

DTIC FILE COPY

(2)

AGARD-CP-421

AGARD-CP-421

AD-A198 664

AGARD

ADVISORY GROUP FOR AEROSPACE RESEARCH & DEVELOPMENT

CONFERENCE PROCEEDING No. 421

AGARD CONFERENCE PROCEEDING No.421

**Advanced Technology for Aero Gas  
Turbine Components**

DTIC  
ELECTE  
DEC 04 1987  
S H D

NORTH ATLANTIC TREATY ORGANIZATION



DISTRIBUTION AND AVAILABILITY  
ON BACK COVER

87 11 21 144

DISTRIBUTION STATEMENT A

Approved for public release;  
Distribution Unlimited

AGARD-CP-421

NORTH ATLANTIC TREATY ORGANIZATION  
ADVISORY GROUP FOR AEROSPACE RESEARCH AND DEVELOPMENT  
(ORGANISATION DU TRAITE DE L'ATLANTIQUE NORD)

AGARD Conference Proceedings No.421  
ADVANCED TECHNOLOGY FOR AERO GAS TURBINE COMPONENTS



Accession For	
NTIS GRA&I	<input checked="checked" type="checkbox"/>
DTIC TAB	<input type="checkbox"/>
Unannounced	<input type="checkbox"/>
Justification	
By	
Distribution/	
Availability Codes	
Dist	Avail and/or Special
A-1	

Papers presented at the Propulsion and Energetics Panel 69th Symposium held in  
Paris, France, 4-8 May 1987.

## THE MISSION OF AGARD

The mission of AGARD is to bring together the leading personalities of the NATO nations in the fields of science and technology relating to aerospace for the following purposes:

- Exchanging of scientific and technical information;
- Continuously stimulating advances in the aerospace sciences relevant to strengthening the common defence posture;
- Improving the co-operation among member nations in aerospace research and development;
- Providing scientific and technical advice and assistance to the Military Committee in the field of aerospace research and development (with particular regard to its military application);
- Rendering scientific and technical assistance, as requested, to other NATO bodies and to member nations in connection with research and development problems in the aerospace field;
- Providing assistance to member nations for the purpose of increasing their scientific and technical potential;
- Recommending effective ways for the member nations to use their research and development capabilities for the common benefit of the NATO community.

The highest authority within AGARD is the National Delegates Board consisting of officially appointed senior representatives from each member nation. The mission of AGARD is carried out through the Panels which are composed of experts appointed by the National Delegates, the Consultant and Exchange Programme and the Aerospace Applications Studies Programme. The results of AGARD work are reported to the member nations and the NATO Authorities through the AGARD series of publications of which this is one.

Participation in AGARD activities is by invitation only and is normally limited to citizens of the NATO nations.

The content of this publication has been reproduced  
directly from material supplied by AGARD or the authors.

Published September 1987

Copyright © AGARD 1987  
All Rights Reserved

ISBN 92-835-0433-X



*Printed by Specialised Printing Services Limited  
40 Chigwell Lane, Loughton, Essex IG10 3TZ*

## RECENT PUBLICATIONS OF THE PROPULSION AND ENERGETICS PANEL

### Conference Proceedings

Testing and Measurement Techniques in Heat Transfer and Combustion  
AGARD Conference Proceedings No.281, 55th A Meeting, May 1980

Centrifugal Compressors, Flow Phenomena and Performance  
AGARD Conference Proceedings No.282, 55th B Meeting, May 1980

Turbine Engine Testing  
AGARD Conference Proceedings No.293, 56th Meeting, Sep/October 1980

Helicopter Propulsion Systems  
AGARD Conference Proceedings No.302, 57th Meeting, May 1981

Ramjets and Ramrockets for Military Applications  
AGARD Conference Proceedings No.307, 58th Meeting, October 1981

Problems in Bearings and Lubrication  
AGARD Conference Proceedings No.323, 59th Meeting, May/June 1982

Engine Handling  
AGARD Conference Proceedings No.324, 60th Meeting, October 1982

Viscous Effects in Turbomachines  
AGARD Conference Proceedings No.351, 61st A Meeting, June 1983

Auxiliary Power Systems  
AGARD Conference Proceedings No.352, 61st B Meeting, May 1983

Combustion Problems in Turbine Engines  
AGARD Conference Proceedings No.353, 62nd Meeting, October 1983

Hazard Studies for Solid Propellant Rocket Motors  
AGARD Conference Proceedings No.367, 63rd A Meeting, May/June 1984

Engine Cyclic Durability by Analysis and Testing  
AGARD Conference Proceedings No.368, 63rd B Meeting, May/June 1984

Gears and Power Transmission Systems for Helicopters and Turboprops  
AGARD Conference Proceedings No.369, 64th Meeting October 1984

Heat Transfer and Cooling in Gas Turbines  
AGARD Conference Proceedings No.390, 65th Meeting, May 1985

Smokeless Propellants  
AGARD Conference Proceedings No.391, 66th A Meeting, September 1985

Interior Ballistics of Guns  
AGARD Conference Proceedings No.392, 66th B Meeting, September 1985

Advanced Instrumentation for Aero Engine Components  
AGARD Conference Proceedings No.399, 67th Meeting, May 1986

Engine Response to Distorted Inflow Conditions  
AGARD Conference Proceedings No.400, 68th A Meeting, September 1986

Transonic and Supersonic Phenomena in Turbomachines  
AGARD Conference Proceedings No.401, 68th B Meeting, September 1986

Advanced Technology for Aero Engine Components  
AGARD Conference Proceedings No.421, 69th Meeting, September 1987



#### **Working Group Reports**

##### **Aircraft Fire Safety**

AGARD Advisory Report 132, Vol.1 and Vol.2. Results of WG11 (September and November 1979)

##### **Turbulent Transport Phenomena (in English and French)**

AGARD Advisory Report 150. Results of WG 09 (February 1980)

##### **Through Flow Calculations in Axial Turbomachines**

AGARD Advisory Report 175. Results of WG 12 (October 1981)

##### **Alternative Jet Engine Fuels**

AGARD Advisory Report 181. Vol.1 and Vol.2. Results of WG 13 (July 1982)

##### **Suitable Averaging Techniques in Non-Uniform Internal Flows**

AGARD Advisory Report 182 (in English and French). Results of WG 14 (June/August 1983)

##### **Producibility and Cost Studies of Aviation Kerosines**

AGARD Advisory Report 227. Results of WG 16 (June 1985)

##### **Performance of Rocket Motors with Metallized Propellants**

AGARD Advisory Report 230. Results of WG 17 (September 1986)

#### **Lecture Series**

##### **Non-Destructive Inspection Methods for Propulsion Systems and Components**

AGARD LS 103 (April 1979)

##### **The Application of Design to Cost and Life Cycle Cost to Aircraft Engines**

AGARD LS 107 (May 1980)

##### **Microcomputer Applications in Power and Propulsion Systems**

AGARD LS 113 (April 1981)

##### **Aircraft Fire Safety**

AGARD LS 123 (June 1982)

##### **Operation and Performance Measurement of Engines in Sea Level Test Facilities**

AGARD LS 132 (April 1984)

##### **Ramjet and Ramrocket Propulsion Systems for Missiles**

AGARD LS 136 (September 1984)

##### **3-D Computation Techniques Applied to Internal Flows in Propulsion Systems**

AGARD LS 140 (June 1985)

##### **Engine Airframe Integration for Rotorcraft**

AGARD LS 148 (June 1986)

##### **Design Methods Used in Solid Rocket Motors**

AGARD LS 150 (April 1987)

#### **Other Publications**

##### **Airbreathing Engine Test Facility Register**

AGARD AG 269 (July 1981)

##### **Rocket Altitude Test Facility Register**

AGARD AG 297 (March 1987)

##### **Manual for Aeroelasticity in Turbomachines**

AGARD AG 298/1 (March 1987)



## THEME

The development of advanced components for new aero gas turbine propulsion systems rests on a wide range of practical and theoretical technologies. The subject was last reviewed at the 32nd PEP Meeting in 1968, and this meeting provided engineers and scientists with an opportunity to discuss recent progress in these technologies and identify requirements for further research.

The scope of the meeting included: compressors, both sub- and supersonic, axial and radial; requirements and objectives for components and component integration in the complete engine; turbines, including cooling effects; combustors and afterburners, including mechanical and materials aspects; advanced propellers, and associated drive systems.

\*\*\*



Le développement de composants avancés de turbo-machines aérobies pour de nouveaux systèmes de propulsion, repose sur un large éventail de techniques théoriques et pratiques. Le PEP a traité ce sujet pour la dernière fois à sa 32ème réunion en 1968. Ce nouveau Symposium a donné aux ingénieurs et aux scientifiques l'occasion de discuter des progrès récents dans ces techniques, et d'identifier les thèmes de futures recherches.

Les exposés et discussions ont porté sur les points suivants: spécifications et objectifs pour les composants, et leur intégration au moteur complet; compresseurs subsoniques, axiaux et radiaux; turbines y compris effets de refroidissement; chambres de combustion et systèmes de réchauffe, avec les aspects mécaniques et matériaux; hélices avancées et leurs systèmes d'entraînement.

#### PROPULSION AND ENERGETICS PANEL

Chairman: Dr W.L. Macmillan  
Project Manager  
EHF Communication Satellite  
Defence Research Establishment  
Ottawa, Ontario K1A 0Z4  
Canada

Deputy Chairman: Ing. Principal de l'Armement P. Ramette  
DRET  
26 Boulevard Victor  
75996 Paris Armées  
France

#### PROGRAMME COMMITTEE

Mr J.F. Chevalier  
SNECMA  
Centre d'Essais de Villaroche  
77550 Moissy-Cramayel, France

Dr G. Maoli  
FIAT s.p.A.  
Via L. Bissolati 57  
00187 Roma, Italy UK

Professor F. Breugelmans  
Von Kármán Institute for Fluid Dynamics  
72 Chaussée de Waterloo  
1640 Rhode Saint Genèse, Belgium

Mr S. Strøm  
A/S Kongsberg Vapenfabrikk  
P.O. Box 25  
3601 Kongsberg, Norway

Professor L. Fottner  
Universität für Strahltriebwerke  
Werner Heisenbergweg 39  
8014 Neubiberg, Germany

Professor A. Üçer  
Middle East Technical University  
ODTÜ  
Makina Muh. Bölümü  
Ankara, Turkey

#### HOST NATION COORDINATOR

Ing. Principal de l'Armement P. Ramette  
DRET, 26 Boulevard Victor, Paris, France

#### PANEL EXECUTIVE

Dr Egbert Riester  
AGARD—NATO  
7 rue Ancelle  
92200 Neuilly sur Seine  
France

#### ACKNOWLEDGEMENT

The Propulsion and Energetics Panel wishes to express its thanks to the National Delegates from France for the invitation to hold this meeting in Paris and for the facilities and personnel which made the meeting possible.

## CONTENTS

	Page
RECENT PUBLICATIONS OF PEP	iii
THEME	v
PROPULSION AND ENERGETICS PANEL	vi
	Reference
<u>SESSION I – REQUIREMENTS AND DESIGN CONSIDERATIONS</u>	
THE COMING REVOLUTION IN TURBINE ENGINE TECHNOLOGY by J.S.Petty and R.E.Henderson	1
OPTIMISATION OF MILITARY COMPRESSORS FOR WEIGHT AND VOLUME by K.R.Garwood	2
AN EXAMINATION OF THE IMPACT OF POTENTIAL ADVANCES IN COMPONENT TECHNOLOGY FOR FUTURE MILITARY ENGINES by M.R.Litchfield and M.G.Philpot	3
SPECIFICATION DU MOTEUR ET DE SES COMPOSANTS A PARTIR DES MISSIONS DE L'AVION par A.Lardellier et J.Dufau	4
APPLICATION OF HIGHLY LOADED SINGLE-STAGE AXIAL-FLOW COMPRESSORS IN SMALL JET ENGINES by R.Mönig, K.D.Broichhausen and H.E.Gallus	5
INTERET DE LA GEOMETRIE VARIABLE POUR LES TURBOMOTEURS DE FAIBLE PUISSANCE par H.Vigneau, R.Rodellar et J.Silet	6
Paper 7 withdrawn	
OPERATION OF GAS TURBINE ENGINES IN DUST-LADEN ENVIRONMENTS by M.G.Dunn, C.Padova and R.M.Adams	8
<u>SESSION II – TURBINES</u>	
A RESEARCH PROGRAM ON THE AERODYNAMICS OF A HIGHLY LOADED TURBINE STAGE by R.G.Williamson, S.H.Moustapha, J.P.Huot and U.Okapuu	9
EXPERIMENTAL EVALUATION OF A TRANSLATING NOZZLE SIDEWALL RADIAL TURBINE by R.J.Roelke and C.Rogo	10
AN INTEGRATED AERO/MECHANICAL PERFORMANCE APPROACH TO HIGH TECHNOLOGY TURBINE DESIGN by J.Hourmouziadis and G.Albrecht	11
DESIGN AND TEST OF A HIGH BLADE SPEED, HIGH WORK CAPACITY TRANSONIC TURBINE by R.C.Kingcombe, J.D.Bryce and N.P.Leversuch	12
ADVANCED TECHNIQUES EMPLOYED IN BLADE COOLING RESEARCH by H.E.Rogers, C.Graham and K.McNicholas	13
THE UNSTEADY GAS FLOW THROUGH STATOR AND ROTOR OF A TURBOMACHINE by K.M.Förster	14
ETUDE ET ESSAIS D'UNE PETITE TURBINE RADIALE POUR GROUPES AUXILIAIRES DE PUISSANCE par Y.Ribaud, C.Fradin et C.Mischel	15

DESIGN AND AERODYNAMIC PERFORMANCE OF A SMALL MIXED FLOW GAS GENERATOR  
TURBINE  
by U.Okapuu

16

SESSION III - COMBUSTION

Paper 17 withdrawn

SIMULATION NUMERIQUE DE L'INTERACTION DIFFUSEUR - TETE DE CHAMBRE  
par D.Jeandel, G.Brun, S.Meunier et M.Desaulty

18

Paper 19 withdrawn

DEVELOPMENT OF A PLENUM CHAMBER BURNER SYSTEM FOR AN ADVANCED VTOL  
ENGINE  
by J.S.Lewis, T.W.Murray and D.Steele

20

PUMPING SYSTEMS AND FLOW INTERFACES FOR RAPID RESPONSE ELECTRONIC  
REHEAT CONTROLS  
by T.C.Yates and T.S.Smith

21

SESSION IV - HIGH SPEED PROPELLERS

AERODYNAMIC PERFORMANCE OF A SCALE-MODEL, COUNTER-ROTATING UNDUCTED FAN  
by T.J.Sullivan

22

GEAR SYSTEMS FOR ADVANCED TURBOPROPS  
by D.A.Wagner

23

NUMERICAL METHODS FOR PROPELLER AERODYNAMICS AND ACOUSTICS AT DFVLR  
by N.Kroll, D.Lohmann and J.Schöne

24

ETUDE DE L'AERODYNAMIQUE DES HELICES POUR AVIONS RAPIDES  
par J.M.Bousquet

25

ANALYSIS OF POSSIBLE TRANSMISSION ARRANGEMENTS APPLICABLE FOR DRIVING  
SINGLE OR TWIN COUNTER-ROTATING FANS ON PROPFAN ENGINES  
by L.Battezzato and S.Turra

26

SESSION V - COMPRESSORS

TRANSONIC BLADE DESIGN ON ROTATIONAL STREAM SURFACES  
by F.Klimetzek and E.Schmidt

27

INVESTIGATION OF DIHEDRAL EFFECTS IN COMPRESSOR CASCADES  
by F.A.E.Breugelmans

28

Paper 29 withdrawn

ETUDE PHENOMENOLOGIQUE DU FLOTTEMENT DE BLOCAGE SUR LA BASE DES  
RESULTATS D'UNE THEORIE LINEARISEE  
par P.Ferrand

30

POSSIBILITIES FOR ON-LINE SURGE SUPPRESSION BY FAST GUIDE VANE ADJUSTMENT  
IN AXIAL COMPRESSORS  
by W.Rieß and U.Blöcker

31

RADIAL COMPRESSOR DESIGN USING AN EULER SOLVER  
by J.T.Bildal and A.Wilson

32

Paper 33 withdrawn

SECONDARY FLOW MEASUREMENTS WITH L2F-TECHNIQUE IN CENTRIFUGAL  
COMPRESSORS  
by H.Krain

34

	Reference
<b>METHODE DE PREVISION DES LIMITES DE FONCTIONNEMENT EN DEBIT DES COMPRESSEURS CENTRIFUGES</b> par H.Miton, G.Senatore et J.Chauvin	35
<b>DESIGN AND DEVELOPMENT OF AN ADVANCED F100 COMPRESSOR</b> by C.M.Love	36
<b>Paper 37 Withdrawn</b>	
<b>CONCEPTION ET ESSAIS D'UN ETAGE DE TETE D'UN COMPRESSEUR HP AVANCE</b> par M.Goutines et H.Navière	38
<b>EXPERIMENTAL INVESTIGATION OF A SUPERCRITICAL COMPRESSOR ROTOR BLADE SECTION</b> by R.Fuchs, R.Kaymaz, H.Starken and W.Steinert	39
<b>CALCUL DES ECOULEMENTS SECONDAIRES DANS UN COMPRESSEUR AXIAL MULTIETAGE</b> par F.Falchetti et J.Brochet	40

# THE COMING REVOLUTION IN TURBINE ENGINE TECHNOLOGY

by

James S. Petty & Robert E. Henderson  
Turbine Engine Division

Air Force Wright Aeronautical Laboratories (AFWAL/POT)  
Wright-Patterson Air Force Base, Ohio USA 45433

## SUMMARY

A major change in turbopropulsion technology development philosophy is now being pursued by the US Air Force Wright Aeronautical Laboratories (AFWAL) which will provide revolutionary advancements in overall operational performance capability for future military aircraft and aerospace weapons systems. An historical perspective illustrates the significance of the advancements being pursued, with engine thrust-to-weight used as the principal performance figure-of-merit. The High Performance Turbine Engine Technologies (HPTET) effort, an initiative begun in 1982, is discussed. The overall goal of the HPTET effort is to provide the advanced materials, innovative structural concepts and advanced aerothermodynamics to double turbopropulsion capability by the year 2000. This is being accomplished through an aggressive, highly integrated technology development effort. The Aero Propulsion and Materials Laboratories within AFWAL are partners in this effort.

## INTRODUCTION

Today, a synergistic convergence of new technologies across the materials and turbopropulsion communities is beginning to occur. Encouraging developments in turbomachinery aerothermodynamics, lightweight high temperature materials, and new innovative engine structural concepts are pointing the way toward a radical departure from the way turbine engines have been designed and built in the past. The situation is rather similar to that of the late 1930s and early 1940s when a major jump in aircraft propulsion capability occurred because of the development of a new type of engine -- the turbine engine -- both in England by Sir Frank Whittle and in Germany by Dr Hans von Ohain. The revolution starting today is not the result of a new engine cycle, but rather the result of the convergence of new developments in aerothermodynamics, materials and structures. The result will be no less dramatic, however.

To accelerate the development and application of these new emerging technologies, and to maximize their early payoff, the Aero Propulsion and Materials Laboratories within the Air Force Wright Aeronautical Laboratories (AFWAL) organization have joined together in a new initiative entitled "High Performance Turbine Engine Technologies" (HPTET). The objective of this initiative is to develop the critical technologies required to double turbopropulsion capability by the year 2000 for a broad range of future Air Force systems. To accomplish this, it was also necessary to develop a new integrated approach to the development and demonstration/assessment of new emerging technologies.

The HPTET initiative began in 1982 as an advanced technology development study in the Aero Propulsion Laboratory. With the realization that advanced materials development was a pacing item, the AFWAL Materials Laboratory joined the initiative as a partner in 1984. In 1985, six U.S. turbine engine companies (Allison Gas Turbine Division, Garrett Turbine Engine Company, General Electric, Pratt & Whitney, Teledyne CAE, and Williams International) joined with the Air Force in developing corporate long range plans to accomplish the ambitious goal of the HPTET initiative by the turn of the century. These companies have also made substantial commitments of company resources to their long range plans.

To appreciate the level of technical advancement being pursued under the HPTET initiative, one must put things in proper perspective. A commonly used figure-of-merit for describing advancements in turbopropulsion operational capability and performance is engine thrust-to-weight (T/W) ratio. This is of particular significance when dealing with high performance, air superiority aircraft where maximum T/W capability is of the utmost importance. Hence, when one speaks of doubling propulsion capability, in terms of T/W this represents a 2X advancement over that provided by contemporary turbine engines. However, doubling T/W does not come easy and, relative to today's fighter engines, will require a number of dramatic, if not revolutionary, changes in engine design as we know it today. This is not to say that the engine of tomorrow will be a totally different design concept from the turbine engine of today. It will still utilize rotating machinery and will still contain the same basic core components -- compressor, combustor and turbine. A number of technological barriers will be broken, however, in internal aerodynamics, materials, structural design and operating temperatures. This, in conjunction with the technology availability target date of the year 2000, makes the engine of tomorrow truly a revolutionary leap beyond what we can provide with today's technology. The overall goal of the HPTET initiative is to provide in the next 12-15 years the same degree of technological advancement that took the past 30-40 years to accomplish.

The following paragraphs will endeavor to place the HPTET initiative in historical perspective, describe the HPTET technical/management approach, discuss some of the promising candidate technologies and present some of the potential payoffs to future Air

## Force systems.

AN HISTORICAL PERSPECTIVE

To better appreciate the extent of advancement being pursued under the HPTET initiative, a brief look at how far the turbine engine has come over the past 40 years is in order. As a basic for comparison, engine thrust-to-weight will be used as the performance figure-of-merit. Figure 1 shows an historical evolution of the turbine engine in terms of T/W dating back to the first operational jet engine -- the German Junkers Jumo 004B. Although this illustration is complex, it highlights advancements made in terms of propulsion system specific thrust (engine thrust per unit airflow through the engine) and specific weight (engine weight per unit airflow through the engine), the ratio of which provides lines of constant thrust-to-weight. From this illustration, one can derive a trend of propulsion system advancements realized over the past 30-40 years.

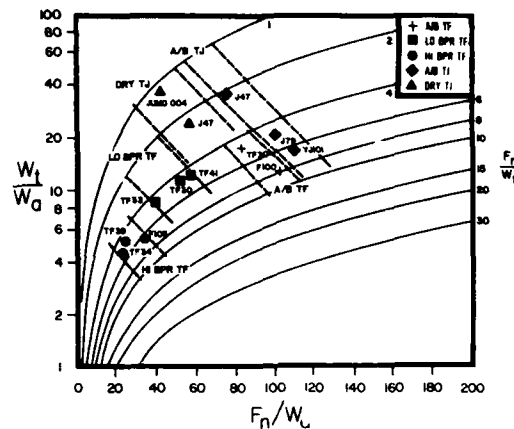


Figure 1. Turbine Engine Thrust/Weight History

Although many engines are represented in Figure 1, only two will be briefly examined to provide historical perspective. In the early 1940s, Germany introduced the first operational jet engine, the Junkers Jumo 004B. Truly a revolutionary advancement in propulsion capability over the high performance aircraft piston engines of the time, the 004B represents the beginning of the jet age as we know it today. The T/W ratio of the 004B was only 1.25, but it provided the twin-engine Messerschmitt Me262 aircraft with a maximum air speed of 540 miles/hour in level flight -- a formidable threat to the Allied air forces during the War. The 004B was a relatively heavy engine with a turbine inlet temperature of only 1300°F (700°C). This operating temperature is of particular significance when one notes that our most modern engines today utilize hot section cooling air with temperatures approaching 1300°F. Still there was no doubt that in the 1940's, this German jet engine represented a huge leap in propulsion system operational and performance capability and a major departure from conventional aircraft engine design philosophy. Figure 2 is a photograph of the Jumo 004B, a design not significantly different from today's jet engines -- an axial compressor and turbine, and a multi-can combustor, the principal core components of any jet engine. Again, it became operational with the Me262 shown in Figure 3, a twin-engine aircraft which first flew in July 1942 and entered service in July 1944, principally against Allied bomber formations. Although a very lethal weapon system in its day, the Me262/004B combination had poor reliability and range -- many aircraft were lost due to engine mechanical problems and high fuel consumption. Those successfully returning from a mission often required partial, if not complete engine overhaul. But, again, the 004B did represent a major advancement in overall aircraft engine capability and initiated a new era in terms of aircraft propulsion.



Figure 2. Junkers Jumo 004B



Figure 3. Messerschmitt Me262

Referring back to Figure 1, one will also note an engine introduced approximately thirty years after the 004B, the F100. The F100 represents a very significant advancement in propulsion capability relative to the 004B; not only does it exhibit a T/W capability 6 times that of the 004B, it also advanced aircraft operational capability



into a whole new flight regime -- the ability to climb vertically and accelerate at the same time. Through advancements in materials, permitting higher temperature and lighter weight structural design, the F100 is the fleet leading fighter engine in the U.S. arsenal today. Operating at turbine inlet temperatures greater than 2500°F (1370°C) and with full afterburning, this low bypass, augmented turbofan engine produces nearly 25,000 pounds of thrust with an installed T/W ratio of nearly 7.4. Figure 4 shows a cross-sectional view of the F100. To some extent it is similar to the 004B. It has a multi-stage axial compression system (turbofan configuration), an annular combustion system and a multi-stage axial turbine, the first stage of which is air-cooled. The F100 is also equipped with a large multi-zone afterburner and an axisymmetric convergent-divergent variable-geometry exhaust nozzle. It is used in two military-only applications by the U.S. today, the F-15, a twin-engine aircraft, and the F-16, a single engine aircraft (Figure 5).

The next generation air superiority aircraft currently undergoing prototype development is the Advanced Tactical Fighter (ATF). Although not shown in Figure 1, the engines for this aircraft will be substantially more advanced than the F100, having higher operating temperatures and higher T/W capability, but perhaps more importantly, allowing the ATF to cruise supersonically without afterburning. Figure 6 is a photograph of a mock-up of one of the ATF demonstrator engines, the Pratt & Whitney XF119. (General Electric also has an ATF demonstrator engine, the XF120, under development.) Externally, the XF119 may appear similar in configuration to the F100, at least forward of the exhaust nozzle. Internally, however, a number of differences exist, including incorporation of advance high temperature materials, structural design changes, substantially reduced parts count, and much higher operating temperature capability. One very visible and significant difference, of course, is the addition of a two-dimensional convergent-divergent exhaust nozzle with both thrust vectoring and thrust reversing capability. Another significant, but less obvious, change to this engine is the incorporation of a full-authority digital electronic control system, without which the many variable features required of this engine would not be possible.

With this brief historical review, one could conclude, as shown by the bold arrow of Figure 7, that propulsion system advancements have nearly reached their limit in terms of further improvements in T/W capability. In fact, there are some today who feel turbine engine propulsion is a "sunset" technology that has reached its improvement plateau, the further advancement of which simply would not show a worthwhile return for the research dollar invested. This could not, however, be further from the truth. The balance of this paper will focus on

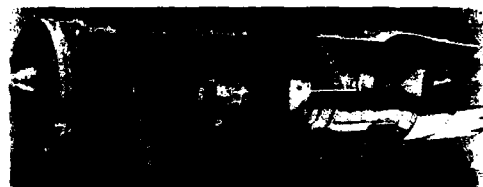


Figure 4. Pratt &amp; Whitney F100 Turbofan Engine

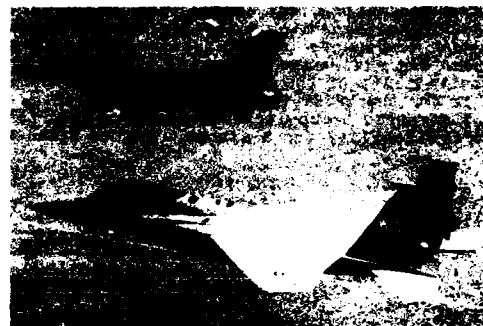


Figure 5. F-15 and F-16 - Modern USAF Fighters

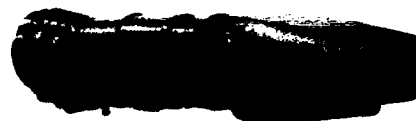


Figure 6. Pratt &amp; Whitney XF119 ATF Engine Demonstrator Mockup

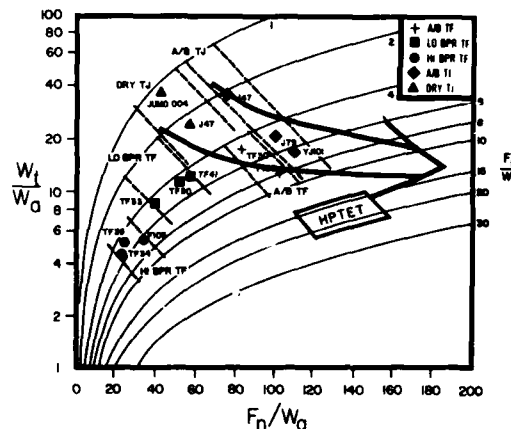


Figure 7. Future Thrust/Weight Trend and the HPTET Initiative

the HPTET initiative and those technology developments currently underway or in planning which will assure a revolutionary advancement in propulsion system capability by the turn-of-the-century. The gridded box of Figure 7 represents that region in terms of T/W for which HPTET is currently focused, drawing upon the most advanced three-dimensional aerodynamic design systems, new high temperature composite and fiber-reinforced metal matrix and ceramic materials, and structural design innovations not heretofore considered for turbomachinery applications. Like the introduction of the 004B engine in 1940, the HPTET initiative also represents a new era in propulsion system design and performance capability, an era which will far surpass engine operational capability today or in the near future.

#### TECHNOLOGY FLOW IN THE HPTET INITIATIVE

Although the development of advanced technology is the most visible part of the HPTET initiative, the integration of the flow of advanced technology from the technology base in aerodynamics, materials and structures, through its use in the design of advanced engine components, to the assessment/verification of those technologies in real engine operating environments is also a key part of ensuring the maximum and most rapid availability of the new technologies at the most reasonable cost. The Air Force is doing this for the HPTET initiative by integrating its turbopropulsion exploratory development and advanced technology demonstrator programs to provide a clear path from the laboratory to availability for a system. Figure 8 shows this integration schematically. At

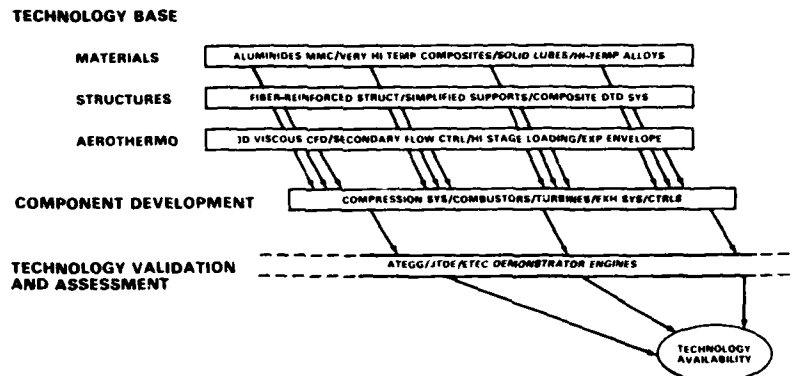


Figure 8. Technology Flow in the HPTET Initiative

appropriate points in time, the best applicable technologies are integrated in the design of advanced turbine engine components, which in turn are integrated into advanced technology demonstrator engines. These demonstrators, which include the Advanced Turbine Engine Gas Generators (ATEGG), Joint Technology Demonstrator Engines (JTDE), and Expendable Turbine Engine Concepts (ETEC), are then tested under realistic operating conditions to verify the component technologies and to assess the interactions of these components in a realistic engine environment. The close integration between these three levels -- tech base, component design, and engine demonstration -- requires that the engineers at each level remain constantly aware of the relationship of their activity to the whole. The result of doing this will provide a much more rapid transition of technology from the lab to the field.

#### THE REVOLUTIONARY NEW TECHNOLOGIES

To the engineer, the most exciting part of the HPTET initiative is the pursuit of new, and in some cases radically different, technologies for use in future turbine engines. A large number of potentially attractive new developments are emerging in materials and aerothermodynamics, which in turn are leading to innovative new structural concepts. The synergism resulting from the combinations of these developments, and a new freedom being given to the design engineer to think in new ways, are leading to the potential for a major increase in turbomachinery capability. A number of these emerging developments will be highlighted in the next few paragraphs.

##### Advanced Aerothermodynamics

Advances in aerothermodynamic design capability are required, not only to maximize the specific thrust of future engines, but also to reduce weight by reducing the number of rotating stages in the compressor and turbine, making the combustor and exhaust nozzle more compact, and eliminating the afterburner where possible. The following paragraphs describe some of the areas needing development and the potential payoffs offered.

o **3-D Viscous Aerothermodynamic Models:** The development of accurate 3-D computational fluid dynamic (CFD) codes for turbomachinery has led to a surge of

aerodynamic design advances in the past few years. Figure 9 is a photograph of an advanced low pressure turbine vane designed by Pratt & Whitney using a 3-D code and tested in an advanced demonstrator engine. Present codes are for inviscid flows, but are moving toward the incorporation of viscous flow modeling capability. Accurate and efficient CFD codes are needed to enable the design engineers to maximize component efficiency while minimizing weight and parts count.

o **Advanced Compact Compression Systems:** A major advance in compression system aerodynamic design occurred in the early 1970s with the development of high through-flow technology by Dr Arthur Wennerstrom of AFVAL's Aero Propulsion Laboratory. The continuing development of this technology, combined with new concepts such as swept airfoils and the use of advanced CFD tools, is leading to very compact compression systems which produce in only a few stages the same pressure ratios which required over a dozen stages a few years ago -- and without any efficiency degradation. Figure 10 is a photograph of a swept-blade compressor stage presently undergoing evaluation in Dr Wennerstrom's facility. Additional development is required to make these compressors even more compact and lightweight. Other compressor concepts, including centrifugal and mixed-flow compressors, also need to be further developed for small engine applications.

o **Near-Stoichiometric Combustors:** To maximize specific core power (gas generator exhaust gas power per unit air flow rate), and to eliminate the need for afterburning (reheat) in some applications, the combustor exit gases need to approach stoichiometric combustion temperature. This requires that nearly all of the air entering the combustor be used in combustion, leaving very little for liner cooling and exit temperature pattern factor (a measure of combustor exit temperature uniformity) tailoring. In addition, the combustion process must be carefully managed to eliminate fuel-rich areas which could produce visible smoke in the engine exhaust. The combustor must also be capable of stable operation at very low fuel-air ratios for engine idle and deceleration. Finally, to minimize weight the combustion system must be as compact as possible. All of this requires considerable advancement in combustor modeling and design, and may involve innovative concepts such as staged combustion and variable geometry.

o **Enhanced Cooling Techniques:** It will probably not be possible to eliminate all cooling air requirements for the turbines of future engines, even with the application of very high temperature non-metallic composites, such as carbon-carbon. For example, the need to cope with stoichiometric temperature hot streaks from the combustor will require that the turbine nozzle vanes be cooled as efficiently as possible. Present materials and cooling techniques would require excessive cooling air, which could seriously degrade performance and efficiency. Improved cooling techniques are needed for both non-metallic materials and for advanced metal alloys.

o **Short, High Pressure Ratio, Multi-Function Exhaust Nozzles:** As the engine specific thrust increases, so does the exhaust nozzle pressure ratio. This is true for fighter engines and, especially, for engines for high Mach number applications. As a result, the nozzle will tend to become larger and heavier. Additionally, future exhaust nozzle requirements may include thrust reversing, and pitch and yaw thrust vectoring. New concepts need to be developed for exhaust nozzle aerodynamic and mechanical design to minimize weight and size, and for the high Mach number applications, to integrate the exhaust nozzle into the airframe as efficiently as possible.

#### Advanced Materials

The key to the successful achievement of the HPTET initiative goal of doubling capability is the development and application of new, advanced materials not previously available for use in turbine engines. Some of these new materials are listed in Table I. They range from very high temperature composites to new high temperature aluminum alloys, and also include non-structural materials such as lubricants. Each of these materials offers the possibility of a major improvement in a number of critical design areas

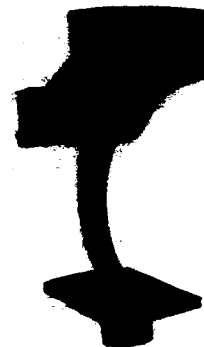


Figure 9. 3-D Low Pressure Turbine Vane Design

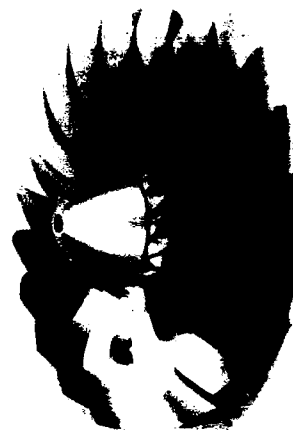


Figure 10. Advanced Fan Design with Swept Blades

throughout the engine, such as use temperature or specific strength (strength/density).

TABLE I. HPTET MATERIALS REQUIREMENTS

ENGINE COMPONENT	STATE-OF-THE-ART MATERIALS	HPTET MATERIALS REQUIREMENTS	CANDIDATE MATERIALS
COLD SECTION (Fan/Compressor)	Titanium (to 800°F) (425°C) Nickel (to 1200°F) (650°C)	2-3X Specific Strength 1200-1800°F 650- 980°C	Ti Aluminide Compos. Ti Composites Glass Composites Hi-Temperature Al
HOT SECTION (Combustor/Turbine Augmentor/Nozzle)	Nickel (to 1900°F) (1040°C) Cobalt	3-5X Specific Strength 2700°F with Adv Cooling 1480°C 3000-4000°F Uncooled 1650-2200°C	Ceramic/C-C Composite Adv Aluminide Compos. Refractory Metals
NON-STRUCTURAL (Bearings/Lubes)	350°F Liquid Lubes 175°C Metal Bearings	up to 1500°F 815°C	Solid Lubes to 1500°F Liquid Lubes to 800°F Ceramic Bearings

o Carbon-Carbon Composites: Carbon-carbon composites are some of the highest payoff, highest risk materials presently under development. Their potential for very high use temperature -- up to 4000°F (2200°C) -- and high specific strength make them well worth pursuing. Carbon-carbon composites have been available for a number of years, and are presently in widespread use in aircraft brakes, and as major heat-shield components in the Space Transport Systems -- the Space Shuttles. The major problem which prevents their use in turbine engines at present is the difficulty in providing oxidation protection for the thousands of operational hours required of man-rated engines. Progress has been made in improving oxidation resistance by "inhibiting" the carbon matrix and by providing improved surface protection. Unfortunately, most of these schemes seriously degrade the strength of the composite, rendering it less attractive for structural uses. Much more research remains to be done to provide thinner, more effective coatings, extending possibly to the protection of the individual fibers. Because of their potential, research on carbon-carbon composites is undergoing aggressive development in many countries.

o Ceramic-Matrix Composites (CMC): The technology of high temperature ceramics has advanced considerably in the past decade. Modern ceramics are far tougher than earlier ceramics, and much less prone to fracture due to thermal shock or mechanical loads. However, their brittle failure mode does not make them particularly attractive for use in man-rated engines, where a much more "graceful" failure mode is desirable. Properly designed, ceramic-matrix composites have the high specific strength of ceramic fibers, the high temperature capability of ceramics and a more graceful failure characteristic. Presently, ceramic-matrix composites are limited to temperatures less than approximately 2500°F (1400°C), due to limitations of the available fibers and matrix materials. France and Japan are currently leaders in CMC technology, although research is underway in many countries. Figure 11 is a photograph of an experimental CMC turbine for a small missile engine. It was produced by Societe Europeenne de Propulsion (SEP) of France and is presently undergoing test evaluation in the United States. Under the HPTET initiative, research is underway or planned to identify and develop new ceramic matrix and fiber systems with temperature capabilities in the 3000-4000°F (1650-2200°C) range.

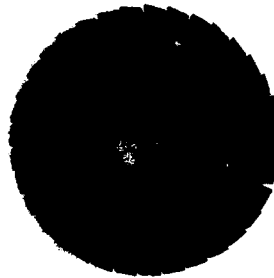


Figure 11. Small Turbine Rotor of Ceramic-Matrix Composite

o Metal-Matrix Composites (MMC): Metal-matrix composites, consisting of high strength ceramic fibers imbedded in a high specific strength metal matrix, are presently being fabricated into engine components for testing. The use of MMC will produce major weight reductions in both static and rotating engine structures because of their high specific strength and high stiffness. A particularly attractive combination for the near future consists of silicon carbide fibers in a titanium aluminide matrix, which will provide high specific strength with a use temperature of up to 1800°F (980°C). Work is underway on this and other MMC systems to identify compatible component materials and to develop fabrication techniques.

o High Temperature Alloys: These include metal alloys, made stronger, lighter and with higher temperature capability. Rapid solidification-rate powder metallurgy offers the possibility of developing new alloy combinations, not producible normally, tailored for greatly increased strength, toughness, oxidation resistance and temperature capability, or desired combinations of these. Research is planned or presently underway to provide useful 900°F (480°C) aluminum, 1800°F (980°C) titanium and 2700°F (1480°C)

columbium (niobium) alloys by the late 1990s, or earlier. If successfully developed, the high temperature aluminum alloy may displace much of the titanium presently used in engines, and the high temperature titanium much of the nickel -- in each case with a significant reduction in weight.

o **Aluminides:** Intermetallic compounds containing aluminum show great promise for increasing oxidation resistance and use temperature of titanium and nickel. Alpha<sub>2</sub> titanium aluminide (Ti<sub>3</sub>Al) parts are presently undergoing evaluation in demonstrator engines in the United States, and gamma titanium aluminide (TiAl) parts will be evaluated in the near future. TiAl is particularly attractive, not only because of its lower density, but because it does not burn -- a problem with titanium alloys at present. Unfortunately, it has very low ductility at room temperature and is extremely difficult to fabricate. New techniques, such as powder metallurgy, are providing considerable progress toward the future use of this material, which could replace nickel alloys throughout much of the engine -- at half the weight. Further in the future, nickel aluminides may extend the use temperature of nickel to near 2200°F (1200°C). However, much work remains to be done to determine alloy constituents and processing methods.

o **Non-Structural Materials:** Non-structural materials include bearings and lubricants. At present, turbine engine lubricants are generally limited to about 350°F (175°C). This low use temperature often requires air-oil or fuel-oil heat exchangers in current engines. At high Mach numbers, where the inlet air temperature may be beyond 800°F (425°C) and the fuel is in demand as a heat sink for airframe, cockpit and electronics, very high temperature lubricants and bearings are a requirement. Work is presently being undertaken to develop liquid lubricants usable to 600°F (315°C), and solid lubricants usable to 1500°F (815°C). Current turbine engine bearings are of steel alloys, but these are not suitable for the high temperatures contemplated in future engines. Ceramic bearings are under development for high temperature use -- a ceramic bearing has been operated for nearly 100 hours at 1200 °F (650°C) with a solid lubricant. This technology is being pursued, not only for limited-life engines, but for long-life man-rated engines of the future.

#### Structural Innovation

The new materials discussed above must be applied intelligently to engine structures to realize their full potential. In many cases, particularly for the composite materials, simple materials substitution into existing structural designs or concepts is ineffective. It is necessary to rethink the way engines are designed -- to invent new innovative structural concepts that take advantage of the strengths of the new materials while avoiding their weaknesses. For example, fiber-reinforced composite materials generally have great strength in tension along the fibers, but much less strength in compression and in shear across the fibers. Some of the structural concepts being considered are discussed below.

o **Hollow Fan and Compressor Blades:** Substantial weight savings can be realized by using hollow blade designs in the fan and the first stages of the compressor. The large, low aspect ratio blades resulting from high through-flow aerodynamics, the development of high specific strength metal-matrix composite materials, and the development of new manufacturing methods such as super plastic forming/diffusion bonding (SPF/DB) are making possible the development of lightweight, hollow blades without sacrificing necessary ruggedness or aeroelastic rigidity.

o **Integrally Bladed Rotors:** A significant part of the weight of a rotor with inserted blades is in the material used for the blade attachment region and the additional disk material required to withstand the centrifugal pull of the attachment. Integrally bladed rotors (IBRs or "blisks") offer a substantial rotor weight saving by eliminating the additional material required in the blade, rim and disk to handle the attachment loads. Figure 12 shows the potential for weight saving by using blisk technology in an advanced compressor rotor design. Blisks have not been attractive in the past because of the lack of repair techniques for damaged blades. However, the recent development of such repair techniques, and the weight reduction potential of blisks are making them increasingly attractive for use in large engines. Blisk compressors for large engines have been tested in the Air Force's Advanced Turbine Gas Generator (ATEGG) and the Air Force/Navy Joint Technology Demonstrator Engine (JTDE) programs.

o **Diskless Rotors:** The very high specific strengths in tension of the new composite materials make it possible to replace the disks in conventional rotor designs with fiber-reinforced rings. This leads

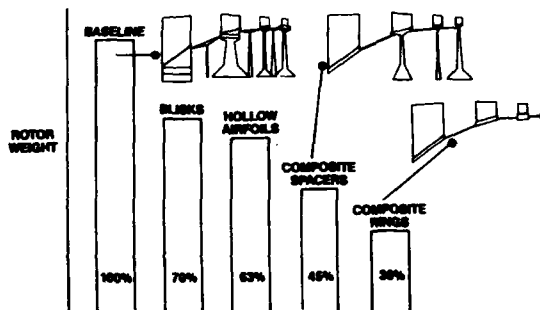


Figure 12. Effect of Structural Innovation on Compressor Rotor Weight

to substantial weight reductions, particularly for high through-flow systems which require high rotor rim speed. Returning to Figure 12, the payoff from the use of metal-matrix composite ring structures in an advanced compressor rotor, when coupled with integral blading, is a weight reduction of as much as 75%. Similarly, new turbine structural designs now being studied offer weight savings of over 50% in the turbine rotor.

o Rotor Support Structures: The very high structural stiffness attainable through the use of fiber-reinforced composite materials offers the possibility of lighter and simpler rotor support structures. One of the more interesting possibilities presently under investigation is the "pedestal" support. In this concept, the rotor is overhung on a single support structure which is integral with the engine case. Other equally innovative concepts are under study. The potential weight savings and simplification of the engine structure should be considerable.

o Static Structures: Again, the very high strength and potential structural stiffness of advanced composite materials offers possibilities for the simplification of the engine static structural design. Contemporary U.S. turbofan engine designs typically have three main frames and five bearing compartments. Advanced structural design approaches will attempt to eliminate at least one main frame and one bearing compartment. In addition, current U.S. design practice is generally to use different components for managing aerodynamic and mechanical loads, and to use redundant load paths for reliability and safety. In the future, aerodynamic structures will also carry mechanical loads; for example, the compressor exit guide vanes in the combustor diffuser may carry the rotor loads from a pedestal support. In addition, the level of load path redundancy must be reduced as much as is practical, ideally to the point at which the cost in additional weight is negligible.

o Controls/Accessories: The engine controls and accessories, including the engine gearbox and power take-off, account for approximately 20% of the weight of the F100 fighter engine. As the weight of the rest of the engine is reduced using the innovations described above, the controls and accessories weight will become more important unless similar innovative measures are taken for them. Some of the possibilities under investigation include: High temperature electronic engine controls with reduced cooling requirements; Cases, actuators and pumps of composite materials; Electric actuation, and; Elimination of the power take-off shaft and gearbox through the use of buried accessories.

Lastly, some rather unique concepts are being studied for specialized engine applications. One of these is the use of endothermic fuels for high Mach weapon system applications. An endothermic fuel is one which can be dissociated, or "cracked", in the presence of heat and a catalyst into higher energy components, such as hydrogen and toluene, absorbing considerable energy in the process. Such fuels lie midway between conventional hydrocarbon fuels and cryogenic fuels, such as liquid hydrogen or methane. Endothermic fuels possess densities comparable to conventional fuels, but offer substantially higher heat capacity and energy density, making them particularly suitable for regeneratively cooling engine and airframe structures.

In addition to the developments in aerothermodynamics, materials and structures, the overall engine design and its thermodynamic cycle also need to be viewed in an innovative manner. For example, by placing the last stage of the fan on the high pressure compressor rotor ("core-driven fan stage") to reduce the low pressure turbine work required, it may be possible to eliminate the vanes between the high and low pressure turbine stages, with an attendant saving in weight and complexity.

#### DURABILITY/REPAIRABILITY/MAINTAINABILITY

Although the goal of the HPTET initiative is to double propulsion capability, the lessons of the past must not be forgotten -- high performance cannot be secured at the expense of the "ilities": durability, repairability, maintainability, etc. The desire for higher performance and lower engine weight will result in simpler engines, in many cases, with fewer parts. Some preliminary design studies indicate that it should be possible to make these future engines very easy to disassemble for maintenance. However, many of the engine components will be made of the new materials described above, especially the composites, with which there is little or no inspection or repair experience. As a result, it will be necessary to develop non-destructive inspection and repair techniques for these materials before they can be used effectively in operational engine applications. The present Air Force Engine Structural Integrity Program (ENSIP) was developed for engines with critical components made of monolithic metals. The extension of ENSIP principles to include brittle and composite materials remains to be done.

#### THE COST

As one might expect, the total cost of accomplishing the goal of doubling turbopropulsion capability will be high. A combined Government/industry estimate for a full technology-limited program places the cost at approximately \$5000 million over the next 14 years. Although seemingly high, it represents only a modest increase (approximately 20%) to the cost of a more evolutionary technology development process which would result in far less capability advancement by the turn-of-the-century. Regardless of resource availability, however, the HPTET initiative has led to a new research and development approach. Should the additional research funding not be

forthcoming, either the broad scope of effort would be reduced or some relaxation of the HPTET goal relative to its demonstration by the year 2000 would be necessary.

#### THE PAYOFF

The potential payoffs of the HPTET initiative in terms of increased weapons systems capability are substantial. Figure 13 is an example of the potential payoff for an advanced engine technology applied to a future tactical fighter with supersonic cruise capability. With an aggressive evolutionary engine technology development approach, this fighter will be 45% lower in take-off gross weight than permitted by current technology. With the revolutionary HPTET approach, this fighter can also be given V/STOL (vertical/short take-off and landing) capability with no mission penalty. Other examples of potential payoff include: An F-15 size interceptor aircraft capable of cruising beyond Mach 3 for a radius of over 1000 miles; A new high Mach propulsion system capable of operating beyond Mach 4, but also possessing a subsonic specific fuel consumption lower than today's fighter engines; Expendable engines providing twice the range of contemporary systems for a variety of strategic and tactical missiles.

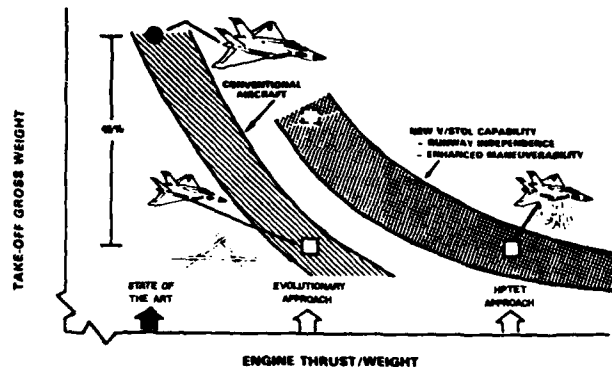


Figure 13. HPTET Payoff for a Future Tactical Fighter Design

There are, of course, also substantial payoffs for the commercial side of the turbine engine business: High bypass turbofan and propfan engines with very high overall pressure ratios will be able to operate at very high turbine inlet temperatures with little or no cooling air required for the engine hot section. This could substantially reduce specific fuel consumption and, hence, operating costs. In addition, engine parts count will be reduced, and many of the remaining parts will be simplified, reducing both cost and weight.

These are just a few examples of the potential payoff of the HPTET initiative. In fact, there will probably be no part of the U.S. turbopropulsion community which will not feel the impact and benefits. Almost all types of systems presently using turbomachinery will be affected, and many systems not presently using turbomachinery will find it to be an attractive propulsion system alternative.

#### CONCLUSIONS

The HPTET initiative is an appropriate undertaking to begin at this time because of the promise offered by a number of new and emerging technologies, and the attendant potential payoff to future Air Force systems.

Planning for this initiative began in 1982, and today over \$40 million in exploratory development contracts are underway. The AFWAL Aero Propulsion and Materials Laboratories have committed their resources to HPTET, and they have been joined in this commitment by the U.S. turbine engine industry.

Recently, at the urging of the Deputy Undersecretary of Defense for Research and Advanced Technology (DUSDRE/R&AT), the other Services (Army and Navy), Defense Advanced Research Projects Agency (DARPA), and NASA have joined with the Air Force in developing a coordinated long range plan embracing the goal of the HPTET initiative. The resulting Integrated HPTET (IHPTET) plan will be a joint DoD/NASA initiative involving the principal US Government organizations and industry involved in aircraft and missile turbine engine development. It will guide nearly all U. S. military turbine engine exploratory and advanced technology development through the next decade.

## DISCUSSION

**H.J.Lichtfuss, Ge**

You have mentioned a SFC reduction of 30% to 40% for the HPTET engine. This is more than for the Prop Fan engines. Can you please explain how you will get this? Or is it mainly the result of non using the afterburner at supersonic speeds?

**Author's Reply**

The goal of 30—50% reduction in SFC under the HPTET initiative relates principally to supersonic, air superiority propulsion systems, currently equipped with reheat systems. To achieve this SFC improvement, dry engine specific thrust will be improved to the point where the system may be eliminated. This alone should provide 30—40% improvement in SFC; the balance would be achieved through component performance improvements.

**A.Habard, Fr**

What overall pressure ratio(s) do you expect allowed by new materials?

**Author's Reply**

A number of emerging new materials will permit future compressors to operate at higher temperature; however, the HPTET program is not focused on any specific engine cycle requiring certain overall pressure ratios. For example, emerging nickel and titanium aluminide materials offer the potential for higher operating pressures and temperatures in the compression system. Hence, these materials could be applicable to the needs of high pressure ratio, high bypass subsonic systems as well as some low pressure ratio (but high temperature) high Mach turbojet compression systems.

**R.Fletcher, UK**

In your paper, you identify main activities, by which you will achieve very significant improvements in engine performance, namely improved aerodynamics, the use of new materials and innovative design. Is it possible for you to quantify the relative importance of each in achieving your objectives?

**Author's Reply**

There is no doubt that materials coupled with structural design innovation are prime drivers in the HPT technology development initiative. However, this is not to the exclusion of advanced aerodynamics. The key to successfully achieving the goals of HPTET rests in the component designer's ability to effectively marry 3D aerodynamics with the new emerging high strength-to-weight materials. For example, we must be able to accommodate the advancements in 3D, swept leading edge, long-chord airfoil shapes and the new integral blade-and-ring structural design approach using fibre-reinforced metal-matrix composite materials.



## OPTIMISATION OF MILITARY COMPRESSORS FOR WEIGHT AND VOLUME

### AUTHOR

K R GARWOOD  
Chief Design Engineer  
Lift Engines and Future Technology Demonstrators

ROLLS-ROYCE plc  
PO Box 3, Filton, Bristol  
BS12 7QE  
Tel: 0272 791234 Telex 44185

### SUMMARY

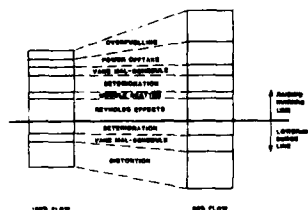
The high pressure compression system for future fighter engines has been projected at two different proven technology standards. For a given cycle of approximately 175 lbs and 25.1 overall pressure ratio, three compressors have been evaluated, ranging from a seven stage unit with medium loading, to a five and a four stage unit with high loading. Test data of the original research parent compressors and two project specific units was commonised to the engine size and conditions. It is shown that apparent benefits between machines are negated and no significant advantage for lower work per stage could be identified at a given blading technology standard. Relative to the seven stage unit a weight advantage of 20% is gained by the adoption of a four stage unit, and is associated with an aerofoil count reduction of 15%.

Introduction of higher specific strength metals already under development will enable a 8% weight reduction to the five stage compressor. Application of these advanced metals to a three stage compressor of higher loading has the potential of a unit weight reduction of 35% relative to the five stage machine.

### BASIC ENGINE REQUIREMENTS

It is important to datum the physical size of the engines under discussion, since both aerodynamics and manufacturing processes favour large machines. Internal studies have indicated that an engine of about 20,000 lb thrust reheated is just over optimum size for maximum thrust:weight ratios. Significantly smaller engines are hampered by machining limitations, whereas the larger machines are starting to be affected by the 'square cube' law. This paper will concentrate on an engine cycle of approximately 175 lbs fan mass flow, and an engine inlet diameter of 29 inches. Typical overall compression ratios are 25-28:1 with fan pressure ratios ranging from 3.5:1 to 4.5:1. This mix of compression system, and the elevated combustion outlet temperatures compared to today's in-service engines, offers cycles capable of compromising for the conflicting demands of the 'Multiple Mission', requirements of high dry thrust, and yet excellent loiter fuel burn, high mach number at low levels and yet agile and surge free at high altitude and low mach numbers.

It is taken as accepted that the future fighter aircraft will be inherently unstable by design. This, in conjunction with 'fly by wire' systems, places an onerous burden on the engine designer, and the airframe designer. The airframe designer has to strive to suppress intake lip vortices, wall separations, and any other unsteady flow generators within the intake, under the adverse flight conditions that are encountered. The stability margin of the engine is lowest at the high altitude, low flight mach number region of the flight envelope, which is also coincident with the anticipated worst intake conditions. In order to assess the high pressure ratio compressor requirements it is first necessary to establish the inlet distortion characteristics. Fortunately, design style of wide chord, unshrouded rotors leads to a more favourable inherent distortion attenuation in the fan. Similarly, current blading techniques tend to give favourable pressure gradients through the fan, leading to improved fan inner work potential. This has tended to suppress the degree of unsteady flow generated at exit to the fan that can exist even with steady inlet flow (Reference 1).



The HP compressor is therefore, subjected to the attenuated pressure distortions of the fan, and the implicit temperature distortion resulting from the pressure attenuation. Indicative stability margin assessment for the HP compressor is given on Figure 1. The compressors discussed in this paper assume a given fan technology and require the same surge margins.

FIG 1  
TYPICAL CORE STABILITY REQUIREMENTS

### COMPRESSOR DESIGN OPTIONS

Having now set the cycle, and the parameters for designing particular blading, it is necessary to consider the stressing requirements of the HP turbine. From the cycle peak temperatures, and estimates of efficiency potential, required turbine life, the turbine blade stress level, chord, and hub:tip ratio were determined. Hence the HP shaft speed is fixed and the actual process of selecting a suitable compressor can now commence.

For projecting, compressor aerodynamic loading can most easily be expressed by the term

$$\frac{\Delta H}{U^2} \cdot \frac{1}{N}$$

Where  $\Delta H$  = Enthalpy rise across the HPC  
 $U$  = Last rotor hub blade speed  
 $N$  = Number of compressor stages

Whilst this is strictly only correct for a compressor of similar radius ratios and similar through flow mach numbers, it is applied for indicative variations ignoring these limitations. Refinements to include these effects are normally made during the detailed design stage.

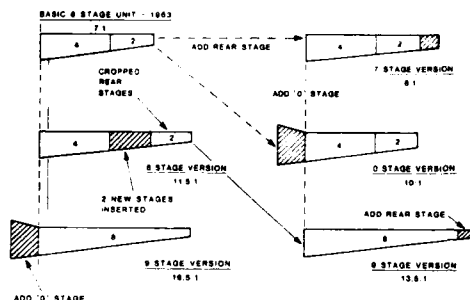


FIG 2  
MEDIUM LOADED COMPRESSOR HISTORY

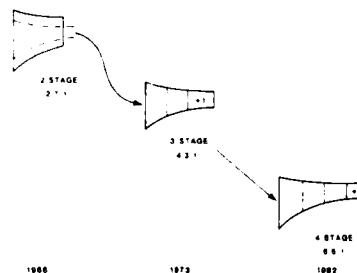


FIG 3  
HIGH LOADED COMPRESSOR HISTORY

Of the compressors available within Rolls-Royce, two units, with different loading values, were suitable for consideration. Both units had their origins in the mid to late nineteen sixties and their family pedigree is shown in Figures 2 and 3. The degree of scaling and cropping to achieve the given shaft speed at the cycle flow is given in Figures 4 and 5 for each compressor. At this stage, recorded test data were corrected for changes in exit hub:tip ratio, and the actual tip clearances and mechanical standards. This reduced the differences in the measured performance of the two units to similar levels of surge margin and efficiency.

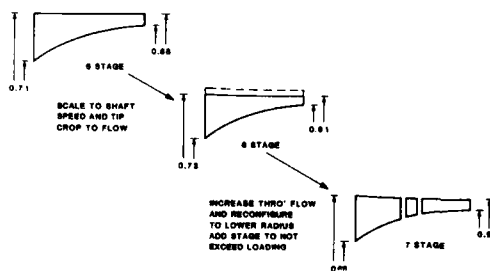


FIG 4  
MEDIUM LOADED COMPRESSOR DERIVATION

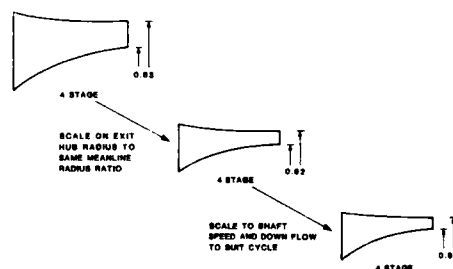


FIG 5  
HIGH LOADED COMPRESSOR DERIVATION

Since there was no identified performance deficit for the higher loading, a further study, using these loadings was undertaken. Simply, the exit flow function ( $W/T/P$ ) from the compressor being fixed by cycle considerations, the question of exit mach number and exit hub:tip ratio could now be addressed.

Given:  $W/T/P$

Then: Selecting exit mach number fixes exit area

And: Selecting exit hub:tip at given mach numbers fixes available blade speed (RPM fixed by Turbine)

and hence, for a given compressor loading, the number of stages to achieve the required pressure ratio is fixed solely by the choice of exit hub:tip ratio. (Figure 6).

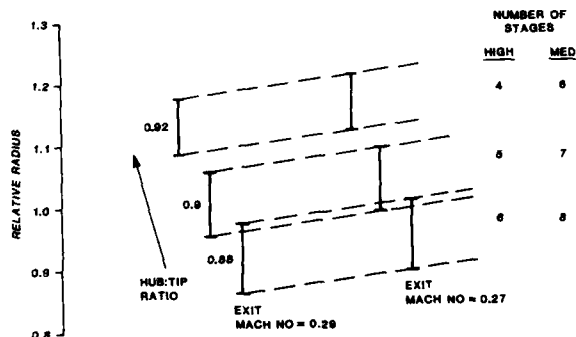


**FIG 6**  
**COMPRESSOR EXIT CONFIGURATIONS**

In view of the fact that fighter engines continue to utilise passive clearance controls on the HP compressor, there is a tendency towards the lower exit hub:tip ratio, and hence minimising the potential performance degradations associated with high hub:tip ratio blading with proportionately larger tip clearances.

Considering the two levels of compressor loading, these particular compressors were further projected at constant exit mach number.

- A - 4 stage, high loading, 0.92 exit hub:tip
- B - 5 stage, high loading, 0.9 exit hub:tip
- C - 7 stage, medium loading, 0.9 exit hub:tip

These three units are driven by the same turbine, at the same shaft speed, and each fulfil the cycle requirements. The requirements of aspect ratio and Reynolds number are incorporated in the projecting and the resulting annuli are compared in Figure 7. In all cases, only a variable inlet guide vane would be necessary for part speed operation, although advantages during light up and low speeds might be derived from the use of variable first stage vanes.

Performance predictions of the three units indicated similar efficiencies for all three. Although the potential efficiency of the seven stage unit was marginally higher, this was negated by the necessity of meeting minimum chord/Reynolds requirements, resulting in significantly lower than optimum aspect ratios for the work input per stage. As a result of these low aspect ratios the surge margin indicated for the seven stage machine was calculated to be some 3% greater than the five and four stage compressors. Adoption of the lower chords would have implied thicker than optimum leading and trailing edges. An advance in blade profile design was assumed to allow this effect to be accommodated. If the lower chords were adopted to capitalise on the apparent efficiency potential, then the computed surge margin would be the same at high Reynolds numbers, but would be significantly less, and unacceptable at the critical high altitude low mach number conditions.

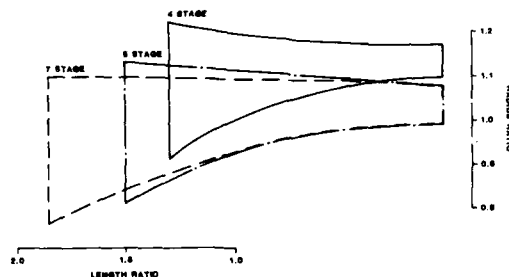


**FIG 7**  
**ANNULUS GEOMETRIES**

These compressor performance assessments were achieved by blade row stacking of initial designs. The methods used were developments of a recent RAE Pyestock model (Reference 2 and 3). As with all these methods, despite their accounting systems for loss, mach number, aspect ratio, hub:tip ratio

and clearances, they are by nature historical. the degree of empiricism based on well developed, medium loaded compressor designs has to be extended to outside the normal applicability in order to estimate the characteristics of any new, more highly loaded machine. As such, much of the adaptation of the RAE Pyestock method was to incorporate observed phenomena from the limited high loading results that had become available. Modelling of the parent compressors utilising the new amendments, gave very encouraging results for both the medium and high loaded compressors.

The following table gives the leading parameters of three compressors studied at the common exit mach number and flow function.

COMPRESSOR	A	B	C
No STAGES	4	5	7
INLET HUB/TIP RATIO	.73	.70	.88
EXIT HUB/TIP RATIO	.82	.9	.9
RELATIVE EXIT HUB RADIUS	112	100	100
RELATIVE LENGTH RATIO	86	100	125
RELATIVE No AEROFOILS	85	100	106
RELATIVE COMPRESSION VOLUME	76	100	128
RELATIVE COMPRESSOR VOLUME	102	100	119
RELATIVE WEIGHT (VIGV ONLY)	93	100	116

#### INITIAL PITCHING

During the projecting phases of an engine it is not necessary to finess the pitching of the HP compressor. Although in essence the axial gaps within the machine are dependant on absolute chord, an analysis of engine proven compressors of similar exit flow function indicates that an allowance of 6 to 7 mm air gap axially between blade rows should be taken as the mean during the projecting phase. Any bleed porting from the casing would need particular evaluation and could well extend this air gap, and would preferably be taken at the exit of the stator.

The physical chord of the blades can be selected from any of the following

- Basic Interference Diagram (Resonance Avoidance)
- Required Aspect Ratio
- Critical Reynolds Number
- Leading or trailing edge thickness maximum thickness
- Circumferential Pitching

Of the above, normally the aspect ratio and critical Reynolds number dominate during the projecting phase, with the others being refinements as a particular design is progressed to maturity.

Blade aspect ratios are primarily chosen from consideration of stage temperature rise and reaction, and the required flow range which is a function of the amount of variable geometry to be adopted, and the position of the stage in the compressor. Typically, rear stages demand lower aspect ratios, although caution must be exercised regarding the first stage of fixed geometry. It has been the general experience that residual pressure ratios down stream of variable geometry to the order of 4:1 are acceptable for ease of starting and quiescent blades. More recent testing of relatively high pressure ratio per stage, and high work coefficient compressors has indicated that 4:1 may be optimistic, and hence additional variable geometry could be necessary.

Performance of the compressor at altitude would traditionally have been assessed using "Wassell" Reynolds corrections to flow, efficiency and compression ratio. Whilst the "Wassell" method of performance correction is blade chord dependant, more recent controlled testing (Reference 4) has revealed that at low Reynolds numbers "Wassell" can be optimistic. Subsequently, this has been found to be particularly true of blades with any form of leading edge imperfection, such as would represent typical long service/hostile environment blades. Consequently, since this degradation in performance would build in an additional unnecessary surge margin burden, all compressors are sized on individual blade row chord for their critical Reynolds number at the worst flight condition. Typically, a chordal Reynolds number of  $1.5 \times 10^5$  is selected at this worst case.

## EXPERIMENTAL DATA

The two parent compressors, of two levels of work were both sponsored by RAE Pyestock though the 1970's within a normal general research contract. Both of the units were designed and tested at Rolls-Royce. Under a different contract between MoD (PE) and Rolls-Royce, using joint funding, both a four and five stage machine were designed and tested. They represent the machines A and B from the previous table.

Machine A, the four stage unit was designed at a large physical size of approximately 24" exit diameter. Typical rig design of bolted discs and heavy casing were utilised for speed and cost. A strutted intake, equivalent to an engine standard, and a diffuser with simulated combustor head formed the inlet and exit to the machine. In all other respects, such as blade leading edge thickness, bleed ports, tip clearances, axial pitching, surface roughness and root sealing the compressor was to engine standards. Machine B, the five stage unit was designed for use as an engine compressor. Again, testing was accomplished using an engine equivalent strutted intake, with a diffuser and simulated combustor head at exit. Between the two units a commonality of instrumentation standard was maintained.

The blading standard of the two units was purposely held to a common philosophy. Pitch/chord ratio selection was based on diffusion loading and mach number. Deviation rules, profile types and incidences were consistent between the two units, as was the design pressure ratio and exit mach number. In order to compare the performance of these two physically different size machines, the data sets have been reduced to the conditions that would appertain at a common flow installed behind a 4:1 compression ratio fan, at sea level static conditions. Figure 8 shows the performance differences that exist between the two units when the data is reduced in the way described. It should be noted that these comparisons are made for the first build of each unit, and no stage matching or normal compressor developments are incorporated in the results. They consequently represent the closest comparison known to the author of a constant technology applied between different stage numbers for the same overall duty.

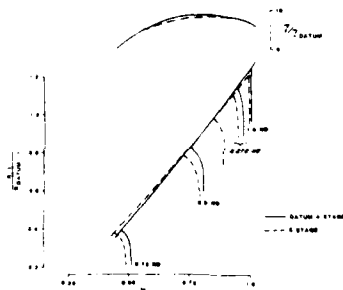


FIG 8  
COMPARISON OF 4 & 5 STAGE COMPRESSORS

The peak efficiency flow relationship is essentially identical between the two machines, although the mass flow speed relationship is marginally different. Likewise, at all speeds above approximately  $80\% N_H/\sqrt{T_2}$  the surge boundary is sensibly the same. Below  $75\% N_H/\sqrt{T_2}$  the surge boundary was not established for the four stage machine due to blading excitation. Subsequent analysis has indicated that a non-optimum variable vane schedule was utilised for this test. However, the indications are that the four stage unit would be more difficult to handle through the low speed region compared to the five stage unit. Engine testing of the five stage unit has proven that this unit has more than adequate capabilities in the start up/low idle region. Although, the four stage unit is worse, it is still expected to be acceptable.

## FUTURE TRENDS

Changing to the four stage unit from the five results in a saving of 7% of module weight, which then translates into approximately 20% of engine weight, would make a small, but worthwhile contribution towards the continued striving for higher thrust weight ratios which must be achieved without sacrifice of component efficiencies, either at maximum rating or at off design conditions. Of similar order of merit is the consideration of the number of parts, and number of part numbers that would be associated with the lower stage number unit, impacting directly on initial cost, and cost of ownership. However, hidden within the accounting systems for the engine remain large compromises for stability margins. There is a tendency of transonic blading to have the efficiency peak closer to the stability limit (e.g., Reference 5) and an estimate of the efficiency penalty for large inherent stability margins are of the order of 1 to 15%. To capitalise on this potential by the development of Active Control Systems could therefore, enable an increase in thrust for the same engine weight of 1 - 1.5% without any increase in combustor outlet temperature. This becomes more significant as the compressor loading is increased as the difficulty of achieving peak efficiency on the engine working time, with large stability margins is compounded with increases in blade relative mach numbers, and hence loading.

Future engine cycles for fighter engines will raise the combustor outlet temperatures towards stoichiometric conditions and also raise the combustor inlet temperatures as cycle pressure ratios rise. It must be considered doubtful that combustor volumes will continue to decrease as the difficulty to fulfil requirements of emissions, low smoke and carbon formation are amplified towards stoichiometric conditions. It is therefore, imperative that the basic turbo machinery masses are reduced. Advances in aerodynamics such that loadings ( $\Delta H/U^2/N$ ) are increased by a further 25% are currently being pursued. In order to capitalise on the potential of these high loadings, with the design restraint of exit hub/tip ratio, it is necessary to raise the shaft speed, and allow a further reduction in stage numbers.

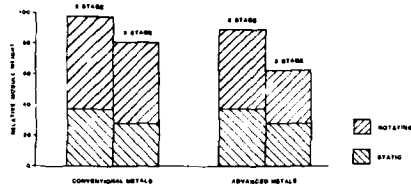


**FIG 9**  
**APPLICATION OF ADVANCED MATERIALS**

Design studies for a similar cycle as datum in terms of maximum compressor delivery temperature, and maximum combustor outlet temperature indicate that on a common materials technology basis, a weight reduction of 20% for the HP compressor could be anticipated (Figure 9). When the increase in the specific strength of compressor materials to the order of 10 - 15% becomes available, then the datum five stage machine could enjoy weight reduction of some 8%, whereas the high blade speed unit could benefit by a further 10 to 20% reduction. The increases required in compressor delivery temperature therefore demand that these increases in specific strength are also maintained at the elevated temperatures.

### CONCLUSIONS

At the engine size of approximately 175 lbs and 29 inch inlet diameter, design studies indicate that a weight saving of a four stage highly loaded compressor compared to a seven stage medium loaded compressor is of the order of 20%. Analysis of compressor test results, when evaluated at the required physical size and limitations of the HP turbine collapse apparent benefits of different machines to minimal differences. A direct comparison between a four and a five stage compressor for the same duty and same turbine, indicates that the lower stage number was only of problem in the low speed region, but not so limiting as to prevent engine application. Forthcoming increases in the specific strength of compressor materials will enable a weight reduction of the five stage unit of 8% whereas these high strength materials in conjunction with increase aerodynamic loadings will permit a weight saving of some 35% relative to the five stage unit, of which approximately half the decrease is due to the increased aerodynamic loading.

### REFERENCE

1. Schaeffler, A. and Miatt, D C, "Experimental Evaluation of Heavy Fan - High Pressure Compressor Interaction in a Three Shaft Engine Part 1 - Experimental Set Up and Results ASME Journal of engineering for Gas turbines and Power, Vol 107, Number 4, October 1985, Pages 828 - 832
2. Howell, A R. and Calvert, W J, "Axial Flow Compressor Performance Prediction by Stage Stacking - Determination of Stage Aerodynamics. NGTE R81002.
3. Rolls-Royce Internal Note. GN25583, June 1982
4. Schaeffler, A, "Experimental and Analytical Investigation of the Effects of Reynolds Number and Blade Surface Roughness on Multi Stage Axial Flow Compressors." ASME Journal of Engineering for Power, 79GT 2.
5. Law, C H. and Wennerstrom, A J, "Performance of Two Transonic Axial Compressor Rotors Incorporating Inlet Counterswirl". ASME Journal of Turbomachinery Vol 99 January 1987, Pages 142 - 148.

### ACKNOWLEDGEMENTS

The views expressed in this paper are those of the author, and form no commitment by the Company. The work has been carried out with the support of the Procurement Executive Ministry of Defence. Thanks are due to Rolls-Royce, Bristol, Compressor Aerodynamics and Design Offices where this work was performed.

### DISCUSSION

G. KARADIMAS, Fr

Has the exit absolute Mach number the same value on your design for the 5, 4 and 3 stages compressors, or do you accept higher Mach number on the 3 stages compressor ?

Author's Reply

The 4 and 5 stages machines have an equivalent Mach number. The 3 stages machine has a slightly high Mach number, just about 0.3.

G. KARADIMAS, Fr

As you showed us, for the 4 and 3 stages compressors you accept higher hub to tip ratio. Do you find, in the last stages, similar secondary phenomena, or is there a great difference ?

Author's Reply

We attempted to find it on our design approach, because we allowed for change on blockage, and change on stage efficiency. Therefore, we modified the work we were putting on the last stages. This, as far as we can determine, indicates the effect of assuming similar efficiencies.

L. FOTTNER, Ge

Could you comment on the application of inverse or prescribed velocity profile technology, or involved end-bend profiles in those compressors ?

Author's Reply

In those compressors, we use essentially standard design methods. As we go to the end walls, the incidence selection is modified. In particular, near the walls, we have a fairly large negative incidence relative to the standard axisymmetric through-flow. This has the effect of overcambering the leading edges of all the stator blades. We do not account for the trailing edge variation deviation.

# AN EXAMINATION OF THE IMPACT OF POTENTIAL ADVANCES IN COMPONENT TECHNOLOGY FOR FUTURE MILITARY ENGINES

by  
M.R. Litchfield and M.G. Philpot  
MOD(PE)  
ROYAL AIRCRAFT ESTABLISHMENT  
Pyestock  
Farnborough  
Hants, UK  
GU14 0LS

## SUMMARY

The paper examines the prospects for major advances in gas turbine engine component technology over the next 20 years. For future military engines and aircraft, these advances could lead to considerably higher thrust/weight ratios than are currently available. The gains in engine performance resulting from various specific technology advances are outlined and their impact on the sizing and performance of a typical combat aircraft are considered. In conjunction with these future projections, an examination is also made of the influences of main engine cycle parameters, such as overall pressure ratio, bypass ratio, and rating philosophy on the mass and performance of the aircraft/engine combination.

## 1. INTRODUCTION

Aircraft gas turbine technology has advanced steadily ever since the first jet aircraft entered service in the 1940s and there is no sign yet that the pace of progress is slackening. Improvements in engine performance continue to be made as a result of the introduction of new materials or materials processing routes, advances in hot parts cooling technology and increased aerodynamic and mechanical design capabilities. The gains are reflected in engines having higher cycle pressure ratios and temperatures, reduced turbomachinery stage numbers and - of particular importance for combat aircraft applications - higher thrust/unit volume and higher thrust/weight ratios (see, for instance, Ref 1). Indeed the latter aspects have such a significant impact on overall fighter size and performance that combat specific thrust (ie maximum thrust/unit inlet airflow) and engine thrust/weight ratio are generally regarded as among the most significant indicators of technology level. Progress tends to be measured by the increase in thrust/weight ratio of one engine generation compared with the preceding generation. The engines in current service, eg RB199, F100, F404 have thrust/weight ratios of 7 to 8; the next generation of engines, which will power the advanced tactical fighters due to come into service during the 1990s will have thrust/weight ratios of 10 or more. For the generation beyond that, some technology projections are so encouraging that a figure of 20 is being widely canvassed as a target that should be achievable within a few years of the turn of the century.

The selection of the most appropriate engine cycle and design for a future fighter is however considerably more complex than simply seeking the highest possible thrust/weight ratio. At base level the choice of aircraft concept and matching engine cycle will depend on the role, or roles, that the new fighter is intended to fulfil. These are typically defined in terms of a set of mission requirements (range, speed, form of combat, etc) and point performances. Candidate designs are iterated and refined to achieve the "best" solution to meet the requirements, "best" often being regarded as minimum possible aircraft size and weight. Engine fuel consumption and thus the fuel mass required to complete the missions can be very significant here. Different mission requirements can lead to significant differences in preferred engine cycle. For example, an attempt was made to define a common solution to the USAF and USN tactical aircraft requirements of the 1990s (Ref 2). Although both wanted more payload-range, improved manoeuvrability, increased combat persistence and easier supportability, the basic mission requirements - air superiority for the Air Force, combat air patrol for the Navy - were sufficiently mismatched to lead to different optimum cycles. While the core cycle parameters (overall pressure ratio, combustor exit temperature and throttle ratio) were similar, the bypass ratios were considerably different - 0.25 for the Air Force, compared with 1.0 for the Navy. The dependence of cycle choice, particularly bypass ratio, on mission requirements is also shown up in several other studies, for both CTOL and STOVL aircraft (References 3 to 7).



The aim of this paper is to investigate the relationships - sometimes conflicting - between the main engine cycle parameters and the three key performance indicators: specific thrust, specific fuel consumption and thrust/weight ratio. Account is taken of the potential technology advances, both evolutionary and revolutionary, over the next 10 to 20 years. The inherent influences of the cycle parameters over the performance indicators will be examined and the further contributions to increased thrust/weight ratio from new methods of mechanical design and new lightweight materials identified. However, increased thrust/weight cannot be considered as an end in itself. It is important to assess the impact of such engine improvements on the overall aircraft system. This aspect is also addressed in the paper. In the interests of brevity, the discussion will be confined to "conventional" fighter engine designs, of two spool fixed cycle architecture; the bypass and core streams are assumed to be remixed prior to entry to a normal afterburning system, with the total flow being exhausted through a variable area propelling nozzle.

## 2. ENGINE CYCLE PARAMETERS AND ENGINE PERFORMANCE

### 2.1 Choice of Cycle Parameters

The primary aero-thermodynamic parameters which can be selected within certain limits for a gas turbine cycle are:

- (a) bypass ratio (bpr)
- (b) fan pressure ratio (fpr)
- (c) cycle temperature, defined throughout this paper as turbine stator outlet temperature (SOT)
- (d) overall pressure ratio (oapr)

In addition there are secondary parameters such as component efficiencies and cooling air flows. Technological improvements can be quantified by advances in SOT and efficiency, reductions in cooling flow at a given effectiveness, and increases in pressure ratio per stage. There will, of course, be interactions between some of the primary and secondary parameters, for example between SOT and turbine cooling air flow.

Some of the primary parameters can be interdependent depending upon the way in which the engine is configured. For the normal mixed engine configuration, at a given technology level (constant component efficiencies, bleed flows, etc), the mixing constraint ensures that bpr is dependent on the values of the other primary parameters. In particular, if the engine core efficiency (SOT, oapr, and efficiencies) is fixed, then bpr and fpr are uniquely related.

### 2.2 The Effect of Fan Pressure Ratio and SOT

Thermodynamically there is freedom to select fpr over a wide range, according to the requirements of the cycle selected. In practice there are two constraints on the upper limit. For weight reasons, it is important to limit the number of turbomachinery stages; increasing fpr to a point where further fan or low pressure (LP) turbine stages have to be added, may be counter-productive (this point is discussed again later in quantitative terms). Secondly in a mixed, reheated engine configuration, sufficient bypass air must be supplied to ensure adequate cooling of the jet pipe and exhaust components.

As noted above, the constraint of equalizing core and bypass pressures before entry to the reheat system ensures that a particular bypass ratio will be defined by the level of fpr chosen, provided that SOT remains constant. For a particular combination of core efficiencies and bleeds, Figure 1 shows how bpr increases with SOT for fixed levels of fpr. This bpr increase occurs because the gain in SOT enables the core to become smaller whilst still providing sufficient power output to drive the fan. As will be seen, the effect of these trends on performance is small, but they can have a significant effect on thrust/weight ratio.

Considering first the effect of fpr on maximum specific thrust in reheat, it is first of all necessary to establish the maximum allowable fuel/air ratio (far) in the reheat system. Theoretically, the fuel/air ratio can be increased until stoichiometric conditions are reached at 0.068 far. In practice, stability problems within the reheat system mean that lower limiting values of far have to be used. These instabilities are complex phenomena whose characteristics vary from one design to another in a way that bears little relation to the cycle. For the purposes of this paper, the limiting far has been fixed arbitrarily at 0.06 for all engine cycles considered. A slightly higher figure might have been selected, but this would not have significantly affected the results.

The variation of maximum specific thrust with fpr and SOT is shown in Figure 2. Maximum thrust is virtually independent of SOT, but increases significantly with fpr. These effects are caused by the fact that, when fpr and far are fixed, the pressures and temperatures in the exhaust nozzle are almost constant. Thus neither of the contributions (velocity or pressure) to thrust are altered. The gain in specific thrust

with fpr is due mainly to the increase in the pressure thrust contribution. The overall specific fuel consumption (sfc) in full reheat is similarly dependent on fpr, but independent of SOT (Figure 3) because at the same far the amount of fuel used within each cycle is approximately constant.

Turning now to the situation with reheat off ("dry" operation), the variations of specific thrust with SOT and fpr are broadly similar to the reheat case, see Figure 4. Specific thrust tends to fall slightly as SOT is increased, but again the major effect is the increase with fpr, which arises directly from the increase in nozzle pressure ratio. Dry operation is habitually used for the endurance parts of the aircraft mission, so the effect on sfc is the main factor of interest. Figure 5 shows that sfc increases considerably as fpr is increased, essentially because of the resultant loss in propulsive efficiency. The trend is only slightly offset by increasing SOT.

The choice of fpr thus has a major impact on overall engine performance and a requirement for high combat specific thrust is in conflict with a requirement for good sfc at throttled back conditions. The key importance of fpr is illustrated more clearly in Figure 6, which shows sfc loops for engines having the same core cycle and design mass flow, but differing fpr's. A fighter aircraft whose primary role is one of combat air patrol, where 75% of its available fuel would be used at a setting of 25%-50% of maximum dry thrust, would favour a low fpr. The best choice for an air superiority fighter, however, in which perhaps 75% of the available fuel load is used at maximum thrust conditions, would be the highest available fpr with its consequent low bpr.

For such an air superiority fighter, the logical end point is an engine design with an extremely high fpr, but no reheat system with its attendant mass and complication. Additional turbomachinery stages could be an acceptable penalty in these circumstances. Figure 7 shows that by increasing fpr to a value of about 8, and increasing SOT to aid mixing and dry sfc, a maximum dry thrust can be obtained approximately equal to the maximum reheated thrust for the 4.5 fpr engine shown in Figure 6. This high thrust is also obtained at a much reduced sfc compared to the reheated case. The severe sfc penalty at part thrust is however clear. Even with an SOT increased by about 100°C above the levels used in Figure 6, the sfc at low thrusts is 20%-30% higher than the reheated designs. For all except a very restricted range of missions, this characteristic could be a considerable disadvantage. The ideal cycle would be one which has the good high thrust sfc of a high specific thrust, high fpr engine together with the low dry sfc of the low fpr cycle - is a variable cycle engine. Cycle variability is a major topic in its own right and consideration of it must lie beyond the scope of this paper. Suffice it to say that while the thermodynamic attractions are apparent, the engineering problems are far from negligible.

### 2.3 The Effect of Overall Pressure Ratio

The main effect of oapr is on the sfc under dry operating conditions. In order to obtain high core efficiency, the highest possible oapr needs to be utilized. Assuming constant component efficiencies, Figure 8 shows that increasing oapr from 20 to 30, at fixed fpr and SOT, reduces dry sfc by about 7%, but has negligible effect on reheated performance; the reason for this is that the increased thermal efficiency of the core due to increasing oapr is utilized in making the core smaller; the net effect is therefore similar to increasing SOT. It is worth noting in passing that the same effect, both qualitatively and quantitatively would result from increasing each of the turbomachinery component efficiencies by about 2%.

Figure 8 is valid provided that there is no limitation to increasing oapr. In practice, materials, stress and temperature limitations place constraints on allowable oapr, and the effect of these can be considerable. Figure 9 shows a family of SOT schedules for a set of postulated engine designs having different design oapr's. All engines have the same fpr at the sea-level static design point, and are limited to the same maximum HP compressor exit temperature. The oapr of each engine varies from 20 where SOT is not limited at all on compressor exit temperature grounds, to 30 where the limiting compressor temperature operates from a low engine inlet temperature. The effects for a typical supersonic flight condition, where engine inlet temperature and therefore compressor exit temperature is relatively high, are illustrated in Figure 10. At the higher design oapr levels, the temperature limitation forces the engine to be throttled back, with major penalties on both sfc and thrust, throughout the combat range. For the particular case shown, which is purely illustrative, but has a compressor exit temperature typical of current designs, the maximum thrust of the 30 oapr design is reduced by 20% at the flight condition shown and sfc is increased by 10%.

Combat engines are currently being designed with oapr's of around 25:1. Because it is very difficult to cool HP compressor components, further advances depend on material improvements. However, there is little doubt that improvements to metal alloys will quickly achieve the additional capability required for a 30 oapr design, and further increases are in prospect with continued materials development.

The approach to selection of oapr is therefore clear. The highest possible cycle pressure ratio should be chosen, but only up to the point where compressor limitations start restricting operation in important parts of the flight envelope. In a diverse combination of requirements (a subsonic combat air patrol and supersonic intercept, for

instance), the choice of  $\phi_{apr}$  will tend to be determined by the intercept mission, where too high a value of  $\phi_{apr}$  could potentially result in an oversized engine, in order to meet the supersonic thrust requirement.

### 3. ENGINE THRUST/WEIGHT RATIO

#### 3.1 Cycle Effects

It has been shown that increasing the fan pressure ratio increases combat specific thrust, while increasing the cycle temperature allows core size to be reduced. The latter step may be expected to improve thrust/weight ratio, but the situation is less clear in the case of fan pressure ratio. Although thrust is improved, the increase in fpr is accompanied by an increase in core size, while the fan itself may require an additional stage. Engine mass is therefore likely to be significantly increased. In order to investigate these effects quantitatively, it is necessary to estimate the changes in engine mass. At this stage it will be assumed that engine architecture, materials and construction methods remain essentially unchanged.

Precise estimation of engine mass is not possible without detailed design drawings and for a parametric study of the type described in this paper, it is necessary to resort to some simple approximate method. The approach used here is similar to a method developed by NASA (Ref 8) and is based on empirical correlations for the masses of the individual major components. By definition it is founded largely on past and current experience and has limitations if used well outside that experience. But for present purposes it gives useful, first order results and, in particular, allows the effects of changing the sizes and numbers of components to be quantified.

Considering first the effect of increasing fan pressure ratio, the current trend towards much higher fpr has been made practicable by the great strides of the last few years in compressor aerodynamic design. Whereas present generation military engines have fans with a fpr lower than 3.0 in three stages, it is now possible to achieve well over 4.0, still in three stages and with little increase in fan mass. Research designs are also being produced to achieve such pressure ratios in two stages, although because of the considerably greater blade chords needed, such fans are likely to produce a mass saving only if constructed largely from lightweight non-metallic materials. Whether the baseline design has two stages or three as the fpr is increased beyond, say 4.5, it may eventually become necessary to add a fan stage, in order to maintain acceptable fan loadings. For the reheated engine arrangement considered in this paper, one extra fan stage is predicted to add around 5% to the total engine mass.

A further and larger increase results from the increasing core size. In this case the change is more progressive as it is related more to core engine diameters and lengths than changing stage numbers. In fact, for fixed overall pressure ratio and cycle temperature, there is likely to be a decrease in the number of HP compressor stages as fpr is increased, but the dimensional growth dominates. With the core and LP turbine representing 30% to 40% of the total engine mass, the effect is significant. An increase in fpr from 3.7 to 5.0 is predicted to increase total mass by at least 20%. Thus, although there is a 10% increase in specific thrust, thrust/weight ratio actually reduces by at least 10%. This decrease, together with an added fan stage, causes the difference in the two bands plotted in Fig 11.

Fig 11 shows thrust/weight ratio plotted against cycle temperature and, as expected, increasing SOT leads to an improvement in thrust/weight ratio. As was shown by Fig 1, at any given fan pressure ratio and specific thrust, bypass ratio is highly dependent on cycle temperature and increasing the latter allows core size to be reduced considerably. Turbine temperatures have continued to increase as a result of advancing cooling technology and improved materials. The engines being developed for the 1990s will have SOTs in excess of 1800K, ie up to 200°C more than the temperatures of the previous generation. Technology demonstrator programmes are already considering SOTs of 2000K and more (Ref 9) and there is a good prospect of advancing to 2200K with metal blades and discs, and in excess of 2400K if acceptable ceramic-based components can be perfected. The temperature plots throughout this paper have been drawn on the projection that such temperatures will be attainable within the next 20 years.

Although the general thrust/weight ratio trend is upward, there is again a complication due to component loading. As the core size reduces, the aerodynamic loading on the LP turbine has to increase in order to maintain the power required to drive the fan. Fig 12 shows the variation in turbine loading and indicates where it would be necessary to increase, first of all from a single turbine stage to two stages and then to three, in order to avoid gross overloading and unacceptable losses in efficiency. The intrinsically lower bypass ratio of the higher fpr cycles gives them an advantage in this respect. Each time a turbine stage is added there is a significant increase in engine mass, indicated on Fig 11 by the step changes in the curves.

Taking the above factors into account, Fig 11 shows that, without changing engine layout or conventional metal construction, cycle improvements over the next 10 to 20 years will allow thrust/weight ratios to be increased from the value of around 10 of the 1990 generation of engines to 12 or 13. Engines having moderate fan pressure ratios will continue to have some advantage over those with high fan pressure ratio.

### 3.2 Materials and Structure Changes

The gains in thrust/weight ratio to be obtained from the cycle and from aerothermodynamic improvements, such as further increases in stage loading, are clearly significant, but considerable further gains can be achieved by attacking the root causes of engine mass, ie the materials. Hitherto, the combinations of stress, temperature and reliability required in aero-engines have precluded the use of anything but premium metal alloys - titaniums for the front end, nickel and cobalt-based alloys for the hot parts. There is however an increasingly intensive effort to develop suitable non-metallic materials, eg polyimides, carbon-carbon, monolithic and composite ceramics, etc. The technology of such materials has progressed to the point where they can now be considered, at least for certain static components. More widespread application, including their use for rotating components, remains a matter for some speculation, with views ranging from strong optimism to considerable scepticism. In general however the question is not whether such developments will take place, but when. Accordingly, in the discussion that follows a distinction is made between near term technologies which could be available within ten years, for the initiation of a new project, and technologies that appear to lie nearer the twenty year time-frame.

In order to assess how new materials and mechanical design techniques will impact on thrust/weight, it is useful to consider the mass breakdown of a typical 1990s technology level metal engine (Fig 13). The important point to note is that the basic powerplant, ie the turbomachinery and associated casings, accounts for less than half the total. The reheat system with its fuel supply and the exhaust nozzle account for nearly 30%, while the main engine fuel and control system, auxiliary gearbox, lubricating oil system and other accessories account for over 25%. There is thus considerable scope for reducing mass without making any radical changes to the rotating turbomachinery. Mass savings have been evaluated for a number of potential nearer term technologies, for which research bases exist or are in the process of being developed:

Jet pipe and exhaust nozzle in carbon-carbon	7-9 %
Fan casing and bypass duct in polyimide	3-4 %
Replace oil system (including sump, coolers, filters) by gas bearings	4-6 %
Use ceramics for reheat flameholders, turbine stator vanes and shrouds, etc	2-3 %
Make wider use of high temperature titanium and lightweight metal composites; and "blisc" construction for rotating components	2-3 %
Simplify gearbox and drives, or replace by turbo-driven system	1-2 %
Simplify fuel system and controls, use plastic casings, fibre-optic transmission	4-5 %
	<hr/> 23-32%

Clearly, not all of the above items may reach fruition, or the projected savings may not be fully realized, but even so there are good prospects for achieving mass savings of around 25%, compared with the all metal engine architectures that have been used hitherto. Indeed one or two of the above savings are already being designed into the 1990s generation of engines. When these developments are added to the gains in prospect from the cycle, it can be seen that thrust/weight ratios of around 15 will become possible.

Turning now to the more speculative uses of non-metallic materials, the most likely progression of applications is the use of fibre-reinforced polyimides for the fan blades, ceramic-based materials for turbine stators and possibly also the combustor, ceramic-based turbine rotor blades and ultimately ceramic turbine discs or bliscs. With their much lower density such materials will allow blade speeds to be increased as well as component sizes and weights to be reduced. However their full exploitation demands a completely different approach to mechanical design and the overall mass savings are therefore difficult to quantify without carrying out proper design studies. Such studies lie outside the scope of this paper, but it may tentatively be estimated that the mass of the turbomachinery could be reduced by up to a third, compared with a conventional all-metal design. The further saving to the overall engine mass is therefore likely to be in the region of 15%. Taken with the savings already enumerated, it is evident that thrust/weight ratios close to 20 should ultimately be attainable, while still retaining the basic concept of a mixed flow two spool engine with a reheat system.

It is however necessary to observe that attainment of such high thrust/weight ratios depends on a number of highly speculative technology items. While it is possible to predict with some confidence that technology readiness for thrust/weight ratios of up to 15 will be demonstrable within the space of the next 10 years, the further advance to 20 is much less certain. Realization of such figures within the next twenty years will be dependent on maintaining aggressive and extensive technology research programmes on both materials and mechanical design methods and, not least, adequately demonstrating their reliability to Service customers.

#### 4. THE EFFECT OF T/W ON AIRCRAFT MASS

The ultimate value of the big improvements in engine thrust/weight ratio discussed in the preceding section depends on how they affect the overall aircraft system. To evaluate this effect, a Multivariate Optimisation (MVO) technique for combat aircraft design developed at RAE<sup>10</sup>, has been used to establish the likely improvements in overall take-off mass. The technique involves taking an example of a suitable mission requirement together with a set of point performance requirements, and obtaining the optimum values for a set of variables defining the aircraft configuration (eg wing planform, fuselage shape and size, engine size) that minimise the empty mass of the aircraft while satisfying all of the requirements.

Apart from those that are incapable of being scaled (crew, weapons, etc) all components can be scaled independently to fit the given requirements laid down. To ensure that all of the configurations produced have acceptable geometry, a set of constraints are applied during the design synthesis, such that, for instance, the fuselage should be large enough to accommodate all of the items specified.

In combination with a set of point performance requirements, two missions have been investigated:

- (a) an intercept mission which uses the majority of its fuel in reheat in travelling at supersonic speed at high altitude followed by a combat phase,
- (b) a typical long loiter mission, in which the majority of the fuel is used at subsonic speed with engines well throttled back.

Baseline current technology engine T/W values for the appropriate size of engine have been taken as 10.5 for a 3.7 fpr engine, and 9.0 for a 4.5 fpr. From the improvements detailed in Sections 3.1 and 3.2 it is reasonable to assume nearer term T/W improvements of 50%, leading to figures of 15.0 and 13.5 respectively. In order to isolate the effects due to the engine, the airframe and avionics technologies are assumed to remain constant.

The results are shown in Tables 1 and 2. Both tables show similar results; the effect of reducing engine mass by approximately 35% is to reduce fuel usage by between 3.3% and 6.3%, and to reduce take-off mass by between 6.3% and 8.1% depending upon the mission and the cycle being examined. The increase in engine T/W results in an associated reduction in the structural mass of the fuselage, which in turn allows a decrease in wing size and hence aerodynamic drag. Therefore the engine thrust requirement can also be reduced, leading to a smaller engine and further mass savings. With the benefits of these effects, the total saving on take-off mass amounts to about 1.7 times the saving on engine mass alone.

Intuitively it would be expected that the savings predicted would vary depending on the mission and particular engine cycle chosen. However in the examples chosen here, the engines range from a 'leaky turbojet' (bpr = 0.25) to a conventional fighter (bpr = 0.66), and the missions involve significantly different fuel usage requirements in dry and reheat operation. Yet the variation in the trade-off against engine mass is seen to be remarkably insensitive to either cycle or mission requirement, within the range investigated.

The calculations reported here may be slightly pessimistic in their trade-offs. Although the various aircraft components were scaled, the basic aerodynamics (wing planform, sweep, etc) were left unchanged. As a result, any reduction in engine mass (which is sited behind the centre of gravity) was balanced simply by repositioning the wing fore and aft in the fuselage or by increasing the fuselage length. A comprehensive approach would re-optimize the aerodynamics and would tend to increase the saving. Nevertheless the present results compare reasonably well with other work. Denning and Mitchell<sup>7</sup>, in investigating the effect of various propulsion parameters on advanced STOVL aircraft, obtained a reduction of 11% in take-off gross weight (TOGW) for an increase in engine T/W from 10 to 15. Lehman and Crafa<sup>6</sup> obtained a 4% reduction in TOGW for a supersonic interceptor and 5% for a Navy VSTOL aircraft as a result of a 20% increase in T/W. Extrapolating these figures to a 50% increase in T/W would give a TOGW gain of around 10%. In a more general US study, which considered the effects of improving aircraft and engine technologies together for a supersonic cruise STOL fighter, Dollyhigh and Foss<sup>11</sup> varied aircraft thrust/weight and engine thrust/weight independently. Their results indicate that improvements in engine T/W tend to give a better return as aircraft thrust/weight is improved, but the effect becomes small at high engine thrust/weight. For the typical aircraft thrust/weight of about 1.2, as considered in the present work, their results show an 8% to 10% reduction in TOGW for an increase in engine T/W from 10 to 15.

Thus while the results of the present study are on the low edge of the band, there is general agreement that an increase from 10 to 15 in engine T/W yields an aircraft TOGW reduction of the order of 10%. References 7 and 11 also considered the step from 15 to 20 engine T/W and both found a further 5% reduction in TOGW, thus indicating that the gains become less marked at very high values of engine T/W.

## 5. DISCUSSION

It is clear that increasing engine thrust/weight ratio brings considerable dividends to the aircraft. Moreover, since airframe and aircraft systems technologies are currently advancing at a similar pace to engine technology, the gains will be compounded. Reference 11 suggests that the potential 10% reduction in TOGW resulting from the increase in engine T/W over a 10 year timespan, will be augmented by a similar gain due to aircraft improvements, giving a total reduction of over 20% for an aircraft having the same level of performance. The improvements can equally be exploited in an aircraft of unchanged TOGW but greatly enhanced range and/or point performance.

Engine weight thus has an important influence on the overall aircraft, but the paramount need to match the engine cycle to the aircraft mission requirements in the most effective way must not be forgotten. Modern fighters normally have a take-off fuel fraction of at least 30% of TOGW, compared with the 10% or less represented by the engine itself. Fuel consumption needs must therefore be balanced carefully against the need for maximum possible combat thrust. Even though cycle parameters and engine thrust/weight ratio are to some extent interdependent, as demonstrated in the first part of this paper, the cycle must normally be chosen in the first place to meet the mission fuel usage requirements, with thrust/weight ratio subsequently being maximised to the extent permitted by the available technology.

In this paper it has been established that technology advances within the next 10 years will make it possible for engine thrust/weight ratios of up to 15 to be achieved. Further increases to around 20 are also in prospect, in a longer time-frame, but such an expectation depends on bolder technical steps and must be regarded as much more speculative. Moreover, the fact that the benefits to the aircraft appears to follow a law of diminishing returns reinforces the indication that continuing to increase engine thrust/weight ratio must eventually cease to be cost effective. Even for the nearer term prospect, it must be recognised that the technology levels involved are very advanced and, for example, involve extremely high cycle temperatures. It may prove extremely difficult to exploit such technology developments fully while at the same time keeping adequate control over the costs of ownership.

In the current financial climate, Air Forces are becoming more concerned about reducing overall life cycle costs, especially in the light of past problems, and this has highlighted the need for a disciplined approach to engine structural development. Within the US, this approach has led to the development of ENSIP (Engine Structural Integrity Program) requirements<sup>12</sup>, in which many of the possible problems which can occur in engine service can be identified and rectified within the research, definition and demonstrator phases of a project, ie prior to full development of in-service engines. Similarly in the UK, Ruffles<sup>13</sup> has described how adequate research and development ahead of project launch is necessary to create a competitive technology base, and how failure to make that investment will increase project development costs.

So although engine technology will undoubtedly continue to proceed along the path to higher thrusts from smaller and lighter powerplants, increasing importance will be applied in the future to the reduction of life cycle costs. This could lead to future research efforts being aimed more at reducing such costs and especially in improving reliability and maintainability, rather than at simply achieving the ultimate in performance and low weight.

## 6. CONCLUSIONS

In a mixed configuration, maximum reheated engine thrust is almost solely dependent upon the level of fan pressure ratio used. Although having negligible effect upon engine thrust at the design point, increased SOT enables engine mass to be reduced through the reduction in core size. Within a conventional layout, a combination of SOT, reduced stage numbers and advanced lightweight materials for static components will enable the technology readiness for a T/W value of 15 to be achieved within a timescale of 10 years. Advances above this value will require a more radical approach to mechanical design with the widespread use of ceramics and other non-metallic materials in the rotating components. By these means values of up to 20 may be achievable, within a 20 year timescale. At a constant aircraft technology level, an improvement in engine T/W from 10 to 15 is likely to produce an overall take-off weight saving of about 10%. A further gain of 5% is likely if engine T/W is increased to 20.

Advances in materials and mechanical engineering technology will provide the greater contribution towards these improvements, but the choices of fan pressure ratio and cycle temperature will also be significant. In general, for maximum engine T/W, fan pressure ratio should be kept relatively low and SOT made as high as possible. However, because of the over-riding need to select the cycle to provide the best balance between fuel usage and thrust requirements for specified missions, achievable T/W will depend ultimately on the application for which the engine is designed.

## REFERENCES

1. Armstrong, F.W., "The aero-engine and its prospects - 50 years after Griffith", Aeronautical Journal of the Ro Aero.Soc. December 1976.
2. Kamman, J.H., Perryman, D.C., "Propulsion system requirements for advanced fighter aircraft", AIAA-82-1143 June 1982.
3. Plourde, G.A., Sims, R.E., Cea, R.A., "Fighter engine cycle selection", AIAA-83-1300 June 1983.
4. Tonskotter, H., "Aspects of advanced fighter engine design on the basis of equal technology", AIAA-84-1271 June 1984.
5. Herrmann, O., Biehl, W., "Effect of engine technology on advanced fighter design and cost", J Aircraft v 23 n 6 June 1986.
6. Lehman, C., Crafa, V.J., "Engine cycle selection for advanced technology engine studies", ASME 81-GT-191 March 1981.
7. Denning, R.M., Mitchell, N.A., "Critical propulsion system parameters for future STOVL combat aircraft", American Helicopter Society. 42nd Annual Forum Proceedings. June 2-4 1986 PP1047-1056 Vol II.
8. Sagerser, D.A., Leiblein, S., Krebs, R.F., "Empirical expressions for estimating length and weight of axial-flow components of VTOL Powerplants", NASA TM X-2406 December 1971.
9. Ruffles, P.C., "Reducing the cost of aero engine research and development", Aerospace v 13 n 9 November 1986.
10. Lovell, D.A., "The application of Multivariate Optimization to combat aircraft design", RAE Technical Report to be published.
11. Dollyhigh, S.M., Foss, W.E., "The impact of technology on fighter engine requirements", SAE 851841 October 1985.
12. Tiffany, C.F., Cowie, W.D., "Progress on the ENSIP approach to improved structural integrity in gas turbine engines/An overview", ASME 78-WA/GT-13 December 1978.

## ACKNOWLEDGEMENT

The authors would like to thank Mr D A Lovell for undertaking the airframe optimization work described in Section 4.

Table 1

## 3.7 FAN PRESSURE RATIO ENGINE

Fuel Usage	Intercept Mission			Long Loiter Mission		
	75% R/H, 25% Dry			36% R/H, 64% Dry		
	Datum (T/W = 10.5)	Improved (T/W = 15)	Saving	Datum (T/W = 10.5)	Improved (T/W = 15)	Saving
Engine Mass (kg)	1662	1100	562 (33.8%)	1612	1059	553 (34.3%)
Fuel Used (kg)	4479	4196	283 (6.3%)	4220	4020	200 (4.7%)
Take-off Mass (kg)	14883	13874	1009 (6.8%)	14484	13571	913 (6.3%)
Saving Take-off mass	1.79			1.65		
Saving Engine Mass						

Table 2

## 4.5 FAN PRESSURE RATIO ENGINE

Fuel Usage	Intercept Mission			Long Loiter Mission		
	60% R/H, 40% Dry			38% R/H, 62% Dry		
	Datum (T/W = 9.0)	Improved (T/W = 13.5)	Saving	Datum (T/W = 9.0)	Improved (T/W = 13.5)	Saving
Engine Mass (kg)	2016	1262	754 (37.4%)	1969	1281	688 (34.9%)
Fuel Used (kg)	4509	4240	269 (6.0%)	4329	4187	142 (3.3%)
Take-off Mass (kg)	15303	14060	1243 (8.1%)	15163	13995	1168 (7.7%)
Saving Take-off mass	1.65			1.70		
Saving Engine Mass						



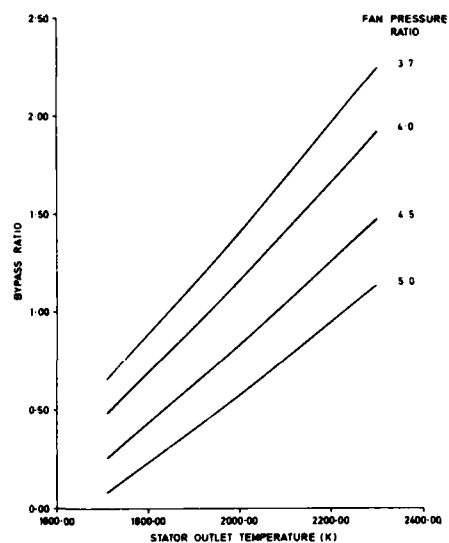


FIGURE 1: THE VARIATION OF BYPASS RATIO WITH SOT (SEA LEVEL STATIC CONDITIONS, OAPR = 24)

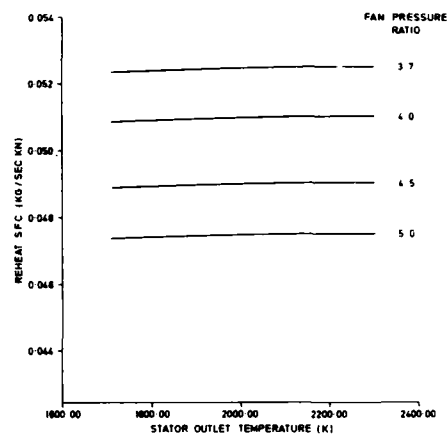


FIGURE 3: THE VARIATION OF REHEATED S.F.C. WITH SOT (SLS, OAPR = 24)

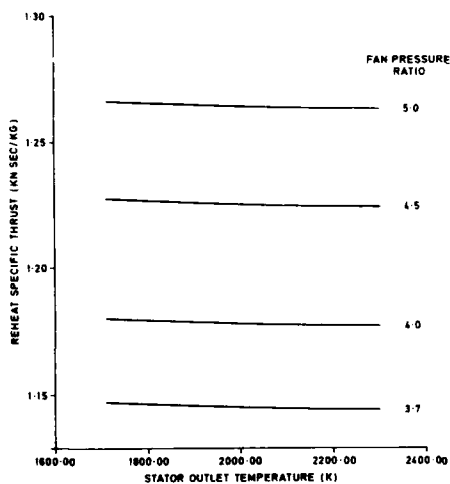


FIGURE 2: THE VARIATION OF REHEATED SPECIFIC THRUST WITH SOT (SLS, OAPR = 24)

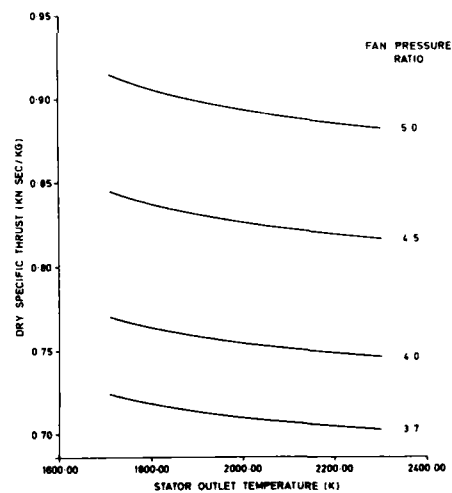


FIGURE 4: THE VARIATION OF DRY SPECIFIC THRUST WITH SOT (SLS, OAPR = 24)

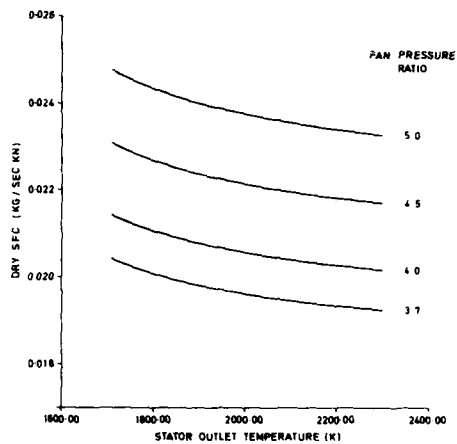


FIGURE 5: THE VARIATION OF DRY S.F.C. WITH SOT (SLS, OAPR = 24)

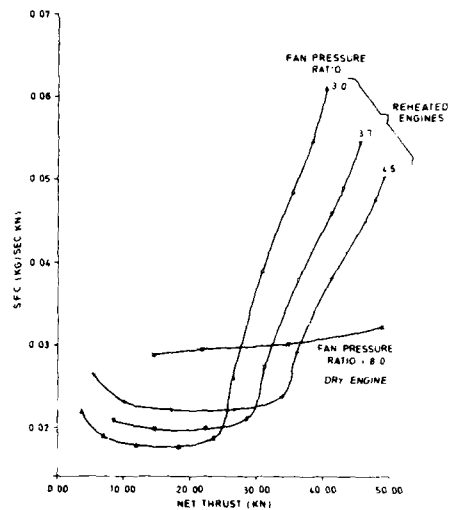


FIGURE 7: COMPARISON OF REHEATED AND DRY ENGINE S.F.C. AT SLS CONDITIONS (OAPR CONSTANT)

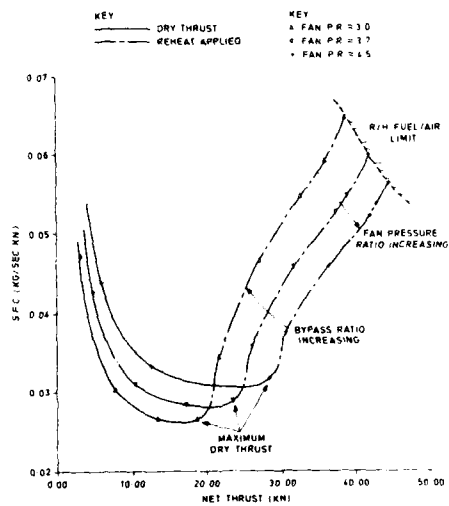


FIGURE 6: TYPICAL S.F.C. VARIATION FOR REHEATED ENGINES (MACH 0.8/SEA LEVEL, OAPR CONSTANT AT DESIGN POINT)

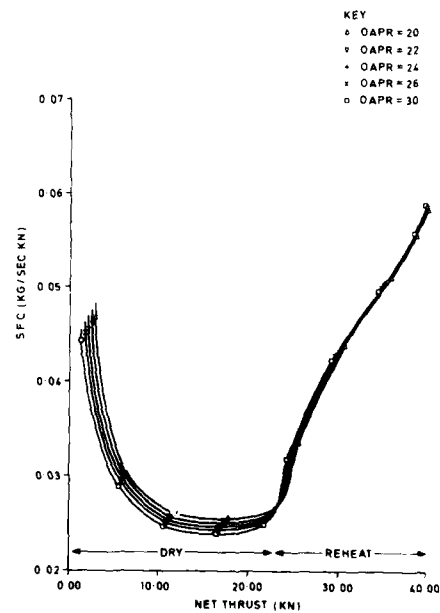


FIGURE 8: S.F.C. VS THRUST AT MACH 0.6/3.05 KM (FPR CONSTANT AT SLS CONDITIONS)

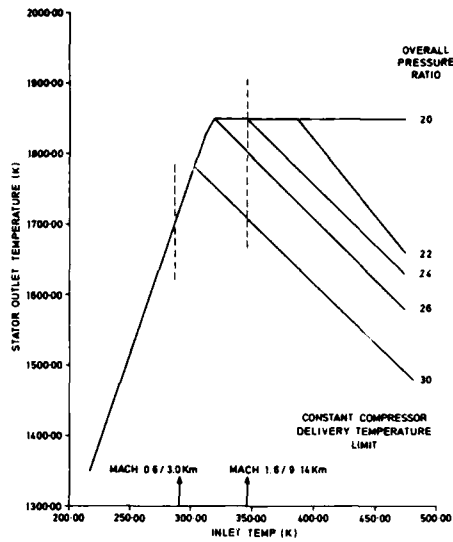


FIGURE 9: FAMILY OF SOT SCHEDULES FOR VARYING OAPR

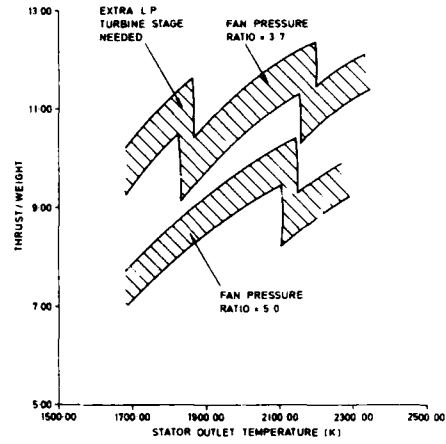


FIGURE 11: PREDICTED VARIATION OF ENGINE T/W WITH SOT

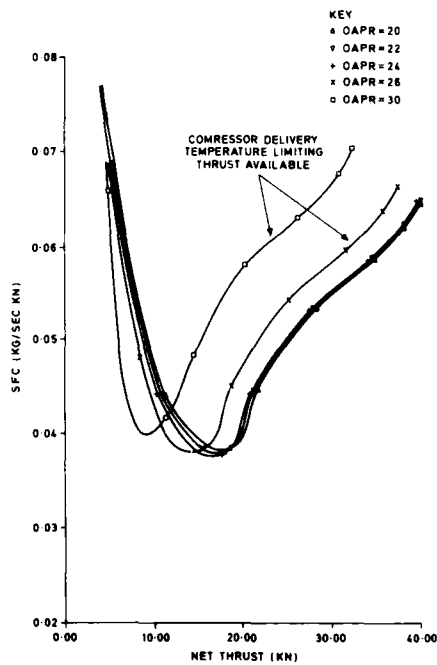


FIGURE 10: S.F.C. VS THRUST AT MACH 1.6/9.14 KM (FPR CONSTANT AT SLS CONDITIONS)

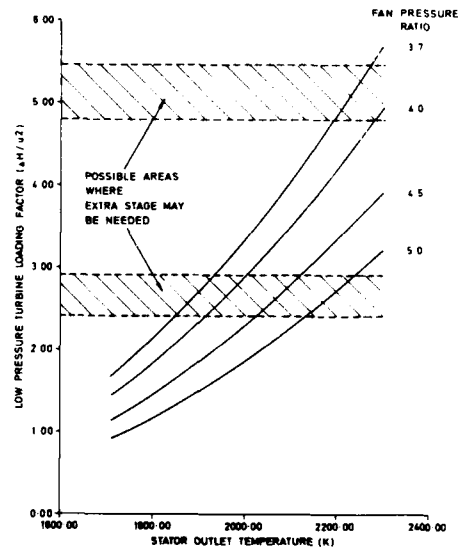


FIGURE 12: THE VARIATION OF L.P. TURBINE LOADING WITH SOT

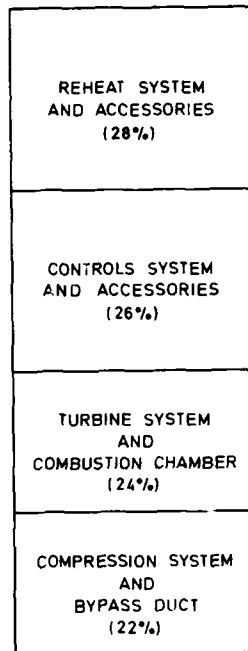


FIGURE 13: MASS BREAKDOWN OF TYPICAL REHEATED MILITARY ENGINE

### DISCUSSION

A. LARDELLIER, Fr

Does the breakdown of weight include equipments and nozzle ? Which type of nozzle was assumed ?

Author's Reply

Yes, the weight includes the nozzle and accessories. A variable area convergent nozzle was assumed, both for the weight and also for the thrust and discharge coefficients used.

**SPECIFICATION DU MOTEUR ET DE SES  
COMPOSANTS A PARTIR DES MISSIONS DE L'AVION**

par

A.Lardellier et J.Dufau  
S.N.E.C.M.A.  
Centre de Villaroche  
77550 Moissy Cramayel  
France

**1 - INTRODUCTION**

Le souci de définir avec précision les caractéristiques de taille et de cycle du moteur afin de pouvoir spécifier ses composants est depuis toujours une nécessité pour le motoriste.

La SNECMA a procédé dans le passé à des études paramétriques utilisant des modèles simplifiés d'avion. Ces études ont permis de définir dès 1976 le cycle du moteur M88 que nous connaissons aujourd'hui.

Il est apparu nécessaire de disposer d'un outil d'estimation plus performant, afin de mieux prendre en compte les exigences opérationnelles. Celui-ci fait l'objet de la présentation qui suit.

**2 - METHODE**

Le coût et la durée de développement d'un avion de combat et des systèmes associés (radar, moteurs etc.) nécessitent, dès le stade de l'avant-projet, l'utilisation d'outils puissants permettant d'appréhender suffisamment tôt les technologies nécessaires à sa réalisation. Le motoriste n'échappe pas à cette règle lors de la conception des moteurs de la génération future.

L'intégration cellule-moteurs doit être réalisée avec les objectifs suivants :

- réalisation des missions assignées à l'avion
- coûts minimaux.

Afin de répondre à ces critères, la SNECMA s'est dotée d'un outil d'aide à l'optimisation des cycles moteurs. Celui-ci permet de calculer les tailles avions et moteurs en vue de réaliser une mission donnée.

Son organigramme général est le suivant :

- calcul du cycle moteur
- calcul de la masse et encombrement moteur
- calcul de l'avion (masse et aérodynamique)
- calcul de la mission.

On notera que le calcul de la masse et de l'encombrement du moteur dépend essentiellement de son débit total ; en ce qui concerne l'avion, sa masse ainsi que ses caractéristiques aérodynamiques dépendent de la taille des moteurs, de ses capacités d'emport de carburant interne et de sa configuration aérodynamique.

En règle générale la taille du moteur (débit) est fixée par la réalisation d'exigences opérationnelles telles que distance de décollage, facteurs de charge au combat, limite du domaine de vol requis.

La taille de l'avion, à moteurs donnés dépend alors essentiellement de sa capacité à réaliser ses missions sur plein interne.

La méthode de résolution est représentée figure n° 1.

Les calculs du cycle thermodynamique ne feront pas l'objet de développement particulier au cours de cet exposé. On supposera disponibles les résultats suivants, nécessaires à la suite du calcul :

- poussées spécifiques et consommations spécifiques au plein gaz sec et plein gaz avec postcombustion,
- consommations spécifiques aux poussées nécessaires en régime de croisière,
- paramètres internes de fonctionnement tels que températures et pressions issus de chaque composant.

Nous nous intéresserons par contre au fonctionnement et aux résultats issus des autres phases du calcul :

- dimensionnement moteur,
- dimensionnement avion,
- calcul des missions.

## 2.1. DIMENSIONNEMENT DU MOTEUR

Celui-ci est effectué en deux phases :

- dimensionnement aérodynamique,
- dimensionnement mécanique.

### 2.1.1. Dimensionnement aérodynamique

Le dimensionnement aérodynamique des composants réalisé en avant-projet est basé sur des méthodes monodimensionnelles de calcul des veines des principaux composants (compresseurs et turbines).

Cependant les résultats qui en sont issus sont compatibles avec l'expérience SNECMA des constituants des moteurs militaires actuels LARZAC, M53, M88.

L'utilisateur du logiciel fournit les hypothèses servant au dimensionnement telles que :

- débit spécifique à l'entrée et à la sortie du composant,
- charge par étage (compresseurs et turbines),
- vitesse maximale en bout d'aubage,
- rapports de moyeux.

Les données supplémentaires proviennent du cycle thermodynamique. On peut citer parmi celles-ci :

- taux de compression ou de détente,
- rendement,
- débit réduit d'entrée,

au point de dimensionnement pour chaque compresseur ou turbine.

Le programme détermine alors le nombre d'étages, et la veine aérodynamique du composant, le nombre d'aubes (rotor et stator) et la vitesse de rotation.

Le dimensionnement aérodynamique est assorti de deux contraintes :

- égalité des vitesses de rotation des composants d'un même corps,
- compatibilité des veines entre les différents corps.

L'ensemble des dimensions est alors transféré aux programmes de dimensionnement mécanique.

#### 2.1.2. Dimensionnement mécanique

Outre les données géométriques issues de l'étape précédente, l'exécution de ce programme nécessite :

- la définition de la technologie de réalisation de chaque composant,
- les hypothèses sur les matériaux utilisés, en fonction de l'époque visée.

A défaut de définition explicite de ces données, le programme choisit les matériaux de chaque composant en fonction des températures internes en cherchant toujours à minimiser la masse.

Dans l'hypothèse où les régimes et dimensions des composants des ensembles tournants du moteur s'avèrent incompatibles avec les caractéristiques mécaniques du meilleur matériau disponible le programme calcule les caractéristiques du matériau pour savoir réaliser le dimensionnement mécanique. Si l'accroissement des caractéristiques des matériaux dépasse la valeur prévisible à l'horizon visé, il est nécessaire de redéfinir la veine. La logique de calcul est explicitée figure n° 2.

Les programmes aérodynamiques traités sont les suivants :

- Compresseur BP
- Compresseur HP
- Turbine BP
- Turbine HP.

Le dimensionnement mécanique porte sur :

- Compresseur BP
- Compresseur HP
- Turbine BP
- Turbine HP
- Aubes
- Carters.

Le canal de post-combustion et la tuyère ne figurent pas parmi les programmes de dimensionnement. Cependant leur masse est estimée au moyen d'une loi simple en fonction du débit moteur.

Les résultats fournis par cette phase de calcul sont :

- dessin simplifié du moteur (voir figure N° 10),
- masse du moteur,
- centre de gravité du moteur.

## 2.2. MODELISATION DE L'AVION

Au cours du déroulement de cette partie du programme sont évaluées les données nécessaires aux calculs des missions, à savoir :

- masse de l'avion,
- capacité d'emport carburant,
- caractéristiques aérodynamiques :
  - coefficient de trainée,
  - surface de référence,
  - trainées des emports externes.

Le calcul d'un avion s'effectue à partir de la taille des moteurs qui l'équipent et de la formule désirée pour la cellule (voir figure n° 3).



Outre le critère d'emport de carburant interne fixé pour la réalisation des missions qui lui sont assignées deux contraintes internes permettent de figer la géométrie :

- respect de la loi des aires,
- centrage donnant une marge statique négative donnée.

Le choix de ce critère a été dicté par la tendance actuelle sur les avions de combat et se justifie par la nécessité d'agilité au combat.

Les paramètres qui interviennent dans la réalisation d'un avion sont très nombreux aussi le programme a-t-il été conçu en vue d'offrir deux modes de fonctionnement :

- avion de géométrie externe "connue",
- avion "nouveau".

Dans le second cas, le plus fréquemment rencontré lors d'une étude paramétrique "cycle - avion - mission" les données géométriques sont calculées à partir de corrélations statistiques établies sur les avions existants.

Parmi les choix principaux offerts à l'utilisateur nous pouvons citer :

- choix de la motorisation,
- choix de la formule aérodynamique,
- choix du type et de l'emplacement des entrées d'air,
- choix parmi un catalogue de l'armement emporté et de l'emplacement de l'emport,
- choix de l'emport externe de carburant si celui-ci est nécessaire à la réalisation de la mission,
- choix du domaine de vol et plus particulièrement Mach maximum réalisable à l'altitude de 36 090 ft.

La logique de constitution de l'avion s'appuie sur des contraintes géométriques simples qui permettent d'appréhender les dimensions de chaque "partie", ainsi :

- la taille des moteurs, leur débit, leur nombre et le Mach maxi du domaine de vol permettent de déterminer la taille et la longueur des entrées d'air (fonction de leur emplacement sur la cellule) ;
- la visibilité arrière du ou des pilotes permet de déterminer le dièdre minimum de la voilure ou son allongement maximum ;
- la largeur et la longueur du cockpit sont déterminées par l'emploi de matériels existants ;
- le volume et le diamètre de la pointe doivent permettre l'utilisation d'un radar de combat ;
- la cellule doit dégager un espace suffisant à l'escamotage du train.

Les allongements, effilements et épaisseurs relatives de voilure, empennage, dérive ou plans-canards sont fixés, sauf indication contraire, par le choix de la formule aérodynamique (voir figure n° 4).

Le calcul de la géométrie de l'avion est également assorti d'une estimation de sa masse et de ses caractéristiques aérodynamiques.

L'évolution des matériaux de construction des cellules d'aéronefs nous a conduit à offrir la possibilité d'utilisation de matériaux composites sur certaines parties de l'avion.

Ce sous-programme fournit un schéma de l'avion (figure n° 11).

### 2.3. CALCUL DES MISSIONS

Les données du calcul des missions peuvent être dissociées en deux familles :

- données issues des phases précédentes,
- données propres à la définition des missions.

La première famille est constituée par :

- les performances du moteur,
- la masse de l'avion,
- la quantité de carburant emportée,
- les caractéristiques aérodynamiques de l'avion.

La seconde famille se présente comme l'enchaînement séquentiel de phases discrètes :

- décollage,
- accélération à altitude constante,
- montée à vitesse ou Mach constant,
- croisière à vitesse constante,
- largage des charges externes,
- calcul de performances ponctuelles,

(vitesse ascensionnelle, marge et limite de manoeuvre).

Les caractéristiques de chaque phase de mission peuvent être soit des données du problème (cas de la recherche d'un cycle et d'un avion adapté) soit des inconnues (recherche de l'impact sur la mission de variations de caractéristiques moteur par exemple).

### 2.4. RESULTATS

Pour un cycle donné les résultats sont constitués par :

- la taille du moteur et sa masse,
- un plan simplifié de la veine sur lequel figurent néanmoins les principales caractéristiques des composants (nombre d'aubes, matériaux, contraintes et température métal),
- la taille de l'avion et son bilan de masse,
- un plan trois vues simplifié de l'avion.

### 3 - VALIDITE

Ce logiciel, relativement complexe, étant basé sur des lois statistiques pour ce qui concerne la définition de l'avion et de ses caractéristiques se devait d'être validé et étalonné si nécessaire sur des avions existants.

La validation, effectuée en trois étapes à porté sur :

- le calcul des masses et des capacités d'emport interne en carburant,
- la précision de détermination des caractéristiques aérodynamiques des avions,
- la crédibilité et la précision des résultats de calcul des missions.

Les deux premières étapes ont été elles-mêmes décomposées en deux. Le calcul s'est déroulé une première fois en figeant toutes les caractéristiques géométriques connues des avions sur lesquels a porté la validation puis une deuxième fois avec en unique donnée les tailles, masse et débit du moteur équipant la cellule.

La troisième étape a été effectuée en ne fournissant outre les données de la mission, que les caractéristiques thermodynamiques du cycle (TEF, taux de dilution, taux de compression global, taux de PC).

Après quelques modifications, le logiciel aujourd'hui en usage fournit des résultats se situant dans une fourchette de  $\pm 5\%$  autour de la réalité, au moins en ce qui concerne les formules aérodynamiques validées :

- delta
- delta canards
- double delta canards
- aile haute en flèche + empennage.

### 4 - APPLICATION DE LA METHODE

La méthode décrite précédemment permet de réaliser d'autres types d'études que l'on peut regrouper en trois ensembles principaux :

- Missions données : cycles et avions variables
- Avion et missions figés : influence du cycle
- Avion et cycle donnés : calcul des missions.

Nous vous proposons de montrer ici trois exemples d'application de la méthode :

- influence de la masse moteur à type d'avion et mission donnés ;
- influence du taux de post-combustion sur une mission de croisière supersonique ;
- influence des paramètres de mission sur le cycle et la taille de l'avion.

#### 4.1. INFLUENCE DE LA MASSE DU MOTEUR

Il est communément admis que le coût d'acquisition d'un avion militaire est proportionnel à sa masse à vide. La recherche pour les moteurs du meilleur rapport poussée sur masse répond aussi à cet objectif. Il a paru intéressant de chiffrer les répercussions sur la taille d'un avion remplissant son éventail de missions d'une variation de masse des moteurs l'équipant. Cette évaluation a porté sur une mission d'attaque au sol de type LO - LO - LO avec un avion bimoteur de formule double delta canards en supposant que la marge statique devait être conservée.

L'augmentation de masse du moteur se traduit par une augmentation de taille et donc de masse de l'avion que l'on peut attribuer à :

- conservation de la marge statique,
- emport supplémentaire de carburant (plein interne) nécessaire à la réalisation de la mission.

Pour un avion bimoteur, on retiendra qu'une augmentation de 5 % de la masse de chaque moteur se traduit au total par + 1,4 % masse environ sur la cellule et + 2,75 % de carburant en plus soit au total 2,2 % sur la masse à la mise en route (figure n° 5).

Une possibilité intéressante du modèle est de pouvoir établir, dans le cadre d'utilisations semblables à cet exemple, des coefficients d'influence liant performances moteur, performances avion et critères de mission.

Nous avons calculé sur cette mission LO-LO-LO l'amélioration de consommation spécifique qui permettrait de compenser l'accroissement d'emport de carburant calculé auparavant.

L'augmentation de masse de mise en route est minimale lorsque l'on assure le centrage sans augmenter la capacité d'emport de carburant. Dans cette hypothèse il est nécessaire de diminuer la consommation spécifique du moteur de 1 % (voir figure n° 5).

#### 4.2. INFLUENCE DU TAUX DE POST-COMBUSTION

En règle générale, sur les avions de combat supersoniques, l'accélération et la croisière au delà de  $M = 1$  sont effectuées avec post-combustion (soit au plein gaz PC soit en intermédiaires PC). Il faut cependant remarquer que les temps de fonctionnement dans ces conditions sont restreints, les missions qui nécessitent ce type de fonctionnement étant principalement des missions de type interception à haute altitude. Le problème devient différent lorsque l'on demande à l'avion de pouvoir croiser en supersonique pendant de longues distances.

On peut alors s'interroger sur l'intérêt d'améliorer les consommations kilométriques de l'avion en adoptant des moteurs sans post-combustion. Une étude visant à évaluer les tailles des avions ainsi équipés a été réalisée au moyen du logiciel Avion - Moteur - Mission.

La mission choisie pour effectuer la comparaison se décompose comme suit :

#### MISSION CROISIERE SUPERSONIQUE

- Décollage PG PC
- Montée à l'altitude et au Mach de croisière
- Croisière supersonique sur 70 % du rayon d'action
- Combat à 36 000 ft ; M 1,8
- Retour symétrique

Deux rayons d'action ont été envisagés :

- R1 = 600 Nm
- R2 = 400 Nm.

Le Mach de croisière choisi a été M = 1,6 à Z = 50 000 ft.

Les moteurs secs double corps - double flux mélangés sur lesquels a porté l'étude sont défavorisés par l'évolution du taux de dilution dans le domaine de vol. Ceci conduit à un rapport  $F_{\text{combat}}/F_{\text{décollage}}$  plus faible que celui des moteurs avec post-combustion.

Le point dimensionnant n'est plus alors la capacité à réaliser le rayon d'action mais le facteur de charge à Z = 36 090 ft, M = 1,8.

Les tailles des avions et des moteurs strictement nécessaires à réaliser le rayon d'action ne permettent pas d'assurer le taux de virage au combat.

Les résultats figure n° 6 montrent que le gain obtenu par l'amélioration de  $C_s$  en croisière, sur la mission considérée, ne se répercutent pas sur l'avion. La cause principale est l'accroissement du débit moteur nécessaire.

#### 4.3. INFLUENCE DES PARAMETRES DE MISSION

La mission de pénétration supersonique décrite au paragraphe précédent a également servi de support à une étude visant à chiffrer l'influence sur l'avion et le moteur des deux principaux paramètres de la mission à savoir le Mach de croisière et le pourcentage de rayon d'action effectué en supersonique.

Le cycle thermodynamique des moteurs défini par :

- $\lambda = 0,3$
- $\pi_{BP} = 4,2$
- $\pi_{GL} = 26,5$
- TPC = 2100°K

a été choisi lors d'une étude préliminaire.

La formule aérodynamique de l'avion : double delta-canards ; bimoteur.

Les masses au décollage des avions obtenus sont plus sensibles au pourcentage de pénétration supersonique à effectuer qu'au nombre de Mach auquel s'effectue la mission (voir figures n° 7, n° 8 et n° 9).

5 - CONCLUSION

L'intégration dès le stade avant-projets des contraintes opérationnelles définies par les objectifs de missions et la prise en compte des caractéristiques de masse et d'aérodynamique des avions de combat, permet :

- \* de définir le cycle moteur le mieux adapté à l'ensemble des missions à réaliser,
- \* de cerner les difficultés technologiques de réalisation du moteur (matériaux, tailles),
- \* de chiffrer les conséquences d'évolutions des paramètres moteurs sur la réalisation des moteurs.

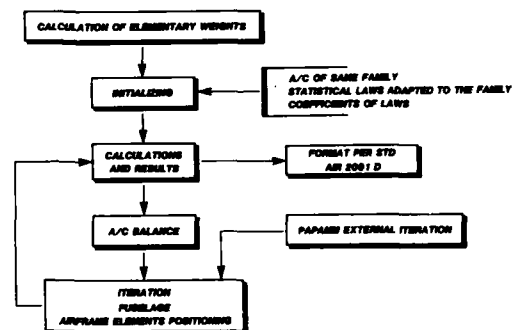


FIGURE 5 : INFLUENCE DE LA MASSE DU MOTEUR  
EFFECT OF ENGINE WEIGHT

Δ ENGINE WEIGHT	Δ AIRFRAME WEIGHT	Δ FUEL WEIGHT	MFC
0 %	+ 1.4 %	+ 2.75 %	0
0 %	+ 1 %	0	- 1 %

FIGURE 6 : COMPARAISON MOTEUR SANS/AVEC POST COMBUSTION  
ENGINE COMPARISON WITH/WITHOUT A/E

Δ A/C WEIGHT	+ 40 %
Δ ENGINE AIRFLOW	+ 100 %
Δ LOAD FACTOR	- 57 %

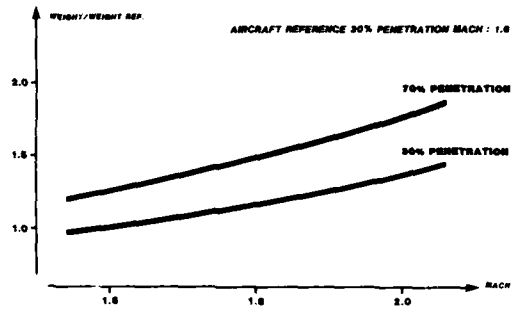
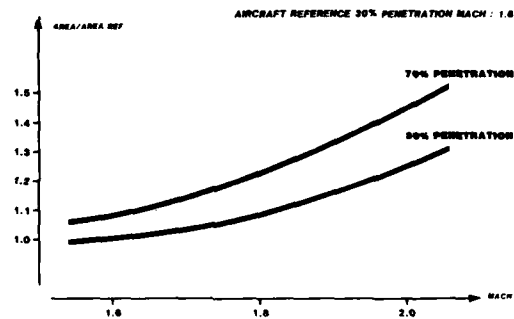
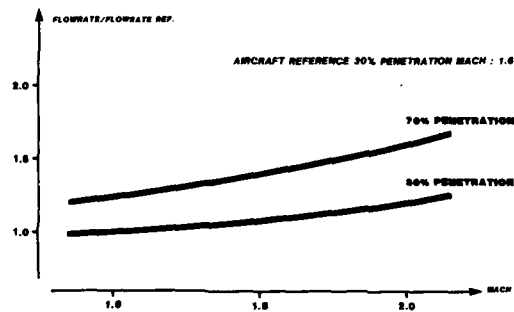
FIGURE 7 : EVOLUTION DE LA MASSE AVION  
CHANGE OF A/C WEIGHTFIGURE 8 : COMPARAISON DES SURFACES DE VOILURE  
COMPARISON OF WING AREASFIGURE 9 : EVOLUTION DU DEBIT MOTEUR  
CHANGE OF ENGINE FLOWRATE



FIGURE 10: COUPE DU MOTEUR OBTENUE APRES DIMENSIONNEMENT MECANIQUE  
ENGINE CROSS-SECTION OBTAINED AFTER STRESSING

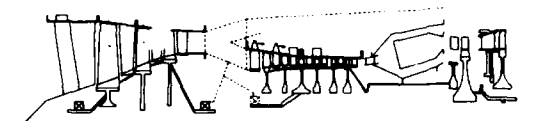
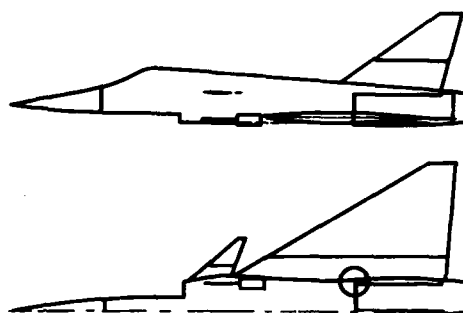


FIGURE 11 : DESSIN DE L'AVION  
AIRCRAFT CONFIGURATION



### DISCUSSION

A.S. ÜÇER, Turkey

Could you give some examples of the data necessary to characterize the aircraft and mission on the computer ?

Réponse de l'Auteur

Les données propres à la mission ne sont pas très nombreuses. Elles concernent essentiellement les performances ponctuelles, telles que :

- distance au décollage
- facteurs de charge en combat
- limites de manoeuvre

D'autres données sont relatives aux vitesses de montée de l'avion, à l'altitude de croisière et aux accélérations.

# APPLICATION OF HIGHLY LOADED SINGLE-STAGE MIXED-FLOW COMPRESSORS IN SMALL JET-ENGINES

R. Mönig<sup>\*)</sup>, K.D. Broichhausen<sup>\*)</sup>, H.E. Gallus<sup>\*)</sup>

<sup>\*)</sup>  
Institut für Strahlantriebe und  
Turboarbeitsmaschinen, RWTH Aachen  
Templergraben 55  
5100 Aachen, West Germany

<sup>\*)</sup>  
Motoren- und Turbinen-Union  
München GmbH  
Dachauer Str. 665  
8000 München 50, West Germany

## Summary

The predominant requirements on small jet-engines are high power-to-weight ratio and low specific fuel consumption in combination with structural simplicity. The consequent demands on the compressor can be fulfilled either by a conventional two-stage unit or by an extremely loaded single stage. This single stage compressors has to be able to perform a sufficiently large massflow and total pressure ratio. Consequently the application of a mixed-flow compressor with supersonic flow at rotor- and stator-inlet (supersonic mixed-flow compressor) turns out to be advantageous. The conception of a jet-engine with a supersonic compressor demonstrates the significantly reduced size compared to other engines of the same thrust class.

## Nomenclature

$C_0$	flight speed	$T$	temperature
$D$	diameter	$u$	circumferential speed
$F$	thrust	$Y$	utilizable comp. power
$F$	specific fuel consumption	$\alpha$	absolute flow angle
$H$	height	$\beta$	relative flow angle
$h$	specific enthalpy	$\nu$	hub/tip ratio
$M$	Mach number	$\kappa$	ratio of specific heat
$\dot{m}$	massflow	$\pi$	pressure ratio
$n$	rotational speed	$\eta$	efficiency
$Q$	heat of reaction		

## Subscripts

$C$	compressor	$t$	total
$CC$	combustion chamber	$0$	stagnation properties
$F$	fuel	$1$	upstream of rotor
$I$	intake	$2$	upstream of stator
$m$	mean	$3$	downstream of compressor
$m$	mechanical	$4$	upstream of turbine
$NO$	nozzle	$5$	upstream of turbine rotor
$r$	relative	$6$	downstream of turbine
$s$	isentropic		

## 1. Introduction

The overall dimensions of jet-engine compressors used in small turbojet and turboshaft engines are strongly limited by application purposes. Thus for these engines highly loaded compressor stages are required, in order to obtain a high total pressure ratio and a low specific fuel consumption.

Tab. 1 outlines the characteristic features of various small jet-engines [1,2]. The specific fuel consumption is mainly placed in the range between 105 and 130 kg/kNh. Only the two bypass-engines (K and N) have a considerably lower fuel consumption. Generally efficiency of jet-engines tends to become slightly better with increasing power. In the observed class of engines, however, a significant and uniform dependence of fuel consumption on the available thrust is not observed.

Regarding the compressor, the considered engines can be divided into two main classes. The lowest thrust class is characterized by use of single stage centrifugal compressors. Multistage compressors are commonly used in the upper thrust range beyond 2.5 kN.

Fig. 1 reveals that the massflow increases in a nearly linear way with the static thrust. The turbine inlet temperatures, commonly placed between 1040 and 1280 K, is only of secondary importance with respect to the required massflow. The engines with compara-

tively high massflow and low turbine inlet temperatures (SOT) are placed in the upper range of the screened region. Engines with higher SOT are located near the lower limiting line.

The low massflow of less than 2.5 kg/s in the thrust class beneath 1.5 kN can be easily performed by conventional single stage centrifugal compressors. The increased massflow of jet-engines with higher thrust requires the application of axial flow low pressure stages or, at least, advanced conceptions of transonic centrifugal compressors (engines S and X).

The average stage-characteristics of the various compressor units are presented in Fig. 2. Gas-generators with multi-stage axial flow compressors commonly have a stage pressure-ratio in the range of 1.2 to 1.6. Their design massflow is generally situated between 5.0 and 8.0 kg/s.

The application of two-stage axial flow/centrifugal compressors, however, leads to an average stage pressure ratio of about 2.5 and a lower massflow between 1.0 and 6.0 kg/s (exception: engine Y with a massflow of 13.5 kg/s).

The pressure ratio of single stage centrifugal compressors is generally placed beyond 3.5 (except engine A, having a pressure ratio of 2.8). In most cases their massflow is lower than 2.0 kg/s (exception: engines X and S, having a massflow of 9.6, respectively 5.8 kg/s).

Another point of interest is the utilizable power  $P_u$  added to the flow by each compressor stage (Fig. 2). For the subsequent classification a stage efficiency of 86% and an inlet temperature of 280 K is assumed. It is obvious that the power of most compressor stages in small jet-engines is located in the range of 100 to 500 kW. Only a few engines have a lower (A) or considerably higher (S, X, Y) power per stage between 1000 and 1500 kW. This category of increased power is also reached by supersonic axial flow compressors.

These engines are characterized by supersonic velocities from hub to tip in at least one axial gap of the stage. Prior developments of different compressor types at NACA (3), ONERA (4), AFARL (5) and the RWTH Aachen (6) revealed:

- \* impulse-type rotors with supersonic inlet and exit flow are appropriate for a high total pressure rise at high efficiency, but
- \* the high supersonic Mach numbers ( $M = 1.7$ ) of the absolute flow lead to high shock and separation losses in the stator and unsatisfying stage efficiency (7).
- \* Shock-rotors operating with a strong shock-wave in the inlet-section and a critical rotor outlet normally have a slightly lower efficiency, but
- \* the subsonic axial flow and moderate supersonic absolute flow ( $M = 1.4$ ) upstream of the stator leads to a superior stage efficiency and uncritical off-design performance (8).

The design point of such a supersonic axial flow compressor with shock-rotor is marked by the solid square in Fig. 2. The essential features of this compressor stage are shown in Fig. 3. The relative velocity at rotor inlet and the absolute velocity at stator inlet is supersonic. The tandem stator proved to be necessary in order to combine high diffusion with high flow turning at satisfying efficiency. The design point is marked by:

- \* rotational speed :  $n_0 = 23043$  rpm
- \* inlet Mach number :  $M_1 = 0.69$
- \* exit Mach number :  $M_{1r} = 0.48$
- \* corrected massflow :  $\dot{m} = 11.7$  kg/s
- \* total pressure ratio :  $\pi_t = 3.05$
- \* total efficiency :  $\eta_t = 82.0 \%$

These design data are validated by experimental rig-tests (9). This conception additionally promises to be convenient for compressors with an even higher specific power. For an application as single stage compressor in a small jet-engine the performance data have to be consistent with thermodynamic requirements of the engine.

## 2. Thermodynamics of small jet engines

According to the applications of small, low-cost jet-engines, certain geometrical, thermodynamical and also mechanical restrictions have to be considered. In the present case the following conditions were specified:

- \* flight mission at sea level with  $M_0 = 0.8$
- \* thrust at flight conditions  $F_0 = 2.7$  kN
- \* turbine inlet temperature  $T_{t4} = 1250$  K (uncooled blades)
- \* outer diameter  $D_{max} = 400$  mm

Regarding these data the subsequent thermodynamic study was restricted to single shaft engines. Total pressure losses in intake, combustion chamber and exit nozzle were considered according to empirical data [10]. The efficiency of the compressor stage, generally decreasing with increasing total pressure ratio, is described by an empirical function:

$$\eta_{ts-c} = 1 - C_1(C_2 + \sqrt{C_3^2 + (\pi_t - C_3)/C_4}) \quad (1)$$

where:  $C_1 = 0.120$  ,  $C_2 = 0.901$   
 $C_3 = 7.236$  ,  $C_4 = 7.521$

This total-pressure dependent maximum compressor efficiency is shown in Fig.4. Published data of investigated transonic axial and centrifugal compressor stages are marked by solid symbols. The general efficiency trend is reproduced by the assumed function. Regarding the turbine, efficiency variations have not been carried out. For design purposes the total efficiency was assumed to be 88.0 percent.

Single stage supersonic compressors of the proposed shock-in-rotor type are expected to be appropriate for total pressure ratios up to 5. With respect to a generalized optimization the compressor total pressure ratio was varied between 2 and 10.

For a given total pressure rise the same thrust may be obtained at high massflow and low turbine inlet temperature or at smaller massflow and higher turbine inlet temperature. Thus a temperature range of 1000 K to 1250 K was covered. As a result of these calculations, the overall efficiency

$$\eta_0 = \frac{F c_0}{\dot{m}_F Q_R} \quad (2)$$

and the specific fuel consumption

$$F_S = \dot{m}_F / F \quad (3)$$

is plotted versus the specific thrust

$$\sigma = F / (\dot{m} \sqrt{2c_p T_0}) \quad (4)$$

in Fig.5. Solid lines represent constant turbine inlet temperatures, broken lines refer to constant total pressure ratios. It is evident that the overall efficiency is primarily affected by the total pressure ratio. The specific thrust, however, mainly depends on the turbine inlet temperature. In order to achieve a satisfying efficiency, a minimum total pressure ratio of about 4 is required. Furthermore, it is obvious that at total pressure ratios of about 6 the decreasing efficiency of single stage compressors nearly compensates the thermodynamic benefit.

In regard of the specified performance data the necessary massflow and the specific fuel consumption can be determined from Fig.6. The total pressure ratio is varied from 4 to 6. The turbine inlet temperature covers the range between 1000 and 1250 K. In order to check the influence of leakage, a rated leakage from 0 to 3 % at the compressor outlet has been assumed. It is evident that the specific fuel consumption is affected by leakage to a high degree. Regarding a supersonic compressor with a total pressure ratio of 5:1 zero leakage leads to a minimum consumption of 141 gk/kNh. For 3 % leakage, however, the corresponding fuel consumption increases to 154 gk/kNh. With respect to the comparatively high total massflow a reduction of the rated leakage to less than 3 % appears to be probable. Nevertheless this unfavourable case was assumed for the subsequent geometry variations. In view of a low thermal turbine loading the turbine inlet temperature is chosen to be 1050 K. The necessary massflow is determined to be 8.2 kg/s.

### 3. Geometry of jet-engines with highly loaded single stage compressors

The efficiency of supersonic compressors, operating with strong passage-shocks is affected by the inlet Mach number to a great extent. The shock losses may be restricted to an acceptable level only if the supersonic inlet Mach number is sufficiently low. Thus, the following aerodynamic conditions were specified for the rotor:

- \* inlet absolute Mach number  $M_1 = 0.7$
- \* inlet relative Mach number  $M_{1r} = 1.4$
- \* inlet flow without swirl  $\alpha_1 = 90^\circ$
- \* outlet relative Mach number  $M_{2r} = 1.0$
- \* flow turning angle  $\Delta\beta = 46^\circ$

As a result, the corresponding circumferential speed at the compressor inlet can be determined from

$$v_{1m} = \frac{M_1 \sqrt{\kappa R T_{t1} / (1 + \frac{\kappa-1}{2} M_1^2)}}{\tan(\arcsin(M_1/M_{1r}))} \quad (5)$$

Conservation of energy leads to the equation for the circumferential speed at the rotor outlet:

$$u_{2m} = \sqrt{D + \sqrt{D^2 - C^2/(1-A)}} \quad (6)$$

where:

$$A = \frac{(\kappa - 1)M_{2r}^2 \cos^2 \beta_2}{2(1 + \frac{\kappa-1}{2}M_{2r}^2)}$$

$$B = \frac{M_{2r}^2 \cos^2 \beta_2 \kappa R T_{12}}{1 + \frac{\kappa-1}{2}M_{2r}^2}$$

$$C = c_p(T_{12} - T_{11})$$

$$D = (C(1-A) + B/2)/(1-A)$$

Thus, the circumferential speed at the rotor-inlet and -outlet can be determined for a given total pressure ratio, Mach number level and flow angle. Assuming total pressure rise, stage efficiency, and relative flow turning to be constant reveals that a lower circumferential speed is required in case of decreasing the relative outlet Mach number. This fact can be easily explained by the absolute circumferential speed downstream of the rotor, increasing with higher diffusion inside the rotor. Thus compressor stages incorporating shock rotors generally need a lower circumferential speed compared to impulse-type stages. Consequently the mechanical loading of shock-rotor stages is considerably lower. Nevertheless it is high in comparison to conventional axial flow compressors.

For the shock-rotor, the variation of total pressure ratio with circumferential speed, mean outlet radius and rotational speed is shown in Fig.7. The broken lines - each one representing a constant outlet radius - are of exponential shape due to the nearly quadratic dependence of rotational speed and energy transfer. The region of technical relevance for single stage jet-engine compressors is marked by screening.

The required rotational speed of the compressor can be determined by means of Fig.8. The hub/tip ratio at the rotor inlet and the absolute inlet Mach number has been varied in the range of 0.6 to 0.8. The relative Mach number is 1.4. An increase of the absolute inlet Mach number yields decreasing circumferential speed with respect to the constant relative Mach number. The also increasing massflow per unit area leads to a smaller inlet diameter at constant hub/tip ratio. Thus there are two phenomena of reverse effect on the rotational speed. In the observed Mach number range the decreasing circumferential speed is of primary importance. The rotational speed therefore decreases with increasing Mach number. For given massflow and inlet Mach number and consequently constant inlet cross-section, an increasing hub/tip ratio of course requires a larger mean radius and a lower rotational speed.

Conservation of mass additionally yields the blade height at the rotor-inlet and -outlet. The hub- and tip-radius at the rotor inlet, dependent on compressor massflow and rotational speed, is given in Fig.9. Increasing rotational speed leads to smaller inlet radius due to the constant circumferential speed predetermined by eq. (1). In the case of high massflow and high rotational speed the extremely small hub/tip ratios may cause mechanical problems. The increased blade-height, on the other side, is expected to be favourable in respect of the tip-clearance and end-wall boundary layer losses.

The corresponding properties at the rotor outlet are shown in Fig.10. The outlet diameter becomes considerably large for low rotational speeds. A comparison shows that for a given rotational speed the outlet radius is always larger than the inlet radius, due to the higher circumferential outlet speed. Thus it is evident that only a mixed flow compressor is able to satisfy all the requirements. The passage shape is influenced by the rotational speed. The difference between outlet- and inlet-radius decreases with increasing rotational speed due to the constant ratio  $u_{2m}/u_{1m}$  and decreasing radius.

Since the shaft-speed affects the turbine geometry as well, it is necessary to consider the corresponding turbine-geometry before the final lay-out. For an approximate determination of the turbine geometry, some additional conditions have to be specified:

- |  |                       |
|--|-----------------------|
| * inlet Mach number                    | $M_4 = 0.25$          |
| * stator outlet Mach number            | $M_5 = 1.0$           |
| * turbine outlet Mach number           | $M_6 = 0.4$           |
| * absolute flow angle at stator outlet | $\alpha_5 = 17^\circ$ |
| * absolute flow angle at rotor outlet  | $\alpha_6 = 90^\circ$ |

The rotational speed of the turbine is already given by the compressor speed. The assumed flow angles in combination with balance of power lead to the necessary circumferential speed at the rotor inlet. The required radius is obtained from this circumferential speed and the known rotational speed. The outer turbine diameter is chosen to be constant.

Fig.11 shows the compressor and turbine geometry of the proposed jet-engine for various hub/tip diameter ratios at the compressor inlet. The rotational speed decreases from the left-hand to the right-hand side. A higher hub/tip ratio leads to increasing outer diameter of compressor and turbine. Furthermore, the shape of the mixed flow compressor becomes more radial and the aspect ratio of compressor and turbine decreases significantly.

Additionally, a remarkable increase of jet-engine thrust can be performed by increasing the massflow. In Fig.12 the geometry of compressor-rotor and turbine is shown for a jet-engine with a thrust of 5 kN. The flow path geometry of this engine is very similar compared to the smaller jet-engine. Thus increasing the static thrust is not expected to cause serious problems.

Irrespective of thrust, the rotor passage geometry can be expected to have a significant influence on the flow losses inside the rotor. A small hub/tip ratio on the one hand will lead to a comparatively high Mach number level at the tip region of the leading edge and may therefore contribute to higher shock-losses. High hub/tip ratios, however, lead to a low blade height. Thus, losses caused by wall-, corner-, and tip-clearance effects may rise considerably. Therefore, the rotor geometries of moderate diagonal shape promise to be advantageous with respect to efficiency.

Fig.13 shows a possible lay-out of a mixed flow supersonic rotor for Freon operation. The profiles are designed along quasi-streamlines and stacked radially upon their centres of mass. The profile- and passage-design was carried out by means of a streamline-curvature calculation method. The governing equations are based on a scheme proposed by Novak /11/. Substantial modifications and extensions, however, were necessary in order to achieve stability and accuracy for transonic and supersonic flow conditions. Particularly the treatment of flow domains with supersonic axial flow, strong shock-waves and near-choking conditions was subject to further improvements /9/. Additionally, semi-empirical models were used in order to consider shock-, boundary layer-, and separation-losses /8/.

An appropriate supersonic stator with splitter-blades is shown in Fig.14. The profile angles of the stator will be exactly adapted to the measured flow properties of the rotor. Additionally, the passage- and profile-shape and the position of the splitter-blades will be optimized experimentally. Based on the preliminary dimensions of mixed-flow compressor and turbine, two small jet-engines are outlined in Fig.15. The static thrust of the smaller jet-engine (marked by screening) is approximately 3.7 kN. The second engine (hatched) has a static thrust of about 6.8 kN.

Fig.16 shows two other jet engines having a static thrust in the range of 3.7 kN. The first one uses a three-stage axial flow compressor, the second operates on the basis of a two-stage axial-flow/centrifugal compressor. The significantly lower size of the proposed jet-engine with mixed-flow compressor outlined in Fig.15 leads to a higher loading capacity and lower manufacturing costs.

#### 4. Conclusion

Single stage jet-engine compressors have to have a sufficiently high total pressure ratio in order to fulfill the established standards regarding overall efficiency and specific fuel consumption. Centrifugal compressors are generally able to satisfy these demands. Nevertheless the application is restricted to engines with low massflow and consequently low thrust. Supersonic mixed-flow compressors are promising with respect to a higher massflow and likewise high total pressure ratio. Thus the application of single stage compressors can be extended to engines with increased thrust. Furthermore, the frontal area of those engines is considerably lower compared to engines with centrifugal compressors. The overall length decreases significantly in comparison with jet-engines using multi-stage compressors. Thus mixed flow supersonic compressors are expected to be advantageous with respect to power-to-weight ratio and manufacturing costs.

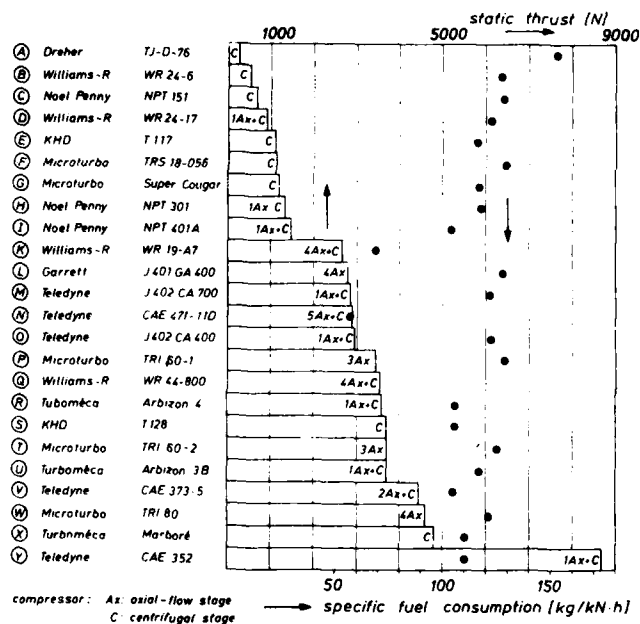
#### References

- /1/ Bridgman, L., Taylor, J.W.R.:  
"Jane's All the World's Aircraft", 1974 - 1982
- /2/ Fricke, H.:  
"Antriebe von Flugkörpern und Drohnen", DGLR 82-086

- /3/ Klapproth, J.F.:  
"A Review of Supersonic Compressor Development", Transactions of the ASME, Journal of Engineering for Power, 1961
- /4/ Paulon, J., Reboux, J., Sovrano, R.:  
"Comparison of test results obtained on plane and annular, fixed or rotating supersonic blade cascades", ASME-Paper 74-GT-49
- /5/ Wennerstrom, A. J., Buzzel, W. A., De Rose, R. D.:  
"Test of Supersonic Axial Compressor Stage Incorporating Splitter-Vanes in the Rotor", ARL TR 75-0165, 1975
- /6/ Simon, H., Bohn, D.:  
"Experimental Investigations of a Recently Developed Supersonic Compressor Stage (Rotor and Stage Performance)", ASME-Paper 74-GT-116, 1974
- /7/ Broichhausen, K. D., Gallus, H. E.:  
"Influence of Shock and Boundary-Layer Losses on the Performance of Highly Loaded Supersonic Axial Flow Compressors", AGARD 1986
- /8/ Broichhausen, K. D., Gallus, H.E., Monig, R.:  
"Off-Design Performance of Supersonic Compressors with Fixed and Variable Geometry", ASME-Paper 87-GT-116, 1987
- /9/ Gallus, H.E., Bohn, D., Broichhausen, K.D.:  
"Theoretische und experimentelle Ergebnisse der Untersuchung an zwei unterschiedlichen Überschallverdichterstufen", Jahrbuch der DGLR 1976, Nr. 83-166
- /10/ Hill, P.G., Peterson, C.R.:  
"Mechanics and Thermodynamics of Propulsion", Addison-Wesley Publishing Comp., 1965
- /11/ Nowak, R. A.:  
"Streamline Curvature Computing Procedures for Fluid-Flow Problems", Transactions of the ASME, Journal of Engineering for Power, 1967

#### Acknowledgement

The presented study has been carried out with the support of the German "Bundesamt für Wehrtechnik und Beschaffung". The authors are grateful for the promotion and the kind permission to publish this paper.



Tab.1 Survey on small jet-engines

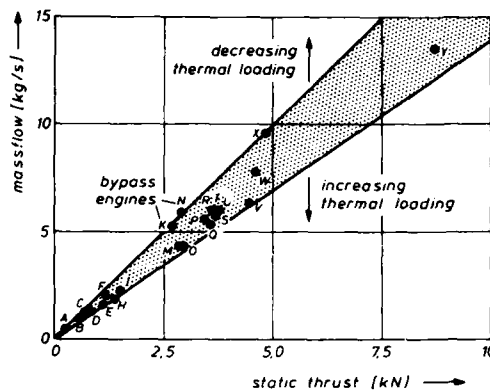


Fig.1 Thrust and massflow of small jet-engines

Fig.2 Compressor characteristics of small jet-engines

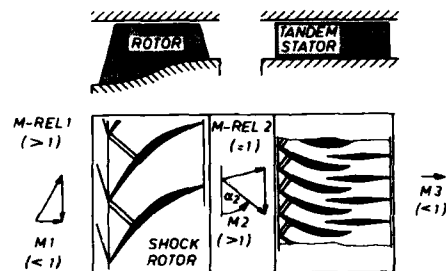
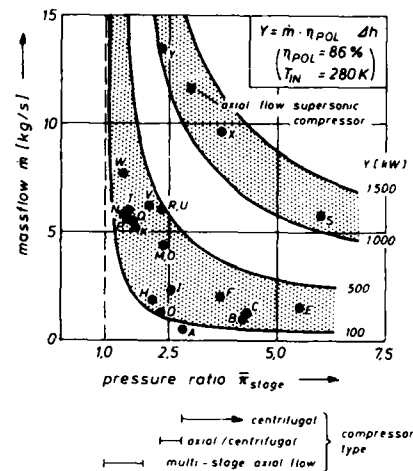
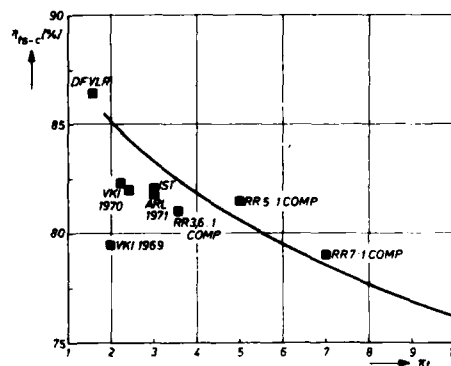


Fig.3 Axial flow supersonic compressor

Fig.4 Efficiency of single stage transonic compressors





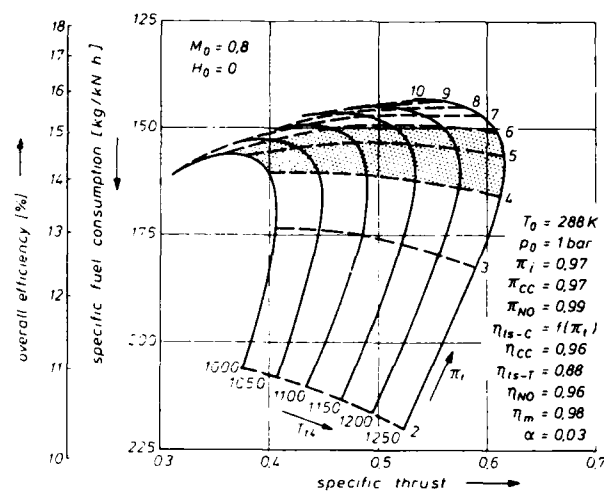


Fig.5 Thermodynamics of small jet-engines

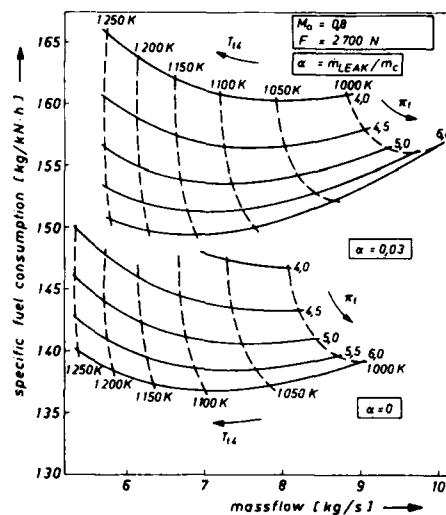


Fig.6 Leakage influence on fuel consumption

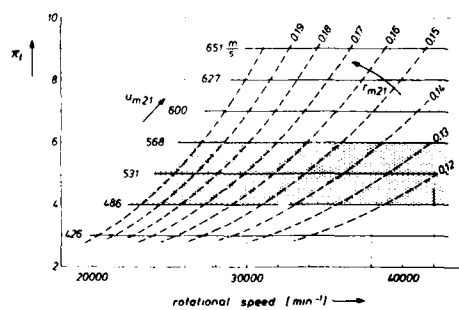


Fig.7 Rotor outlet geometry for supersonic compressors with shock-rotor

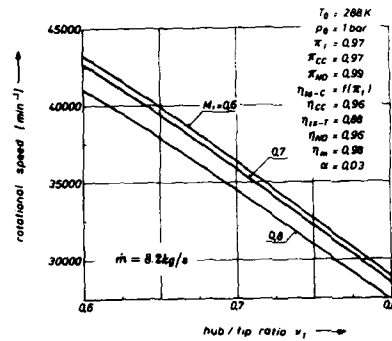


Fig. 8 Required speed for supersonic compressors

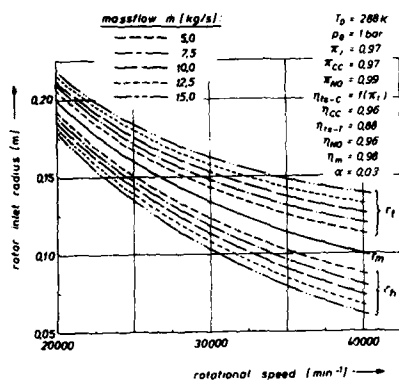


Fig. 9 Rotor inlet geometry for 5:1 compressor

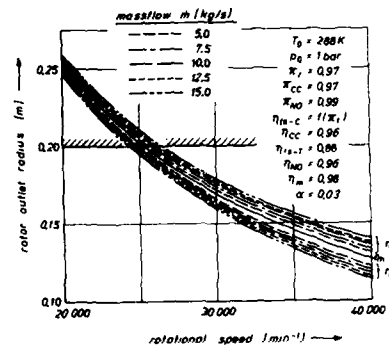


Fig. 10 Rotor outlet geometry for 5:1 compressor

Fig. 11 Geometry of the turbo-unit for 2.7 kN engine

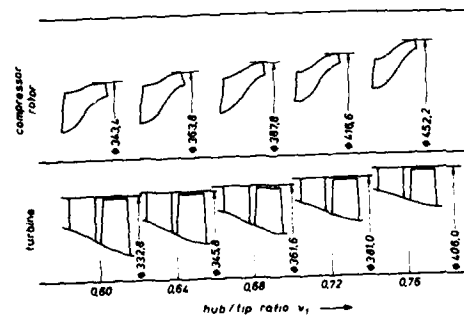
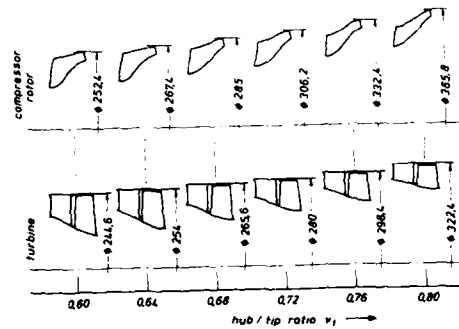


Fig. 12 Geometry of the turbo-unit for 5.0 kN engine

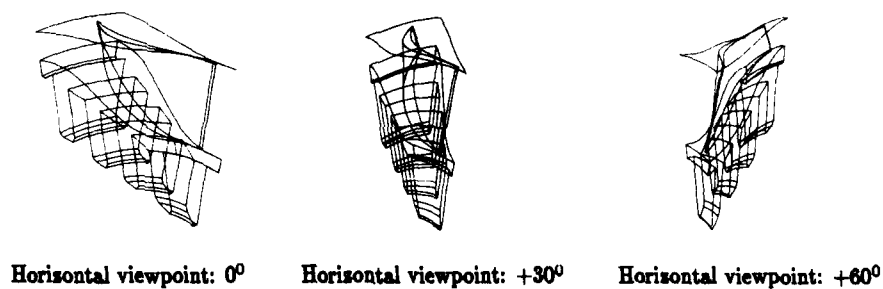


Fig.13 Design of a mixed-flow compressor rotor

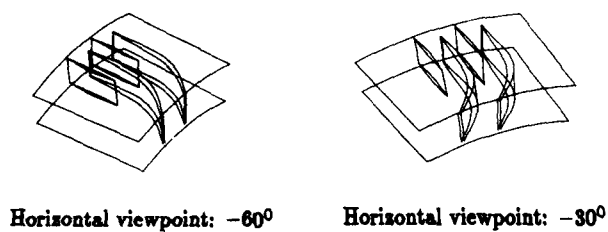
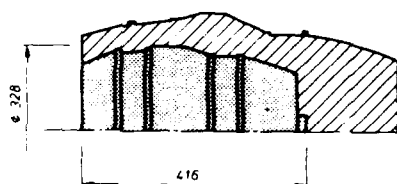
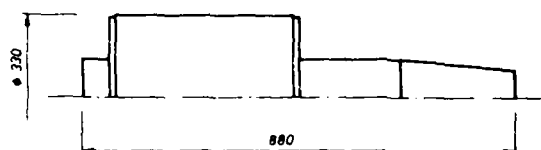


Fig.14 Tandem stator for mixed-flow compressor

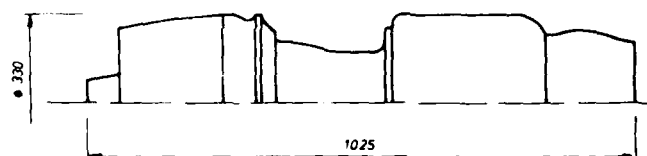
Fig.15 Small jet-engines with mixed-flow compressor



- IST - static thrust 3.7 kN
- ▨ IST - static thrust 6.6 kN



MICROTURBO TRI 60 - static thrust 3.7 kN



TURBOMECA ARBIZON IV - static thrust 3.6 kN

Fig.16 Small jet-engines with multi-stage compressor

# DISCUSSION

Y. RIBAUD, Fr

Travaillez-vous avec une société industrielle et avez-vous conçu de tels rotors avec écoulement mixte ?

Author's Reply

Concerning the first point of your question, we did not work together with an industrial company.

The mixed - flow compressor has been designed and it is in construction now. Thus, experimental investigations in our test rig have not yet been carried out.

P. BELAYGUE, Fr

Pourriez-vous nous donner quelques précisions sur les limitations de chambre de combustion que vous avez prévues dans votre étude paramétrique ?

Author's Reply

Our work primarily dealt with the design of the mixed-flow supersonic compressor. This additional viewgraph shows an example of compressor, combustion chamber and turbine. It might be necessary to use an additional diffuser downstream of the compressor unit.

# INTERET DE LA GEOMETRIE VARIABLE POUR LES TURBOMOTEURS DE FAIBLE PUISSANCE

par  
H. VIGNAU — R. RODELLAR — J. SILET  
Société TURBOMECA  
Bordes  
64320 Bizanos  
France

## RESUME

Pour réduire la consommation spécifique des turbines à gaz de faible puissance, différents cycles de turbomoteurs à turbine libre et à turbine liée sont étudiés. Le moteur à débit variable permet de réduire de manière significative la consommation spécifique à charge partielle. La variation de puissance est obtenue par changement du débit des composants à géométrie variable ; le moteur fonctionne à pression, température entrée turbine et vitesse de rotation constantes. Les hypothèses à prendre en compte pour ces systèmes à géométrie variable doivent être affinées pour préciser les gains potentiels de telles solutions. Les résultats de l'étude menée sur un compresseur centrifuge à taux de compression de 8,5 et à diffuseur radial à calage variable montrent qu'une variation de débit de 50 % peut être obtenue avec des écarts de rendement limités et une sensibilité au jeu faible.

## 1. INTRODUCTION

Il y a toujours eu une demande pressante auprès des motoristes pour diminuer la consommation spécifique de leurs moteurs et de nombreux efforts ont été déployés dans ce sens au cours des dernières décennies.

Si l'on prend par exemple le cas des applications aéronautiques, l'amélioration du rendement s'est toujours faite sur la base de cycles simples. L'élévation de la température à l'entrée des turbines, autorisée par le développement d'alliages réfractaires plus résistants, combinée à l'augmentation du rapport de pression, a conduit à des améliorations progressives de rendement (Réf. 1). Ces gains ont été d'autant plus significatifs que les progrès dans les méthodes de calcul d'écoulement et de structure ont permis d'améliorer les performances des composants.

Mais pour une puissance donnée, la diminution de taille due à l'augmentation de puissance spécifique, conduit à des limitations aussi bien en rapport de pression, qu'en rendement de composants. Et ces limitations, d'autant plus sévères que le moteur est petit, laissent présager, dans le cas de cycles simples, des gains limités.

Par ailleurs, un moteur est dessiné pour un point donné du domaine d'utilisation et les performances hors adaptation sont optimisées pour satisfaire une mission donnée. Dans le cas de la motorisation des hélicoptères, c'est surtout la consommation à puissance partielle (50 % à 60 % de la puissance nominale) qu'il s'agit de privilégier. Pour les moteurs à géométrie fixe, les possibilités de compromis sont limitées et ceci se traduit inévitablement par un accroissement de la consommation spécifique à charge partielle.

Par contre, le concept de géométrie variable, offre la possibilité de réduire les consommations spécifiques en permettant de faire fonctionner les composants plus près des conditions optimales sur toute l'étendue de la mission, que ce soit le compresseur, la turbine ou le récupérateur s'il y en a un. Mais les gains potentiels dépendent beaucoup des pertes inhérentes à de tels systèmes, qu'il s'agisse des jeux nécessaires à leur fonctionnement ou des fuites qu'ils induisent, pénalités qui n'existent pas dans le cas de systèmes à géométrie fixe.

Si historiquement la géométrie variable a été introduite dans les compresseurs multi-étages, les auteurs 1) analysent son intérêt dans le cas du compresseur centrifuge mono-étage qui a tendance à devenir le seul étage de compression des turbomoteurs de faible puissance et 2) présentent les performances d'un compresseur centrifuge à 8,5 de taux de compression obtenues au banc d'essai avec un diffuseur radial à calage variable.

## 2. TURBOMOTEURS DE PETITE PUISSANCE : SITUATION ACTUELLE ET EVOLUTIONS POSSIBLES.

### 2.1 Situation actuelle :

Tout en recherchant une augmentation de puissance spécifique et une diminution de consommation spécifique, l'architecture retenue par les constructeurs, pour les turbomoteurs les plus récents de la classe des 500 ch, est des plus simples. Il s'agit d'une configuration à turbine libre avec :

- un étage de compression centrifuge,
- un étage de turbine haute pression axiale,
- un étage de turbine de puissance axiale.

C'est le cas par exemple du TM 319 (fig. 1) développé par la Société TURBOMECA (Réf. 2 et 3).

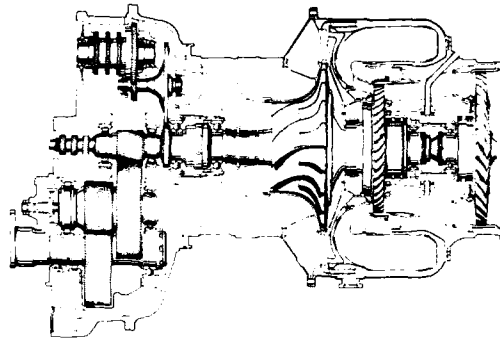
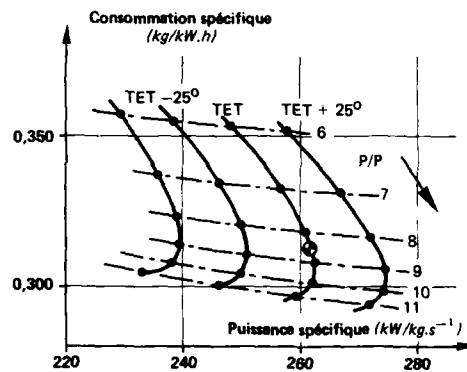


Fig. 1 - Architecture du turbomoteur TM 319

Le rapport de pression retenu, 8,5, qui est proche de l'optimum de puissance spécifique (fig. 2), peut être obtenu en un seul étage avec un bon rendement et une plage de fonctionnement suffisante sans géométrie variable. La température choisie correspond aux possibilités d'une turbine non refroidie en matériau monocristallin.

Turbomoteur à turbine libre

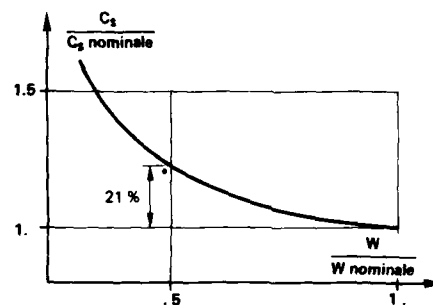
Fig. 2 - Variation de la consommation et de la puissance spécifique en fonction du rapport de pression et de la température à l'entrée de la turbine



Bien que les composants du moteur, notamment la turbine libre et le compresseur, soient optimisés pour obtenir un bon compromis à charge partielle, on note une augmentation de 21 % de la consommation spécifique à 50 % de la puissance nominale sur l'arbre (fig. 3).

Turbomoteur à turbine libre

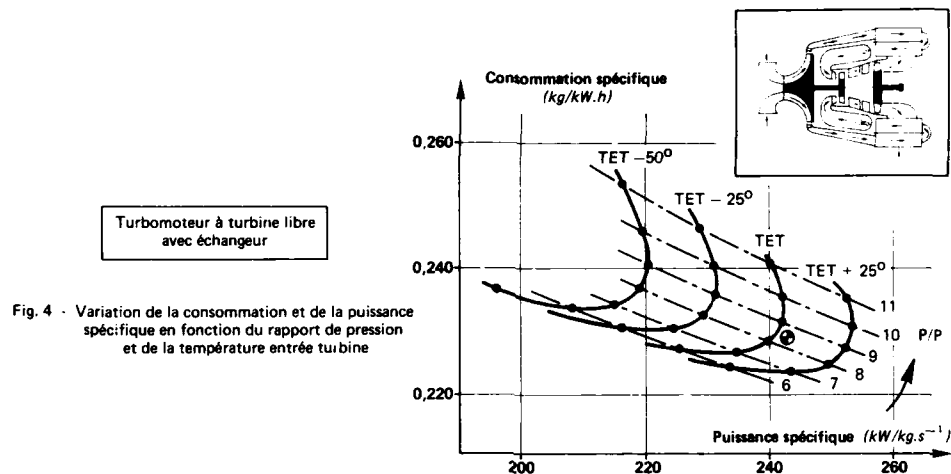
Fig. 3 - Evolution de la consommation spécifique en fonction de la puissance sur l'arbre



Différentes possibilités peuvent être envisagées pour améliorer cette situation, aussi bien pour un turbomoteur à turbine libre que pour un turbomoteur à turbine liée, dans le cas d'un cycle simple ou avec échangeur aéro. L'apport de la géométrie variable est étudié dans les chapitres suivants.

## 2.2 Améliorations possibles du turbomoteur à turbine libre.

L'adjonction d'un échangeur aval réchauffant l'air entrant dans la chambre de combustion, avec des calories prélevées à la sortie de la turbine de puissance, permet un gain significatif de consommation spécifique. Il est à noter que le rapport de pression de 8,5 s'accommode bien d'un cycle avec échangeur aval puisqu'une augmentation du rapport de pression, à même température entrée turbine, entraînerait une augmentation de consommation spécifique (fig.4).



Avec l'hypothèse d'une efficacité d'échangeur de 80 % sur la base du cycle du TM 319, le gain de consommation spécifique est de 27 % à la puissance nominale et reste presque constant sur toute la plage de fonctionnement (fig. 5).

La température à l'entrée de l'échangeur décroissant en fonction de la puissance, une amélioration supplémentaire peut être obtenue à charge partielle si l'on maintient une température plus élevée. Cela peut-être obtenu par diminution, aux faibles puissances, de la perméabilité de la turbine libre. Un distributeur de turbine libre à calage variable permet ainsi un gain supplémentaire de 7 % de consommation à charge partielle (fig. 6).

En partant de la puissance nominale, on rencontre une limitation de marge au pompage (P).

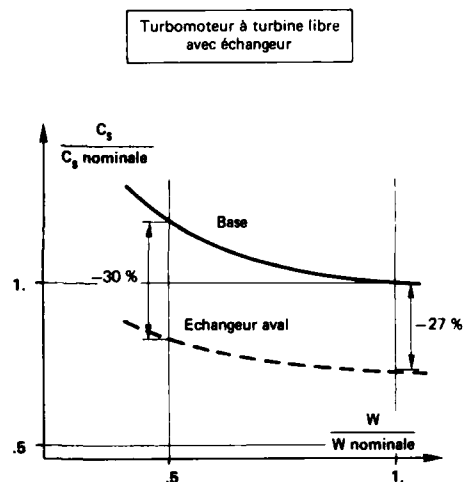


Fig. 5 - Evolution de la consommation spécifique en fonction de la puissance sur l'arbre

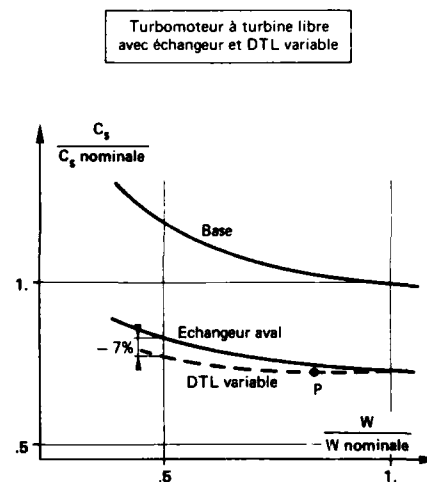
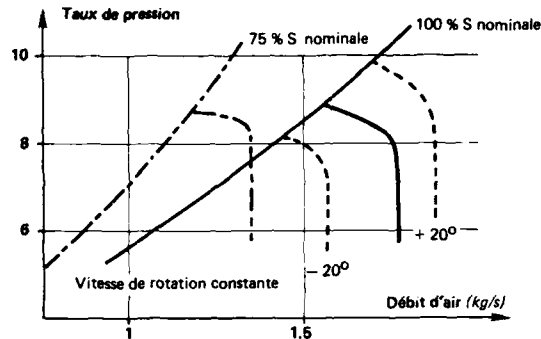


Fig. 6 - Evolution de la consommation spécifique en fonction de la puissance sur l'arbre

Pour s'affranchir de cette limitation, on peut envisager l'introduction d'une géométrie variable sur le compresseur. Comme le montre la figure 7, seul un diffuseur radial à calage variable permet de répondre à la question ; une grille de prérotation à calage variable ne permet pas en effet de modifier la ligne de pompage du compresseur.

— base  
 - - - grille de prérotation  
 - · - - diffuseur radial à calage variable

Fig. 7 - Amélioration des plages de fonctionnement d'un compresseur centrifuge à  $P/P = 8,5$



Il est ainsi possible de maintenir une consommation spécifique quasiment constante jusqu'au tiers de la puissance nominale (fig. 8), en respectant respectivement les limites de température entrée turbine et de température entrée échangeur (E).

### 2.3 Améliorations possibles du turbomoteur à turbine liée.

Le cycle du TM 319 peut aussi être envisagé pour une configuration à turbine liée avec un seul étage de détente centripète.

Sans géométrie variable, si les performances à la puissance nominale sont comparables à celles du turbomoteur à turbine libre, il n'en est pas de même à charge partielle où les évolutions du rendement compresseur à vitesse constante sont peu favorables.

Si l'on envisage par contre le même degré de complexité que précédemment, c'est-à-dire un diffuseur radial à calage variable et une variation de capacité de la turbine (Réf. 4 et 5), on peut obtenir un gain substantiel de consommation à charge partielle (fig. 9).

Bien sur, l'adjonction d'un échangeur aval permet dans cette configuration aussi une diminution de 30 % de la consommation spécifique à 50 % de la puissance nominale sur l'arbre.

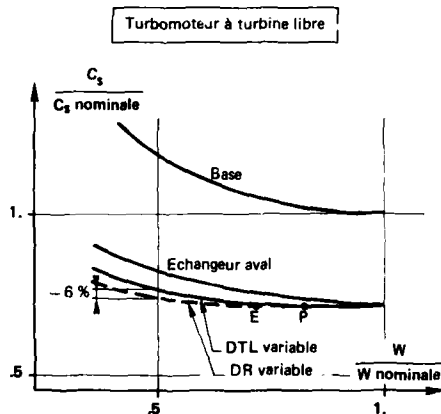


Fig. 8 - Evolution de la consommation spécifique en fonction de la puissance sur l'arbre

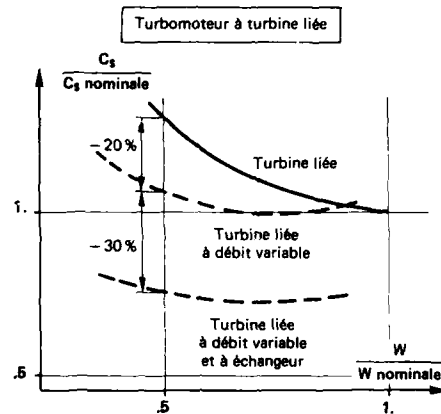


Fig. 9 - Evolution de la consommation spécifique en fonction de la puissance sur l'arbre

### 3. DIFFUSEUR RADIAL A CALAGE VARIABLE

Les études de cycles précédentes ont montré l'intérêt du diffuseur radial à calage variable et ont conduit à définir, réaliser et essayer un prototype adapté à un compresseur centrifuge à taux de pression de 8,5.

#### 3.1 Caractéristiques globales de la diffusion

Les compresseurs centrifuges à fort rapport de pression nécessitent l'utilisation d'un système de diffusion efficace à la sortie du mobile pour transformer l'énergie cinétique en pression.



Dans le cas étudié, un ralentissement très important (entre un nombre de Mach  $M_2 = 1,2$  en sortie du mobile et un nombre de Mach  $M_6 = 0,15$  à la sortie du diffuseur) doit être effectué avec une efficacité de diffusion  $\xi_{26}$  au moins égale à 0,70.

$$\xi_{26} = \frac{CP_{26}}{CP_{26} \text{ idéal}} \quad \text{avec} \quad CP_{26} : \text{Coefficient de récupération en pression statique}$$

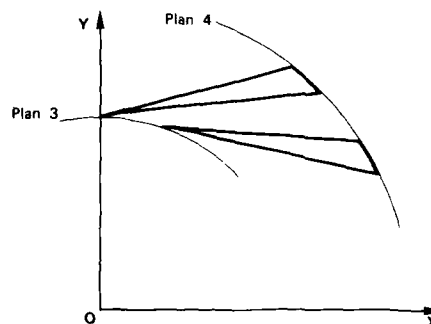
$$CP_{26} : \frac{P_{st_4} - P_{st_2}}{P_{t_2} - P_{st_2}} = \frac{\text{accroissement de pression statique}}{\text{pression dynamique à l'entrée}}$$

Simultanément, la forte composante tangentielle de l'écoulement absolu en sortie du mobile doit être annulée, ce qui correspond à une déviation de l'écoulement de  $70^\circ$  au travers de l'ensemble de diffusion.

Ces deux conditions peuvent être remplies par plusieurs types de diffuseurs : aubés, à canaux, à « pipe », à aubes en tandem, mais seuls les diffuseurs aubés ou à canaux permettent, par rotation, de faire varier la section de passage au col tout en maintenant des incidences satisfaisantes sur les aubages. Pour des raisons de tenue mécanique des aubes, un diffuseur à canaux (fig. 10) a été choisi pour expérimenter un système à calage variable.

- Nombre de Mach à l'entrée  $M_3 = 1,15$
- Nombre de pales  $Z_{34} = 19$
- Rapport des sections sortie/entrée  $S_4/S_3 = 2,35$
- Rapport des diamètres sortie/entrée  $\phi_4/\phi_3 = 1,62$
- Angle de divergence du canal  $2\theta = 10^\circ$
- Diffuseur de hauteur constante  $H_3 = H_4$

Fig. 10 - Caractéristiques du diffuseur



### 3.2 Principe du diffuseur radial à calage variable

La définition du diffuseur radial à calage variable est issue de considérations aérodynamiques et d'effet de jeu.

#### 3.2.1 Aérodynamique

L'ensemble de diffusion doit rester adapté pour des variations de débit importantes. Le choix du centre de rotation de l'aubage (fig. 11) doit :

- limiter les variations d'extension radiale du diffuseur lisse pour assurer son bon fonctionnement, ce qui implique de placer le centre de rotation à proximité du bord d'attaque de l'aube.
- conserver une bonne adaptation de l'aubage à l'écoulement incident dans le domaine d'utilisation, malgré la variation d'angle de calage.

La plage de débit étudiée, de 75 à 125 % du débit nominal, correspond à une variation de calage du diffuseur de  $\pm 5^\circ$ .

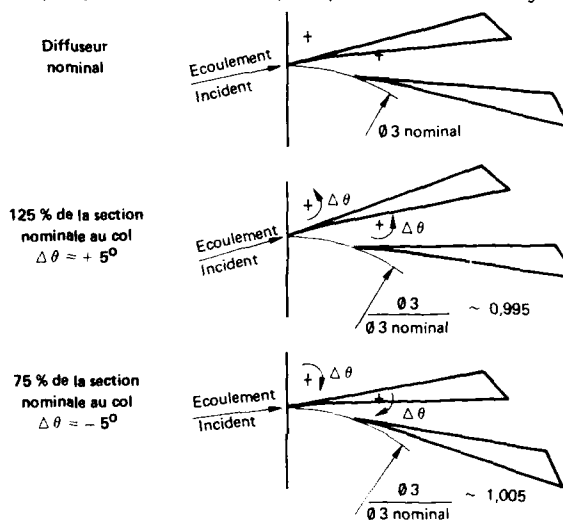


Fig. 11 - Diffuseur radial à calage variable. Choix du centre de rotation

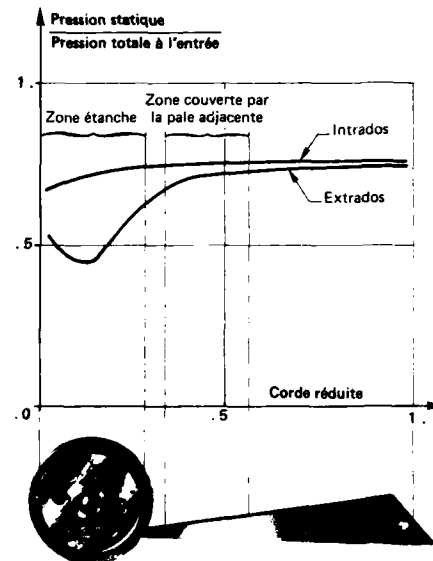
### 3.2.2 Effet de jeu

Les systèmes à calage variable essayés à ce jour, sur les diffuseurs radiaux de compresseurs centrifuges (réf. 6 et 7) et sur les distributeurs de turbines centripètes (réf. 8), sont fortement pénalisés par les effets du jeu sur les performances. La diminution du rendement constatée est de l'ordre du point par pourcent de jeu relatif aux extrémités des aubes.

Un calcul «aube à aube» transsonique (réf. 9) avec simulation des pertes a permis de calculer la distribution des pressions statiques sur l'intrados et sur l'extrados de la pale (fig. 12).

De façon à réduire les effets de jeu, des flasques tournants solidaires des aubages dans la partie captation suppriment les fuites intrados/ extrados dans la zone des forts gradients de pression. Les flasques tournants de la pale adjacente permettent de limiter les fuites dans la zone centrale. Enfin, vers la sortie du diffuseur, les fuites sont limitées par le faible écart de pression et par le laminage de l'air dû à l'épaisseur locale de l'aubage.

Fig. 12 - Distribution de pression statique dans le diffuseur au point nominal



### 3.3 Définition du montage d'essai du compresseur

Le montage d'essai a été défini afin de relever les performances du compresseur pour différents calages du diffuseur radial et pour différents jeux aux extrémités des aubages sans démontage de la machine.

Le principe de fonctionnement retenu est schématisé figure 13.

La commande en rotation est effectuée par une couronne qui entraîne l'aubage par l'intermédiaire d'un maneton.

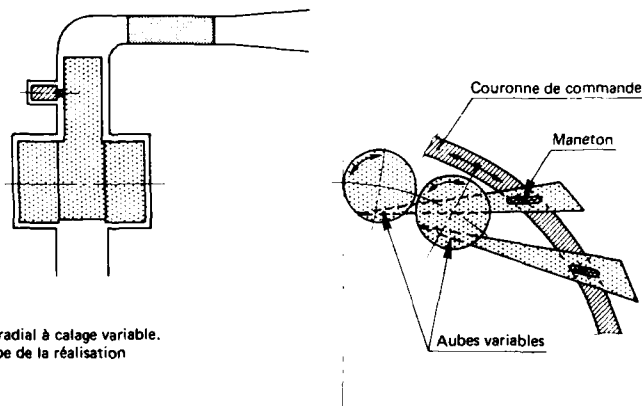


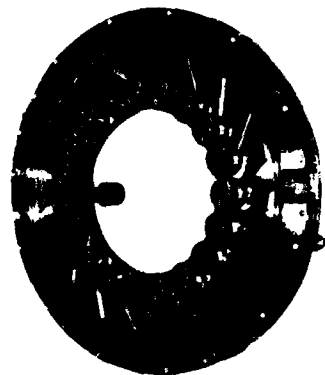
Fig. 13 - Diffuseur radial à calage variable.  
Principe de la réalisation

L'ensemble des problèmes mécaniques posés :

- efforts de commande des aubages variables,
  - dilatations thermiques relatives des différentes pièces (la température des gaz pouvant aller jusqu'à  $350^{\circ}\text{C}$ ),
  - déplacement relatif du flasque avant par rapport au flasque arrière pour le réglage du jeu aux extrémités des aubes (la mesure du jeu étant effectuée par des capteurs de proximité),
- a été pris en compte pour la définition du montage d'essai.

La figure 14 montre l'ensemble des aubes positionnées sur le flasque avant et liées à la couronne de commande.

Fig. 14 - Diffuseur radial à calage variable :  
flasque avant



### 3.4 Résultats d'essais

#### 3.4.1 Résultats globaux

Les performances du compresseur ont été mesurées pour quatre calages du diffuseur radial correspondant à 75, 85, 100, 125 % de la section au col nominale.

Pour un jeu nul aux extrémités des aubes, les différents diagrammes compresseurs sont présentés fig. 15.

Le taux de compression (total / statique) est donné pour différents débits et vitesses de rotation réduits. On remarque que le débit et la limite de pompage varient proportionnellement à la section au col du diffuseur tant que la roue mobile n'est pas bloquée. Cela confirme l'étude théorique présentée précédemment (fig. 7). Il en est de même pour le taux de pression qui varie peu avec le débit pour une vitesse de rotation donnée.

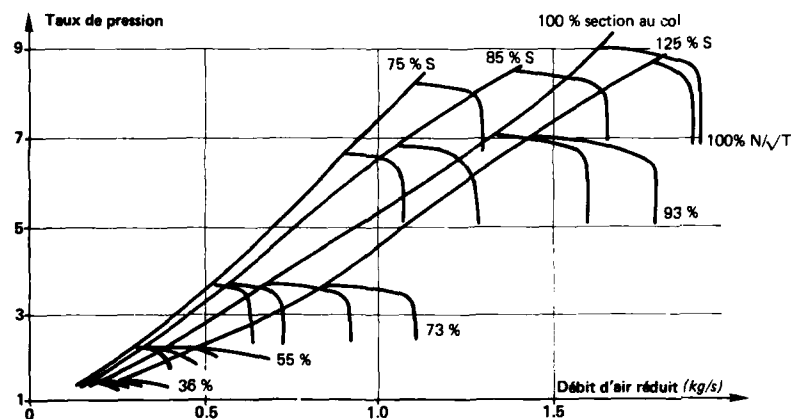
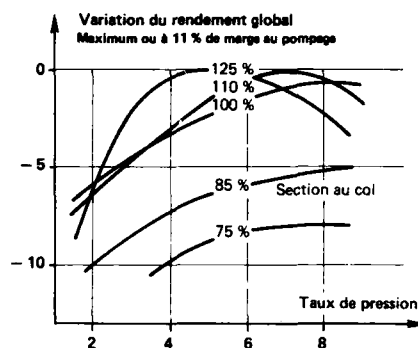


Fig. 15 - Influence du calage du diffuseur radial sur les performances

La variation du rendement (maximum ou à 11 % de marge au pompage sur chaque isovitesse) est donnée fig. 16 en fonction du taux de pression, pour différents calages du diffuseur radial.

L'optimum de rendement se déplace vers les forts taux de pression lorsque l'on ferme le diffuseur radial ; cela résulte de l'adaptation relative de la roue et du diffuseur radial.

Fig. 16 - Influence du calage du diffuseur radial sur le rendement



### 3.4.2 Analyse des résultats

L'analyse détaillée des performances montre que l'augmentation de rendement mesurée lors de l'ouverture du diffuseur radial est due aussi bien à la roue (fig. 17) qu'au diffuseur (fig. 18).

L'évolution du taux de diffusion réel  $MR_2$  de la roue ramené au taux de diffusion idéal  $MR_{2i}$  (suivant la formulation proposée référence 10) est présentée fig. 17 pour différents calages du diffuseur radial. Les performances du mobile s'améliorent par ouverture du diffuseur radial ; ces améliorations sont limitées par le blocage de l'avant roue. Pour les faibles débits, les performances du mobile sont limitées par la désadaptation en incidence.

L'évolution de la perte de charge du diffuseur radial ramenée au facteur de charge aérodynamique  $D_{34}$  (Généralisation du facteur de LIEBLEIN ; réf. 11 ; pour un écoulement radial) est présentée fig. 18 pour différents calages du diffuseur radial. Les performances du diffuseur s'améliorent à l'ouverture, essentiellement du fait de la diminution du facteur de charge aérodynamique.

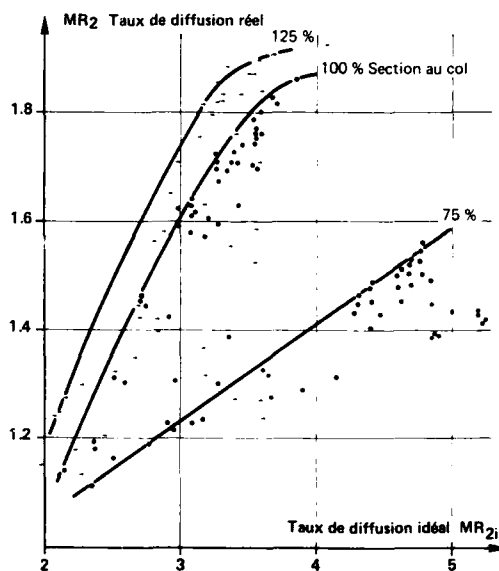


Fig. 17 - Influence du calage du diffuseur radial sur les performances de la roue

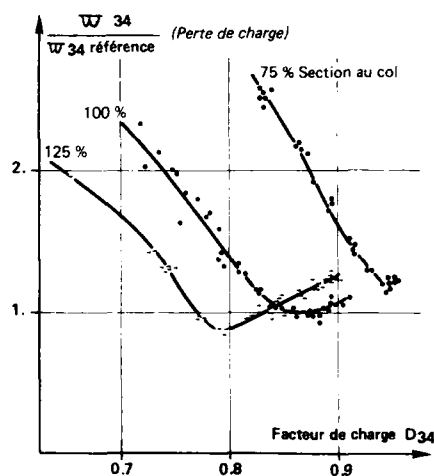


Fig. 18 - Influence du calage du diffuseur radial sur ses performances

### 3.4.3 L'influence du jeu

L'influence du jeu aux extrémités des aubes sur les performances est présentée fig. 19 pour différents calages du diffuseur radial et pour une vitesse de rotation de 93 % de la vitesse nominale.

L'augmentation du jeu amène une augmentation proportionnelle de la section au col et autorise des fuites d'air de l'intrados à l'extrados des aubes. Cela se traduit par un déplacement des caractéristiques vers les forts débits lorsque le diffuseur est bloqué (75 % et 85 % de la section au col nominale) sans toutefois dégrader le niveau de rendement. Lorsque le diffuseur n'est pas bloqué, les performances ne sont pas affectées par un jeu de 3 % aux extrémités des aubes.

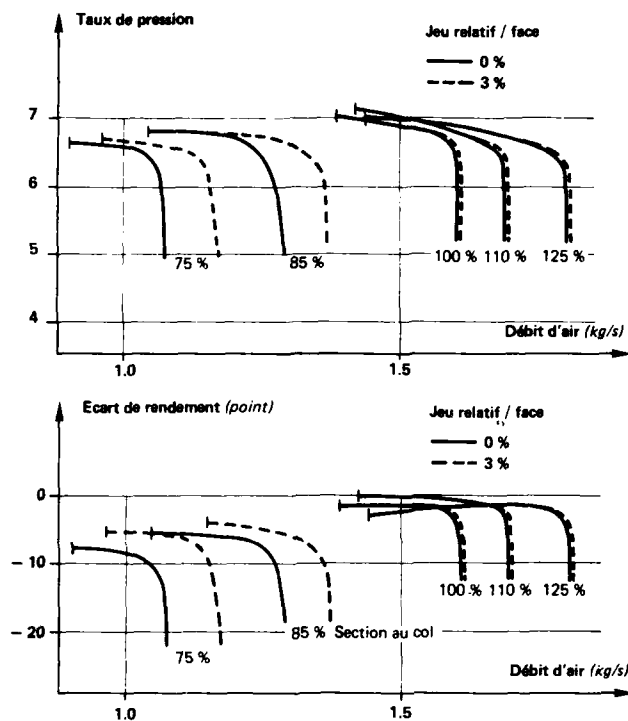


Fig. 19 - Influence du jeu aux extrémités des aubes sur les performances

## 4. CONCLUSION

Les études paramétriques effectuées sur des cycles de turbomoteurs de la classe des 500 ch, montrent l'intérêt de la géométrie variable pour réduire la consommation de carburant à charge partielle.

Dans cette taille de moteur où la compression s'effectue en un seul étage centrifuge, la combinaison d'un diffuseur radial à calage variable et :

- d'un distributeur de turbine de puissance à calage variable dans une configuration à turbine libre et échangeur aval,
- d'un distributeur variable de turbine centripète dans une configuration à turbine liée avec ou sans échangeur aval,

permet d'obtenir une consommation spécifique sensiblement constante de 40 % à 100 % de la puissance nominale.

Une réalisation de diffuseur radial à calage variable, adaptée à un compresseur centrifuge de 8,5 de taux de pression, a été faite.

Les essais montrent :

- qu'une variation de débit de 50 % peut être obtenue à une vitesse donnée pour une faible variation de rendement et de taux de pression,
- que la sensibilité au jeu est faible.

Ces résultats permettent de conforter les gains potentiels que montre l'étude paramétrique présentée.

# REFERENCES

1. P. BELAYGUE : Problèmes des hautes températures dans les petites turbomachines - AGARD Lecture Series N° 229 on high temperature problems in Gas Turbine Engines, 1977.
2. J. SILET : TM 333 and TM 319 turboshafts : Two new powerplants for helicopters ; présenté au symposium : New developments of European powerplants for helicopters - Octobre 1986.
3. M. GIRAUD : Power level influence on architecture of small helicopter turboshaft engines. ASME paper 86-GT-191.
4. C. ROGO and E.H. BENSTEIN : Variable cycle turboshaft technology for rotorcraft of the '90s - J. PROPULSION - Vol. 2, N° 1, January-February 1986, pp. 73-80
5. C. ROGO : Variable area radial turbine fabrication and test program - Report N° NASA CR-174663 - May 1984.
6. C. RODGERS : Variable geometry gas turbine radial compressors ASME Paper 68-GT-63.
7. H. GREENWALD : Vane seal - UNITED STATES PATENT OFFICE 3,489,339 - Patented January 13, 1970.
8. P. MEITNER and A. GLASSMAN : Off-design performance loss model for radial turbines with pivoting, variable - area stators - NASA TP 1708 - AVRADCOM Technical Report 80-C-13.
9. G. MEAUZE : Détermination de la région de captation d'une grille d'aubes supersoniques - AGARD 68th Specialists' meeting - 10-12 September 1986.
10. D. JAPIKSE : The computation and use of the MR 2 centrifugal compressor relative diffusion characteristic - CREARE CPD-188 - November 1977.
11. LIEBLIN, SCHWENK and BRODCRICK : Diffusion factor for estimating losses and limiting blades loadings in axial-flow compressor blade elements - NACA RM E53D01 - 1953.

## DISCUSSION

Y. RIBAUD, Fr

L'emploi d'un échangeur aval apparaît très intéressant. Avez-vous déjà essayé un tel échangeur sur turbomoteur, et si oui, quel est l'accroissement de poids du moteur lié à l'échangeur ?

Réponse de l'auteur

Un échangeur intégré à un turbomoteur n'a pas été essayé. Toutefois, les essais d'éléments d'échangeur ont montré la possibilité d'obtenir un niveau d'efficacité supérieur à 80 %. L'accroissement de la masse du moteur, due à l'introduction d'un échangeur, sera essentiellement fonction du niveau d'efficacité retenu.

## OPERATION OF GAS TURBINE ENGINES IN DUST-LADEN ENVIRONMENTS\*

By

M.G. Dunn and C. Padova  
 Calspan Advanced Technology Center  
 Buffalo, New York 14225

and

R.M. Adams  
 Hq. Defense Nuclear Agency  
 Alexandria, Virginia 22310

Abstract

Results are reported for a measurement program designed to investigate the performance deterioration of gas turbine engines and the associated auxiliary equipment difficulties when operating in dust-laden environments. Three TF33 turbofan engines and one J57 turbojet engine have been tested with two different dust blends. The predominant damage mechanism in all of the engines was compressor blade erosion. The length of dust exposure time required to cause engine damage was dependent upon power setting and dust concentration. The turbine inlet temperature for these engines was too low to realize deposition of glassy material on the hot section components.

The Environmental Control System (ECS) was monitored to ascertain the relative amount of ingested material and the size distribution of that material that makes its way to the ECS. A significant fraction of the dust is not centrifuged out of the flow and does end up in the control system air. These particles have a mean size on the order of 6  $\mu$ m.

The engine parameters most indicative of degradation have been identified and are discussed. Even with an eroded compressor significant thrust can be generated by unconventional operation of available compressor bleeds.

1. INTRODUCTION

This is the third in a series of three technical papers describing the results of a measurement program designed to ascertain the operation of gas turbine engines in dusty environments. Reference 1 presented results obtained for two different TF33 turbofan engines and one J57 turbojet engine when exposed to a single dust blend. The TF33 turbofan is a derivative of the J57 which evolved by removing the first three stages of the J57 compressor and replacing them with two fan stages. The third stage turbine of the J57 was enlarged and an additional low pressure stage was added. The J57 compressor has basically the same flow path as the TF33 aft of the fan stages, but the high pressure compressor blades are constructed of steel instead of titanium for the models tested. It was initially thought that perhaps the titanium was more susceptible to erosion than would be the steel blades. This did not turn out to be the case as is described in (1). Upon completion of the first turbojet measurements, the engine was torn down and the results presented in (1) concentrated on the damage sustained by that engine. The principal damage mode was compressor blade erosion. Previously reported (3-5) encounters with dust clouds involving T56, RB.211, and JT-9D engines resulted in significant glassy deposits on the hot section components becoming the foremost damage mode.

It is also important to develop a predictive capability so that one can extrapolate the results reported in (1) to other engines and other operating conditions for which data are not available. Detailed measurements of compressor and turbine erosion are available as a result of this measurement program because one of the TF33s and the J57 were both torn down for detailed inspection. Refurbished blades as well as new blade profiles were provided so that comparisons of the wear characteristics could be made. Reference (2) provides a discussion of the analysis effort.

The technology program currently underway at Calspan in the area of propulsion research utilizes a unique facility that allows one to subject operating engines to adverse environments without endangering either an airplane or a flight crew. Reference (1) describes the facility and some of the results obtained from the first two TF33 turbofan engines and the J57 turbojet engine. Reference (2) describes the analysis effort that was undertaken to extrapolate the results to other engines and other operating environments. The purpose of this paper is to discuss results obtained for a third TF33 operated at conditions similar to one of the previous TF33s but with a dust mixture significantly different than used in (1).

\*The research reported in this paper was sponsored by the Defense Nuclear Agency under contract DNA 001-83-C-0182.

This paper also addresses the results from tests where the engine high pressure compressor bleed air was sampled for dust. From previous reports of aircraft encounters with volcanic clouds (3-5) it is known that a portion of the engine ingested material ends up in the environmental control air supply. For all of the encounters, the crew has reported an acid-like smell with other indications of the volcanic cloud. For the engines used here, the air supply for the cabin air conditioning system is taken downstream of the 16th stage compressor from the diffuser casing at a location on the outer shell. The necessary plumbing was installed on one of the TF33 engines so that samples of the material contained in the compressor bleed air could be collected and analyzed. In addition, the same sampling system was used to collect samples of material leaving the fan discharge for later analysis. The results of this analysis will be described later in this paper.

The remainder of this paper will provide a very brief summary of the experimental technique, a summary of the material composition, a discussion of results and a set of conclusions and recommendations.

## 2. EXPERIMENTAL APPARATUS AND TECHNIQUE

A sketch of the dust injection system, the dust tube, and the engine mounting system as they are located within the engine test cell is given in Figure 1. The primary components of the dust ingestion system are the reservoir, the weighbelt feeder, the compressed air system, and the dust tube. A bellmouth is placed at the entrance to the dust tube to help with flow quality. The engine is mounted from an H-frame and is independent of the test stand as illustrated.

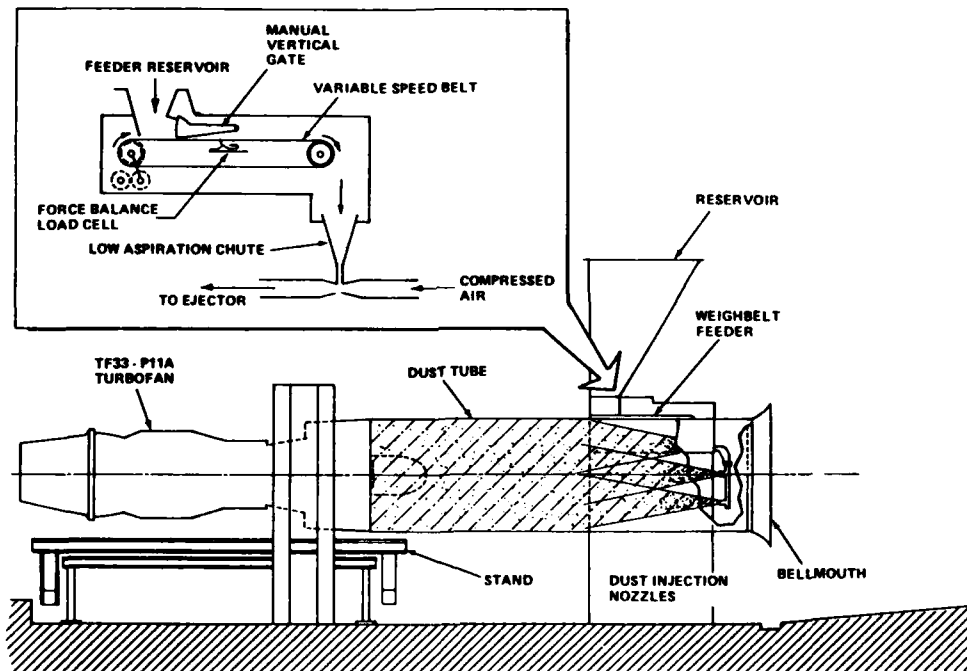


Figure 1 Schematic of dust injection system.

### 2.1 The TF33-P-11A Engine

The particular engine of interest in this program was the TF33-P-11A turbofan built by Pratt/Whitney Aircraft. To subject this engine to the proposed environment one needs: (1) a substantial thrust bed, (2) a substantial enclosure to protect the surroundings in the event of a catastrophic engine rupture or fire, (3) a noise suppression structure to attenuate the engine noise level emanating from the fan, the core, and the jet exhaust, (4) a cell which provides a sufficient flow of well-behaved air, and (5) an appropriate fuel storage and delivery system.

The TF33-P-11A engine used here was taken from an RB-57F aircraft. The TF33-P-3, P-5, and P-9 engines are currently in use on the C-135B, the EC-135B and C, and the B52-H aircraft. The TF33-P-7 and P-7A engines are used on the C-141 and the TF33-PW-100A engine is used on the E-3A. The sea level static takeoff parameters for the P-2 model are approximately 8,200 Kg (18,000 lbs) thrust, inlet airflow of 209 Kg/s (460 lb/s), bypass



airflow of 120 Kg/s (264 lb/s), turbine inlet temperature of 870°C (1600°F), turbine discharge temperature of 480°C (895°F), and compression ratio of approximately 13.5:1. The engine is equipped with an intercompressor bleed valve which is used to increase the surge margin at low speed. Some models of the TF33 are equipped with a bleed valve override so that the valve can be maintained in the closed position during crosswind taxi and thus avoid low speed engine surge. The TF33-P-11A is one of these engines.

## 2.2 The Dust Injection System

The dust injection system used here is the same system that was described in (1) and sketched in Figure 1. A 3.65m (12 ft) long dust pipe provides a conduit to the engine face. The dust pipe contains a cluster of six nozzles through which the dust is introduced at the upstream end. This combination of multiple nozzles and length of dust pipe is used to establish a uniform and equilibrated dust cloud just upstream of the fan face. It is important that the velocity of the dust particles be in equilibrium with the local velocity of the air stream ahead of the engine face in order to correctly simulate the encounter with a stabilized cloud. From this initial state of dispersion, the air and the dust particles are accelerated and turned by the bullet nose to the engine face similar to what occurs in flight.

The dust is delivered to each of the six nozzles as a high-loading air-particle dispersoid which is transported by compressed air. Both the particulate material and the carrier airflow are carefully metered. The carrier airflow is constant at all feed rates and engine power settings. The lines are sized to limit the airflow to 2% of inlet air and deliver the particles into the inlet air at a release velocity which is closely matched to the local value.

## 2.3 Dust Blend #1 and #2

In the series of TF33 and J57 dust ingestion tests, two different blends of dust have been used to represent dust environments. A detailed description of blend #1 was given in (1) and was composed of 1/3 Hollywood sand + 2.5/9 Corona Clay + 1/3 Mt. St. Helens ash + 0.5/9 Bentonite. The particle size distribution of each of the components in the mix is also given in (1). Blend #2 was constructed in order to increase the glass content of the mixture and to lower the melting temperature of the glass in that mixture. To achieve this purpose, the Mt. St. Helens ash was replaced with a greater amount of black scoria which was obtained from Twin Mountain quarry at Des Moines, New Mexico. An analysis of the scoria performed by the University of Nebraska and the National Soil Survey Laboratory (7) produced the result given in Table 1. On the basis of these results, it was assumed that the scoria glass fraction was on the order of 85%.

Table 1. Summary of glass fraction analysis for black scoria.

Glass Fraction - University of Nebraska		
250 $\mu$ m portion:		
	glass for sure :	76%
	glass likely but too opaque :	7.3%
	partly glass (nitrophere) :	3.3%
	crystalline for sure:	14.4% (plagioclase and pyroxene)
	nominal glass fraction :	80 - 85%
Glass Fraction - National Soil Survey Laboratory		
40%	100 to 250 $\mu$ m size	: 94% glass (37.6% glass)
22%	47 to 100 $\mu$ m size	: 88% glass (19.4% glass)
35%	< 47 $\mu$ m size	: 70% glass (26.6% glass)
100%	weighted sum 83.6% glass fraction	

The next important matter was to specify the appropriate mixture to be used for the engine measurements. This blend was specified by RDA (G. Rawson) (8) and is given in Table 2. As was noted earlier, the intent of this new blend (blend #2) was to increase the glass content from approximately 8% to approximately 34% and to significantly reduce the melting temperature of the glass in the mixture.

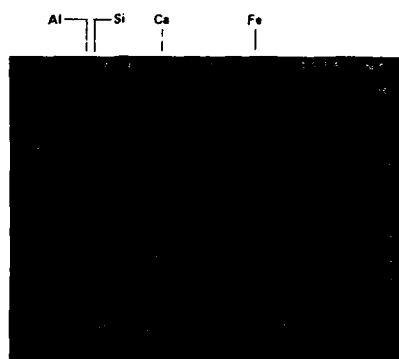
Figures 2(a) and (b) are a micrograph of the scoria magnified 100 times and the elemental composition spectrum of the scoria. The elemental spectrum is consistent with the University of Nebraska analysis illustrating prominent peaks at silicon, aluminum, calcium and iron. Figures 3(a) and (b) are a micrograph and an elemental composition for Mt. St. Helens ash. Comparison of Figure 2(a) with Figure 3(a) illustrates that the Mt. St. Helens ash can reasonably be represented by a sphere whereas the scoria has the shape of platelets.

Table 2. Definition of blend #2 for use in TF33-P-11A engine.

<u>Hollywood Sand</u>		
premix recipe:	15% of	<106 $\mu\text{m}$ size bin
	85% of	106 $\mu\text{m}$ to 250 $\mu\text{m}$ size bin
<u>Corona Clay</u>		
premix recipe:	75% of	<106 $\mu\text{m}$ size bin
	25% of	106 $\mu\text{m}$ to 250 $\mu\text{m}$ size bin
<u>New Mexico scoria</u>		
premix recipe:	100% of	<250 $\mu\text{m}$ size bin
<u>Bentonite</u>		
as available:	100% of	<106 $\mu\text{m}$ size bin
Mixing recipe of premixed materials above:		
26% Hollywood sand + 26% Corona clay + 42% scoria + 6% Bentonite		



(a) MICROGRAPH OF SAMPLE MAGNIFIED 100 TIMES

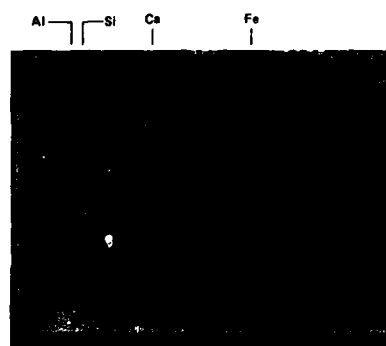


(b) ELEMENTAL COMPOSITION SPECTRUM

Figure 2 Scanning electron microscope micrograph and composition spectrum of black scoria.



(a) MICROGRAPH OF SAMPLE MAGNIFIED 20 TIMES



(b) ELEMENTAL COMPOSITION SPECTRUM

Figure 3 Scanning electron microscope micrograph and composition spectrum of Mt. St. Helens ash sample (unprocessed ash).

## 2.4 EXPERIMENTAL PROCEDURE

Prior to dust exposure, the engine was sent through a set of preliminary runs for the purposes of: (1) checking engine, instrumentation, and facility operation; (2) generating pre-exposure engine baseline data; and (3) providing operating personnel with engine handling characteristics during rapid accelerations and decelerations. Baseline data in the "as installed" configuration were important in order to monitor the engine deterioration with increased dust exposure.

To perform a dust exposure measurement, the engine throttle is advanced to the predetermined EGT value, several minutes are allowed for the engine to thermally stabilize, the dust feed system is initiated by turning on the injecting air at the MA-1A start cart and then starting the weighbelt feeder. All available engine monitoring parameters are recorded just prior to dust initiation, many times during ingestion, and immediately after the dust flow is terminated. Control cab and control room readings are taken simultaneously. Throughout the run, the engine pressure ratio (EPR) corresponding to the initial EGT set point is held constant.

The selected EGT set points were picked for descent, cruise and military rated thrust (MRT) and are based on typical in-flight data collected by the USAF Strategic Air Command. Also before each dust exposure run, dust weight flow is calculated to match the desired dust concentration. The calculation involves several steps. First, an EGT for the given TIT set point is inferred from the Pratt/Whitney-furnished EGT vs. TIT plot. Secondly, baseline plots of EPR vs. EGT/T<sub>T2</sub> are used to infer an EPR value from the measured EGT and T<sub>T2</sub>. Thirdly, the corresponding corrected engine air weight flow is determined from bellmouth pitot-probe measurements. Finally, the dust ingestion concentration is multiplied by the air volumetric flow rate to give the target dust weight flow.

When the engine had ingested the total amount of material prescribed for the run, the feeder was stopped and the injected air shut off. At the end of each exposure, a set of readings was taken before shutting down and readings were taken at two or three intermediate power settings in order to establish a deteriorated engine baseline. The engine was run through several rapid acceleration/deceleration cycles to determine the engine response. The acceleration schedule consisted of moving the throttle from idle to an intermediate power setting in six seconds, holding the throttle steady for several seconds, and returning the throttle to idle in six seconds.

## 3. DISCUSSION OF RESULTS

The results to be presented here will be divided into three basic parts; (a) a comparison between the results obtained for two TF33 engines that were exposed to significantly different dust blends but for a similar test matrix, (b) a description of the wear characteristics on the component parts for one of the TF33 engines using photographs taken during the tear down, and (c) a discussion of the ECS and fan bypass sampling.

### 3.1 Results obtained using two TF33's and two dust mixtures

This section of the paper will describe the results obtained for the two TF33 engines when they were subjected to different dust blends. One of the engines that will be discussed here was tested in a group of two TF33s and one J57 all exposed to the blend #1 mixture. This particular engine (TF33 engine #2) experienced a test matrix similar to that of TF33 engine #3 the last engine tested. Engine #2 was exposed to the dust mixture described earlier as blend #1. The primary damage mode for all of the engines exposed to this mixture was compressor blade erosion. However, on the basis of in-flight experiences (3-5), deposition of glassy material is known to occur on hot section components during encounters with volcanic material. Late in the measurement program, it was determined that the Mt. St. Helens ash was composed of about 25% glassy material instead of the initially believed 80%. This raised the obvious question regarding the results obtained with these engines; did glassification not occur because the TIT was too low or did it not occur because the glass concentration of the blend was too low?

The third TF33 was therefore dedicated to a glassification study. The question to be answered was: at the operating temperatures of the TF33 engine, will naturally occurring glass melt in the combustor and subsequently deposit on the hot section components of the machine? For this purpose, the Mt. St. Helens ash was replaced with a low melting temperature glassy material, black Twin Mountain scoria, and the relative fraction of the scoria in the mix was increased. The new mixture to be used for TF33 engine #3 was termed blend #2. Viscosity-temperature calculations were performed by Cranmer (6) demonstrating that the viscosity of black scoria in the 2000°F temperature range was on the order of 50 times less than that of the Mt. St. Helens ash. The test matrices to which engine #2 and engine #3 were subjected are given in Tables 3 and 4, respectively.

Table 3 Dust ingestion matrix for engine #2.

Run #	Load kg	Conc, mg/m <sup>3</sup>	Exposure Time		Power -	TIT °C	EGT °C
			This run, hrs.	Cum. Hrs.			
61	26	120	0.38	0.38	MRT	918	477
62	34	240	0.25	0.63	MRT	875	463
63	33	480	0.125	0.76	MRT	873	461
64	80	240	0.75	1.51	cruise	679	340
65	140	240	1.40	2.91	cruise	677	338
66	200	480	1.0	3.91	cruise	682	343
70	27	120	0.52	4.425	cruise	715	363
71	26	-	0.30	4.725	idle	530	265
Total dust load = 566 kg Total exposure time = 4.725 hrs							

Table 4 Dust ingestion matrix for engine #3.

Run #	Load kg	Conc, mg/m <sup>3</sup>	Exposure Time		Power -	TIT °C	EGT °C
			This run, hrs.	Cum. Hrs.			
98	47.7	480	0.25	0.25	Cruise	682	344
99	94.5	900	0.25	0.50	Cruise	682	344
100	67.3	480	0.25	0.75	MRT	918	477
101	129.1	900	0.25	1.00	MRT	918	477
103	49.5	480	0.25	1.25	Cruise	682	344
Total dust load = 388.1 kg Total exposure time = 1.25 hrs.							

### 3.2 Description of engine damage

At the conclusion of run #71, engine #2 had ingested 566 kg of blend #1 over a time period of 4.725 hours. Because the engine is disassembled from the tail cone towards the fan, the discussion of results will also proceed in that direction. The damage description will be illustrated with photos taken from the tear down of TF33 engine #1; TF33 engine #2 was not disassembled but a borescope inspection revealed very similar damage. The first hot section components to be removed were the low-pressure turbine stages and nothing unusual was observed with these parts except for a light dusting of dirt on the blades which could easily be removed with the finger. The high-pressure turbine rotor was the next component removed and it also had a light layer of dust on the blade surface as shown in the photograph of Figure 4. The most interesting feature of this photograph is not the dust, but rather the manner in which the dust illustrates the flow pattern over the suction surface of the rotor blades. The dust appears to collect only in the midspan region of the blade.

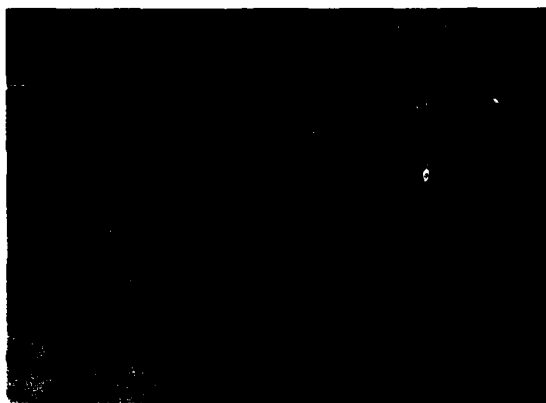


Figure 4 Photograph of HP turbine rotor.

The HP nozzle guide vane (NGV) has a thermal barrier coating and compressor discharge air is directed through an internal cavity of the vane to provide forced convection cooling. The only influence of the dust on the NGV was to remove a portion of the thermal barrier coating in the stagnation region of the vane as shown in the photograph of Figure 5. There was also a light dusting of material on the suction surface of the NGV that could easily be removed. However, no evidence of glassified material was found on the NGV surfaces.



Figure 5 Photograph of HP turbine nozzle guide vane.

The combustor was then removed and found to be in reasonably good condition. No evidence of glassified material was found anywhere in the combustor system. There was a light dusting at one location in the #8 combustor can as shown on the photograph of Figure 6. This material was loose and did not appear to have any adverse influence on the operation of the device. Figure 7 is a photograph of one of the burner nozzles that again illustrates a light dusting of material, but nothing of sufficient quantity or solidity to be troublesome. The small diameter tubing leading to the pressure transducer that measures burner pressure and then communicates with the fuel-flow controller was carefully inspected. There was a very small accumulation of light dust in this tube, but the line would have to be considered unobstructed.



Figure 6 Photograph of inside surface of #8 combustor can.

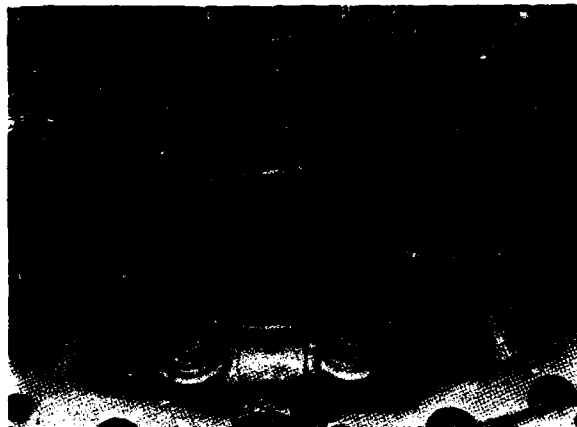


Figure 7 Photograph of burner nozzles.

The high-pressure compressor was the next major component to be removed from the engine and at this point the damage mechanism became obvious. The 16th stage compressor blade tip was seen to be badly eroded as illustrated in the photograph of Figure 8. For this stage, the squealer is nearly gone and the leading edge in the 70% to 100% span region is badly worn away. What one cannot see from the photograph is that the tip region of the blades were worn to a knife edge, so sharp that great care had to be taken in handling the rotor disc. The wear pattern on the 13th stage blade is shown to be similar to what was seen for the 16th stage. Again the squealer is nearly gone and the leading edge of the blade in the 70% to 100% span region is badly worn. Figure 9 is a photograph comparing new blades with blades taken from stages 10, 12, 14, and 15 of the engine. A blade tip tear is clearly shown in Figure 9 for the 10th stage blade. Stages 12, 14, and 15 clearly demonstrate bad tip wear with 14 and 15 being particularly bad. Figure 10 is a photograph of the suction surface of one blade from each of the HP compressor stages. Figure 11 is a photograph of the 10th stage compressor disc illustrating that the blade selected for presentation in Figure 4 was typical and not an isolated case.



Figure 8 Photograph of 16th stage HP compressor disc.



Figure 9 Photograph of 15th, 14th, 12th, and 10th stage HP compressor blades.



Figure 10 Photograph of HP compressor blades.

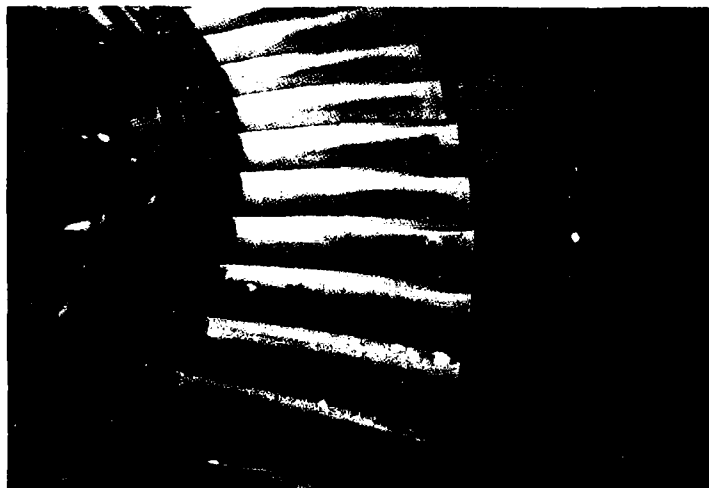


Figure 11 Photograph of 10th stage HP compressor disc.

The low-pressure blades were also worn and damaged, but not as badly as the HP blades. Figure 12 is a photograph of the 4th stage LP disc as it was being removed from the machine illustrating a saw tooth wear pattern near the trailing edge in the tip region. This particular pattern was not present on all of the 4th stage blades, but it was present on a large fraction of them.

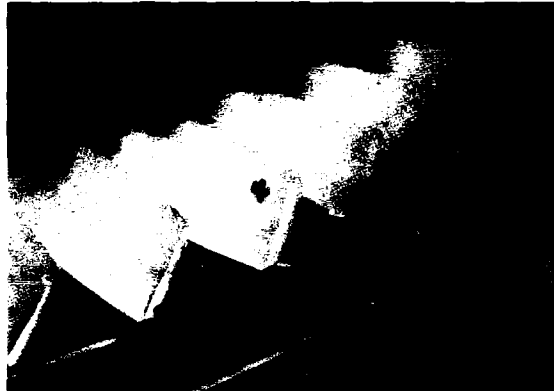


Figure 12 Photograph of 4th stage of LP compressor.

The internal cavities of the engine collected significant quantities of dirt as can be seen from the photograph given in Figure 13. This dirt was compacted but it could be easily removed by scraping with a soft object. For analysis purposes, large amounts were collected in this way.

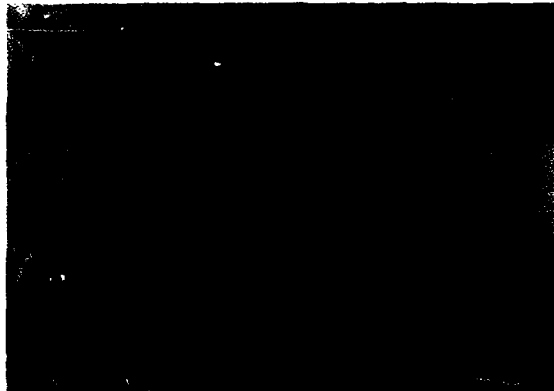


Figure 13 Photograph of internal cavities of engine #1.

Because glassification was not observed in engine #2, the blend was changed as discussed above and a third TF33 was installed in the test cell. The test conditions to which the third TF33 engine was subjected are given in Table 4. At the conclusion of Run #103, the engine had accepted a total load of 388.1 kg over a total exposure time of 1.25 hours. Of this exposure time, 0.75 hours was at cruise power and 0.5 hours was at MRT. The maximum dust concentration to which the engine was exposed was almost twice the highest value previously used. The very prominent St. Elmo's glow reported in (1) was again observed for dust blend #2. Because of the higher power settings and the higher dust loadings, the glow was much brighter than shown in the photographs of (1).

At the completion of each run, a detailed internal inspection (borescoping) of the engine was performed. Easy access was possible to the combustor, the HP turbine nozzle guide vane, the LP rotors, the 16th stage compressor blades and the 1st and 2nd stage LP compressor blades. The borescope used to perform these examinations is a 6 mm diameter Olympus unit with a controllable head. The unit is equipped with a 35 mm camera so that internal photographs of the machine could be and were taken for future reference.

Also at the completion of each dust ingestion run, the engine was required to undergo several acceleration-dwell-deceleration (6 sec - 2 sec - 6 sec duration) cycles to insure proper throttle response. First indication of significant engine damage usually surfaced during the acceleration portion of this sequence in the form of a tailpipe surge, one of which is shown in the photograph of Figure 14.



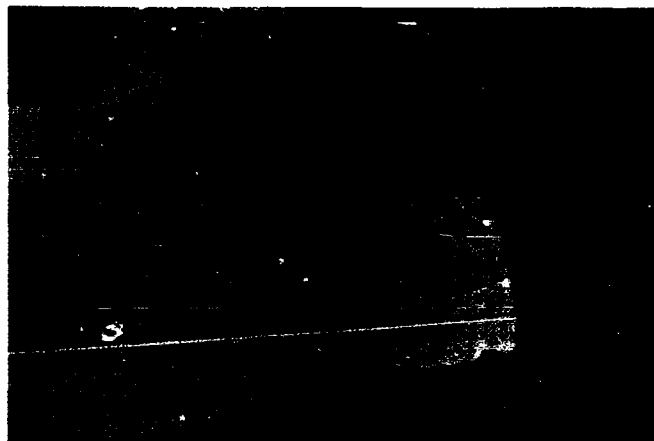


Figure 14 Tailpipe surge for TF33 engine #2.

In order to easily advance the engine to the cruise power condition for Run #103, the anti-ice system was turned on and the bleed valve was held in the open position. The power lever angle (PLA) is slowly advanced until achieving a  $P_{T7}$  of 5.5. The PLA is then retarded to obtain a  $P_{T7}$  of about 3.0 and the bleed valve is switched to the closed position. The engine can then be easily accelerated to a  $P_{T7}$  in the 8 to 9 range and the operator has good control of the engine (MRT corresponds to  $P_{T7}$  of about 10).

At no point during the measurements was glassification observed on any of the components. The primary damage mechanism for this engine was the same as it had been for the two previous TF33s and the J57, erosion of the compressor blading. The pattern of the erosion was very similar to what had been previously seen. While the engine #3 measurements were being performed, a separate combustor measurement program reported in (9) was also underway. The material used in (7) was consistent with blend #1 and blend #2 compositions. However, the turbine inlet temperature in (7) could be varied over quite a large range as could the dust concentration. As these combustor measurements were completed, it became obvious that the reason why glassification was not observed in the TF33 was that the turbine inlet temperature was about 200° to 300°F too low to melt and deposit any of the dust constituents.

By way of comparison, the two TF33 engines exposed to dust blend #1 which contained Mt. St. Helens ash accepted considerably larger amounts of dust and operated somewhat longer than engine #3 (see (1)). Engine #1 was operated at a dust concentration of 120  $\text{mg}/\text{m}^3$  and at a power setting of descent (for 1.45 hours) and cruise (for 10.42 hours) for a total loading of 860 kg over 11.87 hours of exposure. Engine #2 was operated at dust concentrations in the range 120  $\text{mg}/\text{m}^3$  to 480  $\text{mg}/\text{m}^3$  at power settings of idle (0.3 hours), cruise (3.15 hours), and MRT (0.76 hours) for a total loading of 572 kg over 4.73 hours of exposure.

The total time at MRT was about the same for engine #2 and engine #3. However, engine #2 accepted 93 kg of blend #1 during this time and engine #3 accepted 196.4 kg of blend #2. It is known from (3) that either higher power settings or higher dust concentrations have a tendency to deteriorate the machine at a more rapid rate. Because of the much higher loading for engine #3, it is difficult to be certain whether the rapid deterioration of this engine was due to the erosive characteristics of the scoria material or if it is the result of the higher concentrations at the higher power settings.

### 3.3 Dust sampling in bypass and ECS

During testing of engine #2, the by-pass air and bleed air to the ECS were sampled. This sampling was planned for the purpose of obtaining preliminary measurements of dust density and size in order to assess whether or not a threat to crew and electronic equipment in the cabin exists.

Among the questions to be answered were:

- (a) What is the level of dust release at the compressor bleed which is used for the ECS air?
- (b) Does this level scale with the dust concentration at the engine inlet?
- (c) Is there significant pulverization of the dust as it moves along the compressor?
- (d) How much pulverization takes place in the fan and how much in the compressor stages further downstream?
- (e) How does bleed dust concentration vary with throttle setting?

The sampling system which was used for these measurements consisted of a cylindrical heat resistant filter bag, a short admission line, a remotely operated valve and, in the case of by-pass sampling, a 2.54 cm (1-inch) diameter probe facing into the by-pass discharge flow. For sampling in the compressor bleed air, the admission valve was mounted directly to the bleed air flange which is located at the 10 o'clock position on the rear compressor housing. An orifice plate was used to meter the airflow in the bleed. The high pressure service airbleed level of 1.0% of core engine airflow at cruise thrust was selected as typical to evaluate airbleed content. For sampling in the by-pass discharge, the 2.54 cm probe was installed facing the stream inside the collector duct also at the 10 o'clock position. The remainder of the sampling system was the same in the two measurements. In each case the collection time was remotely controlled by opening and closing the solenoid valve at the desired times in the test sequence. The amount of dust sample collected in the filter bag was determined by weighing the filter before and after the test.

As a result of the sampling, dust amounts ranging from 10 to 235 grams were obtained from the ECS. These results are presented in Table 5. Prior to test Run #65, a limited effort was devoted to implement the sampling system for the ECS bleed. During Run #65, the first bulk sample of dust from the ECS air was obtained in the filter. Comparison of the pretest and post test weight of the filter bag indicates that 32.2 grams of dust were collected over a sampling time of 10 minutes. During this time, the engine operated at cruise power in air with a dust concentration of 240 mg/m<sup>3</sup>, resulting in a total amount of ingested dust equal to 14.5 kg (32 lb) during the sampling time. A larger sample was obtained in Run #66 at the same engine power setting but at higher dust concentration in the inlet air (480 mg/m<sup>3</sup>). In this case, the threefold increase in sampling time and twofold increase in dust density resulted in a total amount of ingested dust equal to 102 kg (225 lb). This was followed by a sequence of three runs in clear air which were scheduled to investigate the possibility of accelerating the engine beyond the critical rpm level.

Table 5 Summary of test conditions and results at dust sampling in bleed and bypass air.

Run No.	Total Dust Ingested (Kg)	Sampling Time/Location (mm)	Amount Collected (g)	Rate of Collection (g/min)
65	14.5	10/ECS	32.2	3.2
66	102	30/ECS	235	7.5
67-69	0	-	-	0
70	26.6	30/ECS	63	2.1
71	23	16/BYPASS	10	0.63

TOTAL DUST INGESTED = WEIGHT FEED RATE x SAMPLING TIME

After Run #69, before changing to the installation of the sampling system in the by-pass duct, one more collection in the ECS bleed produced 63 grams in 30 minutes during Run #70. In this run, the engine operated at cruise power and ingested 26.6 Kg (58.5 lb) during the sampling time (at a concentration of 120 mg/m<sup>3</sup>).

After Run #70, the sampling was moved to a location in the by-pass discharge duct. On the first run attempted after this change, it was not possible to accelerate the engine beyond a near idle power setting. The by-pass sampling was carried out at this low thrust setting for 16 minutes, and 23 Kg (50.4 lb) of dust were ingested by the engine during this time. The dust in the ECS system results in erosion of the plumbing at the pick-off point on the engine. Figure 15 is a photograph of the ECS air duct taken soon after Run #71.



Figure 15 Photograph of ECS plumbing.

The rate at which samples of dust were collected from the bleed air and by-pass air are also indicated in Table 5. From these and the measured feed rate of the input dust the value of two important parameters which characterize the contamination of the bleed air were computed. The absolute level of contamination of the bleed air at any inlet dust concentration is defined as the fraction of the input dust that shows up in the bleed. In the three cases sampled, the value of this fraction was approximately constant with an average value of 2.2 parts per thousand. The efficiency of the particle collection process at the ECS bleed can be obtained from this contamination level and the estimated air mass flow in the bleed manifold. In our case, the latter was 0.5% of the total mass flow into the engine. This results in a 45% particle collection efficiency in the ECS bleed. The collection efficiency depends primarily on the geometry of the engine near the ECS bleed and the local air velocity. The engine geometry is fixed and the contribution of changes in the local air velocity to the collection efficiency, with moderate changes in thrust setting, is expected to be small. Thus, the collection efficiency is relatively independent of thrust setting, its measured level can be used to estimate the absolute level of contamination for the bleed air at power settings other than cruise. For example, at MRT the increase in ECS airflow of about 50% would produce an absolute level of contamination for the bleed air equal to 3.4 parts per thousand of input dust feed rate.

A quantitative indication of the degree of pulveriation is contained in Figures 16 and 17. These results of particle size distribution were obtained using the two independent techniques of wet size analysis (Microtrac) and air jet dry size analysis (Alpine Air Jet Sieve). The average size of the particles collected in the ECS after passing 16 stages of the compressor was about 6 microns. However, the average particle size of the material collected in the by-pass was also on the order of 6 microns. The average particle size for the input material was on the order of 38 microns. It is suggested that most of the pulverization takes place in the initial rotating stages of the engine.

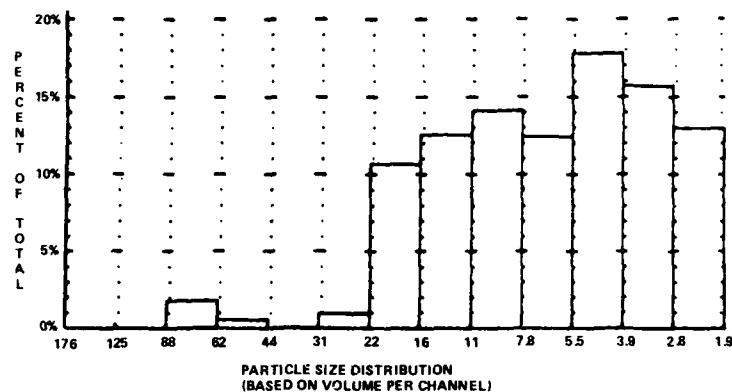


Figure 16 ECS run #66 average particle diameter = 6 microns.

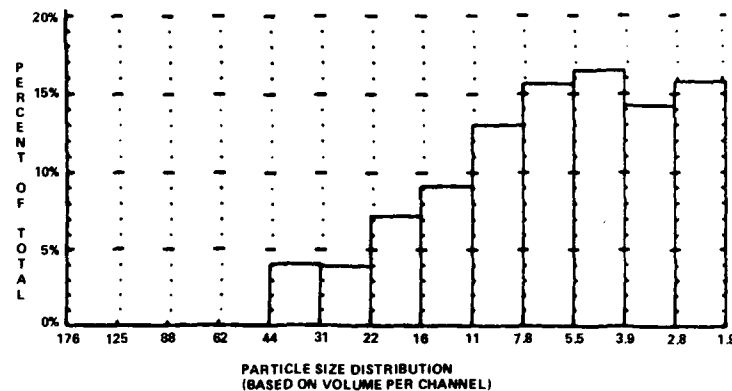


Figure 17 Bypass air run #71 average particle diameter = 6 microns.

The observations noted above should prove useful in determining safety precautions relative to cabin contamination. A well-known danger (10) which comes from breathing air with suspended particles is that they may form permanent deposits in the lungs. Fine particles are most dangerous. Because their settling velocity is a fraction of 1 mm/s, they remain suspended for long times and are easily recirculated by air currents. Fine particles of sizes between 0.5 and 10  $\mu\text{m}$  are most likely to be retained in the lungs. The nasal passages tend to trap particles larger than 10  $\mu\text{m}$ , while particles below 0.5  $\mu\text{m}$  are mostly exhaled again.

#### 4. CONCLUSIONS

Two TF33-P-11A engine have been subjected to two different dust mixtures and the performance deterioration has been monitored. In addition, samples of dust have been collected from the ECS and the fan by-pass. The thrust settings, the dust concentrations, and the melting temperature of the mixture were different for the two engines.

The most important damage mechanisms for this engine is compressor erosion. Glassification was not observed with either dust blend under any of the power settings. The reason for the lack of glassification is now known to be the result of the turbine inlet temperature being too low to produce significant melting of the material.

A significant amount of dust was captured in the ECS system. The particle size distribution suggested the particles are fractured in passing through the compressor and at the ECS bleed they are predominately 6  $\mu\text{m}$  and below. Samples collected at the fan exit were also fractured, having particle sizes of 6  $\mu\text{m}$  and below. The suggestion is that the dust pulverization occurs in the early fan and compressor stages.

#### 5. REFERENCES

1. Dunn, M.G., Padova, C., Moller, J.E., and Adams, R.E. "Performance Deterioration of a Turbofan and a Turbojet Engine Upon Exposure to a Dust Environment," paper to be presented at the 32nd International Gas Turbine Conference, Anaheim, CA, May 31 - June 4, 1987.
2. Batcho, P.F., Moller, J.C., Padova, C., and Dunn, M.G., "Interpretation of Gas Turbine Response Due to Dust Ingestion," paper to be presented at the 32nd International Gas Turbine Conference, Anaheim, CA., May 31 - June 4, 1987.
3. Mitchell, H.J. and Gilmore, F.R., "Dust-Cloud Effects on Aircraft Engines - Emerging Issues and New Damage Mechanisms," RDA-TR-120012-001, March 1982.
4. Chambers, J.C., "The 1982 Encounter of British Airways 747 with the Mt. Galunggung Eruption Cloud," AIAA paper 85-0097, AIAA 23rd Aerospace Sciences Meetings, 14-17 January 1985, Reno, Nevada.
5. Smith, W.S., "International Efforts to Avoid Volcanic Ash Clouds," AIAA paper 85-0101, AIAA 23rd Aerospace Sciences Meeting, 14-17 January 1985, Reno, Nevada.
6. Cranmer, D., "Private correspondence from Cranmer (Aerospace Corp.) to G. Rawson (RDA)," August 1985.
7. Holzhey, S., "Private correspondence from Holzhey (Soils Conservation Service) to Dunn (Calspan)," October 1985.
8. Rawson, G., "Private communication from G. Rawson (RDA consultant) to C. Padova (Calspan)," August 1985.
9. Padova, C. and Dunn, M.G., "Dust Deposition Measurements in an Allison T56 Hot Section Simulator," work in progress at Calspan.
10. Steere, N.V., CRC Handbook of Laboratory Safety, CRC Press, 2nd Edition, 1985.

### DISCUSSION

D.K. HENNECKE, Ge

You stated that you didn't observe glassification because the turbine entry temperature was too low. But a portion of the particles is passing through the combustor primary zone whose temperature is essentially independent of the turbine inlet temperature of the particular engine.

#### Author's Reply

The low turbine inlet temperature is the principal cause for the absence of glassification in the TF33. The melting and deposition process depends on the entire temperature history experienced by the individual particles. Residence time in various regions of the combustor are more important than the peak temperature encountered. For example, a fine particle swirling with the gas flow may soften as it traverses the primary combustion zone and then become hard again as it goes through the dilution zone to a relatively low temperature turbine inlet. Furthermore, each TF33 combustor can have a complex geometry with six fuel nozzles and six entries of swirled primary air. I believe that such a geometry leads to a shorter residence time of the fine particles in the primary combustion zone.

Y. RIBAUD, Fr

Pensez-vous que les pièges à poussière permettent un meilleur fonctionnement du moteur dans une atmosphère volcanique ?

#### Author's Reply

Yes. It is a solution possible for small engines. Separators of various design are used on helicopter installations. They are not used on engines with a large airflow, such as the TF33.

J. HOURMOUZIADIS, Ge

You have mentioned that volcanic ash was deposited on the pressure side of a turbine inlet guide vane. Have you observed any such deposits on the suction side, and if so, on what part of the airfoil ?

#### Author's Reply

No. There were no deposits over most of the suction side. Only near the leading edge and over a small fraction of the chord, perhaps one or two percent.

A. BROOKS, US

Why is it not viable to separate sand and dust in engines larger than helicopter engines ?

Author's Reply

In principle, some separator designs could be scaled up to large engines. For example, as you know, there are separators that use streamline curvature in the axial planes of the engine inlet to cause dust to migrate to the inlet perimeter where suction is applied in order to reject the particles overboard. These separators have low losses and could be scaled up. In practice, however weight penalties and subsystem complexities associated with the larger dimensions appear to have discouraged such installations. To my knowledge, separators are currently used only for engines with airflow up to about 20 Kg/s (  $\approx$  50 lb/s). The TF33 has an airflow of 209 Kg/s (460 lb/s).

Verbally, you also mentioned that there should be substantial centrifuging of the dust occurring naturally in the fan stages. I want to emphasize that our measurements indicate that centrifuging is rather insignificant.

W.A. VAN BODEGOM, N1

Is dust damage considered incidental ?

Are there any (official) instructions/procedures concerning operating in dusty environments ?

Author's Reply

For commercial aircraft, one may consider dust damage from encounters with airborne clouds to be incidental. There are official instructions for encounter avoidance on a case by case basis. At present, there are no official procedures to follow, should the encounter take place. For example, FAA Advisories were issued in the past for known eruption areas.

For some military aircraft, encounters with airborne dust clouds cannot be considered incidental. In parallel to this program, there are efforts directed to provide means for early detection of the cloud. Then, the pilot may avoid or choose a course to minimize damage, within mission constraints. In our measurement program we are developing procedures that will allow the pilot to best manage its engine resource while damage occurs.

# A RESEARCH PROGRAM ON THE AERODYNAMICS OF A HIGHLY LOADED TURBINE STAGE

by

R.G. Williamson  
Head, Gas Dynamics Laboratory  
National Research Council of Canada  
Ottawa, Ontario  
K1A 0R6  
CANADA

and

S.H. Moustapha  
Staff Aerodynamicist

J.P. Huot  
Senior Aerodynamicist

U. Okapuu  
Chief, Turbine Research  
and Design

Pratt and Whitney Canada Inc.  
Longueuil, Québec  
J4K 4X9  
CANADA

## SUMMARY

The paper brings together some of the main conclusions drawn from recent work in an on-going experimental program of research on the aerodynamics of a highly loaded turbine stage. Detailed data have been secured relating to the aerodynamic performance of transonic nozzles of high turning angle (tested with two different outer wall contours) and the influence of the stage environment on such measurements. Further work addressed rotor performance (as affected by blade loading), and also overall stage performance. The ultimate objective of the work is the extension of turbine design methods to regimes combining high stage loadings with high pressure ratios, with special emphasis on small blade sizes.

## LIST OF SYMBOLS

bxn vane axial chord  
bxr rotor axial chord  
Cx axial velocity, m/s  
Cp<sub>0</sub> nozzle local total pressure loss coefficient  
(P<sub>01m</sub> - P<sub>02</sub>)/(P<sub>01m</sub> - P<sub>s2m</sub>)  
 $\overline{Cp_0}$  circumferential average of C<sub>p0</sub>  
 $\overline{Cp_0}$  area weighted radial average of C<sub>p0</sub>  
ΔH change in stagnation enthalpy, J/kg  
 $\dot{m}$  mass flow rate, kg/s  
M absolute Mach number  
 $\overline{M_n}$  overall area weighted mean Mach number at plane 2  
Mr relative Mach number  
N rotational speed, rpm  
Nr N/√T<sub>01m</sub> relative to design value  
P pressure  
Pr P<sub>01m</sub>/P<sub>s2m</sub>  
PR P<sub>01m</sub>/P<sub>03m</sub>  
T temperature, K  
U Blade speed, m/s  
α local flow angle, deg. from axial  
 $\overline{\alpha}$  circumferential average of α  
 $\overline{\alpha}$  area-weighted radial average of α

## Subscripts

1,2,3... plane number (Fig 5)  
m mean  
s static

## INTRODUCTION

Gas turbine engines designed for the propulsion of light helicopter and small turboprop aircraft generally incorporate single stage axial gas generator turbines, for reasons of compactness and simplicity. To achieve acceptable fuel consumption, such turbines must operate with relatively high stage pressure ratios. The resulting large enthalpy drop,  $\Delta H$ , calls for high rotor blade speeds for the achievement of good turbine efficiency.

However, considerable benefits to engine weight, cost and handling characteristics would result if blade speeds could be kept low without compromising turbine efficiency. The results of one design study (of a 600 hp turboshaft/turboprop engine) indicated that if the rotor blade diameter were reduced so that the gas generator turbine stage loading ( $\Delta H/U_m^2$ ) increased by 37% over conventional levels, the weight of the turbine rotor would reduce by 31%, the number of rotor blades by 24%, and the polar moment of inertia of the turbine rotor by 39%. The latter is particularly important for turboshaft versions of small engines, where rotational inertia has a strong influence on the handling characteristics of light helicopters. The only major disadvantage of such increased stage loading is the predicted reduction in turbine efficiency.

A research program on the aerodynamics of a highly loaded turbine stage was therefore undertaken. This was a cooperative activity involving the National Research Council of Canada and Pratt and Whitney Canada, and had as its objective the extension of turbine design methods to regimes combining high stage loadings with high pressure ratios, with special emphasis on small blade sizes. Results have been reported in detail in References 1, 2, 3 and 4, and it is the intention here to attempt to highlight some of the main conclusions of this work.

## STAGE DESIGN

The design parameters selected pertain to a small, single stage gas generator turbine having a stage loading of 2.47, a flow factor of 0.64, and a pressure ratio of 3.76. Figure 1 shows a comparison of the design point of this NRC/PWC turbine with other similar designs, as reported in References 5, 6, 7, 8 and 9. Bearing in mind that these parameters were selected in the mid 1970's, it is evident that the target was ambitious.

The aerodynamic difficulty of the design is further illustrated by the design point velocity triangles of Figure 2. Both nozzle and rotor involve supersonic exit Mach numbers and high flow turning angles ( $76^\circ$  in the vane and over  $126^\circ$  in the rotor blade) to accommodate the high stage work requirements. Conditions were more severe at the root where Mach numbers and rotor blade turning angles were higher.

The nozzle had 14 vanes of aspect ratio 0.6, based on mean true chord. Trailing edges were quite thick, with 20% blockage, to accommodate cooling requirements. Vane sections, shown in Figure 3, were stacked such that the trailing edge was straight (no tilt) and radial (no lean) in the meridional and axial views. The meridional view, also shown in Figure 3, illustrates one of the variables in the research program, viz nozzle outer wall contouring. Secondary flow losses in the nozzle passages might be expected to be significant, due to the low aspect ratio, high vane loading, and turning angles involved, so that alleviation of the radial component of pressure gradient by contouring was deemed worthy of exploration. Two nozzle builds of differing meridional outer wall profiling were available, one with a conical outer wall contour from inlet to exit (nozzle C), the other with a more rapid "S" wall contour starting in the vicinity of the throat. In order to maintain the same throat area between nozzle builds, it was necessary to restagger the C nozzle vanes  $0.72^\circ$  open compared to those of the datum S version. Dimensions of test hardware shown in Figure 3 are approximately three times typical engine size.

Rotor blade design in a highly loaded turbine generally poses some conflicting requirements. The research turbine was designed for sub-impulse conditions at the blade root with a resultant large flow deflection ( $130^\circ$ ) and high inlet relative Mach number (0.8). The tip section was designed to have surface velocity distributions and loading such that there would be a minimum pressure difference across the tip from pressure to suction surface to decrease the tip leakage flow and its adverse effects on stage performance. Design tip clearance was 1.5% span; due to a manufacturing error the actual clearance during the tests was 2.3% span. Details are shown in Figure 4.

From weight and cost considerations it is advantageous to minimize the number of rotor blades in a turbine. However, without increasing the stage reaction this implies higher blade loading, for the same axial chord, and possible performance penalties. In order to investigate the effect of Zweifel loading coefficient for this class of turbine, three rotor configurations were tested, each employing the same blading and designated by the number of blades in the build. The resulting Zweifel loading coefficients are shown in Table 1. In the case of Rotors 45 and 34, the blades were closed by  $0.7^\circ$  and  $3.0^\circ$  respectively, in order to maintain the same stage reaction between rotor variants.



## TEST ARRANGEMENTS

The test facility (Fig. 5), which has been described in References 1, 2, 3 and 4, was designed to accommodate single turbine stages of about 53 cm o.d. with blade heights up to 7.5 cm. Turbine power was absorbed in a water brake dynamometer with a speed range up to 10,000 rpm. Air was drawn through the rig by an exhaust plant, and was prewarmed by thorough mixing with the output of a propane combustor.

Plenum conditions, which were assumed to represent inlet stagnation conditions, were sensed by sixteen partially shielded thermocouples equispaced around the circumference, and by four static pressure tappings.

In order to allow for circumferential variations in static pressure at nozzle exit, mean wall exit static pressures were derived from subsurface chambers connected to circumferential slits extending over one nozzle blade pitch. Provision was made at nozzle exit (plane 2) for radial/circumferential traversing by a wedge probe equipped with a partially shielded thermocouple. Similar radial/circumferential traversing capability was also available at rotor exit (plane 3), together with hub and tip static pressure tappings at five circumferential locations. Rotor exit conditions could also be sensed by four total pressure rakes, each with five probes disposed at centers of equal areas, equispaced circumferentially in the exit duct (plane 4). The rakes, located some six axial chords downstream of the rotor exit (a location previously found to best represent engine measured performance) could be aligned and locked to conform with the mean exit swirl angle. A straightening cascade restored axial flow in the downstream ducting, where further mixing of remaining temperature nonuniformities could occur. Four rakes of partially shielded thermocouples, located at approximately nine rotor diameters from rotor exit (plane 5), were used to determine the final mixed-out temperature of the exit flow. Insulation of the entire rig, and careful adjustment of inlet temperature to maintain exit temperature within  $\pm 1^\circ\text{C}$  of cell ambient temperature, combined to reduce heat transfer in the downstream mixing process. A discussion of instrumentation accuracy and averaging procedures is contained in Reference 2.

## PROGRAM OBJECTIVES

The detailed program objectives fall naturally into two groups, the first relating to nozzle performance, and the second to behaviour of the overall stage.

The nozzles, incorporating high flow turning angles, transonic flows, complex wall shapes, thick trailing edges and aerofoil twist, were expected to present problems in terms of analytical predictions. It was therefore proposed to secure benchmark data for comparison with calculations, to help in the extension of design methods to these more difficult circumstances.

Although the possible benefits of contoured walls had been explored in simpler test environments (i.e. with lower swirl angles, Mach numbers and blade loadings, and in two-dimensional cascades, e.g. Refs 10 and 11) there appeared to be a clear need for detailed data from a large scale rig operated under realistic conditions.

Such a test capability also lent itself to an investigation of the influence of downstream conditions on nozzle performance. The rig was large enough to conduct detailed surveys of flows at nozzle exit, even with a representative rotor in operation. By performing such tests with various rotors and operating conditions, and also with no rotor present, it was hoped to assess the influence of the stage environment on nozzle performance.

With respect to objectives relating to the complete stage, it was believed that direct measurement of the overall performance of a highly loaded, high pressure ratio stage at realistic Mach and Reynolds numbers would provide a useful benchmark. Comparison of overall stage performances secured with each of the two nozzle wall contours would permit direct assessment of the practical usefulness of such contouring. Finally, by changing the number of rotor blades in the disc, the effect of rotor blade loading on overall stage performance could be explored.

Results are discussed first in terms of the nozzle behaviour, and then from the standpoint of overall stage performance.

## NOZZLE PERFORMANCE DATA

### Surface Mach Number Distributions

The analytical method selected here for comparison is based on a time marching solution of the Euler equations, and is due to Denton (Ref. 12). The method calculates the inviscid three-dimensional flow field, and has transonic capability. Appropriate cusps are required at leading and trailing edges.

Measured static pressures along the vane surfaces at midspan, and midway between vanes on both endwalls, were converted isentropically to Mach number using the measured upstream stagnation pressure. The results are compared with the analytical

predictions in Figures 6 and 7 at an area weighted mean exit Mach number of 1.04 (nominal total/static pressure ratio,  $P_r$ , of 2.3).

There is remarkable agreement between measurement and calculations, the only real differences arising in regions of decelerating supersonic flow just downstream of the throat, indicative of the impingement of an oblique shock wave emanating from the trailing edge of the adjacent vane. Confirmation of the presence of the shock wave was provided by surface flow visualization which showed excellent agreement with the implications of the measured pressure distributions at midspan and on the endwall.

Generally similar agreement between calculation and experiment was found at all values of nozzle pressure ratio tested, covering subsonic, transonic and supersonic exit conditions (Ref. 2).

#### Nozzle Exit Traverse Data

Nozzle exit traversing was conducted with a three-hole wedge probe (automatically nulled for flow angle) at 11 circumferential positions spanning one vane pitch. The circumferential average of readings at a given probe immersion has been used to produce the radial distributions of Figures 8 to 11.

Figure 8 shows radial distributions of nozzle exit flow angle for the basic S nozzle, operated at design pressure ratio. The three sets of data indicate the influence of downstream conditions, which range from a "no rotor" case, through rotor running at off-design conditions, to the complete stage operation at design point. (The nozzle could be maintained near its design point, with essentially constant total to static pressure ratio, while rotor speed and stage total/total pressure ratio were varied, since the rotor remained choked down to values of stage pressure ratio near 2.4.) It is immediately evident that the influence of the downstream conditions was felt more strongly at the hub than near the tip, although some change is apparent in all regions. Also shown in Figure 8 is the trailing edge bisector angle. Comparison of this with the flow angle distributions gives some indication of the three-dimensionality of the flow.

Similar data for the C nozzle are presented in Figure 9. The influence of downstream conditions on the inner region of the annulus is, if anything, more noticeable than with the S nozzle, although the tip was little affected. The distribution of flow angle under stage design conditions is somewhat more uniform than was found with the S nozzle, although the overall level is lower.

The distributions of total pressure loss coefficients for the two nozzles, shown in Figures 10 and 11, again support the conclusion that the influence of downstream conditions can be significant. For the S nozzle, the generally beneficial effect on the near hub region of rotor operation is somewhat offset by apparent adverse effects beyond 20% span, a situation which is less evident with the C nozzle results of Figure 11.

The data of Figures 8 to 11 relate to nozzle operation near its design point, i.e. with generally supersonic exit conditions. Other work, reported in Reference 3, explored rotor effects down to values of  $P_r$  as low as 1.2, and has confirmed that rotor influences are still evident at low Mach numbers. The results of these experiments are summarised for nozzle C in Figure 12, in which overall area weighted mean values of flow angle and total pressure loss coefficient are plotted against mean exit Mach number. Local flow velocities first reach sonic values near the vane suction surface/hub wall intersection well before the mean exit Mach number reaches unity, leading to performance degradation at relatively low values of overall mean exit Mach number. The transonic deterioration in performance evident in the isolated cascade tests on the nozzle (i.e. without rotor) appears significantly worse than that measured in a stage environment, at least for this nozzle. (It is noted that upstream propagation of downstream conditions in supersonic flow can occur in boundary layers. Moreover, high flow swirl angles at nozzle exit lead to an effective axial component of velocity substantially below the sonic level at all test conditions.)

As indicated in the bar charts of Figure 13, relatively small differences in nozzle design (in this case only the outer wall contour) can have significant impact on the way in which nozzle performance is influenced by stage environment. In this Figure the overall performances of the S and C nozzle builds are compared, including separate evaluations of their hub and tip contributions to total pressure losses for three nominally similar downstream test conditions.

It is apparent that, whereas for nozzle C the hub total pressure losses are reduced substantially by rotor presence, the reduction is much less for nozzle S. Although losses very close to the hub wall are reduced in both cases, the larger separated region in nozzle C permits greater gains from beneficial rotor influence. In the case of nozzle S, the smaller gains are reduced further by the appearance of increased losses in the 20 to 100 percent span region (Fig. 10). This region is also affected in terms of exit angles (Fig. 8), and the results suggest greater three-dimensionality of the S nozzle exit flow compared to that of the C version (Fig. 9). (The three-dimensionality of the S nozzle exit flow is also reflected in the value of

the corrected mass flow parameter, which was 4 percent lower than found for the C nozzle despite the nominal similarity in geometric throat area.)

Behaviour of the tip contributions to nozzle total pressure losses (Fig. 13) also differs between the S and C builds, some slight increase in loss with rotor presence being apparent for the S variant. One of the results of these detailed differences in behaviour is that in terms of overall total pressure loss  $C_{p0}$ , the performance of the S nozzle is only slightly affected by rotor operation, although overall nozzle exit flow angle  $\alpha$  is substantially increased by the flow angle changes induced by the rotor. It is interesting to note that in terms of  $C_{p0}$ , the relative overall performances of the two nozzles are reversed by rotor operation (Fig. 13).

It appears that some loss components, such as those associated with certain accumulations of low energy fluid from secondary flows, might be less susceptible to downstream effects than losses associated with, say, a region of hub flow separation. The actual extent of improvement due to the rotor would also depend on the details of the "no rotor" test conditions.

Information on another aspect of rotor influence on nozzle performance is available in Figure 14. This compares distributions of nozzle exit mean swirl angle across the span for three different rotor designs operating at the same nominal design point, with the no rotor case included for comparison. The rotational speed, blade design, stage pressure ratio and nozzle pressure ratio are all essentially constant, the only variable being the number of blades on the disc (i.e. blade loading). It is apparent that rotor design is another parameter contributing to the observed influence on nozzle performance.

#### CONCLUSIONS FROM NOZZLE EXPERIMENTS

It may be appropriate at this stage to review the main conclusions stemming from the experiments on nozzle performance. It has been shown that surface Mach number distributions were well predicted by a three-dimensional Euler flow solver. Data have also been presented which indicate some increase in nozzle losses and flow underturning at higher Mach numbers. There seems little doubt that the main conclusion from this work is that the performance of a nozzle can be significantly affected by conditions downstream of the nozzle exit. The sensitivity of the nozzle performance to rotor presence depends on the details of the nozzle exit flow field and on the rotor design and operation. In summary, it appears that performance assessment of nozzles of high turning angle may require testing with an appropriate rotor.

#### OVERALL STAGE PERFORMANCE

The second main aspect of the research program concerned the overall performance of a highly loaded turbine stage, as affected by nozzle wall contouring and rotor blade loading.

Figure 15 shows the efficiency map for the basic stage, with nozzle S and rotor 51. For rotational speeds from 80% to 100% of design, the efficiency is largely independent of pressure ratio over a considerable range, where the rotor remains choked. Efficiency would be expected to decrease at pressure ratios beyond design, influenced by rotor shock losses, and to increase for stage pressure ratios below about 2.4, as the rotor unchokes and overall Mach numbers are reduced. The behaviour with decreasing speed reflects increasing rotor incidence and relative inlet Mach number, and reduced reaction. The efficiency measured at the design point was just over 80%.

As was noted earlier, a high design value of stage loading had been chosen. It is, however, of interest from the standpoint of future designs, to attempt to derive some indication of stage performance at even higher values of stage loading. Such estimates have been derived in the present investigation, as shown in Figure 16. The points represent off-design conditions, and thus may be taken as lower bound estimates of attainable efficiencies for a gas generator turbine of the present size.

#### Influence of Nozzle Wall Contour on Stage Performance

Some understanding of the influence of the two particular nozzle wall contours on stage efficiency may be gained from Figures 17 and 18 which illustrate directly the contributions of the nozzle. Figure 17 shows the radial distribution of total pressure losses for the two nozzle variants, as measured at design point with rotor 51. The superiority of the C contour version is readily apparent, and would be expected to lead to better stage performance. However, a comparison of mean exit swirl angles (Figure 18) suggests that other performance parameters must be considered. As noted earlier, the vanes in the C build were re-staggered 0.72° open (i.e. with less turning) to maintain a constant throat area. As seen in Figure 18, with the C nozzle producing about 1° less flow turning on average than the S variant, the mean flow angle at exit of the two builds differed by 1.8°. This combination of re-stagger and aerodynamic underturning of the C nozzle led to rotor incidences which were locally as much as 5° below the design values. In such circumstances, measurable effects on stage efficiency might be expected.

A comparison of overall stage efficiencies for the S/51 and C/51 builds at design point is presented in Table 2, evaluated with different measurement techniques. It is seen that overall efficiency with the C nozzle is slightly inferior to that with the S build, regardless of the measurement technique adopted. It appears that for the C nozzle configuration, off-design rotor incidence outweighed lower nozzle losses. In order to realize the potential of the C nozzle, some re-design to accommodate the measured flow angles would be required.

The selection of efficiency evaluation methods listed in Table 2 is intended to illustrate how choice of measurement plane and technique can influence the calculated value of overall efficiency. For example, total pressure could be evaluated from rotor exit traverse data (plane 3), from measurements from fixed rakes at plane 4 (about 6 axial chords downstream of the rotor), or from continuity assumptions and other inlet and exit measurements. Total temperature could also be derived in different ways, from measurements far downstream (plane 5) or at rotor exit, or inferred from dynamometer torque readings. (In methods 4 and 5, no allowance for disc windage and bearing friction losses has been incorporated.) As a point of interest, total/static efficiencies are also shown. In general, efficiencies quoted in the text have been derived using Method 1.

#### Effect of Rotor Blade Loading

The final stage variable of interest was rotor blade loading, which was explored using the three builds of 51, 45 and 34 identical rotor blades. Figure 19 compares the mean radial distributions of rotor exit flow angle for the three rotor builds. The data, obtained from radial/circumferential traversing at rotor exit, have been re-cast in the relative (rotating) frame of reference. The differences in blade angle due to the re-stagger are also indicated.

The baseline rotor 51 and rotor 45 both show the expected underturning at mid-span and the overturning near the walls associated with classical secondary flow mechanisms. Centres of secondary vortices are at about 25% and 75% span, and tip leakage effects are significant. Rotor 34, on the other hand, with its high blade loading, clearly has a much more three-dimensional flow field at exit. A strong vortex centered near 40% span appears to be associated with the high flow turning in the lower aspect ratio passage between blades. A similar phenomenon was noted in earlier cascade testing of the rotor blades at high pitch/chord ratios (Ref. 13).

Data presented in Figure 20 were derived from averaging locally measured values of total pressure and total temperature from radial/circumferential traverses conducted at rotor exit. As would be expected, the strong three-dimensionality of the exit flow from rotor 34 reduced its efficiency, particularly in the mid-span region.

For completeness, Table 3 presents the calculated design point efficiencies of all the nozzle/rotor builds tested, evaluated using the methods of Table 1. The general internal consistency of the data is apparent, together with the spread of several percentage points depending on the calculation method adopted.

#### CONCLUSIONS FROM STAGE EXPERIMENTS

The measured overall efficiency of the basic highly loaded stage was just over 80%, which conformed closely with design predictions. Lower bound estimates of efficiency were derived from off design operation for even higher stage loadings, and may be helpful in selecting future design parameters. Although direct measurement of nozzle total pressure loss coefficient had suggested that conical outer wall contouring would be superior to S wall contouring, the expected gains in overall stage performance were not realised. The shortfall was believed to be associated with the magnitudes of nozzle exit flow angles achieved.

Blade loadings in excess of normal values were explored, with design mean Zweifel coefficients up to 1.18. It was found that such increases reduced stage efficiency by about 2% percentage points. The reduction was shown to be associated with a significant increase in the three-dimensionality of the rotor flow field.

#### ACKNOWLEDGEMENT

The authors are indebted to Messrs. B.J. Day and D.L. Logan for their invaluable technical contributions to the extensive experimental program.

#### REFERENCES

1. Moustapha, S.H. and Williamson, R.G., "Investigation of the Effect of Two Endwall Contours on the Performance of an Annular Nozzle Cascade". AIAA Journal, Vol. 24, No. 9, pp 1524-1530. Sept 1986.
2. Williamson, R.G. and Moustapha, S.H., "Three-Dimensional Cascade Testing of Turbine Nozzles at High Exit Mach Numbers". ASME Journal of Fluids Engineering, Vol. 108, No 3, pp 313-320. Sept 1986.

3. Williamson, R.G., Moustapha, S.H. and Huot, J.P., "The Effect of a Downstream Rotor on the Measured Performance of a Transonic Turbine Nozzle". ASME Journal of Turbomachinery, Vol. 108, No. 2, pp 269-274, Oct. 1986.
4. Moustapha, S.H., Okapuu, U. and Williamson, R.G., "The Influence of Rotor Blade Aerodynamic Loading on the Performance of a Highly Loaded Turbine Stage". ASME Journal of Turbomachinery, Vol. 109, No. 1, pp , Jan. 1987.
5. Crow, D.E., Vanco M.R., Welna, H. and Singer, I.D., "Results from Tests on a High Work Transonic Turbine for an Energy Efficient Engine", ASME Paper No. 80-GT-146, 1980.
6. Liu, H.C., Booth, T.C. and Tall, W.A., "An Application of 3D Viscous Flow Analysis to the Design of a Low Aspect Ratio Turbine", ASME Paper No. 79-GT-53, 1979.
7. Ewen, J.S., Huber, F.W. and Mitchell, J.P., "Investigation of the Aerodynamic Performance of Small Axial Turbines". ASME Paper 73-GT-3, April 1973.
8. Okapuu, U., "Some Results from Tests on a High Work Axial Gas Generator Turbine", ASME Paper 74-GT-15, March 1985.
9. Bryce, I.D., Litchfield, M.R. and Leversuch, N.P., "The Design, Performance and Analysis of a High Work Capacity Transonic Turbine", ASME Paper 85-GT-15, March 1985.
10. Haas, J.E. and Boyle, R.J., "Analytical and Experimental Investigation of Stator Endwall Contouring in a Small Axial Flow Turbine", NASA TP-2309, September 1984.
11. Morris, A.W.H. and Hoar, R.G., "Secondary Loss Measurements in a Cascade of Turbine Blades with Meridional Wall Profiling", ASME Paper 75-WA/GT-13, November 1975.
12. Denton, J.D., "A Time Marching Method for Two and Three-Dimensional Blade to Blade Flow". ARC R&M 3775, 1975.
13. Moustapha, S.H., Paron, G.J. and Wade, J.H.T., "Secondary Flow in Cascades of Highly Loaded Turbine Blades", ASME Journal of Engineering for Power, Vol. 107, No. 4, pp 1031-1038. Oct 1985.

TABLE 1

ROTOR BLADE LOADINGS

Number of blades	Zweifel coefficient		
	Hub	Mean	Tip
51	.69	.77	.79
45	.79	.87	.90
34	1.07	1.18	1.23

TABLE 2

DESIGN POINT TURBINE EFFICIENCY (%)

Method	Pressure measurement	Total Temperature measurement	S/51	C/51
1	Po rakes, plane 4	Mixing pipe rakes, plane 5	80.0	79.8
2	Po traverse, plane 3	Mixing pipe rakes, plane 5	83.0	82.0
3	Po traverse, plane 3	Traverse, plane 3	79.4	78.7
4	Po rakes, plane 4	Dynamometer (N, m)	79.7	78.6
5	Continuity (Po1m, To1m, Ps3m, m, a)	Dynamometer (N, m)	81.9	80.8
6	Wall Ps plane 3	Mixing pipe rakes, plane 5	70.8	69.2

TABLE 3

DESIGN POINT TURBINE EFFICIENCY (%)

Method	S/51	S/45	S/34	C/51	C/34
1	80.0	79.8	77.6	79.8	77.6
2	83.0	82.7	81.6	82.0	81.3
3	79.4	79.5	76.3	78.7	76.0
4	79.7	79.3	77.7	78.6	78.2
5	81.9	81.6	78.3	80.8	78.3
6	70.8	69.7	68.4	69.2	68.1

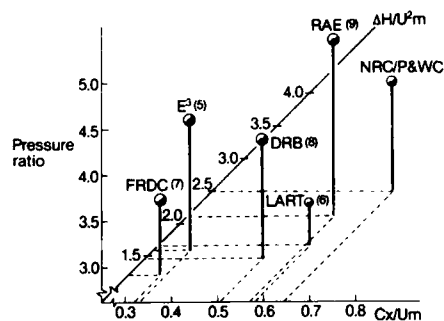


Fig. 1 High pressure research turbine characteristics

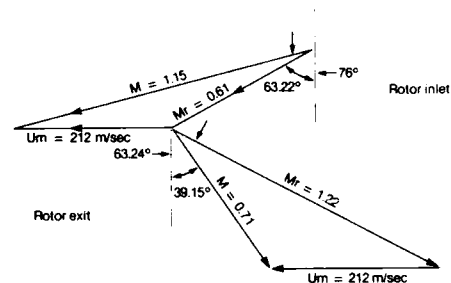


Fig. 2 Design point velocity triangles at midspan

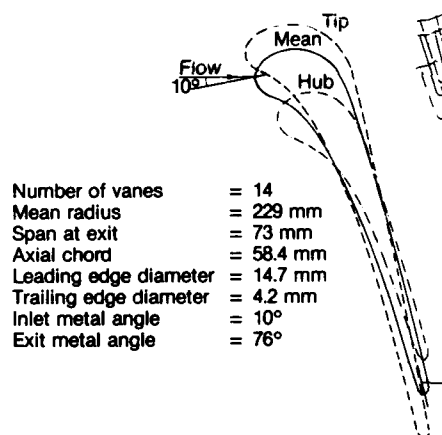


Fig. 3 Vane sections & midspan geometric parameters

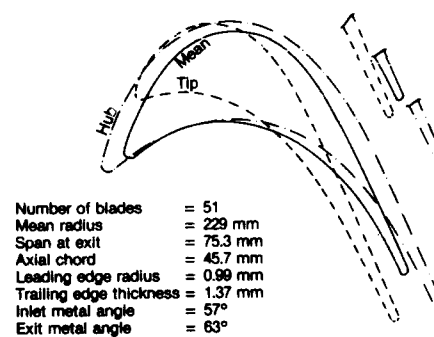


Fig. 4 Blades sections & midspan geometric parameters

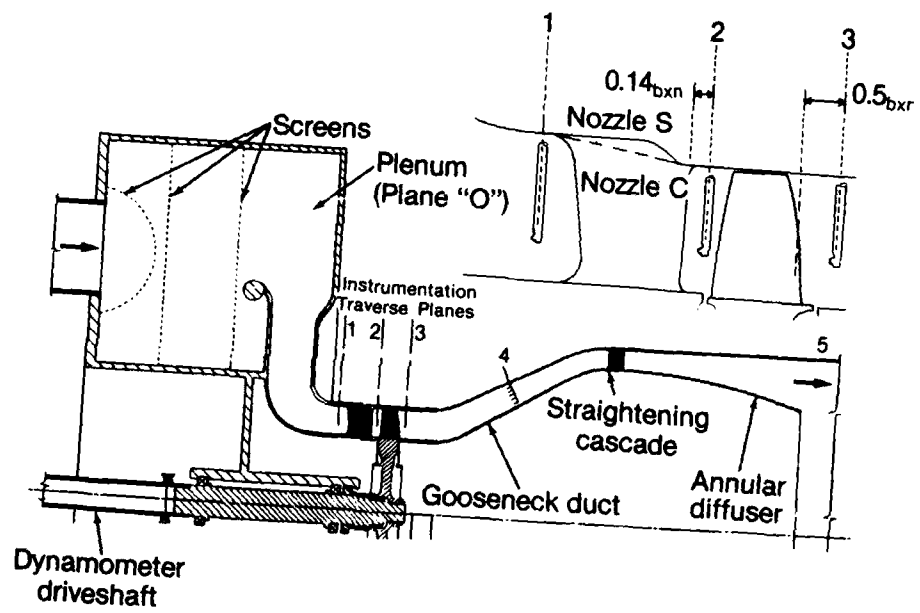


Fig. 5 The highly loaded turbine rig



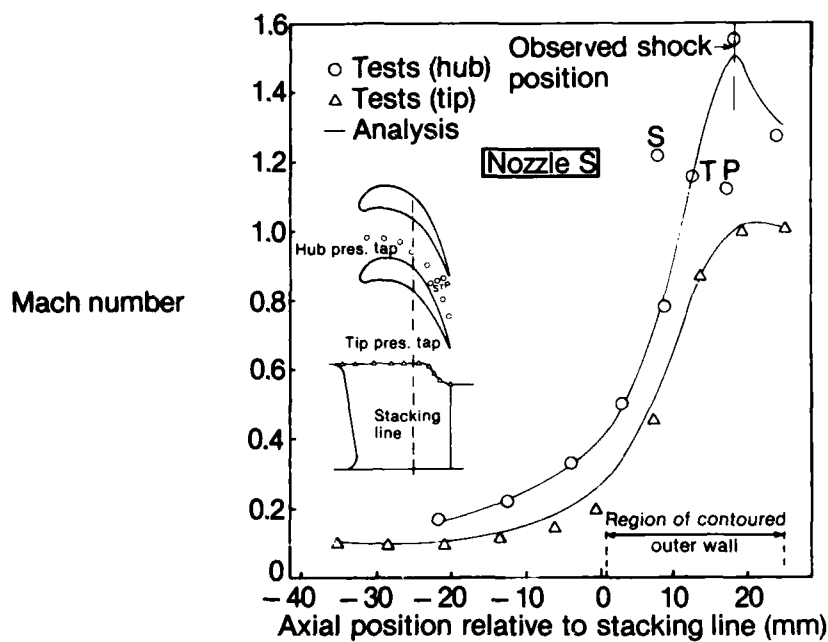


Fig. 6 Nozzle endwall Mach number distributions ( $Pr = 2.3$ )

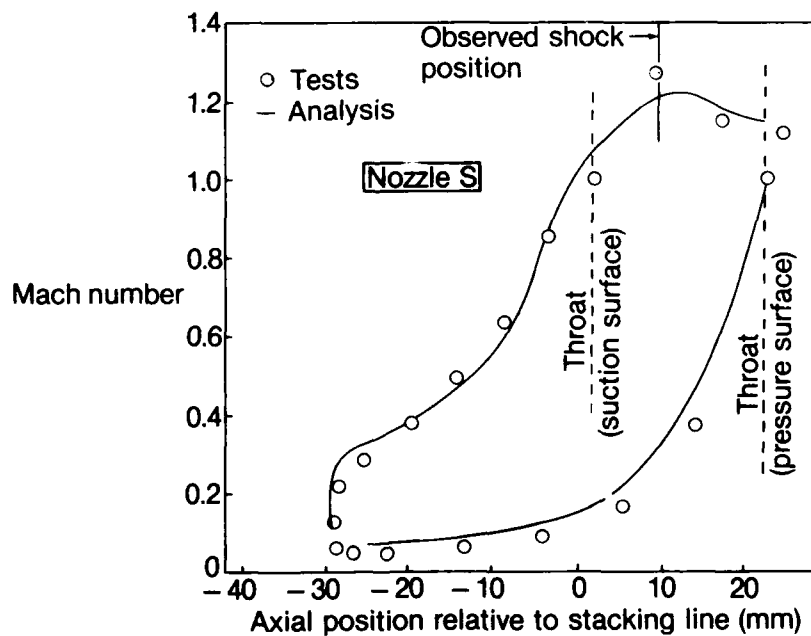


Fig. 7 Vane surface Mach number distribution at midspan ( $PR = 2.3$ )

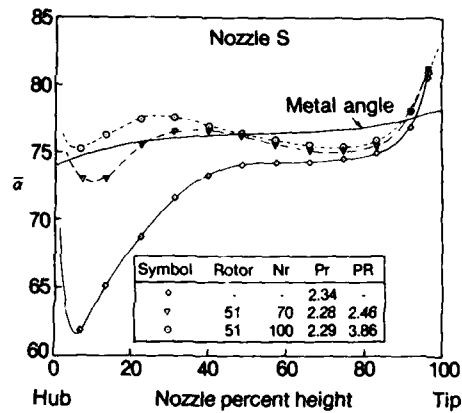


Fig. 8 Effect of rotor operating condition on radial distribution of circumferentially averaged nozzle exit flow angle

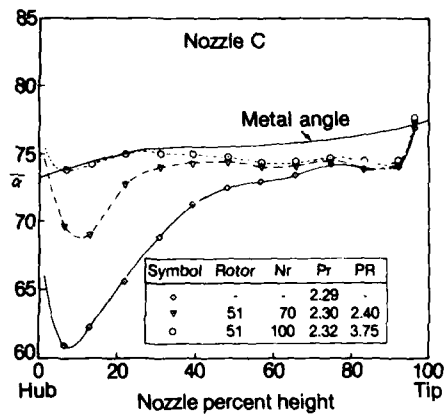


Fig. 9 Effect of rotor operating condition on radial distribution of circumferentially averaged nozzle exit flow angle

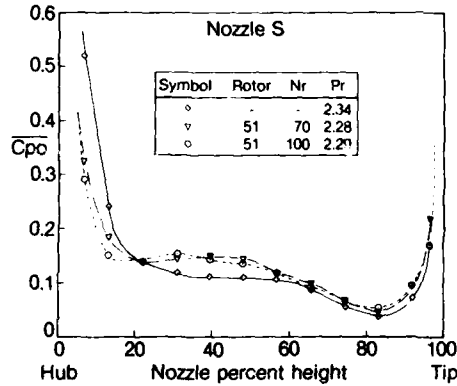


Fig. 10 Effect of rotor operating condition on radial distribution of circumferentially averaged nozzle total pressure loss coefficient

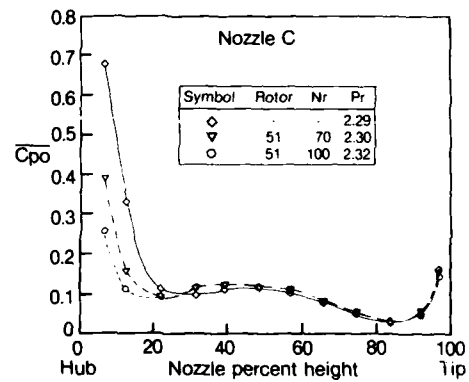


Fig. 11 Effect of rotor operating condition on radial distribution of circumferentially averaged nozzle total pressure loss coefficient

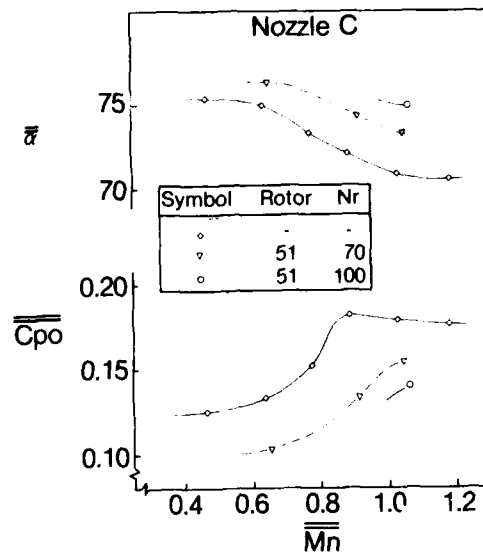


Fig. 12 Effect of stage operating conditions on overall nozzle performance

	$\overline{C_{po}}$	$\overline{C_{po_H}}$	$\overline{C_{po_T}}$	Nr	PR
Nozzle 'C'	0.179	0.269	0.101	-	-
	0.152	0.209	0.104	70	2.40
	0.140	0.187	0.099	100	3.75
Nozzle 'S'	0.168	0.242	0.105	-	-
	0.168	0.222	0.121	70	2.46
	0.163	0.216	0.118	100	3.86

(Rotor 51,  $\overline{M_n} \approx 1.05$ ,  $Pr \approx 2.3$ )

Fig. 13 Comparison of effect of rotor operation on performance of two nozzle variants

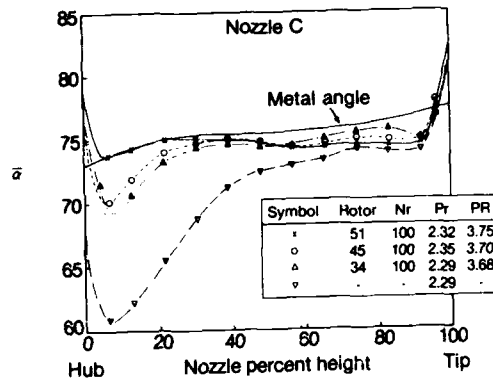


Fig. 14 Effect of rotor blade number on radial distribution of circumferentially averaged nozzle exit flow angle

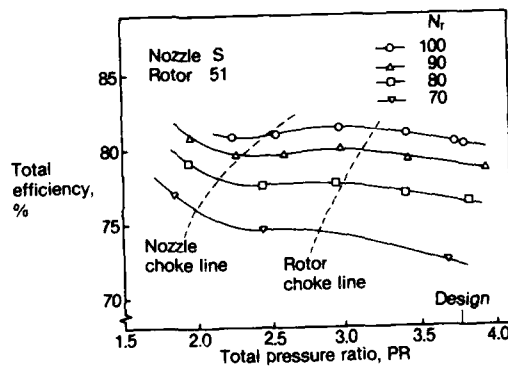


Fig. 15 Variation of efficiency with pressure ratio for the basic stage

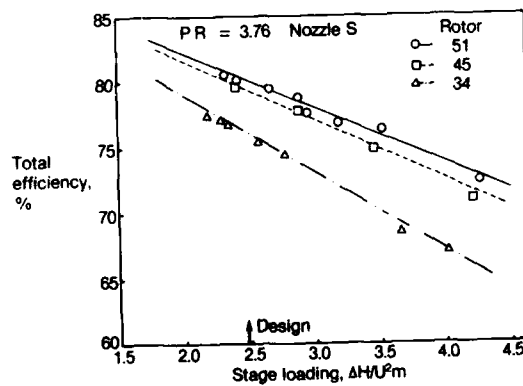


Fig. 16 Effect of stage loading on efficiency

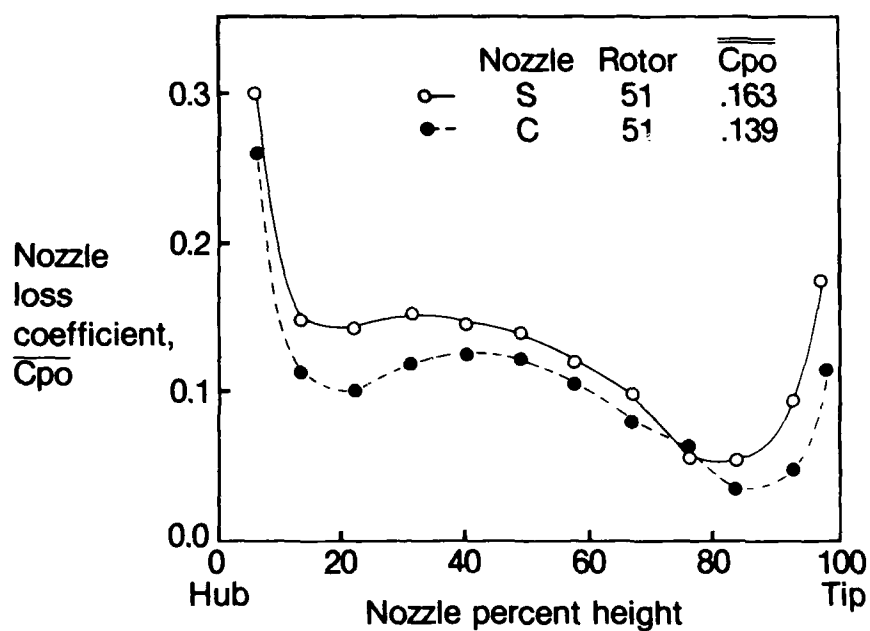


Fig. 17 Radial distribution of circumferentially averaged nozzle total pressure loss at design conditions

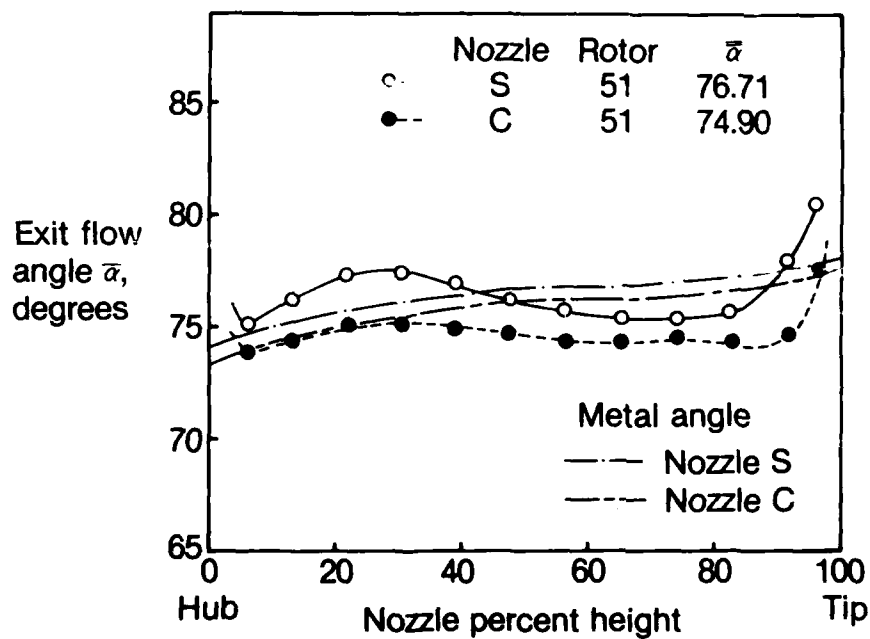


Fig. 18 Radial distribution of circumferentially averaged nozzle exit flow angle at design conditions

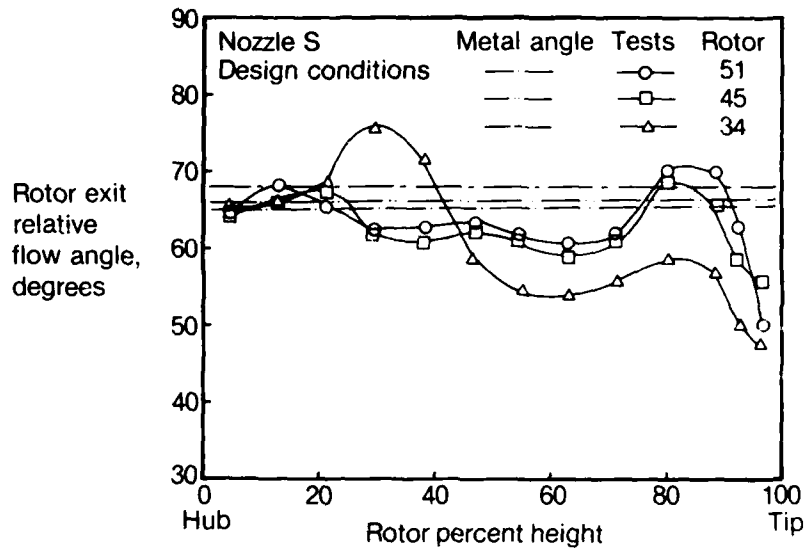


Fig. 19 Radial distribution of rotor exit relative flow angle

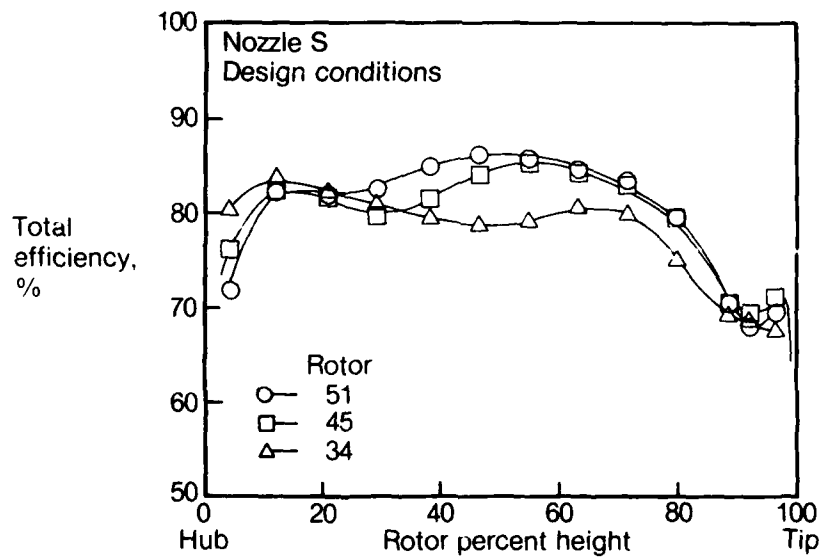


Fig. 20 Radial distribution of stage efficiency at design conditions

## DISCUSSION

Y. RIBAUD, Fr

Why is the efficiency so bad, is it because of high hub ratio ?

### Author's Reply

We feel that the source of the relatively low level of efficiency obtained with this turbine lies in the combination of high stage loading ( $\Delta H/U^2$ ) and high pressure ratio, as illustrated in Fig. 1. The former determines the large amount of flow turning in the rotor, with resulting narrow flow passages and high streamline curvatures. The latter establishes the high levels of gas velocity within the rotor passages. The combination of the two causes large amounts of local diffusion on blade surfaces, as well as shocks within and downstream of the covered channel of the blade. It is likely that the present design could be somewhat improved by refinements to the blade shape, indicated by three-dimensional analyses which were not available at the time of the original design. However, it is unlikely that the efficiency of this turbine (at its design target pressure ratio and rotational speed) could be radically increased as long as the present constraints on trailing edge thickness, tip clearance and blade aspect ratio remain in force.

It should be emphasized that the objective of this research was to establish aerodynamic "design rules" for turbines in an operating regime which is generally associated with low efficiency. In certain application, the benefits to engine weight, cost, and rotational inertia may outweigh increased fuel consumption, provided this can be kept within reasonable bounds.

J. MOORE, US

Could you comment on the large difference in rotor flow shown in Figure 19 between the 45 and 34 blades configurations ?

Was this caused by a change in the stator exit flow distribution ?

### Author's Reply

The significant change in the flow field at high blade loadings is believed to be associated with the low aspect ratio of the rotor blade passages. Earlier work by S.H. Moustapha (Reference 13) on a non-rotating rig which simulated this rotor blade geometry, has shown a similar effect at low values of blade passage aspect ratio.

## EXPERIMENTAL EVALUATION OF A TRANSLATING NOZZLE SIDEWALL RADIAL TURBINE

Richard J. Roelke  
Research Engineer  
NASA Lewis Research Center  
21000 Brookpark Road  
Cleveland, OH 44135

and

Casimir Rogo  
Project Manager  
Aerodynamic Components  
Teledyne CAE  
1330 Laskey Road  
Toledo, OH 43612

## SUMMARY

An experimental performance evaluation was made of two moveable sidewall variable area radial turbines. The turbine designs were representative of the gas generator turbine of a variable flow capacity rotorcraft engine. The first turbine was an uncooled design while the second turbine had a cooled nozzle but an uncooled rotor. The design, fabrication and testing were carried out by Teledyne CAE under a series of government contracts. Performance measurements were taken over a turbine flow range of 2:1 in the Contractor's warm (121 °C) air facility. The cooled nozzle turbine was evaluated both with and without coolant flow.

The test results showed that the moveable nozzle wall is a viable and efficient means to effectively control the flow capacity of a radial turbine. Peak efficiencies of the second turbine with and without nozzle coolant were 86.5 and 88 percent respectively. These values are comparable to pivoting vane variable geometry turbines; however, the decrease in efficiency as the flow was varied from the design value was much less for the moveable wall turbine. The measured turbine performance over the entire flow range was within one point of the estimated turbine performance used in a previously conducted variable flow capacity engine analysis which showed significant fuel savings. Several design improvements were identified which should increase the turbine efficiency one or more points. These design improvements include reduced leakage losses and relocating the vane coolant ejection holes to reduce mainstream disturbance.

## INTRODUCTION

A major programmatic thrust at the NASA Lewis Research Center is to improve the performance and fuel economy of small (0.9 to 2.3 kg/sec airflow size) gas turbine engines. Significant performance improvements of this engine class have been made over the years with optimized engine cycles, improved small component performance and the incorporation of higher temperature materials and cooling technology. Further fuel savings may be made (Ref. 1) by utilizing ceramics in the hot section, allowing higher temperatures and reduced coolant flows, and developing nonconventional cycles such as regenerative engines. These approaches increase the engine's thermal efficiency. Another approach to reducing the total fuel burned is to improve the part-power fuel consumption. This is particularly important for an engine that operates over a wide power range as in a rotorcraft application. Here the objective of a reduction of total fuel consumption can be effectively made by a variable flow capacity engine.

Typically, engines are designed to be most efficient at a selected operating condition (or power level), for a given application, and increased fuel consumption is accepted at other power levels. As is well known, the increased fuel consumption is due to higher losses as the engine components operate off-design. In the variable flow capacity engine, the components are operated at constant conditions during the entire flight and the engine power is modulated by changing engine airflow. This is accomplished by operating the turbomachinery at their design values of speed, pressure ratio and turbine inlet temperature and utilizing variable geometry for airflow management. The variable capacity engine was included in an Army study (Ref. 2), where it was concluded that the lack of data on variable geometry made the evaluation of the cycle difficult and that research efforts should focus on the critical variable geometry loss/leakage issues in the engine components. Later Army sponsored studies (Refs. 3 and 4), provided in-depth analyses of the losses and performance of variable nozzle area gas generator radial turbines. These studies showed fuel savings for the variable flow cycle compared to a simple cycle, if the aerodynamic penalties of the variable geometry could be kept low.

The latter two studies focused on the variable geometry gas generator turbine since this was one of the riskiest components in the engine and the one about which very little information existed. For this turbine, two methods were considered to vary the nozzle area. One was by translating the nozzle sidewall and the second was by pivoting the vanes or the trailing edge portion of the vanes. The results indicated that the translating sidewall method had the same or lower losses than the pivoting vanes, but lacked substantiating data. An experimental program was recommended to obtain data for the translating sidewall turbine.



A series of Army funded - NASA managed contracts were awarded to Teledyne CAE to obtain turbine performance data on the translating sidewall concept. Initially, a variety of moving sidewall configurations were tested to establish a data base and identify the one or two concepts with the best performance. An existing uncooled turbine design was used for those tests. Information gained from the test program was then incorporated into the turbine design of Ref. 4 and a second research turbine built. The purpose of the second turbine was to determine the effect of nozzle vane coolant flows and improved vane leakage control on turbine performance.

The testing was done at the Contractor's site. Tests were conducted with air at a temperature of 121 °C and a pressure of 164 kPa. Overall stage performance and selected flow surveys were taken. This paper summarizes the results of the program.

#### TURBINE DESIGN

A cross section of a conceptual variable flow capacity engine is shown in Fig. 1. The engine has a two-stage compression system, a reverse flow combustor, a radial gas generator turbine, and an axial flow power turbine with a forward output shaft. All the turbomachinery in the engine has variable geometry. The compressors have variable inlet guide vanes and translating sidewall diffusers, while both turbines have variable area nozzles. There is no variable geometry in the combustor. A single mechanical linkage simultaneously actuates all variable geometry components with a single control.

Several cycle and mechanical variations of this engine were studied and analyzed for a defined rotorcraft mission (Refs. 3 and 4). A design life of 4000 hr with projected year 1990 materials was specified. Both cooled and uncooled rotors were considered for the gas generator turbine. Design parameters of one of the selected engines are listed in Table I. Comparison of the performance of this engine with a comparable technology simple cycle showed a seven percent fuel savings for the variable cycle engine. Additional study details may be found in Ref. 4.

The engine studies formed the basis of the variable geometry turbine designs. Two turbine designs were recommended. One design had an inlet temperature of 1370 °C with a cooled nozzle and rotor, while the other turbine had an inlet temperature of 1205 °C, a cooled nozzle and an uncooled rotor. The lower temperature design was selected for the test program. The design engine airflow, i.e., the flow corresponding to the nominal setting of the variable geometry, and the airflow range were selected based on the vehicle power demands and an optimization study made to minimize the total fuel burned for the mission. Results indicated a flow variation of 2:1 was required with the design airflow set at 78 percent of the maximum flow. The two methods considered for turbine flow control, the pivoting vane and moving sidewall nozzles, are shown in Fig. 2. The variable geometry losses associated with the pivoting vanes are leakage flows between the vanes and sidewalls and incidence changes as the vanes are rotated. The losses associated with the moving sidewall are leakage flows on the telescoping side of the nozzle plus sudden expansion and contraction losses as the sidewall is moved.

#### First Test Turbine.

As mentioned earlier, the initial turbine utilized in the test program was an existing design of Teledyne CAE. The turbine had been designed some years earlier, but the design conditions were sufficiently close to those specified for this program. A variation of the design was also used in a test program to evaluate the pivoting vane turbine and could therefore serve as a reference against which to compare the moving sidewall turbine. To adapt the turbine for use in this program the machine was scaled up (to a rotor diameter of 355.6 mm) to match facility and Reynolds number requirements and the nozzle hardware was redesigned to accept various kinds of moving sidewalls. The nominal design conditions for this turbine are listed in Table II and the meridional flow path is shown in Fig. 3.

The test objective for this turbine was to evaluate several stator configurations. Typical geometries are shown in Fig. 4. Both straight and contoured sidewalls as well as various vaneless space geometries were tested. Figure 4(a) shows a sudden expansion or dump into the vaneless space as the nozzle is closed down. The next configuration, Fig. 4(b), depicts a diffusing ramp in the vaneless space that is actuated by and follows the moving wall. The intent is to reduce sudden expansion losses. The next illustration, Fig. 4(c), shows a converging vaneless space where the flow is accelerated smoothly as the nozzle is opened to its maximum area. However, this configuration still results in a sudden expansion at closed down areas. In Fig. 4(d), the vaneless space wall travels with the nozzle wall and the flow dump occurs in the rotor inducer where there are lower relative velocities than in the vaneless space.

In each configuration, one of the nozzle sidewalls was always in a fixed position and aligned flush with the inlet and vaneless space walls. The opposite sidewall was then positioned to either increase or decrease the flow area from the nominal setting. At the nominal setting, both walls are aligned flush with the rotor inducer. All nozzle vanes of the first turbine were solid and no coolant flow was simulated.

Tests with this turbine were also conducted with variable geometry at the rotor exit. This consisted of rings that were inserted into the flow just downstream of the rotor to control the rotor reaction as the stator was closed down. The stage efficiency decreased for all rotor exit ring tests and will not be reported on further in this paper. Additional design and configuration details are included in Ref. 5.

## Second Test Turbine

The second research turbine was essentially the design executed in Ref. 4 with some modifications made based on the results of the first turbine tests. Design parameters are listed in Table III. The flow path of the turbine, as taken from an engine layout, is shown in Fig. 5. The use of current cooling technology and year 1990 materials required coolant in the nozzle vanes, sidewalls, and rotor shroud, plus a small amount to purge the rotor backface cavity. No rotor coolant was required. All coolant flows except the shroud flow was simulated in the test turbine. The nozzle was designed with straight sidewalls and a converging vaneless space. The test turbine was built so either the hub or shroud walls could be moved. Photographs of the two rotors and nozzle vanes are shown in Fig. 6.

## Vane Seals

During the design and test phases of the program, careful attention was given to the leakage flow around the nozzle vanes. The gap between the sidewall cutout and the vane profile was nominally 0.4 mm. Tests were run with this gap open, completely sealed with a rubberized sealant and finally with a metal wiper seal. The seals are shown in Fig. 7. A cross section of the "L" shaped seal is shown in section B-B. Based on pressure measurements, it appeared that the leakage flow followed a path as shown in the figure which caused significant losses. In the first turbine, Fig. 7(a), only a portion of the vane clearance gap was sealed with the wiper seal. The region is shown by the cross hatched area in the figure. The application of the wiper seal to this small area was very effective; however, the seal was extended to most of the vane perimeter for the second turbine. The effectiveness of the seals is discussed later in this paper.

## APPARATUS AND TEST PROCEDURE

The research turbines were evaluated in a test facility at Teledyne CAE. A cross section of the test apparatus is shown in Fig. 8. Compressed air at a nominal pressure of 164 kPa was heated to about 121 °C and ducted to the inlet plenum of the turbine. Within the inlet plenum the flow passed through two screens to smooth the flow before entering the turbine. After leaving the turbine, the air was ducted to facility exhausters. The turbine pressure ratio was set by changing the exit pressure. Power was absorbed by a waterbrake which also served to control the speed. Between the turbine and waterbrake was an in-line torque meter which measured the shaft torque and rotational speed.

The instrumentation installed in the test rig is shown in Fig. 9. At station 1, about one-half vane chord upstream of the nozzle, measurements of total temperature, total pressure and wall static pressure were taken. At this same location, surveys of flow angle and pressure were taken from wall to wall to verify the flow uniformity at the turbine inlet. At station 2 were located wall static pressure taps and an angle/total pressure survey probe. The survey probe was used to measure from wall-to-wall axially and over a distance of one and one-half vane pitches circumferentially. Wall static pressures were measured on the inner and outer walls at stations 3 and 4. A radial survey probe for measuring angle, total pressure and total temperature was located at station 3. At station 4, twelve values each of total pressure and temperature were measured with fixed rakes. The coolant and mainstream flow rates were measured with calibrated flow orifices.

For each turbine configuration tested, the nozzle sidewalls were moved in increments (usually four) from full open to 50 percent closed by means of jack screws with a pneumatic assist. Stops were provided to repeat the nozzle area settings accurately as the nozzle configurations were changed. The nozzle sidewall position could also be set and/or measured with a depth gage through access holes in the nozzle assembly. The first turbine was set up so that at the flush wall condition the nozzle area was 80 percent of the maximum area, whereas it was 78 percent for the second turbine. The nozzle assembly of the second turbine used to simulate vane coolant flows is shown schematically in Fig. 10. The coolant entered a small plenum behind the hub sidewall and then flowed through a series of small holes into the mainstream to simulate vane and wall cooling. A small amount of coolant also entered the mainstream from the rotor backface plenum.

All testing with the first turbine was conducted at design speed and pressure ratio. For each nozzle configuration, stage performance data were taken over a range of flow areas. Based on the results of those tests, five geometries were selected for detail flow surveys at the nozzle and rotor exits. Testing with the second turbine was limited to fewer nozzle configurations but for expanded operating conditions. Data were taken at speeds of 60, 80, and 100 percent of design and for a range of pressure ratios above and below the design value. Data were also taken with and without nozzle coolant flows.

The turbine efficiency was calculated from both torque measurements and the turbine temperature drop. Measured values of tare torque (for bearing, seals and windage losses) were added to the shaft torque to get the total turbine torque. Comparison of the efficiencies calculated from the two methods, as well as mass averaged efficiency values from surveys, showed very good agreement. Torque derived efficiencies were intended to be the primary basis for performance comparisons but recurring mechanical

problems with the waterbrake and torquemeter gave occasional erratic results. Therefore, most of the comparisons were made based on temperature derived efficiencies.

#### RESULTS AND DISCUSSION

This section presents a summary of the test results of the two research turbines and the impact of those results on the variable flow capacity engine. Over the span of seven years of this program much valuable research has been accomplished and information gathered. Therefore, of the voluminous amount of data, only the most salient results are presented here. A great deal of additional information is contained in Refs. 3 through 7.

##### First Research Turbine

The first turbine build was tested without any leakage control at the location where the vanes passed through the nozzle sidewall. The test build consisted of a moveable hubwall with a vaneless space dump, see for example Fig. 4(a). The resulting measured turbine efficiency is shown in Fig. 11 by the symbol labeled "no seal." The test was repeated first with the clearance gaps totally sealed with a rubber compound and then with the flexible metal wiper seal shown in Fig. 7(a). The turbine performance from both of these tests was the same and is indicated by the symbol labeled (1) in Fig. 11. The turbine air flow decreased 7.4 percent and the efficiency increased 2-1/2 points for the sealed vane tests when compared to the unsealed vane test. The wiper seal employed is typical of what could be used in an engine and was used for the remainder of the turbine tests.

A summary of the overall performance results with the first research turbine is given in Fig. 12. The peak efficiency ranged from 87 to 87.3 percent for the different turbine builds and occurred, as expected, with flush aligned nozzle walls. All of the nozzle configurations with the straight sidewalls performed similarly. The contoured nozzle configurations were definitely lower in performance and had different flow characteristics. The nozzle contouring was rather arbitrarily added to the straight wall design and its incorporation into the vane design was not individually optimized. This may explain its lower performance. There was very little difference in performance between moving the hub or shroud walls. At intermediate flow reductions (i.e., 65 percent of the maximum nozzle area), the moveable shroud wall builds performed slightly better than moveable hub wall builds, but the reverse was true at greater flow reductions. The change in efficiency from the peak value to the value at 50 percent nozzle flow area was approximately 2-1/2 points for the moving hub wall and 3-1/2 points for the moving shroud wall. The choice of which wall to move may be selected on the basis of mechanical actuation considerations.

Based primarily on results such as those shown in Fig. 12, two straightwall nozzle configurations with converging vaneless spaces were selected for detailed stator exit flow surveys. The pressure and flow angle measurements taken between two adjacent vanes are shown in Fig. 13. Surveys were taken for four nozzle areas with a moveable shroud wall and one nozzle area with a moveable hub. The rotor was installed and rotating during the surveys. The nozzle wall position is indicated on the figure. High pressure losses (Fig. 13(a)), occurred along the shroud as the nozzle shroud wall was moved into the flow stream indicating probable flow separation. A loss core was also measured near the hub side. This may have been due to air flowing in the vane clearance gap between the main channel flow and the plane of the wiper seal. Locating the wiper seal nearer to the mainstream, as shown in Fig. 14(b), should reduce this hub loss, however this seal change was not evaluated for either turbine. The dashed line in Fig. 13 represents the measured loss with the moveable hub wall. In this case, any recirculating clearance gap flow is shifted from the hub side to the shroud side. However, that by itself does not account for the large pressure loss measured near the shroud. Overall mass weighted pressure losses are listed in the figure.

The angle measurements (Fig. 13(b)), show that changes in flow direction occurred mostly over two-thirds of the channel on the shroud side. As the nozzle area was reduced, the flow angle measured from radial was increased, which is consistent with continuity considerations. The maximum change in flow angle as the nozzle area was changed occurred at 80 percent of the inducer width and equaled 10°.

##### Second Research Turbine

The effect of vane leakage flow on the performance of the second test turbine is shown in Fig. 15. These leakage tests were conducted in a similar manner to the first research turbine. Tests were run at design speed with the vane gap completely sealed and then with the wiper seals installed. Data were taken for a range of pressure ratios at two nozzle area settings, 78 (flush wall) and 100 percent of the maximum area. For the higher pressure ratios tested, the loss in efficiency was about one-fourth point for the flush walls and about one and one-fourth points for the maximum flow area. These losses are greater than those of the first turbine and may be due to the different pressure gradients around the redesigned vane profile.

The effect of nozzle coolant flow on turbine efficiency is shown in Fig. 16 for a stator with flush aligned walls operating at design speed and pressure ratio. A reference test was made with no coolant flow to either the nozzle or rotor backface cavity. The resulting efficiency is shown by a triangle. Data were also taken with a constant coolant flow of 1 percent to the backface cavity and for a nozzle coolant flow range

of 0 to 6 percent. As can be seen, as the nozzle coolant flow was increased the turbine efficiency first increased and then decreased. At the design coolant flow of 5.6 percent, the efficiency was 1.6 points less than the reference value when all coolant flows were zero.

The nozzle coolant was then fixed at 5.6 percent of the mainstream flow as the nozzle flow area was varied. Since the wall position determined the primary flow, cooling was increased or decreased in direct proportion to the vane surface area exposed to the mainstream thus simulating an engine application. The results while operating the turbine at design speed and pressure ratio are summarized in Fig. 17.

All data in the figure were obtained with straight nozzle sidewalls, a converging vaneless space, and vane wiper seals. Both moveable hub and shroud wall geometries are included. The top curve is for a turbine without coolant flow and could represent a machine utilizing a ceramic nozzle assembly. The bottom curves are for 5.6 percent nozzle coolant flow and 1.0 percent rotor backface flow. The peak efficiencies for the cooled and uncooled turbines were 86.4 and 88.0 respectively. The moveable hub and shroud wall geometries performed similarly except for the cooled turbine at the 50 percent closed position. At that condition, the moveable hub turbine efficiency was 2.2 points higher than the moveable shroud turbine. This increased loss, with the moveable shroud, is probably due to the location of the flow disturbance caused by the coolant ejected into the clearance gap, see Fig. 10. This gap coolant enters the rotor hub region where there is low reaction and flow diffusion. A similar effect occurs with the moving hub wall but with a lower loss due to the higher reaction along the rotor shroud. It is felt that the efficiency levels shown in Fig. 17 can be increased by: 1) reducing the leakage loss by relocating the wiper seal as discussed earlier; and 2) redesigning the vane coolant circuit to locate the ejection holes in the mainstream for all wall positions. The latter improvement would apply only to the cooled turbine.

#### Comparison with Pivoted Vane Turbines

Shown in Fig. 18 is a comparison of the performance of the two moveable sidewall turbines with pivoting vane turbines. Many of the turbines compared had different design requirements and applications and so the comparison is made on a nondimensional basis. The moveable sidewall turbines used in these comparisons were the best performing configurations of the first and second test turbines. The Teledyne pivoting vane turbine, listed in the figure, was the design used for the first moveable wall turbine and therefore had the same rotor and vane profiles.

The two moveable wall turbines and the Teledyne pivoting vane turbine had peak efficiencies of generally the same level (not shown in the figure), but the moveable wall turbines maintained substantially higher efficiencies as the flow was varied. The efficiency difference would be even greater than shown if the pivoting vane turbine had realistic vane endwall clearances. During that test program, for each vane angle set, the nozzle sidewalls were drawn against the vanes to eliminate the clearance gap.

The moveable wall turbines also compared well against the two turbines of Refs. 8 and 9. Those two turbines were evaluated for reasons other than variable geometry. In each case, a series of integral machined nozzles were designed to match a single rotor. Each nozzle was uniquely designed for a given stagger angle and in some instances, the number of vanes was changed to obtain an optimum condition. Also, the integral nozzle assembly resulted in no leakage loss. If those turbines were true variable geometry designs, their efficiency loss would be expected to increase from that shown.

#### Comparison of Measured and Predicted Turbine Performance

The efficiency of the moveable sidewall turbine was estimated for use in the variable flow capacity engine cycle calculations of Ref. 4. It was arrived at by adding a leakage loss and a sudden contraction or expansion loss to a predicted radial turbine performance map. The change in efficiency from the design point is shown in Fig. 19 by a solid curve. The change in efficiency from the peak efficiency of the cooled moving hub wall turbine, taken from Fig. 17, is shown for comparison. The research turbine slightly exceeded the estimated performance for flows larger than design flow and was slightly lower at low flows. In general, the test results compare well with the estimate. A redesigned nozzle coolant circuit, as discussed earlier, should raise the efficiency level in the low flow range. The absolute level of turbine efficiency used in the engine cycle calculations was about one point higher than the experimental values. However, a further reduction in seal loss would raise the overall efficiency level of the moveable sidewall turbine. A further increase in turbine efficiency could be realized if ceramics were used in the nozzle reducing or eliminating the coolant flows.

A more recent cycle analysis of the variable flow capacity engine, utilizing the test results of this program, was made and is reported in Ref. 10. The approach differed from the earlier study, Ref. 4, in that the turbomachinery was not kept at constant conditions for the entire mission. Engine power was varied by a combination of RPM and variable geometry changes during the flight. The resulting fuel consumption was compared to the "best" 1984 engines and an advanced technology engine of the 1990's. The results indicated that the variable geometry engine had fuel savings of 26 percent compared to the best 1984 engine, and 11 to 14 percent compared to the 1990's engine in the 60 percent power range.

## SUMMARY OF RESULTS

A performance evaluation was made of a moveable sidewall variable area radial turbine applicable to a variable flow capacity rotorcraft engine. The primary results of the investigation follow.

1. The moveable nozzle sidewall concept is a viable method to efficiently control the flow capacity of a radial turbine. The investigation quantified the performance of turbines with cooled and uncooled nozzles and the effect of variable geometry leakage flows.
2. Peak efficiencies at design speed and pressure ratio of 86.4 and 88 percent were measured for cooled and uncooled turbines respectively. The efficiency decrease from the peak value was about 5 points at 50 percent flow and 2-1/2 points at 100 percent flow for the best performing configurations.
3. The level of the turbine performance was one point or less over the entire flow range from the component estimate used in a variable flow capacity engine cycle which showed significant fuel savings. Several design improvements were identified which should increase the turbine efficiency one or more points.
4. The moveable wall and pivoting vane variable geometry concepts had about the same maximum efficiency, but the efficiency decreased significantly less as the flow was changed with the moveable wall.
5. The best performing turbine configuration had straight nozzle sidewalls and a converging vaneless space. Similar performance results were obtained with either the hub or shroud wall moveable except for the cooled nozzle configuration at 50 percent flow area. For that case, the moveable hub performed better.
6. A flexible metal wiper seal proved to be an effective means of controlling leakage flow around the nozzle vanes.

## REFERENCES

1. Vanco, M.R.; Wintucky, W.T.; and Niedzwiecki, R.W.: An Overview of the Small Engine Component Technology (SECT) Studies. AIAA Paper 86-1542, June 1986.
2. Easterling, A.E.: A Comparative Study of Simple, Regenerative, and Variable Capacity Cycles for Gas Turbine Engines. USAVRADCOM-TR-81-D-1, Oct. 1980.
3. Large, G.D.; and Meyer, L.J.: Cooled, Variable-Area Radial Turbine Program. NASA CR-165408, 1982.
4. Rogo, C.; and Holbrook, M.R.: Cooled Variable Nozzle Radial Turbine for Rotorcraft Applications. (Teledyne-CAE-1759, Teledyne CAE; NASA Contract NAS3-22005) NASA CR-165397, 1981.
5. Rogo, C.; Hajek, T.; and Chen, A.G.: Variable Stator Radial Turbine. (Teledyne-CAE-1987, Teledyne CAE; NASA Contract NAS3-23163), NASA CR-174663, 1984.
6. Rogo, C.; Hajek, T.; and Roelke, R.: Aerodynamic Effects for Moveable Sidewall Nozzle Geometry and Rotor Exit Restriction on the Performance of a Radial Turbine. Advances in Aerospace Propulsion, SAE-P-131, SAE, 1983, pp. 71-81.
7. Rogo, C.: Variable Area Radial Turbine Fabrication and Test Program. (Teledyne-CAE-2231, Teledyne CAE; NASA Contract NAS3-23173) NASA CR-175091, 1986.
8. Kofskey, M.G.; and Wasserbauer, C.A.: Experimental Performance Evaluation of a Radial-Inflow Turbine Over a Range of Specific Speeds. NASA TN D-3742, 1966.
9. Kofskey, M.G.; and Nusbaum, W.J.: Effects of Specific Speed on Experimental Performance of a Radial Turbine. NASA TN D-6605, 1972.
10. Rogo, C.; and Benstein, E.H.: Variable Cycle Turbohaft Technology for Rotorcraft of the '90s. J. Propulsion Power, vol. 2, no. 1, Jan.-Feb. 1986, pp. 73-80.

TABLE I. - VARIABLE FLOW CAPACITY ENGINE CONDITION  
AT 71 m/s FLIGHT VELOCITY AND 82 PERCENT POWER

Inlet pressure, kPa	103.4
Inlet temperature, °C	17.2
Compressor pressure ratio	16
Compressor efficiency, percent	78.3
Combustor pressure drop, percent	3
Combustor efficiency, percent	99.5
GG turbine inlet temperature, °C	1205
GG turbine inlet pressure, kPa	1602.4
GG turbine efficiency, percent	88
Power turbine exit pressure, kPa	107.6
Power turbine exit temperature, °C	578
Power turbine efficiency, percent	88
Shaft power (82 percent of maximum), kW	515
Airflow, kg/s	1.63
Fuel consumption, kg/kW-hr	0.257

TABLE II. - FIRST RESEARCH TURBINE  
EQUIVALENT DESIGN CONDITION AT  
80 PERCENT FLOW

Airflow, kg/s	1.28
Pressure ratio	4.50
Speed, rpm	16540
Specific work, kJ/kg	87.88
Work factor	0.93
Tip diameter, mm	355.6
Tip speed, m/s	306.7

TABLE III. - SECOND RESEARCH TURBINE DESIGN  
CONDITIONS AT 78 PERCENT FLOW

	Engine	Equivalent (2x size)
Rotor inlet temperature, °C	1205	14.5
Inlet pressure, kPa	1602.4	101.4
Airflow, kg/s	1.77	1.44
Rotor speed, rpm	71000	15940
Tip diameter, mm	176.7	353.4
Tip speed, m/s	656.9	294.9
Pressure ratio	4.094	4.54
Specific work, kJ/kg	442.5	88.7
Total efficiency, percent	87.3	87.3
Work factor	1.03	1.03
Nozzle coolant, percent	5.6	5.6
Rotor backface coolant, percent	1.0	1.0

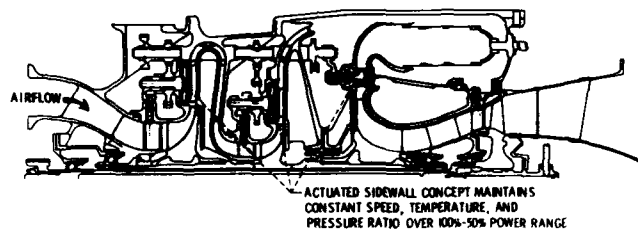
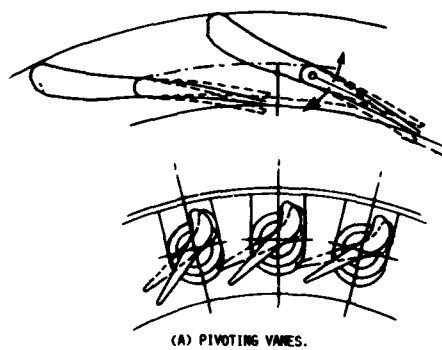


FIGURE 1. - CONCEPTUAL VARIABLE FLOW CAPACITY ENGINE.



(B) MOVING SIDEWALLS.

FIGURE 2. - VARIABLE NOZZLE AREA CONCEPTS.

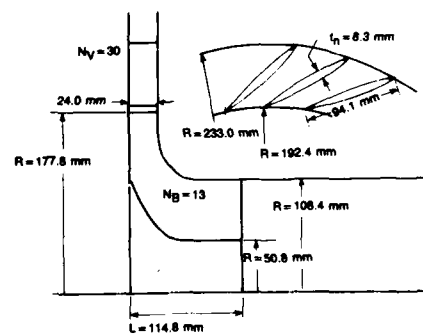


FIGURE 3. - FIRST RESEARCH TURBINE FLOWPATH.

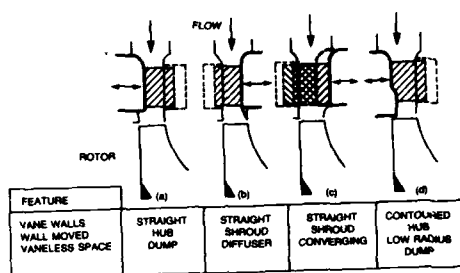


FIGURE 4. - TYPICAL CONFIGURATIONS TESTED.

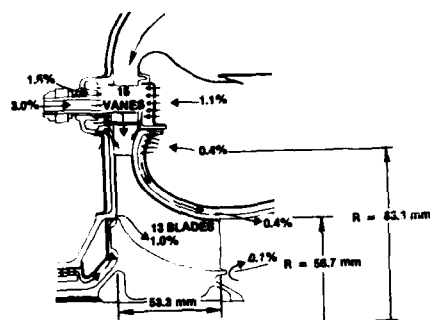


FIGURE 5. - SECOND RESEARCH TURBINE SHOWN IN ENGINE LAYOUT.

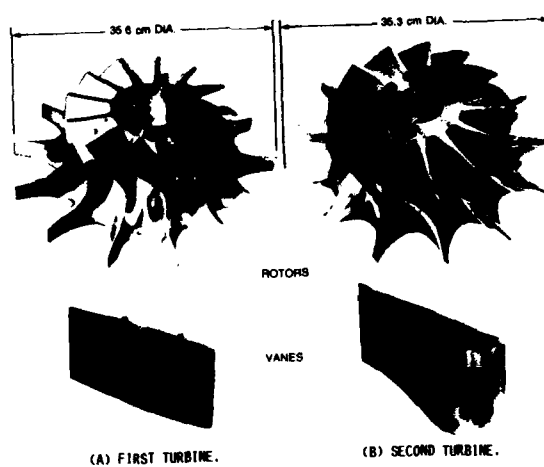


FIGURE 6. - RESEARCH TURBINE BLADING.

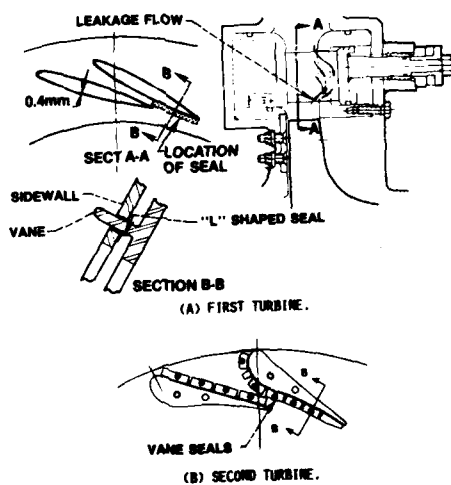


FIGURE 7. - VANE LEAKAGE CONTROL SEALS.

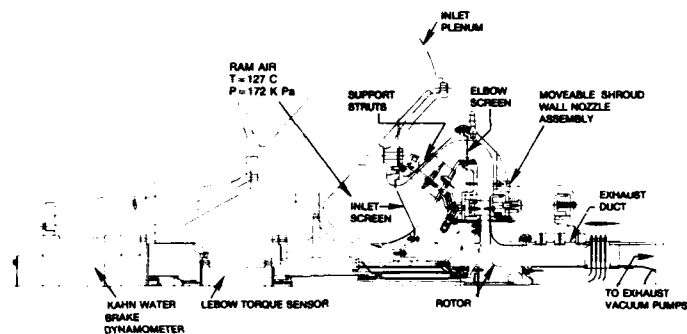


FIGURE 8. - TURBINE TEST RIG CROSS SECTION.

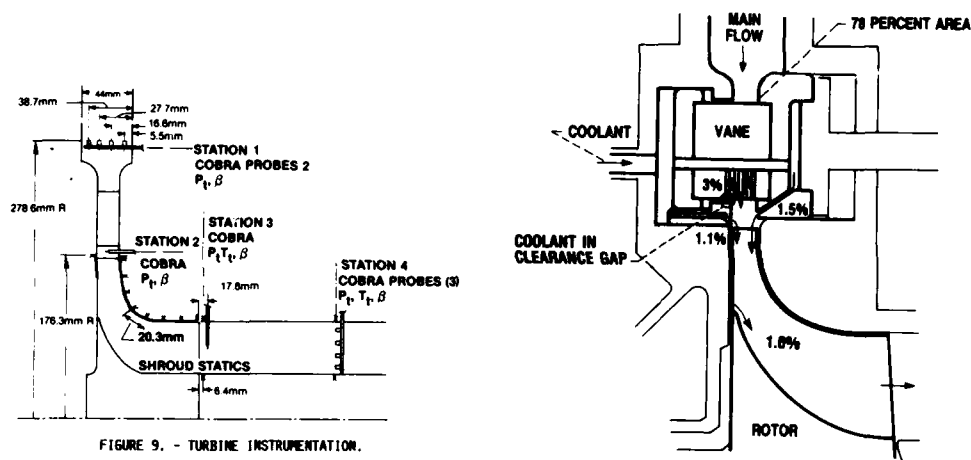


FIGURE 9. - TURBINE INSTRUMENTATION.

FIGURE 10. - SECOND RESEARCH TURBINE SHOWING SIMULATED COOLANT FLOWS.

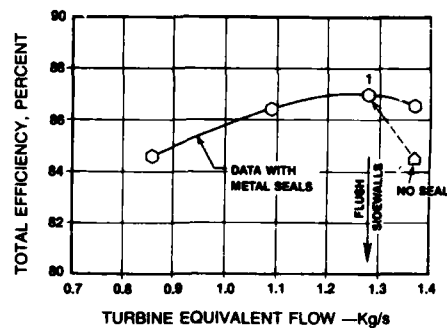


FIGURE 11. - NOZZLE LEAKAGE EFFECT ON STAGE PERFORMANCE OF FIRST TURBINE.



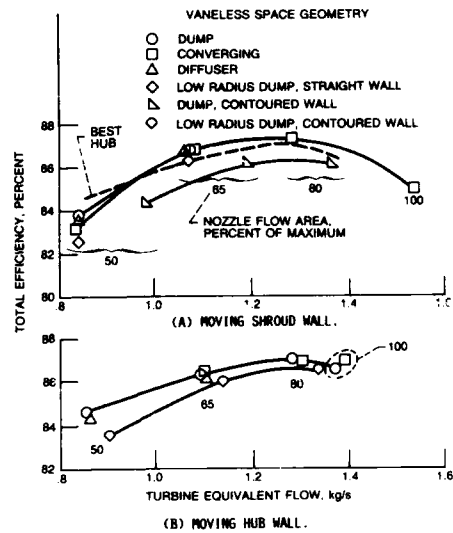


FIGURE 12. - OVERALL PERFORMANCE OF FIRST RESEARCH TURBINE DESIGN SPEED AND PRESSURE RATIO.

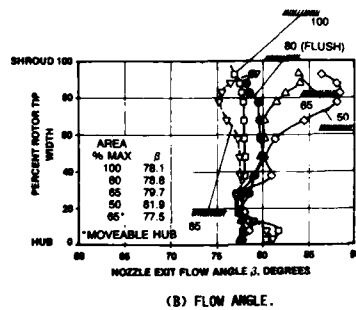
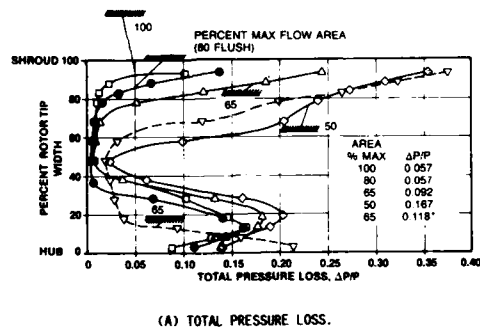


FIGURE 13. - NOZZLE EXIT SURVEY OF FIRST TURBINE.

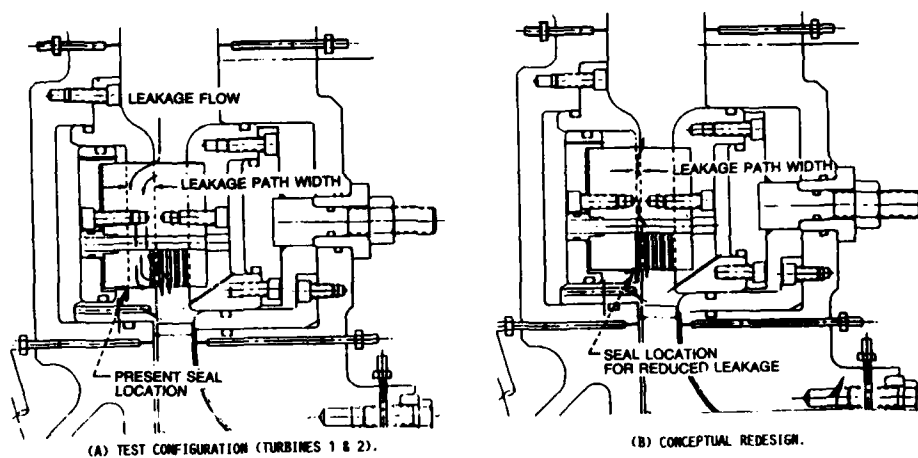


FIGURE 14. - RELOCATION OF NOZZLE SEALS TO REDUCE SIDEWALL LEAKAGE.

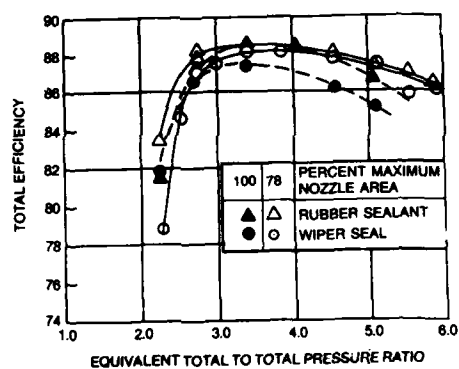


FIGURE 15. - EFFECT OF NOZZLE SEALS ON PERFORMANCE OF SECOND RESEARCH TURBINE AT DESIGN SPEED.

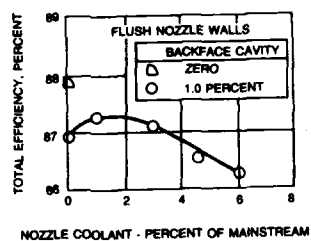


FIGURE 16. - EFFECT OF NOZZLE COOLANT ON TURBINE EFFICIENCY. DESIGN SPEED AND PRESSURE RATIO.

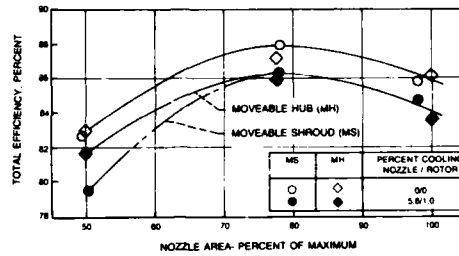


FIGURE 17. - SECOND TURBINE PERFORMANCE AT DESIGN SPEED AND PRESSURE RATIO.

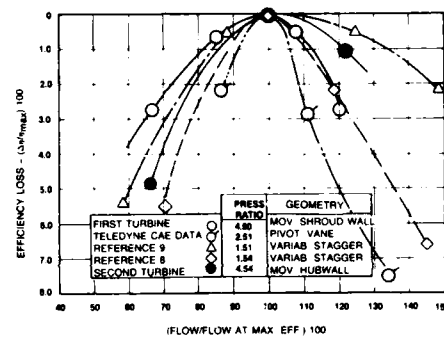


FIGURE 18. - COMPARISON OF MOVEABLE SIDEWALL AND PIVOT-VANE TURBINE PERFORMANCE.

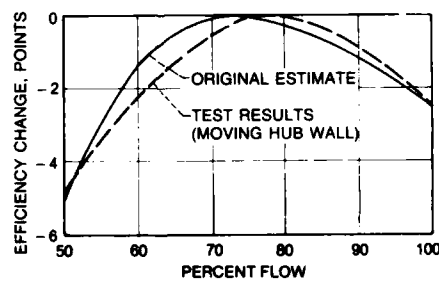


FIGURE 19. - COMPARISON OF ESTIMATED AND MEASURED CHANGE IN TURBINE EFFICIENCY WITH FLOW.

DISCUSSION

U. OKAPUU, Ca

In your figure showing the variation of turbine efficiency with the amount of cooling air injected, is the efficiency shown that of the primary stream only, or does it also include the energy change in the cooling air?

Author's Reply

The efficiency shown, I believe, includes the energy change of both the mainstream and coolant flows. The likely explanation for the increase in efficiency at low coolant flow rates is that the injected coolant at the vane trailing edge energizes the vane wake and therefore, improves the nozzle exit flow field.

R.G. WILLIAMSON, Ca

I understand that the contours chosen were somewhat arbitrary. Could you comment on the use of any contour in circumstances in which there is little hub/tip static pressure gradient?

Author's Reply

The effect of contoured sidewalls on the control of the loss distribution in the nozzle was not fully understood when this program was started (~ 6 years ago), nor for that matter is it today. In that light it was decided to include sidewall contouring in some of the configurations to observe if a benefit in turbine performance resulted.

# AN INTEGRATED AERO/MECHANICAL PERFORMANCE APPROACH TO HIGH TECHNOLOGY TURBINE DESIGN

by

J. Hourmouziadis and G. Albrecht

MTU MOTOREN- UND TURBINEN-UNION MÜNCHEN GMBH

Dachauer Str. 665

8000 München 50

GERMANY

## SUMMARY

Modern aero engine concepts set very high technology standards for the component design. This is particularly true for turbines getting smaller in an increasingly hot environment. Precise control of the air system, the clearances and the deformations of the hardware become an important contributor to the overall performance and the life of the turbine.

This situation suggests attempting an integrated approach to the aero/mechanical design. Analytical and experimental experience from an advanced technology gas generator program is used to define the requirements on the engineering sciences involved. Some aerodynamic, performance and cooling problems to be solved in a common approach with the mechanical design for radial clearance control, hot gas path sealing and life are discussed. Attention is drawn to the interactions between these individual aspects of the design.

## SYMBOLS

$h$	mm	Blade height
$s$	mm	Tip clearance
$\alpha$	m/m.K	Thermal expansion coefficient
$\eta$	-	Isentropic total to total efficiency
$\eta_0$	-	Isentropic efficiency with zero tip clearance

## 1. INTRODUCTION

Advanced aero engine concepts are very demanding on the component design, with aerodynamic performance requirements rising continuously in an increasingly hostile mechanical environment. Particularly with turbines getting smaller and hotter, very close attention has to be paid to the deformations of the hardware, which is only possible if the thermal behaviour is carefully controlled. Presently aerodynamics define the geometry, then cooling is introduced usually penalising performance and finally mechanical design has to make a component with sufficient life while keeping radial clearances and leakage flows under control.

Future developments strongly suggest an integrated approach to these engineering problems. For example aerodynamic design, initiating the whole process, will have to consider features that reduce the heat transfer from the hot gas to the airfoil or can accept the introduction of film cooling without performance penalty. Computation of the pressure field using modern numerical methods can provide timely information on risk areas where hot gas ingestion from the main stream into cavities can happen. It can also indicate the locations where the reintroduction of cooling or leakage air into the main flow will cause minimum losses. Furthermore aerodynamics can assist mechanical design with the prediction of secondary flows defining the evolution and transformation of the flow field passing through a cascade.

Some aspects of such an integrated approach will be discussed in this paper. They will be limited to the following problem areas:

- Radial clearance effects and control
- Hot gas path sealing
- Cooling and secondary flows

Most of the experimental results reported here were obtained in a demonstrator and high pressure turbine rig program over several years. The advanced technology demonstrator GNT 1 shown in Fig. 1 is the single spool gas generator of a 1000 kW class turboshaft engine described by Weiler and Trappmann (1) and Weiler (2). It consists of an axial/radial compressor, a reverse flow combustor and a single stage transonic axial turbine. The program was sponsored by the German Ministry for Research and Technology.

## 2. AERODYNAMIC EFFECTS OF TIP CLEARANCE

Tip clearance is well known to have strong detrimental effects on efficiency. Data for shroudless turbines from refs. 3 to 8 is plotted in Fig. 2 showing the change of isentropic efficiency  $\eta$  relative to the zero clearance value  $\eta_0$  versus tip clearance  $s$  relative to the mean annulus height  $h$ . Authors data from cold rig and hot demonstrator results are also included. Test results in the former case can be reproduced very well giving a high level of reliability for the clearance changes. Relative running clearances  $s/h$  could be determined with an accuracy of  $\pm 0.3\%$ . In a hot engine environment the assessment is extremely difficult, however the data shown in Fig. 2 could be traced quite closely. It was collected when the liner coating broke out in two distinct and well identified steps.

Considering the accuracy of determining the running clearance, the scatter is surprisingly low. An exchange rate of 2% efficiency for 1% clearance can be deduced from the diagram, a rather discouraging fact. The turbines investigated cover a large variety of pressure ratios, aspect ratios and reaction. Obviously the exchange rate has not been sensitive to the designs of the past decades. Ludwig (9) and Haas and Kofsky (6) proposed a relationship between the slope of the curve and the degree of reaction. This conclusion however was drawn using total to static efficiency, which does not appear to be an appropriate parameter. The exhaust kinetic energy of the turbine, which is part of the losses in that definition, is particularly sensitive to any mismatch of the guide vane and rotor blade throat areas resulting indirectly

from a change in tip clearance. From the profile pressure distribution point of view, this conclusion does not appear reasonable either. For a given work output and size of the blading the total aerodynamic loading is the same and the pressure drop across the profile is of the same order of magnitude for an impulse and a reaction design.

There are two ways of attacking the tip clearance problem. On one hand the aerodynamic design can be refined to reduce its sensitivity to clearance effects, on the other hand a sophisticated mechanical design can be applied to minimise clearances. Most of the published work is concerned with the former. Booth (10) has presented a comprehensive literature survey complementing the experimental and numerical studies reported by Booth, Dodge and Hepworth (11), Wadia and Booth (12) and Wadia (13). The proposed improvements generally try to increase the resistance to the cross flow in the clearance gap. The suggested configurations include:

- Blade tip running in grooves
- Winglets
- Variation of the geometry of the blade tip
- Cooling air from the blade blowing into the radial gap
- Reduction of work extraction close to the tip

Some of these concepts shown schematically in Fig. 3 were investigated in an extensive cold rig programme at MTU. The high pressure turbine of the demonstrator with an outer diameter of 210mm and an aspect ratio of 1 was used. Clearance was varied using three liners of different diameter.

Experimental data indicating a positive effect on the slope of efficiency versus clearance with blade tips running in circumferential grooves in the casing have been reported by Kofskey (14) and Haas and Kofskey (6). The latter are also plotted in Fig. 2. It can be seen that the exchange rate was reduced from 2.0/1 to about 1.5/1. No further published data is available. Such a configuration was part of the test programme and is included in the authors rig results shown in Fig. 2. The previous observations could not be confirmed. No effect of the grooves on the slope of the curve could be identified.

Blade tip treatment is limited by mechanical constraints. Winglets investigated by Patel (7), Booth, Dodge and Hepworth (11) and Adams and Hepworth (15) cannot be introduced for turbine blades because the higher weight leads to unacceptable stresses in the blade root. Knife edge tips should not be used with abrasive liner coatings and are not strong enough for running-in configurations. The hollow or grooved tip shown in Fig. 3 was tested and compared with the flat tip. Both results are included in the rig data of Fig. 2. An efficiency improvement was expected corresponding to about 15% reduction in tip leakage flow observed in the water tunnel experiments of Booth, Dodge and Hepworth (11). The results however were negative. No effect on performance could be identified.

The experimental and analytical studies of Wadia and Booth (12) promised an improvement with air injection at the tip. A method which could also satisfy cooling requirements in a high pressure turbine blade. The effect, obviously caused by the blockage reducing the amount of high energy gas leaking across the blade tip, was confirmed in the rig. It did not change the slope of the efficiency versus clearance curve but reduced the overall level of loss.

Reduction of the work done close to the tip is usually incorporated in every turbine design and is limited by the loading capability of the mean section. The radial work redistribution potential of the turbine was rather small and was not included in the study.

The available information on efforts to reduce aerodynamic turbine sensitivity to tip clearance effects is not very promising. It indicates that the flow phenomena and the parameters involved are not understood yet. A lot of fundamental research like that reported by Graham (16) and Sjolander and Amrud (17) as well as numerical analysis is still required to identify applicable solutions. At present design work will have to concentrate on mechanical clearance control.

### 3. MECHANICAL TIP CLEARANCE CONTROL

The mechanical aspect of the problem is by all means just as challenging as the aerodynamic aspect. The engine operating conditions demanding high levels of performance are shown in the compressor map in Fig. 4. The design targets for an optimum clearance control can be summarised in the requirements for minimum clearance for steady state stabilised high power settings and sufficiently small values for the acceleration of the cold engine.

Although the number of engineering publications is limited, the amount of patent applications is a clear indication of the importance of the problem. Its complexity is illustrated in Fig. 5 showing the interacting design parameters. Minimising tip clearance is limited by the engine configuration, the installation and the operational constraints including manoeuvre load deflections. Manufacturing and assembly tolerances as well as eccentricities present further limitations. These effects make it necessary for unshrouded turbines to set a minimum clearance avoiding rubbing at the blade tip under normal conditions. The most severe problem however is the adaption of the expansion rates of the rotor and the casing during engine transients as has been discussed by Hennecke and Trappmann (18), Lagrange (19) and Hourmouziadis and Schrieck (20). Since the disc is defined by stress and life requirements, it is the thermal response of the casing that will have to be adapted to that of the rotor. For a typical small high pressure turbine configuration shown in Fig. 6 the evolution of clearance versus time for an acceleration from stabilised idle and a deceleration from stabilised TO rating is shown in Fig. 7. The following targets have to be met for the thermal response in engine operation.

- The stabilised steady state diameter increase of the casing should be of the same order as the thermal expansion of the disc.
- This reduces the risk of rubbing in a hot restart situation,
- it also provides sufficient margin for tolerances and bearing clearances to avoid rubbing during the starting procedure of the engine. When liner segments in an outer casing are used, attention should be paid to the fact that the inner diameter decreases when the segments heat up fast in a cold outer ring during starting.
- The transient thermal behaviour of the casing should be designed to be slow and should be adapted to the time constants of the disc.

- This would limit the tip clearance increase during a cold engine acceleration
- and would further reduce the running in risk from a hot restart.
- If the above ground rules are observed, the risk of rubbing the blade tip when the engine is shut down from a high power setting is very low.

The main difficulty encountered meeting these targets is the high temperature at the outer part of the casing resulting from the high pressure ratio compression systems used in advanced engines. Overcoming these problems requires a sophisticated design philosophy outlined in Fig. 8.

The casing structure is resolved into a supporting ring taking the loads and separate liner segments. The lowest theoretically possible temperature of the supporting ring is that of the surrounding air, 100 to 200 K hotter than the compressor discharge. As mentioned before, that is already almost too high for the desired low thermal expansion levels. This means that a careful design is necessary to isolate this part of the casing from the hot gas path and avoid any further heat flux into the ring. Fortunately this also satisfies the requirement for a slower thermal response. Furthermore thermal stresses as well as the deterioration of material properties are reduced.

The shielding function is taken over by the liner segments, which themselves have to be protected from the hot gas temperatures. The application of thermal barrier coatings is one way of doing this. Attwood (21) has presented some considerations about their application. Two methods of incorporating the Yttria stabilised Zirconia coating in the turbine casing are being investigated.

- The thermal barrier material is embedded in a honeycomb structure bonded to the segments. This is a design that has been successfully developed for the HPT of a military engine. It has two disadvantages. Firstly too much heat is conducted through the honey comb material to the liner. Secondly the honey comb metal is too hard, so that the blade tips wear out in case of rub.
- The improved solution is a coating sprayed directly on the liner segments with a suitable bonding sublayer.

In both cases the abradable properties of the coating are not particularly good. Contact between the blade and the casing will have to be avoided, even if hardened tip caps are used.

Cooling is the other way of keeping liner temperatures low. Impingement cooling is applied through holes in the supporting ring. Film cooling is also very efficient. Small, closely controlled amounts of air are introduced upstream of the liner.

The supporting ring itself is also cooled by the liner impingement air. Heat convection and radiation from the segments to the ring is inhibited by a perforated sheet of metal. The outer diameter of the ring is protected by a heat shield from the radiation of the combustor.

If these measures do not suffice to ensure the necessary thermal behaviour of the casing, materials like Incoloy 907 with lower thermal expansion coefficients (Fig. 9) have to be considered. Further slowing down of the thermal response can be accomplished by local accumulation of material and thickening of the support ring. Research is also being performed for future application of ceramic materials in the structure.

#### 4. HOT GAS PATH SEALING

Isolation of highly stressed parts from the temperatures of the main flow has become a dominating design feature for advanced engines. It requires a very comprehensive secondary air system that helps avoid hot gas ingestion into cavities, supplies the necessary cooling air and minimises leakages. This has to be coupled with a careful design of gas seals to provide the necessary resistance to the pressure drop between the main flow and the cavities.

A particular problem arises with transonic guide vanes in highly loaded turbines. The structure of the flow in such a guide vane is shown in Fig. 10 in the experimental Schlieren photograph and the time marching prediction taken from Happel, Dietrichs and Lehmann (22). Two compression shocks originate at the trailing edge. Shock a) is reflected on the suction side b) and propagates downstream. The suction side shock c) is usually stronger and is of significant influence to the pressure field behind the cascade. An important side effect of these phenomena is the pitchwise pressure distribution at the guide vane exit shown schematically in Fig. 11. The pressure drop across the shock is of the order of 1 bar depending on the operating conditions. The area between guide vane and rotor blade usually communicates with cavities where a constant pressure prevails. An example is shown in Fig. 11 at the casing, in the structure designed to take the thermal loads. Although the average pressure drop over the connecting gap may be negative, the distribution along the pitch would lead to hot gas entering the cavity behind the shock and leaving it at the low pressure main stream region. This results in recirculation zones downstream of every individual guide vane passage overheating structurally highly loaded parts.

Minimising these effects sets three targets to be achieved by mechanical design.

- Reduce the size of the cavities
- Provide sufficient through flow of cooling air
- Increase the resistance to the recirculating flows.

For the situation at the casing described above, achieving adequate control of the sealing air is rather difficult. This is due to the relative movements of the guide vane and the supporting ring. Recirculation however was significantly reduced by filling the cavity and introducing a sealing strip as shown in Fig. 12.

Solving the problem at the hub is just as difficult, because the seal is situated between a static and a rotating part and cooling air has to be supplied to the rotor in the same vicinity. In this case the two functions of the air system have to be separated. Fig. 13 shows a configuration taking these considerations into account. A cover plate design is used to increase the pressure of the cooling air and to guide it to the disc rim and the blade. Preswirl is introduced to keep the temperature of the cooling flow low. The pressure drop across the front seal is adjusted to provide the necessary through

flow. A double seal concept has been selected to reduce the size of the cavity and to minimise the leakage flow. It should also reduce the pitchwise pressure gradients by mixing processes between the seals.

## 5. SECONDARY FLOWS AND COOLING

The high combustor temperature levels in advanced engines require a very complex cooling philosophy to provide sufficient life with as low a performance penalty as possible. One aspect that needs particular attention are secondary flows. They dominate the rearrangement of the temperature field along the blade passage, transporting hot gases across the main flow. This requires again an integrated approach to aerodynamics, heat transfer and cooling as well as mechanical design.

The three principal secondary flow structures in a gas turbine are shown in Fig. 14.

- The rotational motion induced by the trailing edge shed vorticity when forced vortexing is applied to the aerodynamic design. Since potential vortexing is effectively not used any more for modern turbines, this secondary flow is always present. However 3D Euler predictions and test experience indicate that the motion is quite slow not exceeding about 1/20th of a revolution per passage length in axial turbomachinery.
- The passage vortices on both end walls are generated by the boundary layers at the hub and at the casing. The secondary velocities involved are one order of magnitude larger and they transport large amounts of fluid across the passage.
- The horse shoe vortices on both end walls represent the fastest secondary motion. The pressure side leg of these vortices is transported by the passage vortices towards the suction side, where these flows concentrate. Their structure is quite complex, the amount of fluid affected however is rather small.

The transport of hot gases around the passage by these secondary flows is the important aspect from the cooling point of view. The evolution of the temperature field from the inlet to the exit of a turbine guide vane is shown schematically in Fig. 15. The temperature distribution entering the passage is assumed to be axisymmetric and cold at the end walls, particularly at the hub. At the exit plane the trailing edge shed vorticity has shifted the mid section hot gases only slightly towards the casing on the pressure side and towards the hub on the suction side. The passage vortices give the strongest contribution pushing the hot gas region onto the pressure side across the span of the airfoil. The horse shoe vortex carries the incoming boundary layer and part of the flow close to the end walls into the main stream.

This is a qualitative description of the characteristics of secondary flows. Prediction techniques are not yet sufficiently reliable for design work, one has to resort to experimental results. Fig. 16 shows the flow visualization in a turbine guide vane discussed by Dietrichs (23). At the casing the effects of both the horse shoe and the passage vortex can be clearly seen at the inlet. At the hub exit however the motion across the passage can not be identified. The particularly strong acceleration in the inlet guide vanes of high pressure turbines, with typical exit to entry velocity ratios of about 10, appears to lead to very thin boundary layers at the hub. This results in low intensity secondary flows.

It is quite evident that these phenomena have to be accounted for in advanced designs. For example two conclusions can be drawn from Fig. 15.

- Near the trailing edge of the airfoil the hot gases have accumulated on the pressure side. This is quite useful information for the definition of the cooling system.
- If film cooling is to be used for that part of the guide vane, it is evident that it will have to be introduced in the rear part of the passage. Any cooling air injected further upstream would be washed away from the airfoil onto the end walls and would be less effective.

## 6. CONCLUDING REMARKS

Blade tip clearance control remains one of the dominating problems in unshrouded high pressure turbines. In spite of a lot of experimental work in the recent past, no reliable solutions for aerodynamic control have yet emerged. Numerical methods are available today and should be used to attack the problem. There are many parameters involved in mechanical control and they are well known. Difficulties arise when trying to integrate them in the design.

Gas path sealing and cooling pose a further challenge to advanced engine design. New problems are encountered with highly loaded transonic turbines. Although applicable solutions already exist some of the design tools still need to be improved. Reliable secondary flow prediction techniques are needed which can be developed based on the broad experimental data available today.

## 7. ACKNOWLEDGEMENT

The authors would like to express their gratitude to H. Kneissl from the turbine test group and to H. J. Dietrichs from the turbine aerodynamics group who provided the test results, and to the German Ministry for Research and Technology who sponsored the program with the registration number LFT 8303/4. The responsibility for this publication lies with the authors.



## 8. REFERENCES

1. W. Weiler and K. Trappmann  
Die Versuchstriebwerke GNT 1 und WD 1000 und ihre Anwendungen  
DGLR Annual Meeting, 17 - 19 October 1983, München, Germany
2. W. Weiler  
Gasgenerator neuer Technologie (GNT 1) - Aktueller Entwicklungsstand  
4th BMFT-Statusseminar, Aeronautical Research and Technology, 28 - 29 April 1986, München
3. C. Rogo  
Experimental Aspect Ratio and Tip Clearance Investigation on Small Turbines  
SAE Paper 680448, 1968
4. D. E. Holeski and S. M. Futral Jr.  
Effect of Rotor Tip Clearance on the Performance of a 5-Inch Single-Stage Axial-Flow Turbine  
NASA TM X-1757, 1969
5. J. S. Ewen, F. W. Huber and J. P. Mitchell  
Investigation of the Aerodynamic Performance of Small Axial Turbines  
Journal of Engineer for Power, October 1973, pp. 326 - 332
6. J. E. Haas and M. G. Kofskey  
Effect of Rotor Tip Clearance and Configuration on Overall Performance of a 12.77-Centimeter Tip Diameter Axial-Flow Turbine  
ASME Paper 79-GT-42, March 1979
7. K. E. Patel  
Research on a High Work Axial Gas Generator Turbine  
SAE Paper 800618, April 1980
8. J. D. Bryce, M. R. Litchfield and N. P. Leversuch  
The Design, Performance and Analysis of a High Work Capacity Transonic Turbine  
ASME Paper 85-GT-15, March 1985
9. L. P. Ludwig  
Gas Path Sealing in Turbine Engines  
NASA TM-73890, April 1978
10. T. C. Booth  
Tip Clearance Effects in Axial Turbomachines  
VKI Lecture series 1985-05, 15 - 18 April 1985
11. T. C. Booth, P. R. Dodge and H. R. Hepworth  
Rotor-Tip Leakage: Part I - Basic Methodology  
ASME Paper 81-GT-71, March 1981
12. A. R. Wadia and T. C. Booth  
Rotor-Tip Leakage: Part II - Design Optimization through Viscous Analysis and Experiment  
ASME Paper 81-GT-72, March 1981
13. A. R. Wadia  
Numerical Calculations of Time Dependent Three-Dimensional Viscous Flows in a Blade Passage with Tip Clearance  
AIAA Paper 83-1171, June 1983
14. M. G. Kofskey  
Experimental Investigation of three Tip-Clearance Configurations over a Range of Tip Clearance using a Single-Stage Turbine of High Hub to Tip Radius Ratio  
NASA TM X-472, May 1961
15. N. G. Adams and H. K. Hepworth  
Cantilevered Stator Vane Tip Leakage Studies  
AIAA Paper 85-1136, Juli 1985
16. J. A. H. Graham  
Investigation of a Tip Clearance Cascade in a Water Analogy Rig  
ASME, Paper 85-IGT-65, September 1985
17. S. A. Sjolander and K. K. Amrud  
Effects of Tip Clearance on Blade Loading in a Planar Cascade of Turbine Blades  
ASME Paper 86-GT-245, June 1986
18. D. K. Hennecke and K. Trappmann  
Turbine Tip Clearance Control in Gas Turbine Engines  
AGARD-CP-324, October 1982
19. J. P. Lagrange  
Maitrise des jeux axiaux et radiaux - situation actuelle et perspectives  
AGARD-CP-324, October 1982

20. J. Hourmouziadis and R. Schrieck  
Technologie moderner Wellentriebwerke für Hubschrauber  
MTZ 47 (1986) 6, pp. 243 - 249
21. R. S. Attwood  
Shroud Segments for Unshrouded Blade Turbines  
AGARD-CP-390, May 1985
22. H.-W. Happel, H. J. Dietrichs and K. Lehmann  
Computation of Transonic 2D Cascade Flow and Comparison with Experiments  
AGARD-CP-401, September 1986
23. H. J. Dietrichs  
Steigerung der Energieausnutzung in gekühlten Hochtemperatorturbinen  
4th BMFT-Statusseminar, Aeronautical Research and Technology, 28 - 29 April 1986, München

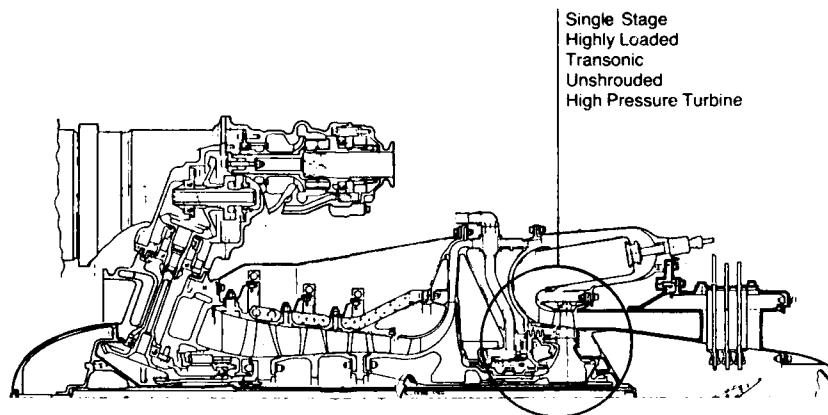


Fig. 1 Advanced Technology Demonstrator GNT 1

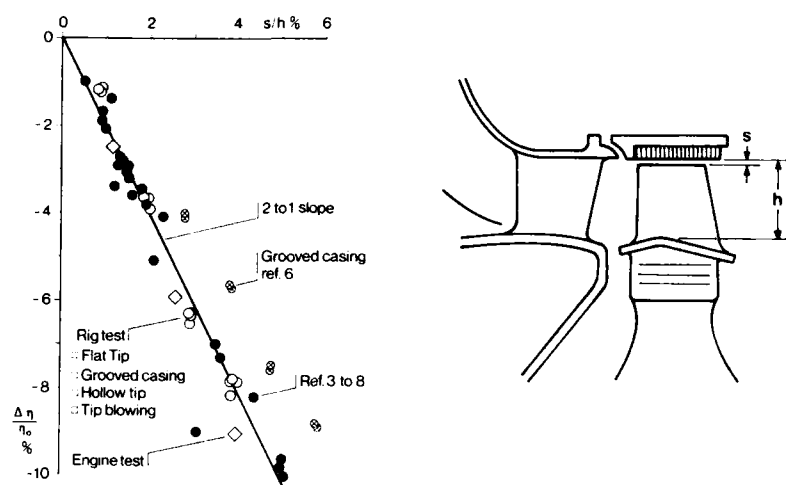


Fig. 2 Effects of Tip Clearance on the Efficiency of Single Stage Shroudless Turbine

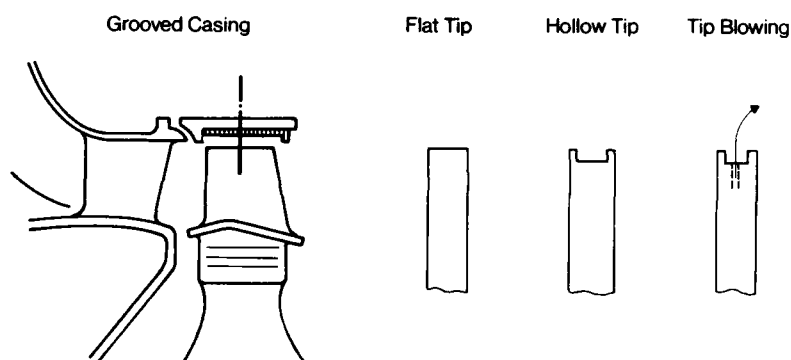


Fig. 3 Blade Tip Treatment Configurations

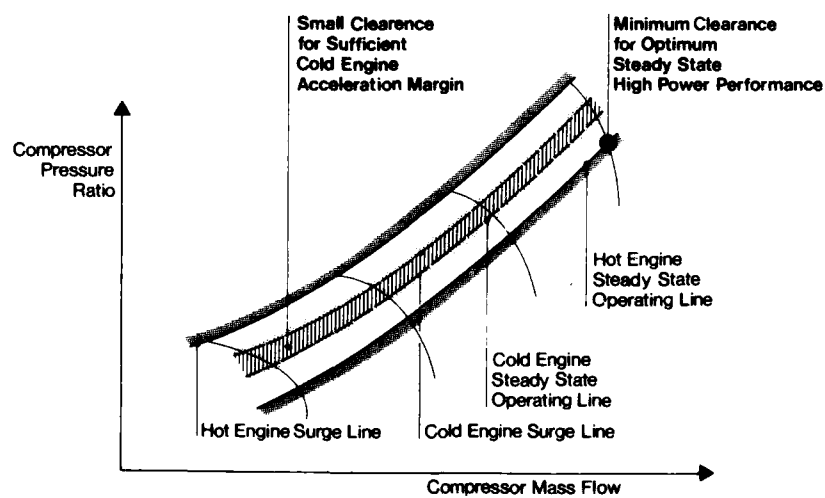


Fig. 4 Engine Operating Conditions Requiring Low Turbine Tip Clearance

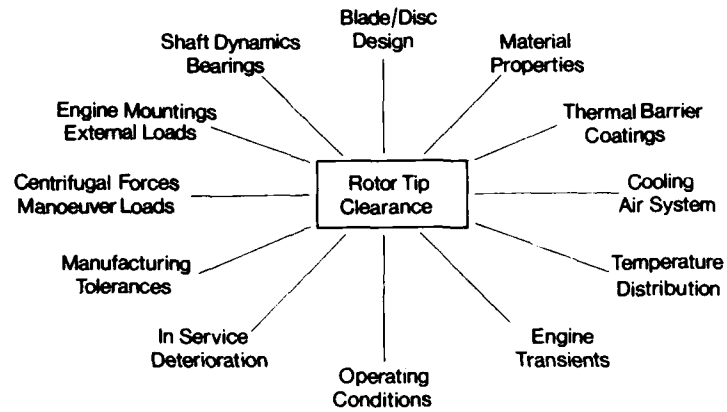


Fig. 5 Design Parameters Affecting Tip Clearance in Unshrouded Turbines

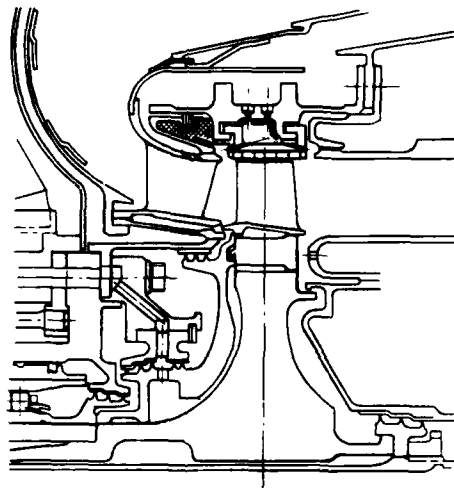


Fig. 6 High Pressure Turbine Concept for Thermal Expansion Control

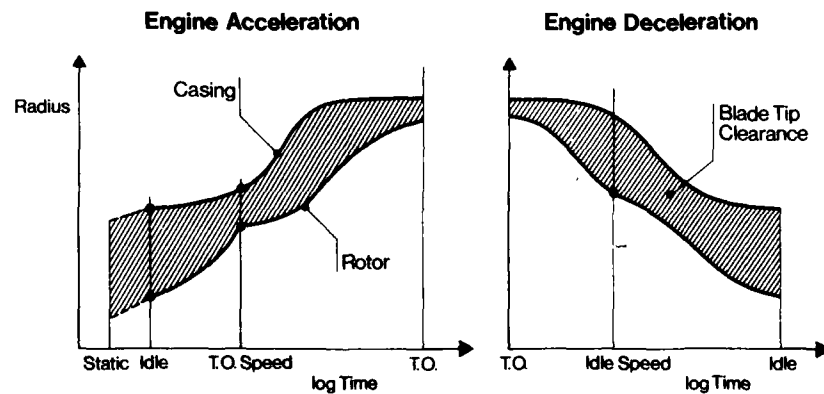


Fig. 7 Evolution of Turbine Blade Tip Clearance Engine Transient Operation

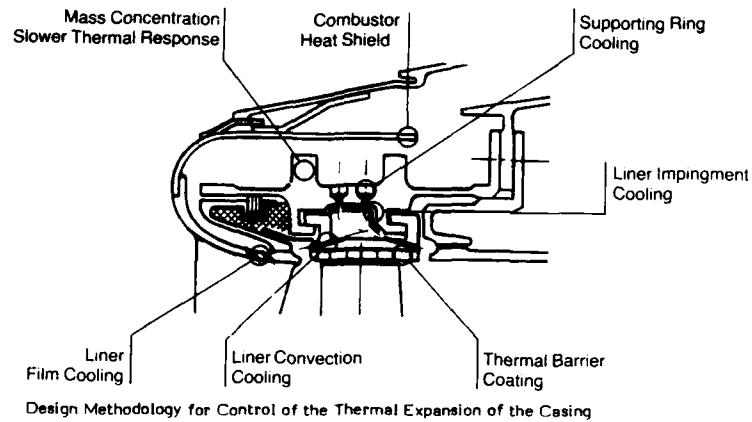


Fig. 8

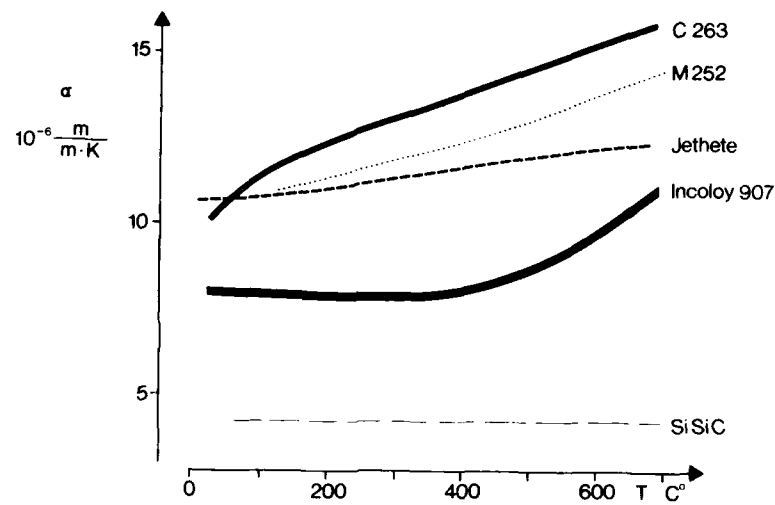


Fig. 9

Thermal Expansion Properties of High Temperature Alloys

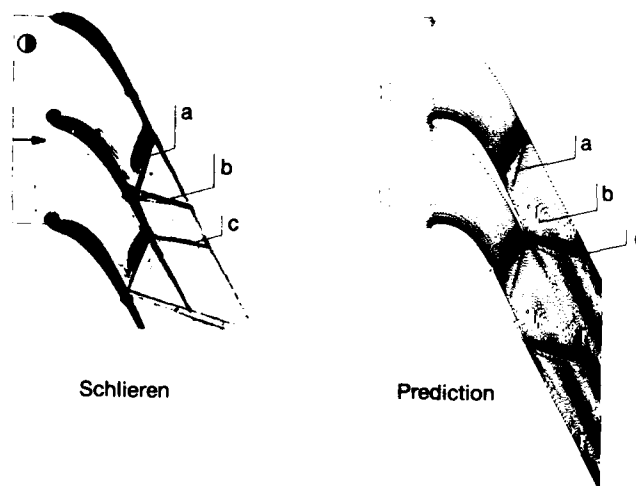


Fig. 10

Shock Structure in the Guide Vane of a Transonic Turbine

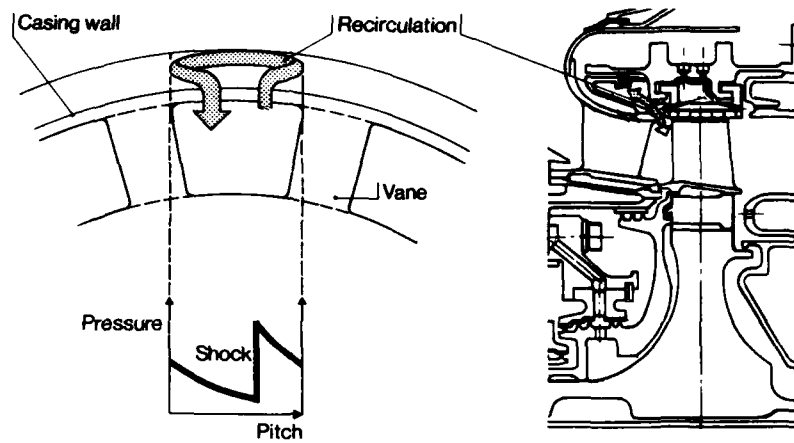


Fig. 11 Secondary Air System Effects in Transonic Turbines

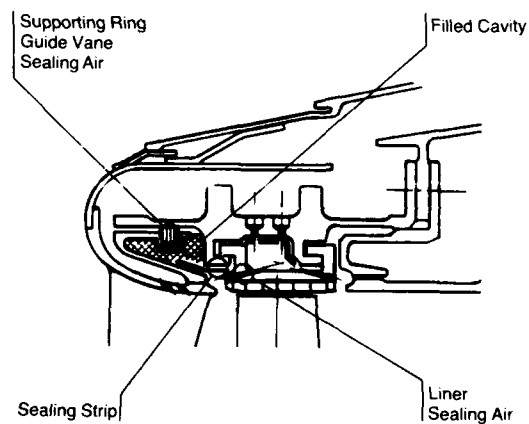


Fig. 12 Gas Path Sealing at the Casing

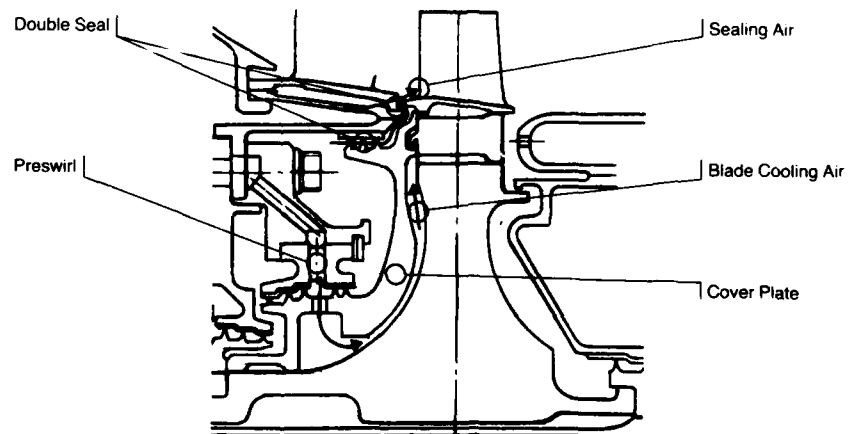


Fig. 13 Gas Path Sealing at the Hub

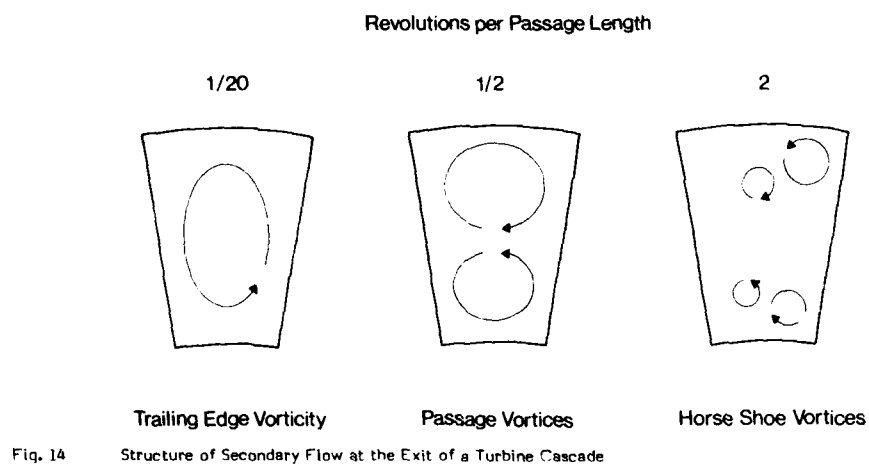


Fig. 14

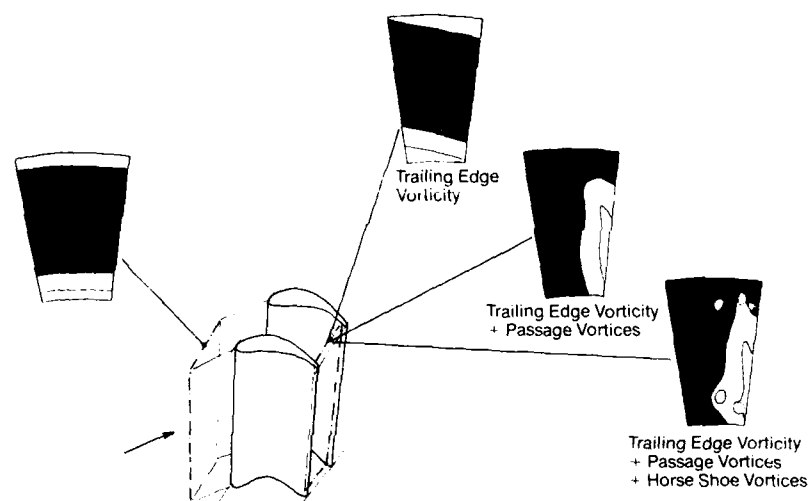


Fig. 15

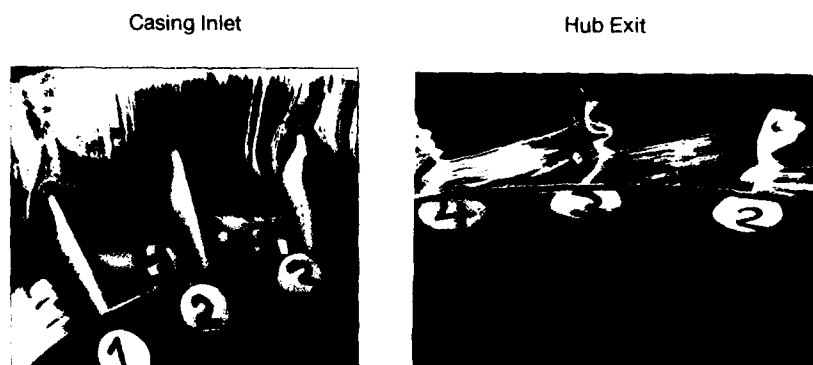


Fig. 16

Transonic High Pressure Turbine Flow Visualization in the Inlet Guide Vane

DISCUSSION

A.S. ÜÇER, Turkey

In figure 7 you are showing the variation of blade tip clearance. How this clearance was measured ?

**Author's Reply**

Figure 7 is a qualitative presentation of the thermal transients in the engine. Clearance cannot be measured directly. It is assessed from material and air system temperature measurements and the computed thermal expansion of the parts. At the beginning of an engine program, this estimation is not very accurate. With accumulating experience, after about 100 test hours, this estimation becomes quite reliable. Absolute clearance under all operating conditions including transients can be calculated better than 1 % s/h.



# DESIGN AND TEST OF A HIGH BLADE SPEED, HIGH WORK CAPACITY TRANSONIC TURBINE

by

R.C. Kingcombe, J.D. Bryce, N.P. Leversuch

Royal Aircraft Establishment, Pyestock,  
Farnborough, Hampshire, GU14 0LS, England

## SUMMARY

A high rim-speed turbine has been designed and tested at RAE Pyestock. A major objective in the design was to achieve high aerodynamic efficiency at high work capacity by way of reduced stage loading - facilitated by high blade speed. The design includes three-dimensional features such as a parabolic distribution of exit angle and compound trailing-edge lean on the nozzle guide vane and a thick root, highly tapered rotor blade - necessary in an engine turbine to moderate blade stress.

The paper describes the design approach and presents and discusses the results of cold flow rig tests undertaken at RAE Pyestock. Measurements included NGV and rotor blade surface static pressures as well as detailed traverses.

## 1 INTRODUCTION

The need to develop a single stage HP core turbine which has both high aerodynamic efficiency and high work capacity has been the subject of much recent research effort. At such high work capacity engines often adopt 2-stage HP turbines to drive the core. However, modern advances in materials technology on both blades and discs permit increases in turbine blade speed sufficient to generate the desired work capacity in a single stage, whilst maintaining a high level of turbine efficiency. The major contribution to high efficiency is the moderate level of turbine stage loading achievable when operating at high blade speed. The turbine has the following parameters:

work capacity $C_p \Delta T/T$	285 J/KgK
aerodynamic loading $\Delta h/U^2$	1.46
blade speed $U/\sqrt{T}$	14 m/s $\sqrt{K}$
flow coefficient $V_A/U$	0.41
rotor mean hub/tip ratio	0.87
flow function $Q\sqrt{T}/P$	0.76 (kg/s) $\sqrt{K}/(kN/m^2)$

This duty is compared with some other research turbines on Fig 1. Included on the figure are some American turbines <sup>1,2,3</sup> and a previous research turbine designed and tested at RAE Pyestock<sup>4</sup>. This turbine had a very high work capacity ( $C_p \Delta T/T = 306$ ) and a high aerodynamic loading of 2.1 using a moderate level of blade speed ( $U/\sqrt{T} = 12$ ). It achieved a rig efficiency of 87% at a tip clearance of 1.4% of blade height. The high rim speed turbine aimed to demonstrate considerably higher aerodynamic efficiency at the higher blade speed and lower loading.

An important feature in modern turbine design, contributing to high aerodynamic efficiency, has been the choice of three-dimensional geometry for the aerofoils. One of the first to incorporate such features was the AIRESEARCH turbine<sup>5</sup> which featured pronounced compound trailing-edge lean on the NGV, together with radial work distribution. Successful incorporation of three-dimensional geometry to advanced HP turbine design requires computer codes to predict the three-dimensional flow in complex turbine passages. For this turbine, the Denton three-dimensional inviscid time-marching computer program<sup>6</sup> was applied extensively to the aerodynamic design.

## 2 AERODYNAMIC DESIGN

The turbine annulus is shown on Fig 2. It features cylindrical end-walls on the NGV and equal and opposite flare of 7.2° on the inner and outer walls of the rotor blade, which is shroudless.

The assumed NGV and rotor losses were derived from both published correlation methods<sup>7,8,9</sup> and other turbine data. The NGV mean loss was assumed to be 0.08, resulting from a profile loss (profile, trailing edge and shock) of 0.04 together with a secondary loss of 0.04. The manner in which the loss was distributed across the annulus is shown on Fig 3(a) where it can be seen that the secondary loss has been concentrated in the inner and outer 30% of the span. There was some optimism fed into the assumed level of secondary loss, which it was hoped to minimise by three-dimensional design.

On the rotor, the profile loss (profile, trailing edge and shock) was assumed to be 0.08, the secondary loss 0.08 and the overtight leakage 0.04. These components were distributed as shown on Fig 3(b). It can be seen that because of the NGV wakes and loss cores, some effect of the secondary loss may be felt even at mid-height. The tip clearance loss is concentrated in the outer annulus region.

A throughflow analysis study was then carried out to select the blade velocity triangles. A parabolic forced vortex of NGV outlet angle was specified in order to concentrate most work in the most efficient central region of the flow and also to unload the end wall sections to help reduce secondary flow and loss. A similar parabolic variation of rotor exit angle was chosen for the same reasons. The variation of inlet and outlet gas angles and Mach numbers is shown on Fig 4. The NGV exit Mach numbers are slightly supersonic (about 1.05 to 1.1 at root and mean sections) and the rotor gas exit Mach numbers relative to the blade are low supersonic (1.0 to 1.1 at root, mean and tip sections). The exit swirl from the rotor blade is at a mean value of about  $25^\circ$ . The reaction varies from 37% at the root to about 43% at the tip. The throughflow analysis, with the above losses, yields a total-to-total adiabatic efficiency of 91.5%. This is a gas path figure and excludes bearing losses and disc windage. At this high rim speed, and for the rig disc which has protruding bolt heads, provisional estimates of bearing loss and windage indicate a penalty of about 1½% on turbine efficiency.

### 3 BLADE DESIGN

Preliminary blade profiles were selected using a quasi-three dimensional design method<sup>10</sup> which allowed blade-to-blade calculations to be carried out including the effect of change of streamtube height and rotational effects. Final design was carried out using early versions of the Denton three-dimensional time-marching program<sup>6</sup>. After the design had been committed for manufacture further predictions were carried out on an improved version of the program<sup>11</sup>. It is these predictions that are presented in this Paper.

Trailing-edge thicknesses of 0.89 mm and 0.85 mm were selected for the NGV and rotor respectively together with wedge angles of  $4^\circ$ , so that the design would be mechanically practical in an engine, in which the aerofoils would have to be cooled.

#### 3.1 Nozzle guide vane

A constraint on the choice of NGV numbers was the decision to use the existing transonic turbine casing for the testing of this design. Thus, despite the optimum number of vanes being around 36, 40 vanes were chosen. Use of this casing, which has cylindrical end-walls, also prevented incorporation of end-wall profiling.

The NGV stacking was chosen on the basis of previous work and published results<sup>5</sup>. A significant advantage in controlling NGV secondary flows stems from compound trailing-edge lean such that the suction surface displays concavity in the hub to tip direction on the back surface of the vane. This is illustrated on Fig 5. This lean introduces radial pressure gradients on the aerofoil limiting movement of the blade boundary layer into the end-wall region. This has the effect of reducing the secondary loss. The maximum tangential lean was limited to  $25^\circ$  at the end-walls. Seven design sections were selected and were stacked on the trailing-edge line in a constant axial plane but varying in the pitchwise direction as shown on Fig 5.

The final vane is illustrated on Fig 6 by a computer picture together with a photograph. The pressure distribution at hub, mean and tip sections is shown on Fig 7. Illustrated are the predictions carried out with the improved Denton program<sup>11</sup> after the vane had been committed to manufacture. There is generally smooth acceleration of the flow up to the throat region, with modest peak Mach numbers, reaching 1.14 on the hub section suction surface. Predicted contours of static pressure on the suction and pressure surfaces are shown on Fig 8. The patterns indicate largely two-dimensional flow with a slight static pressure gradient away from the end-wall towards mid-span in the region up to the throat. It should be noted that the three-dimensional shaping of the blade is only slight in the leading-edge region, giving very small effects in this area.

#### 3.2 Rotor blade

This blade features deliberate choice of a thick root highly tapered design in order to simulate the engine turbine requirement to minimise root centrifugal stresses by tapering the blade sections from root to tip. The thick root philosophy has also been used to minimise diffusion within the rotor row which can occur at the junction of the pressure surface with the hub platform. The Mach number at the forward pressure surface has been raised to avoid significant pressure diffusion in the hub/end-wall region, thereby reducing the tendency of the end-wall boundary layer to migrate towards the suction surface augmenting the secondary flow.

The blade profiles were stacked so that the centroids of each section were on a radial axis. It was considered that this was the most appropriate from the point of view of stressing constraints in an actual engine turbine.

A study of trailing-edge losses and aspect ratio led to the conclusion that the optimum number of blades was around 60 and the prime number of 59 was selected. This gave reasonable blade lift coefficients. The radius of the leading-edge circle was varied linearly from 2.5 mm at the hub to 1.25 mm at the tip. The resulting blade is shown on Fig 9. The predicted Mach number distribution at hub, mean and tip sections is shown on Fig 10. These distributions show a peaky, non-uniform distribution of surface Mach number on the suction surface with an undesirable over-expansion at the point of maximum curvature. This over-expansion and the subsequent recompression become worse towards the tip of the blade. This will induce local shocks and accompanying viscous effects which would cause loss of performance. Such peaky distributions were not predicted at the time of committing the design to manufacture, but were predicted by the improved time-marching program<sup>11</sup>. If the opportunity had been available the distribution would have been improved by modification of the profiles. In other respects, the distribution is satisfactory and in particular the lack of hub pressure surface diffusion can be seen. Fig 11 shows the predicted static pressure contours on the suction and pressure surfaces of the rotor blade in meridional view. It can be seen that the flow around the nose and on the forward part of the suction surface is largely two-dimensional. The early over-expansion on the suction surface at about the point of maximum curvature can be seen as a finger of low static pressure extending from the tip down towards the root

region. There is a pronounced gradient of static pressure acting towards the tip on the suction back surface at the position of peak Mach number.

#### 4 TEST RIG

The blading was manufactured and tested in a cold-flow turbine test rig at RAE Pyestock. A schematic layout of the instrumentation is shown on Fig 12. Air from plant compressors was fed to the turbine via a calibrated venturi-nozzle airmeter and exhausted to atmospheric pressure. The shaft torque was measured using a phase-shift torque meter and the power was absorbed by a high speed water dynamometer. All pressures were measured by transducers via Scanivalves and temperatures were sensed by chromel-constantan thermocouples. All readings were logged by a computer based data acquisition system which determined 'on-line' turbine performance from the measurements.

The most reliable and consistent measure of turbine temperature drop was from the measured torque together with shaft speed and the measured mass flow rate. Neither the downstream thermocouples nor the Kiel rakes were used in the determination of efficiency. For this purpose, the outlet total pressure was determined from the mean wall static pressure and a calculation for the mean flow Mach number. This calculation uses the measured mass flow rate, annulus area and mean swirl angle across the annulus determined from comprehensive (35 point) radial traverses supplemented by 350 point area traverses. This yields an absolute level of turbine total to total adiabatic efficiency which is estimated to be accurate to better than  $\pm 1.0$  percentage points. Being based on measured shaft power this efficiency includes the effect of windage and bearing loss. From internal estimates, and a separate set of tests specifically to measure this windage which are still in progress, the gas-path efficiency is believed to be about 14% higher.

Other important measurements were static tappings on both the NGV and the rotor. There were 30 tappings distributed around the NGV surface at each of 15% and 50% annulus heights and there was a total of 34 tappings on the rotor blade, 9 at 20% annulus height, 7 at 50% annulus height and 18 at 80% annulus height. The rotor measurements were taken out via a rotating Scanivalve with measured corrections for the centrifugal pumping effect. The tappings were not all on one blade or in one passage but are distributed around the 40 vanes and 59 rotors. In addition there are NGV exit and NGV passage end-wall static tappings. Running tip clearance was also measured using electrical contact type probes with stepper-motor drive to achieve a resolution of  $\pm 0.01$  mm.

Testing was carried out over a range of turbine speed from 80% to 110% and pressure ratios from 2.0 to 4.2. Test Reynolds numbers at design point, based on true chord and blade exit conditions, were  $3.6 \times 10^6$  for the NGV and  $0.56 \times 10^6$  for the rotor.

#### 5 TEST RESULTS

At turbine pressure ratios above about 2.4 the turbine was choked and the measured mass flow function was 0.8% higher than design. This was a creditable reflection on the throat discharge coefficient assumed in the design and on the accuracy of setting the nozzle throats in the rig.

The variation of turbine efficiency with speed and pressure ratio is shown on Fig 13. It can be seen that the performance improves with speed but that peak efficiency occurs at lower than design pressure ratio. At 110% of design speed, higher efficiency than at design speed is only obtained over a narrow range of pressure ratio. The shape of this 110% characteristic is unexpected, compared with the shape of the characteristics at other speeds. The measured efficiency at design point was 89.2%. The measured tip clearance at design speed was 0.37 mm, which represents 0.9% of annulus height.

##### 5.1 NGV performance

The measured distribution of surface isentropic Mach number at NGV mid-height is shown on Fig 14 compared with the three-dimensional time-marching predictions. It can be seen that close agreement is obtained on the pressure surface and on the suction surface up to the throat. There is evidence of a weak shock on the suction surface at about 65% axial chord, with subsonic conditions indicated over the remainder of the instrumented portion of the blade. It was not possible to install tappings in the thin trailing-edge region. The distribution at 15% annulus height shows similar results with an ever weaker shock at about 65% axial chord. The end-wall NGV exit static pressures indicate isentropic outlet Mach numbers of 1.03 and 0.96 at the hub and tip respectively, compared with 1.13 and 0.99 at design. With the 0.9% higher flow than design, these lower outlet Mach numbers are consistent with a small error in NGV throat discharge coefficient in the design. Otherwise the NGV appears to be operating close to design, with no indication of serious extra loss.

##### 5.2 Rotor blade performance

The rotor blade surface static pressures were measured using a rotating Scanivalve with a correction for the centrifugal pumping effect between the tapping on the blade and the pressure transducer on the axis of rotation. Because there is no measure of relative inlet total pressure to the rotor, the surface static pressures were non-dimensionalised with respect to the highest indicated static pressure, and isentropic Mach numbers calculated. Because of uncertainty over the total pressure, the level of isentropic Mach number indicated by the measurements is also slightly suspect. The possible error is largest at the low Mach numbers and so will most affect comparisons on the pressure surface. The variation of this isentropic Mach number at design conditions is shown on Fig 15 at 3 annulus heights and compared with a three-dimensional inviscid time-marching synthesis. This synthesis is not based on the design values of outlet static pressure, but on the measured values which are lower. The reason for this difference is discussed below with reference to the traverse results. Comparison of Figs 10 and 15 shows that this has led to the prediction of higher surface Mach numbers, with a considerable over-expansion of the flow on the suction surface at about 75% to 80% axial chord which is considerably more pronounced towards the tip. The measurements confirm the trends indicated by the synthesis but show even higher suction surface peak Mach numbers. A peak Mach number of greater than 1.5 is measured at 80%

annulus height and this must introduce higher than design loss towards the tip. The measurements also show the over expansion of the flow at around the point of maximum curvature on the suction surface (35% to 40% axial chord) as discussed above with the rotor blade design.

Fig 16 shows the variation of measured and synthesised isentropic Mach number distribution on the rotor blade at 80% annulus height at speeds of 90%, 100% and 110% of design, all at design pressure ratio. It can be seen that there is moderately good agreement between measurement and synthesis on the early part of the suction surface where the higher Mach number at lower shaft speed are due to increased incidence of the airflow onto the rotor. This indicates that the incidence onto the rotor is as designed and helps substantiate the conclusion that the NGV exit flow is close to design intent.

### 5.3 Downstream traverse measurements

Area traversing was carried out downstream of the rotor by a series of 19 circumferential sweeps separated by 2.5 mm radial increments. On each sweep 19 readings were taken at points  $\frac{1}{4}^\circ$  apart circumferentially, covering one complete NGV pitch. Total pressure, static pressure and yaw angle were recorded using a 3-hole wedge probe nulled at each point. Fig 17 shows contours of exit swirl angle which clearly shows that there is a large region of flow, extending in from the tip, where there is significant underturning of the flow. This is attributed to the effect of the overtip leakage flow and the underturning associated with the strong shock wave in the tip region of the rotor as seen on the rotor static pressure distributions. This overall reduction in rotor outlet angle is causing a reduction in work output as well as an increase in pressure loss from the shock. The low swirl in the tip region means that significantly higher swirl is required in the mid-span and root region in order to achieve design work. The design swirl is  $25^\circ$ , compared with over  $30^\circ$  from Fig 17 in the mid-span and root region. This would help to explain why the turbine characteristic (Fig 13) peaks at lower than design pressure ratio. This effect also explains why the measured outlet static pressure is lower than the design value, because, with close to design flow but higher swirl, the flow has a higher Mach number and hence higher total-to-static pressure ratio.

Contours of outlet total pressure are shown on Fig 18. The most striking feature is the predominantly radial variation of total pressure again confirming the dominance of the rotor losses in the tip region. Although traversing could not be carried out very close to the inner wall, there is no indication of secondary loss cores from the NGV.

## 6 CONCLUSION

A high rim speed, high work capacity single stage shroudless transonic turbine has been designed and tested at RAE Pyestock. The turbine demonstrated a measured efficiency of 89.2% at design conditions at a tip clearance of 0.9% of blade height. This includes the effect of bearing and windage losses which are estimated to be equivalent to about  $1\frac{1}{2}\%$  efficiency. The gas-path efficiency was therefore about 90% to 91%.

Static tappings on the NGV indicated no major problems on the aerofoil. The other limited information available, indicated that the NGV loss was close to design and it should be noted that some optimism was included for the effect of three-dimensional design on the level of secondary loss. On the rotor, a rather peaky Mach number distribution was obtained on the suction surface. The early peak is associated with an overexpansion of the flow over the maximum curvature of the profile. This can now be predicted by more up-to-date versions of the Denton three-dimensional time-marching inviscid computer program than were available when the design was committed to manufacture. The distribution would have been improved by modification of the profile if the opportunity had been available.

The second factor causing some loss of performance was identified from both the downstream traverses and the rotor static tappings. The underturning of the rotor blade tip clearance flow in the outer annulus region is causing the rest of the blade to operate with higher outlet swirl in order to obtain the design work. Thus the outlet Mach number is higher and the downstream static pressure lower than design in the mid-span and root region. This gives rise to considerably higher suction surface peak Mach numbers on the rotor blade which must induce higher than design loss.

Overall the turbine demonstrated reasonable levels of aerodynamic efficiency with areas identified where small improvements could be made.

### ACKNOWLEDGEMENT

The authors are indebted to many colleagues at RAE Pyestock who helped progress and support the work reported on this turbine. In particular, thanks are due to Mr G.C. Horton for assistance in running and plotting the computer predictions.

### REFERENCES

- 1 D.E. Crow, M.R. Vancro, H. Welna, I.D. Stringer, 'Results from tests on a high work transonic turbine for an energy efficient engine.' ASME 80-GT-146 (1980)
- 2 W. Tall, 'Understanding turbine secondary flow', Paper No.14, 49th Meeting of Propulsion, Energetics and Panel.' AGARD (1977)
- 3 U. Okapuu, 'Some results from tests on a high work capacity axial gas-generator turbine.' ASME-74-GT-81 (1974)
- 4 J.D. Bryce, M.R. Litchfield, N.P. Leversuch, 'The design, performance and analysis of a high work capacity transonic turbine.' ASME 85-GT-15 (1985)

- 5 M.C. Liu, T.C. Booth, W.A. Tall, 'An application of three-dimensional viscous flow analysis to the design of a low aspect ratio turbine.' ASME 79-GT-33 (1979)
- 6 J.D. Denton, 'Extension of the finite area time-marching method to three-dimensions.' Von Karman Institute Lecture Series 84 (1976)
- 7 S.C. Kacker, U. Okapuu, 'A mean line prediction method for axial flow turbine efficiency.' ASME 81-GT-58 (1981)
- 8 D.G. Ainley, G.C.R. Mathieson, 'A method of performance estimation for axial flow turbines', Aero. Res. Co. R&M 2974 (1951)
- 9 J. Dunham, P.M. Came, 'Improvements to the Ainley-Mathieson method of turbine performance prediction.' ASME 70-GT-2 (1970)
- 10 J.D. Denton, 'A time-marching method for two- and three-dimensional blade-to-blade flow.' Aer. Res. Co. R&M 3775 (1975)
- 11 J.D. Denton, 'An improved time-marching method for turbomachinery flow calculation.' ASME 82-GT-239 (1982)

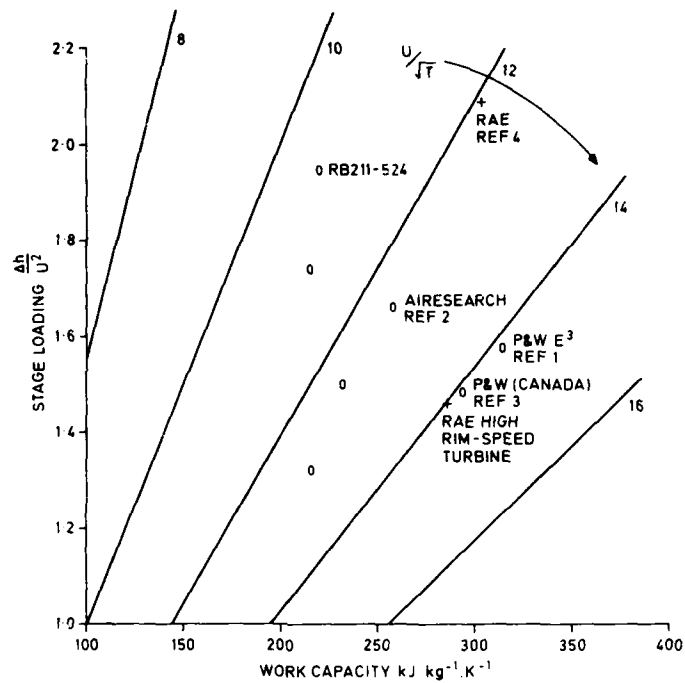


FIG 1 SINGLE STAGE HP RESEARCH TURBINES

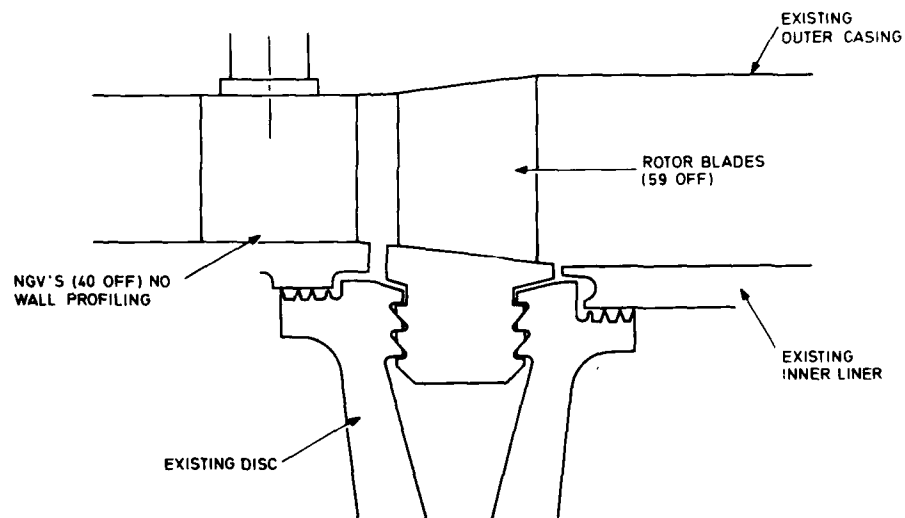


FIG 2 HIGH RIM SPEED TURBINE ANNULUS

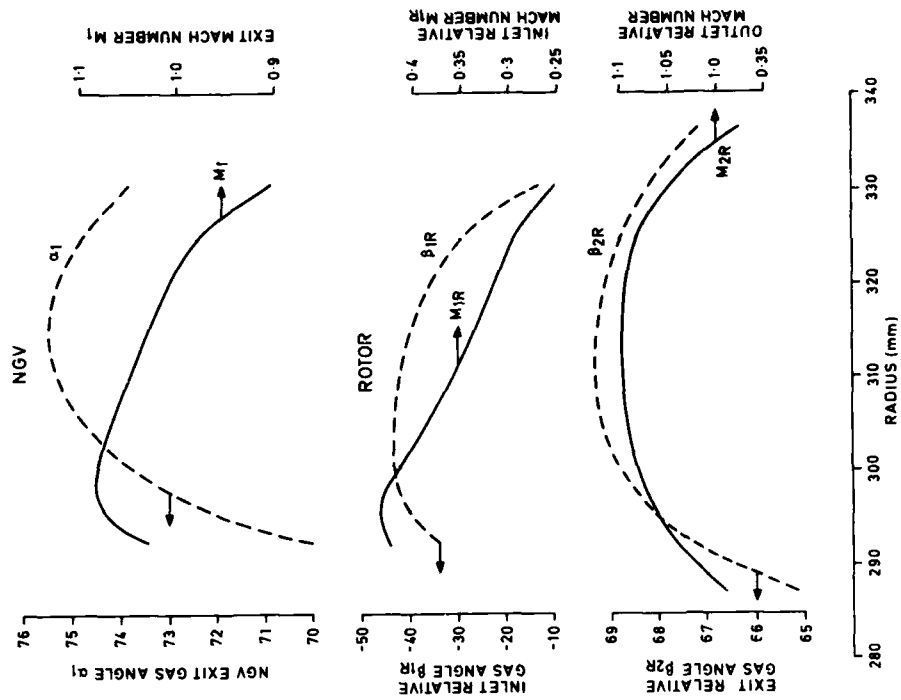


FIG 4 DESIGN THROUGHFLOW ANALYSIS

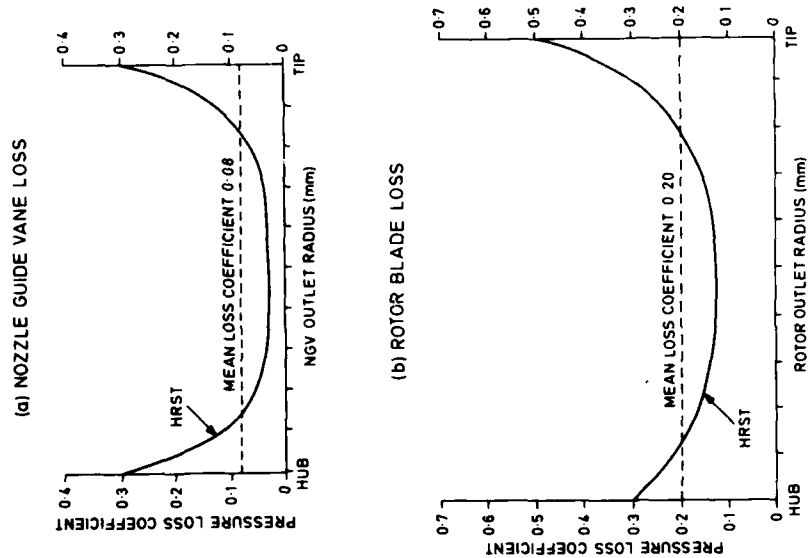


FIG 3 NGV AND ROTOR BLADE PRESSURE LOSS COEFFICIENTS

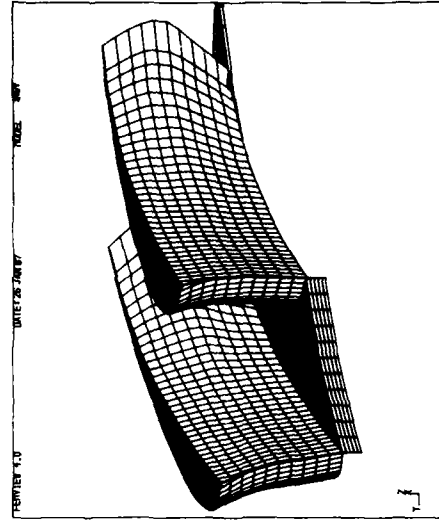


FIG 6 NOZZLE GUIDE VANES

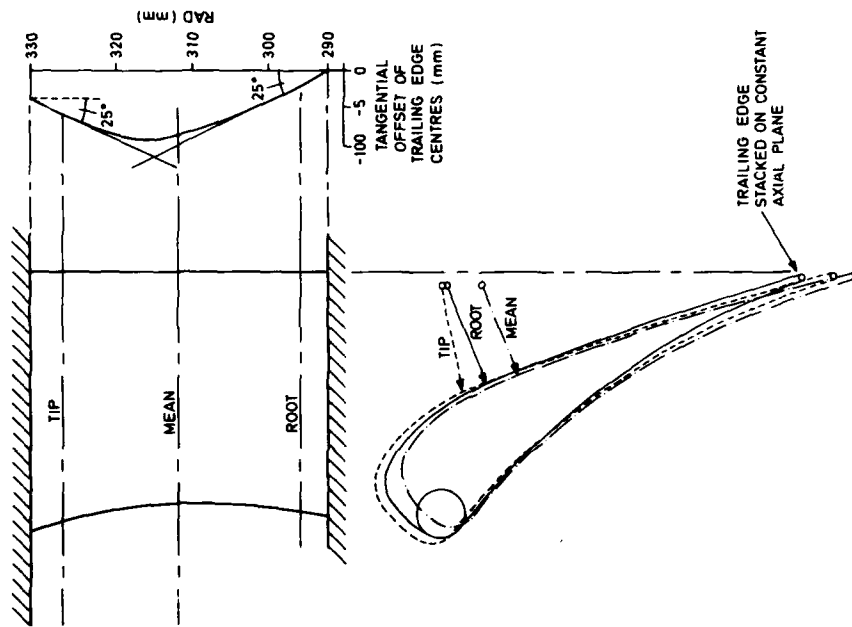
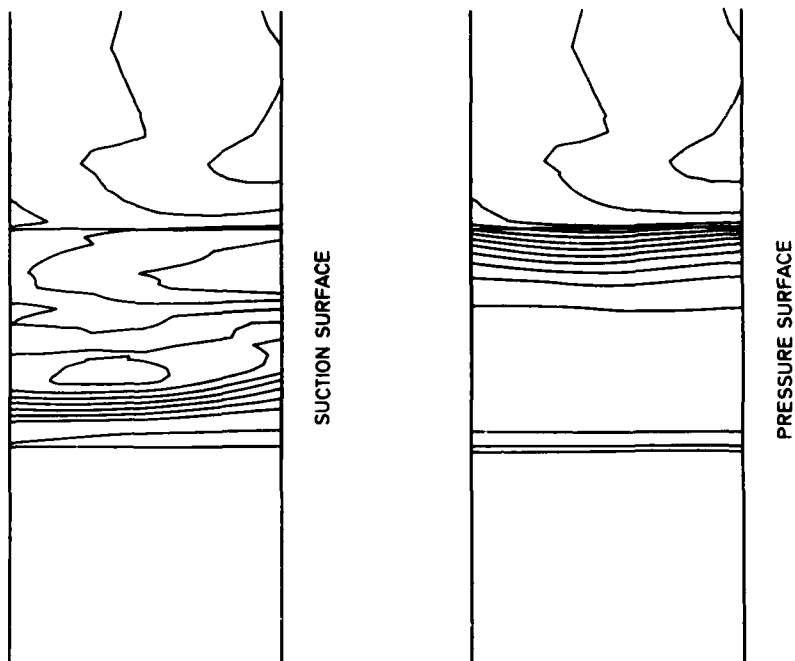


FIG 5 NGV AERFOIL STACK





12-9

FIG 8 PREDICTED NGV STATIC PRESSURE CONTOURS

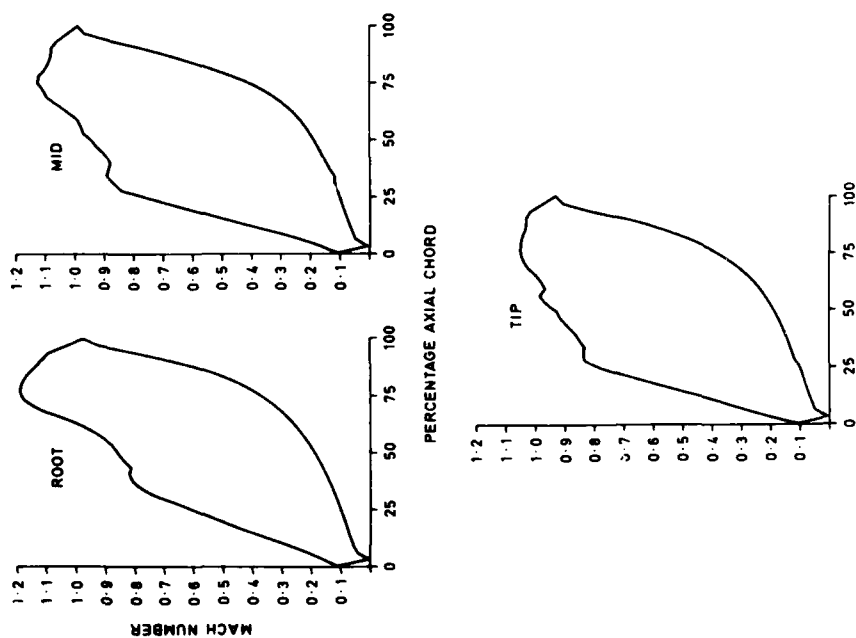


FIG 7 PREDICTED NGV MACH NUMBER DISTRIBUTION

12-10

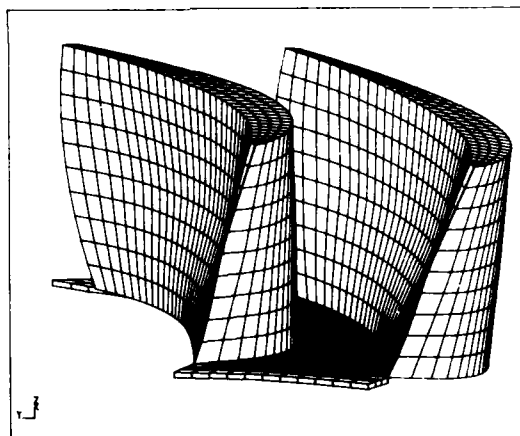


FIG 9 ROTOR BLADES

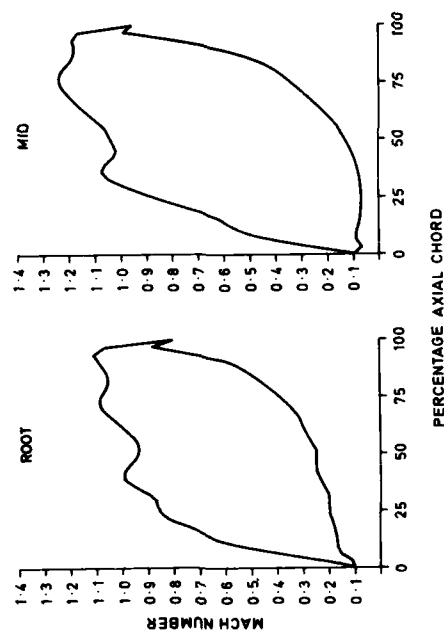


FIG 10 PREDICTED ROTOR BLADE MACH NUMBER DISTRIBUTION

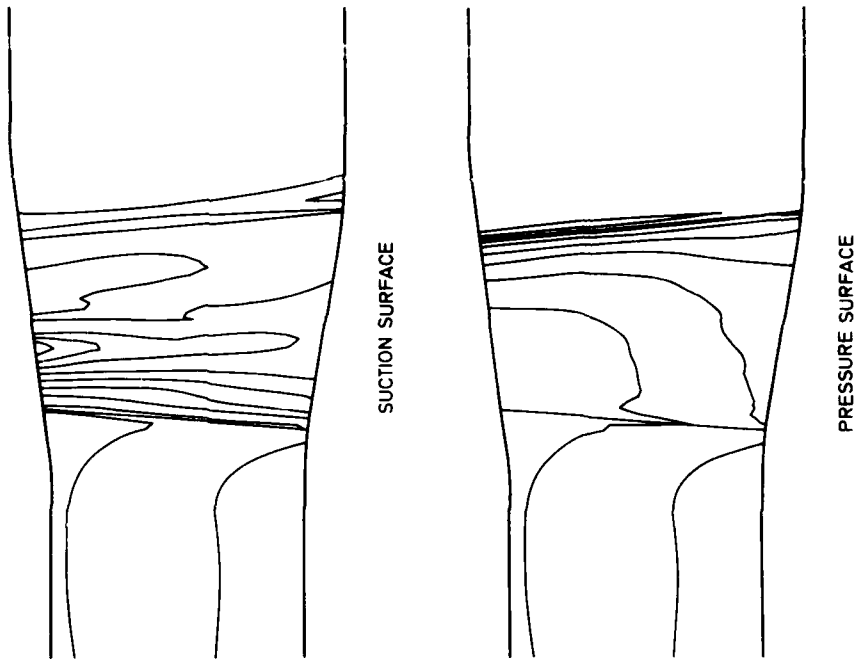


FIG 11 PREDICTED ROTOR BLADE STATIC PRESSURE CONTOURS

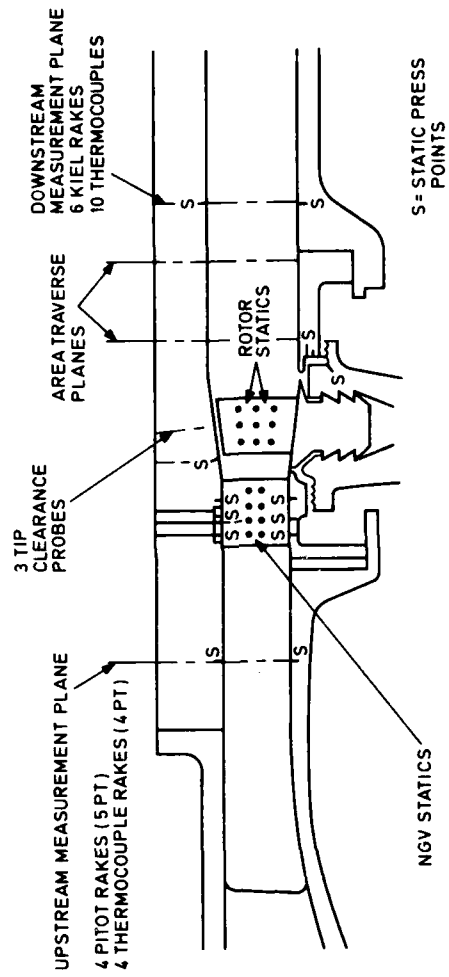


FIG 12 TURBINE TEST RIG AND INSTRUMENTATION

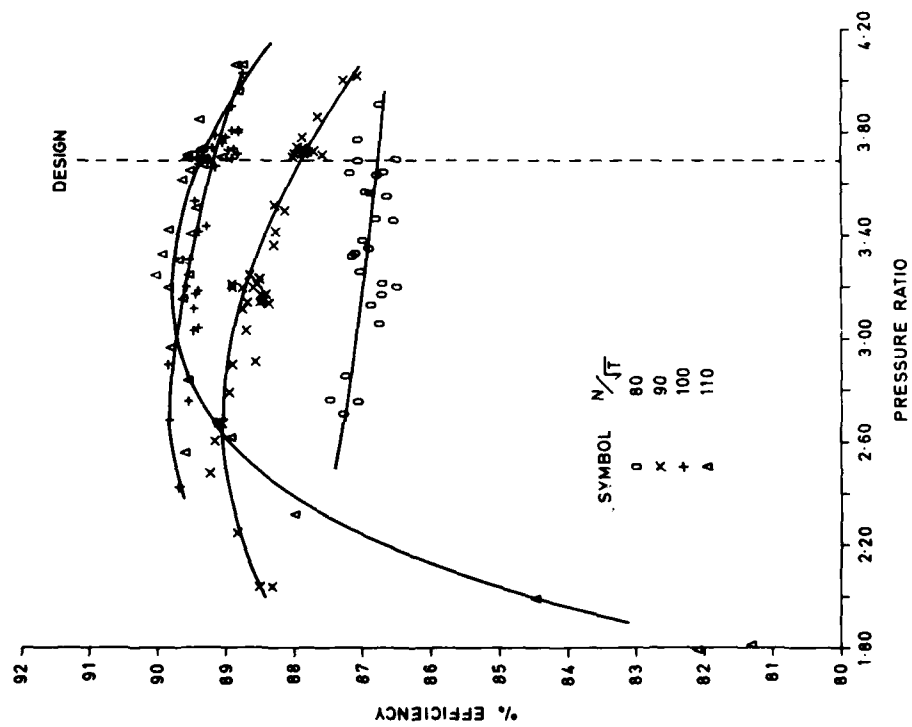


FIG 13 MEASURED TURBINE PERFORMANCE

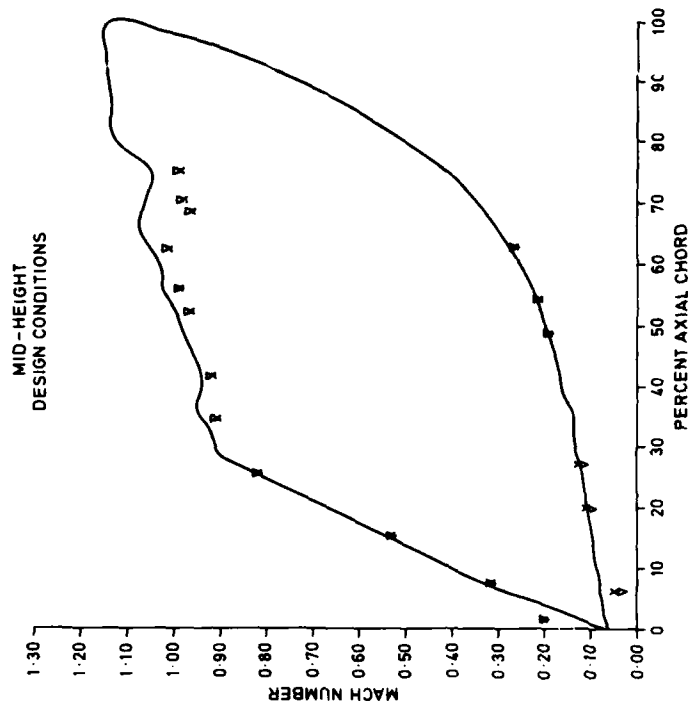


FIG 14 NGV MACH NUMBER DISTRIBUTIONS

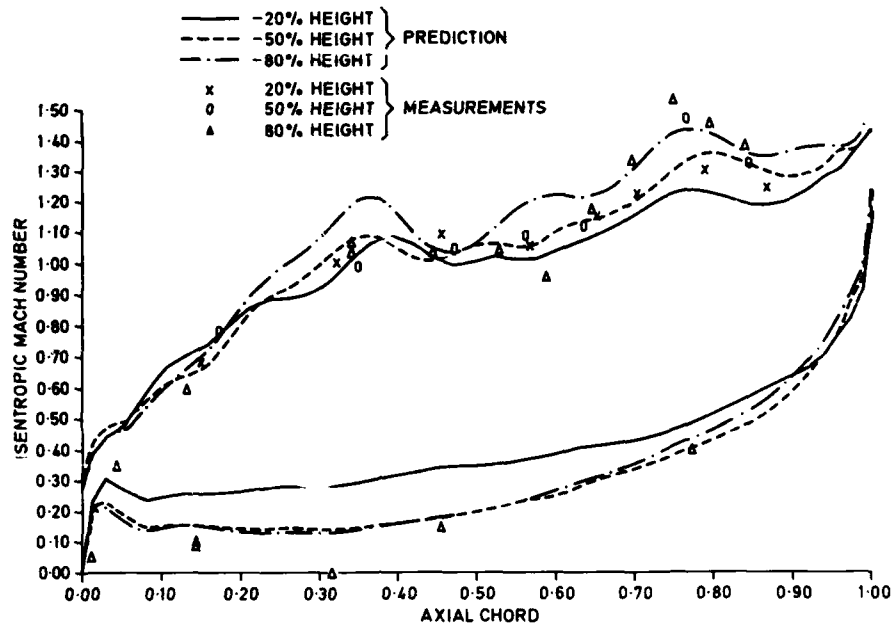


FIG 15 ROTOR BLADE MACH NUMBER DISTRIBUTIONS

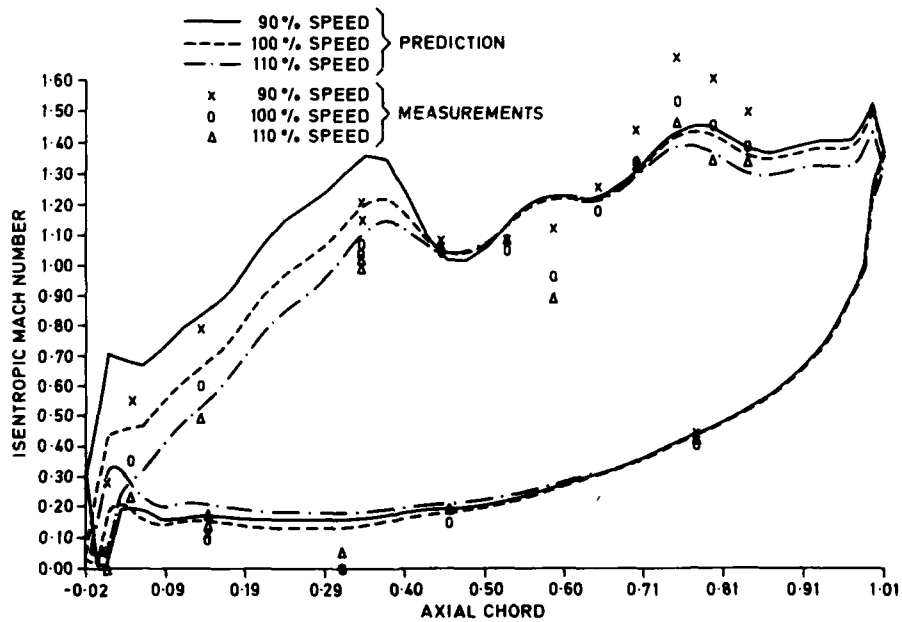
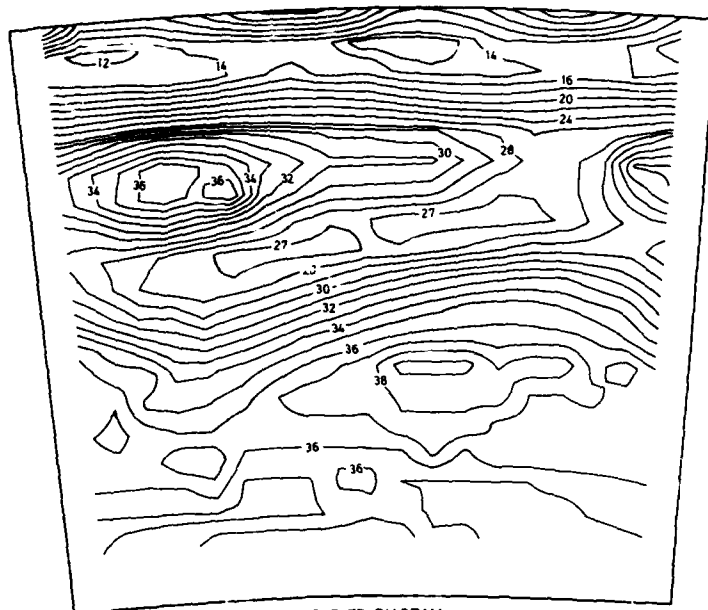
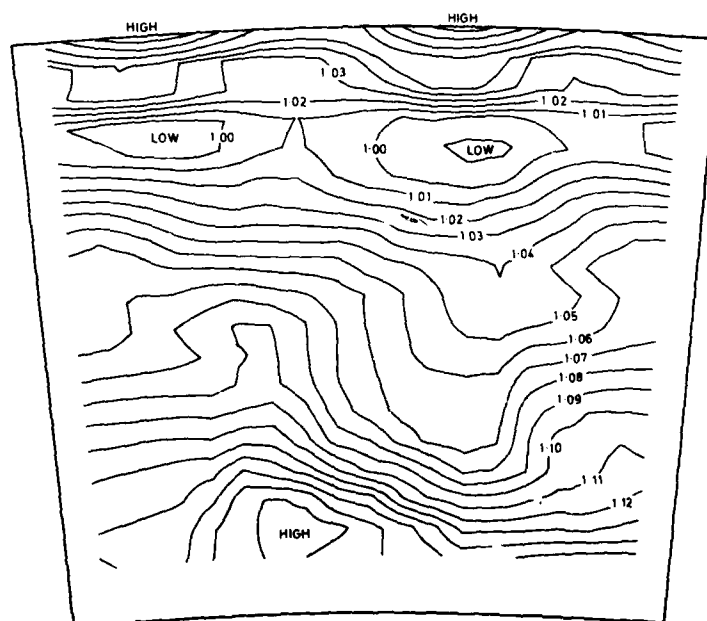


FIG 16 ROTOR BLADE MACH NUMBER DISTRIBUTIONS



OUTLET DIAGRAM  
FLOW DIRECTION

FIG 17 CONTOURS OF FLOW DIRECTION



OUTLET DIAGRAM  
TOTAL PRESSURES  $\text{N/m}^2 \times 10^5$

FIG 18 CONTOURS OF TOTAL PRESSURE

DISCUSSION

A.S. ÜÇER, Turkey

Do you use any deviation prediction method in your design ?

Author's Reply

Deviation corrections are much lower on turbines than on compressors because the blade boundary layers are much thinner on turbines. In this design, allowance was made for deviation by carrying out some continuity calculations between the throat and downstream and allowing for appropriate throat blockage. The outlet angles predicted by the inviscid design methods were thus higher than those required in the turbine.

H.B. WEYER, N1

How did you correct for the centrifugal effects on the rotor blade pressure measurements ?

Author's Reply

The centrifugal pumping effects on the rotor static pressure measurements were calculated from the known radius, measured speed and a calibration based on a disc rim static pressure measurement .

R.G. THOMPSON, US

What reference temperature was used to represent the rotating column of air when measuring the rotating blade static pressure ?

Author's Reply

The mean temperature of the rotating column of air was determined from the calibration of a disc rim static pressure measurement as mentioned in the previous answer. There was one reading on the rotating disc near the rim and a second reading on the stationary structure at the same radius. This allowed the mean gas temperature in the rotating column to be calculated and this same temperature was used in the calculation of the corrections for the rotor static pressure measurements.

J. MOORE, US

Were the 3D flow calculations performed for the stator and rotor combined or for the two blade rows independently ?

Author's Reply

Most of the design work was carried out with separate calculations for the nozzle and rotor rows. This allowed the maximum amount of detail to be obtained from the limited overall grid size that could be run on the



computer. However, some calculations were performed on the nozzle and rotor combined as a stage in order to determine the radial gradients at exit from the nozzle arising from interaction between the blade rows. In these calculations, the flow between the nozzle and rotor was circumferentially averaged at each radial station so that the time-meared interaction was calculated, not the instantaneous flow for one relative position of the nozzle and rotor.

J. HOURMOUZIADIS, Ge

The original turbine you reported on two years ago at the ASME was much more advanced. What was the real reason why you decided to make such a conservative design and put all the advancement into the tip speed of your turbine ?

**Author's Reply**

It was for the efficiency gain over the earlier design. Because of the much higher Mach numbers on the blading, the efficiency of the former turbine was significantly lower, at about 86 % or 87 %. In order to make a turbine of this duty competitive with a two-stage design, higher aerodynamic efficiency than that obtained previously would be required. Advances in materials technology allowed a higher turbine blade speed to be selected to give a more competitive turbine at higher efficiency. The attainment of 89 % to 90 % efficiency at higher blade speed in the turbine described is not necessarily any easier or less advanced than the previous turbine design.

# ADVANCED TECHNIQUES EMPLOYED IN BLADE COOLING RESEARCH

MISS H E ROGERS, SENIOR TECHNOLOGY ENGINEER  
ADVANCED TURBINE TECHNOLOGY DEPARTMENT

MR C GRAHAM, HEAD ADVANCED TURBINE  
TECHNOLOGY DEPARTMENT

MR K McNICHOLAS, SENIOR TEST ENGINEER  
ADVANCED PROJECTS DEPARTMENT

ROLLS ROYCE PLC, P O BOX 3, FULTON, BRISTOL, BS12 7QE, ENGLAND

## SUMMARY

As the demand for improved performance of advanced gas turbine engine components continues, the environment within an engine, in which the turbine must operate, has become more hostile. The operating temperatures of turbines have increased such that not only the first stage, but in many cases the second stage requires some form of cooling.

The design of an advanced cooling system for moderately cooled second stage blades was undertaken as part of a demonstrator project. The design process, involving complex computer modelling, and hot rig testing of the blades, is described in part 1 of this paper. The test results confirmed that substantial increases in cooling efficiency can be gained by introducing small scale turbulators into radial hole cooling systems.

Part 2 describes a development temperature measurement technique based on a video camera operating in the near infra-red region. The results of the video pyrometry were validated from results obtained from a series of demonstrator hot rig tests. Also discussed are a number of problems relating to surface temperature measurement, in particular, the method used to achieve artificially matured blade surfaces.

## INTRODUCTION

Increasing demand for improved performance from advanced gas turbine engines has resulted in hotter gas temperatures at which the turbine has to operate. Consequently, the requirement for advancing turbine blade cooling technology continues to be of great importance.

The penalties of cooling can be twofold, reduction of the hot core air flow and compromise of the blade aerodynamics.

Therefore, it is in the interest of the turbine designer to develop a cooling system that uses the minimum amount of cooling air and that will not compromise the external aerodynamic performance of the blade.

An advanced demonstrator programme, based on an uprated 2 stage high pressure turbine, required the second stage blade to be cooled to achieve the required life. A family of cooling systems was designed, incorporating small scale turbulators to enhance the performance of a radial hole cooling geometry, suitable for thin aero-efficient aerofoils.

The design process can now utilise complex computer models to predict the performance of new designs, prior to testing under conditions representative of the engine environment. The results obtainable from the latter enable assessment of the new designs and also verification and improvement of the prediction methods used in the design process.

The conclusions and inferences that can be made from any tests are dependent on the quality of results obtained. Hence, the development of the measurement techniques used in testing plays an important part in blade cooling research.

Thus it was with this in mind that the testing of the innovative blade designs was used for the development of a further advanced measurement technique, video pyrometry, in conjunction with the already established technique using thermal paints.

The design and test of the new blade cooling standards is described in the first part of this paper, and the development and results of the video pyrometry technique, detailed in the second.

### PART 1 - ADVANCED RADIAL HOLE BLADE COOLING TECHNOLOGY

The high pressure (H.P.) second stage rotor blade (Fig 1) of the demonstrator project was used as a vehicle to enable the cooling performance of a simple row of square ribbed radial (S.R.R.) holes to be measured. This also served as a manufacturing driver in the development of core/casting technology.

The moderate amount of cooling required by the second stage H.P. blade enabled a radial pass, low pressure fed cooling system to be adopted - it was anticipated that S.R.R. holes had the potential to achieve cooling efficiencies of 100% with moderate length: diameter holes.

The Company's suite of computer programs for the prediction of aerodynamic and cooling performance was used to execute the design of a number of cooling standards of design, and to assess their behaviour at engine conditions.

The comparison of these designs was achieved by both use of the prediction methods and hot cascade testing.

#### DESIGN AND PREDICTED PERFORMANCE

The second stage H.P. blade used as the vehicle for this work is shown in Fig 2.

The configuration consists of 8 square radial holes in the leading edge and central region of the blade shape. The design variants were:-

- \* plain walled passages, Datum
- \* passages with 2 walls ribbed
- \* passages with 4 walls ribbed

The designs were analysed at conditions representative of engine type test conditions.

The effect of the ribbed surfaces on the pressure drop and heat transfer in the radial passages was modelled using data from a number of sources including Norris (Ref 1) and Burggraf (Ref 2).

The predicted performance of each standard was compared, relative to that of the plain walled standard, for mid span mean cooling effectiveness and cooling efficiency, as derived by Holland and Thake (Ref 3). See Table 1 below.

Table 1. Predicted performance

COOLING SYSTEM	COOLING FLOW % OF DATUM	COOLING EFFECTIVENESS % OF DATUM	COOLING EFFICIENCY % OF DATUM
DATUM, PLAIN WALLS	100	100	100
2 RIBBED WALLS	33	68	157
4 RIBBED WALLS	25	61	175

The prediction process enabled temperature contour plots through a number of different radial blade sections to be obtained. These were then combined to generate a surface temperature plot (butterfly plot). Both section and surface contour plots for one standard of cooling are shown in Figure 3.

#### MANUFACTURING

Manufacture of the square radial hole blades required advances in both core and casting technology. Reinforced silica tubes were used and grooves 'machined' into the tubes in batches. The square shape of the cores facilitated the machining process.

Initially grooves were cut using a grinding wheel. This was found to be unsatisfactory as bad scratches raised in the cores resulted in an unacceptably high scrap rate.

Use of lasers to make the grooves gave much better results as the 'grinding scratches' were avoided.

Initial casting trials had a problem with location of the core tubes within the blade section. These were subsequently facilitated by development of the shell material.

The castings were x-rayed and flow checked before modification for rig testing.

### TESTING

Static hot cascade testing was carried out to enable the relative cooling performance of the different blade design standards to be measured at representative temperatures and pressures.

Two test blades were placed in an annular segment between 'flanking' pairs of blades to create representative gas paths. The rig was run to correct non-dimensional engine conditions and the length of test varied dependent on the measurements required. The test rig is described more fully in Part 2.

In this series of testing the design verification tests were run using thermal paints to measure blade surface temperature. The gas conditions during the thermal paint test runs were as below:

Cascade Inlet gas temperature	1326K
Cascade exit gas pressure	60 psi
Coolant gas inlet temperature	825K
Coolant gas inlet pressure	79 psi

A number of different temperature band paints were run for each design standard to enable a composite picture to be established for each blade. Fig 4 shows a non-dimensional contour plot of the plain walled, Datum, blade standard - cooling effectiveness levels have been taken to make allowance for variations in mainstream and coolant gas conditions from test to test.

Development of the video pyrometry measurement techniques as detailed in Part 2, looked at a simulated thermal paint test run to enable direct comparison with thermal paint test results.

The video pyrometry technique was extended to use as a real time measurement technique to investigate transient behaviour. Tests were run to examine behaviour of the cooling system during simulated cyclic running.

### BLADE COOLING PERFORMANCE

In this section, results from the cascade tests are compared with the predicted performance.

The measured reduction in cooling flow due to the presence of the ribs is less severe than predicted, see Fig 5. This, in part, is reflected in the greater measured cooling effectiveness enhancement due to the ribs, as shown in Fig 6.

The cooling efficiency, however, allows the effect of mass flow variation to be separated out, giving a true indication of relative cooling performance. In this case the measured improvement in cooling efficiency due to the ribs is predicted with reasonable accuracy, see Fig 7.

In order to improve the modelling of the effect of friction due to ribs, the cooling flow behaviour was analysed in detail. The resultant increases in friction due to the ribs, test measurement compared with prediction, is shown in Fig 8. This information has now been incorporated into the design process.

### PART 2 - VIDEO PYROMETRY OF TURBINE BLADES

A measure of the efficiency of a cooling system can be derived from the blade surface temperature under operating conditions. This is achieved using two well established techniques - thermocouples and thermal paints. Although both techniques achieve the desired results, both have limitations. Thermocouples, for instance, are prone to mechanical failure whilst thermal paints are limited by the amount of time that can be spent at operating conditions before being adversely affected by high temperature and gas erosion. Although both methods achieve the desired results, i.e. surface temperature measurement, both are essentially invasive, requiring direct contact with the blade surface.

An alternative to direct surface contact methods is optical pyrometry.

### TURBINE BLADE TEST RIG

Traditionally, Rolls-Royce has used hot rig testing for verification of design and mechanical integrity of engine components. Rigs, both dynamic and static, are designed to mimic engine environmental conditions.

The test rig used for this series of static turbine blade tests consists basically of a high pressure air supply feeding a tandem combustion system. During test running, the hot combustion gases are transferred via a dog leg shaped duct to the cascade section. Here, the blades are orientated so that they meet the gas stream at the correct angle of incidence.

During testing, all performance and health monitoring parameters are scanned by a high speed analogue/computer system. Thus, pertinent test data can be readily available on completion of testing either for performance analysis or for transfer to main frame computer storage.

The development of video pyrometry was aided by the unique construction of the turbine test rig in having two line of sight windows, one upstream and the other downstream of the cascade test section. Both viewing ports were readily accessible, allowing ease of installation and subsequent adjustment. Services to and from the camera such as electrical power, cooling air, video leads etc, were readily accommodated within the test cell without modification.

Video testing was carried out from the downstream window, the camera and its environmental box being mounted on a platform attached to the port window flange. Originally, it was thought that rig vibration during running would induce camera microphony, resulting in a degradation in picture quality. Subsequent experience showed that there was no picture degradation or distortion, the test rig proving remarkably free from vibration.

Focusing of the camera was straightforward. The target blades were illuminated by a tungsten light source and the lens system was then focused until the TV monitor image appeared clear and sharp, this position then being noted and fixed. Initially, the focus was considered satisfactory when a visually sharp image was obtained. Later, this technique was modified by overlaying a graticule on the target blades surface. The benefit of this technique was that focusing was made more precise, the blade surface area under observation was made easier to calculate and positions of primary importance could be readily identified and related as X Y coordinates. Also pixel area change over the blade curvature can be readily assessed

The view of the test cascade from the downstream observation window allows only the suction side to be viewed, and then only partially. The amount of blade surface visible is dependent on the camber and stagger of the individual blade and its position within the cascade. Under normal circumstances the test blades are positioned in the centre of the cascade in order to minimise wall effects and gas stream temperature gradients.

#### PYROMETRY

Pyrometers operate on the well established principal that a surface, particularly metal, when heated to a sufficiently high temperature, will emit energy in quantities that are proportional to the surface temperature. Therefore, if the emitted intensity can be calibrated, then the temperature of the emitting surface can be determined.

The active photo sensitive area of a video camera is composed of photo-conductive material deposited on a conductive film. The target can be assumed to consist of a large number of elements, the size being determined by the size and accuracy of focus of the scanning electron beam. As with the photo sensor of the engine control pyrometer, the photo-sensitive element reacts to light, producing an electrical voltage proportional to the emitted intensity. This relation between illumination and the signal current can be shown as:

$$\frac{I_s}{I_c} = \left( \frac{E_s}{E_c} \right)^\gamma$$

in which:

$I_s$  = the signal current at illumination  $E_s$

$I_c$  = the signal current at calibration illumination  $E_c$

$\gamma$  = the gamma of the tube

If a tube gamma of one is assumed, then the current will be directly proportional (Ref 4) to the illumination of the target. Thus the camera tube is acting in the same manner as an optical pyrometer to changes in light levels.

It is well known that heated bodies emit radiation which is characterised principally by the temperature of the body. Thus an increase in temperature is accompanied by a corresponding increase in energy. Thus, as the emitted light from a body is directly related to its absolute temperature and the voltage signal produced in the camera target is proportional to the light intensity then a suitably configured camera may be said to act as a radiation detection instrument.

#### TEST BLADE - ARTIFICIAL MATURING

In practice, it is found that no surface behaves as an ideal emitter and invariably the emittance at a particular wavelength is less than that for the ideal surface, the ratio of the emitted value to the ideal surface value being defined as emissivity ( $\epsilon$ ). Although the distribution of energy emitted throughout the wavelength spectrum from a real surface usually follows the trend predicted for a black body, there can be irregularities in the distribution that cause variations in emissivity with wavelength.

It is fortunate that blade surfaces, in general, are not strongly selective emitters, particularly in the higher operating temperatures associated with combustion.

This does not imply that blades operating under the same conditions necessarily have the same emittance value.

Consider the hypothetical case of a turbine blade under test for comparison with new design marks of a similar type. The original blade may have been exposed to a considerable amount of testing time at high operating conditions and consequently achieved a stable emissivity state. A newly manufactured blade installed alongside the original, now matured blade, would be continually changing surface condition during initial running. As chief engineers are not particularly well disposed to unwarranted - long term test running, maturing of the new blade by extensive high temperature running is not condoned.

To overcome this problem, a novel approach was proposed, that of artificially producing a mature blade. This was achieved by spray coating a sample blade with a high temperature resistant paint and baking it in an oven at 1100°C for 30 minutes. By baking the blade at conditions higher than those expected during rig testing, all intermediate surface melt conditions, up to 1100°C, were effectively removed. On cooling, the blade exhibited a uniformly smooth, dark blue matt surface. There were no special handling restrictions placed on the blade, other than common sense handling, as the surface was found to have a good bond and proved to be relatively scratch resistant.

In order to check emissivity ( $\epsilon$ ), the sample blade was instrumented with thermocouples, the beads being secured in blind holes. The blade was then heated using an R.F. coil. Temperature measurements were then taken at nominally 50°C intervals, in the case of blade metal temperature by the thermocouples and surface temperature by a hand-held optical pyrometer. Analysis of the results indicated that over the 600-860°C temperature range investigated, there was no detectable change in values. This was later confirmed from an earlier, and more detailed investigation into the paint, were it was found that the emissivity ( $\epsilon$ ) value was held constant at the final surface formation. For the baked blade situation, the final emissivity value was found to be approx .9, this figure being confirmed by the findings from the earlier investigation.

#### CAMERA

The camera used throughout these trials was an Insight series 75 unit fitted with an extended red Newvicon tube. This camera, being physically small (155mm x 62mm x 38mm), is ideal for situations where space is at a premium. In all respects, the camera operates as a normal video system conforming to CCIR standards. However, the unit does have a number of selectable options and adjustments that are not normally found on video cameras.

The camera options utilised for this investigation are summarised below:

- \* Auto gain ON/OFF - selecting auto gain OFF prevents the gain circuits from artificially increasing sensitivity at low light levels.
- \* Selectable black level TRUE/AUTO - as the type of tube used in this camera is sensitive to changes in reference blade signal level, the selection of TRUE black level prevents reference signal drift.
- \* Shading correction HORIZONTAL - VERTICAL - CENTRE - adjustment compensates for tube dark current shading and lens vignetting.

As mentioned previously, the tube fitted in the camera unit was an extended red "Newvicon", a silicon based vidicon target. The advantages of using this type of tube are, sensitivity up to the near infra-red, high quantum efficiency (almost 100%) plus good resistance to tube target "burn-in".

The lens system used for these tests was a "NIKON" 105mm with a remote aperture and focus control.

#### CALIBRATION OF CAMERA AND LENS SYSTEM

The camera and lens system was calibrated against a black body radiator of known performance and stability over the temperature range thought most likely to be encountered during the blade test.

Throughout these tests, the camera lens system was fitted with a KODAK Wratten 87C I.R. filter. This was incorporated to prevent any stray visible light that might have entered the environmental box, via the front window, from causing a response in the camera. In addition by combining the filter cut-off  $<0.8\mu\text{m}$ , with the camera tubes falling sensitivity  $>0.95\mu\text{m}$ , a comparatively narrow band filter was effectively produced. Theoretically, there is little flame radiation and interference from combustion gas thermal emissions in this waveband (Ref 5).

On reaching a designated temperature, readings - in the form of luminance values were taken over the full range of lens apertures. From this collected data a series of curves of temperatures vs luminance for the different aperture selections were produced (Fig 9). For a video camera, the slope of the curve is a function of the tube gamma and is also indicative of the accuracy obtainable from the system and of its dynamic range.

A camera having a tube gamma of one, for example, has a target voltage response that is directly proportional to changes in light intensity. Thus, a camera system configured to this standard would have good temperature resolution, but at the expense of the temperature range that can be accommodated. For a camera having a tube gamma of .65 (say), the temperature range that can be accommodated would be increased, but at the expense of measurement accuracy.

#### EXTRANEOUS RADIATION AND BLADE TEMPERATURE MEASUREMENT

If the radiation sensed by the camera tube has been emitted exclusively by the target blades, then direct surface measurements are possible. This is something of an ideal case and is unlikely to be achieved in practice. The more common sources of extraneous radiation are from flame - direct and reflected; from adjacent structures and blades and depending on total pressure and gas temperature - from gas emissions. An investigation into extraneous radiations was considered in some detail. In order to make the required corrections, it was necessary to assume that any additional radiation falling within the field of view of the camera would result in the same response as that due to a black body radiating at the equivalent temperature (Ref 6).

As stated previously, the combustion system for this rig is situated some distance from the cascade test section and is not in direct line of sight of the downstream viewing port. Because of this feature, it was considered unlikely that there would be any direct flame interference. This was subsequently borne out during test running. However, there remained the possibility of combustion gas radiation, particularly that from water vapour. In the wavelength band in which the camera was operating, the most likely interference would be from wings of the  $H_2O$  fundamental line at 1.1  $\mu$ . A previous investigation at similar inlet temperature conditions, though at higher pressures, had shown that waveband broadening interference was a distinct possibility. This phenomenon results in degradation of the video images and is characterised by an apparent haze or shimmer.

With the camera positioned and focused on the blade cascade, there remained a sight path that allowed an uninterrupted view of the inner wall of the test section (Fig 10). By monitoring the wall luminance at the following conditions, the effect of combustion emissions were evaluated.

- \* prior to combustor light up - to obtain a datum luminance level.
- \* after combustor light up - to assess possible flame reflections.
- \* at test conditions - for flame reflections and gas absorption.

As the test section is cooled by a continuous flow of water the inner wall temperature is prevented from reaching temperature levels where it would begin to emit sufficient radiation to become detectable by the camera at the aperture selected. It was considered that if flame were present, either as transients or featured over a period of time, or if radiation were emitted into the upstream test section from the leading edges of blades, these effects would cause a change in the datum luminous value.

Similarly with gas absorption, as the wall datum luminance did not decrease with an increase in gas temperature, it can be inferred that there was negligible gas absorption at the test conditions.

Though the emissivity value for the paint had been determined originally from a sample blade, as it was obtained at conditions that were not truly representative i.e. at atmospheric conditions, no adjacent blade etc. Therefore this evaluation could only be considered as a good working approximation.

Under normal engine operation conditions a turbine cascade operates in a confining structure of NGV's, adjacent blades and platforms, in conditions that can be said to be thermally stable. Under these conditions the blade enclosure can be considered to be a good approximation to a black body source. In the test rig situation where these particular blades were tested a similar situation occurs, however, because of the absence of NGVs, the structure is not totally enclosed. As a result, some reflected radiations escape into the upstream void and though the  $\epsilon$  value of the enclosed surfaces of the blade will still tend towards unity, however because of the broken enclosure, a value of unity is unlikely to be achieved. The enclosure or cavity effect produced by the blades influences the surface emissivity of the blade under observation. In general terms it can be said that the greater the penetration into the cavity, the closer to unity the surface  $\epsilon$  value becomes (Ref 7). Thus, the original laboratory derived emissivity value  $\epsilon$ , though a good datum figure is not satisfactory as an overall blade surface correction factor when converting luminance observed values to corrected surface temperatures.

To assess the surface emissivity changes across the blade chord, the following semi-empirical evaluation methods were used (Ref 8):

- \* during the 'standard cycle' the cooling airflow was reduced to zero. At this condition the blade surface will rapidly attain inlet gas temperature. As this temperature is known the blade temperature is also known. Thus as we have an observed luminance value for a known blade temperature at a given lens aperture the effective emissivity ( $\epsilon_a$ ) can be derived. This method is particularly effective for resolving trailing edge  $\epsilon_a$  values.
- \* by restoring the cooling airflow to the blade, whilst maintaining inlet conditions, a second set of luminance values are obtained. However, as the blade temperature has changed (restored cooling air) the surface temperature at a known position across the chord must be obtained, either via a thermocouple or alternatively must be able to be determined, perhaps from previous results.

These results were then plotted to produce an emissivity correction curve (Fig 11).

#### TEST OBJECTIVE

The test objective was to investigate and verify that a video camera could operate as an optical pyrometer under rig test conditions and could achieve an acceptable degree of temperature measurement accuracy, as determined from thermal paint test results.

#### TESTING

To investigate the video pyrometry technique three test schedules were used.

- \* Thermal Paint Schedule - design point conditions - as detailed in part 1.
- \* Standard schedule - from a constant cascade inlet condition, step reduction of coolant pressure ratio.
- \* Simulated cyclic running - thermal cycle comprising of two accel/decel and steady state segments.

The later two schedules were run at off design conditions. Both schedules are shown in figures 12 and 13.

In order to correlate the video recordings and the analogue computer readings, a video time clock was linked into the recording system. The clock was set in operation by a trigger pulse from the computer when an inlet temperature of 700°C was achieved. Consequently, all pyrometry data could be merged with the relevant test data.

For the scheduled testing, two standards of data logging were used:

- \* Standard schedule - essentially steady state running - a 5 sec scan rate of all parameters.
- \* Simulated Cycle - accel/decel running - a 2 secs scan rate - logging only minimum, health monitoring parameters.

#### RESULTS

From the plotted values (fig 14) it can be seen that the results from the video pyrometry are in close agreement with those of the thermal paint, the error at the blade trailing edge being approx 5°C, at the 50% chord width position approx 15°C. The error in temperature can be attributed to incorrect assessment of the degree to which the adjacent blade enclosure effect causes the emissivity value to shift towards unity.

#### CONCLUSIONS

1. Square ribbed radial hole cooling systems can achieve high cooling efficiencies of about 100%.
2. 4 ribbed walls give the most efficient configuration of the 3 standards investigated.
3. The modelling of the complex heat transfer processes in the presence of small scale rib turbulators in the design cycle has proved to be reasonably accurate.
4. A real time, low costs, pyrometry system based on a Newvicon camera, has been demonstrated. The results from a series of hot cascade rig tests were in close agreement with results obtained from the thermal paint tests.
5. The artificial maturing of the target blades by an application of a high temperature resistant paint, allowed direct comparison between adjacent blades, that under normal circumstances, may not exhibit the same surface emissivity values.



6. The technique allows limited cyclic running to be undertaken, though there is a limit imposed by the temperature window that can be accommodated by any aperture selection. The temperature window at F8 for the conditions reported, was approx 200°C.
7. If linked to a suitable computer, digitised video data can be readily transferred to other computers for updating or creation of a data base, for use in thermal prediction programs.

#### REFERENCES

1. Norris, R H  
Some simple approximate Heat Transfer Correlations for Turbulent flow in Ducts with Rough Surfaces  
ASME Winter Annual meeting, December 1970 on Augmentation of Convective Heat and Mass Transfer.
2. Burggraf, F.  
Experimental Heat Transfer and Pressure Drop with Two-Dimensional Discrete Turbulence Promoters Applied to Two Opposite Walls of a Square Tube.  
ASME Winter Annual Meeting, December 1970 on Augmentation of convective Heat and Mass Transfer.
3. Holland, M J and Thake, T F  
Rotor Blade Cooling in High Pressure Turbines  
AIAA 80-4061
4. Wezel, Ru Van.  
Video Handbook  
Newnes Technical Books - 1981
5. Ludwig, C.B., Malkmus, W., Reardon, J.E., and Thomson, J.A.L.  
Handbook of Infrared Radiation from Combustion Gases  
NASA SP 3080 1973
6. Gibberd, G.J.  
Background work for a Gas Turbine Radiation Pyrometer  
RR sponsored final year thesis, Bristol University (86/22) 1986.
7. Barber, R.  
A Radiation Pyrometer designed for Inflight Measurement of Turbine Blade Temps.  
Paper delivered at ASAE National Air Transportation Mtg, New York. No 690432 1969
8. Buchele, D.R.  
Surface Pyrometry in Presence of Radiation from other sources with application to Turbine Blade Temperature Measurement  
NASA 1754 1980
9. Insight Vision System Maintenance Manual
10. Quantel Intellect 100 Service Manual

#### ACKNOWLEDGEMENTS

1. The authors gratefully acknowledge the support of the Ministry of Defence (Procurement Executive) for all of the work, and the kind permission of Rolls-Royce plc, to publish this paper.
2. Insight Vision Systems Ltd, Malvern.

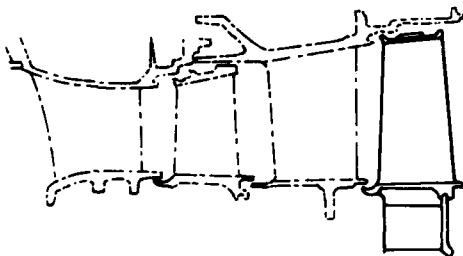


Fig. 1. HP Demonstrator Turbine.

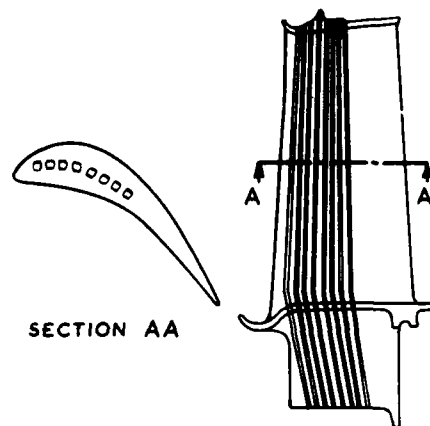


Fig. 2. Demonstrator Blade.

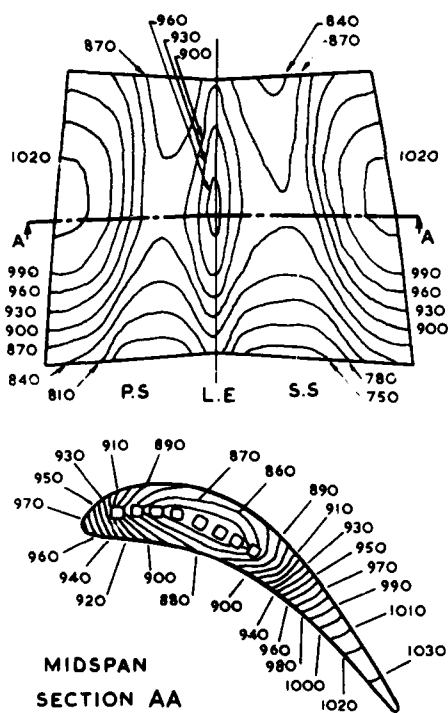


Fig. 3. Temperature Contour Plots  
 — Surface and Section.  
 — Predicted.

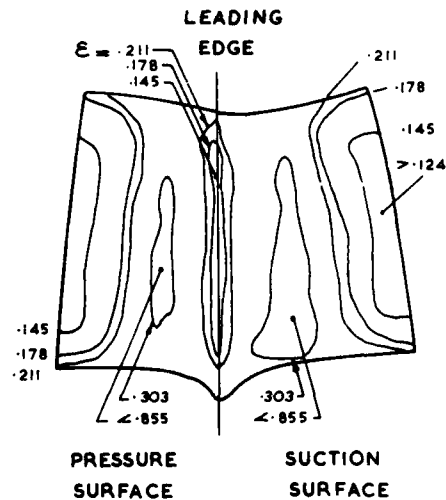


Fig. 4. Plain Walled Standard  
 — Effectiveness Contour Plot.  
 — Test Result.

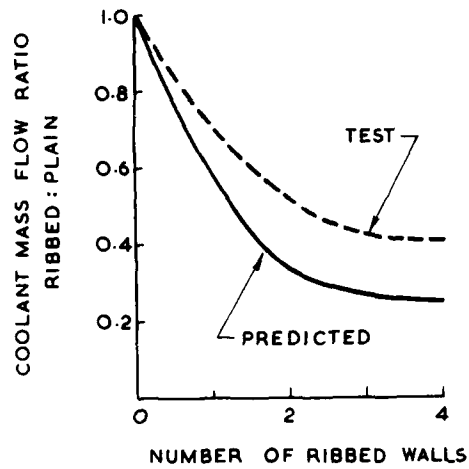


Fig. 5. Coolant Mass Flow.

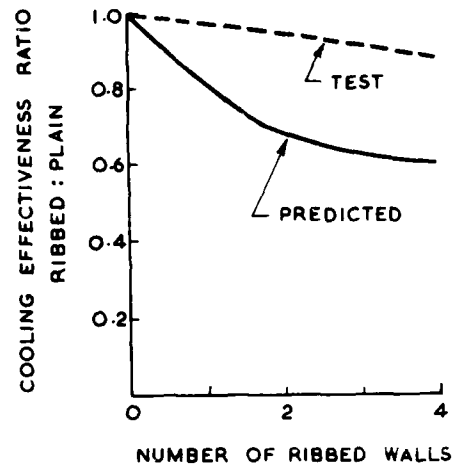


Fig. 6. Cooling Effectiveness.

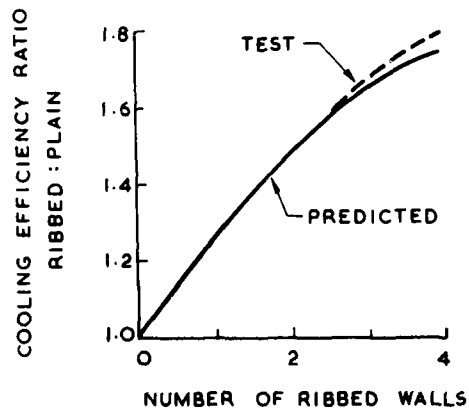


Fig. 7. Cooling Efficiency.

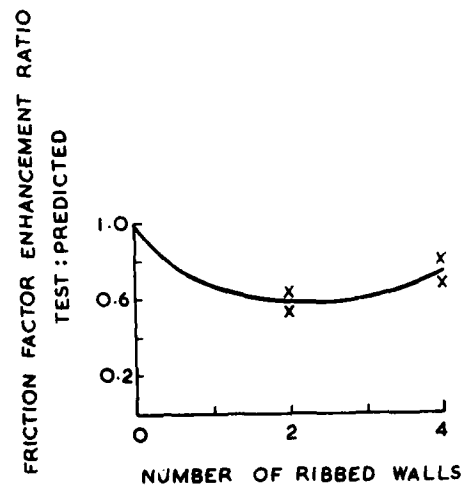


Fig. 8. Friction Factor Enhancement.

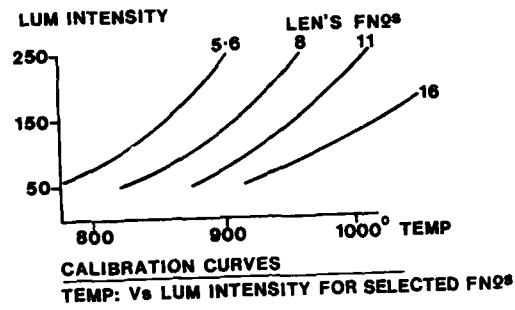


Fig. 9.

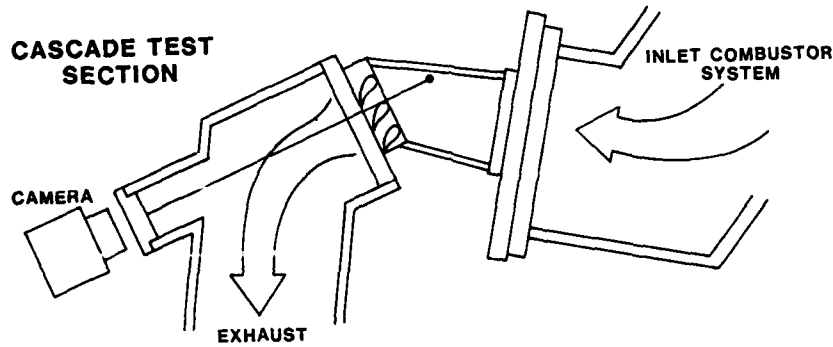


Fig. 10.

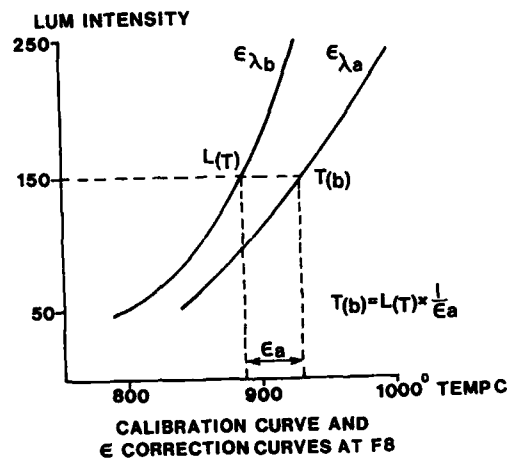


Fig. 11.

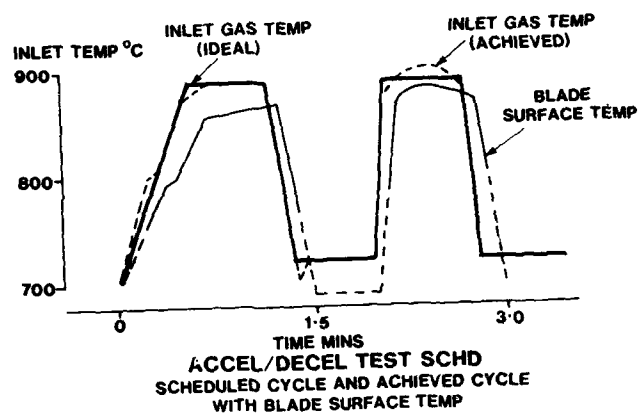


Fig. 12.

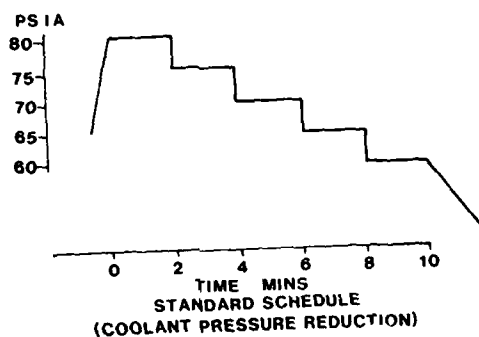


Fig. 13.

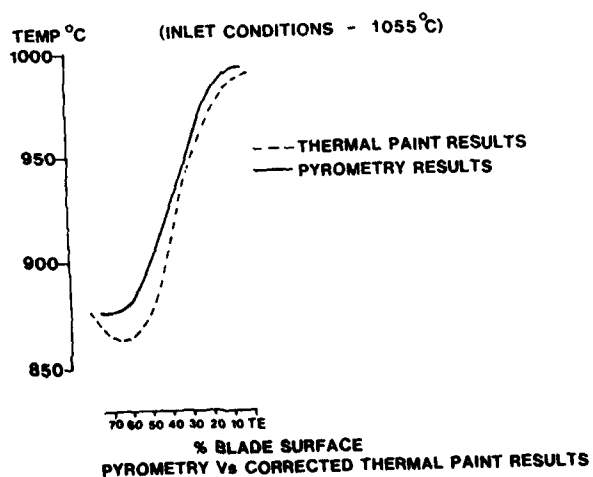


Fig. 14.

DISCUSSION

D.K. HENNECKE, Ge

In your prediction scheme, do you have a correlation to account for the effect, not only of ribs, but also of rotation (Coriolis and buoyancy forces) on flow and heat transfer ?

Which is it ?

Author's Reply

The prediction method used does employ a "correlation" to model the effect of the ribs. This draws on information from a number of sources.

In modelling the cooling systems for comparison with the hot cascade test results, which are a static case, rotation effects need not be included.

G. WINTERFELD, Ge

You showed a very interesting comparison between the Video-Radiation Technique and the Thermal-Paint-Technique on a relative basis. Could you give figures on the absolute accuracy, in degrees centigrade, of the Video-Radiation Technique ?

Author's Reply

It is difficult to give an accuracy level for temperature sensitive paints in general. However, our comparisons with thermocouple results show it to be in relatively good agreement. For these particular tests, the paint laboratory felt that paint test results should be within  $\pm 15^\circ$  to  $\pm 20^\circ\text{C}$ .

J. HOURMOUZIADIS, Ge

Did you select the square form of the holes because the cooling effect is good ? If so, do you expect any increase in thermal stresses at the corners of the squares ?

Author's Reply

The reason for choice of squares holes was to aid the manufacturing process and thus reduce costs of production.

A.S. ÜÇER, Turkey

Have you compared predicted and measured temperature distributions ? What about the comparison ?

Author's Reply

Comparison of the predicted and measured temperature distributions was good in the leading edge and central regions where the cooling system has greatest effect, 5-10°C deltas being seen. Trailing edge region temperatures still compared reasonably well, within 20°C.

# THE UNSTEADY GAS FLOW THROUGH STATOR AND ROTOR OF A TURBOMACHINE

by

K.M.Förster, Prof.Dr.-Ing.

Institut für Aerodynamik und Gasdynamik der Universität Stuttgart  
Pfeffenweidring 21, D - 7000 Stuttgart 80

## Summary

The difficulties of computing unsteady transonic flow in multiply connected domains with a minimum of neglects and approximations have been overcome by using

- individual computational grids fixed to each cascade,
- a novel grid-less finite difference scheme,
- physically real in- and outflow boundaries.

The resulting computer program is capable of computing the inviscid, plane gas-flow through stator and rotor of a turbomachine stage made up from arbitrarily shaped (thick, round-nosed) blades of arbitrary spacing, up to local Mach Numbers of 1.8.

## 1. Introduction

Answering the needs of the industry a large number of computational methods for the flow through turbomachine cascades has been developed, the overwhelming majority tackling steady flow. This, however, is only a crude approximation to reality and in order to get a better picture one has to compute the true unsteady flow through the multistage sequence of steady and rotating rows of blades. Now the computation of an unsteady and, as is now necessary in many applications, transonic flow is a formidable task in itself, but in the case of the turbomachine it is further complicated by

- the large-scale mutual movement of every two neighbouring cascades which thus cannot be covered by one common computational grid, and
- the singular grid points which occur inevitably in multiply connected domains and result not only in additional and non-vectorizable coding but also decrease the overall accuracy.

The first problem can be solved by a grid-coupling technique developed several years ago and used successfully for unsteady flows with large-scale moving boundaries (see /1/, /2/).

The second problem is posed already in computations of steady flow - for instance, in using H-grids where it produces the well-known spikes protruding from the blade's nose - but there it is not going to cause serious trouble. In unsteady computations, however, with their changing and eventually reversing flow around the nose such singularities are bound to result in disaster, at least after computing through very many time-steps. Therefore an acceptable computational scheme for unsteady flows should avoid this problem altogether. A good choice with respect to this would be the Finite Element Method, but for hyperbolic problems as presented by unsteady compressible flows it still seems to be not yet fully developed if one is not willing to accept the existing hybrid methods (spatial discretization by the FEM, integration in time by, say, Runge-Kutta-methods) as satisfactory; furthermore, the FEM's developmental expense is very high. Also the Finite Volume Method, though straightforward in concept and simple to implement, suffers from the afore-mentioned hybrid character and, in its cell-center-implementations, additionally from a serious decay of accuracy in stretched and sheared arrangements of cells. So what can we do?

## 2. A grid-less Finite Difference Scheme

### 2.1 Design

An efficient way to circumvent all problems connected with singular grid-points is to skip grids at all. This seems to be a baffling statement, but regarding the Finite Element Method quickly shows that it may be quite natural to ask: what is a grid good for? In discretizing spatial derivatives by difference quotients we need to know the relative positions of one point's neighbours, and the notion of a (regular) grid greatly facilitates the description of these relations - at the price of compulsory regularity. So, if we find another, perhaps not so elegant but more general way of describing the said relations we may do away with the grid at all, and so with the associated problems, too.

A simple example (with only first order of accuracy) may serve to illustrate our idea:

Consider an arbitrary cluster of points 1,2,3. Then for an arbitrary function  $u$  the sought-for partial derivatives  $u_x, u_y$  of  $u$  in (0,0) can be computed on the basis of three Taylor expansions:



$$u_l = u + x_l u_x + y_l u_y + O(2), \quad l = 1, 2, 3$$

yielding a linear equation:

$$\begin{bmatrix} 1 & x_1 & y_1 \\ 1 & x_2 & y_2 \\ 1 & x_3 & y_3 \end{bmatrix} \begin{bmatrix} u \\ u_x \\ u_y \end{bmatrix} = \begin{bmatrix} u_1 \\ u_2 \\ u_3 \end{bmatrix} \xrightarrow[\text{Rule to give}]{\text{solved by Cramer's}} u_x, u_y \text{ (and } u) \text{ to first order.}$$

It is easy to extend this procedure to second order of accuracy using a cluster of six points. Of course, to yield robust expressions for the partial derivatives, the linear system of equations must be well conditioned. It can be proved (see Theilemann /3/) that the matrix becomes singular if the six points used are situated on the section of a cone and so this situation must be avoided. This can be done by considering not only six but eight neighbouring points and picking, by some not stringent "Design Rules", those giving the best condition number and the smallest truncation error of the Taylor expansion of the sought-for derivatives.

Upon this basis, an explicit algorithm of the Runge-Kutta type can now be constructed in the following way (see also fig.1): to advance the point number  $i$  at time  $n$  to the time  $n+1$ , in the first step the cluster of eight neighbouring points is used in the manner described above to compute six auxiliary points in the time-plane  $n+(1/2)$ . From these, in the second step, the derivatives  $u_x$  and  $u_y$  are formed in a like manner and used to compute the new values at time  $n+1$ .

## 2.2 Properties

First, an analytical investigation of the new scheme was made. The accuracy was tested by extending the well-known Modified Equation Approach (Warming and Hyett /4/) to two spatial dimensions, resulting in a condition for second order of accuracy which is not stringent and can be easily controlled during the design process of the computational grid, along with the afore-mentioned design rules.

Second, the stability of the scheme was investigated by computing the amplification factor for a variety of stretched and sheared configurations of the cluster of points involved. For some rather extreme configurations a very mild instability was found for which a stabilizing term can be computed (after acquiring some "feeling", however, it proved less time consuming but equally accurate to guess the necessary damping factors for the actual computation).

Because the tests done so far had to be carried out with a linearized version of the novel scheme we added a series of numerical tests of the complete nonlinear case using an exact, non-trivial solution of the gasdynamic equations. For this we picked the well-known Ringleb Flow (a two-dimensional steady solution of Chaplygin's equation) for the following reasons:

- choosing appropriate streamlines as solid boundaries, this solution simulates a channel flow roughly equivalent to the flow between blades,
- using the appropriate set-up, the Ringleb Flow can be used for testing schemes for the two-dimensional unsteady case as well as for the steady one,
- there exists a complete set of auxiliary programs for this test (in /5/).

Some significant results from these numerical tests are reproduced in fig.2. There is no unfavourable difference in accuracy compared with good conventional schemes, and nearly none at all between regular and irregular clusters of points.

Summing up, the statement is justified that the new scheme combines, on one side, the accuracy and geometric versatility of the Finite Element Method with the perspicuity and ease of implementation of the Finite Difference Method on the other side. Its disadvantage, compared with the latter, is the larger memory requirement, but this drawback is eased by the high and equally distributed numerical accuracy resulting in a comparatively low number of computational points (see below). The computation time per point does not differ much from conventional explicit finite difference methods because the computation of all coefficients resulting from the irregular clusters is done once only for a given geometry of the turbomachine stage.

## 3. Details of actual turbomachine computations

### 3.1 Overall discretization

As a model we adopted a turbine stage with a given parallel flow from minus infinity onto an infinite plane stator cascade perpendicular to the onflow followed by a similar "rotor" moving parallel to the stator with prescribed "circumferential" speed or angle of attack, the outflow going to plus infinity. All flow angles are left to adjust themselves.

It is clear that such a set-up continuously produces pressure waves running up- and downstream. Although there exists now (mainly due to Moretti) a sound philosophy for the treatment of artificial inflow and outflow boundaries we wanted to avoid any risk and consequently regarded the physical domain as unbounded, that means we had to provide for an appropriate computational domain both upstream and downstream. Because the computation time is finite (it terminates when after a start from rest the periodic flow through the stage is achieved) it suffices to extend the computational space up- and downstream only so far that these limits are reached by the spatial loops after slightly more than half the computational time (for reasons and details see 3.2 below). Afterwards the spatial loop limits are reduced one mesh per time step so that at the end of the computation only the domain of interest from, perhaps, one blade spacing ahead and



two behind the stage proper is computed. Such an extension need not be costly in memory space and/or computing time. It pays anyway to divide the computational space not only into the two mutually moving subdomains wrapped around the two cascades but to restrict these subdomains to the absolute minimum and to couple them to simple regular grids in the singly connected on- and outflow regions. These two two-dimensional grids need not be large because the onflow as well as the outflow, being subsonic, becomes essentially one-dimensional within a rather short distance, about three blade spacings before and four behind the stage (the actual value can easily be controlled during the computation). Consequently we may append here one-dimensional grids (which are very cheap in memory space and computational time), extending to the spatial limits mentioned above.

The resulting computational domain looks like fig.3. To give some numbers from sample computations:

- grids A and F use 400 resp. 800 points,
- grid B has  $40 \times 14$ , grid E  $70 \times 18$  points, and
- the grid-less subdomains C and D comprise 860 points each.

A sample of one such subdomain is shown in fig.4; all points which would be singular when using a grid-bound instead of the grid-less method are encircled.

### 3.2 The starting procedure

Time and again when modelling critical parts of a computation, we have found that it is always safe to stick as closely as possible to what happens physically. So in starting the computation we "start the flow" by "opening a valve" - modeled by a (one-dimensional) compression wave immediately upstream of the stator at time  $t = 0$ . Then, when this wave travels downstream through the stage, the rotor is "started rotating" in such a way that its blades are not attacked under a too incorrect angle (in this case the real flow would answer with a separation, the computation answers by blowing up).

This starting procedure implies the following economical use of the computational domain (see fig.5):

For  $t = 0$  the flow assumes a constant state upstream of the compression wave and is at rest downstream. According to the theory of hyperbolic equations the physical disturbances travel down- and upstream with the gasdynamic characteristics (resp. the shock emerging from the convergent compression wave far downstream), whereas the computational disturbances proceed along numerical characteristics whose speed is in between the true and the difference characteristics which are the diagonals in the  $x,t$ -grid. It is a matter of taste if one simply uses the difference characteristics or searches for the numerical ones to fix the limits of the spatial loop at a given time.

### 3.3 Trailing edge treatment

The common practice with regard to the trailing edge is the implementation of some approximate form of the Kutta Condition, mostly by setting the angle of the velocity vector to halving the tangents to the contour. This works more or less satisfactory with steady flows, in the unsteady case, however, the Kutta Condition is not valid at all any more.

We have chosen the following way out (which basically resembles the train of thought leading to the grid-less scheme):

at contour points the boundary condition makes use of the given direction of the wall. At the trailing edge this direction is not unique, and thus the trailing edge is not a valid boundary point in the sense of numerical mathematics. Consequently we exclude it - what we are completely free to do! - and instead take a nearby point in the field which is computed with the help of a neighbouring cluster as all other field points. And - though it is not necessary - it is perfectly alright to push this field point very near to the trailing edge until geometrically they merge. We just have to choose the computational cluster in such a way that the upstream influences from the upper and lower side of the blade have equal weight upon the computation.

## 4. A sample computation

### 4.1 Geometry of sample stage

The blades of stator and rotor were laid out on the basis of the NACA 0020 airfoil

$$y_{NA20} = \pm d (0.2948 \sqrt{x} - 0.126 x - 0.3516 x^2 + 0.2843 x^3 - 0.1015 x^4)$$

whose median line was bent according to

$$y_{ml} = (x - x_0) \tan \alpha + (x - x_0)^3 \beta$$

To reduce the resulting slinness in the rear part,  $y_{NA20}$  was additionally thickened by a function

$$f(x) = 1 + g x^2$$

so the final shape of the contour is given by

$$y = y_{NA2D} f(x) + y_{NL}$$

The constants are  $d = 0.1$ ,  $x_0 = -0.1286$ ,  $\gamma = 2.0$  for both blades

and  $\alpha = 0^\circ$ ,  $\beta = -0.65$  for the stator,

$\alpha = -20^\circ$ ,  $\beta = 0.7$  for the rotor.

The resulting shape is shown in fig.6.

The blade spacing was chosen as  $g = 1.12$  or, related to the length of the chord,

$$g/c = 0.8 \quad \text{for the stator} \quad \text{and} \quad g/c = 0.93 \quad \text{for the rotor.}$$

It should be remarked that  $g$  need not be the same for stator and rotor. The spatial periodicity interval, however, is determined by the condition of commensurability and so may then become very large and consuming, both in memory space and computation time. For instance, if a real stage comprises  $m$  stator blades and  $m+1$  rotor blades, the periodicity interval is equal to the complete circumference and the size of the two-dimensional subdomains and consequently also the computation time are roughly the  $m$ -fold of the case with equal spacing.

The gap between the two cascades was chosen as 0.15 which is a small realistic value. Smaller spacings, e.g. 0.1, are perfectly alright with the computational procedure but - via the CFL Condition - prolong the computation time because of the then rather small clusters in the overlapping area of the two grid-less subdomains.

#### 4.2 Sample starting conditions and some results

As starting conditions we took an unsteady compression wave accelerating the flow at rest downstream of it to a velocity  $u_0 = 0.7$ , and the circumferential speed was determined by the condition  $A = 52^\circ$ , see fig.7. These conditions resulted in a periodic state of flow with a time-average onflow Mach Number of 0.25. The space-averaged velocity vectors for four times equally distributed over one period are shown in fig.8, the individual (non-averaged) fluctuations are of course considerably larger.

Such fluctuations are better displayed by, for instance, a sequence of isobar plots. Fig.9 shows two pictures, one half-period apart, from a cinematographic film made up of such plots. Such a film (as shown during the presentation of this paper) of course gives a much more vivid impression of the unsteady flow than a lot of diagrams. Nevertheless, already the comparison of the two pictures in fig.9 shows a lot of details which are characteristic for such an unsteady flow through the given cascade.

- First, there is a local supersonic region on the rear part of the rotor's suction side marked by the shaded area. Its boundary, the sonic line, does not coincide with an isobar as would be the case for homentropic steady flow. The differences are a measure for the unsteadiness.

Second, let us compare the pressure distribution

- first on the suction side of the stator blades. For  $t = T/4$  the minimum is very broad, centered at about two-third-chord and stretching nearly to the trailing edge with a steep pressure rise there. One half-period later it is much narrower, the center is at about half-chord and the gradient toward the trailing edge much more soft;
- second on the forward part of the suction side of the rotor blades. The difference is striking: whereas for  $t = T/4$  there is a continuous decrease in pressure corresponding to a continuous acceleration, one half-period later we see a sharp decrease in pressure followed by an equally sharp rise before the final acceleration along the rest of the suction side begins, and it is quite clear that such an enormous counter-pressure gradient will, in real flow, cause massive separation.

These circumstances are shown once more by fig.10, plotting the pressure coefficient from our inviscid computation along the contours over one period, and fig.11 where the results of a quasi-steady boundary-layer calculation based upon the inviscid unsteady solution are shown: for large parts of each period the calculation fails because the separation criterion is exceeded.

It is this behaviour of unsteady turbomachine flow which underlines the need for unsteady computations, and in fact for viscous ones, so this paper presents just the first step.

Also the following diagrams are to be seen under this proviso:

Fig.12 shows the oscillation of the forces and moments exerted upon the stator and rotor blades - they are by no means harmonic, and would still be changed when incorporating the influence of viscosity.

#### 4.3 Off-design starting conditions

As mentioned above the results of the preceding section have been won for an angle  $\beta_0 = 52^\circ$  corresponding to the so-called shockless entrance upon the rotor blades. One can of course also examine off-design cases:

- fig.13 shows the velocity-relations and the pressure distribution along the contour for the case  $\beta_0 = 41^\circ$ , leading to a time averaged  $M_{\infty} = 0.259$ ,
- fig.14 gives the same for  $\beta_0 = 79^\circ$ ,  $M_{\infty} = 0.248$ .

The afore-mentioned details show up here, too, partly enlarged, partly diminished.

#### 5. Acknowledgment

Most of the work presented in this paper is the result of a close cooperation between the author and L.Theilemann leading to the latter's dissertation /3/.

#### 6. References

- /1/ Förster,K., Technically oriented algorithms for unsteady pipe flow. Computer Meth.in Appl.Mech.and Engin. vol.2(1973), p.279-303
- /2/ Förster,K., The crossing of two high-speed trains in a tunnel. Proc.4th Int.Symp.Aerodynamics&Ventilation of Vehicle Tunnels, paper C3 BHRA, Cranfield 1982
- /3/ Theilemann,L., Ein gitterfreies Differenzenverfahren. Dissertation, Universität Stuttgart 1983
- /4/ Warming,R.F. and B.J.Hyett, The modified equation approach to the stability and accuracy analysis of finite-difference-methods. J.Comp.Phys. vol.14(1974), p.159-179
- /5/ Förster,K.(ed.), Boundary algorithms for multidimensional inviscid hyperbolic flows. Notes on Num.Fluid Mech. vol.1, Vieweg, Wiesbaden 1978

## 7. Figures

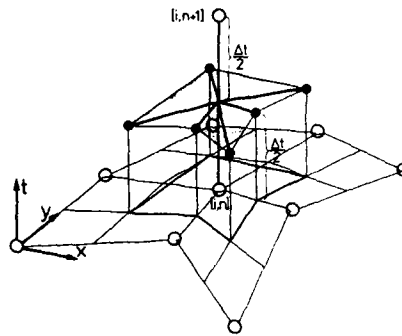
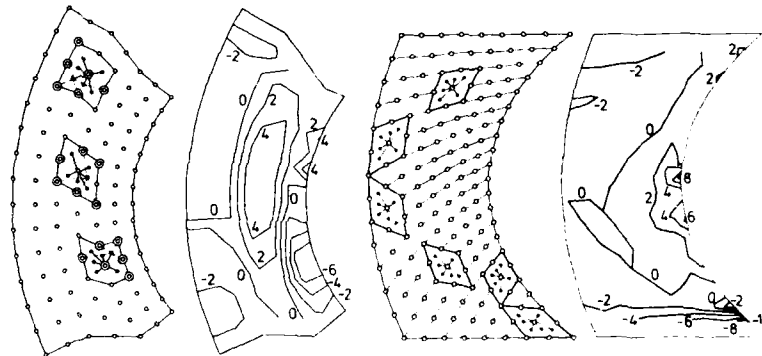
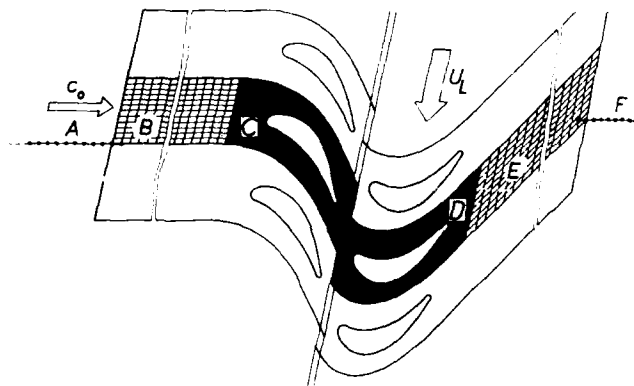


Fig.1 Runge-Kutta type algorithm

Fig.2 Distribution of the relative error in pressure  $(p/p_{\text{exact}} - 1)10^3$  for a regular, distorted grid (left pair) and for irregularly chosen clusters (right).Fig.3 Composition of physical domain from one-dimensional (A, F) and two-dimensional (B, E) regular grids and grid-less subdomains (C, D).  $c_0$  and  $u_L$  see fig.7.

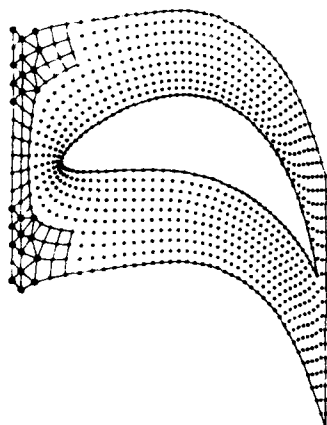


Fig.4 Sample distribution of points in grid-less method. Irregular points in a ev. grid encircled.

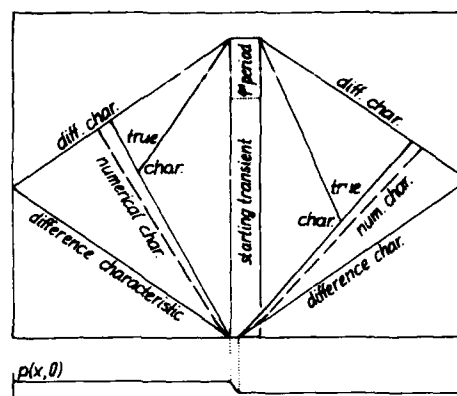


Fig.5 Above: limits of disturbed and undisturbed regions in the  $x,t$ -plane. Ch characteristics Below: initial pressure distribution with unsteady compression wave.

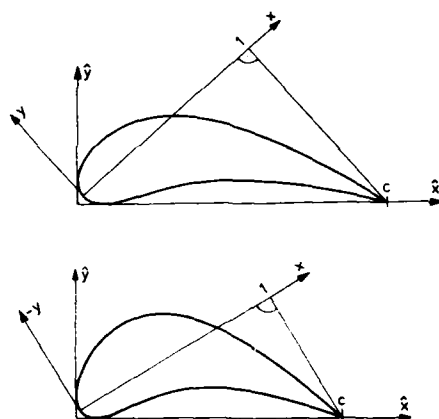


Fig.6 Shape of stator (above) and rotor blade (below) used in sample computation.  $c$  chord length.

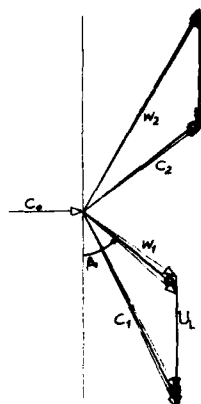
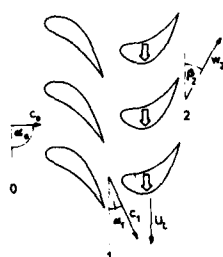


Fig.7 (left) Layout of stage.

Fig.8 (right) Space-averaged velocities,  $c$  absolute,  $w$  relative  
index 0 far upstream  
1 between cascades  
2 far downstream

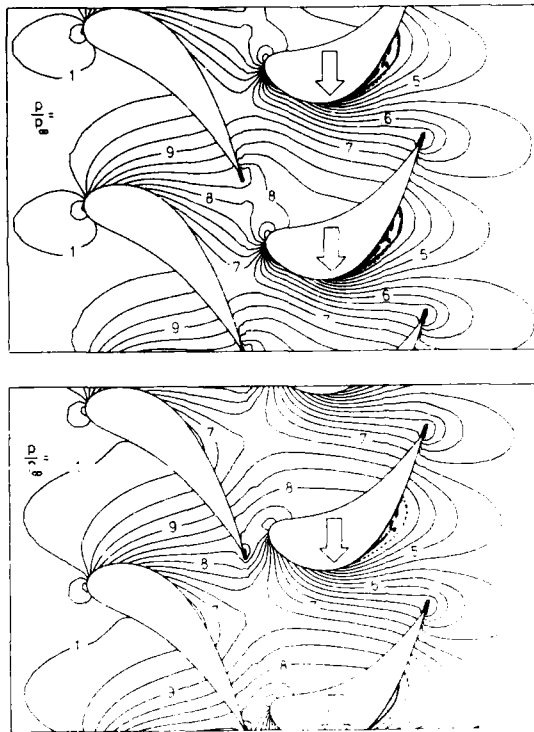


Fig.9 Isobars for  $t_0 - T/4$  (above) and  $t_0 + T/4$  (below). Shaded area: supersonic flow.

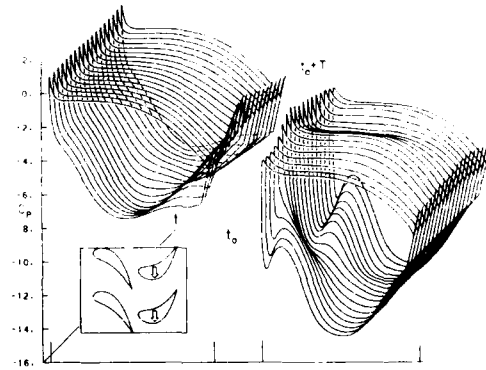


Fig.10 Distribution of pressure coefficient (time as parameter) along the contours of stator (left) and rotor blade (right).

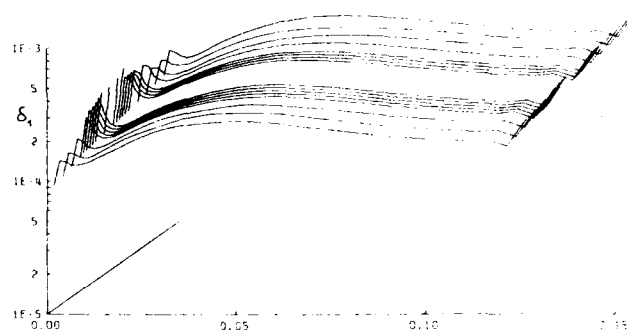


Fig.11 Displacement thickness of boundary layer on pressure side of rotor (time as parameter). No curve: separation.

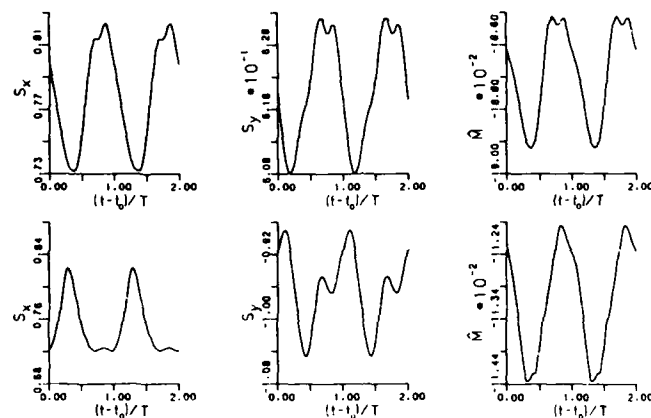


Fig.12 Oscillations of forces (axial:  $S_x$ , circumferential:  $S_y$ ) and moments  $M$  (around geometric center of gravity of blade). Stator: above, rotor: below.

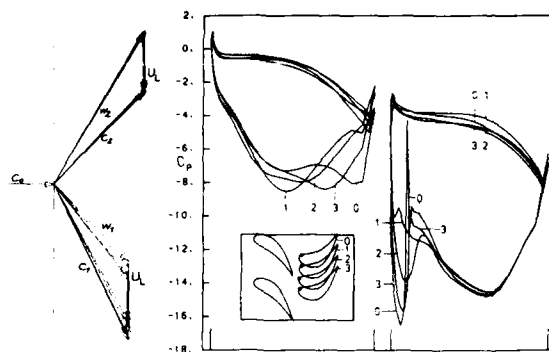


Fig.13 Velocity configuration and distribution of pressure coefficient for off-design: lower circumferential speed.

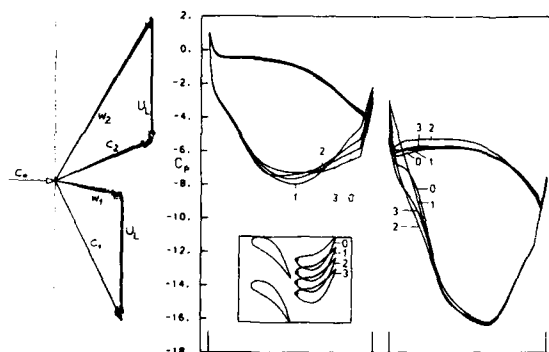


Fig.14 Velocity configuration and distribution of pressure coefficient for off-design: higher circumferential speed.

DISCUSSION

J. HOURMOUZIADIS, Ge

The rotating blade didn't show any significant pressure distribution fluctuation on the rear point. The major fluctuation within the suction peak was in a front part. Do you have an explanation for this phenomena ?

**Author's Reply**

Being no turbomachine specialist, I paid no special attention to this point yet and I can just report on what the computation produced. Figure 10 of the written version indeed displays some pressure fluctuations at the rotor's trailing edge though they are considerably smaller than those at the stator. A close (post-conference) inspections of the film revealed, however, that the domain influenced by these fluctuations is very small. This may be due to the assumption of inviscid flow which remains attached all the time, whereas in real flow an eventually detached and periodically pulsating boundary layer would produce much larger and farther spreading fluctuations.



# ETUDE ET ESSAIS D'UNE PETITE TURBINE RADIALE POUR GROUPES AUXILIAIRES DE PUISSANCE.

Y. RIBAUD, C. FRADIN et C. MISCHÉL  
(\*) (\*) (\*\*)

- (\*) Office National d'Etudes et de Recherches Aéronautiques.  
29, Avenue de la Division Leclerc - 92320 CHATILLON CEDEX, FRANCE.  
(\*\*) MICROTURBO  
Chemin du Pont de Rupé, 31019 TOULOUSE CEDEX, FRANCE.

## SOMMAIRE

Le projet d'une petite turbine centrifuge d'un taux de détente de l'ordre de 3,6 a été entrepris par la Société MICROTURBO, avec la coopération de l'ONERA pour la partie calculs et analyse des résultats d'essais.

En premier, le but et les contraintes liés à la mission demandée sont soulignés. Les calculs préliminaires conduisent au dessin de la forme des pales du distributeur et à celles de la roue.

Puis y sont effectués les calculs quasi-tridimensionnels. Les essais à froid de la turbine sur le banc et les essais correspondants à chaud sur le turbomoteur permettent d'évaluer les performances.

L'intérêt des calculs de prédimensionnement et de détermination des champs d'écoulement est confirmé au vu des hautes valeurs des rendements isentropiques obtenus.

Les sondages de l'écoulement en aval de la roue d'échappement, au point de fonctionnement nominal, permettent de mieux connaître la structure du fluide.

## NOMENCLATURE

j	jeu entre roue et carter
k	rapport entre les chutes d'enthalpie statique et totale
m	coordonnée méridienne
N	vitesse de rotation (tr/mn)
P	pression
Q	débit masse (kg/s)
Re	nombre de Reynolds
T	température
$U_{e,r}$	vitesse périphérique de la roue
$V_t$	vitesse tangentielle
$V_j$	vitesse de jet
w	vitesse relative
Z	nombre de pales
$\alpha$	angle de l'écoulement ou de la pale par rapport à la direction tangentielle
$\Delta H_T$	chute d'enthalpie totale
$\sigma$	solidité méridienne (inverse du pas relatif méridien)
$\mu$	coefficient de travail ( $V_{t,e,r}/U_{e,r}$ )
$\eta$	rendement
$\Pi_i$	taux de détente (totale/totale), mesures par sonde NASA
$\omega$	vitesse de rotation (rd/s).

**INDICES**

e	entrée
T	conditions totales
st	conditions statiques
is	conditions isentropiques
R	conditions relatives
V	volumique
r	roue
3	entrée turbine
4	sortie turbine.

**1 - INTRODUCTION**

Actuellement les turbines radiales sont surtout utilisées dans des environnements relativement froids, par exemple, dans les G.A.P. (Groupe Auxiliaire de Puissance) (1) pour les avions ou les hélicoptères ou dans les cycles de Brayton, pour des applications spatiales ou pour des stations sous-marines (2).

Des turbines à gaz terrestres de faible puissance fonctionnent également souvent avec des turbines radiales (3) surtout dans la gamme comprise entre cent et deux mille kilowatts. Cependant, l'application principale reste le turbocompresseur pour camions et voitures (4, 5).

Enfin nous devons souligner les recherches importantes entreprises sur les matériaux céramiques et appliquées aux petites turbines à gaz (6, 7, 8). Ceci constitue une tentative pour démontrer que la turbine radiale sera utilisée tôt ou tard dans les petits turbomoteurs à haute température pour la propulsion des voitures et des hélicoptères.

Ici nous étudions une turbine d'un taux de détente de 3,6 montée dans un petit turbomoteur d'une puissance comprise entre 40 et 70 kW. L'étude a été conduite par la société MICROTURBO avec la coopération de l'ONERA pour les calculs théoriques et l'analyse des résultats d'essais dans le but de déterminer avec précision le rendement de ce type de turbomachine. En effet, si une certaine expérience a été acquise dans le domaine des taux de détente assez bas par contre pour des taux de détente supérieurs à 3, peu de résultats ont été publiés.

**2 - BUTS**

Les objectifs de la société MICROTURBO sont donnés dans le tableau 1

TABLEAU I

## CARACTERISATION GLOBALE DU PROJET DE LA TURBINE RADIALE

CONDITIONS ENTREE DISTRIBUTEUR

Pression totale  $P_{T_3} = 3.81$  bars - Température totale  $T_{T_3} = 953^\circ\text{K}$

Débit masse (air + gaz) -  $Q = 0.67$  kg/s

VITESSE DE ROTATION

$N = 59200$  tr/mn

PERFORMANCES

$Q\sqrt{T_{T_3}} / P_{T_3} = 5.43$  -  $N / \sqrt{T_{T_3}} = 1918$  -  $P_{T_3} / P_{T_4} = 3.63$

$$\eta_{is,T} > 82\%$$

NOMBRES SANS DIMENSION

Nombre de tours spécifique

$$Ns = \frac{\omega \cdot \sqrt{Q_{v4}}}{(\Delta H_{T, is})^{0.75}} = 0.58$$

Nombre de Reynolds

$$Re_{\theta_{e,r}} = 2.2 \cdot 10^6 \text{ (à chaud)}$$

$$Re_{\theta_{e,r}} = 6 \cdot 10^6 \text{ (à froid)}$$

Rapport de la vitesse périphérique sur la vitesse de jet

$$u_{e,r}/V_j = 0.69$$

3 - PREDIMENSIONNEMENT DE LA TURBINE RADIALE3.1. Contraintes prescrites par la société MICROTURBO

- Le diamètre d'entrée du distributeur est de 220 mm.
- L'espace lisse entre le distributeur et la roue doit être suffisant pour éviter l'érosion des bords de fuite de la grille distributrice due à la centrifugation par la roue et aux rebonds de particules solides (9).
- Le jeu radial relatif au niveau de l'échappement de la roue est 2.3% (10).
- L'usinage de la roue adaptée aux essais à froid sur le banc d'essais impose que le passage minimum en pied entre deux pales soit supérieur à 7.8 mm.
- Le projet de la turbine a été établi en utilisant les résultats expérimentaux de MICROTURBO et les études théoriques effectuées à l'ONERA.

### 3.2. Expérience acquise par MICROTURBO

L'expérience acquise par MICROTURBO sur la turbine TCS 14 conduit aux règles suivantes :

- les pertes dans le distributeur sont estimées à 3,6% de la pression totale d'entrée ;
- le nombre de pales de la roue est choisi égal à 13. Jusqu'à présent le travail effectué sur ce sujet a montré que les pales intercalaires ne sont pas très utiles (11) pour les roues de turbines radiales ;
- un coefficient de travail égal à 0,886 est choisi en accord avec le nombre trouvé expérimentalement dans l'étude de la TCS 14. Ce nombre est de 4 points supérieur à la valeur théorique  $\mu = 1-2/Z_r$  (12) ;
- le rapport de moyeu à l'échappement doit être supérieur à 0,41 pour réduire les risques de vibration des pales près de leur bord de fuite et donc éviter leur rupture.

### 3.3. L'estimation du rendement à partir de l'approche ONERA

Nous nous sommes appuyés sur l'expérience acquise par ALCATEL sur une turbine radiale (3). Nous avons choisi la plus haute valeur de rendement trouvée lors des essais et nous avons corrigé cette valeur expérimentale pour tenir compte des variations des nombres adimensionnels, tels que le nombre de tours spécifique, le nombre de Reynolds (13), le nombre sans dimension lié au jeu radial, entre la turbine ALCATEL et celle correspondant à notre étude. En utilisant cette approche le rendement isentropique total fut estimé à 84% alors que la valeur prévue par MICROTURBO était légèrement plus faible et égale à 82%.

### 3.4. Les calculs de dimensionnement effectués par l'ONERA

Ils sont basés principalement sur les idées suivantes :

- Avec l'aide de la technique de la transformation conforme, le passage d'une grille axiale à une grille radiale conduit à définir la solidité méridienne et donc à relier cette grandeur au nombre de pales et au rapport de rayon du distributeur.

De nombreux essais effectués à la NASA LEWIS montrent que pour un angle d'entrée de l'écoulement  $\alpha = 90^\circ$  et un angle de sortie de l'ordre de  $15^\circ$ , la valeur optimum de  $\sigma$  est environ 0,75 (14). Grâce au travail théorique de ce centre de recherches, il est possible de relier le rendement isentropique statique et l'angle optimum à la sortie du distributeur par l'intermédiaire du nombre de tours spécifique.

- Dans le repère mobile, le rapport des vitesses relatives entre la sortie et l'entrée de la roue le long de la nappe de courant moyenne doit être suffisant pour éviter tout décollement le long des pales :  $2 < W_4/W_{e,r} < 2,5$

- L'énergie cinétique de sortie doit être minimisée :  $1,03 < k < 1,05$

- Enfin l'angle de calage des pales en sortie de la roue d'échappement en tête doit rester supérieur à  $30^\circ$  pour faciliter l'usinage et pour limiter la contraction de la section causée par l'épaisseur de la pale.

Le canal méridien correspondant est tracé sur la figure 1 sur laquelle sont portés les principaux paramètres géométriques et aérodynamiques.

#### 4 - FABRICATION DES ROUES

Pour les essais sur le banc de turbines froides, la roue utilisée comprend deux parties en alliage léger : une partie radiale et une roue d'échappement axiale. Par contre, sur le turbomoteur, une pièce de fonderie en acier réfractaire est employée. Malgré la vitesse périphérique élevée, le niveau des contraintes reste modéré. Une vue en perspective de la turbine radiale est présentée sur la figure 2.

#### 5 - CALCULS D'ÉCOULEMENT

##### 5.1. Deux types de distributeur ont été définis :

Le premier type est déterminé uniquement à partir de considérations géométriques tandis que le second type est obtenu en partant d'une grille axiale à hautes performances, et en lui appliquant la transformation conforme permettant le passage de cette grille à la grille radiale équivalente. Le premier type de distributeur est caractérisé par des pales à forte courbure (Figure 3). Tandis que la technique par transformation conforme donne des pales de forme très différente, avec une courbure peu prononcée excepté au bord d'attaque (Figure 4). Le calcul d'écoulement dans ces grilles peut être effectué à l'aide d'une méthode numérique résolvant les équations d'Euler instationnaires (15). Les résultats obtenus sur le premier type de grille ne sont pas satisfaisants car il apparaît deux zones à gradient de pression positif sur l'extrados (Figure 5). Au contraire le second type de grille est caractérisé par une accélération progressive de l'écoulement sur les deux faces du profil (Figure 6). Il faut préciser que ces calculs donnent avec précision la direction moyenne de l'écoulement à la sortie du distributeur.

5.2. Les calculs d'écoulement dans la première roue (Figure 7) définie par MICRO-TURBO lors de la présente étude ont été effectués en utilisant le code de calcul quasi-3D de KATSANIS (16). Ce code donne accès à l'écoulement moyen et à l'écoulement de pale à pale linéarisé. Dans ces calculs, les pertes jouent un rôle fondamental à l'échappement du fait de l'existence d'un équilibre radial de pression dépendant fortement du moment cinétique de sortie. Nous avons pris soin de choisir un niveau de perte compatible avec le niveau de rendement estimé de la roue, tandis que les variations d'enthalpie normalement à l'écoulement méridien sont ignorées. Les résultats relatifs à la roue d'origine (Figures 8, 9 et 10) mettent en évidence un déficit de charge de pale à pale dans la partie hélicoïde de la veine méridienne, ce qui se traduit par des recompressions locales exagérées. Une seconde roue présente une veine méridienne plus pincée et une roue d'échappement allongée de manière à obtenir des profils de vitesse beaucoup plus réguliers, comme cela apparaît sur les figures 8, 9 et 10, les évolutions correspondantes étant dessinées en trait continu.

#### 6 - EXPERIMENTATIONS SUR TURBOMOTEUR

Les premiers essais de cette turbine (second type de distributeur et première roue) ont été effectués directement sur le turbomoteur complet. Ils ont donné entièrement satisfaction puisque dès le premier essai la consommation spécifique demandée au projet du turbomoteur complet, soit 500 g/CV h, environ a été obtenue (Figure 11). On note que

le rendement de turbine est plus haut que prévu (Figure 12), cette situation est expliquée par le fait que la turbine est effectivement meilleure que prévue et que le rendement du compresseur est légèrement inférieur à nos prévisions.

Nous devons aussi souligner que le rendement maximum de turbine est obtenu pour une puissance mécanique dépassant 80 kW même si le turbomoteur était initialement conçu pour la gamme 40 à 70 kW.

## 7 - ETUDES EXPERIMENTALES SUR LE BANC D'ESSAI

Sur la figure 13 sont portées les principales sections de mesure. Le débit masse est mesuré au niveau de la canalisation amont à l'aide d'un diaphragme calibré. Les résultats d'essais montrent que, à la vitesse réduite nominale (1918) et au taux de détente nominale (3,63), le col du distributeur semble bloqué et que le débit réduit d'entrée est plus grand que la valeur fixée au projet (Figure 14). Les évolutions des rendements isentropiques total et statique sont données en fonction de la vitesse réduite, pour le taux de détente nominal (Figure 15). Il apparaît que le rendement total est nettement plus élevé que la valeur prévue par le projet MICROTURBO.

Notons néanmoins que des calculs récents effectués par la NASA (17) sur une turbine radiale, dans le même domaine de nombres adimensionnels (nombre de tours spécifique, nombre de Reynolds, taux de détente et jeux radiaux) donnent un rendement isentropique total à total de 0.915. Nous en concluons que l'analyse aérodynamique des pertes effectuées par la NASA concorde de manière significative avec nos résultats d'essais.

Pour un taux de détente plus modéré de 3.2, un rendement isentropique total maximum de 0.91 est encore atteint. De plus, le rendement s'écarte peu de sa valeur maximale dans un grand domaine de vitesse réduite et ceci pour tous les taux de détente étudiés.

## 8 - SONDAGES EN SORTIE DE ROUE AU POINT NOMINAL

Les sondages de l'écoulement au moyen d'une sonde type NASA (18) donnent accès à la température d'arrêt, la pression totale et la direction de l'écoulement.

Connaissant bien l'énergie cinétique absolue restante, il est possible de préciser le rendement isentropique total. Ainsi, au point nominal, on obtient, en tenant compte avec exactitude de cette énergie cinétique restante, un rendement isentropique total de 0.93 (fig. 16) au point nominal. Ces sondages mettent aussi en évidence la structure de l'écoulement.

Dans la partie centrale de la veine, la vitesse méridienne est uniforme et le moment cinétique résiduel est très faible (fig. 17). Ces résultats sont conformes aux hypothèses admises lors du projet. Par contre, les sondages soulignent le rôle primordial du jeu sur la structure de l'écoulement : il apparaît que les effets du jeu se font sentir sur une profondeur égale à vingt fois la longueur de celui-ci. Notons également que cette structure en dard, près du carter externe, conforme à ce que l'on pouvait imaginer d'un point de vue qualitatif, semble favorable à l'utilisation d'un diffuseur lisse radial en aval de la roue ou d'un redresseur.

## 9 - CONCLUSION

Cette étude montre que les petites turbines radiales, avec des taux de détente de l'ordre de 3.5 à 4 peuvent donner des performances élevées, comme cela a été démontré à la lumière des résultats obtenus tant sur le banc d'essai que sur turbomoteur.

Ce travail de coopération entre une société industrielle et un organisme de recherche a été très profitable si nous considérons qu'un rendement total de 93 % a été obtenu dès le premier essai. Ceci démontre aussi que l'expérience acquise sur les turbines radiales à taux de détente modéré est aussi utilisable sur les turbines à haut taux de détente.

Des progrès sont peut-être encore réalisables en calant avec précision l'angle de l'écoulement à la sortie du distributeur et en diminuant l'allongement axial de la turbine pour minimiser les pertes par frottement.

Dans le futur, la taille du GAP pourra être réduite par accroissement de la vitesse de rotation. Une réduction de la consommation spécifique pourra être atteinte par un accroissement de la température à l'entrée de la turbine et de la vitesse périphérique.

Les progrès réalisés tant sur les matériaux ceramiques que sur les alliages métalliques devraient permettre prochainement de définir des petits turbomoteurs simples et robustes d'une puissance mécanique de l'ordre de 50kW et avec une consommation spécifique inférieure à 320 g/CV.h.

Enfin, soulignons l'importance des mesures fines de l'écoulement issu de la roue tout particulièrement hors adaptation. En effet, de tels renseignements seraient d'une grande utilité pour mieux cerner le rôle d'un éventuel redresseur en aval de la roue en vue de la minimisation de l'énergie cinétique restante.

## REMERCIEMENTS

Nous tenons à remercier la DRET, Groupe 7, du Ministère de la Défense, dont le soutien et la confiance nous ont été très précieux pour mener à bien cette étude.

## REFERENCES

1. RODGERS, C., "Power dense gas turbine APUs", ASME GT 124.
2. SAWYER's, "Gas turbine engineering handbook", Volume II, Applications.
3. MERIGOUX, J.M., "Mise au point d'une turbine radiale" (Radial turbine optimization), Entropie n° 66 - 1975.
4. JAPIKSE, D., "Turbocharger turbine design and development", TN 65, July 79 - Creare Hanover - Newhamphshire.
5. BHINDER, F.S., "Turbocharger and related problems - Modern developments in the design and performance of radial flow turbines", V.K.I. lecture series 1982-01.
6. GROSECLOSE, Lance E., JOHNSON, Richard A., "Status of the AGT 100 - Advanced gas turbine technology update", ASME 85 GT 205.

15-8

7. KIDWELL, J.R., KREINER, D.M., "AGT 101 - Advanced gas turbine technology update", ASME 85 GT 177.
8. NAPIER, James C., ARNOLD, J.P., "Advancements in application of ceramics to the Gemini radial-flow gas turbine", ASME GT 183.
9. CLEVENGER, W.B., TABAKOFF, W., "Dust particle trajectories in aircraft radial turbines", Journal of Aircraft - Vol. 13 n° 10 - October 76.
10. FUTRAL, S.M., Jr, HOLESKI, D.E., "Experimental results of varying the blade shroud clearance in a 6.02 inch radial inflow turbine", NASA TN D-5513, 1970.
11. FUTRAL S.M., Jr, WASSERBAUER, Ch. A., "Experimental performance evaluation of a 4.59 inch radial inflow turbine with and without splitter blades", NASA TN D-7015.
12. ROHLIK, Harold E., "Radial inflow turbine", NASA SP-290, Volume 3.
13. NUSBAUM, W.J., WASSERBAUER, ch.A., "Experimental performance evaluation of a 4.59 inch radial inflow turbine over a range of Reynolds number", NASA TN D-3835.
14. STEWART, N.L., GLASSMAN, A.J. "Blade design - Turbine Design and Application", Volume 2, NASA SP 290.
15. BERTHEAU, F., RIBAUD, Y., MILLOUR, V., "Transonic blade to blade calculation in an axial, radial or mixed flow cascade equipped with splitter blades", ASME 85 GT 86.
16. KATSANIS, Th., Mc NALLY, N.D., "Revised Fortran program for calculating velocities and streamlines on the hub shroud mid channed stream surface of an axial, radial or mixed flow turbomachine or annular duct", NASA TN D 8430 - 8431 - 1977.
17. CIVINSKAS, Kestutis C., POVINELLI, Louis A., "Application of a quasi-3D inviscid flow and boundary layer analysis to the hub shroud contouring of a radial turbine", NASA T.M. 83669, AIAA-84-1297.
18. GLAWE, G.E., KRAUSE, L.N., and DUDZINSKI, T.J., NASA TN D-4816 - october 1968.



## CANAL MERIDIEN DE LA TURBINE

Figure 1

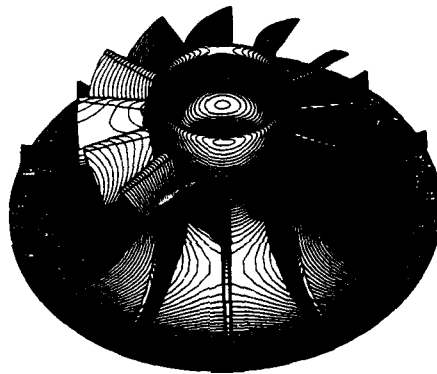
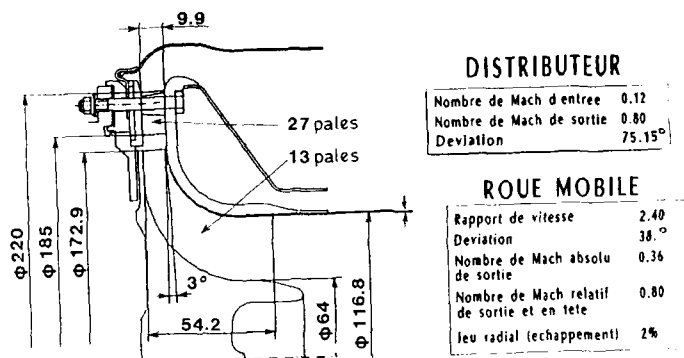
VUE EN PERSPECTIVE  
DE LA ROUE DE TURBINE

Figure 2

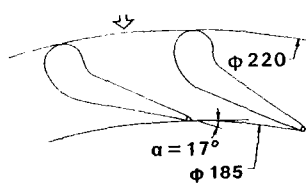


Figure 3

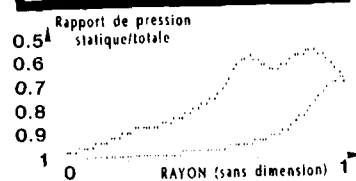
DISTRIBUTEUR DEFINITION GEOMETRIQUE  
- PREMIER TYPE -

Figure 5

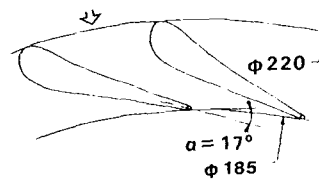
REPARTITION DE LA PRESSION STATIQUE  
LE LONG DES PALES DU DISTRIBUTEUR  
- PREMIER TYPE -

Figure 4

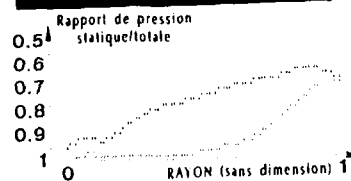
DISTRIBUTEUR OBTENU PAR TRANSFORMATION  
CONFORME - SECOND TYPE -

Figure 6

REPARTITION DE LA PRESSION STATIQUE  
LE LONG DES PALES DU DISTRIBUTEUR  
- SECOND TYPE -

# DIFFERENCES GEOMETRIQUES ENTRE LES DEUX ROUES

Figure 7

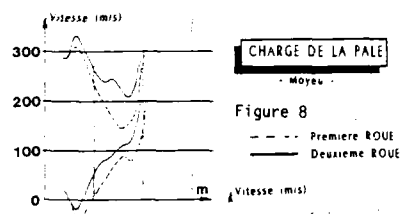
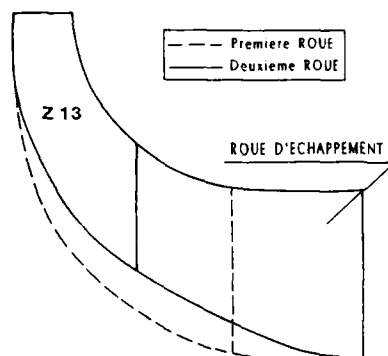


Figure 8

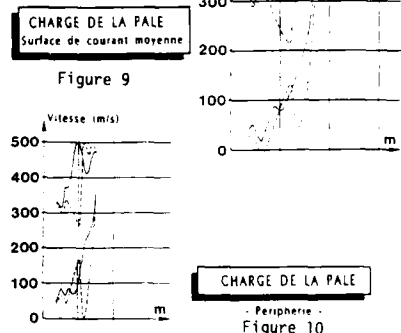


Figure 9

CHARGE DE LA PALE  
Peripherie  
Figure 10

## RESULTATS D'ESSAIS A PARTIR DES EXPERIMENTATIONS SUR TURBOMOTEUR

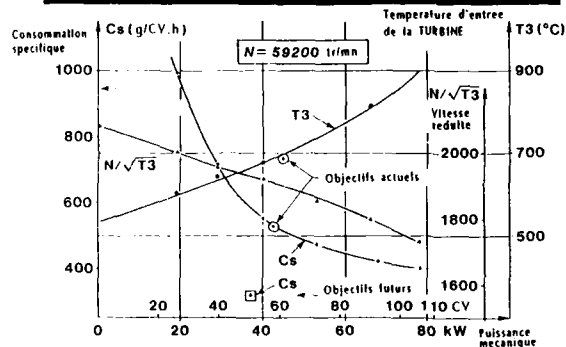


Figure 11

## RENDEMENT ISENTROPIQUE TOTAL DE TURBINE A PARTIR D'ESSAIS SUR MOTEUR

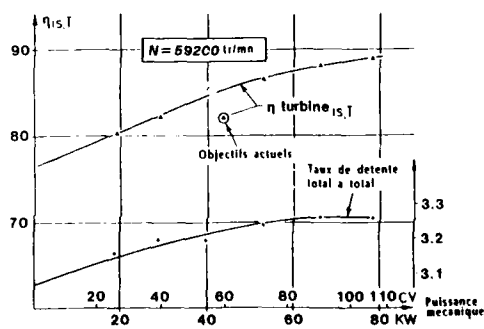
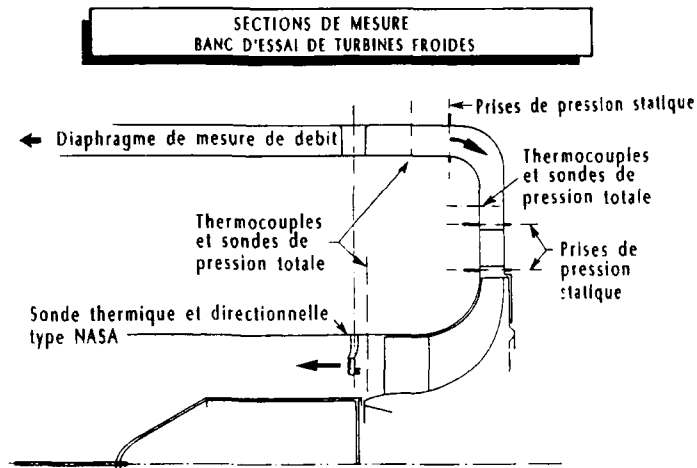


Figure 12

Figure 13



**DEBIT MASSE REDUIT EN  
FONCTION DE LA VITESSE REDUITE**

Figure 14

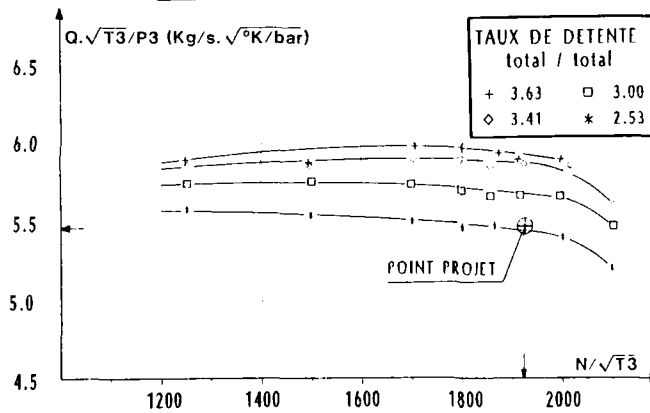
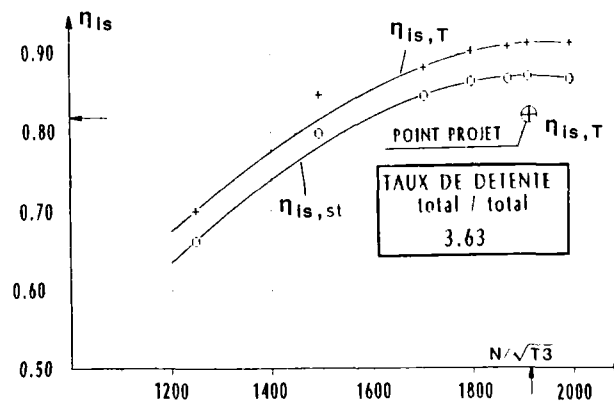


Figure 15

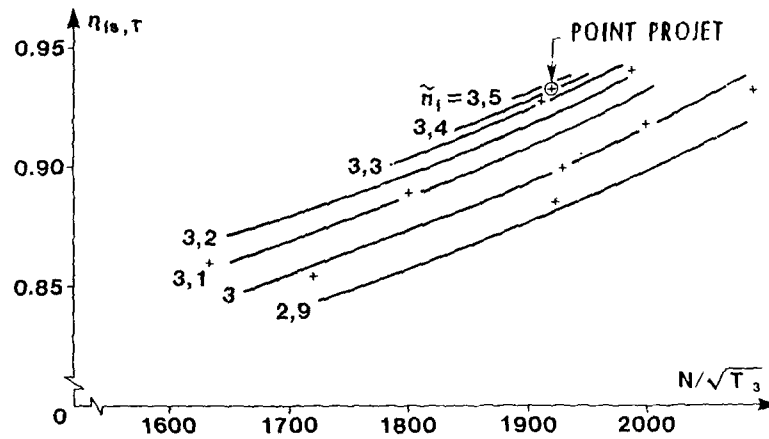
**RENDEMENT ISENTROPIQUE D'ETAGE  
BANC D'ESSAI DE TURBINES FROIDES**



# RENDEMENT ISENTROPIQUE TOTAL BANC D'ESSAI DE TURBINES FROIDES

Figure 16

- Mesures par sonde NASA -



## NOMBRE DE MACH AXIAL A L'ÉCHAPPEMENT - POINT PROJET

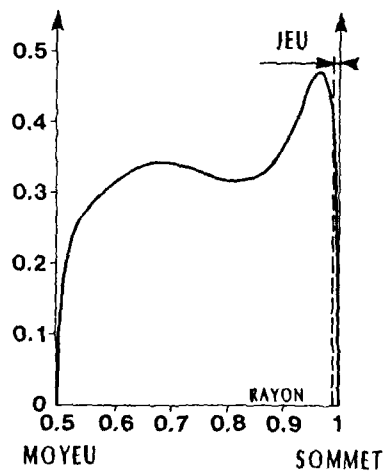
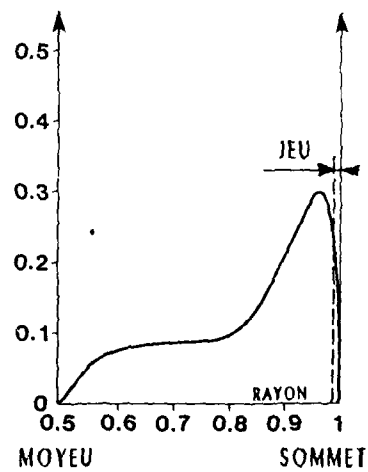


Figure 17

## NOMBRE DE MACH TANGENTIEL A L'ÉCHAPPEMENT - POINT PROJET



DISCUSSION

A.S. ÜCER, Turkey

Can you comment on the life expectancy of the rotor ?

Author's Reply

The life of the rotor is about one hundred an fifty hours or even more.

## DESIGN AND AERODYNAMIC PERFORMANCE OF A SMALL MIXED-FLOW GAS GENERATOR TURBINE

Ü. Okapuu

Chief, Turbine Aerodynamics  
Pratt & Whitney Canada Inc.  
C.P./Box 10  
Longueuil, Qué. Canada J4K 4X9

### SUMMARY

Design details and results from aerodynamic rig tests are presented for four variants of a mixed-flow turbine having a design target pressure ratio of 3:1.

This experimental turbine, designed to satisfy the aerodynamic requirements of a gas generator turbine in a hypothetical small turboprop engine, demonstrated a design point efficiency substantially in excess of that predicted for a single stage axial turbine of equivalent duty.

Design and material implications are discussed and potential constraints identified.

### INTRODUCTION

The single-stage gas generator turbine in small, two-spool aircraft engine applications continues to show size, weight and cost advantages when compared to its more complex multi-stage counterpart. Aerodynamic efficiency, the only significant weakness of high work single-stage turbines, has therefore been the target of continuous research at Pratt & Whitney Canada for more than two decades.

Results from tests on Radial turbines (e.g. [1]) and high work Axial turbines (e.g. [2, 3]) eventually caused speculation regarding the feasibility of combining the demonstrated benefits of each, in a hybrid turbine type which has come to be referred to as the Mixed-Flow Turbine (MFT). As shown in figure 1, the MFT differs from Axial and Radial Turbines in that its inflow angle is 60 deg from the axial direction, when viewed in the meridional projection.

The rotor blade speed of the Axial gas generator turbine is principally governed by its disc rim speed, which has a maximum permissible value dictated by blade fixing and disc life requirements. The maximum span of an uncooled blade is also given by its (target) time between overhauls, temperature, and hub/tip metal area ratio. Hence, for a given power, the efficiency of the Axial turbine is limited by its mechanical constraints to blade speed and blade span.

Owing to its shape, the rotor of the Radial turbine can accommodate blade elements with hub/tip metal area ratios in excess of 10:1, substantially greater than what is achievable with efficient Axial turbine blades. In addition to this, the relative gas temperature reduces towards the hub, making the blade stronger in the region of highest stress. Taking advantage of these properties of the Radial rotor, its blade span can be much increased relative to its Axial counterpart. This has the effect of a higher blade speed at rotor inlet (hence reduced flow turning within the rotor) and a larger flow area (hence a lower gas velocity within the rotor flow passages). Pressure losses being related to gas velocity, the net effect is higher efficiency. An additional bonus is the substantially lower (absolute) velocity at the exit of the Radial rotor.

The major weakness of the Radial turbine concept lies in the fact that, due to its shape, its rotor blades and disc must be integral with one another. A rotor made from a high temperature alloy suitable for blades, which are exposed to the hot gases, does not have optimum properties at the bore, where ability to resist low cycle fatigue is important. It is therefore desirable to minimize bore stresses, and reducing the centrifugal pull of the blades is one way to do this.

The blades of the Radial turbine must be aligned radially, for minimum centrifugal stress. Blade orientation at rotor leading edge, therefore, calls for a radial inflow direction (when viewed along the axis of rotation) relative to the rotor, for minimum entry loss. On the other hand the MFT, owing to its non-radial orientation (in the meridional projection), can have its leading edge aligned to accept an inflow having a swirl component in the relative frame of reference, while retaining the radial orientation in its blade elements. This fortuitous quirk of geometry permits the reduction of blade height at rotor leading edge by trading off Coriolis work against flow turning, thereby reducing the centrifugal pull of the blades and, in consequence, stresses at the bore of the rotor.

The MFT geometry also holds the promise of additional benefits over the Radial geometry, such as compactness and an improved resistance to erosion. The major unknown, however, was aerodynamic efficiency: whether the excellent performance of the Radial turbine could be matched by the MFT. This, and related questions were addressed by the research program described in the following paragraphs.

### THE DESIGN POINT

An experimental turbine which is configured for a realistic engine application will produce the most useful design data. The application chosen for this study was a small, two shaft turboprop engine with a single stage power turbine, a single stage centrifugal compressor and front end drive. This engine was sized to generate 600 horsepower when flying at 563 km/h (350 mph) at 7620 m (25,000 ft) altitude. At this operating condition, engine pressure ratio was 11:1, gas generator turbine speed 39,528 r/min,  $\Delta H = 303.8$  kJ/kg (130.6 BTU/lb), inlet temperature 1286 K (1854°F) and pressure ratio approximately 2.9, its exact value depending on efficiency attained. This became the "design point" for the research turbine.

Figure 1 compares the turbine concepts, all three optimized for this application. The exducers of Radial and MF rotors have identical radii, and an (absolute) exit Mach number of 0.30. Both have an average gas velocity of 314 m/s (1030 ft/sec)

within the rotor, but  $AN^2$  of the longest hot blade element (a measure of hub/tip metal area ratio required for adequate blade life) is only  $5.1 \times 10^{10}$  (in  $\times \text{rpm}$ )<sup>2</sup> for the MFT, compared to  $9.2 \times 10^{10}$  for the Radial turbine. By contrast, the Axial turbine has an exit Mach number of 0.41, average gas velocity of 405 m/s (1328 ft/sec) and  $AN^2 = 3.7 \times 10^{10}$ .

Figure 2 shows a simplified layout of the engine hot end, with Axial and MF gas generator turbines. It appears that engine diameter and length are not affected by the choice of turbine type. A Radial gas generator turbine, on the other hand, would have called for a larger diameter, but would have permitted some reduction in engine length. The efficiency of the Axial turbine was predicted to be a disappointing 84% (owing to compromises introduced in order to optimize the overall expansion efficiency). Sufficient experimental data exist to inspire confidence in this estimate [4]. A somewhat less reliable extrapolation of (earlier) test results with Radial turbines indicated that 89.5% efficiency is achievable with that turbine type. Pressure losses in the inter-turbine duct were also lower in the case of the Radial turbine, due to its larger exit area. The combination of enhanced turbine efficiency and reduced duct loss was predicted to improve the Specific Fuel Consumption of the engine by approximately 6%, relative to its Axial turbine version. A similar improvement in specific power was indicated. Would the MFT do as well?

### THE NOZZLE AND THE ROTORS

Figure 3 shows the midspan velocity triangles of the MFT at its design point. The velocity triangles shown here correspond to the actual test hardware, which differed somewhat from the original design intent due to manufacturing deviations. The swallowing capacity of the turbine, for example, proved to be higher than intended due to excessive nozzle throat openings, causing the exit Mach number to be 0.33.

It is evident that the MFT geometry produces the required power with relatively low Mach numbers and a modest amount of flow turning, compared to the equivalent Axial turbine.

Figure 4 shows a segment of the nozzle. Its vanes, which lie on a 60 degree conical surface, are bowed in the spanwise direction at their leading edges. This feature was introduced in order to reduce the aerodynamic loading of the vanes next to their endwalls, thereby reducing secondary flows and associated pressure losses. The most highly loaded vane section is therefore at midspan, shown in Figure 5. In addition to the measured pressure distribution, Figure 5 also shows this distribution as predicted for the tested geometry by the inviscid flow analysis program used in the design of the nozzle. Agreement with measurements is within the experimental error, and the nozzle is seen to be conservatively designed, with little local diffusion.

Four rotors were tested with this nozzle. Three had the same blade shape, with radial blade elements, differing only in the number of blades and/or meridional chord. The fourth had non-radial blade elements in its inlet portion, blade tips leaning into the flow, with the same camberline at the hub as the other three. All rotors had their blade leading edges oriented 25 degrees off the meridional plane, at midspan. Figure 6 is a photograph of rotor ALPHA. Rotor geometries are summarized in the following table.

Rotor	No. of blades	Characteristics
ALPHA	20	baseline design
BETA	14	same meridional projection as ALPHA
GAMMA	20	same as ALPHA, except with non-radial blade elements in inlet portion
DELTA	20	same as ALPHA, except with trailing edges cut back by 4.6 mm (0.18 in.)

Static pressures on rotor blade surfaces were not measured, but were calculated for several operating conditions by a three-dimensional Euler code. The results of this inviscid channel flow analysis are shown in Figure 7 for rotor BETA operating at its peak efficiency conditions of 106% design speed and a (total/total) pressure ratio of 2.5. The curves show the calculated static pressure on the suction and pressure surfaces of the rotor blades, normalized to the inlet (relative) total pressure, at hub, mean and tip respectively. A third curve, showing the drop in relative total pressure due to Coriolis work, is also plotted for reference.

Pressure on the suction surface is seen to be generally reducing in the streamwise direction. The exceptions are the front portion of the blade at the hub, and the trailing edge uncovered surface where recompression is predicted to take place along the whole span of the blade. The pressure surface sees a reduction in pressure everywhere. It is also evident from the small difference between relative total pressure and static pressure, on the pressure surface, that the velocity there is generally low.

The most meaningful representation of pressure distribution is that along streamlines. Figure 8 shows a series of curves of constant Rothalpy, for the suction and pressure surfaces of the same case. Rothalpy is a quantity which is conserved along a streamline in a rotating frame of reference, hence the curves represent streamlines as predicted by the present inviscid analysis. It appears from Figure 8 that on the suction surface the streamlines follow the hub and tip contours of the rotor quite well, hence the suction surface pressure distributions on Figure 7 closely represent those experienced by the flow. The pressure surface streamlines, on the other hand, do not follow the hub and shroud contours of the rotor. Streamlines which begin near the hub migrate up the blade to the shroud. Therefore the pressure surface distributions along the hub, mean and tip shown in Figure 7 do not represent those along streamlines. However, these Figure 7 curves may be cross-plotted for any of the pressure surface streamlines shown in Figure 8. The result of this indicates that practically no recompression occurs along any of these streamlines.

## THE EXPERIMENTAL FACILITY

Aerodynamic testing of the four turbines was carried out on the rotating test rig shown in Figure 9. A 1000 hp compressor supplied air at approximately 138 kPa (20 psia) through a heater and a Venturi flow meter to the inlet of the turbine. A second, 500 hp compressor evacuated the exit of the turbine. A combination of valves allowed the pressure ratio across the turbine to be fixed at any desired value. The power generated by the turbine was absorbed by a water brake dynamometer. The air supply to the turbine was heated to a temperature such that its exit temperature became equal to that of the test cell.

Turbine power, hence efficiency, was calculated from the measured temperature drop across the turbine. A generous mixing length (several pipe diameters) was provided downstream of the rotor, to produce an accurate average of exit temperature. Conduction errors were eliminated by thermal insulation of the exhaust duct and by the matching of exhaust temperature with test cell temperature. Rotor exit total pressure was measured by fixed rakes placed 38 mm (1.5 in) (slightly more than the blade height at rotor exit) downstream of rotor trailing edge, aligned with the flow at each test point. Temperature and pressure at nozzle inlet were similarly measured by fixed rakes; these were found to be quite uniform. Temperature based efficiency was preferred to that derived from the dynamometer, since the latter has to be corrected for disc windage and bearing friction losses, a potential source of errors. Rotational speed at the design point of the turbine was 22,800 r/min.

The basic measurements of temperature and pressure at the inlet and exit planes of the turbine were complemented by measurements of static pressure in the nozzle vanes, along rotor shroud and in the exhaust duct. Radial-circumferential traverses of temperature, pressure and flow angle were also taken at a plane immediately downstream of the rotor trailing edge. Rotor tip clearance was measured by means of a contact probe, under running conditions. The following paragraphs present the highlights of the aerodynamic test programme.

## RESULTS FROM AERODYNAMIC TESTS

Figures 10-13 show the measured variation of efficiency with pressure ratio at constant normalized speed, for rotors ALPHA, BETA, GAMMA and DELTA respectively. Efficiency and pressure ratio are based on total pressures. Mechanical constraints related to rig operation prevented testing at 100 percent speed. The results shown are for a tip clearance of one percent of exducer span, or 0.34 mm (0.0135 in).

Some general conclusions may be drawn from all four part load maps. Peak efficiencies in excess of 90% were obtained with all turbines. Interpolating for design speed, peak efficiency is seen to occur at a pressure ratio lower than design, which was 3.2 under rig conditions. The four turbines differ from one another mainly in their rate of decrease in efficiency, as the pressure ratio is increased, at any given speed.

Nozzle exit traverses permitted the calculation of relative flow angle at rotor inlet, hence rotor incidence. Figure 14 leads to the conclusion that the optimum incidence is approximately  $-20$  degrees, and that the leading edges of all rotor blades should have been oriented at  $40$  or  $45$  degrees instead of the present  $25$  degrees. Whether this would move the efficiency peaks over to the design pressure ratio, as expected, remains to be confirmed by further tests.

This result was not totally unexpected since earlier tests have indicated that Radial turbines benefit from a large negative incidence: even under operating conditions when the average flow at rotor inlet is aligned with the blades, circulation about each blade causes a local induced incidence which the sharp leading edges cannot tolerate.

Another conclusion which can be drawn from these test results is that the performance of rotors with 20 blades differs relatively little from rotor BETA which has 14 blades. In fact, BETA appears to reach the highest peak efficiency of the four, by a small margin, although GAMMA has the highest efficiency at design point pressure ratio and speed. Here one is faced with the frequently recurring problem with flow in ducts involving local diffusion, where wetted area must be judiciously traded off against the risk of flow separation, for minimum pressure loss. It would appear that the pressure distribution shown in Figure 7 for BETA operating at peak efficiency (with  $-20$  degrees incidence) represents a good design in regard to blade loading and rate of local diffusion. It is possible that this design could be further improved by a further reduction in the number of blades, if three-dimensional flow analysis indicates that local diffusions can be held to their present values by an appropriate shaping of blades.

Rotor exit traverses of pressure, temperature and flow angle for rotor BETA (Figure 15) indicated that rotor exit flow is significantly underturned and possibly separated over the outer 50 percent of the exducer portion of the blade. This phenomenon has also been previously observed on radial turbines. The fact that local streamline efficiency is nearly 100 percent in the inner half of the rotor suggests that the low energy boundary layers, generated within the rotor, are flung radially outward and emerge from the rotor near its shroud, causing the poor performance observed in that region. There were also indications that the leakage flow through the rotor tip clearance gap contributes to the underturning of the flow in the same manner as it does in the case of unshrouded axial turbine rotor blades. The situation was compounded in the present case by the relatively large uncovered turning at exducer tips, ranging from  $16$  to  $22$  degrees for the four rotors tested.

Rotor ALPHA was also tested with two tip clearances. Its efficiency was found to change by  $0.9$  points for a tip clearance change of one percent of blade span, measured at rotor exit. This, too, is in line with previous results with radial turbines, and amounts to approximately half the sensitivity of a typical, unshrouded axial turbine blade. Since the axial turbine for the same duty must have shorter blades, for equivalent life, it may be concluded that the MFT (and also the radial turbine) is substantially less sensitive to rotor tip clearance than the axial turbine.

## STRUCTURAL CONSIDERATION

At present, Axial Turbine rotors are with few exceptions assembled from cast, high temperature alloy blades and forged discs, the two mechanically joined by "fir-tree fixings", carefully designed interlocking lobes which permit the centrifugal load of the blades to be uniformly transferred to the disc. The blades, operating at high metal temperatures, will thus enjoy



the good creep resistance properties of high temperature (cast) alloys, while the disc is able to resist low cycle fatigue by virtue of the strong forging alloys developed for the purpose.

However, the MFT rotor cannot utilize fir-tree fixings nor other types of mechanical attachments. In applications where the rotor is expected to undergo many stress cycles before it is replaced, present casting alloys appear only marginally adequate. The problem with integrally cast rotors is aggravated by the fact that the rate of solidification varies from one part of the rotor to another: the massive hub cools slowly, and its material properties could prove much inferior to expectations. Techniques for routinely producing fatigue resistant castings are being developed, but these still seem some years in the future. A complicating factor here is the difficulty of inspecting massive castings for flaws.

One possible way around the creep/fatigue problem is the bi-metallic rotor (Figure 16). If a cast ring of blades were to be bonded to a forged hub, without degrading the properties of the parent materials, a very strong rotor could be obtained. Recent experiments with diffusion bonding of cast MAR M-247 to forged IN100 have indicated that a strong bond can be obtained without a significant deterioration of the original properties of either material. The process consists of holding the mating surfaces in contact under high pressure and temperature for a period of time, during which the constituents of the alloys migrate across the interface, creating the bond. The details of the process, surface treatments, bonding pressure, temperature and time, and subsequent heat treatments are at present a proprietary art jealously guarded by those who possess the knowledge.

However, the bonding for a complete MFT rotor is considerably more complex than that of simple specimens, owing to its complicated shape. This, and the problem of inspecting the bond surface, are at present the major obstacles to the immediate application of the MFT to conventional gas turbine engines for aircraft propulsion.

While the rotor blades of the MFT are substantially lighter than those of the Radial turbine, the hub still has to be massive due to the required axial extent of the rotor. Much of the material in the hub is not needed to carry the blades; it merely increases stresses at the bore. Figure 17 presents some ideas of how the hub might be constructed, to minimize bore stresses. None of these schemes is free of problems, but the Extended Blade rotor seems the most attractive configuration at this time.

A detailed, three-dimensional stress analysis of the rotor is clearly called for, due to its complex shape. Such areas as the platform leading edge may prove quite critical: the "scalloping" of the disc, a standard feature with radial turbines intended to relieve the local stresses in the platform at its largest radius, cause an overhang of the blades in the case of the MFT. A trade-off study will determine the amount of overhang which produces the lowest stresses in this area. Transient stress analysis is also required: changes to engine operating conditions may set up large temperature gradients within the rotor, causing sizeable transient stresses calling for innovative design solutions for their relief. The problems do not appear insurmountable, only very complex.

Another potential problem related to the durability of radial inflow turbines is that of erosion. The vulnerability of Radial turbine nozzles to particle erosion has been well documented over the years. For example carbon particles, originating in the combustion chamber, may be carried into the turbine where they enter the rotor at a lower velocity than the surrounding stream of gas. The advancing (suction) surfaces of the rotor blades catch up with the particles and fling them outward, against the uncovered surfaces of the nozzle vanes. The residual fragments of the particles continue to bounce back and forth between the rotor and the nozzle until their mass/drag ratio becomes small enough for them to be swept through the rotor by the gas stream. This mechanism is inherent to the Radial turbine geometry. With non-radial entry (such as in the MFT) the erosion of nozzle vanes, which is the more severe problem, will be considerably alleviated.

This erosion process is gradual, however; it will not cause a dramatic failure. The problem can be eliminated by an inlet particle separator and a well-developed, carbon-free combustor.

## CONCLUSION

Rotating rig testing has shown that the Mixed Flow Turbine is capable of surpassing the aerodynamic efficiency of the Axial turbine by a significant margin, and matching (and possibly exceeding) that of the Radial turbine, especially in small sizes. Why, then, has it not found a wide acceptance in gas turbine engines for aircraft propulsion?

The answer appears to lie in the high cost of development of a mechanically reliable rotor: even the remotest possibility of rotor disc failure is unacceptable in aero engines. The complex shape of the MFT rotor has until recently prevented reliable stress analyses to be carried out on this component. The technologies to manufacture and inspect a bulky rotor are still under development [5]. The "square-cube law" makes the MFT less attractive for large gas turbine engines, and the incentive for the required massive R&D expenditures has been lacking in that segment of the industry which could best afford it.

Given time, it is expected that the MFT will first find a home in single-shaft engine applications where a large number of operating cycles between overhauls is not required. The technology for this already appears to be at hand.

### THREE GAS GENERATOR TURBINE TYPES

For the same small turboprop application

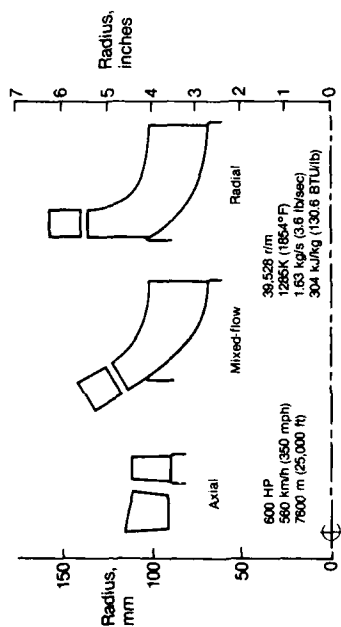


Figure 1

### MFT ROTOR

### MIDSPAN MACH NUMBER TRIANGLES

At design point

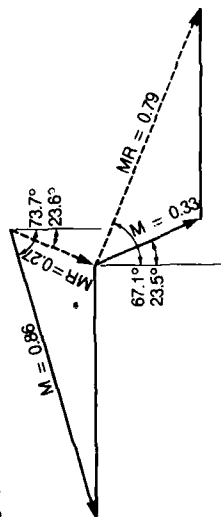


Figure 3

### AXIAL AND MIXED FLOW GGT FOR 600 HP TURBOPROP

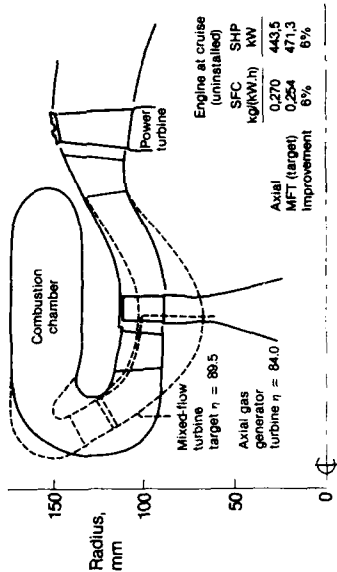


Figure 2

### SEGMENT OF MFT NOZZLE



Figure 4

## STATIC PRESSURE DISTRIBUTION

At nozzle midspan

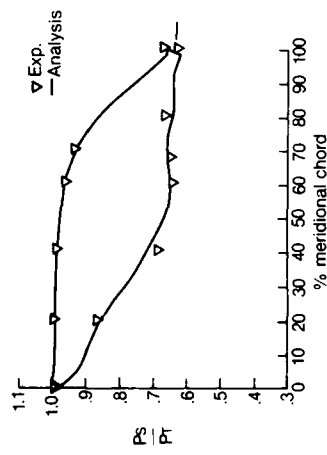


Figure 5

## ROTOR BETA AT PEAK EFFICIENCY

Calculated pressures on blade surfaces normalized to inlet relative total pressure

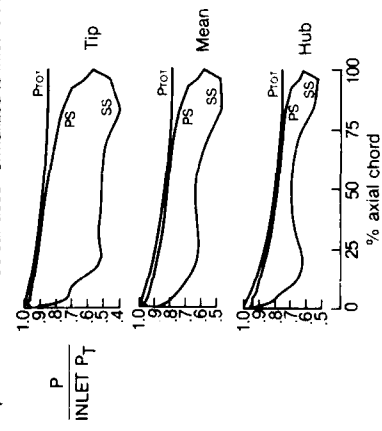


Figure 7

## EXPERIMENTAL ROTOR ALPHA

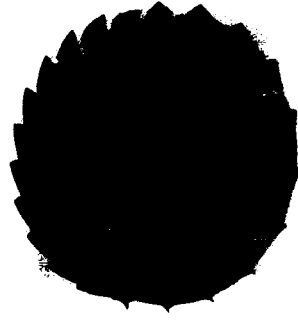


Figure 6

## ROTOR BETA AT PEAK EFFICIENCY LINES OF CONSTANT ROTHALPY

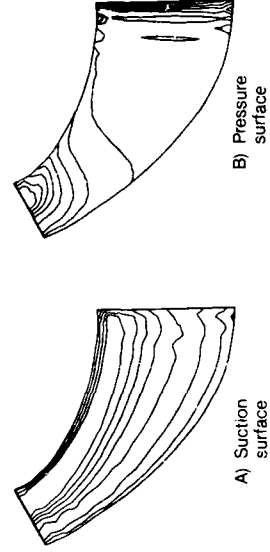


Figure 8

## MIXED-FLOW TURBINE TEST RIG

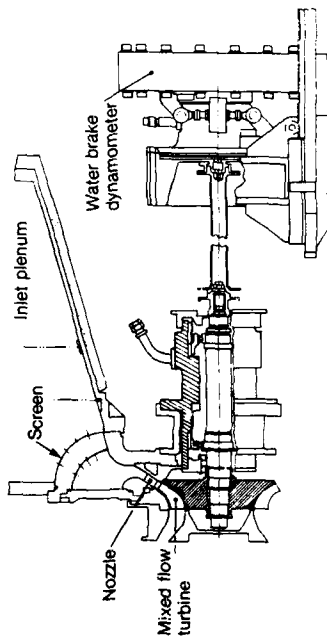


Figure 9

## TEST RESULTS

ROTOR BETA (1% tip clearance)

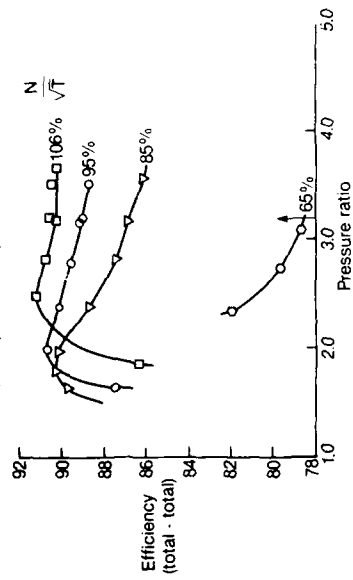


Figure 11

## TEST RESULTS

ROTOR ALPHA (1% tip clearance)

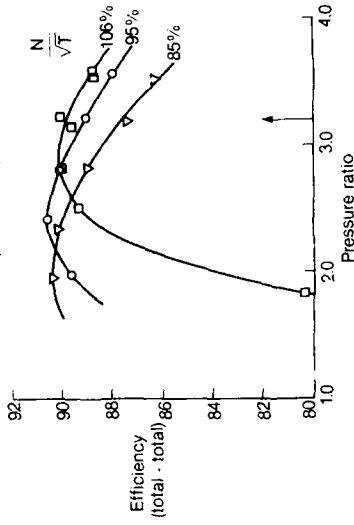


Figure 10

## TEST RESULTS

ROTOR GAMMA (1% tip clearance)

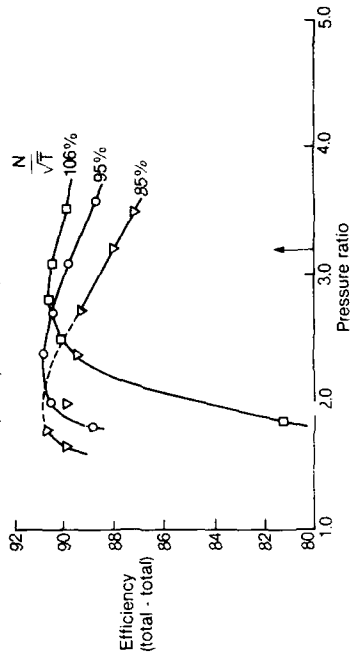


Figure 12

# TEST RESULTS SUGGEST THAT PEAK EFFICIENCY OCCURS AT NEGATIVE INCIDENCE

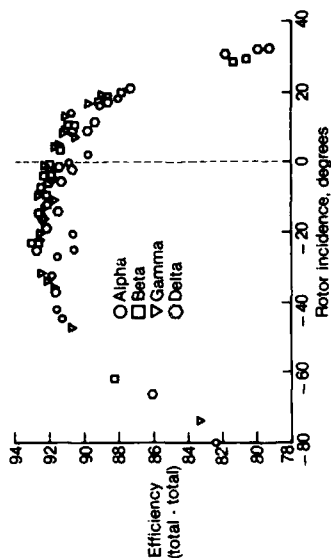


Figure 14

## DUAL ALLOY ROTOR

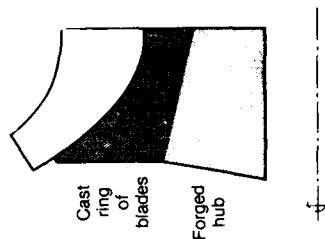


Figure 16

# TEST RESULTS

## ROTOR DELTA (1% tip clearance)

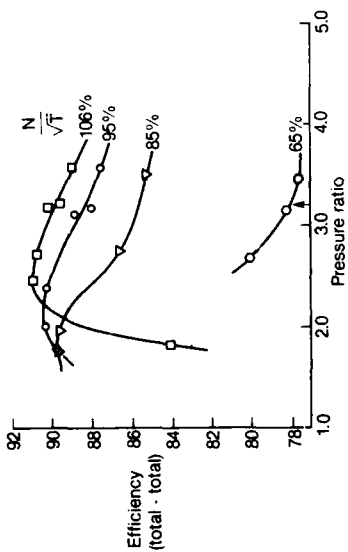


Figure 13

## ROTOR EXIT TRAVERSE RESULTS

### ROTOR BETA

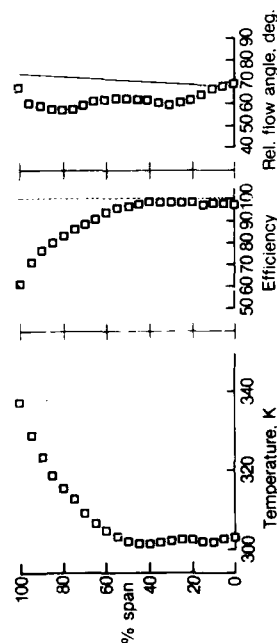


Figure 15

## POSSIBLE SHAPES FOR STRUCTURALLY EFFICIENT DUAL ALLOY ROTORS

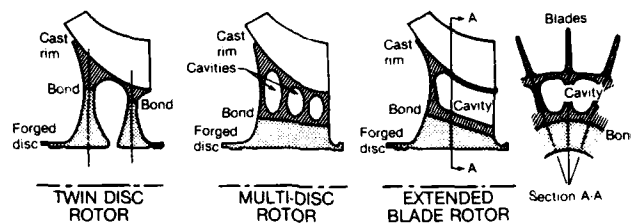


Figure 17

### REFERENCES

1. OKAPUU, Ü and CALVERT, G.S.:  
An Experimental Cooled Radial Turbine, AGARD C.P. No. 73 (pp 10-1 to 10-10), 1971.
2. OKAPUU, Ü:  
Some Results from Tests on a High Work Axial Gas Generator Turbine, ASME paper 74-GT-81, 1974.
3. PATEL, K.V.:  
Research on A High Work Axial Gas Generator Turbine, SAE paper 800618, 1980.
4. KACKER, S.C. and OKAPUU, Ü.:  
A Mean Line Prediction Method for Axial Flow Turbine Efficiency, ASME Journal of Engineering for Power, Vol. 104 pp 111-119, Jan. 1982.
5. LANE, J.M.:  
Cooled Radial In-Flow Turbines for Advanced Gas Turbine Engines, ASME paper 81-GT-213, 1981.

### ACKNOWLEDGMENTS

An experimental research project of this type is always a team effort. Special acknowledgments for major contributions are due to Manfred Mueller, who carried out the experimental program and data interpretation, and to Tony Yee, who performed the aerodynamic analysis of nozzle and rotor flow passages. Significant contributions were also made by Andrew Byrne, Robert Seto, and the late Pieter deNeeve. The project was partially funded by the Transportation Development Centre of Transport Canada under the program management of W.H.D. Hanchet (now retired), whose support and encouragement in no small measure contributed to the success of the program.

# DISCUSSION

P. BELAYGUE, Fr

Où situez-vous, en taux de détente, le domaine d'intérêt des turbines mixtes ?

## Author's Reply

The range of optimum applicability of the MFT is not well understood at present.

As to pressure ratio, efficient operation can be expected up to the limit loading of the exducer, which is likely to occur at pressure ratio in excess of 7 or 8 : 1, the exact value depending on design details. Structural limitations are likely to be encountered well before this maximum is reached, however, but these will again depend on design details and the material(s) used for the rotor. The pressure ratio of 2.9 : 1 of the present research turbine therefore appears to lie at the low end of MFT applicability. However, it is noteworthy that even at such a modest pressure ratio, well within the capability of the Axial turbine, the MFT performed some five efficiency points better. A portion of this difference is due to effects of small size (tip clearance, trailing edge thicknesses) which affect the performance of the Axial turbine much more than the MFT. It would therefore follow that in very small sizes the MFT will outperform the Axial turbine at any pressure ratio.

As to the place of the MFT in the specific speed spectrum, it would be reasonable to expect it to fill the gap between the low specific speed regime dominated by the Radial turbine and the high specific speed regime where the Axial turbine reigns supreme.

R.G. THOMPSON, US

What is the source or mechanism of the variation of stage efficiency as a function of downstream total pressure probe location ?

## Author's Reply

Various test programs on our turbine rig have shown that the observed efficiency of a turbine depends quite strongly on the location of the downstream measurement plane for total pressure. Tables 2 and 3 of Paper N° 9 illustrate this : the efficiency of turbine configuration S/51 can be taken as 80.0 or 83.0 percent, depending on the choice of measurement plane. Unfortunately, this fact does not seem to be widely recognized within the gas turbine industry, with the result that misleading conclusions may be drawn from comparisons of test results from different test facilities.

The main mechanism of the reduction of average total pressure (hence efficiency) with downstream distance is thought to be the mixing of the rotor exit flow field. Endwall vortices, having their axes essentially in the streamwise direction, require an especially long distance to dissipate. Therefore, pressure measurements taken close to rotor trailing edge will include a component of total pressure which will not be available after mixing. This situation is expected to be most pronounced in small turbines having low blade aspect ratios, where secondary losses predominate.

The practice of Pratt & Whitney Canada has been to measure total pressure at more than two blade chords downstream of the rotor trailing edge, in the case of Axial turbines. Efficiency computed from such measurements have been found to agree best with efficiencies deduced from performance measurements on engines. Lacking a corresponding calibration for Mixed-Flow turbines, we chose a similar distance for the current series of tests.

H. VIGNAU, Fr

Quel est l'intérêt du concept de turbine "mixte" pour augmenter le coefficient de travail et réduire les vitesses périphériques, comparativement aux turbines radiales ?

Author's Reply

Compared to the equivalent Radial turbine, the blade diameter at rotor inlet is substantially lower for the MFT. It is indeed interesting to note, therefore, that the MFT achieves efficiencies equal to or better than the Radial turbine of the same duty, in spite of the higher work coefficient ( $\Delta H/U_{TIP}^2$ ) of the MFT.

The larger amount of flow turning within the MFT rotor, implied by its higher  $\Delta H/U_{TIP}^2$ , can be expected to cause greater pressure losses. However, the span of the rotor blade, at its leading edge, is higher in the case of the MFT, producing a more favourable passage aspect ratio and (relative) tip clearance. It would appear, therefore, that these features of the MFT compensate for any additional losses caused by its greater turning angle.

J. MOORE, US

In looking at the static pressure distribution in the mixed flow rotor, it may be helpful to remove the centrifugal pressure field or alternatively to look at the distribution of an isentropic relative Mach number. This is found to be useful when considering boundary layer development in centrifugal compressor impellers, for example.

Author's Reply

We thank Professor Moore for his suggestions. We will explore them at the next opportunity.



# SIMULATION NUMERIQUE DE L'INTERACTION DIFFUSEUR TETE DE CHAMBRE

par  
D. JEANDEL\*, G. BRUN\*, S. MEUNIER\*\*, M. DESAULTY\*\*  
\*Ecole Centrale de Lyon  
36, avenue Guy de Collongue  
BP 163 - 69131 Ecully Cedex  
France  
\*\*SNECMA Villaroche  
77550 Moissy Cramayel  
France

## RESUME

La conception du diffuseur et de la tête d'une chambre de combustion de turboréacteur doit être réalisée, non seulement en recherchant une perte de charge faible mais aussi en s'assurant de la stabilité de l'écoulement autour du tube à flamme.

Parmi les méthodes dont dispose la SNECMA pour atteindre ces objectifs, figure un logiciel de calcul elliptique, de type "éléments finis" développé par l'Ecole Centrale de Lyon.

Cette méthode de calcul, grâce à son maillage triangulaire, se caractérise par ses capacités à prendre en compte des configurations géométriques complexes.

Sa validation sur diverses configurations élémentaires et industrielles a permis de démontrer la robustesse de l'algorithme de calcul et son aptitude à décrire les caractéristiques principales de l'écoulement.

## NOMENCLATURE

A	Matrice de quantité de mouvement
$B_\phi$	Matrice pour une grandeur scalaire
$C_p$	Chaleur massique à pression constante
C1, C2	Constantes de la loi logarithmique
$C_\mu, C_\epsilon, C_{\epsilon_2}$	Constantes du modèle k- $\epsilon$
$C_\phi, D_\phi, Pr_\phi$	Constantes dans l'équation de bilan d'une grandeur scalaire
$\vec{F}$	Second membre de l'équation discrétisée de quantité de mouvement
$G_\phi$	Second membre de l'équation discrétisée de $\phi$
k	Energie cinétique de la turbulence sans dimension
$K=(K_{ij})$	Tenseur de diffusivité artificielle
L	Echelle caractéristique de longueur
$\vec{n}$	Vecteur unitaire normal à la frontière
Ni	Fonction de base du maillage fin
N2i	Fonction de base du maillage grossier
nn2	Nombre de nœuds du maillage grossier
$\bar{p}^*$	Pression moyenne généralisée
$\bar{p}_{2h}^*$	Pression généralisée discrétisée
Pr	Nombre de Prandtl
$\bar{Q}$	Quantité de mouvement moyenne sans dimension
$\bar{Q}_h$	Quantité de mouvement moyenne discrétisée
Re	Nombre de Reynolds
rh	Opérateur divergence discrétisé
rj	Composante de rh
Rt	Nombre de Reynolds turbulent

18-2

$S$	Second membre de l'équation de continuité
$T$	Température instantanée sans dimension
$\vec{T}$	Vecteur unitaire tangent à la frontière
$Th$	Maillage fin du domaine
$T2h$	Maillage grossier du domaine
$\bar{u}$	Vitesse moyenne sans dimension
$\overline{u''*u''}$	Tenseur de Reynolds
$\overline{u''*\theta''}$	Flux turbulent
$U_0$	Vitesse de référence
$U_f$	Vitesse de frottement
$\Gamma$	Frontière du domaine
$\delta$	Distance à la paroi où sont imposées les conditions limites
$\Delta t$	Pas de temps
$\epsilon$	Taux de dissipation de l'énergie cinétique de la turbulence
$\phi$	Variable scalaire instantanée
$\phi''$	Fluctuation d'une grandeur scalaire
$\lambda$	Conductivité thermique
$\mu$	Viscosité dynamique
$\nu$	Viscosité cinématique
$\Omega$	Domaine de calcul
$\rho$	Masse volumique instantanée sans dimension
$\bar{\rho}$	Masse volumique moyenne sans dimension
$\sigma_{T,k}, \sigma_{\epsilon}$	Nombres de Prandtl Schmidt pour $T, k, \epsilon$

## INTRODUCTION

Un contrôle rigoureux du champ aérodynamique au niveau du diffuseur et de la tête de chambre de combustion de turboréacteur est essentiel pour atteindre l'ensemble des performances requises pour ce type de foyer.

Parmi les méthodes numériques de simulation disponibles, l'utilisation des éléments finis, qui permet de décrire de façon réaliste les contours d'une géométrie industrielle est particulièrement attractive.

Une telle méthode, dont le développement a été assuré par l'Ecole Centrale de Lyon est couramment utilisée à la SNECMA aux divers stades de conception :

- Lors de l'avant projet, la viscosité est supposée constante. Cette approche pessimiste permet de ménager les marges nécessaires à la reproductibilité des performances lors de la fabrication des chambres en série.
- Une analyse fine de zones critiques de l'écoulement est réalisée au moyen d'une procédure de sous domaines.
- Le calcul quantitatif des pertes de charge est ensuite obtenu par le biais du même code mais en modélisant la turbulence par une approche du type  $(k, \epsilon)$ .

Dans une première étape, nous décrivons les principes physiques et numériques de la méthode de calcul dans le cas le plus général, c'est-à-dire intégrant le modèle de turbulence  $(k, \epsilon)$ .

Ensuite quelques exemples extraits des cas de validation sur configurations de laboratoire démontreront le caractère prédictif du logiciel.

Enfin, l'utilisation industrielle sera illustrée par plusieurs applications à des foyers expérimentaux de la SNECMA.

## 1. EQUATIONS D'EVOLUTION ET CONDITIONS AUX LIMITES

Les équations instantanées d'évolution sont obtenues à partir des principes fondamentaux de conservation de la masse, de la quantité de mouvement et de l'enthalpie. Ces équations sont écrites sous forme sans dimension par

l'introduction d'une longueur de référence, d'une vitesse et d'une température caractéristiques de l'écoulement. Ces grandeurs nous conduisent à construire les nombres sans dimension classiques :

$$Re = \frac{U_0 \cdot L_0}{\nu} \quad \text{et} \quad Pr = \frac{\mu C_p}{k}$$

Les caractéristiques physiques du fluide telles que la viscosité dynamique ou la conductibilité thermique sont supposées constantes. La masse volumique, quant à elle, est reliée à la température par une équation d'état déduite de l'équation des gaz parfaits en supposant que l'effet des variations de pression sur la masse volumique est négligeable. Ecrite sous forme sans dimension l'équation d'état prend alors la forme simplifiée :

$$P = \frac{1}{T}$$

Le traitement des phénomènes turbulents conduit à décomposer les variables en une partie moyenne et une partie fluctuante. Pour ce qui est de la pression et de la masse volumique, on utilise la décomposition classique de Reynolds. Pour la vitesse et la température, on utilise par contre la décomposition de Favre (1) définie comme suit :

$$\vec{x}(x, t) = \tilde{\vec{x}}(x, t) + \bar{\vec{x}}(x, t) \quad \text{où} \quad \tilde{\vec{x}}(x, t) = \frac{\rho \vec{x}}{\bar{\rho}}$$

Les termes de corrélation qui apparaissent du fait de la décomposition sont modélisés en utilisant une hypothèse du type Boussinesq. On écrit alors pour les tensions de Reynolds :

$$\overline{\rho \vec{u} \vec{u}} = \frac{2}{3} (\bar{\rho} k + \frac{1}{Re} \text{div} \tilde{\vec{u}}) \vec{I} - \frac{1}{Re} (\text{grad} \tilde{\vec{u}} + \text{grad}^T \tilde{\vec{u}})$$

et pour le flux turbulent de température :

$$\overline{\rho \vec{u} \theta} = -\frac{1}{Re \sigma_T} \text{grad} \tilde{T}$$

où le nombre de Reynolds turbulent est donné par :

$$\frac{1}{Re} = C_\mu \bar{\rho} k^2 / \epsilon$$

$k$  est l'énergie cinétique de turbulence définie par :  $k = \frac{1}{2} \langle u_i u_i \rangle$  et  $\epsilon$  est son taux de dissipation.

Les équations gouvernant l'évolution des grandeurs scalaires turbulentes  $k$  et  $\epsilon$  font l'objet d'une modélisation analogue à celle adoptée classiquement dans le cas incompressible (2).

Le système fermé d'équations porte sur les variables dépendantes suivantes :

- . quantité de mouvement moyenne  $\vec{Q} = \bar{\rho} \tilde{\vec{u}}$
- . pression généralisée  $\bar{p}^*$
- . température moyenne  $\tilde{T}$
- . masse volumique moyenne  $\bar{\rho}$
- . deux échelles caractéristiques de la turbulence  $k$  et  $\epsilon$

Ce système s'écrit alors (cf (3)) :

$$\bar{p} = \frac{1}{T}$$

$$\frac{\partial \bar{p}}{\partial t} + \text{div} \vec{Q} = 0$$

$$\frac{\partial \vec{Q}}{\partial t} + \text{div} \left( \frac{\vec{Q}}{\bar{\rho}} \otimes \vec{Q} \right) = -\text{grad}(\bar{p}^*) + \text{div} \left( \left( \frac{1}{Re} + \frac{1}{Re} \right) (\text{grad} \frac{\vec{Q}}{\bar{\rho}} + \text{grad}^T \frac{\vec{Q}}{\bar{\rho}}) \right)$$

$$\text{avec} \quad \bar{p}^* = \bar{p} + \frac{2}{3} \left( \frac{1}{Re} + \frac{1}{Re} \right) \text{div} \frac{\vec{Q}}{\bar{\rho}} + \bar{\rho} k$$

$$\frac{\partial \tilde{T}}{\partial t} + \frac{\partial}{\partial t} \left( \frac{\vec{Q}}{\bar{\rho}} \cdot \text{grad}(\tilde{T}) \right) = \frac{1}{\bar{\rho}} \text{div} \left( \left( \frac{1}{Re Pr} + \frac{1}{Re \sigma_T} \right) \text{grad} \tilde{T} \right)$$

$$\frac{\partial k}{\partial t} + \frac{\partial}{\partial t} \left( \frac{\vec{Q}}{\bar{\rho}} \cdot \text{grad}(k) \right) = \frac{1}{\bar{\rho}} \text{div} \left( \left( \frac{1}{Re} + \frac{1}{Re \sigma_k} \right) \text{grad} k \right) + P - \epsilon$$

$$\frac{\partial \epsilon}{\partial t} + \frac{\partial}{\partial t} \left( \frac{\vec{Q}}{\bar{\rho}} \cdot \text{grad}(\epsilon) \right) = \frac{1}{\bar{\rho}} \text{div} \left( \left( \frac{1}{Re} + \frac{1}{Re \sigma_\epsilon} \right) \text{grad} \epsilon \right) + C_{\epsilon 1} \frac{\epsilon}{k} P - C_{\epsilon 2} \frac{\epsilon^2}{k}$$

avec

$$P = \frac{1}{\bar{\rho}} \left( \frac{1}{Re} (\text{grad} \frac{\vec{Q}}{\bar{\rho}} + \text{grad}^T \frac{\vec{Q}}{\bar{\rho}}) - \frac{2}{3} \left( \frac{1}{Re} \text{div} \frac{\vec{Q}}{\bar{\rho}} + \bar{\rho} k \right) \text{grad} \frac{\vec{Q}}{\bar{\rho}} \right)$$

où les constantes sont données par :

$$C_u = 0.09 \quad C_\phi = 1.44 \quad C_k = 1.92 \quad \sigma_k = 1.0 \quad \sigma_\phi = 1.3 \quad \sigma_\tau = 0.9$$

Au voisinage des parois solides, la présence de forts gradients sur les variables dépendantes du problème nécessite en toute rigueur l'utilisation de maillages très fins.

On préfère ici adopter des lois d'équilibre qui permettent de reporter les conditions aux limites à une distance  $\delta$  de la frontière physique réelle.

Ces lois ont une forme similaire à celles habituellement employées dans le cas incompressible. On définit une vitesse de frottement notée  $u_\tau$  par la relation :

$$\left( \frac{1}{Re} + \frac{1}{Re_\tau} \right) \frac{\partial \vec{Q}}{\partial n} \cdot \vec{t} = u_\tau^2$$

Les conditions aux limites sont alors calculées par :

$$\begin{aligned} \frac{1}{\bar{\rho}} \frac{\vec{Q} \cdot \vec{t}}{U_\tau} &= C_1 \log \frac{\delta U_\tau}{\nu} + C_2 & \frac{\delta U_\tau}{\nu} > 11.6 \\ \frac{1}{\bar{\rho}} \frac{\vec{Q} \cdot \vec{t}}{U_\tau} &= \frac{\delta U_\tau}{\nu} & \frac{\delta U_\tau}{\nu} < 11.6 \\ \vec{Q} \cdot \vec{n} &= 0 \\ k &= \frac{1}{\sqrt{C_u}} U_\tau^2 & \epsilon &= \frac{1}{k} \frac{U_\tau^3}{\delta} \end{aligned}$$

## 2. METHODE NUMERIQUE DE RESOLUTION

### 2.1 Discrétisation en temps

Les équations du système (1) sont discrétisées en utilisant un schéma semi-implicite en temps défini par :

1. Calcul de  $\vec{Q}^{n+1}$  ( $= \vec{T}^{n+1}, \vec{K}^{n+1}, \vec{E}^{n+1}$ ) par :

$$\begin{aligned} \frac{\vec{Q}^{n+1} - \vec{Q}^n}{\Delta t} + \frac{\vec{Q}^n}{\bar{\rho}^n} \text{grad} \vec{Q}^{n+1} &= \frac{1}{\bar{\rho}^n} \text{div} \left( \left( \frac{1}{Re Pr_g} + \frac{1}{Rt \sigma_g} \right) \text{grad} \vec{Q}^{n+1} \right) \\ &+ C_g \vec{P}^n - D_g \frac{\epsilon^n}{k^n} \vec{Q}^{n+1} \end{aligned}$$

avec

$$\begin{aligned} C_g &= 0.1, \quad \alpha_g = \epsilon^n / k^n \\ D_g &= 0.1, \quad \alpha_g \\ Pr_g &= Pr, 1, 1 \quad (\text{pour, respectivement : } \vec{Q} = T, K \text{ et } E). \end{aligned}$$

2. Calcul de  $\bar{p}^{n+1}$  par l'équation d'état

$$\bar{p}^{n+1} = 1 / \bar{T}^{n+1}$$

3. Calcul de  $\vec{Q}^{n+1}$  et  $\bar{p}^{n+1}$  par les équations couplées :

$$\begin{aligned} \text{div} \vec{Q}^{n+1} &= - \frac{\bar{p}^{n+1} - \bar{p}^n}{\Delta t} \\ \frac{\vec{Q}^{n+1} - \vec{Q}^n}{\Delta t} + \text{div} \left( \frac{\vec{Q}^n}{\bar{\rho}^n} \cdot \vec{Q}^{n+1} \right) &= - \text{grad} \bar{p}^{n+1} + \\ &\text{div} \left( \left( \frac{1}{Re} + \frac{1}{Rt} \right) \left( \text{grad} \frac{\vec{Q}^{n+1}}{\bar{\rho}^{n+1}} + \text{grad} \left( \frac{\vec{Q}^{n+1}}{\bar{\rho}^{n+1}} \right) \right) \right) \end{aligned}$$

On note en particulier que le schéma entraîne une linéarisation des termes convectifs des équations de quantité de mouvement.

## 2.2 Discrétisation en éléments finis

L'écriture d'une formulation faible du problème est obtenue par multiplication par une fonction test, intégration sur le domaine de calcul et application d'une formule de Green sur les termes de plus haut degré de chacune des équations du système (2).

On utilise une double triangulation du domaine de calcul  $\Omega$ . A partir d'une triangulation  $T_{2h}$ , on construit une deuxième triangulation  $T_h$  obtenue en subdivisant chaque triangle de  $T_{2h}$  en 4 triangles égaux comme le montre la figure suivante :



Les variables  $\vec{Q}$ ,  $\vec{T}$ ,  $k$ ,  $\varepsilon$  et  $\bar{p}$  sont alors approchées linéairement sur chaque triangle de  $T_h$ , alors que la pression  $\bar{p}$  est approchée linéairement sur chaque triangle de  $T_{2h}$  (4).

La formulation de Galerkin du problème conduit finalement à un système matriciel de la forme :

$$\begin{aligned} B_{\vec{Q}} \vec{Q}_h &= G_{\vec{Q}} \\ A \vec{Q}_h &= -\text{grad } \bar{p}_h + \vec{F} \\ \text{div } \vec{Q}_h &= S \end{aligned}$$

où  $\vec{Q}_h$ ,  $\bar{p}_h$ ,  $\vec{T}_h$  sont les valeurs approchées aux nœuds des maillages  $T_h$  et  $T_{2h}$ .

Les équations sur les quantités scalaires  $\bar{p}_h$  sont résolues en utilisant une factorisation  $Lx \cdot Dx \cdot U$  de la matrice  $B_{\bar{p}}$ . La matrice  $L$  est triangulaire inférieure,  $D$  est diagonale et  $U$  est triangulaire supérieure.

La présence d'un terme de pression dans l'équation de quantité de mouvement oblige à effectuer un traitement spécial de cette équation. Couplée à la contrainte de continuité, elle est, en effet, résolue en utilisant un algorithme d'Uzawa dont la convergence est réglée par une méthode de gradients conjugués. La contrainte de continuité est alors satisfaite en minimisant sur le domaine  $\Omega_h$  la quantité intégrale :

$$\int (\vec{r}_h)^2 d\Omega \quad \text{avec} \quad \vec{r}_h = \sum_{j=1}^{nn2} \vec{r}_j N_{2j}$$

où  $\vec{r}_h$  est défini par

$$\int \vec{r}_h N_{2i} d\Omega = \int (\text{div } \vec{Q}_h - S) N_{2i} d\Omega \quad \forall i=1, nn2$$

$nn2$  est le nombre de nœuds du maillage  $T_{2h}$ .

Le processus itératif utilisé a été initialement proposé par Buffat et est détaillé dans (5).

Pour éviter l'apparition d'oscillations numériques dans les écoulements où les phénomènes convectifs sont dominants, un schéma de "balancing dissipation" (cf (6), (7)) est employé.

## 2.3 Calcul des conditions aux limites en paroi

Les lois de parois décrites en (1) forment un système d'équations où les deux composantes de la quantité de mouvement sont couplées. Ce système est alors utilisé de façon à fournir des conditions de type Dirichlet sur chacune de ces deux composantes.

Ainsi, connaissant le gradient de  $\vec{Q}^n$  à la paroi à un instant donné, on calcule au pas de temps suivant la vitesse de frottement  $u^{n+1}$  définie sur chaque arête frontière du maillage par :

$$(u_i^{n+1})^2 = \frac{1}{\text{Re}_i} \frac{\partial \vec{Q}^n}{\partial n} \cdot \vec{e}_i$$

La connaissance de  $u^{n+1}$  permet alors de résoudre, à la frontière pariétale, le système d'équations sur  $\vec{Q}$  écrit sous forme faible :

$$\int_{\Gamma} \vec{Q}^{n+1} \cdot \vec{e}_i N_i d\Gamma = \int_{\Gamma} \rho^{n+1} u_i^{n+1} (C1 \cdot \text{Log} \frac{\delta u_i^{n+1}}{v} + C2) N_i d\Gamma \quad \text{si} \quad \frac{\delta u_i}{v} > 11.6$$

ou

$$\int_{\Gamma} \vec{Q}^{n+1} \cdot \vec{e}_i N_i d\Gamma = \int_{\Gamma} \rho^{n+1} \frac{\delta (u_i^{n+1})^2}{v} N_i d\Gamma \quad \text{si} \quad \frac{\delta u_i}{v} < 11.6$$

$$\text{et } \int_V \vec{Q}^{n+1} \cdot \vec{n} N_i dV = 0 \quad k^{n+1} = \frac{1}{\sqrt{C_u}} (U_i^{n+1})^2 \quad \epsilon^{n+1} = \frac{1}{K} \delta (U_i^{n+1})^3$$

Dans la pratique, pour des raisons de stabilité numérique, on introduit une relaxation sur la vitesse de frottement qui induit un processus itératif à chaque pas de calcul  $\Delta t$ .

### 3. ETUDE DE QUELQUES CONFIGURATIONS ELEMENTAIRES

Le problème industriel est décomposable en un certain nombre de configurations élémentaires : écoulement brusque, diffusion, changements de direction, couches limites... etc.

Le bon comportement du logiciel dans chacune de ces configurations est un préalable indispensable à la description satisfaisante de la géométrie globale. Afin de s'assurer de cette représentativité de nombreux cas tests ont été traités.

Les résultats concernant un élargissement brusque et une couche limite sont rapportés.

#### 3.1 Elargissement brusque

Pour effectuer cette étude l'expérience de Kim et Al (8) correspondant à un élargissement brusque isotherme, à un nombre de Reynolds de 44500 est retenue.

Les profils d'entrée de vitesse, d'énergie cinétique et de dissipation sont déduits d'un calcul d'écoulement pleinement développé en canal plan.

Les figures 1 et 2 montrent des visualisations des lignes de courant ainsi que des illustrations des principales quantités caractéristiques de la turbulence.

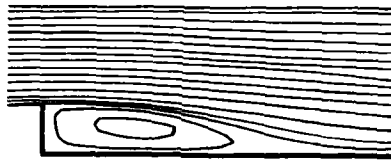


Figure 1 Ecoulement derrière un élargissement brusque

.lignes de courant

*Backward facing step*

*Streamlines*

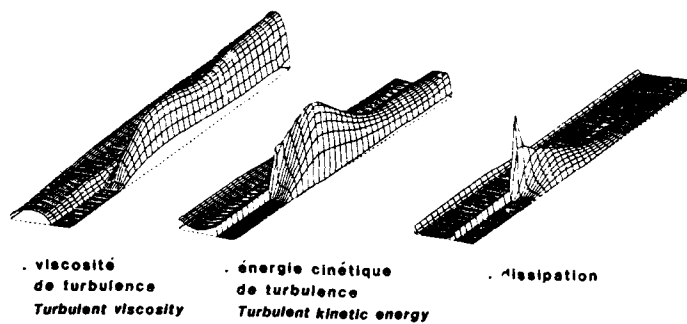


Figure 2 Ecoulement derrière un élargissement brusque

*Backward facing step*

La zone de recirculation, à l'aval de l'élargissement a une longueur d'environ 5 fois la hauteur de la marche  $h$  ; cette valeur est inférieure à celle obtenue expérimentalement par Kim et Al (7h). Cependant, cette sous-estimation semble en partie due au modèle de turbulence utilisé : des résultats comparables ont été obtenus par d'autres auteurs (cf Mansour et Al [9], Taylor et Al [10], Brison et Al [17]). Les pics sur  $k$  et  $\epsilon$  à l'aval de la marche sont, d'autre part, bien prédits.

### 3.2 Couche limite

Dans le cas d'une couche limite, des calculs ont été effectués en se plaçant dans les conditions expérimentales de Cheng et Ng (111), (112)), en situation isotherme (figures 3 et 4).

La vitesse à l'extérieur de la couche limite est alors de 10,4 m/s. Le domaine de calcul s'étend sur une longueur de 200 mm, les profils d'entrée étant déduits des résultats expérimentaux sur  $u$ ,  $k$  et  $\bar{\epsilon}$ .

Les résultats obtenus dans trois sections ( $x = 70$  mm,  $x = 125$  mm et  $x = 182$  mm) sont données par les figures 5 à 7. Les comparaisons concernent les profils de vitesse, d'énergie cinétique de turbulence ainsi que des profils de tensions de Reynolds.

Les résultats montrent une bonne concordance entre profils expérimentaux et numériques. Les valeurs à la paroi semblent, en particulier, prédites de façon correcte par l'utilisation des lois logarithmiques.

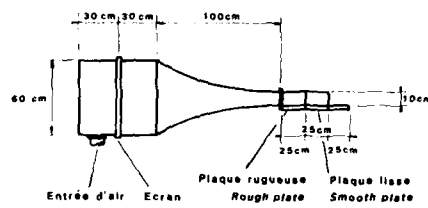


Figure 3 Couche limite  
Boundary layer

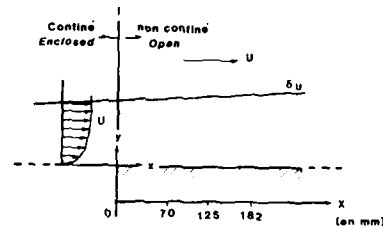


Figure 4 Couche limite  
Boundary layer

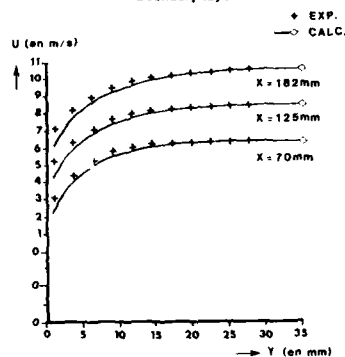


Figure 5 Couche limite - Profils de vitesse  
Boundary layer - Velocity profiles

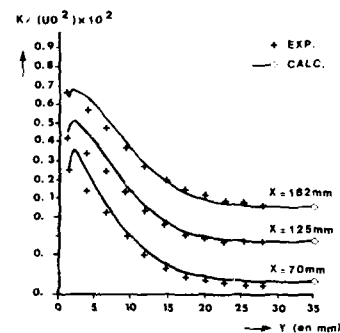


Figure 6 Couche limite - Profils de K  
Boundary layer - Kinetic energy profiles

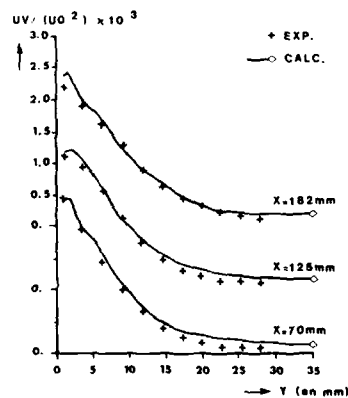


Figure 7 Couche limite - Profils de  $\bar{UV}$   
Boundary layer -  $\bar{UV}$  profiles

#### 4. UTILISATION INDUSTRIELLE

Les divers tests effectués sur des configurations réalistes de tête de chambre ont montré que l'hypothèse consistant à supposer la viscosité constante s'avérait très sévère en ce qui concerne la description de l'aérodynamique, en particulier sur les casquettes, ce qui permet de ménager les marges nécessaires à une bonne reproductibilité des performances sur les chambres de série. Aussi son utilisation est-elle retenue au niveau de l'avant projet.

Elle est associée, pour les zones où une connaissance plus approfondie de l'écoulement est désirée, à une méthode de sous domaines. Dans ce dernier cas, les conditions limites à imposer sur la frontière du domaine détaillé, sont extraites du calcul global.

Cette méthodologie est illustrée sur une configuration de chambre industrielle dont le schéma de principe est rapporté figure 8.

Pour l'étude globale d'aérodynamique extérieure à la chambre, le domaine de calcul sélectionné est constitué d'un plan méridien entre deux injecteurs limité par deux frontières, l'une située à l'entrée du prédiffuseur, l'autre à l'amont des trous primaires.

Des profils de vitesse sont imposés dans les sections de sortie alors qu'un profil de pression est donné à l'entrée du diffuseur. Ce type de conditions limites ne permet pas l'équilibrage naturel des débits entre les différents passages. Aussi, les diverses valeurs de débit dans les sections de sortie sont obtenues à partir d'une schématisation monodimensionnelle ou à partir de résultats expérimentaux. Une alternative à cette méthode, consistant à relier la pression statique en sortie à une vitesse débitante, par l'intermédiaire d'un coefficient de perte de charge déduit de l'expérience, fera l'objet d'une publication ultérieure [13].

Sur les figures 12 et 13, nous avons illustré le cheminement complet qui va de la phase d'avant projet jusqu'au calcul précis des performances. Ainsi, la figure 12 montre comment la méthode à viscosité constante permet, en partant d'une configuration malsaine (12a) caractérisée par des zones de décollement au niveau de l'alimentation des premiers films, d'aboutir à une configuration aérodynamiquement saine (12b).

D'un calcul utilisant le modèle  $(k, \epsilon)$  (figure 13) sont ensuite déduites les pertes de charge de contournement et les pertes de charge entre le diffuseur et le fond de chambre. Si ces pertes de charge ne sont pas encore conformes à l'objectif, il est possible de poursuivre l'étude au moyen du modèle  $(k, \epsilon)$  afin de réaliser les dernières modifications locales nécessaires du prédiffuseur, des casquettes ou des carters.

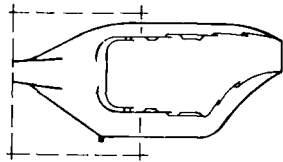


Figure 8 Schéma de la chambre étudiée  
Scheme of the studied combustor

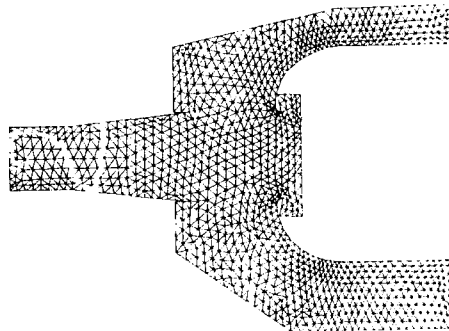


Figure 9 Aérodynamique de la tête de chambre  
Maillage fin  
Aerodynamic study of the combustor dome  
Fine mesh

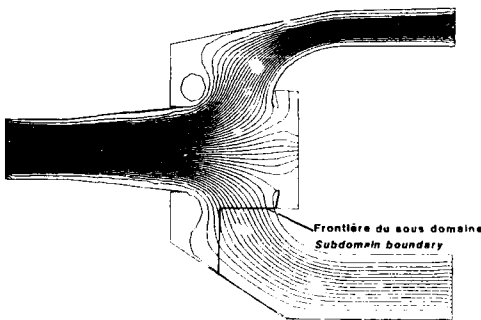


Figure 10 Aérodynamique de la tête de chambre  
Lignes de courant calculées : Modèle à viscosité turbulente constante  
Aerodynamic of the combustor dome  
Calculated streamlines: Constant viscosity model

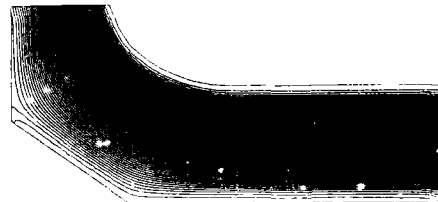


Figure 11 Aérodynamique de la tête de chambre  
Sous domaine: lignes de courant  
Modèle à viscosité turbulente constante  
Aerodynamic of the combustor dome  
Streamlines - Subdomain calculations  
Constant viscosity model



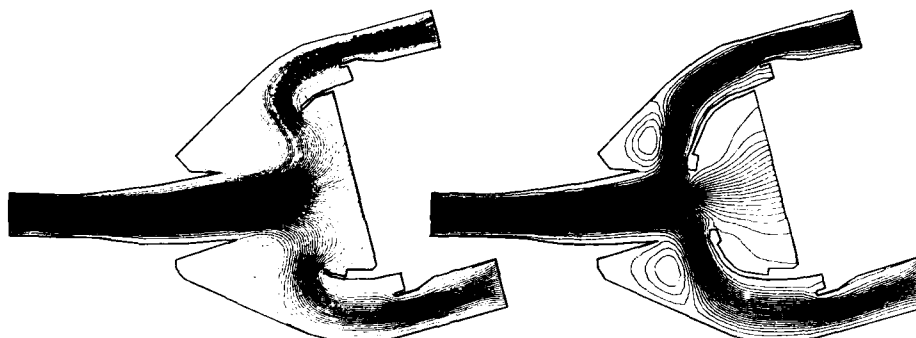


Figure 12 Optimisation de la tête de chambre  
Modèle à viscosité constante  
*Combustor dome optimisation*  
*Constant viscosity model*

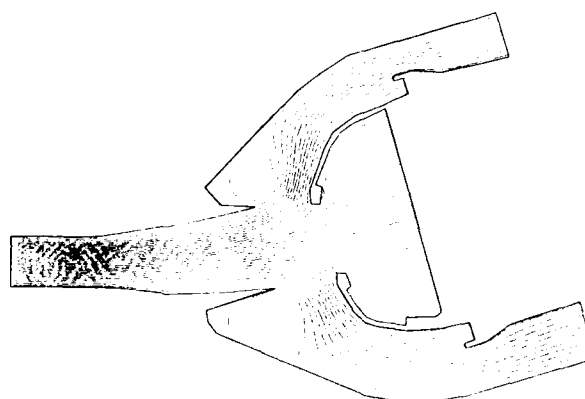


Figure 13 Aérodynamique de la tête de chambre  
Lignes de courant sur des casquettes optimisées  
Modèle K - E  
*Aerodynamic of the combustor dome*  
*Streamlines over optimised cowls*  
*K - E model*

## CONCLUSION

Une méthode de type éléments finis a été développée par l'Ecole Centrale de Lyon et est couramment utilisée à la SNECMA pour tous les problèmes d'interaction diffuseurs - tête de chambre.

Le logiciel employé est elliptique ; le maillage de type triangulaire est bien adapté pour simuler les phénomènes aérodynamiques dans des configurations où la géométrie et la topologie sont complexes.

La turbulence est décrite au moyen d'un modèle ( $k, \epsilon$ ) qui permet une restitution quantitative de l'écoulement. Cependant, au niveau de l'avant projet, un modèle correspondant à une viscosité constante, plus sévère sur le plan de l'identification des zones susceptibles de décoller lui est préféré.

La validité du logiciel a été vérifiée par l'étude de nombreuses configurations élémentaires représentatives des différents types d'écoulement rencontrés au niveau des problèmes d'interaction diffuseur - tête de chambre (couches limites, recirculation, diffusion...).

Sa fiabilité a été obtenue par le passage de cas variés correspondant à des géométries réalistes.

## BIBLIOGRAPHIE

- [1] A. FAVRE. Equations des gaz turbulents compressibles". Journal de mécanique. Vol. n° 3 et 4, 1965.
- [2] W.P. JONES and J.J. Mc GUIRK : "Mathematical Modelling of gas-turbine combustion chambers" AGARD CP 275, 1979.
- [3] W.P. JONES : "Models for turbulent flows with variable density and Combustion", VKI lecture Series 1979-2.
- [4] R. GLOWINSKI : "Numerical methods for non-linear variational problems". Ed. Springer Verlag, 1981.
- [5] M. BUFFAT : "Finite element analysis on a microcomputer of laminar flow". 2nd International Conference on Microcomputer in Engineering development and application of software - Swansea, 1986.
- [6] D.W. KELLY, S. NAKAZAWA, D.C. ZIENKIEWICZ, J.C. HEINRICH : "A note on upwinding and anisotropic balancing dissipation in finite element approximations to convective diffusion problems." Int. Journal Num. Methods and Engineering, vol 15. 1980.
- [7] J.F. BRISON, M. BUFFAT, D. JEANDEL, E. SERRES. "Finite Element Simulation of Turbulent Flows, Using a two Equation Model". Numerical Methods in Laminar and Turbulent Flows, Swansea, Pineridge Press, 1985.
- [8] J. YIM, S.J. KLINE, J.P. JOHNSTON. "Investigation of a reattaching turbulent shear layer : Flow over a backward-facing step". Transactions of the A.S.M.E., J. Fluids Engineering, vol. 102, 1980, pp. 302-308.
- [9] N.M. MANSOUR, J. KIM, P. MOIN. "Computation of turbulent flows over a backward-facing step". Turbulent shear flow symposium, Karlsruhe, 1983.
- [10] C. TAYLOR, C.E. THOMAS, K. MORGAN. "A Modelling flow over a backward-facing step using the F.E.M. and the two equations model of turbulence". Int. J. Num. Meth. Fluids, vol.1, 1981, pp. 295-304.
- [11] R.K. CHENG & T.T. NG. "Some aspects of strongly heated turbulent boundary layer flow". Physics of Fluid 25 (8). August 1982.
- [12] R.K. CHENG & T.T. NG. "Conditional Reynolds stress in a strongly heated turbulent boundary layer with premixed combustion". Physics of Fluid 28 (2). February 1985.
- [13] D. JEANDEL, G. BRUN, S. MEUNIER, M. DESAULTY. Numerical Simulation of Diffusor/Combustor Dome interaction. A paraître Congrès ISABE 1987.

DISCUSSION

J.S. LEWIS, UK

How did you define the downstream boundary conditions ?

Réponse de l'Auteur

Les conditions aux limites en aval (débits) peuvent être obtenues suivant 3 méthodes :

- à partir d'une schématisation monodimensionnelle
- à partir des résultats expérimentaux
- en reliant la vitesse débitante à la pression statique à l'intérieur du foyer par l'intermédiaire d'un coefficient de perte de charge déduit de l'expérience.

Cette dernière méthode fera l'objet d'une publication ultérieure.

# DEVELOPMENT OF A PLENUM CHAMBER BURNER SYSTEM FOR AN ADVANCED VTOL ENGINE

J S LEWIS, T W MURRAY AND D STEELE  
Rolls-Royce plc, Filton, Bristol.

## Summary

Plenum Chamber burning (PCB) continues as one of the most viable options for vertical take-off and landing aircraft with a supersonic capability.

Assessments of the future thrust requirements for such aircraft show that higher levels of temperature rise than previously demonstrated will be required, coupled with the ability to operate efficiently over a wide range of fuel air ratios in an expanded flight envelope.

This paper describes the research and development programmes that were carried out on model and full size rigs to design and evaluate advanced concepts to meet the anticipated requirements.

The system characteristics which were evaluated include pressure loss, ignition, efficiency, thermal integrity and velocity profiles at nozzle exit under non-combusting (dry) and combusting conditions.

The successful achievement of the target levels of performance on the rig will now be followed by further demonstrations on the full engine.

## Background

The development of thrust augmentation technology for vectored thrust engines of the Pegasus type is described in Reference 1. The work in the early 1960's for the supersonic VTOL P1154 aircraft culminated in the BS100 engine (Figure 1) which utilised a boost system for the front nozzles that was given the title of a Plenum Chamber Burner (PCB). Cancellation of the P1154 project resulted in a discontinuation in the design and further development of the PCB systems which had been initially demonstrated on Pegasus rig and engine hardware.

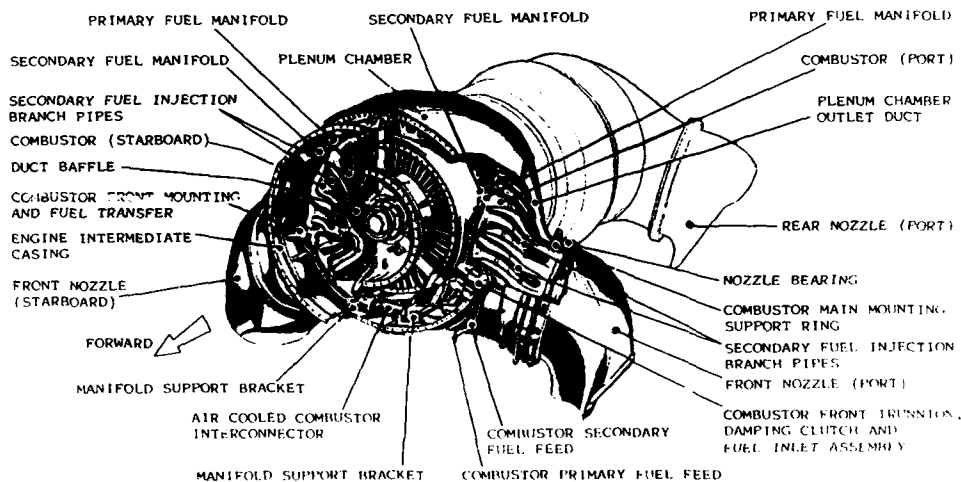


Figure 1 BS100 Engine with Plenum Chamber Burner

Since that time, afterburner technology has evolved particularly for augmented turbofan engines and reappraisals of the requirements of future supersonic STOVL aircraft continue to conclude that a front nozzle PCB system is a major contender (Figure 2).



Figure 2 Future Supersonic STOVL Aircraft

Rolls-Royce has therefore continued with the development of this augmentation system starting with an assessment of the full capabilities and characterisation of the technology associated with the BS100 and then extending the programme to meet the recognised aims of these future projects.

This paper describes the results of the research and development programme that was introduced in Reference 1. The vehicle chosen for this work was an advanced cycle based on the Pegasus geometry installed in what was considered to be a realistic and technologically demanding airframe. The fundamentals of the work described are however applicable to any advanced cold stream burning geometry.

#### TECHNOLOGY TARGETS

Design targets were set for the programme which were considered to represent the future project requirements and would also ensure that the derived performance characteristics would continue to expand the existing design data bank in the most economical way.

The targets for the combustion system were:-

- 1) to achieve a reduction in dry pressure loss compared to that of previously demonstrated systems.
- 2) to achieve substantial increases in thrust boost capability and efficiency.
- 3) to achieve acceptable high altitude stability and light up.
- 4) to demonstrate reliable light up capability at Sea Level Static conditions.
- 5) to demonstrate acceptable thermal and mechanical integrity and
- 6) to achieve the above targets with a reduced non-dimensional volume and installed frontal area.

#### DESIGN STUDIES - PLENUM CHAMBER AND COMBUSTOR

An interactive design technique is used to formulate the main plenum chamber lines taking due account of the required nozzle throat position and other installation requirements.

Scaled perspex models of the plenum chamber including fan delivery casing and nozzle simulation are used at this stage of the design. The models represent one side of the engine (Figures 3 and 4) and are used for the experimental confirmation of overall pressure loss and pressure distribution on air flow rigs in support of the theoretical design specification. Flow visualisation techniques are also employed to assist in the definition of the main combustor flow areas and volumes.

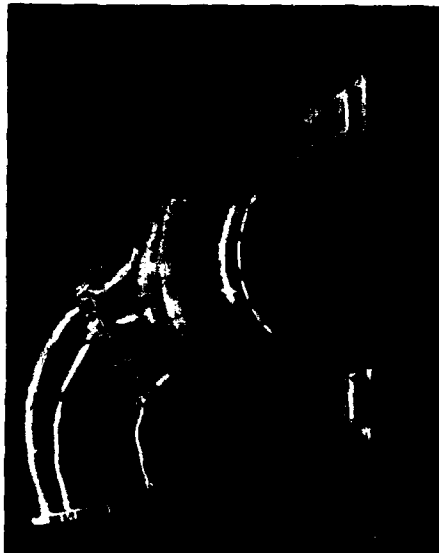


Figure 3 Scaled Perspex Model  
Showing Nozzle in the  
Vertical Position.



Figure 4 Scaled Perspex Model  
View of Nozzle Bearing  
Plane.

Initially, simplified three dimensional surfaces are used to simulate the flame holder arrangement (Figure 5).

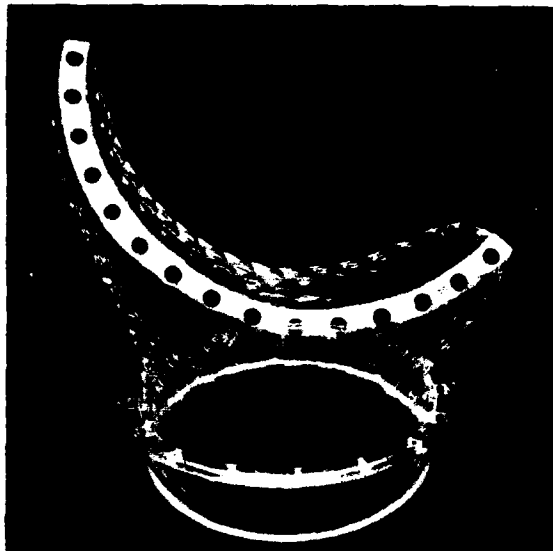
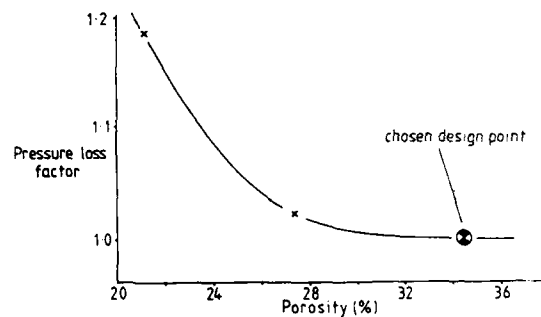


Figure 5  
Simulated Combustor

With this style of combustor studies were carried out to achieve the minimum pressure loss while optimising the surface porosity (magnitude and distribution), the combustor volume and the axial position of the surface relative to the three dimensional inlet diffuser. As shown in Figure 6 the chosen geometry achieves the minimum loss and is also in a relatively stable part of the design characteristic. It is therefore insensitive to small changes that may be necessary because of mechanical design constraints or which arise during the development and manufacture phase of the programme.

As the design progressed, a more realistic surface is produced to support the stressing and lifing studies. (Figure 7).

**Figure 6 Pressure Loss Characteristic**



**Figure 7**  
Combustor Model with  
Realistic Flow  
Distribution

#### DESIGN STUDIES - HEATSHIELD

To achieve the high thrust boost targets with an acceptable thermal integrity, the region between the combustor and the nozzle throat required cooling. The experimental studies showed that a substantial pressure distribution existed at entry to this region (Figure 8) and also in the various sections as the flow turned through the 70° bend (Figure 9).

The cooling design chosen for this region incorporated hot side film cooling and cold side convective cooling. Figure 10 shows the geometry that was used. It featured a maximum of 11 stages of film cooling for the outside of the bend and 5 stages for the inside of the bend including the variable area final nozzle.

A full aerodynamic and heat transfer analysis was carried out to achieve a minimum cooling flow design at the most demanding simulated flight condition and fuelling level. The typical metal temperature distribution is shown in Figure 11 for the 11 cooling stage region. Allowance is made for a hot side cyclic variation in temperature associated with geometric features of the burner.

A more detailed cross-sectional view of the assembly is shown in Figure 12, illustrating the diffuser, primary zone, fuel manifolds and injectors, "colander" combustor, heatshield and variable nozzle.

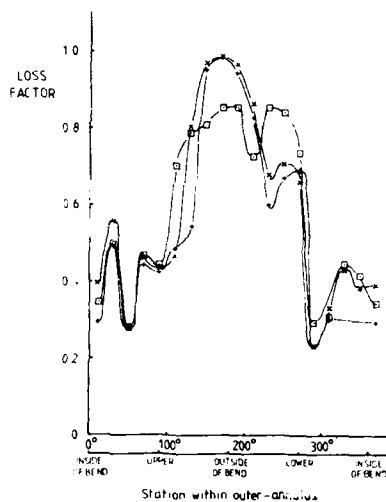


Figure 8 Pressure Distribution at Entry to Heatshield.

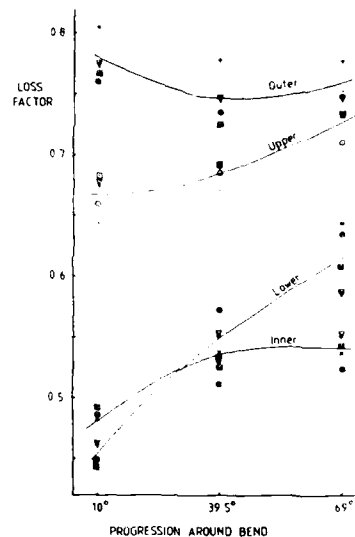


Figure 9 Pressure Distribution Around the Heatshield Bend.

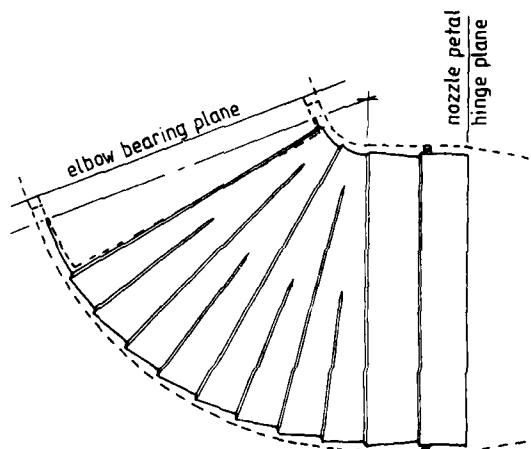


Figure 10 Heatshield Geometry

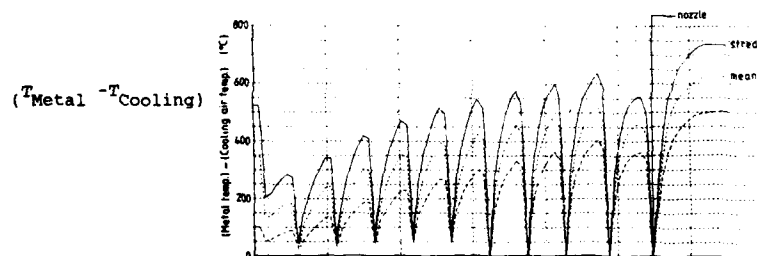


Figure 11 Heatshield Temperature Distribution

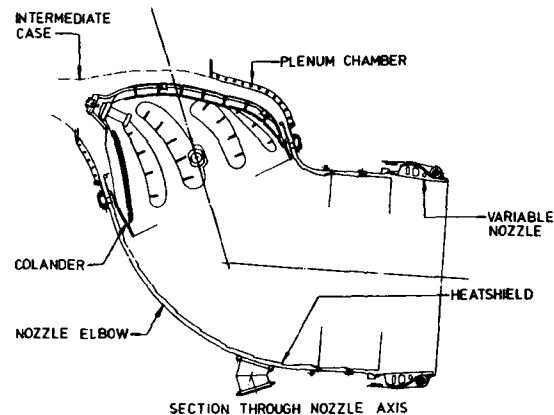


Figure 12  
General Arrangement

#### FULL SCALE RIG PROGRAMMES

A full scale rig programme was then carried out to evaluate the design. The tests included pressure loss assessment, full combustion performance (temperature rise and efficiency), high altitude stability, light up and thermal integrity. The unit was tested in an Altitude Test Facility at RAE Pyestock (Figure 13) where the required conditions of inlet pressure, temperature and mass flow were supplied to one half of the fan delivery annulus and a single nozzle.

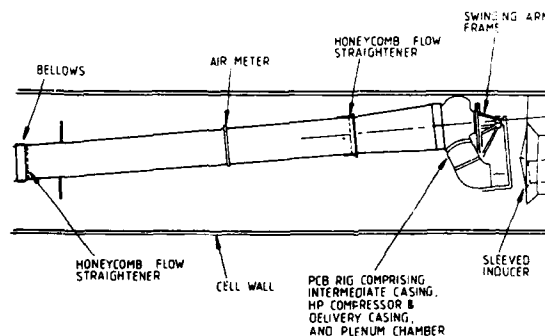


Figure 13 Full Scale Rig Layout

#### PRESSURE LOSS

The overall pressure loss was obtained by traversing a suitable pressure probe at the nozzle exit plane to give a mass weighted mean total pressure which was compared with the inlet total pressure at the fan delivery flame.

The nozzle exit profile was obtained at several settings of the variable nozzle size as shown in Figures 14. Each nozzle setting represented a different Mach number in the plenum chamber and the loss characteristic (Figure 15) was therefore derived. At the design flow function the full scale unit showed good agreement with the values obtained from the scaled model tests and confirmed the substantial reduction in loss of this design compared with earlier designs. However the target pressure loss requirement for advanced designs continues to fall and further work will be required in this area particularly associated with the fuel injector and fuel manifolds. The velocity profiles of the nozzle in the dry case showed a centralised region of 'high' pressure with a bias towards the final outer bend. The ratio of peak to mean pressure was 1.05 for all settings.



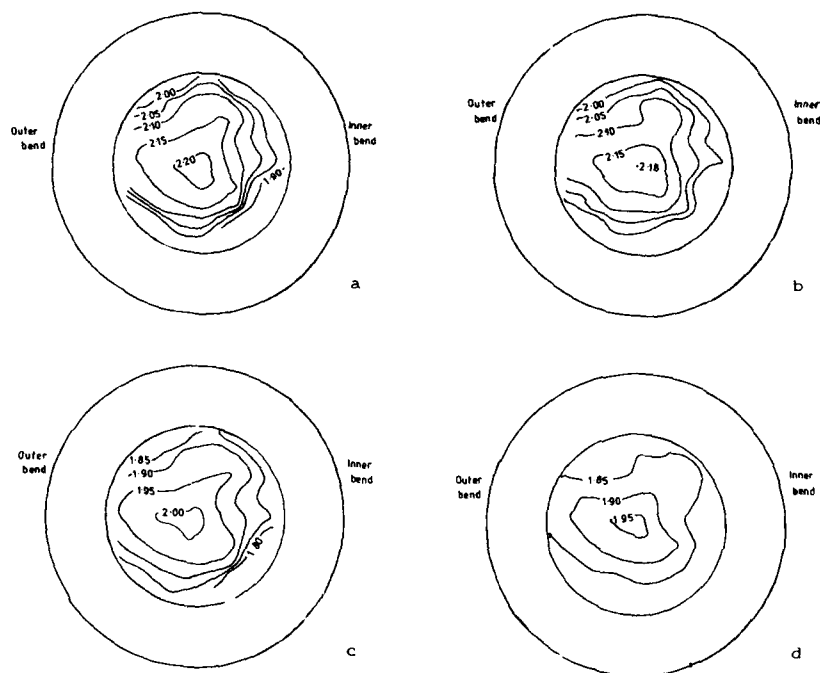


Figure 14 Nozzle Pressure Profiles With Increasing Inlet Mach Number (a to d)

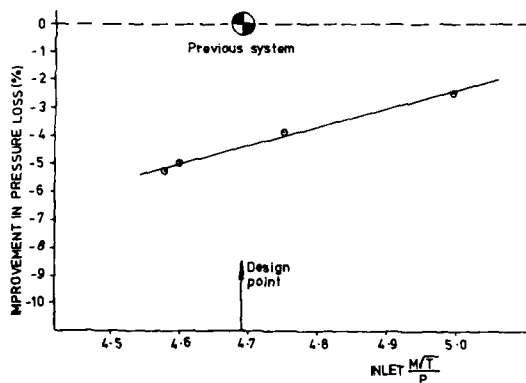


Figure 15  
Full Scale Rig  
Pressure Loss  
Characteristic.

#### HIGH ALTITUDE STABILITY AND LIGHT UP

The high altitude light up and primary zone stability characteristics were obtained and as indicated in Figure 18 met the requirements anticipated for future projects.

The ignition source is a separately fuelled pilot combustor Figure 19 which had been subject to an optimisation programme to achieve the best air loading and fuel air ratio at the critical light up conditions. An igniter was positioned in each combustor at the top of the engine with a cross-lighting zone positioned between combustors at the bottom of the engine.

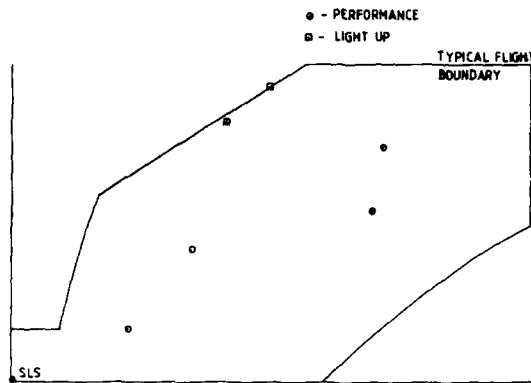
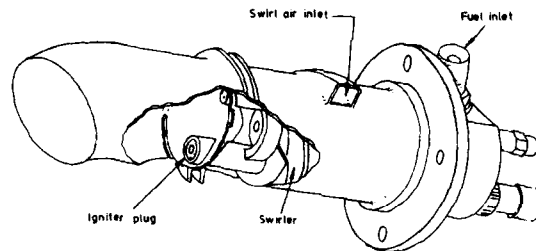


Figure 16 Light-up Boundary

Figure 17 Igniter Arrangement



### PERFORMANCE

The combustion performance was measured over a wide range of flight conditions which were chosen to enable a systematic assessment of the effects of inlet pressure, temperature and flow function or Mach number in the chamber.

At some conditions, a complete traverse was carried out at the nozzle exit plane to give the gas conditions, fuel air ratio and inefficiency due to carbon monoxide and unburnt hydrocarbons. Typical distributions of fuel air ratio, efficiency and temperature rise ratio are shown in Figures 18, 19 and 20.

Fuel-Air Ratio Distribution Ratio

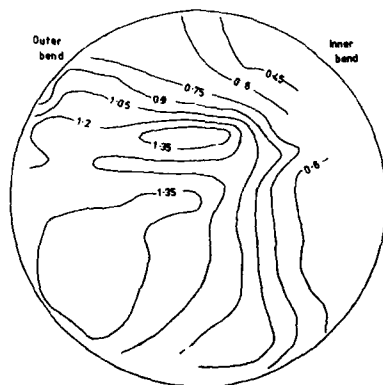


Figure 18 Fuel Air Ratio. Distribution Relative to the Mean Value.

Combustion Efficiency Ratio

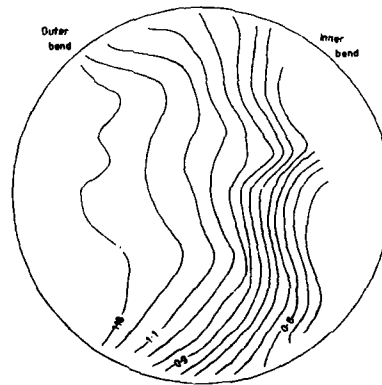
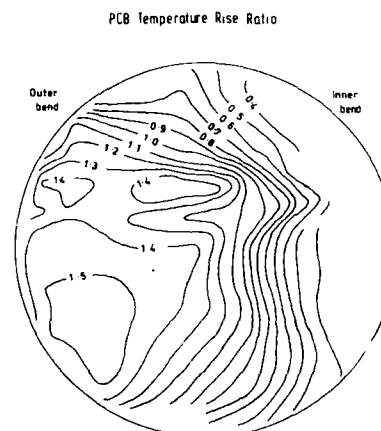


Figure 19 Combustion Efficiency Distribution Relative to the Mean Value.

**Figure 20** Distribution of Temperature Rise Relative to the Mean Value.



Previous work at Rolls-Royce has demonstrated that these profiles can be adjusted by changes to the fuel jet position and size to meet any special needs associated with hot gas ingestion, thermal integrity of the installation or high efficiency at low and intermediate fuel air ratios. For this programme the data was analysed to confirm the combustion performance that was derived from gas dynamic calculations based on pressure and nozzle area measurements at selected conditions. This comparison served as a calibration to be used at the other flight conditions where traversing was not carried out.

The maximum temperature rise ratio set for the project was achieved and efficiencies greater than 95% were measured.

#### THERMAL/MECHANICAL INTEGRITY

The thermal and mechanical integrity of the complete installation was monitored during the test programme.

The metal temperature of the combustor which are used in the finite element stress design programme were satisfactory.

The maximum metal temperatures recorded on the heatshield were also within the required design range.

#### FUTURE PROGRAMME

A full engine evaluation is planned for this system coupled with hot gas ingestion studies on the Tethered Harrier Installation at Shoeburyness.

Further research work to achieve lower pressure losses will also be carried out.

#### REFERENCE

1. A SOTHERAN  
Development of Thrust Augmentation Technology for the Pegasus  
Vectored Thrust Engine.  
SAE Technical Paper Series 821390 - October 1982.

#### ACKNOWLEDGEMENT

This work has been carried out with the support of the Procurement Executive Ministry of Defence.

### DISCUSSION

N.A. BAIRSTO, UK

With a reheat system of this sort, modulation will be an important factor. What level of modulation are you able to achieve ?

#### Author's Reply

The modulation is limited by the degree of complication of the control system (i.e. the fuel metering controls).

In the system described here, a two zone fueling arrangement is illustrated, the minimum level is then set by the primary zone fuel (about 5 % of the maximum) which is set to give a constant fuel air ratio, and the remaining 95 % of the fuel can be introduced to give a smooth thrust modulation up to maximum.

If high efficiency is required at these intermediate levels, then additional fuel control stages will be required with a corresponding penalty of weight and cost.

PUMPING SYSTEMS AND FLOW INTERFACES FOR RAPID RESPONSE  
ELECTRONIC REHEAT CONTROLS

BY

Thomas C Yates  
 Engineering Manager

Trevor S Smith  
 Specialist Engineer

Lucas Aerospace Limited  
 Engine Systems Division  
 Shaftmoor Lane  
 Hall Green  
 Birmingham

SUMMARY

Modern engine controls, including reheat controls, are based on digital electronic techniques and there are many papers published on the use of microprocessors for this purpose. This paper addresses the problems of fuel pumping and metering which are associated with digital electronic reheat controls.

A survey is carried out of various pumping options including main engine and reheat fuel pumping. A technical description of single, twin, and three pump systems, including rotodynamic and positive displacement pumps is given together with comments on the relative advantages and disadvantages of the various options.

A fuel flow interface designed for rapid response reheat control systems is described. The application is a digital electronic control for a future bypass engine. Comparison is made between computer simulation of the control characteristics and test results on the hardware.

The report concludes with some comments on likely future advances in reheat control systems.

1.0 INTRODUCTION

In a modern bypass engine running at full power over 75% of the oxygen entering the engine remains unburnt. Thus there is scope for increasing the thrust and this is accomplished by extending the jet pipe, fitting a variable area nozzle, and burning fuel in the jet pipe. The variable area nozzle is needed to maintain operating pressures and temperatures in the engine unaffected by afterburning (or reheat). The fuel flow rate required for reheat is three to eight times maximum "dry" engine flow so the thrust augmentation is commonly only used for short periods of time for take-off, climb, and combat, and almost exclusively in military aircraft.

For optimum aircraft performance rapid reheat modulation is needed, particularly with modern agile aircraft which have inherently unstable aerodynamic configurations. Less than 1 second from minimum to maximum thrust augmentation is a typical requirement. Modern reheat controls are micro-processor based. Pumps and valves are needed to move and monitor the liquid fuel, and the response of the pumping and valve system is crucial to the achievement of rapid reheat response.

This paper considers various options for overall configuration of reheat control loops and proposes one considered capable of achieving optimum response performance.

Consideration is given to the choice of pumps to give fastest possible response in the re-heat fuelling mode. This is then extended to examining the relationships between fuel flow requirements in the two modes of engine operation viz:- with and without re-heat, and to the optimisation of combinations of pumps to meet the wide range of flows required, with minimum power consumption and heat rejection into the fuel.

The paper describes a system, embodying the re-heat fuel pump and a combination of metering valves and associated pressure drop and shut-off valves, which has been demonstrated on a test rig. Typical response performance results obtained with this system are given and discussed and the paper concludes with a review of possible future developments in this field.

## 2.0 OVERALL SYSTEM CONFIGURATION

A typical bypass engine is shown in figure 1.

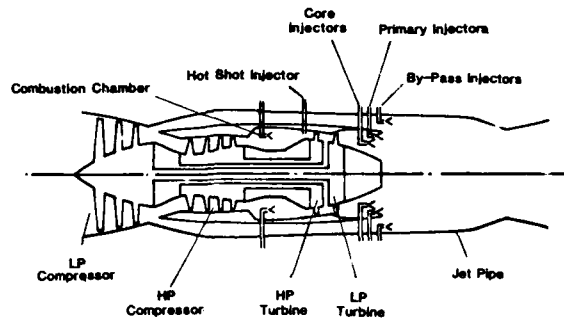


FIG.1 TYPICAL BY-PASS ENGINE WITH REHEAT

In this example afterburner fuel injectors and flame stabilisers are fitted in both bypass and core air streams and the streams are mixed after combustion. This gives a shorter jet pipe than some alternative configurations but necessitates separate metering of core and bypass fuel flows for good efficiency. About 10% of the maximum reheat flow is fed to primary burners with good flame stabilisation in the core jet stream. The fuel flow to these burners is maintained constant irrespective of the degree of reheat and ensures that the other burners are always maintained alight.

Ignition of the primaries is achieved either by a torch, catalytic igniter or a "hot shot" of fuel injected into the main combustion chamber upstream of the turbine. In a modern bypass engine with a high degree of augmentation, reheat is not lit at maximum flow level, because even if the nozzle control could act quickly enough to prevent engine surge the sudden doubling of engine thrust could impair aircraft handling. Nevertheless, for optimum aircraft performance, rapid reheat modulation is needed and this is difficult to achieve with closed loop afterburner control. If nozzle area is selected and there is a closed loop on the fuel flow which varies flow to achieve the desired engine operating conditions, there is a risk of exceeding the stoichiometric fuel air ratio leading to loss of control. The alternative of selecting fuel flow and having a closed loop nozzle control varying nozzle area for desired engine conditions, gives an inherently slow system as the rate of fuel flow change is restricted by the rate of change of nozzle area to ensure the nozzle area does not lag fuel flow excessively causing LP compressor surge or blade flutter.

As the limiting factor is nozzle response, optimum reheat response is achieved if nozzle area is selected and the nozzle allowed to change area as fast as it can. The fuel flow can then be scheduled in accordance with the achieved nozzle area. Such a twin open loop scheduling control gives the fastest achievable reheat response but requires a fast accurate 3 channel multi function reheat control. Such a control, shown diagrammatically in figure 2 is the subject of this paper.

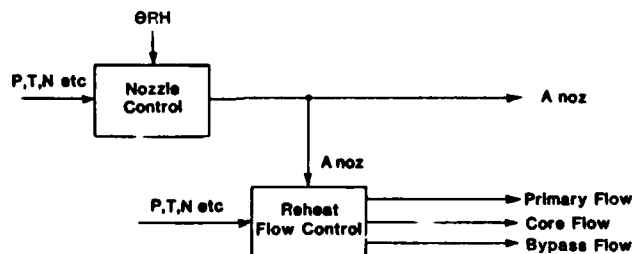


Fig. 2 TWIN OPEN LOOP AFTERBURNER CONTROL

### 3.0 PUMPING SYSTEM

#### 3.1 Reheat Pump Considerations

The choice of reheat pump has a major impact on the ability to achieve fast stable system response.

Many current reheat systems use either a centrifugal pump driven by an air turbine or one having a vapour core created by an inlet throttle. The object of both types of pump is to reduce unnecessary input power at low flows and thereby reduce reheat fuel temperature to acceptable limits. However it is difficult to achieve rapid response with such pumps because of turbine inertia in the case of a turbo pump or the necessarily slow response of the inlet valve in the case of a vapour core pump. Thus pump filling, manifold priming and system response during modulation tend to be undesirably slow. Attempts to improve response by increasing system gain cause stability problems due to the time lags in the pump.

The response problem is best solved by running an engine driven centrifugal pump full and throttling the output to achieve the required reheat flow. Thus full pump pressure and flow is immediately available at all normal running conditions and response is only limited by the response of the metering valves, there being no pump lags to interact and cause stability problems at high system gains. This approach also has the advantage of giving minimum pump weight. Inevitably the fuel temperature rise in the pump at low reheat flow will be somewhat higher with such a pump but the reheat fuel temperature rise can be kept below 75 deg C even at 1/50th of maximum flow. When reheat is off the pump inlet valve can be shut off and the impeller drained so that there is virtually no power consumed.

With such a pump the inlet valve does not need a low gain to ensure stability during reheat operation and so a high gain can be used allowing the pump to fill rapidly so that full flow and pressure becomes available for rapid manifold priming when engaging reheat.

A limiting factor is the water hammer surge which occurs at the instant the pump impeller becomes full and the flow rate in the inlet pipe is suddenly reduced as the metering valve restriction at pump outlet, rather than the inlet valve restriction, becomes the controlling factor. The resultant pressure peak in the LP pipe must be kept low to avoid damage to the pipe. This effect can be minimised by ensuring the metering valves are already in a substantially open position as required for priming and by controlling the gain of the inlet valve over the first part of its opening. This enables the pump to be filled in less than 0.1 sec. and the manifolds to be primed and steady minimum flow to be established in a further 0.4 sec.

#### 3.2 Other Considerations

Having selected the type of reheat pump for rapid response one should then consider the pumping system including main engine and reheat pumps as one system, rather than considering the pumping requirements for each independently. Apart from the requirement of supplying the prescribed fuel flows at appropriate pressures the pumping system must have adequate response and must not raise the fuel temperature to a level at which the fuel becomes chemically unstable.

There exists a wide choice of pumping configurations and those considered here are presented as a representative rather than an exhaustive selection of those possible. Most modern systems use a centrifugal first stage and spur gear second stage pumps for the main engine fuel system with some form of rotodynamic pump for the reheat system. Usually the pumps are driven at a ratio of engine speed through an engine gearbox, but not always. Engines on the Concorde, for example, have centrifugal pumps for starting and first stage, whilst a second stage centrifugal pump is driven from an air turbine powered by engine bleed air.

The main attraction to using a centrifugal pump for supplying fuel for gas turbine engines is that its basic simplicity should result in a very reliable pumping system. This is indeed the experience with the Concorde engine fuel pumps which are giving an MTBF of 200,000 hours.

The main obstacle to the use of simple engine driven centrifugal (CF) pumps is the mismatch between pump delivery pressure requirements over the flight envelope, which leads to excessive power consumption, and hence fuel temperature at flight idling conditions.

It is possible greatly to reduce the CF pump low flow power consumption, at the expense of some mechanical complication and increase in weight. For example a shrouded rotor design, with floating shroud seals and with a multiport diffuser can consume half the power of a similar sized pump with conventional shroud seals and a simple volute, when throttled down to minimum flow.

In this section we first examine the performance of a state of the art shrouded rotor CF pump and compare it with the performance of a conventional system comprising backing pump, gear pump and CF reheat pump.

The inherent incompatibility of relatively low main system flow at high pressure and high reheat flow at low pressure renders the choice of a single CF pump unlikely. A twin rotor unit is therefore examined in alternative configurations. In the first configuration both rotors are driven from a common shaft. The reheat supply rotor chamber is drained when reheat is off. A better two rotor system is possible if separate drives are provided for main flow and reheat pumps, and this is the configuration next considered. In this case, one pump is drained when reheat is off.

We shall therefore consider the following pumping configurations:-

Conventional three pump system	Fig 3
Single CF pump supplying main and reheat flow	Fig 4
Two rotor system with both rotors driven at the same speed	
One configuration has a first rotor generating reheat systems pressure whilst the second adds the extra pressure required for main fuel flow.	Fig 5
An alternative has separate rotors generating pressures for reheat & main engine flow.	Fig 6
Two rotor system with rotors driven at different speeds	Fig 7

To give a basis for comparison the table of data (Table 1) is included. This is an outline flight plan fuel flow and pressure requirement for a typical reheat gas turbine engine. The figures are realistic but fictional and include an allowance for starter jets at cranking speed. The table includes total power consumption for a three pump system in which the reheat CF pump runs dry when reheat is not in use.

### 3.3 Single Centrifugal Pump

The model chosen for our single centrifugal pump has a radial flow shrouded impeller fitted with an integral unshrouded axial flow inlet inducer. The design is based on data generated by research programmes aimed at identifying and reducing loss generating processes including inlet recirculation and shock, disc friction, shroud leakage, diffuser shock and recirculation and mechanical friction.

From table 1, the maximum output required is 5275 gm/sec at 6.83 MPa for the reheat system and 2198 gm/sec at 8.52 MPa for the main engine fuel system, with engine speed 100%. The worst throttled back condition requires a delivery flow of 176 gm/sec with the engine speed at 94.5%. Correcting for the differences in engine speed, the lower flow corresponds to 2.5% of maximum flow. The pressure rise at normal dry maximum flow on such a pump will be well in excess of that required.

The single pump has the tremendous advantage of being the simplest possible arrangement. Its main drawbacks are that reheat flow is delivered at excessive pressure - which is comparatively minor - and the turn down ratio is excessive. The fact that it would be possible for the system to fail completely and irrecoverably should a sufficiently large volume of vapour or air enter the pump so as to deprive it also has to be considered. Some characteristics of the single pump system are given in table 2.

### 3.4 Two CF Pump System with Common Speed

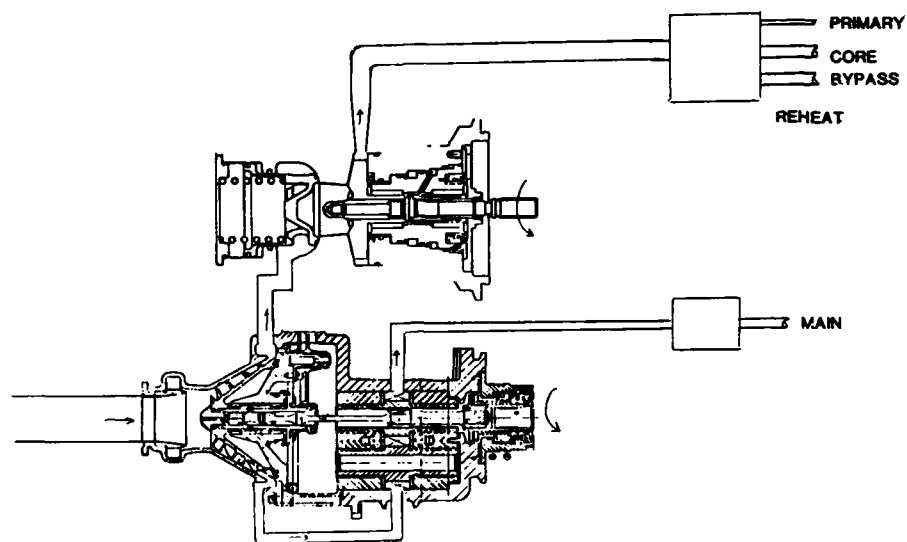
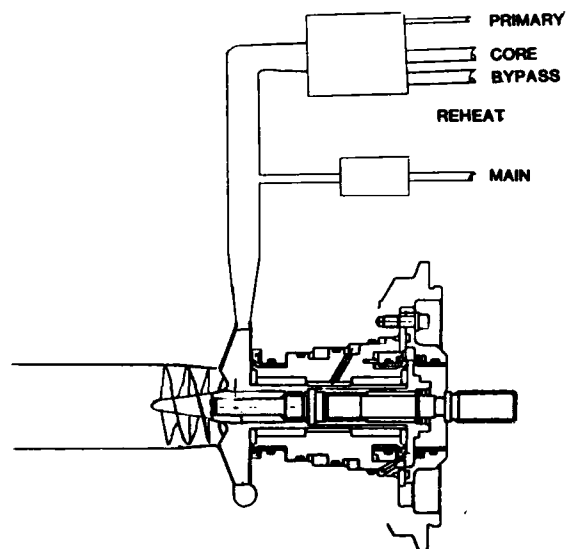
Both rotors are driven from a common shaft. One configuration has a main rotor to deliver the pressure required for the reheat system and a second rotor to provide the extra pressure required by the main system. Table 3 compares this system with the conventional three pump system in table 1.

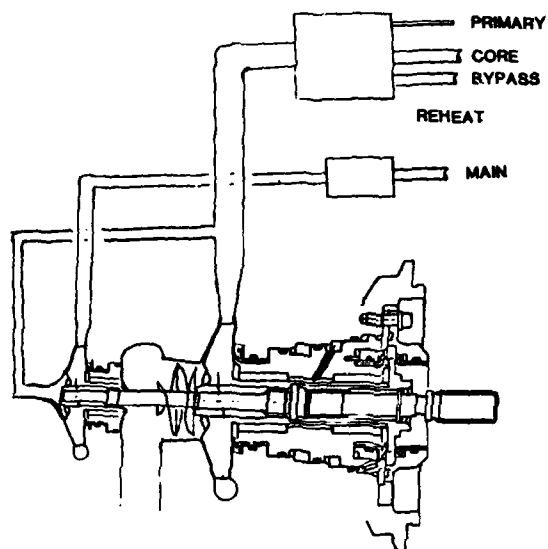
An alternative approach is one in which one pump delivers main engine flow whilst the other delivers reheat flow. This system is analysed in Table 4. In this case the pump dedicated to reheat flow is drained once reheat is not selected.

### 3.5 Two CF Pumps with Differing Speeds

This configuration has one pump dedicated to main fuel supply and the other to reheat supply with conventional shut-off and drain facilities. Each pump is scaled to make maximum flow coincide with maximum efficiency. The performance of such an arrangement is given on table 5 and once again is compared with the conventional three pump system from table 1.

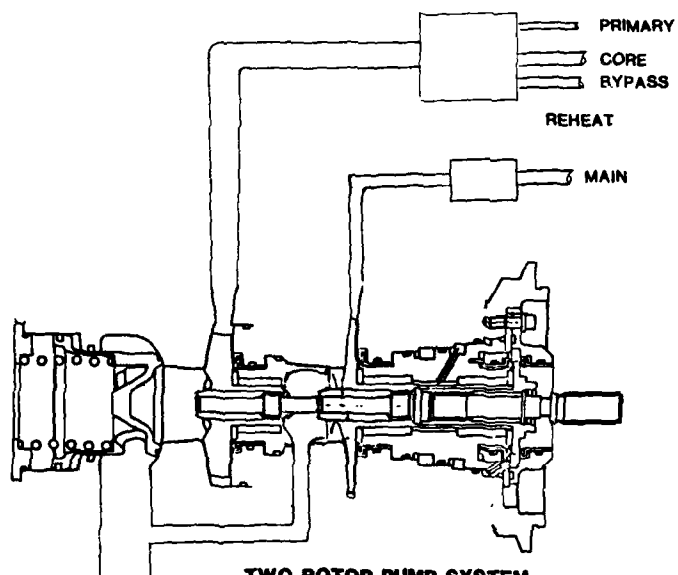


**CONVENTIONAL THREE PUMP SYSTEM****FIG.3****SINGLE PUMP SYSTEM****FIG.4**



**TWO ROTOR PUMP SYSTEM REHEAT AND MAIN IN SERIES**

FIG. 5



**TWO ROTOR PUMP SYSTEM  
ONE MAIN  
ONE REHEAT**

FIG. 6

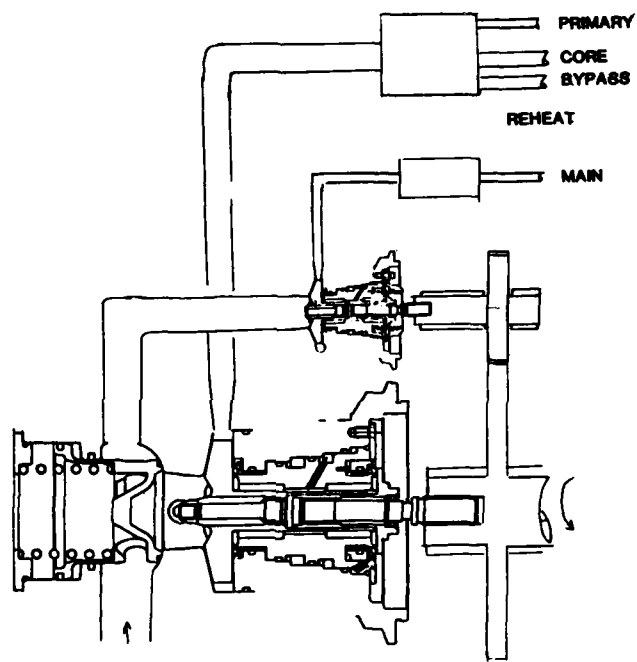
**TWO PUMP SYSTEM**

FIG.7

TABLE 1

CONDITION	% NH (ENGINE SPEED)	FUEL PRESSURE MPa		FUEL FLOW gram/Sec		CONVENTIONAL SYSTEM		
		MAIN	REHEAT	MAIN	REHEAT	KW (TOTAL)	J/Gram (CHANNEL)	TEMP RISE °C
1a SL M1.2 Dry	100.0	8.52	0	2198	0	49.6	22.5	6.0
1b SL " Min RH	100.8	8.52	1.38	"	1295	78.7	22.5	10.6
1c SL " Max RH	100.8	8.52	6.83	"	5275	119	13.0	2.6
2a SL MO Dry	101.3	5.12	0	1480	0	36.5	24.6	9.2
2b SL Min RH	101.3	5.12	1.17	1480	734	60.8	33.0	15.7
2c SL Max RH	101.3	5.12	2.84	1480	2947	82.0	15.3	6.2
3 SL MO Idle	65	0.90	0	100	0	11.3	113	53.2
4a 11 KM M.6 Max	93.1	1.45	0	400	0	21.0	52.8	24.5
Min RH	93.1			"	240	35.7	61.3	28.5
Max RH	93.1			"	945	41.8	22.0	10.2
4b 11 KM M.6 Idle	76.3	0.90	0	100	0	11.3	113.5	53.5
5 Max Flight Idle	94.5	0.90	0	176	0	20.2	115.1	54.5
6 SL MO light up	5 to 10	0.35 fuel Sg 0.75						

Conventional 3 pump system reheat pump drained when reheat off

TABLE 2

Single CF Supply Pump

CONDITION	CF PUMP						CONVENTIONAL SYSTEM		
	FLOW gr/sec	PUMP RPM	PRESS MPa	KW in	J/Gram	TEMP RISE °C	KW Total	J/Gram (Channel)	TEMP RISE °C
SL M1.2 Dry	2198	23160	10.54	67.5	30.7	9.6	49.6	22.5	6.0
" " Min RH	3492	23160	10.57	88.5	25.3	7.1	78.7	22.5	10.6
" " Max RH	7473	23160	8.52	141.1	18.9	4.0	119	13.0	2.6
SL MO Dry	1480	23275	10.52	56.2	37.9	15.2	36.5	24.6	9.2
" " Min RH	2214	23275	10.65	68.4	30.9	11.9	60.8	33.0	15.7
" " Max RH	4427	23275	10.55	103.6	23.4	8.3	82.0	15.3	6.2
SL MO Idle	100	14935	4.09	8.58	86.4	40.7	11.3	113	53.2
11 KM M.6 Max	400	21390	8.50	29.2	73.2	34.1	21.0	52.8	24.5
Dry									
Min RH	240	21390	8.55	32.7	51.2	24.1	35.7	61.3	28.5
Max RH	945	21390	8.88	43.0	32.3	15	41.8	22.0	10.2
" " Idle	100	17531	5.63	13.8	138.0	65.1	11.3	113.5	53.5
Max Flt Idle	176	21712	8.67	27.0	153.7	72.51	20.2	115.1	54.5
SL MO light up		1149 to 2298	.025 to .1						

Best technology tested, engine driven CF pump  
designed for maximum pressure rise and maximum total flow, hence large turn down ratio

TABLE 3

Two CF Stages in Series 1st Stage giving total flow at reheat pressure  
2nd Stage gives required extra pressure for Main System

CONDITION	FLOW gr/Sec	CF PUMP						CONVENTIONAL SYSTEM		
		PUMP RPM	Pressure MPa	Pressure Required MPa	KW in	J/Gram lb	TEMP RISE °C	KW Total	J/Gram (Channel)	TEMP RISE °C
SL M1.2 Dry	2198	21564	9.14	8.52	56.6	25.7	7.3	49.6	22.5	6.0
" " Min RH	3492	21564	9.14	8.52	74.6	21.3	5.2	78.7	22.5	10.6
" " Max RH	7473	21564	6.83	8.52	118.5	15.8	2.6	119	13.0	2.6
SL MO Dry	1480	21671	9.12	5.12	46.8	31.6	12.2	36.5	24.6	9.2
" " Min RH	2214	21671	9.22	5.12	57.6	26	9.5	60.8	33.0	15.7
" " Max RH	4427	21671	9.07	5.12	87.5	19.8	6.6	82.0	15.3	6.2
SL MO Idle	100	12905	3.56	0.9	7.0	70.2	33.0	11.3	113	53.2
11 Km M.6 Max Dry	400	19916	7.39	1.45	23.9	60.0	27.8	21.0	52.8	24.5
" " Min RH	240	19916	7.43	1.45	26.9	18.6	19.8	35.7	61.3	28.5
" " Max RH	945	19916	7.72	1.45	35.8	26.7	12.5	41.8	22.0	10.2
" " Idle	100	16323	4.89	0.9	11.2	111.9	52.8	11.3	113.5	53.5
Max Flt Idle	176	20216	7.50	0.9	22	124.7	58.8	20.2	115.1	54.5
SL MO light up		1069 to 2138		0.35						

TABLE 4

Two CF Pump System with Common Speed

CONDITION	STAGE FLOW Gm/Sec	PUMP RPM	CF PUMP				CONVENTIONAL SYSTEM		
			STAGE KW	TOTAL KW	STAGE J/gram	TEMP RISE °C	POWER IN KW	J/GRAM	TEMP RISE °C
SL M1.2 Dry	2198	28500	47	47.0	21.4	5.4	48.5	22.5	6.0
" " Min RH	1294	28500	29.5	76.5	22.8	10.7	30.6	22.5	10.6
" " Max RH	5275	28500	77.6	124.6	14.7	3.4	74.6	13.0	2.6
SL MO Dry	1480	28641	36.6	36.6	24.7	9.1	36.6	24.6	9.2
" " Min RH	734.3	28641	23.1	59.7	31.5	15.3	26.5	33.0	15.7
" " Max RH	2947	28641	50	86.6	16.9	7.0	50.0	15.3	6.2
SL MO Idle	100	18468	4.3	4.3	43.3	20.7	11.3	112.8	53.2
11 Km M.6 Dry	400	26295	16.0	16.3	40.2	18.9	21.0	52.8	24.5
" " Min RH	240	26295	13.7	29.8	57.2	27.5	14.7	61.3	28.5
" " Max RH	945	26295	21	37.2	22.3	10.6	20.7	22.0	10.2
" " Idle	100	21573	6.9	6.9	68.7	32.8	11.3	113.5	53.5
Max Flt Idle	176	21712	13.8	13.8	78.5	37.5	20.2	115.1	54.5
SL MO light up		1413 to 2826							

Reheat pump drained when reheat off  
Designed slightly comprised to achieve common drive speed  
Both pump models deviate from best tested model

TABLE 5

Separate Main and Reheat CF Pumps

CONDITION	CF PUMP						CONVENTIONAL SYSTEM		
	FLOW Gm/Sec	PUMP RPM	PRESS RISE MPa	KW in	J/Gram	TEMP RISE °C	POWER IN KW	J/Gram (Channel)	TEMP RISE °C
SL M1.2 Dry	2198	34847	8.52	39.5	18.00	3.6	48.5	22.5	6.0
" " Min RH	1294	19072(RH)	7.3	34.8	26.33	12.2	30.6	22.5	10.6
" " Max RH	5275	19072(RH)	6.83	76.00	14.42	3	74.6	13.0	2.6
SL M0 Dry	1480	35020	9.31	31.3	21.28	7.3	36.6	24.6	9.2
" " Min RH	734.3	19167(RH)	7.22	27.4	37.33	17.6	26.5	33.0	15.7
" " Max RH	2947	19167(RH)	7.50	52.90	17.93	7.3	50.0	15.3	6.2
SL M0 Idle	100	22471	3.64	3.16	31.47	14.7	11.3	112.8	53.2
11 Km M.6 Max Dry	400	32185	8.05	12.8	32.03	14.7	21.0	52.8	24.5
Min RH	240	17740	4.14	16.60	69.55	32.5	14.7	61.3	28.5
Max RH	945	17740	4.27	23.5	25.20	11.7	20.7	22.0	10.2
" " Idle	100	26377	5.0	4.90	49.40	23.2	11.3	113.5	53.5
Max Flt Idle	176	32669	7.72	10.1	57.50	27	20.2	115.1	54.5
SL M0 light up		1728 to 2455	0.35						

Reheat pump drained when reheat off  
Speed chosen to use best tested model without deviation

### 3.6 Pumping System Summary

The number of pumping systems considered here is not, of course, exhaustive. For the systems considered, one may draw some general conclusions. Except at maximum flow and at light up the single pump system produces fuel pressures in excess of requirements. It also consumes more power with consequential higher fuel temperatures particularly at the critical flight idle conditions (See table 2).

By sizing the pump so as to produce only the pressure required for reheat, and adding a second pump on the same shaft to add the additional pressure required for main engine flow, one can achieve temperature rises nearer those offered by the conventional system. The maximum temperature rise however is in excess of that with the conventional system (see table 3).

A considerable improvement is obtained by choosing to a two pump system in which one CF pump supplies main engine flow, whilst the other supplies reheat flow and is drained when reheat is switched off (see table 4).

A system which has separate main and reheat CF pumps separately driven at speeds proportional to engine speed, results in some individual temperature rises higher than those obtained in the other systems considered, but the maximum temperature rise is considerably lower (see table 5).

The temperature rise in the system is an important consideration and from this aspect the system which has separate main and reheat centrifugal pumps separately driven at speeds proportional to engine speed is the best choice. To satisfy the requirements for rapid response, minimum power, and minimum fuel temperature rise, a pumping system which has an engine driven centrifugal pump for reheat flow, which is drained when reheat is not selected, is the appropriate choice.

We shall now go on to discuss the reheat fuel metering system.

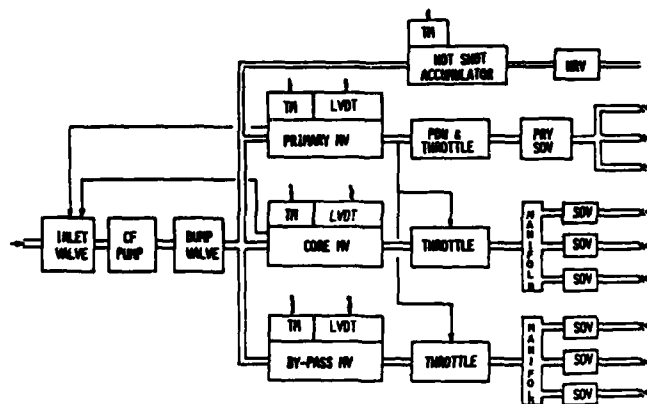
4.0 FAST RESPONSE REHEAT SYSTEM

FIG 8: SYSTEM DIAGRAM

Fig. 8 shows the block diagram of a fast response reheat system that has been rig tested.

The reheat pump has a shut-off valve at its inlet and a dump valve at its outlet. The metering control consists of 3 individual metering controls in parallel with distribution and shut-off valves at the reheat manifolds plus a hot shot control.

The system has demonstrated the ability to reach full reheat, including priming and hot shot within 1.8 sec. from selection. Accurate stable control was maintained throughout.

4.1 Metering Controls

The metering valves are servo controlled by dual coil torque motors with position feedback from LVDT's.

The servo supply is from the main engine HP fuel pump so that the metering valves can be positioned when reheat is 'off' as well as 'on'. This enables the first part of the metering valve travel to be utilised to control the reheat pump inlet valve and save the weight and cost of a separate reheat selection solenoid. It also allows the computer to check correct operation of the reheat metering valves when reheat is 'off'.

Reheat controls are often required to fail freeze in the event of loss of electrical power, this avoids loss of thrust at critical conditions. This is achieved by having equal servo areas at each end of the metering valves and using a symmetrical torque motor and flapper arrangement with opposed servo nozzles. Thus metering valve position is the integral of motor current and zero current results in zero velocity. This null condition is set accurately on build by an adjustable null bias on the torque motors. To ensure that the metering valve does not move at zero current under flow forces or 'g' loads the piston has sliding cap seals or piston rings which give a friction force of about  $\pm 20$  lbf. ( $\pm 89$  newton).

Thus fail freeze is achieved by simply switching off torque motor current, the friction prevents drift, there is no 'jump' prior to freeze and no additional locking solenoid or piston is required. Tests show that, in spite of the presence of friction during normal operation, fast stable response is easily achieved with either analogue or digital position control loops. See test results later.

The pressure drop across the primary metering valve is kept constant by a pressure drop piston and servo throttle valve. In order to save weight and cost the pressure drop piston is placed inside the servo throttle valve. The pressure drop piston acts against a spring to control the opening of a servo nozzle and control servo flow to the throttle valve. The servo flow is taken from upstream of the metering valve and returned downstream so that the servo flow becomes part of the metering valve calibration and there are no parasitic flow losses. The spring preload is altered by bi-metal discs to give fuel temperature compensation and an 'O' ring on the pressure drop piston prevents dirt ingress.

The pressure drop across the bypass and core metering valves could be controlled by similar combined pressure drop and servo throttle valves to those used on the primary control. However somewhat faster response can be achieved by using equalising valves as shown. These throttle so as to make the pressure downstream of the core and bypass metering valves equal to that downstream of the primary metering valve.

The equalising valves are sized to give a high corrective force in the event of hysteresis due to dirt. As well as improved response, the equalising valve arrangement improves reliability due to the lower component count and reduces cost.

#### 4.2 Reheat Selection

The primary and core metering valves are moved to their priming flow positions. This opens ports in series in the two metering valves to supply HP fuel to the pump inlet shut-off valve. The inlet valve then opens allowing the pump to fill and as pressure builds up the dump valve opens, connecting the pump to the metering valves and sealing-off the dump connection. It takes only 0.1 secs from selection to produce full reheat pump delivery pressure and thus establish priming flow, the metering valves already being in the priming position.

The computer controls the opening of the metering valves during priming and closes them down to reach the appropriate minimum reheat position at the instant the manifolds become full so as to prevent overpriming. Priming can easily be achieved in 0.6 sec from reheat selection and if the core and by-pass shut-off valves are at manifold outlet, so that only the spray bars have to be primed, then priming within 0.35 sec of selection becomes possible.

#### 4.3 Hot Shot

The hot shot unit consists of a torque motor, a pilot valve and an accumulator piston. When priming is complete the torque motor is energised to move the pilot valve to the discharge position. This connects one side of the accumulator to the injector and the other side to reheat pump delivery pressure so that a fixed volume of fuel is discharged under pressure. After firing the torque motor is de-energised so that the pilot valve returns to the recharge position and the accumulator is recharged from reheat pump pressure.

The porting in the pilot valve is sufficiently large to allow rapid recharging in about 0.15 sec, ready for repeat firing if reheat fails to light. Rapid recharging and firing is possible because of the high flow and pressure instantly available from the reheat pump without affecting metered flow. If HP fuel from the main engine control were used there would be a risk of causing a transient drop in flow to the main engine. If the accumulator is in the discharged position for any reason during reheat selection then it will recharge before priming is complete.

#### 4.4 Modulation

When light up is detected, flow is increased to the desired level. Rapid stable modulation from minimum to maximum and maximum to minimum in 0.5 sec is possible with an accuracy of better than  $\pm 8\%$  of point during the transient.

At low flow levels even distribution to all the spray bars on the core and bypass manifolds is ensured by having a number of distribution valves each feeding a number of spray bars. The distribution valves have a calibrated flow vs pressure drop characteristic to ensure accurate distribution with a flow accuracy of  $\pm 5\%$  of point.

The valves also act as shut off valves having an elastomeric seal to give a drip tight seal when shut down. When shut down the manifolds are kept full of fuel so that only the spray bars have to be primed, this greatly reduces priming time.

If required the bypass channel can be shut-off at minimum reheat. This is achieved by ports in the bypass metering valve which connect downstream of the metering valve to low pressure. This causes the bypass equalising valve to be held firmly closed by the higher pressure downstream of the primary metering valve. A soft seat on the end stop and a low friction seal on the piston prevent leakage to bypass manifold at this condition.



The large operating force available at the equalising valve makes the error due to seal friction acceptable during metering. When bypass flow is selected the metering valve is rapidly opened and closed to the minimum flow position to prime the flow line and then opened to the flow level required. This allows rapid priming particularly if the distribution/shut-off valves are on the manifold outlet when priming in less than 0.25 sec. is possible.

#### 4.5 Shut Down

Shut down is achieved by moving both the primary and bypass metering valves to the 'off' position. This shuts off the HP servo supply to the pump inlet valve which then closes, under the action of the spring, as servo pressure decays to LP via a fixed restrictor. The inlet valve servo supply ports on the two metering valves are in series so that shut down can be achieved by moving only one of the metering valves in the event of failure of the other valve.

As the inlet valve shuts, the pump starts to empty, pumping a substantial portion of the fuel in the pump to the primary and core sprayers and pulling a vapour core at the eye of the impeller. As the pump empties, pump delivery falls and when it gets sufficiently low the pump dump valve closes, dumping the small volume of fuel remaining in the pump and shutting-off the supply to the metering valves.

The distribution and shut-off valves then close keeping the system full of fuel. The low pressure return line from the hot shot unit and bypass metering valve has a non-return valve to prevent low pressure pressurising the system and cracking the distribution valves. Thus when reheat is off evaporation of the fuel maintains system pressure at the vapour pressure of the fuel corresponding to the fuel temperature. The distribution valves will 'crack' at a pressure which prevents thermal expansion overpressurising the system.

#### 4.6 Test Results

Fig. 9:-

U.V. record showing selection to maximum flow

This shows reheat selection at time zero followed by a short delay as the inlet valve opens and then a sudden rise in pump delivery pressure as the pump becomes full of fuel. The primary flow commences at a high level to give rapid manifold priming and is then reduced to the level required for reheat operation. At the same time the core flow is ramped up to the level required for minimum reheat, this also primes the core spray bars. After a delay for hot shot firing and light-up detection, the core flow is ramped up to maximum level. There is no bypass flow until almost maximum core flow, then a spike of fuel is put into the bypass line for priming and then bypass flow is ramped up from a low level.

This record shows the ability to achieve selection to maximum flow in 1.8 seconds with sequential core and bypass ramps. If the core and bypass shut-off valves are at manifold outlets to reduce priming time and the core and bypass flows are increased together, then selection to maximum flow could be reduced to as little as 1 second.

Fig. 10:-

U.V. record showing minimum to maximum flow and return

In this case reheat flow is initially at a minimum level with bypass flow shut off. As core flow is ramped up to maximum, a spike of flow is put into the bypass line to prime it and then the bypass flow is ramped up after core flow reaches its maximum level.

This record shows the ability to modulate reheat flow from minimum core flow and zero bypass flow to maximum flows in 0.6 seconds including priming of the bypass manifold.

Fig. 11:-

Computer simulation for the same conditions as Fig. 10 showing good agreement with test results.

#### NOTE:

Figs 9 and 10 show linear ramps in metering valve position with time giving a non-linear relationship between flow and time due to the exponential nature of the metering valve profiles.

Fig. 12:- Record of 0.5 second flow ramp.

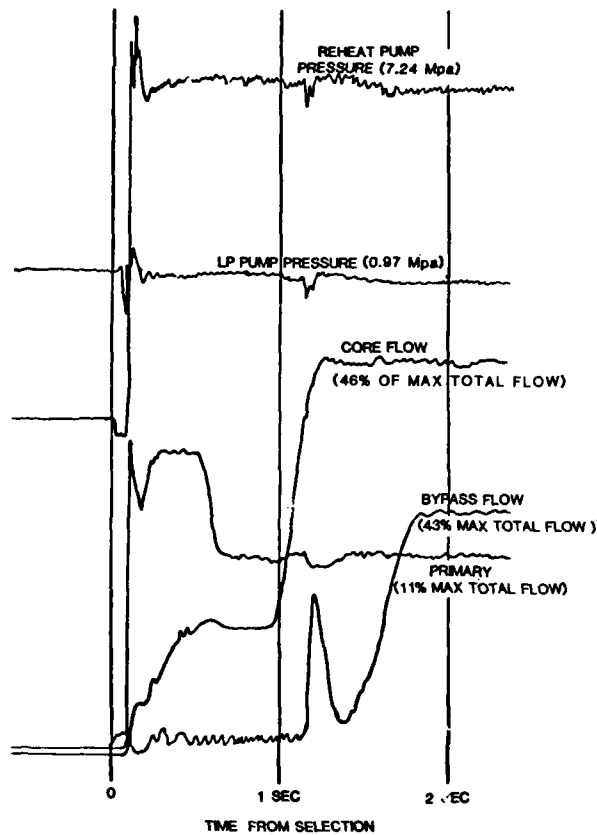
This shows the ability to achieve a 0.5 second flow ramp between minimum and maximum flow inspite of the exponential metering valve profiles.

Fig. 13:- Transient flow error for record in Fig. 12.

This shows that the transient error between demanded flow, as indicated metering valve position, and actual fuel flow does not exceed 8% of point for a 0.5 second flow ramp.

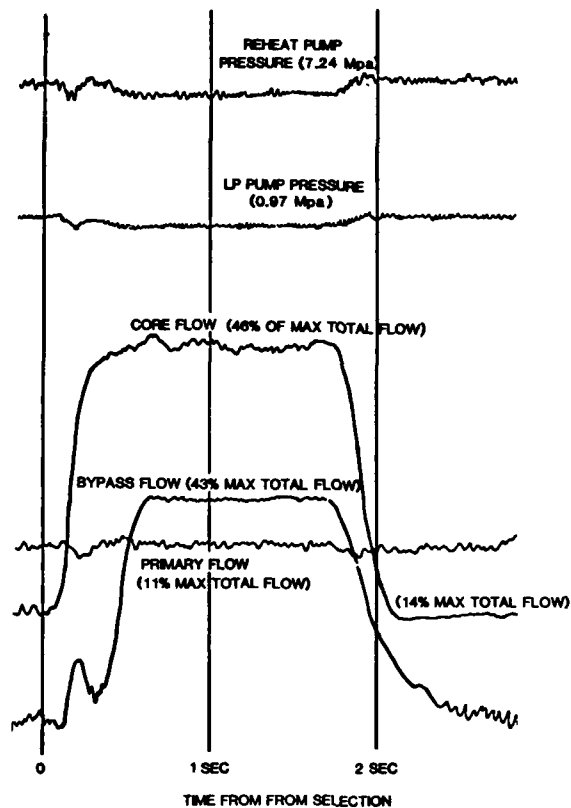
Fig. 14:- Fail freeze

This shows torque motor current, metering valve position and flow vs time for a saw tooth wave position demand, giving full travel of the metering valve in 0.5 sec. Failure is simulated at 0.54 sec by switching current to zero. This results in immediate freeze of the metering valve and flow, with no measurable delay. Fail freeze is maintained indefinitely with no creep.



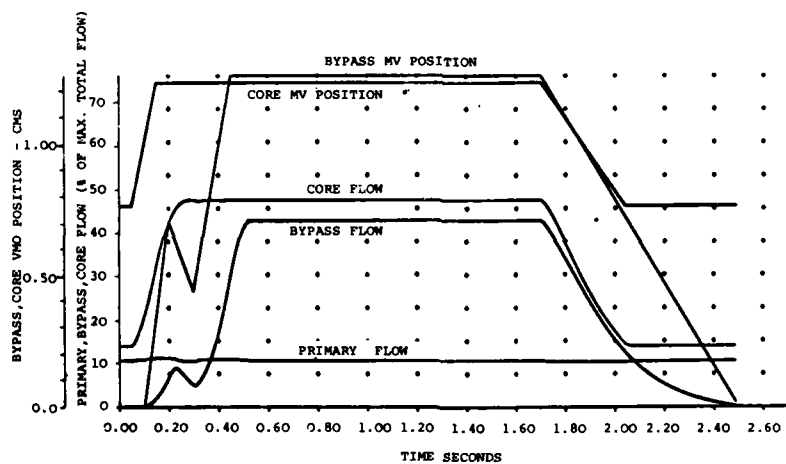
SELECTION TO MAXIMUM FLOW

FIG. 9



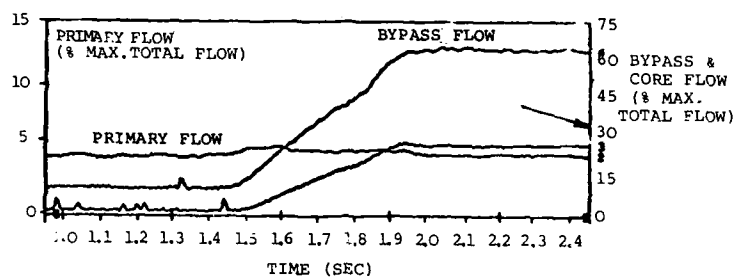
MINIMUM TO MAXIMUM FLOW AND RETURN

FIG. 10



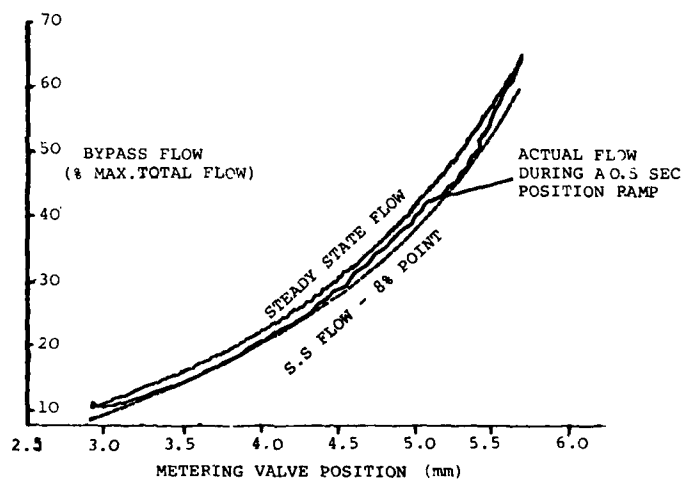
COMPUTER SIMULATION FOR SAME CONDITIONS AS FIG. 10

FIG. 11



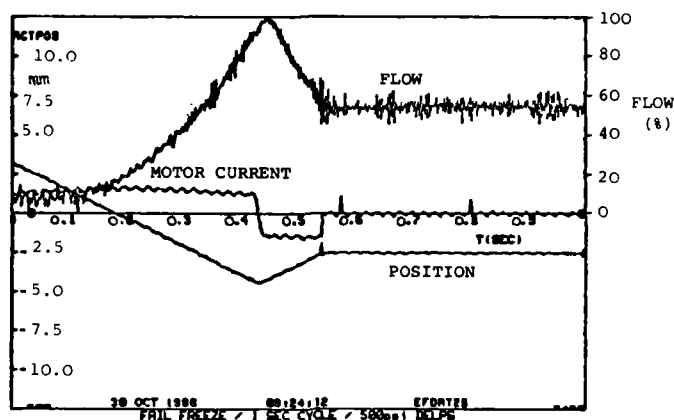
### 0.5 SECOND FLOW RAMP

FIG. 12



### TRANSIENT FLOW ERROR FOR FIG. 12

FIG. 13



## FAIL FREEZE

FIG. 14

### 4.7 Reheat System Summary

The fast response reheat metering system described here has demonstrated the ability to reach maximum reheat within 1.8 seconds from selection and promises even faster response. The system has also demonstrated the ability to modulate flow between minimum and maximum in 0.5 seconds with stable accurate control. Fail freeze at the instant of electrical failure was achieved without the penalty of additional locking solenoids and valves.

### 5.0 CONCLUSIONS

The report has discussed a number of possible pumping systems and shown that with present technologies an engine driven centrifugal reheat pump which is drained when reheat is switched off is a good choice from both the points of view of avoiding excessive heating up of the fuel and of achieving a rapid response reheat system. The reheat valve control described has shown from analysis, simulation and rig results that it is possible to achieve necessary rapid response and high accuracy with a comparatively simple valve metering mechanism.

As always it is possible to see future developments and improvements. These would include for example smart valves in which each valve meters, distributes and shuts off fuel downstream of a single manifold, giving substantial weight saving. It should be possible to develop centrifugal pumps having high efficiency at high turn down ratios allowing a single pump to be used for both reheat and main engine system. Sufficiently accurate flow meters would enable deletion of the pressure drop control in the reheat system. Development of a variable speed drive to interpose between the engine and fuel pump would allow the use of a centrifugal pump which would not need to have particularly good efficiency at high turn down and would remove the necessity for any starter pump.

These may be the subject of future papers.

### 6.0 ACKNOWLEDGEMENTS

The work described in this paper has been carried out with the support of the Procurement Executive of the British Ministry of Defence. The authors are grateful to the Procurement Executive and to the directors of Lucas Industries for permission to publish the paper.

APPENDIX I

CF	Centrifugal
gm/sec	Grammes per second
HP	High Pressure
J/gram	Joules per gramme
KM	Kilometers
KW	Kilowatts
Li	Low Pressure
LVDT	Linear Variable Differential Transducer
M	Mach Number
MPa	Mega Pascal
MTBF	Mean Time Between Failures
NH	Engine High Pressure Shaft Speed
RH	Reheat
SL	Sea Level
UV	Ultra Violet

## DISCUSSION

E.G. HUNT, UK

1) I made the comment that the statement in the report that the vapour core pump is associated with slow response of afterburner thrust is not correct. Many European & American fuel systems use vapour core pumps and meet the specification. The authors have set as their target 1.8 seconds from reheat selection to maximum thrust. I quoted the Tornado as 2.0 seconds from selection to maximum thrust and even this is a limit set by the nozzle actuation system, and not the pump control system.

2) The fuel temperature rise problem is due to the combustion system. Have the authors discussed, with the engine manufacturers, how the design of the combustion system might be modified to obtain lower pressures for fuel atomisation and distribution ?

Author's Reply

- 1) The authors thank Mr Hunt for his comment
- 2) the authors hold frequent discussions with engine manufacturers on the point raised.

N.A. BAIRSTO, UK

Of the pumping systems described, what are the relative weights ?

Do you have to take a system approach to pump selection, to include the weight influence of pump air cooled, fuel cooler, etc... and match this against the temperature rises of each pumping method ?

Author's Reply

The authors agree that it is necessary to take account of a lot of factors other than merely fuel temperature in comparing pumping systems. These include total weight, starting and relighting the engine, pump suction performance, etc.

This was felt to be beyond the scope of the paper presented. It is misleading to quote relative weights of the pumps discussed without considering the effects on the rest of the system.

Of the systems described, the relative weights lightest first, are :

- Single CF pump
- Double impellor pump
- Two shaft system
- Conventional three pump system

The conventional system is probably the only one which meets all present performance criteria.

21-20

J.S. LEWIS, UK

What do you propose to do with the fuel which is drained from the CF pump ? Overboard dumping of fuel is not considered acceptable on reheat cancellation.

**Author's Reply**

Some fuel is dumped from primary manifolds, and core and by pass injectors on cancellation of reheat, and presumably this quantity is acceptable. The quantity of fuel involved in draining a reheat pump will add only a small amount to that already being dumped.



Aerodynamic Performance  
Of a Scale-Model, Counter-Rotating  
Unducted Fan

By: Thomas J. Sullivan  
General Electric Company  
Aircraft Engine Business Group  
Cincinnati, Ohio

Abstract

The aerodynamic performance of a scale-model, counter-rotating unducted fan has been determined and the results are discussed herein. Experimental investigations were conducted using the scale-model propulsor simulator and uniquely-shaped fan blades designed by the General Electric Company under contract to NASA. The blades, designed for a high disk loading at Mach 0.72, 35000 feet altitude max climb condition, are aft-mounted on the simulator in a "pusher" configuration. Data are compared with analytical predictions at the design point and show good agreement.

Nomenclature

J	Advance Ratio	
Mo	Flight Mach Number	
PQA	Power Coefficient	$550 \text{ SHP/A} \rho N^3 D^3$
TQA	Thrust Coefficient	$FEF/A \rho N^2 D^2$
A	Annulus Area, ft <sup>2</sup>	
D	Rotor Tip Diameter, ft	
N	Rotor Speed, rps	
Vo	Free-Stream Velocity, fps	
SHP	Shaft Horsepower	
Q	Rotor Torque, ft-lbs	
$\beta$	Blade Angle at 3/4 Radius, degrees	
$\rho$	Air Density, slugs/ft <sup>3</sup>	
$\eta_{NET}$	Net Efficiency	$J \times TQA/PQA$
FBALC	Rotor Balance Force, lbs.	
FHU	Upstream Face Pressure Force, lbs.	
FHD	Downstream Face Pressure Force, lbs.	
FH	Tare Corrected Hub Force, lbs.	
FPB	Forebody Force, lbs.	
FAB	Afterbody Force, lbs.	
FEF	Effective Thrust, lbs.	
PT-RATIO	Total Pressure Ratio	
TT-RATIO	Total Temperature Ratio	

Subscripts

1	Forward Rotor
2	Aft Rotor

## I. Introduction

The unducted fan engine (UDF<sup>TM</sup>) under development by the General Electric Company has evolved over the past four years from the need for a more fuel-efficient power plant. Conventional high bypass ratio turbofans, which were the engineering development creations of the 1960's and 1970's, have been pushed to practical limits of diameter and weight as thrust demands have grown to 60,000+ lbs. Now, the technology advancements of the 1980's have led to the ultra-high bypass ratio fans with their potential for significant improvements in the fuel economy of modern jet aircraft. The unducted fan engine with high disk loading and counter-rotating blades offers the industry the performance benefits of ultra-high bypass ratio without a large diameter duct and the associated weight penalty [1]. The direct-drive of the variable pitch fan blades from counter-rotating power turbine stages further enhances the engine concept by eliminating the complexity, weight and maintenance problems of a gearbox.

The General Electric UDF<sup>TM</sup> engine, which was flight tested on the Boeing 727 from August 1986 through early 1987, and soon to be flight tested on the McDonnell-Douglas MD-80, operates with 11.67 ft. diameter counter-rotating fan blades. The demonstrator engine blades were designed in early 1984 and followed by an extensive scale-model wind tunnel test program aimed at developing the unducted fan technology needed to meet the engine requirements. Aerodynamic, acoustic and aero-mechanical performance aspects of several counter-rotating blade configurations were investigated in the test program funded by NASA contract and also sponsored by General Electric independent research and development. Since 1984, scale-model testing of General Electric unducted fan designs has been conducted at the Boeing low-speed and transonic wind tunnels, the NASA-Lewis 8' x 6' high speed tunnel and the General Electric anechoic test chamber. NASA-funded programs, such as this, aimed at researching the counter-rotation scheme and the development of thin swept, composite airfoils, have been the natural extension of the single rotation prop-fan program activity initiated by NASA in the mid 1970's [2].

In the following discussion, aerodynamic performance results and analysis from wind tunnel testing of a scale-model counter-rotating unducted fan configuration similar to the full-scale demonstrator engine configuration will be presented. The blade design, manufacture, test in the NASA 8' x 6' wind tunnel and data analysis of this configuration were funded through NASA Contract NAS3-24080. The Boeing transonic wind tunnel test and data analysis of the same configuration were funded through General Electric independent research and development.

## II. TEST RIG DESCRIPTION

The Model Propulsion Simulator (MPS) is a counter-rotating unducted fan engine model propulsion system designed for testing "pusher" type fan blade configurations in either subsonic or transonic wind tunnels [3]. The overall length from the nacelle forebody nose to the aft end of the drive turbine housing is 119.3 inches and the propulsor tip diameter is 24.5 inches.

The MPS SN001 unit was used for testing in the 8 foot x 12 foot Boeing Transonic Wind Tunnel (BTWT). The MPS SN003 unit was used for testing in the NASA-Lewis 8 foot x 6 foot transonic wind tunnel and is nearly identical to the SN001 unit. A photograph of the MPS rig installed in the BTWT is shown in Figure 1. In the wind tunnel, the MPS is mounted on a strut extending from the floor of the test section such that the MPS centerline coincides with the centerline of the test section. For this test, the wind tunnel walls were acoustically treated to allow for the measurement of the unducted fan noise at all critical operating points.

The MPS rig is shown with the pylon attached to a sting off of the support strut. The strut is positioned on a turntable which can be rotated to simulate angles of attack. The pylon is soft-mounted to the nacelle forebody and can be translated axially to two different positions relative to the forward blade leading edge. Testing in the BTWT was performed with and without the pylon installed. In the NASA transonic tunnel, all testing was performed without the pylon and at zero angle of attack.

The nacelle consists of two sections, the forebody and the afterbody. The forebody is an ellipsoid-shaped shell supported from the non-rotating center shaft of the MPS rig. Its shape represents the faired-over inlet and nacelle of an unducted fan engine and was designed to produce diffusion of the airflow just ahead of the counter-rotating blade rows to reduce the shock strengths in the blading. The afterbody shape approximates the outer boundary of the turbine exhaust air exiting an actual engine; it has a short 6 inch diameter section before flaring to encompass the MPS drive turbine housing.

The flowpath hubs provide the attachment and locking mechanisms for the 8 forward and 8 aft rotor blades. The forward, or inner shaft, hub rotates counter-clockwise (aft looking forward) while the aft, or outer shaft, hub rotates clockwise. A portion of the blade hub flowpath, as well as the blade platforms, are dished to provide area-ruling for the blade root thickness where

the through-flow Mach numbers would otherwise be the highest. The inner and outer hubs attach to the metric side of the rotating force balances which, in turn, attach to the rotating shaft.

Propulsor loads are measured by rotating force balances gaged to measure thrust and torque. The rotating force balances incorporate strain gaged flexure beams for thrust and torque load measurement. These balances are installed between the rotating inner shaft and the forward hub and the rotating outer shaft and the aft hub; the balances are completely interchangeable.

The MPS SN002 unit is a vertical assembly mounted in the General Electric Cell 41 Anechoic Chamber. The facility description is shown in Figure 2. The propulsor is located 1.3 fan diameters downstream of the free-jet nozzle exit. The Mach number capability of the free-jet facility for aerodynamic and acoustic testing is from 0 to 0.35. The shape of the MPS SN002 forebody and afterbody in the region near the propulsor blades is identical to the horizontal MPS SN001 and SN003 vehicles. Since the vehicle is driven by a shaft from the bottom and the flow is from bottom to top in the vertical assembly, the forebody does not close but blends into the turbine housing as shown in the photograph of Figure 3. The afterbody contour is the same as the horizontal SN001 shape extending to the 6 inch diameter cylindrical section and then is closed out with an elliptical shape at the top of the model.

Data from the MPS SN001 and SN003 vehicles are presented herein.

### III. INSTRUMENTATION AND DATA REDUCTION

A data reduction program was set up to calculate the important performance parameters from the instrumentation measurements made during the wind tunnel testing of the MPS rig. Standard wind tunnel procedures were used to obtain free-stream total and static pressures and temperatures, tunnel Mach number, velocity, density and Reynolds number. The basic MPS measurements included the blade angle, rotational speed, axial thrust and torque for each of the counter-rotating blade hubs. Force balance measurements were corrected for dynamic effects to get the true thrust and torque values. Four of the blades on each hub are instrumented with three strain gages each. Signals from these strain gages are routed through telemetry to a 14 track magnetic tape and monitoring equipment in the control room.

Five rows of thirteen static pressures are located on the nacelle forebody from the nose to the forward rotor leading edge. Four rows of twelve static pressure are located on the afterbody downstream of the aft rotor trailing edge to the point where the afterbody shape blends into the 6 inch diameter cylinder just ahead of the turbine housing and support strut. Static pressure measurements on the MPS forebody and afterbody as well as in the cavities between rotors were used to correct the forces measured by the hub balances, FBALC1 and FBALC2. A schematic of the MPS in Figure 4 shows the location and direction of all the forces acting on the model. The body pressures are integrated over incremental projected areas assigned to each static pressure tap.

The resultant forces, FFB and FAB, are calculated for both the blades-on and blades-off configurations and used in the equations (below) to define the total effective blade thrust. The hub balance force data are corrected for the upstream and downstream hub face pressure integrals. Static pressure taps on the upstream and downstream faces of the rotors at different radial positions in the cavities beneath the flowpath are area-averaged and represent tare force corrections (FHU and FHD) to the hub balance thrust measurements. The hub forces measured with blades off (FH1 and FH2) are equal to or very nearly zero for both high speed wind tunnel tests.

The MPS effective thrust includes the change in nacelle forces due to the action of the blading. Effective thrust can be calculated as the change in hub thrust, with-blades minus without-blades, plus the change in nacelle body forces (i.e. the forebody and afterbody pressure integrals) with and without blades. Each rotor thrust is credited (or debited) by half of the forebody induced force and half of the afterbody induced drag. The resultant equations (1) and (2) for the effective thrust of each rotor are:

$$\text{FEF1} = \text{FBALC1} + \text{FH1U} + \text{FH1D} - 1/2 [\Delta\text{FFB} + \Delta\text{FAB}]_* - \text{FH1}_{**} \quad (1)$$

and

$$\text{FEF2} = \text{FBALC2} + \text{FH2U} + \text{FH2D} - 1/2 [\Delta\text{FFB} + \Delta\text{FAB}]_* - \text{FH2}_{**} \quad (2)$$

\*Blades On Minus Blades Off  
\*\* Blades Off

The total propulsor effective thrust (3) is the sum of the two individual rotor thrusts:

$$\text{FEF} = \text{FEF1} + \text{FEF2} \quad (3)$$

The total effective thrust (FEF) is then used to determine the propulsor net efficiency:

$$\eta_{NET} = \frac{FEF \times V_0}{550 \text{ SHP}} \quad (4)$$

In summary, the effective thrust is determined by using the blades-on rotor force, first corrected for the tare force (integrated hub face pressure), then corrected for blading induced body forces (blades-on versus blades-off forebody and afterbody pressure integrals), and finally, incremented from the hub force measured with the blades removed.

#### IV. Blade Design

The unducted fan blades, named F7A7, were designed at the Mach 0.72, 35000 ft. altitude max climb flight condition. There are 8 blades in the forward rotor and 8 blades in the aft rotor, each having an activity factor of 150. The blades are designed at a high disk loading (SHP/A) of 86 to minimize the diameter and weight of the full-scale UDF<sup>TM</sup> engine. The aerodynamic design of the unducted fan blades was carried out using the general method described by Smith [4]. The design specified custom tailored airfoil and flowpath shapes designed to have favorable velocity distributions with minimum-strength shocks. The composite construction and moderate sweep cause the blades to deform substantially from the static to the running condition, and a finite-element elastic model was employed to account for this change. However, after the airfoil molds were made, the originally intended stiffness in the chordwise direction was increased, resulting in airfoils with 2-4° more camber than intended in the running condition. Subsequent analysis by GE and NASA [5] have indicated that the tested airfoils might have relatively strong shocks at the trailing edge.

The blades are designed and manufactured in the 24.5 inch diameter scale-model size for wind tunnel testing at sea level atmospheric pressure. The following table shows the aerodynamic design parameters of the F7A7 configuration.

TABLE IV-1

Mach No./Altitude	0.72/35000'
Advance Ratio, J	2.80
Power Coefficient, PQA	4.17
Tip Speed, ft/sec	780
Radius Ratio	0.42
Total Activity Factor	2400
Aero Tip Sweep, FWD/AFT, deg.	33/29

A planform sketch of the MPS forward rotor blade, F7, is shown in Figure 5. The blade is made from a composite material of graphite fibers with a titanium shank and spar extending to approximately 50% of the blade span. The blades are designed with chord, thickness and sweep distributions that will allow aero-mechanical stability over the entire operating range.

#### V. Wind Tunnel Test Data

Aerodynamic testing was conducted in the Boeing Transonic Wind Tunnel (BTWT), the NASA 8' x 6' Wind Tunnel, and the General Electric Anechoic Chamber, Cell 41. The BTWT was configured with acoustic wall panels and the vehicle was tested at tunnel speeds from Mach 0.24 to Mach 0.81. Testing was done with and without the pylon and at angles of attack. Forward-to-aft rotor spacing effects were evaluated and reverse thrust was measured. A circumferentially traverseable rake was used to measure total pressure, total temperature and yaw angle downstream of the aft rotor for certain key aerodynamic test points. Rotor spacing effects were also investigated in the NASA tunnel. Low speed aerodynamic testing was performed in the GE anechoic chamber.

The F7A7 blades were tested in the high speed wind tunnels over a wide range of Mach numbers, pitch angles and rotor speeds. The blades were first set to pitch angles that would give equal rotor torques at design speed and the tunnel was brought up to the test Mach number with the blades windmilling. The rotors were powered to the minimum speed above windmill and data were taken with equal rotor speeds at several increments up to 110% design speed. The tunnel Mach number was then adjusted slightly up and down from the nominal setting and the test was repeated at the same equal rotor speed points. The initial pitch angles tested were chosen to produce the power required along the max climb flight path at 100% speed on both rotors and equal torques per stage.

#### A. Overall Performance

In the Boeing transonic wind tunnel, the data were taken at tunnel speeds from Mach 0.24 to Mach 0.81 without the pylon and at zero angle of attack. The overall performance of the F7A7 blades for these conditions is presented in Figure 6. The power coefficient, PQA, and net efficiency are plotted as a function of the advance ratio of the forward rotor,  $J_1$ . The efficiencies plotted are as-measured and do not account for strain gage effects nor dynamic model calibration. When applied to the test data, these corrections will increase the net efficiency by 2-3 points at the high Mach numbers. Each power line represents a different tunnel Mach number with a different set of pitch angles. The max climb target design point at Mach 0.72 is shown on the performance map.

The net efficiency interpolated on the performance map from the measured data to the design point is 81%. The effects of increasing Mach number can be seen by tracing the fall-off of efficiency along a constant power loading line. The data trend shows that at Mach 0.65 the efficiency at 85%, dropping to 77% at Mach 0.81. At low speed, such as the takeoff condition at Mach 0.24, the net efficiency is 62%.

Blade pitch angle variations were made at the Mach 0.24 and Mach 0.70 test conditions and the performance data are shown in Figures 7 and 8, respectively. The efficiency data when plotted versus the loading parameter,  $PQA/J_1^3$ , collapse to nearly a unique line for most of the pitch angles tested. When the loading differs greatly from the nominal value, the efficiency data will depart from a single line. This is the case at Mach 0.24 (Figure 7) with both rotors open approximately  $5^\circ$  from nominal. The blade loading is significantly higher and the efficiency is 2-3 points less than nominal pitch angle data. At Mach 0.70 (Figure 8), the three pitch angle settings vary only 1-2 degrees from each other and produce efficiency levels within 0.5 point. The most open setting with the blades running slower for the same power absorbed gives slightly higher efficiency.

#### B. Rotor Spacing Effects

Rotor spacing effects were investigated at Mach 0.80 with three different spacings of the rotor pitch-change axes. The spacings varied from the minimum axial distance to blade diameter ratio of .14 to the maximum value of .24. The nominal distance for which most of the wind tunnel testing was conducted was 4.16 inches. Figure 9 shows that for larger spacing between rotors, less power is absorbed by the rotors at the same advance ratio, even though the pitch angles are held constant. The spacing effect on efficiency is shown in Figure 10 by plotting the data versus the power loading parameter,  $PQA/J_1^3$ . The minimum spacing gives the highest efficiency at all Mach 0.8 loading levels, approximately 1.0 to 1.5 points higher than the nominal spacing. The maximum spacing is 2 points worse in efficiency than the nominal spacing. Other F7A7 wind tunnel data (Figure 11) show that at slightly lower Mach numbers, down to Mach 0.67, the nominal to maximum spacing effect is 1-2 points in net efficiency, while the minimum to nominal effect is less. At takeoff Mach 0.25, the test data indicate that rotor spacing has little or no effect on net efficiency.

The proximity of the downstream rotor to the upstream rotor has a pronounced effect on the torque split between rotors. Data are shown in Figure 12 for three different spacings. At equal power and RPM, the total torque remains the same but the split between rotors is different. The torque ratio ( $Q_2/Q_1$ ) decreases as spacing increases since the induced effect of the downstream rotor is diminished. If the spacing was further increased, the effect would continue to lessen to the extreme condition where the downstream rotor is so far removed from the upstream rotor that it acts as an isolated blade row having no effect at all.

#### C. Angle of Attack/Pylon Effects

Aerodynamic performance data taken in the transonic wind tunnel to assess the effect of angle of attack, with and without pylon, at Mach 0.24 and Mach 0.70, are shown in Figures 13 through 16. The three graphs in Figure 13 show the net efficiency, power coefficient and torque ratio parameters as a function of advance ratio for the F7A7 configuration without pylon at Mach 0.24. Data are shown for three angles of attack, 0, 5 and 16 degrees, with constant pitch angles. Similar data are shown in Figure 14 at Mach 0.70 at zero and two degrees angle of attack. Since the model is rotated in the tunnel on a platform by the angle of attack ( $\alpha$ ) the free-stream velocity ( $V_0$ ) in the direction of thrust is equivalent to  $V_0 \cos \alpha$ . Correcting the advance ratio,  $J_1$ , by the cosine  $\alpha$  causes the data to collapse to one curve for all angles of attack on the power coefficient plot. The effect on the torque ratio lines is to spread them farther apart with increasing angle of attack.

The measured thrust is in the direction of the model centerline axis skewed from the free-stream tunnel direction by the angle of attack. The normal force on the blades as a result of the model direction relative to the

airflow was not measured, and its streamwise component is therefore not accounted for in the efficiency calculation. The word "apparent" has been added to the efficiency label to indicate that it is not a true efficiency.

With the pylon installed at the bottom of the model, as shown in the photograph of Figure 1, the test points are repeated at the same Mach numbers and blade pitch angles. The power coefficient, apparent net efficiency and torque ratio data are shown in Figures 15 & 16. Since the pylon drag is not measured by the rotor force balances and not otherwise accounted for in the overall thrust, the apparent efficiency values with pylon on are approximately the same as the pylon off data, but slightly higher. Now, the free-stream velocity correction is no longer appropriate to collapse the power coefficient lines because of the angular momentum change caused by the pylon. The pylon effect is most noticeable in how it affects the level of torque ratio. With increasing angle of attack, the pylon acts like an inlet guide vane producing counter swirl into the forward rotor and loading it relative to the aft rotor. The schematic of the MPS in the wind tunnel, Figure 17, shows that positive angles of attack produce counter-swirl into the forward rotor, negative angles produce pre-swirl.

In Figure 15 at Mach 0.24, the aft-to-forward rotor torque ratio ( $Q_2/Q_1$ ), varies from 1.0 at zero angle of attack to 0.85 at  $5^\circ$  and 0.60 at  $16^\circ$ . The large split in torque per stage, observed from test with constant pitch angles and constant speeds, will be corrected in the installed engine by varying blade pitch angles and maintaining equal speeds as the airplane climbs out from takeoff at some angle of attack. The direction of pitch angle change will also vary from right-hand engine to left-hand engine since the direction of forward rotation is down inboard on the airplane right side and up inboard on the left side. An estimate of the amount of angle change required to offset unequal torques is shown in Figure 18. Data from low-speed tests at Mach 0, .2 and .4 were cross-plotted to obtain the amount of  $\beta_2$  change, holding  $\beta_1$  constant, as a function of torque ratio.

#### D. Mis-Matched Rotor Speeds

Wind tunnel data were taken at Mach 0.72 with unequal rotor speeds over a wide range of RPM's. Figure 19 shows the net efficiency plotted against the loading parameter,  $PQA/J^3$ , for two different speed ratio lines as well as equal rotor speed reference data. Testing was conducted with the aft rotor speed 10% higher and 10% lower than the forward rotor speed. Holding the pitch angles constant, as was necessary in this type of test, means the rotor torque splits are not equal as the RPMs are increased. When rotor 2 is running 10% faster than rotor 1, the ratio of rotor 2 to rotor 1 torque varies between 1.04 and 1.32. When rotor 2 is running 10% slower, its torque varies between 23% and 74% of the rotor 1 torque. The data show that the net efficiency is higher at low loadings when the torques are within 25% of being equal. The lower efficiency line ( $N_2/N_1 = .91$ ), at low loadings, shows torque ratios that are much less matched and consequently, lower efficiencies. At the high loading levels, however, the data show that when the torque ratios are within 25% of being matched, the speed ratio has little effect on the net efficiency. By comparing all the data shown in Figure 19, the test points with torque ratios closest to 1.0 have the highest efficiencies.

#### E. Design Point Data Match

Data were recorded in the high speed wind tunnel near the design Mach 0.72 condition with a circumferentially traverseable rake at the exit of the second rotor. The rake measured total pressure, total temperature and swirl angle at 15 radial locations which spanned from the rotor hub to an outer tip radius approximately 10% above the blade tips. The rake was traverseable through an arc of  $60^\circ$ , from  $135^\circ$  to  $195^\circ$ . Data were taken in five-15 degree increments, without pylon and at zero angle of attack, with the model operating at the tunnel Mach number of 0.70. In addition to the rake measurements, nacelle forebody and afterbody static pressures were measured. The rake and body pressure data were used to compare with the design analytical calculation of the circumferential average flowfield.

Detailed aerodynamic data-match studies were conducted using the test data to determine areas of the blade where improvements could be made to reduce losses. The data match analysis was performed by using a modified version of the circumferential-average flow calculation procedure that is used for designing and analyzing conventional high bypass turbofans. The data match test point was taken at Mach 0.70, design power coefficient of 4.17 and at the design advance ratio of 2.80. The procedure begins by inputting speed and torque for each rotor (measured from test) and adjusting the radial distribution of losses until the net thrust, body static pressure distributions, and the fan exit radial pressure profile are reasonably well matched.

The total airflow is adjusted so that the tip streamline matches the forward rotor blade tip diameter. Figure 20 illustrates the flow field that results when the data are matched. Meridional Mach number contours are

superimposed on the chart with the flow streamlines and calculation stations; the rake plane location is also noted. The peak Mach number of 0.82 occurs inside the blades where the effects of thickness and lean are accounted for in the calculation. A hub boundary layer is specified to represent the flow losses near the hub surface. Figure 21 shows the data match of the pressure and temperature measurements at the discharge rake plane. Since no data between the rotors were taken, it was necessary to assume the loss split. The symbols in these plots distinguish the aerodynamic design intent from the actual test data results. The data match analysis using the test data matches the original design intent quite well over most of the blade span. Locally in the hub region, where the boundary layer affects the test measurements, the blade total pressure falls off and the loss coefficients are higher than design intent.

The distribution of static pressure coefficient as a function of axial length along the forebody and afterbody of the MPS rig are shown in Figure 22. The data matches the theoretical expectations quite well and confirms the static pressure rise on the after body and where the hub necks down to a cylindrical body downstream of the blades.

#### VI. Conclusions

The scale model, counter-rotating unducted fan blades, F7A7, were tested in the Boeing and NASA high speed wind tunnels and the aerodynamic performance has been demonstrated. The following lists the most significant performance results:

- o Aero data were obtained with several blade angle combinations up to Mach 0.81. The measured net efficiency at the max climb Mach 0.72 design point is 81%; at takeoff, the net efficiency is 62%.
- o Large rotor spacings have a significant effect on net efficiency at high Mach numbers.
- o Power coefficient lines at different angles of attack and constant pitch angles, collapse to a single line when the advance ratio is corrected by the  $\cos\alpha$  to account for the skewed thrust direction.
- o The pylon, installed at an angle of attack, acts like an inlet guide vane, producing inlet swirl to the forward rotor. The swirl unloads or loads the forward rotor depending on the direction of rotation relative to the pylon. If pitch angles are held constant, unequal torque splits result.
- o Data taken with unequal rotor speeds show very little effect on efficiency at loadings and torque ratios near the cruise design point. When the torque ratios are substantially different from 1.0, the overall efficiency can be 2-5 points lower than nominal.
- o The design point rake data were analyzed and showed good agreement with the design intent.

#### References

- [1] Stuart, A.R., General Electric Co., "The Unducted Fan Engine," AIAA/SAE/ASME/ASCE 21st. Joint Propulsion Conference, Monterey, California, July 1985.
- [2] Mikkelsen, Daniel C., Mitchell, Glenn A., and Bober, Lawrence J., NASA Lewis Research Center, "Summary of Recent NASA Propeller Research," AGARD Fluid Dynamics Meeting on Aerodynamics and Acoustics of Propellers, Toronto, Canada, Oct. 1-4, 1984.
- [3] Delaney, B.R., Balan, C., West, H., General Electric Company, Humenik, F.M., NASA Lewis Research Center, and Craig, G., The Boeing Company, "A Model Propulsion Simulator for Evaluating Counter-Rotating Blade Characteristics," SAE Aerospace Technology Conference and Exposition, Long Beach, California, October 13-16, 1986.
- [4] Smith, Leroy H., Jr., General Electric Co., "Unducted Fan Aerodynamic Design," ASME Paper to be presented at 32nd. ASME International Gas Turbine Conference, Anaheim, California, June 1987.
- [5] Celestina, M.L., Mulac, R.A., and Adamczyk, J.J., "A Numerical Simulation of the Inviscid Flow Through a Counter-Rotating Propeller," Transactions of the ASME Journal of Turbomachinery, Vol. 108, October 1986, pgs. 187-193.



FIGURE 1

## Facility Description

Schematic of General Electric Free-Jet Noise Facility  
(Cell 41)

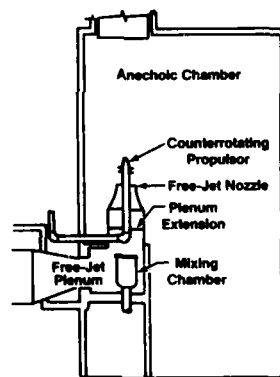


FIGURE 2

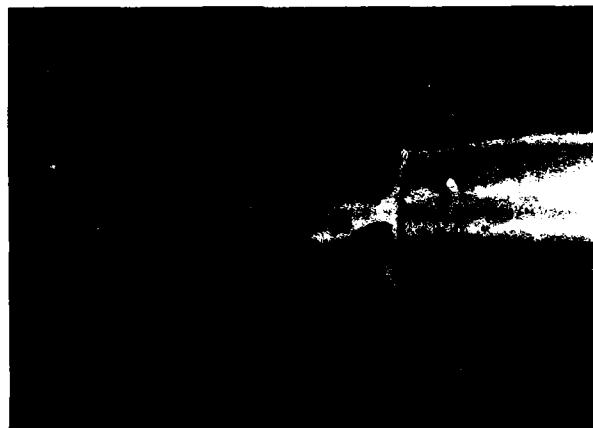


FIGURE 3



## Schematic Description of MPS Forces

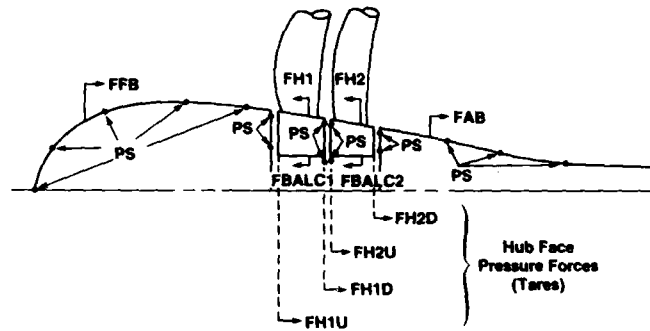


FIGURE 4

## MPS Propulsor Blade Design (F7)

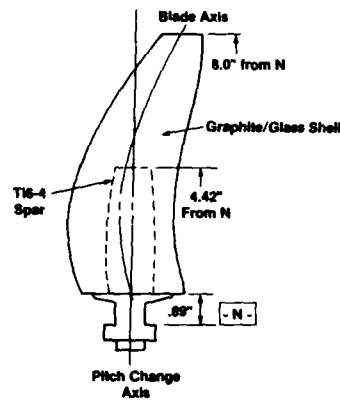


FIGURE 5

## F7A7 Performance Map

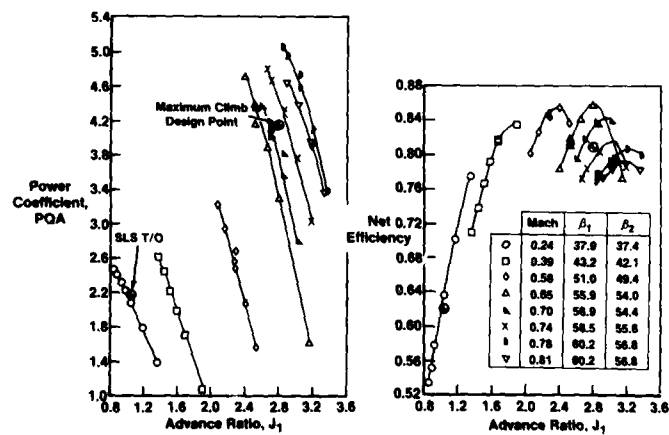


FIGURE 6

### F7A7 Blade Angle Variations at Mach 0.24 Efficiency vs. Loading Parameter

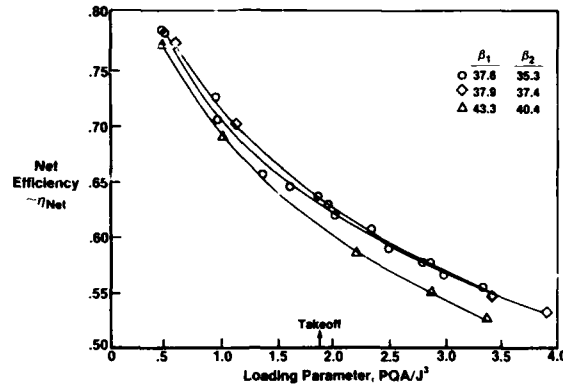


FIGURE 7

### F7A7 Net Efficiency vs. Loading Parameter Blade Angle Variations M = .70

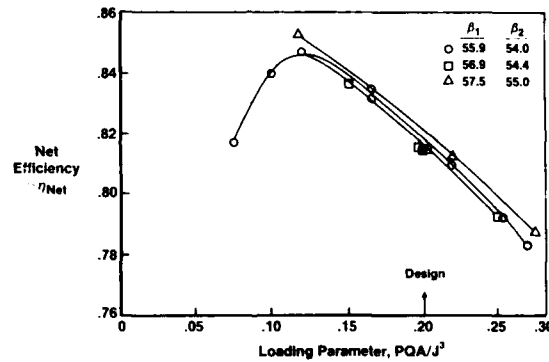


FIGURE 8

### NASA 8' x 6' F7A7 Test Results at M = .8 Total Power Coefficient vs. Forward Advance Ratio

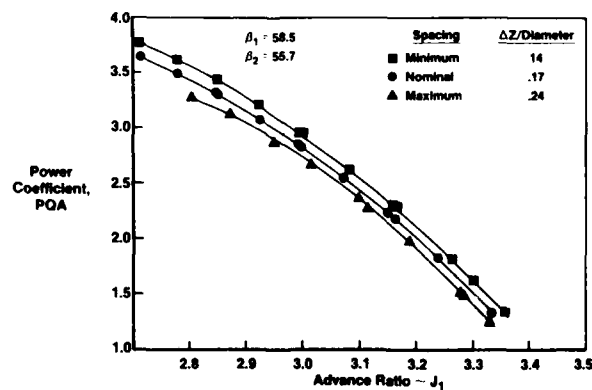


FIGURE 9

### NASA 8' x 6' F7A7 Test Results at $M = .8$ Net Efficiency vs. Power Loading Parameter

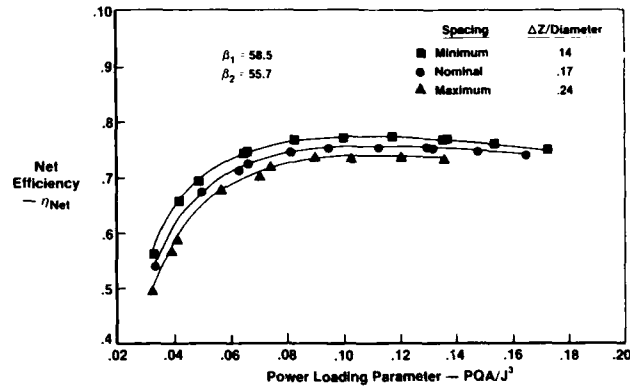


FIGURE 10

### NASA 8' x 6' Rotor Spacing Effects at Mach 0.67

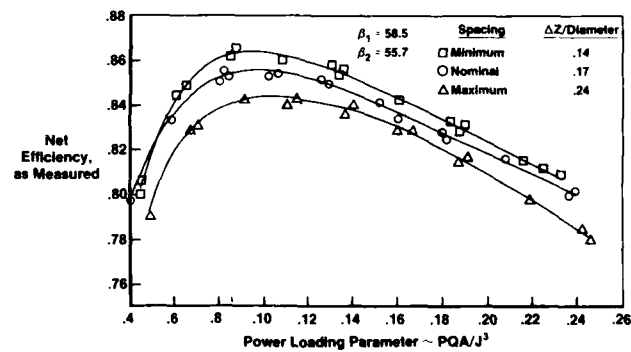


FIGURE 11

### NASA 8' x 6' F7A7 at Mach 0.72 Rotor Spacing Effects on Torque Ratio

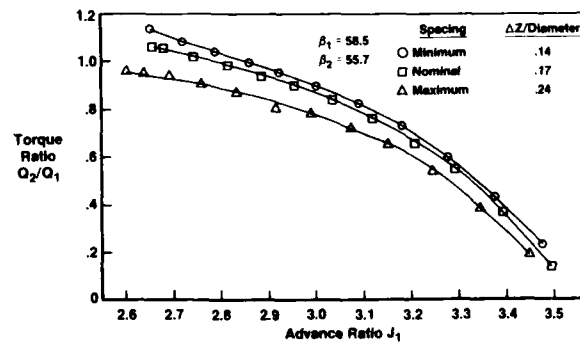


FIGURE 12

### Effect of Angle of Attack, F7A7, Mach 0.24, No Pylon

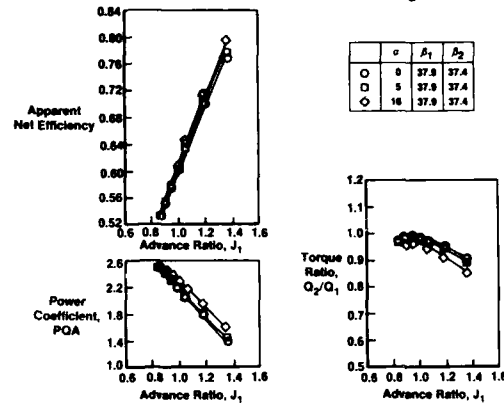


FIGURE 13

### Effect of Angle of Attack, F7A7, Mach 0.70, No Pylon

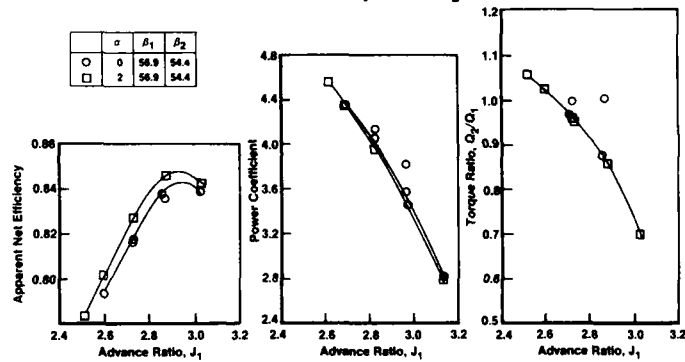


FIGURE 14

### Effect of Angle of Attack, F7A7, Mach 0.24, With Pylon

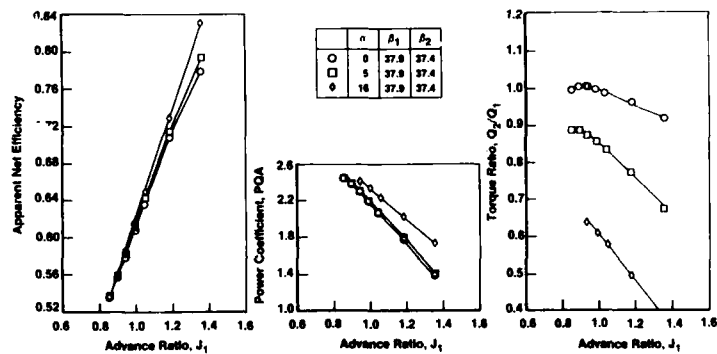


FIGURE 15

### Effect of Angle of Attack, F7A7, Mach 0.70, With Pylon

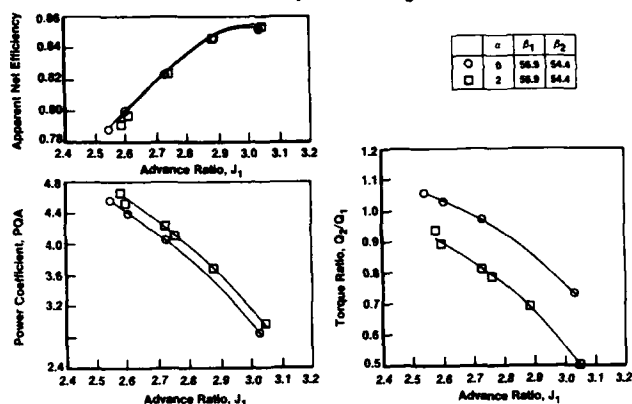


FIGURE 16

### Schematic of MPS in Transonic Wind Tunnel at Angle of Attack, With Pylon

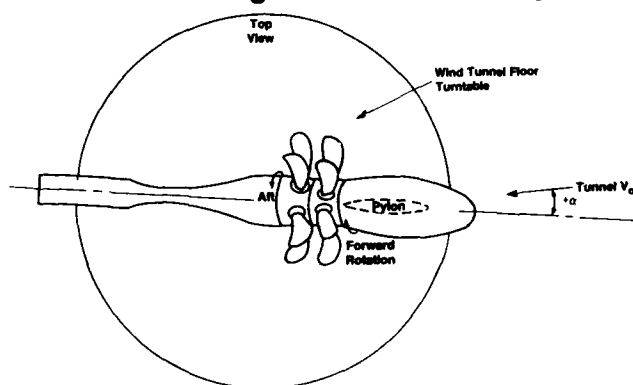


FIGURE 17

### Blade Angle Change Required to Match Torques Mach 0-.4 Equal Speeds, 100% $N_c$ $\beta_1$ Constant

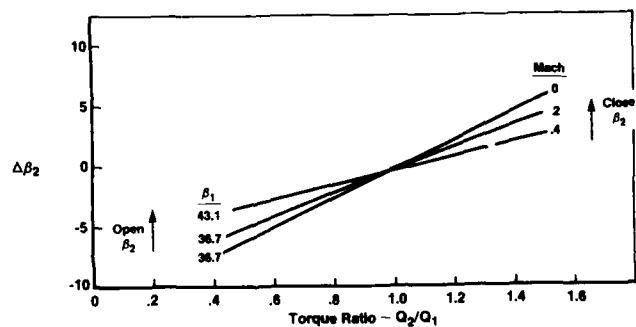


FIGURE 18

# NASA 8' x 6' F7A7 Scale-Model Performance Mach 0.72 Effect of Mis-Matched Rotor Speeds

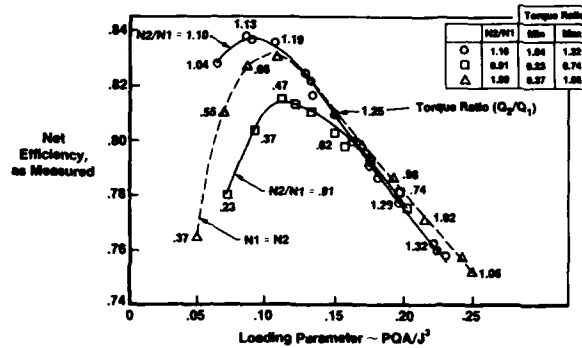


FIGURE 19

## F7A7 Flowfield $M = 0.70$ Meridional Mach Number Contours

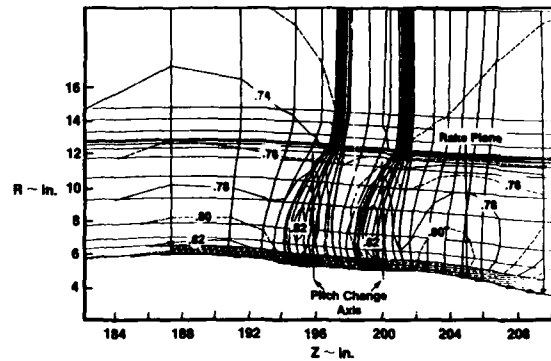


FIGURE 20

## F7A7 Data Match Results Pressure and Temperature Profiles vs. Design Intent Rotor 2 Exit Rake Plane

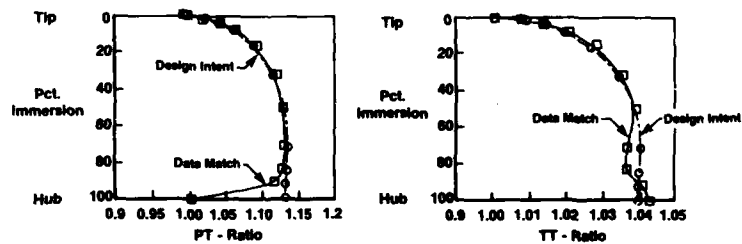


FIGURE 21

### F7A7 Data Match at Mach 0.70 Static Pressure Coefficient Along Forebody and Afterbody

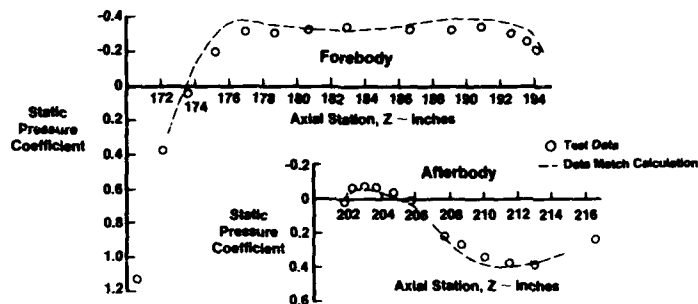


FIGURE 22

### DISCUSSION

R.G. THOMPSON, US

- 1) Was the pitch angle changed from low Mach number to high Mach number ?
- 2) Will the control system include speed sensing and pitch control ?

#### Author's Reply

Approximately three to four pitch angle settings were tested at each Mach number from Mach 0.24 to Mach 0.81. The standard test procedure was to set pitch angles at a selected Mach number which would produce the max climb path power coefficient when the forward and aft rotors were running at 100 % speed and with matched torques. Data were taken at other Mach numbers with equal forward and aft rotor speeds and torque ratios slightly less than or greater than 1.0.

In the full-scale unducted fan engine, the pitch control mechanism will vary the blade angle settings, responding to changes in flight speed and engine power requirements ; equal rotor torques will be maintained at all times.

G. WINTERFELD, Ge

Could you please comment on the effects of the spacing of the rotors on the acoustics of the UDF ?

#### Author's Reply

The UDF scale-model tests which varied the rotor-to-rotor spacing were conducted to obtain both the aerodynamic and the acoustic effects. The maximum spacing ( $\Delta Z/\text{Diameter} = .24$ ) was the most favorable from an acoustic standpoint although the net efficiency was poorer. The larger spacing allows a greater distance for the tip vortex and blade wakes to dissipate thereby reducing the noise interaction levels.

D.W. STEPHENSON, US

Please comment on the degree of agreement in the results between the Boeing and NASA wind tunnel results on unducted fan performance.

Author's Reply

The initial test results obtained from the Boeing wind tunnel test did not correctly account for the MPS support strut and turbine housing blockage interference. When the tunnel velocities are corrected to account for the difference between the free stream measured Mach number and the UDF fan face Mach number, the re-calculated net efficiencies are within 0.5 point of total agreement with the NASA wind tunnel results. The Boeing test data presented in this paper include the interference effects in the efficiency calculation.

H.J. LICHTFUSS, Ge

Do you have measured thrust reverse with the UDF model, and if so, what are the amount of thrust reverse ?

Author's Reply

Reverse thrust measurements from the F7A7 blades have been made in both the Boeing transonic wind tunnel and the NASA high speed wind tunnel. The blades have operated at pitch angles 20°-30° past flat pitch without aero-mechanical instability and have produced approximately 50 % of the takeoff thrust in reverse.

C.A. MOSES, US

You have made some efficiency measurements. Are they what you expected ? How do they compare with the ducted fans and the older propellers ?

Author's Reply

The Unducted Fan is forecast to produce up to 25 to 30 % fuel reduction respect to the old by-pass fans. Efficiency we measured is within a percent of miling the prediction that we had for this blade. There are several others blades under development and we are very close to miling the requirements for the engine cycle that will give us a 25-30 % improvement over ducted fans.

J.M. BOUSQUET, Fr

Do you plan pressure measurements on the blades or laser velocimetry analysis of the flow field on your UDF models ?

Author's Reply

Yes ! Laser velocimeter measurements are planned for future UDF scale-model tests at NASA - Lewis 8' x 6' wind tunnel.



## GEAR SYSTEMS FOR ADVANCED TURBOPROPS

by

Douglas A. Wagner

Supervisor - Mechanical Design

Allison Gas Turbine Division  
 General Motors Corporation  
 P. O. Box 420  
 Indianapolis, Indiana 46206-0420

**ABSTRACT**

A new generation of transport aircraft will be powered by efficient, advanced turboprop propulsion systems. Systems that develop 5000 to 15,000 horsepower have been studied. Reduction gearing for these advanced propulsion systems is discussed in this paper. Allison Gas Turbine Division experience with the 5000 horsepower reduction gearing for the T56 engine is reviewed and the impact of that experience on advanced gear systems is considered. Gear system arrangements are analyzed, including single- and counter-rotation types. The reliability needs for component design and development are also considered. Allison's experience and their research serve as a basis on which to characterize future gear systems that emphasize low cost and high reliability.

**INTRODUCTION**

Allison has been active in the design, development, and production of turboprop gear systems for over forty years. This work has involved both commercial and military applications of large reduction gear systems. The propulsive efficiency of turbine driven propellers suggests that gear systems for these applications will continue to be with us for years to come. It is, therefore, worth while to take note of the lessons learned from existing turboprop gear systems and see what these lessons suggest for future generations of gear systems. The superior fuel efficiency of propellers and propfans when compared to turbofans (Figure 1) has created a resurgent interest in these propulsion devices as a means to mitigate the effects of expected fuel price increases. Propfan propulsion studies have in turn initiated new interest in large reduction gear systems.

This paper will review Allison's experience with the T56 gear system, consider the gear system studies ongoing since the 1970's (sponsored by NASA and Allison), and then suggest characteristics of gear system design that develop from this background.

**T56 GEAR SYSTEM DESCRIPTION**

The T56 gear system is used in many different aircraft. Military applications include the P-3, C130, C-2, and E-2. Commercial applications have included the Lockheed Electra and Convair 580. Over 100 million flight hours of experience have been accumulated since this gear system was first produced for the C130 in 1954.

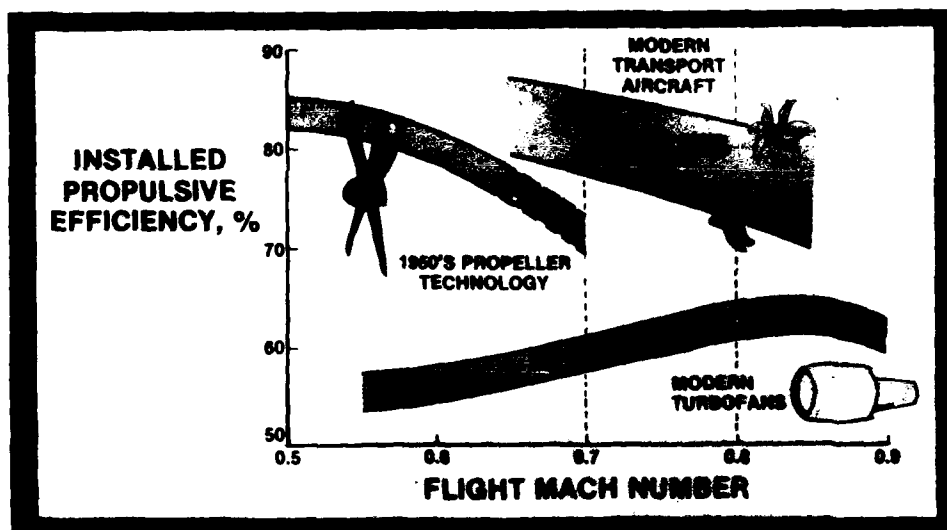


Figure 1. Propulsion Efficiency of Propfans Versus Turbofans.

The T56 gear system (Figure 2) reduces the turbine speed of 13,200 rpm to a propeller rpm of 1020. This overall reduction gear ratio of 13.54:1 is accomplished in two stages. The first stage reduction of 3.125:1 is by a spur gear train, and the second stage reduction of 4.333:1 by a planetary gear train.

In addition to the reduction gearing required by the propeller, an accessory drive gear train (Figure 3) is included for externally mounted accessories such as an alternator, hydraulic pump, starter, and tachometer generator. The accessory drive gear train also drives the pressure oil pump. The externally mounted accessories on the reduction gear assembly are not the same on all engines of a multi-engine aircraft, due to the design requirements of the airframe systems.

The reduction gear assembly also contains the devices or systems which protect the aircraft from excessive propeller drag and negative torque in the event of engine failure

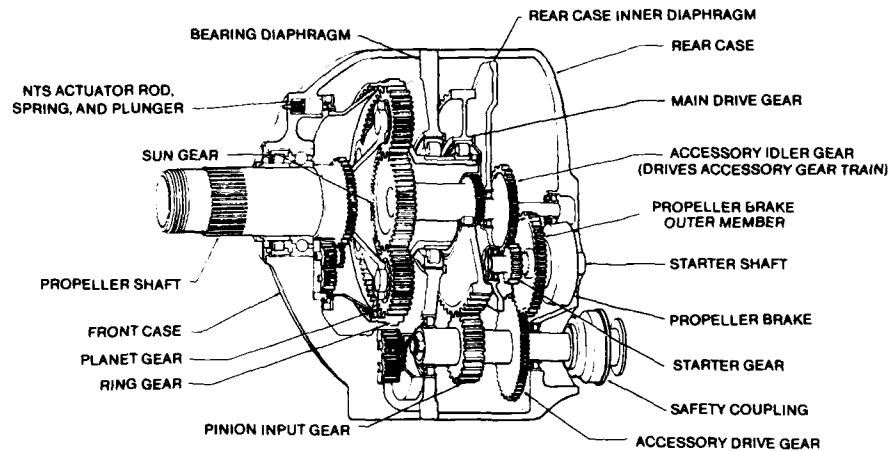


Figure 2. T56 Engine Reduction Gear System.

VS87-1329  
T512

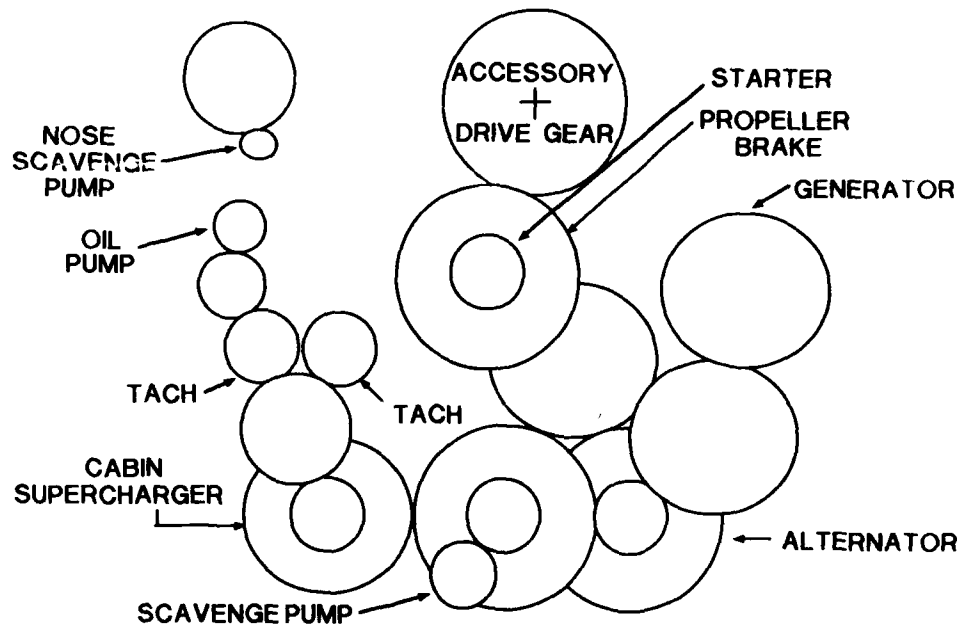


Figure 3. Accessory Drive Gear Train.

on takeoff, climb, cruise, letdown, or approach. It incorporates a propeller brake assembly which prevents rotation of the propeller when feathered in flight.

The case structure is magnesium and the gearing is AISI 9310 steel. While this gear system transmits over 5000 horsepower, its overall weight is only 560 pounds.

#### T56 GEAR SYSTEM PERFORMANCE

The original T56 gear system was designed to operate in a military application at 3750 horsepower during takeoff. The basic life criteria at the time of design was the requirement to complete a 150 hour qualification test without failure. This system has been upgraded over the years (without external change) to the point where it now transmits over 5000 horsepower and demonstrates a reliability of 4000 to 8000 hours MTBUR (mean time between unscheduled removals) and an efficiency of greater than 98.9%.

The reliability experience of the T56 gear system is even more remarkable when one considers the various causes of removal (Figure 4). Over half the removals are due to accessory drive system failures. Approximately 38% are due to main power train bearings and only 1% are associated with main power train gears. The high percentage of accessory drive and main bearing failures is better understood when one remembers that this gear system was originally designed to pass a 150 hour qualification test at an input power of 3750 horsepower.

#### ADVANCED GEAR SYSTEM STUDIES

Allison has participated in a number of gear system studies that started in the 1970's, some of which were NASA sponsored. While these studies focused on large, commercial, propeller or propfan driven aircraft, the results are also applicable to military transports. These studies provided an excellent opportunity for Allison to review their turboprop gear system design and experience and extrapolate to next generation aircraft.

#### RELIABILITY AND MAINTAINABILITY STUDIES

A study (Reference 1) of turboprop systems reliability and maintenance costs was conducted to achieve the following objectives:

- o to identify and understand the overall and relative Reliability and Maintenance Costs (R&MCs) of the gearbox of past and current turboprop systems
- o to quantitatively project the R&MC improvements that could reasonably be expected to occur from these levels to those of new turboprop systems becoming operational in the 1985-1990 time period

The scope of effort consisted of two tasks which correspond to the objectives:

- o Task I--To conduct an analysis of current and past turboprop propulsion systems to determine the principal factors that have affected their reliability and main-

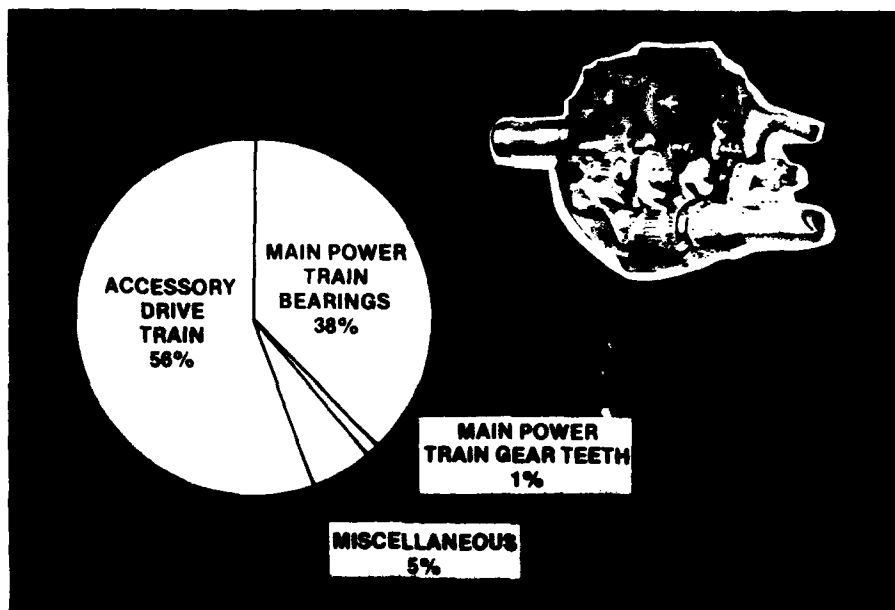


Figure 4. T56 Gearbox Removal Causes.

tenance costs, and to establish an overall baseline comparison with current turbofans.

- o Task II--On the basis of the results of Task I and the incorporation of new design practices, new maintenance practices, and projected technology advances, determine quantitatively the R&MC improvement that could reasonably be expected for systems becoming operational in 1985-1990 over turboprop levels at the time of the study. Recommended actions and R&E programs to achieve the projected advances were to be defined.

In identifying and understanding the overall and relative R&MC's of past and current turboprop systems it was recognized that the real era of turboprop usage by the domestic airlines was in the early to mid 1960's. The Allison T56 (501-D13 commercial) turboprop engine was chosen for analysis of past systems because of wide usage on the Lockheed Electra and Convair 580 commercial airliners. The main drive reduction gearbox, was a military design of the 1950's that was designed on the basis of a scheduled overhaul philosophy. For the airlines, these scheduled overhauls occurred every 4000 to 9000 engine flight hours (TBOs). It was found that the cost of the scheduled overhauls accounted for 40 percent of the total maintenance cost of each of these major modules, and were the primary maintenance cost driver of the system. A very positive conclusion was drawn that a new turboprop system would embody the "On-Condition" philosophy that would eliminate scheduled overhauls. This philosophy would be facilitated by:

- o improved reliability where numbers of parts would be lowered and all parts would be designed for high durability and long life of 35,000 hours where possible
- o improved diagnostics utilizing newly developed automatic conditions monitoring techniques for better fault detection and isolation

Increased modularity was found to be an essential requirement in a new turboprop system. The reduction gearbox of the T56 system incorporated three primary functions: the main drive reduction between the engine and propeller, a drive system for engine accessories, and a drive system for aircraft accessories. Problems in any one system usually required complete gearbox removal, including the propeller. A new system would make the main drive gearbox a simple system for just that purpose, incorporating high reliability in its bearings and gears for minimization of removal of either propeller or gearbox. The engine accessory drive system and aircraft accessory drive system would be individual modules (Figure 5), facilitating access and removal independently of the main drive reduction gear (Reference 2).

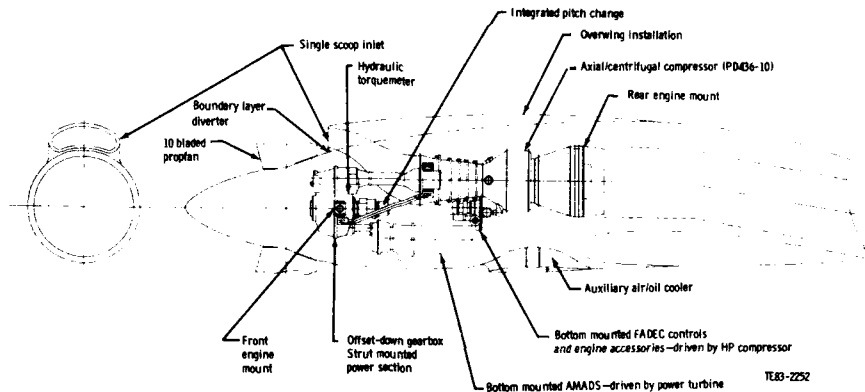


Figure 5. Modular Accessories.

Maintenance costs for the reduction gear system and other propulsion system components were reviewed. The conclusion was that an advanced turboprop and an advanced turbofan, using similar cores, will have very competitive maintenance costs per flight hour.

#### CONFIGURATION STUDIES

Allison has studied the design for turboprop propulsion systems for commercial airliners of the 1990's. These studies have focused on identifying the engine cycles that would result in the most favorable fuel consumption for a 120 passenger advanced technology airplane operating at 0.72 Mach at 32,000 ft. altitude. Several engine configurations were considered, and conceptual designs for engine configurations were defined. The results of the aircraft/engine evaluation indicate that the propfan-powered aircraft has a significantly lower fuel consumption than the turbofan-powered aircraft. This fuel savings is as much as 18.6%. On an economic basis, the comparison shows up to 9.7% lower direct operating cost (DOC) for the propfan. The DOC advantage is primarily caused by less fuel burned and lower propulsion system maintenance cost.

One objective of this design activity was to define, in detail, components for both single-rotation (SR) and counter-rotation (CR) gear systems as they would apply to production propfan airplanes of the 1990s. In the case of the SR gearbox, the dual compound idler gear arrangement (Figure 6) was selected for the preliminary design to take advantage of the accessibility to the propfan drive shaft for propeller controls and to simplify packaging of the accessories and engine with a contoured nacelle. Allison's SR gearbox design is fully compatible with specific needs of advanced pitch change systems. Oil supply and a high-speed drive are provided for the hydraulics and heat rejection requirements of the pitch change.

The differential planetary gearing arrangement (Figure 7) was selected as the favored configuration for the counter-rotating propfan system (Reference 3). This is an in-line design that is very compact. It is also light weight, efficient (99.2% at cruise), and designed for long life (30,000 hr MTBUR). Helical gears were used because of their increased contact ratio, resulting in low vibration levels and enhanced life.

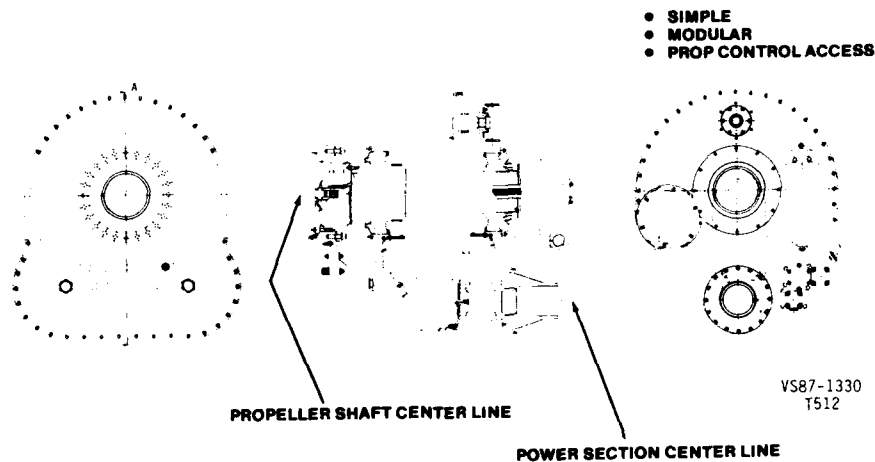


Figure 6. Basic Dual Compound Idler Gearbox Powertrain.

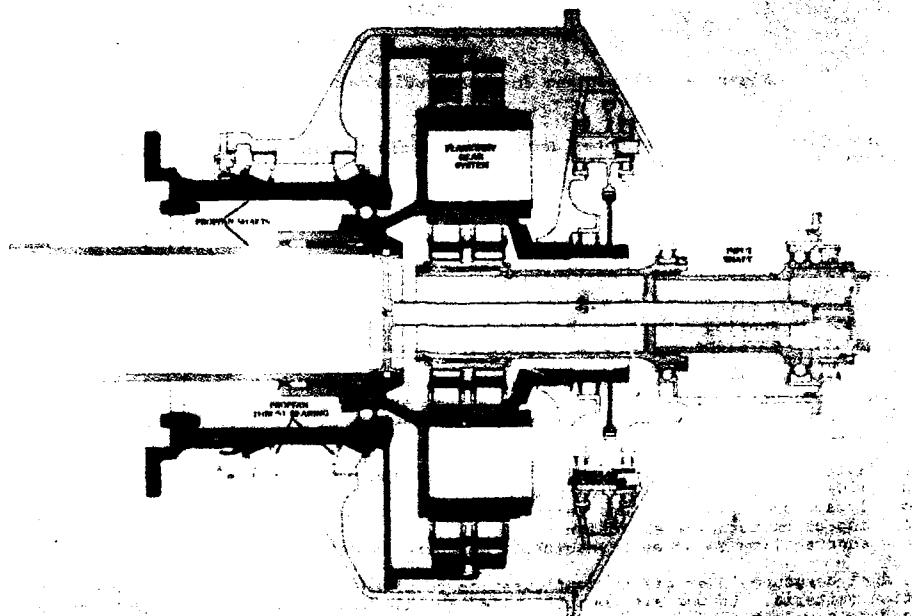


Figure 7. Differential Planetary Gearing for Counter-Rotating System.

A study (Reference 4) was performed to define a single-rotation, 10,000 shp class, advanced technology propfan gearbox. A configuration selection procedure was performed to arrive at the favored gearing and bearing arrangement for the preliminary design phase. This evaluation considered both in-line and offset input-to-output shafting as indicated by the star and dual compound idler gearing types shown in Figure 8.

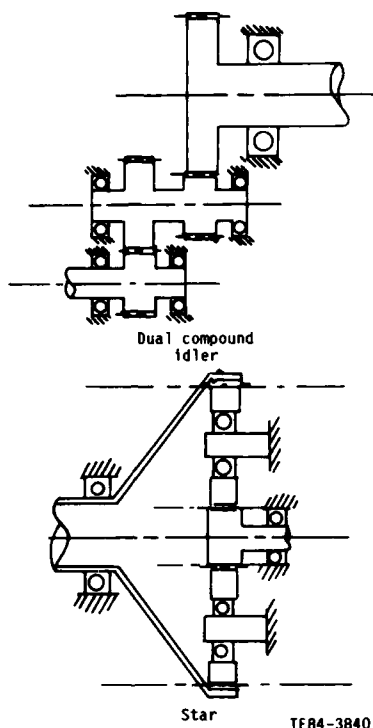


Figure 8. Offset and In-Line Candidate Gearbox Arrangements.

The procedure involved a weighted decision analysis to rank the candidate configurations relative to nine parameters:

- o reliability
- o efficiency
- o maintenance cost
- o acquisition cost
- o propfan pitch change compatibility
- o weight
- o technical risk
- o ease of scaling
- o spatial envelope

Reliability and efficiency, the most important criteria, were essentially the same for all the candidates. The remaining seven parameters favored the dual compound idler system. However, due to the closeness of the results, five additional criteria were used in the evaluation:

- o adaptability of the configuration to over- and under-wing mounting
- o impact on inlet duct efficiency
- o impact on reliability and maintainability of gearbox and airframe accessory drives
- o impact on torque meter design
- o adaptability to an aerodynamically contoured nacelle

The dual compound idler offset configuration received higher ratings for these installation criteria. It was also better suited for use with a hydraulic torque meter, which leads to a weight saving over the phase detector type torque meter required for the star planetary configuration. The overall rating of the dual compound idler offset gearbox was greater.

The dual compound idler gear arrangement selected was composed of a single input pinion, two idler gears, and an output gear, as shown in Figure 6. The idlers are compound gears consisting of two gears per idler. Power is applied to the input pinion gear, split through the idlers, and recombined in the output gear.

Features of this type of gearbox are summarized as follows:

- o load sharing--equalizes loads on each idler and provides for torque meter readout
- o modularity--provides external accessibility
- o prop load isolation--minimizes gear misalignment

The gearbox design included provisions for accessories required by the propfan pitch change system, such as an oil pump and high speed drive, a propfan brake, an airframe accessory drive, a gearbox oil pump, and an oil filter.

Studies were conducted to define a counter-rotation (CR), 10,000-shp class, advanced technology propfan gearbox for a 300 nautical mile commercial mission. This design incorporated the requirements for a tractor wing-mounted CR propfan propulsion system.

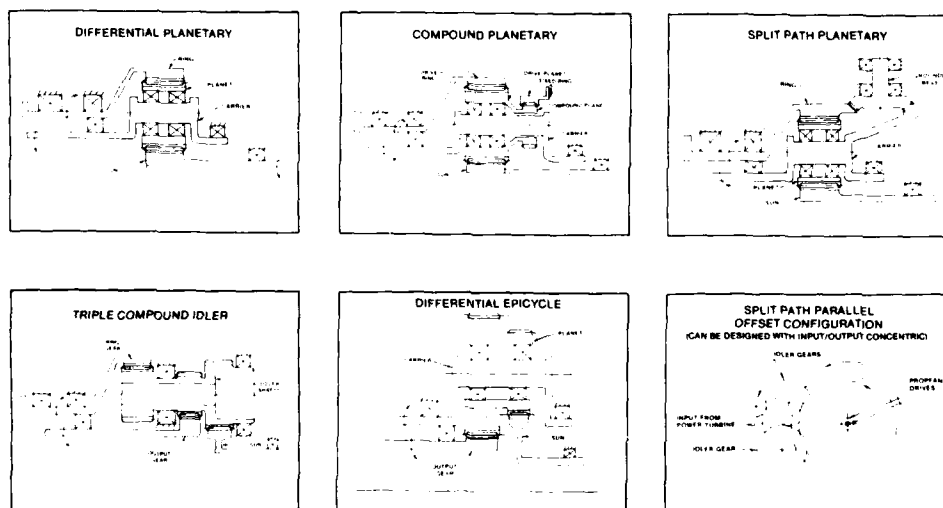
The gearbox study consisted of the following phases:

- o a configuration selection procedure to establish the design concept
- o gear and bearing type selection based primarily on long life and efficiency considerations similar to the single rotation selection.
- o design of the general arrangement including the main gear train, accessory gearing, mounts and lubrication system.
- o design analysis to estimate bearing life, gear stresses, heat rejection to the oil and surroundings, and integrity of the supporting structure.
- o propfan interface requirements.
- o modifications required for converting this tractor gearbox arrangement to a pusher configuration.

Six candidate configurations (Figure 9) were evaluated for the counter-rotating gearbox. The best configuration was determined through a series of competitions between the candidate configurations: differential planetary, compound planetary, split path parallel offset, triple compound idler, differential epicyclic and split path planetary concepts. The differential planetary gear set was selected.

A general arrangement of the advanced technology CR propfan gearbox is shown in Figure 7. The gearbox main power gear train is a differential planetary gear set with four planet gears. The sun gear is driven by the input shaft, the outer output shaft is driven by the ring gear, and the inner output shaft is driven by the planet gear carrier.

The CR gearbox was analyzed for power loss to determine both gearbox performance and cooling requirements. Considered in these calculations were gear power loss, tapered roller bearing power loss, and oil pump loss. The results of the CR gearbox power loss analysis are shown in Figure 10. Efficiency of this gearbox arrangement is very high, 99.18% at cruise and 99.24% at full power.



VSC7-1326  
T512

Figure 9. Counter-Rotation Candidate Configurations.

# GEARBOX POWER LOSS BREAKDOWN

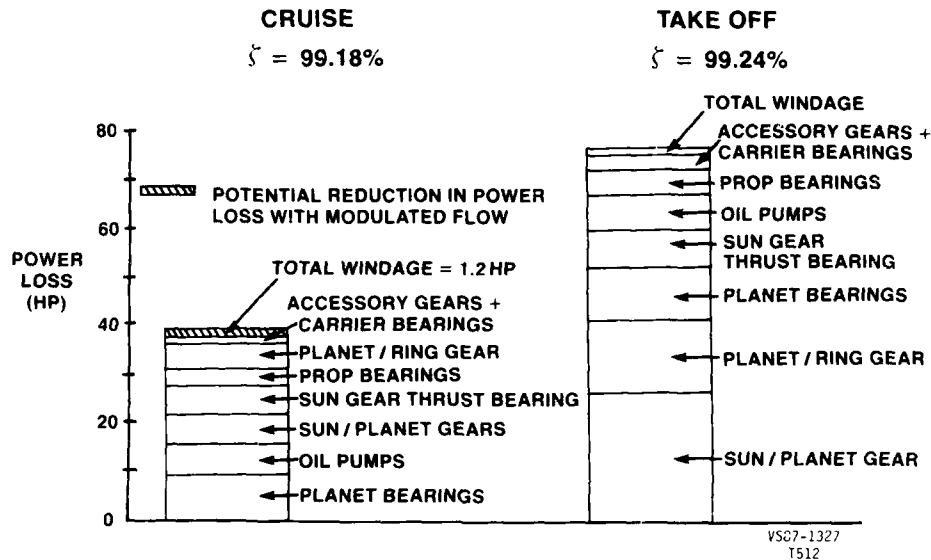


Figure 10. Gearbox Power Loss Analysis.

## CONCLUSIONS

The Allison T56 gear system experience, and the studies reviewed herein, serve to provide excellent guidance for new gear systems.

1. Reduction gearing has been developed to be very efficient. The T56 operates in the 98.9% or better range and new systems will be this efficient also. Overall gear system heat rejection will not be a major detractor in considering their use.
2. The reduction gearing used in the T56 application has been quite reliable, 8000 hours MTBUR in some applications. New gear systems will be even more reliable. They will be designed to meet the needs of modern transports and will be expected to achieve reliability levels equivalent to other major propulsion system components. Gear system components will be selected to achieve a MTBUR of 20,000 hours to 30,000 hours depending on basic system requirements and weight/cost trade-offs.
3. Cost of ownership will be positively influenced by modular design, on-condition repair and condition monitoring that can provide timely notice of impending problems. This suggests that new reduction gear systems will tend to be less complicated than the T56 gear system that has been so very successful.

## REFERENCES

1. NASA; "Study of Turboprop Systems Reliability and Maintenance Costs"; 1978; NASA CR-135192, prepared by Allison Gas Turbine for NASA under Contract NAS 3-20057
2. W. L. McIntire, D. A. Wagner; ASME; "Next Generation Turboprop Gearboxes"; 1982; ASME publication number 82-GT-236
3. D. J. Holt; "Will Propfans Require Gearboxes"; SAE Aero Space Engineering February 1985, Pages 12-17
4. R. D. Anderson, D. A. Wagner, R. E. Devlin, A. S. Novick; AIAA; "Advanced Propfan Drive System Characteristics and Technology Needs"; 1984, AIAA-84-1194



### DISCUSSION

H.I.H. SARAVANAMUTTOO, Ca

It is noted that only 1 % of removals occurred because of the main gear train. Could you say how many of these led to loss of propeller load ? On the T56, being a single shaft engine, overspeed is not a serious problem because of the compressor load. On a free turbine, however, the power turbine may suffer severe overspeeding. It is useful to remember the loss of the second Bristol Britania prototype in 1953, directly resulting from a gear box failure leading to catastrophic power turbine disintegration and fire. Hopefully we are now much better equipped to withstand turbine failures, e.g. by blade containment rings or fused blades, permitting the blades to fail before the disc overspeed.

#### Author's Reply

I am not aware of any instances where tooth failure has led to turbine over speed and/or loss of load.

Our current work recognizes that loss of load on a free turbine machine is serious. This concern is addressed in the mechanical design of the turbine and by features in the fuel control system.

Our gear design effort places a high degree of conservatism in the area of tooth breakage. Our quality control in manufacturing also is very concerned with avoiding tooth breakage.

W.G. ALWANG, US

Do you think that new techniques like acoustic emission will play any significant role in fault detection for future gear box health monitoring systems ?

#### Author's Reply

Yes I do. I believe they will require development but they have potential for improving our understanding of the gear system health.

# NUMERICAL METHODS FOR PROPELLER AERODYNAMICS AND ACOUSTICS AT DFVLR

Kroll, N., Lohmann, D., Schöne, J.

Deutsche Forschungs- und Versuchsanstalt für  
Luft- und Raumfahrt e.V.  
Institut für Entwurfsaerodynamik  
D-3300 Braunschweig-Flughafen  
F.R. Germany

## SUMMARY

In the DFVLR Institute for Design Aerodynamics, linear and nonlinear analysis methods for flow fields around propellers have been developed. Two singularity methods are presented. In the first, a doublet point scheme has been formulated for the calculation of steady and unsteady loads on surfaces having helical motion in an incompressible medium, e.g. propellers in uniform and nonuniform inflows and counter rotating propellers. The second is a surface panel method for computations of steady subsonic flows around propeller blades moving in a compressible medium. The method has been extended for the prediction of acoustic quantities. In order to predict the characteristics of transonic propeller flow fields, the DFVLR Euler code for solving the 3-D Euler equations has been extended. The equations are formulated in a rotating cartesian reference frame. The solution procedure is based on a finite volume method using an explicit Runge-Kutta time stepping scheme. Numerical results for various propeller geometries are presented and compared with experimental data.

## NOTATIONS

$a_\infty$	sound velocity in undisturbed medium	$\hat{i}_x, \hat{i}_y, \hat{i}_z$	unit vectors of the relative cartesian reference frame
$c$	section chord length	$J$	advance ratio, $J = \pi U_\infty / (2R_T)$
$\tilde{c}_l$	time dependent part of lift coefficient	$M_\infty$	axial freestream Mach number, $M_\infty = U_\infty / a_\infty$
$\bar{c}_l$	time averaged lift coefficient	$M_h$	helical tip Mach number, $M_h = (U_\infty^2 + \Omega^2 R_T^2)^{1/2} / a_\infty$
$c_p$	pressure coefficient	$M_{\vec{d}}$	Mach number in radiation direction
$\Delta c_p$	difference of $c_p$ at the lifting surface	$\hat{n}, \hat{n}_0$	unit normal vectors
$C_p$	power coefficient	OASPL	overall sound pressure level
$\tilde{C}_p$	time dependent part of power coefficient, real part	$\Delta p_0 / \rho_\infty$	strength of dipole
$\bar{C}_p$	time averaged power coefficient	$p'$	acoustic pressure at the observation point
$C_T$	thrust coefficient	$p$	pressure
$\tilde{C}_T$	time dependent part of thrust coefficient, real part	$\vec{Q}$	source term vector
$\bar{C}_T$	time averaged thrust coefficient	$\vec{q}$	relative velocity vector without rotational velocity, $\vec{q} = [u, v, w]^T$
$c_{wp}$	profile drag coefficient	$\vec{\hat{q}}$	relative velocity vector, $\vec{\hat{q}} = \vec{q} - \vec{\omega} \times \vec{r}$
$d$	distance between singularity and observation point	$\vec{r}$	position vector
$\bar{d}$	retarded distance	$R_T$	blade tip radius
$d^*$	modified retarded distance	$S_0$	surface
$E$	total energy	$S_p$	panel surface
$\vec{F}$	flux tensor	$t$	time
$H$	total enthalpy	$U_\infty$	propeller advance velocity
		$\vec{V}, \vec{V}_0$	velocity vectors of positions on lifting surface

$v_n$	local induced normal velocity of monopole and dipole	$\Omega$	angular velocity
$\vec{W}$	vector of flow variables	$\phi$	azimuthal angle
$x, y, z$	blade-attached, relative cartesian reference frame	$\rho$	density
$\beta, \beta_t$	stretching factors	$\rho_\infty$	density in undisturbed medium
$\beta_{75}$	blade angle at $0.75 \cdot R_T$	$\xi$	control volume with boundary $\partial \xi$
$\eta_0$	efficiency, $\eta_0 = J C_T / C_P$	$\sigma$	strength of monopole
$\gamma$	azimuthal angle between front and rear propeller	$\delta$	phase shift
$\Phi$	velocity potential	$\theta$	angle between $\hat{n}$ and $\hat{n}_0$
$\kappa$	ratio of specific heats	$\theta'$	angle between $\xi$ and $\vec{V}_0$
$\vec{\omega}$	rotational velocity vector, $\vec{\omega} = [\Omega, 0, 0]^T$	$\xi, \eta, \zeta$	transformed cartesian coordinate system taken into account compressibility

## 1. INTRODUCTION

In the view of a design aerodynamicist, various features of high speed propeller aerodynamics are significant. First, unsteady flow phenomena appear for special configurations and operating conditions. These include the cases of nonuniform or time dependent onflow, unsteady motion and interference between rotating stages. Examples of these are, respectively; the flow field behind a strut, flutter of blades and counter rotating propellers. Second, the flow field is usually transonic. This type of flow field will occur in future applications such as transport aircrafts with advanced propfan propulsion systems operating in high subsonic flight regimes. Third, the complexity of these flow fields generates important acoustic effects. The aforementioned flow phenomena may combine to yield extremely large acoustic quantities.

During the last few years a wide variety of numerical methods for simulating the complex flow fields of rotary wing configurations has been developed. An overview of the methods for propeller and rotor applications is given by Poisson-Quinton [1] and Johnson [2]. At present, numerical methods based on linearized potential theory are routinely used. Their special merits are the simple treatment of complex configurations as well as the requirement of only small computational resources. Contributions concerning singularity methods which approximate the surface with panels are given e.g. by Hess and Valarenzo [3], Long [4] and Luu [5]. These methods provide velocity and pressure distributions on the blade surface. In addition, lifting surface methods, treating the blade without thickness, have been recently reported by Tsakonas et al. [6], Hanson [7] and Runyan and Tai [8]. In some of these papers, as well as in the paper of Das [9], compressibility effects are taken into account by considering the velocity of sound, to be finite. Unsteady propeller aerodynamics at present are mainly calculated by lifting surface methods producing time dependent lift distributions.

In order to treat nonlinear transonic flows associated with high speed propellers, several numerical procedures based on the small-disturbance as well as the full potential equation have been developed. The main limitation of the potential flow model is that the roll-up of the vortex wake and the convection of the tip vortex behind the blade are not taken into account. Recent advances in computer performance and computational techniques have made it possible to solve the three-dimensional Euler equations which admit vortical solutions. Due to the high computational expense, the numerical solution of the Euler equations for rotary wing configurations are at present mainly used for the calculation of steady flows such as the flow field of single rotating propellers in axial flight. Several papers have addressed the prediction of the flow fields of high speed propellers. Bober et al. [10] developed a three-dimensional Euler code for a multi-blade propeller and axisymmetric nacelle combination using an implicit finite difference scheme. Similar methods are used by Bousquet [11] and Kobayakawa et al. [12]. Holmes and Tong [13] applied an explicit finite volume scheme to turbine blade rows and propellers. Celestina et al. [14] presented results of the numerical simulation of the time-averaged inviscid flow field through a counter rotating propeller.

For analyzing the acoustic characteristics of propellers, numerous theoretical studies have been performed in the last few years. Theories have been developed by Farassat [15] and Hanson [16] which allow the prediction of propfan aeroacoustics in the high subsonic speed regime. Similar approaches have been used by Schmitz and Yu [17]. These methods are based on the linearized Ffowcs Williams-Hawkins acoustic analogy in which the equations of fluid motion are transformed into the wave equation for the acoustic pressure. In order to calculate near and far field acoustics caused by nonlinear transonic aerodynamic phenomena, like shock waves, new concepts have been outlined by Korkan et al. [18] and Forsyth et al. [19]. Their approach is based on a nonlinear field method for the calculation of the propeller flow field.

At the DFVLR Institute for Design Aerodynamics, research work concerning several topics of propeller aerodynamics and acoustics has been performed. New airfoil sections for propeller blades have been designed by Horstmann et al. [20]. Acoustic investigations with emphasis on experiments have been carried out by Heller et al. [21]. Furthermore, analysis methods for predicting the flow fields of propellers in axial flight, including linear as well as nonlinear methods, have been developed. The present paper is restricted to the description of these methods. In the following, these are briefly outlined and numerical results are shown and compared with experimental data.

## 2. SINGULARITY METHODS FOR PROPELLER BLADE AERODYNAMICS AND ACOUSTICS

In order to perform preliminary predictions of the aerodynamic coefficients of high speed propeller blades, singularity methods for special applications have been developed. These methods require fewer computational resources compared to nonlinear field methods. However, they are restricted here to inviscid, subsonic and irrotational flow fields.

In the following, two solution procedures for special applications are described. In order to efficiently predict unsteady lift distributions over propeller blades, a Doublet Point Method has been developed. This method is restricted to incompressible flows and simulates the propeller blades as lifting surfaces without thickness. In addition, a Lifting Body Surface Method has been developed to calculate steady pressure distributions on the propeller blades moving in a compressible medium. The results of this method has been used to calculate the signatures as well as the spectra of the acoustic pressure.

### 2.1 Unsteady Lift Distribution in Incompressible Medium

#### 2.1.1 Integral Equation and Solution Method

The Doublet Point Method for the calculation of unsteady propeller aerodynamics is outlined with more details in reference [22]. The method is based on the following equation formulated in a fixed reference frame with the medium at rest at infinity

$$\dot{\mathbf{n}} \cdot \dot{\mathbf{V}} = \frac{1}{8\pi} \iint_{S_0} \int_{-\infty}^t |\dot{\mathbf{V}}_0|^2 \Delta c_p \frac{\partial}{\partial n} \left\{ \frac{\partial}{\partial n_0} \frac{1}{d} \right\} dt_0 dS. \quad (2.1)$$

Here,  $\hat{\mathbf{n}}$ ,  $\hat{\mathbf{n}}_0$  are the normal unit vectors on the lifting surfaces at the position of the observation point and singularity respectively,  $\dot{\mathbf{V}}$  and  $\dot{\mathbf{V}}_0$  are the corresponding velocity vectors and  $d$  is the distance between these two positions.  $S_0$  denotes the area of the lifting surfaces,  $\Delta c_p$  the nondimensional pressure difference and  $t$  is the time assigned to the observation point. The equation (2.1) is similar to the expression given by Dat [23] and can also be obtained from the integral equation deduced by Das [9] using the aforementioned assumptions. The integral equation (2.1) relates the normal velocity at time  $t$  in the position of the observation point to the induced velocity caused by a pressure distribution  $\Delta c_p$  on an arbitrarily moving lifting surface. The unknown function is  $\Delta c_p$  which is a function of location and time.

The numerical solution of equation (2.1) for unsteady propeller aerodynamics is now outlined. The first step is the subdivision of the lifting surface into panels. Instead of a continuous distribution of singularities over the panel, the doublet and the upwash point are located in the quarter and three quarter point of each panel, respectively. This leads to a simple approximation of the surface integration in equation (2.1). This doublet point scheme was introduced by Ueda and Dowell [24] for unsteady wing aerodynamics. Each doublet produces a time dependent single force and together they are simulating the lift distribution of the propeller blade. These forces acting on the panel surface lead to the unknown pressure difference  $\Delta c_p$ . Here, only periodic cases are treated and therefore  $\Delta c_p$  is developed as a Fourier series. The unknowns are now the Fourier coefficients for each panel. Applying the tangential flow condition at each upwash point, a system of linear equations is obtained. The equations are formulated for different times within one period. In the calculation approximately 30 time steps have been used.

In the case of interfering lifting surfaces, such as counter rotating propellers, the complete system has to be solved. In special cases the freestream vector is known in each blade section, e.g. single propellers acting in a given nonuniform onflow. Then a harmonic analysis of the freestream velocity can be performed and for each harmonic only one system of equations is formulated. A quasi steady solution is obtained, if only the zero coefficient of the Fourier series is taken into account and independent sets of equations are built for different times. In the case of steady lift distributions like single propellers with uniform onflow, only one of these systems needs to be solved. The solution of the system of linear algebraic equations yields the Fourier coefficients for the  $\Delta c_p$  for each panel. With these, the discrete time dependent  $\Delta c_p$  distribution over the lifting surface is determined. Integral values such as lift coefficient as well as thrust and power coefficients of the complete propeller can be calculated. The induced drag coefficient is calculated using the expression given in [7].

### 2.1.2 Numerical Results

In the following, numerical results performed by the Doublet Point Method are shown. Figure 1 demonstrates the effect of blade number for steady lift distributions. Three single rotating propellers, having 4, 6 and 8 identical blades, have been examined. The geometry and experimental data for these propellers are described by Biermann et al. [25], [26]. In this calculation the lifting surface of each blade is subdivided into 6 panels along chord and 36 panels along radius. A central body is not taken into account with the Doublet Point Method and each blade terminates with a free end at an inner radius. In the figure, measured and calculated thrust and power coefficients are plotted versus advance ratio. The experimental data, recorded for helical tip Mach numbers lower than 0.3, agree fairly well with the theoretical results. The discrepancies in the power coefficients may be due to viscosity, which is not taken into account in the calculation.

Figure 2 shows results for unsteady propeller aerodynamics. Experimental data for ship propellers acting in a nonuniform onflow are reported by Miller [27]. The propeller used here for comparison has a large blade width (expanded area ratio of 1.2). The axial onflow varies in the circumferential direction. In the calculation performed with the Doublet Point Method only the first blade harmonic of the axial velocity is taken into account. Higher harmonics are relatively small and are neglected. The figure shows on the right side the unsteady, in-phase part of the thrust and power coefficient divided by the design value and on the left side the phase shift. All quantities are plotted versus advance ratio. Here, both, unsteady and quasi-steady calculations with  $7 \times 15$  panels are presented. In addition, experimental data [27] and theoretical results of Tsakonas et al. [6] are shown. In comparison with the quasi-steady solution, the unsteady calculation agrees better with the experimental data.

Figure 3 presents results for a counter rotating propeller, which has two blades for each of the front and rear propeller. On the left side the unsteady part of the lift coefficient divided by the time-averaged lift (determined from the zero Fourier coefficients) is plotted as function of fraction of blade radius and azimuthal angle. This angle varies periodically with time. In the case of a 2- by 2-counter rotating propeller, one period is equivalent to 180 degrees of rotation. For the azimuthal angle  $\gamma=0$ , the lift coefficient of the front propeller shows a drop of up to 30% of the time-averaged lift. A maximal peak of 50% occurs for the rear propeller when it is rotating through the wake of the front propeller. Efficiency of single and counter rotating propellers determined with measured time-averaged thrust and power coefficients are reported in reference [25]. The right part of figure 3 compares the measured and calculated efficiency for a 2- by 2-blade counter rotating and a 4-blade single rotating propeller. An estimated profile drag coefficient of  $c_{wp}=0.015$  is added to the calculated induced drag. The improved efficiency of a counter rotating propeller compared with a single propeller is predicted fairly well with the Doublet Point Method. Calculations presented in the left side of the figure have been performed with  $2 \times 10$  panels and  $3 \times 12$  panels have been used for calculations shown on the right side.

## 2.2 Steady Surface Pressure Distribution on Propeller Blades in Compressible Medium

### 2.2.1 Integral Equation and Solution Method

For compressible flows a Lifting Body Surface Method based on the linearized Ffowcs Williams-Hawkins equation has been developed. Following Lighthill [28], one obtains from the equation for conservation of mass and momentum the general multipole equation for aeroacoustics. The solution of this inhomogeneous wave equation, taking into account the acoustic approximation, represents the pressure as a function of the various possible sources in flow. This solution is a Fredholm integro-differential equation of second order, which contains the acoustic pressure in both the left and right hand sides and has still to be solved.

Integrating the Fredholm integral equation with respect to time and considering the complete time history of the sources, one obtains the potential formulation written in a blade-attached cartesian coordinate system

$$4\pi\Phi = \iint_{S_0} \left[ \frac{\sigma_0}{\tilde{d}(1-M_{\tilde{d}}^2)} \right] dS + \int_{-\infty}^t \iint_{S_0} \frac{\partial}{\partial n_0} \left[ \frac{\Delta p_0/\rho_\infty}{\tilde{d}(1-M_{\tilde{d}}^2)} \right] dS dt. \quad (2.2)$$

The square brackets denote quantities to be taken at emission time.  $\Phi$  represents the velocity potential,  $\sigma_0$  and  $\Delta p/\rho_\infty$  are the unknown strengths of the monopole and dipole and  $\tilde{d}$  is the retarded distance between the singularity and observation point.  $M_{\tilde{d}}$  is the Mach number in radiation direction.  $S_0$  is the surface and  $t$  is the time. The integral equation (2.2) represents the velocity potential as a function of a surface distribution of monopole and dipole. At the body surface the normal velocity is zero, which leads to the boundary condition

$$\frac{\partial \Phi}{\partial n} + \hat{n} \cdot \vec{v} = 0. \quad (2.3)$$

For the numerical solution of the integral equation (2.2), the propeller blades have to be subdivided into surface panels. On each panel a constant source and doublet

distribution is assumed. For the calculation of the velocities induced by the source term (first term of equation (2.2)), there are existing closed form solutions in cartesian coordinates for panels given e.g. Hess and Smith [29] and Kohlmeier [30]. For the evaluation of the dipole term (second term of equation (2.2)), the surface integral has to be cast in another form. This also leads to a physical interpretation of the dipole term. Using the transformed coordinates  $\xi, \eta, \zeta$ , taking into account the compressibility as a kinematic effect, and the fact that in these coordinates the acceleration potential satisfies the Laplace equation [2], [31] the induced normal velocity is given by

$$4\pi v_n = \frac{\partial}{\partial \zeta} \iint_{S_p} \beta_0 \frac{\cos \theta}{d} dS + \frac{\partial}{\partial \zeta} \iint_{S_p} \frac{\beta_t \Delta p / \rho_\infty}{\vec{V}_0} \frac{\cos \theta}{d} dS + \cos \theta \cdot \int_{\xi_b}^{\xi_a} \left( \frac{\partial}{\partial \eta} \int_{-\infty}^t \beta \beta_t \Delta p / \rho_\infty \frac{\cos \theta}{d} dt \right) d\xi \quad (2.4)$$

Here  $\theta$  is the angle between  $\vec{n}$  and  $\vec{n}_0$ ,  $\theta'$  is the angle between  $\vec{V}_0$  and  $\xi$ ,  $\beta$  and  $\beta_t$  are stretching factors and  $d$  is a modified retarded distance between singularity and observation point. The integration of the last term of equation (2.4) can be performed in the case of a translatory motion in a closed form whereas in a helical motion the integration has to be executed numerically. Details are given in reference [32]. For the special case of incompressible flow, equation (2.4) without the first term is the well known integro-differential equation of Prandtl for thin wings. The second term in equation (2.4) describes the bound and the last term the free vortex. The separated terms of bound and free vortices are used later for calculation of lift and drag.

The unknowns of the numerical procedure are the constant strength of source as well as the doublet distribution on each panel. The doublet strength in the chord direction is a discrete Birnbaum distribution which leads to only one unknown for the doublet strength in each blade section. For the additional upwash point a Kutta panel located in the plane of the bisector is used. Applying the zero normal velocity in each upwash point, a linear system of equations is obtained. Using the periodicity, the number of unknowns is reduced to the number for one blade. The solution of the linear equation system results in a steady surface pressure distribution using the perfect gas law. From the pressure distribution and the induced velocities due to the free vortices the coefficients of lift, drag, thrust and power of the propeller are calculated.

## 2.2.2 Numerical Results

The Lifting Body Surface Method has been extensively tested for several applications. Comparisons with results of various numerical methods as well as measurements have shown good agreement [32]. In this paper calculations for a 2-blade advanced propeller are shown.

Figure 4 presents on the left hand side pressure distributions for various blade sections. In the calculation  $29 \times 8$  panels have been used. Although this is a relatively coarse surface grid, the figure shows reasonable pressure distributions. The lift reduces in the direction of the hub as well as the tip. For this propeller only measurements of total forces such as thrust and power are available and reported by Dobrzynski et al. [33]. On the right hand side of figure 4 thrust and power coefficients are plotted versus advance ratio. The full line represents the calculation of the Lifting Body Surface Method and the symbols the experimental data. Since the drag of the nacelle was measured separately here only the forces resulting from the blades are presented in the figure. The comparisons show that the calculated values of thrust are slightly overestimated whereas the values of the power fit the measurements very well. The discrepancies are less than 5%. An explanation for the fairly good result may be that viscous effects in this Mach number range are small.

## 2.3 Near Field Acoustics

In recent years, the acoustic analysis of advanced propellers has received a great deal of attention. The conventional harmonic analysis of propeller noise based on compact sources at an effective radius is not suitable for detailed predictions of the influence of blade geometry on the propeller noise. With a powerful computer, calculations of the acoustic pressure signature due to the blade thickness and steady surface pressure distributions are possible. As a first step some calculations of the signatures and spectra have been performed and will be shown evaluated with the technique equivalent to Farassat's numerical procedure for the subsonic regime [34].

The acoustic pressure

$$p' = - \rho_\infty \frac{\partial \phi}{\partial t} \quad (2.5)$$

at each point in space is the sum of the contributions of all panels. With equation (2.2) equation (2.5) yields an expression first used by Lowson [35] for acoustic calculations. Using the chain rule for moving sources

$$\frac{\partial}{\partial n_0} [f] = \left[ \frac{\partial f}{\partial n_0} + \frac{\cos \theta}{a_\infty} \frac{\partial f}{\partial t} \right] \quad (2.6)$$

for the differentiation of the second term in equation (2.2), the following expression for the induced acoustic pressure

$$-4\pi p' = \frac{1}{a_\infty} \frac{\partial}{\partial t} \iint_{S_0} \left[ \frac{a_\infty \rho_\infty \sigma_0 + \Delta p_0 \cos \theta}{\tilde{d}(1 - M_\infty^2)} \right] dS + \iint_{S_0} \left[ \frac{\Delta p_0 \cos \theta}{\tilde{d}^2(1 - M_\infty^2)} \right] dS \quad (2.7)$$

is obtained. Equation (2.7) is the same used by Farassat [34] for the subsonic regime. The unknowns of the singularity distribution have been calculated with the Lifting Body Surface Method outlined in chapter 2.2.1. The expression (2.7) is evaluated numerically for 256 time steps per revolution resulting in the signature of the acoustic pressure. The spectra are then obtained with a Fourier analysis of the signature.

First results of acoustic calculations in comparison to experimental data [33] are shown in the next two figures. The right side shows results for a microphone position outside the propeller disc plane and the left side for one in the plane. In the upper part, the acoustic signatures and in the lower part the spectra are presented. Figure 5 shows the results for test conditions of  $J=0.57$  and  $M_h=0.57$ . The comparisons between the calculated and measured peak values show good agreement. Reasons for the discrepancies may be acoustic wave reflections in the experiment as well as the fact that the quadrupole term is not taken into account in the calculation. The calculated OASPL corresponds very well with the measured values. In Figure 6 results for the same advance ratio but for a higher helical Mach number of  $M_h=0.76$  are presented. In this calculation the pressure distribution of Figure 4 has been used. The comparisons between calculated and measured data show the same quality as before. In this case the acoustic wave reflections in the measurements are visible in the signature for the microphone positions outside the propeller plane.

### 3. SOLUTION OF EULER EQUATIONS FOR STEADY TRANSONIC PROPELLER FLOW FIELDS

In order to treat transonic flows of high speed propellers, a numerical method for solving the three-dimensional Euler equations has been developed. The Euler equations describe the inviscid transonic flow correctly regardless of the strength of the appearing shocks. Unlike the potential flow model, the Euler equations allow entropy rise through shock waves while mass, momentum and energy are conserved. This leads to an accurate prediction of the location and strength of the shock. An important feature of the Euler equation model for rotary wing applications is that vortical flows are yielded as solutions of the equations. Since vorticity is captured and convected, the complex wake geometry of rotary wing flow fields does not have to be prescribed but is a part of the solution.

#### 3.1 Governing Equations

The governing equations are the unsteady Euler equations in integral conservation form. In a blade-attached cartesian reference frame, which is rotating with a constant angular velocity  $\Omega$  about the x-axis, the equations are written as

$$\frac{\partial}{\partial t} \iiint_{\mathcal{V}} \tilde{W} dv + \iint_{\partial \mathcal{V}} \tilde{F} \cdot \hat{n} dS - \iint_{\partial \mathcal{V}} \tilde{W} (\tilde{\omega} \times \hat{r}) \cdot \hat{n} dS + \iiint_{\mathcal{V}} \tilde{Q} dv = 0 \quad (3.1)$$

Here,  $\mathcal{V}$  denotes a fixed region in the blade-attached coordinate system with boundary  $\partial \mathcal{V}$  and outer normal  $\hat{n}$ . The angular velocity is given by  $\tilde{\omega} = [0, 0, \Omega]^T$  and  $\hat{r}$  is the position vector. The equations (3.1) are formulated such that the vector  $\tilde{W}$  of flow variables does not contain the rotational velocity  $\tilde{\omega} \times \hat{r}$ . In this formulation the vector  $\tilde{W}$ , the flux tensor  $\tilde{F}$  and the source term vector  $\tilde{Q}$  are given by

$$\tilde{W} = \begin{bmatrix} \rho \\ \rho u \\ \rho v \\ \rho w \\ \rho E \end{bmatrix}, \quad \tilde{F} = \begin{bmatrix} \rho \tilde{q} \\ \rho u \tilde{q} + p \hat{i}_x \\ \rho v \tilde{q} + p \hat{i}_y \\ \rho w \tilde{q} + p \hat{i}_z \\ \rho H \tilde{q} \end{bmatrix}, \quad \tilde{Q} = \begin{bmatrix} 0 \\ 0 \\ -\rho \Omega w \\ \rho \Omega v \\ 0 \end{bmatrix}$$

where  $\rho$  is the density,  $p$  is the pressure,  $E$  is the total energy,  $H$  is the total enthalpy and  $i_x, i_y, i_z$  denote the unit vectors of the cartesian reference frame. The relative velocity is defined by

$$\vec{Q} = \vec{q} - \vec{\omega} \times \vec{r}, \quad (3.2)$$

where  $\vec{q} = [u, v, w]^T$ , and the pressure  $p$  is obtained by

$$p = \rho(\kappa - 1) \left( E - \frac{1}{2}(u^2 + v^2 + w^2) \right). \quad (3.3)$$

The vector  $\vec{Q}$  represents the terms due to the rotation of the coordinate system. For  $\Omega=0$ , the system of differential equations (3.1) reduces to the Euler equations written in a nonrotating reference frame.

Physical boundary conditions must be imposed at the solid surface and at the far field. At the solid surface normal velocity has to be zero. The formulation of (3.1), where the vector  $\vec{W}$  of flow variables does not contain the rotational velocity, leads to a uniform rather than a rotating far field. The flow at the far field is assumed to be undisturbed and freestream conditions are prescribed. Furthermore, by applying periodicity, only the flow field around one propeller blade has to be calculated.

### 3.2 Numerical Procedure

The solution method is an extension of the DFVLR-developed, block-structured 3-D Euler code written for a nonrotating reference frame [36]. In the following, the algorithm is briefly described. Details of the method applied to rotary wings are outlined in reference [37]. The solution procedure is based on the finite volume method using an explicit multistage time-stepping scheme originated by Jameson et al. [38]. Semi-discretization of (3.1) decouples spatial and time discretization. The flow field is divided into hexahedral cells by the generation of a body-fitted grid. In the finite volume spatial discretization the Euler equations in integral form are approximated at each cell. The flow variables are associated with the cell centers. The surface integrals are evaluated by assuming that the flow variables are constant on the cell faces and are calculated as the average of their values at the corresponding cell centers. In order to damp out high frequency oscillations in the flow variables and to avoid oscillations in the neighbourhood of shock waves, dissipative terms are added. The terms are formed by a blend of second and fourth differences of the flow variables.

In the finite volume scheme the solid surface boundary condition results in the condition that all convective fluxes are zero at the wall. The only quantities which are required at the wall are the pressure and the volume flux velocity due to the rotation of the coordinate system. The pressure is obtained by linear extrapolation from the interior and the rotational volume flux is known from the grid geometry. The far field boundary conditions are implemented using the concept of characteristic variables.

The spatial discretization results in a system of ordinary differential equations in time which is solved by an explicit 5-stage Runge-Kutta time stepping scheme. Since unsteady flow calculations require enormous computational expense, at this time our interest is focussed on steady flow fields. In this case, various techniques, like local time-stepping, implicit residual averaging [39] and successive grid refinement, are used to accelerate the convergence to the steady state. Furthermore, the technique of enthalpy damping [38] has been applied to the rothalpy which is constant in the case of a propeller in axial flight.

The code is written in a block-structured form which allows calculations with a nearly unrestricted number of grid points on arbitrary grid topologies. The details of the multiblock structure implemented in the program are found in reference [36].

### 3.3 Numerical Results

In the present paper, results for a 2-blade propeller are shown which was tested by NACA [40]. The propeller blades have a rectangular planform and consists of NACA 16-series blade sections. The tests provide pressure distributions on the rotating blade at a number of radial stations.

Figure 7 shows the structure of the field grid which has been used in the calculation. The grid is body-fitted and has an O-O structure, that is, it wraps around the blade in both, chordwise and spanwise directions. This provides a good resolution at leading and trailing edges as well as at the tip of the blade. The grid has been generated algebraically using the transfinite interpolation method [41]. It has a total of 96x20x36 cells, 96 cells around the blade profile, 20 normal to the blade and 36 along the blade span. The outer boundary of the grid around the propeller blade forms a half sphere with its center at the x-axis near the blade trailing edge. The radius of the sphere is about 20 chords, that is 2.6 times the blade radius. Because of the strong twist of the propeller special care has to be taken in constructing the surface grids at the boundaries of the computational domain in order to avoid intersections or excessively skewed cells.



Computations have been performed for transonic flow with axial freestream Mach number  $M_\infty=0.56$  and advance ratio  $J=2.3$ . Figure 8 shows the comparison of the calculated and the measured pressure distributions at four different span sections. The theoretical results are in good agreement with the experiment. The shock at the outer station is resolved in the calculation. The helical tip Mach number is about  $M_t=0.96$ . The difference between theory and experiment may be due to the effect of the boundary layers along the surface which is not accounted for in the calculation.

Figure 9 shows for the same flow conditions crossflow velocities in six different  $x$ -constant planes which are perpendicular to the axis of rotation. The first three planes intersect the propeller blade for  $x=0.3$ ,  $x=0.5$  and  $x=0.8$ , that is, near the leading edge, at the center line, and the trailing edge of the blade respectively. Because of the twist of the propeller the blade surface is directed downwards near the blade leading edge ( $x=0.3$ ) and upwards near the blade trailing edge ( $x=0.8$ ). The last three planes  $x=0.9$ ,  $x=1.2$  and  $x=1.8$  are just behind the blade trailing edge. The crossflow velocities in the different planes show the formation and growing of the tip vortex. Near the blade leading edge only the displacement effect is visible. As the crossplane moves further downstream the crossflow velocities indicate a flow around the tip which then develops into a tip vortex. This vortex leaves the blade trailing edge and approximately follows the path of the blade tip.

#### 4. CONCLUDING REMARKS

Two singularity methods for propeller aerodynamics have been presented. First, a Doublet Point Method for unsteady incompressible flow has been described. Here, single doublets are distributed over the lifting surfaces and an unsteady formulation for the doublet strength is used. Applied to unsteady conditions this formulation is superior to the quasi-steady approach. Interfering lifting surfaces, like counter rotating propellers, are treated directly without iterative treatment.

Second, a Lifting Body Surface Method for steady compressible flow has been outlined. The basic equation is the solution of the linearized Ffowcs Williams-Hawkins equation in potential formulation, which is taken for predicting both aerodynamics and acoustics. Using a source and doublet distribution on the blade, surface pressure distributions of an advanced 2-blade propeller in compressible flows have been computed. The induced velocities of the bound and free vortices are calculated separately. The evaluated aerodynamic coefficients are used to calculate the acoustic signatures as well as the spectra.

Furthermore, a numerical method for the solution of Euler equations has been described in order to predict the characteristics of transonic flows. It is based on the finite volume approach and solves the equations in a blade-attached cartesian coordinate system. An algebraically generated grid around the propeller blade, which has an O-O topology, has been used.

Each of the presented theories has been used for the prediction of special flow phenomena associated with high speed propellers. The various comparisons of theory and experiment are encouraging.

#### 5. ACKNOWLEDGEMENTS

The authors would like to thank S. SCHERR for providing the plot program for the crossflow figures.

#### 6. REFERENCES

- [1] Poisson-Quinton, P. Technical Evaluation Report on the Fluid Dynamics Panel Symposium on Aerodynamics and Acoustics of Propellers. AGARD-AR-213 (1985).
- [2] Johnson, W. Recent Developments in Rotary Wing Aerodynamic Theory. AIAA Journal, Vol. 24, No. 8, pp. 1219-1244 (1986).
- [3] Hess, J.L. Valarenzo, W.O. Calculation of Steady Flow about Propellers by Means of a Surface Panel Method. AIAA-Paper 85-02838 (1985).
- [4] Long, N.L. The Compressible Aerodynamics of Rotating Blades Based on an Acoustic Formulation. NASA-TP-2197 (1983).
- [5] Luu, T.S. Design Concept and Performance Prediction Technique for Potential Flows Collierand, R. Around Advanced Propellers. AGARD-CP-366, pp. 3.1-3.12 (1984).
- [6] Tsakonas, S. Propeller Blade Pressure Distribution Due to Loading and Thickness Effects. Journal of Ship Research, Vol. 23, No. 2, pp. 89-107 (1979).
- Ali, M.R.

- [7] Hanson, D.B. Compressible Lifting Surface Theory for Propeller Performance Calculation. *Journal of Aircraft*, Vol. 22, No. 1, pp. 19-27 (1985).
- [8] Runyan, H.L. Lifting Surface Theory for a Helicopter in Forward Flight. *NASA-CR-16997* (1983).
- [9] Das, A. A Unified Approach for the Aerodynamics and Acoustics of Propellers in Forward Motion. *AGARD-CP-366*, pp. 9.1-9.28 (1984).
- [10] Bober, L.J. Prediction of High Speed Propeller Flow Using a Three-Dimensional Euler Analysis. *AIAA Paper 83-0188* (1983).
- [11] Chaussee, D.S. Kutler, P. Methods Aerodynamiques Utilisees en France Pour L'Etude des Helices pour Avions Rapides. *AGARD-CP-366*, pp. 2.1.-2.15 (1984).
- [12] Kobayakawa, M. Calculations of High Speed Propeller Performances Using Finite Difference Methods. *ICAS-86-3.10.3* (1986).
- [13] Onuma, H. Shiota, Y. Holmes, D.G. Tong, S.S. A Three-Dimensional Euler Solver for Turbomachinery Blade Rows. *ASME Journal of Engineering for Gas Turbines and Power*, Vol. 107, pp. 258-264 (1985).
- [14] Celestina, M.L. A Numerical Simulation of the Inviscid Flow Through a Counterrotating Propeller. Presented at ASME Gas Turbine Conference, June 8-12 (1986).
- [15] Mulac, R.A. Adamczyk, J.J. Farassat, F. Linear Acoustic Formulas for Calculation of Rotating Blade Noise. *AIAA Journal* Vol. 19, No. 9, pp. 1122-1130 (1981).
- [16] Hanson, D.B. Near-Field Frequency-Domain Theory for Propeller Noise. *AIAA Journal*, Vol. 23, No. 4, pp. 499-504 (1985).
- [17] Schmitz, F.H. Yu, Y.H. Theoretical Modeling of High Speed Helicopter Impulsive Noise. *Journal American Helicopter Society*, Vol. 24, No. 1 (1979).
- [18] Korkan, K.D. Numerical Evaluation of Propeller Noise Including Nonlinear Effects. *AIAA Journal*, Vol. 24, No. 6, pp. 1043-1045 (1986).
- [19] Lavante, E. Bober, L.J. Forsyth, D.W. Korkan, K.D. Computational Aeroacoustics of Propeller Noise in the Near and Far Field. *AIAA Paper 87-0254* (1987).
- [20] Horstmann, K.H. Entwicklung von vier Profilen für einen Experimentalpropeller in der Leistungsklasse 750 PS. *DGLR-Nr. 82-067* (1982).
- [21] Köster, H. Quast, A. Heller, H.H. Aeroacoustics at the German-Dutch Wind Tunnel. *SPlettstößer*, ICAS-86-1.6.4 (1986).
- [22] W.R. Dobrzynski, W.M. Schultz, K.-J. Schöne, J. A Doublet Point Method for the Calculation of Unsteady Propeller Aerodynamics. To appear in: *Notes on Numerical Fluid Mechanics*, Vieweg Verlag, Braunschweig (1987).
- [23] Dat, R. Representation of a Lifting Line in an Arbitrary Motion by a Line of Acceleration Doublets. *NASA TT F-12*, 952 (1970).
- [24] Ueda, T. A New Solution Method for Lifting Surfaces in Subsonic Flow. *AIAA Journal*, Vol. 20, No. 3, pp. 348-355 (1982).
- [25] Dowell, E.H. Biermann, D. Hartmann, E.P. Wind-Tunnel Tests of Four- and Six-Blade Single- and Dual-Rotating Tractor Propellers. *NACA Rep. No. 747* (1940).
- [26] Biermann, D. Gray, W.H. Wind-Tunnel Tests of Eight-Blade Single- and Dual-Rotating Propellers in the Tractor Position. *NACA ARR* (1941).
- [27] Miller, M.L. Experimental Determination of Unsteady Propeller Forces. *Proceedings of Seventh ONR Symposium on Naval Hydrodynamics*, Office of Naval Research, pp. 255-290 (1968).
- [28] Lighthill, M.J. On Sound Generated Aerodynamically. I. General Theory. *Proc. Roy. Soc. A* 2.1, pp. 564-587 (1952).
- [29] Hess, J.L. Smith, A.M.O. Calculation of Potential Flows about Arbitrary Bodies. *Progress in Aeronautical Sciences*, Vol. 8, Pergamon Press, pp. 1-138 (1967).

- [30] Kohlmeier, H.H. Eine direkte Berechnungsmethode für Störfelder bewegter Körper in kompressiblen Medien bei Unterschall-Machzahl. DFVLR-FB 85-52 (1985).
- [31] Multhopp, H. Methods for Calculating the Lift Distribution of Wings (Subsonic Lifting-Surface Theory). R.A.E. Report Aero. 2353 (1950).
- [2] Lohmann, D. Oberflächenverfahren zur Berechnung umströmter Körper und Propeller in kompressiblen Medien. DFVLR-IB 129-86/26 (1986).
- [33] Dobrzynski, W.M. DFVLR/FAA Propeller Noise Tests in the German-Dutch Wind Tunnel DNW. Appendix I: Basic Test-programm DFVLR-IB 129-86/3, FAA Report No. AEE 86-3 (1986).
- Heller, H.H.  
Powers, J.O.  
Densmor, J.E.
- [34] Farassat, F. A Review of Noise Prediction Technology with Emphasis on Two Current Methods for Time Domain Calculations. JSV, Vol. 71, No. 3 (1980).
- [35] Lowson, M.V. The Sound Field of Singularities in Motion. Proc. Roy. Soc. A 286, pp. 559-592 (1965).
- [36] Radespiel, R. Progress in the Development of an Efficient Finite Volume Code for the Three-Dimensional Euler Equations. DFVLR-FB-85-31 (1985).
- [37] Kroll, N. Computation of the Flow Fields of Propeller and Hovering Rotor Using Euler Equations. Proceedings of the Twelfth European Rotorcraft Forum. Garmisch-Partenkirchen (1986).
- [38] Jameson, A. Numerical Solutions of the Euler Equations by Finite Volume Methods Using Runge-Kutta Time-Stepping Schemes. AIAA Paper 81-1259 (1981).
- Schmidt, W.  
Türkel, E.
- [39] Jameson, A. Solution of the Euler Equations for Complex Configurations. AIAA-Paper 83-1929 (1983).
- Baker, T.J.
- [40] Maynard, J.D. Pressure Distributions on the Blade Sections of the NACA 10-(3)(066)-033 Propeller Under Operating Conditions. NACA-RM L9L12 (1950).
- Murphy, M.P.
- [41] Kumar, A. Computation of Flow around Delta Wings Based on Euler Equations. DFVLR-IB 129-86/07 (1986).

## 7. FIGURES

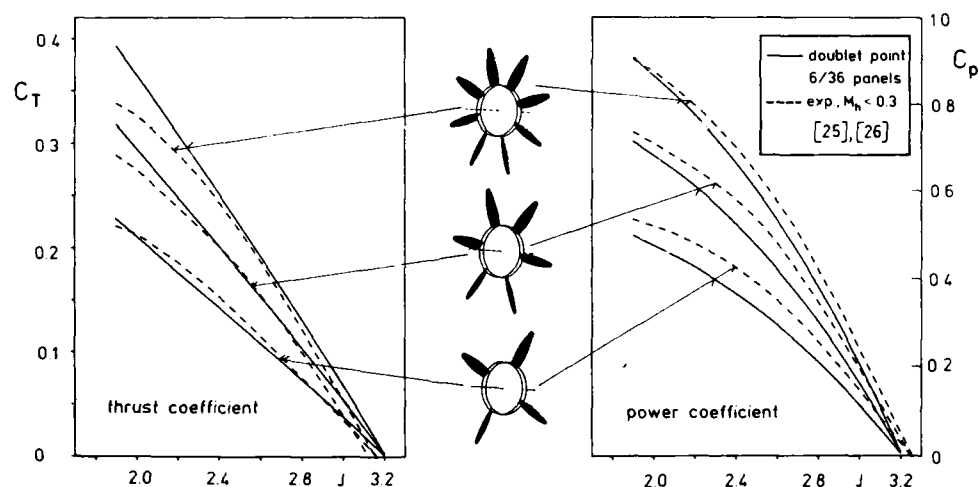


Fig. 1 Comparison between Doublet Point Method calculation and measured data for single propellers having 4, 6 and 8 blades.



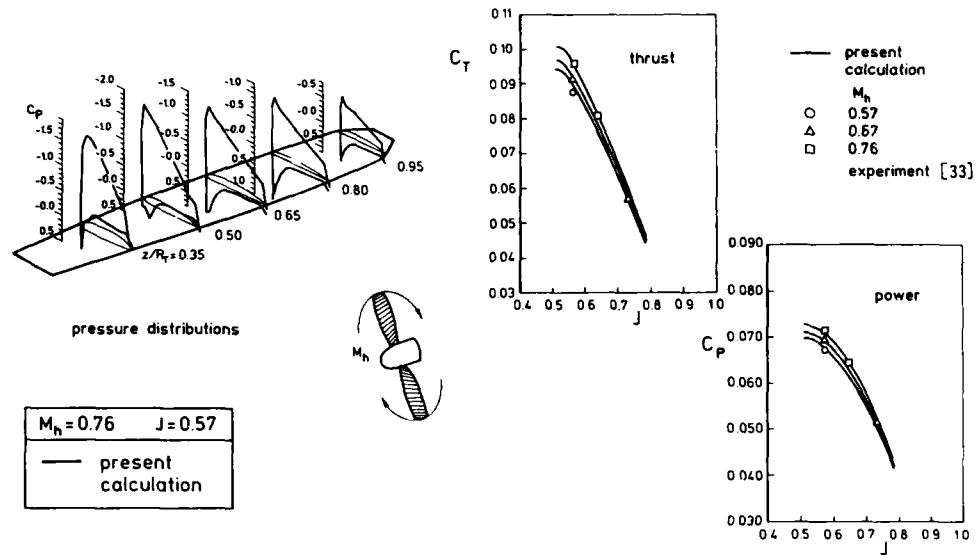


Fig. 4 Pressure distributions for various blade sections and thrust and power coefficients for a 2-blade propeller - Lifting Body Surface Method.

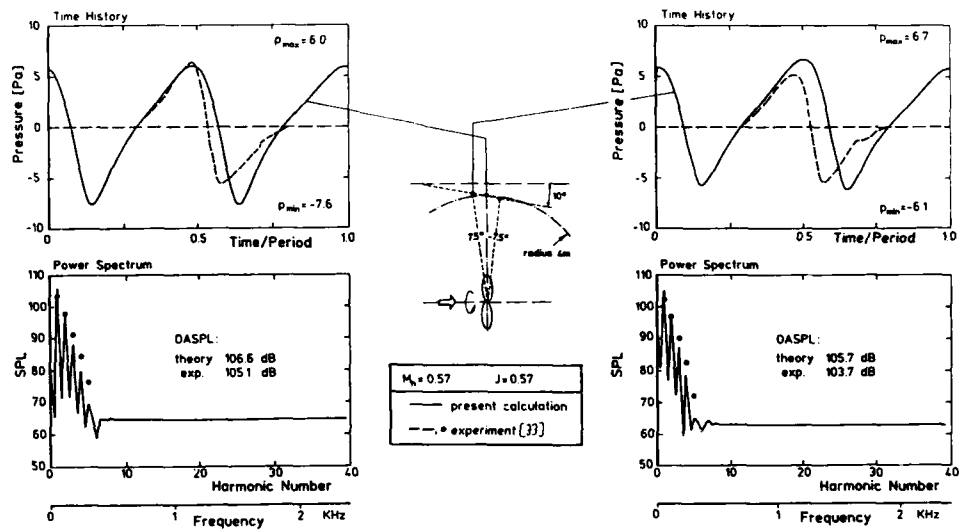


Fig. 5 Comparisons between acoustic experimental data and Lifting Body Surface Method calculations,  $M_h = 0.57$ .

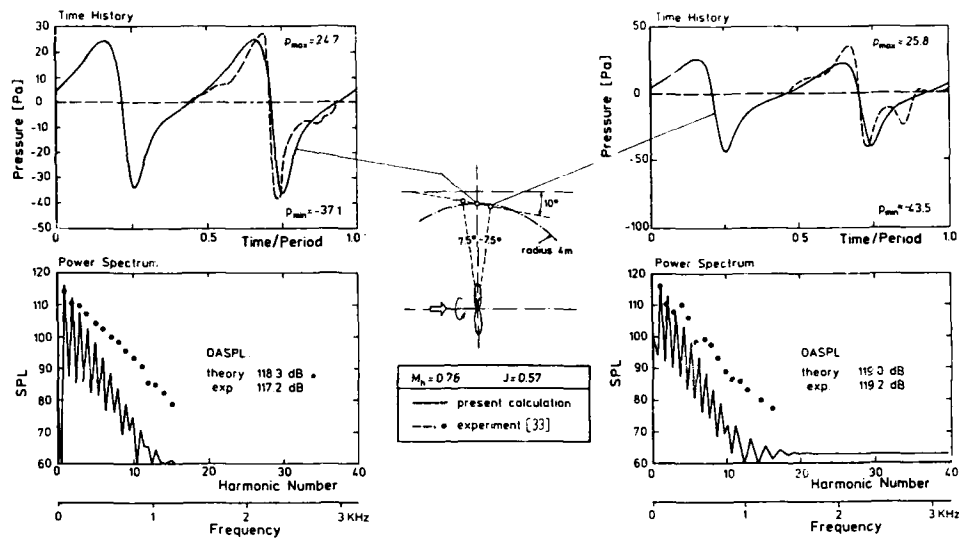


Fig. 6 Comparison between acoustic experimental data and Lifting Body Surface Method calculations,  $M_h = 0.76$ .

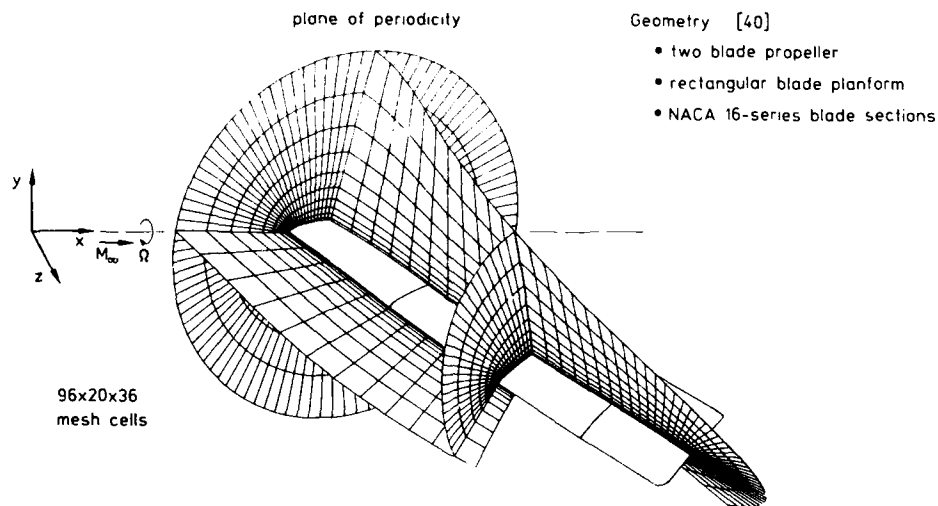


Fig. 7 Parts of the 0-0 type grid around propeller blade.

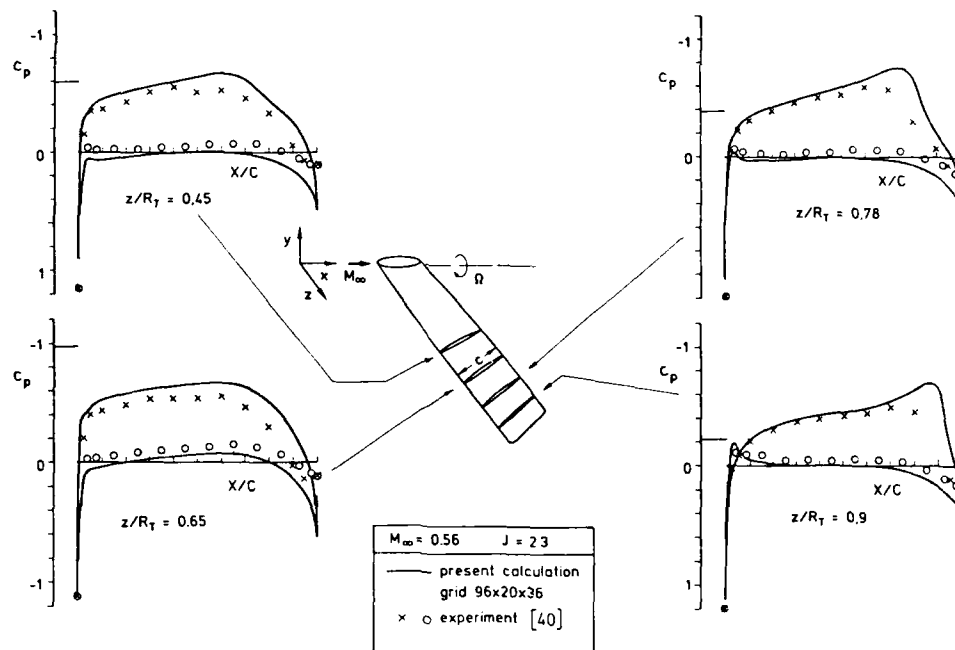


Fig. 8 Comparisons of pressure distributions from measurements and calculations using the Euler equations.

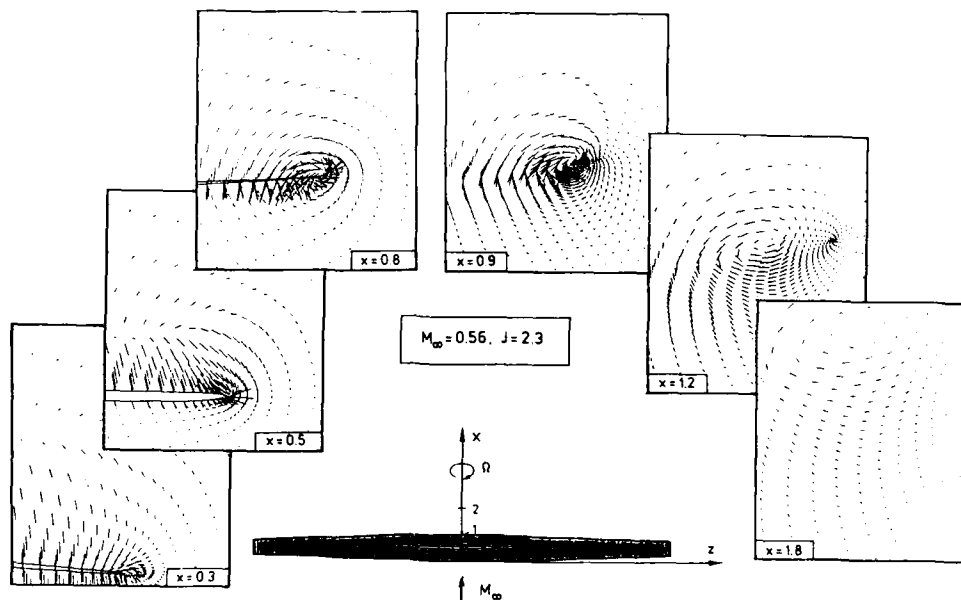


Fig. 9 Crossflow velocities for selected  $x$ -constant planes - solution of Euler equations.

### DISCUSSION

C. PADOVA, US

Please comment on the state-of-the art for inclusion of viscous effects in propeller calculations, particularly in the transonic regime to treat the shock boundary layer interaction.

Author's Reply

At the DFVLR Institute for Design Aerodynamics, presently in the non linear method applied to rotary wing configurations viscous effects are not taken into account. In the linear methods viscous effects are accounted for by a correlation with drag data for wing sections in special cases.

P. PSARUDAKIS, It

1) Can you tell us how do you define the pressure coefficients. I mean, do you define such coefficients to the relative flow in the plane of the propeller, or to something else ?

2) In the method you have developed, you have to simulate the rotational wake of the propeller blades. How do you design such wake and what kind of singularities do you use on the same wake ?

Author's Reply

1) The pressure coefficient  $c_p$  used in the paper is defined as

$$c_p = \frac{p - p_\infty}{\frac{\rho_\infty}{2} (U_\infty^2 + \Omega^2 \cdot z^2)}$$

where  $p$  is the pressure,  $p_\infty$  and  $\rho_\infty$  are the pressure and the density in the undisturbed medium,  $U_\infty$  is the axial advance velocity of the propeller,  $\Omega$  is the angular velocity and  $z$  is the cartesian coordinate in spanwise direction.

2) A wake has to be prescribed for the two singularity methods presented in the paper. In both methods, a rigid wake model is used. The wake forms a pure helix defined by the motion of the propeller. In the case of the Doublet Point Method, the wake is simulated by the path of the discrete doublets. In the Lifting Body Surface Method, discrete vortices are used.

In the method for the solution of the Euler equations, the wake does not have to be prescribed but is a part of the solution.



**ETUDE DE L'AERODYNAMIQUE DES HELICES POUR AVIONS RAPIDES**  
**ANALYSIS OF HIGH SPEED PROPELLERS AERODYNAMICS**

par

J.M. BOUSQUET

Office National d'Etudes et de Recherches Aérospatiales (ONERA)  
 29, avenue de la Division Leclerc - 92320 CHATILLON (FRANCE)

**R E S U M E**

Des études d'hélices pour avions rapides sont menées en France dans le cadre de l'opération CHARME. On présente une synthèse des études aérodynamiques ayant abouti à la définition de l'hélice HT3 dont une maquette a été essayée dans la soufflerie S1 de Modane. Les résultats expérimentaux obtenus sont comparés aux prévisions. Par ailleurs l'intérêt des hélices coaxiales contra-rotatives est présenté du point de vue des performances.

**A B S T R A C T**

Highspeed propellers are studied in the French CHARME research program. A synthesis of aerodynamic developments leading to the HT3 propeller definition and test in S1 Modane wind-tunnel, is presented. The validity of the main calculation methods used in this research, is analysed. Counterrotating highspeed propellers are also studied ; their performance benefits against single rotation propellers are presented.

**NOTATIONS**

B	Nombre de pales
C	Charge au disque $C = P/D^2$
$C_z$	Coefficient de portance (profil)
$C_x$	Coefficient de trainée (profil)
D	Diamètre de l'hélice
$e/l$	Epaisseur relative
h	Enthalpie
I	Rothalpie $I = h(p, \rho) + \frac{W^2}{2} - \frac{r^2 \Omega^2}{2}$
l	Corde
M	Nombre de Mach
n	Fréquence de rotation $n = \frac{\Omega}{2\pi}$
p	Pression statique
$p_i$	Pression d'arrêt
P	Puissance
R	Rayon de l'hélice
r	Rayon
T	Traction
V	Vitesse
$W(\xi)$	Vitesse relative $W = V \cdot \sqrt{1 + \frac{\pi^2}{4} \xi^2}$
$\alpha$	Incidence
B	Calage ( $\xi = 0,7$ )
$\gamma$	Paramètre d'avancement $\gamma = \frac{V_a}{nD} = J$

$\eta$	Rendement $\eta = \frac{YI}{X}$
$\lambda_0$	Pas réduit du sillage
$\xi$	Rayon réduit (ou diamètre réduit)
$\xi_0$	Rayon réduit (ou diamètre réduit) du moyeu
$\rho$	Masse volumique
$\tau$	Coefficient de traction $\tau = \frac{Y}{\rho n^2 D^4} = C_T$
$X$	Coefficient de puissance $X = \frac{P}{\rho n^3 D^5} = C_P$
$\Gamma$	Circulation
$\Omega$	Vitesse de rotation

### 1. INTRODUCTION

Les recherches sur les hélices d'avions rapides font partie du contexte plus général des économies de carburant à réaliser sur les futurs avions de transport.

Pour cerner l'intérêt de ce nouveau type de propulsion, les Services Officiels français (DRET/STPA/DGAC) ont lancé l'opération CHARME (Concept d'Hélice pour Avion Rapide en vue d'une Meilleure Economie) en 1982. Ce programme de recherche est mené en collaboration entre l'Aérospatiale divisions Avion et Hélicoptère, Ratier-Figeac et l'ONERA [1].

L'objectif de cette opération de recherche a été de développer de nouvelles méthodes de calcul adaptées à ce type d'hélice, et d'en vérifier le champ d'application en réalisant une maquette de 1 mètre de diamètre (figure 1) pour essais dans la grande soufflerie transsonique S1 de Modane. Si l'essai de cette maquette baptisée HT3 a eu pour objet principal l'étude du fonctionnement aérodynamique de l'hélice, de nombreuses mesures ont également été faites dans les domaines des structures et de l'aéroélasticité [2] et de l'acoustique [3].

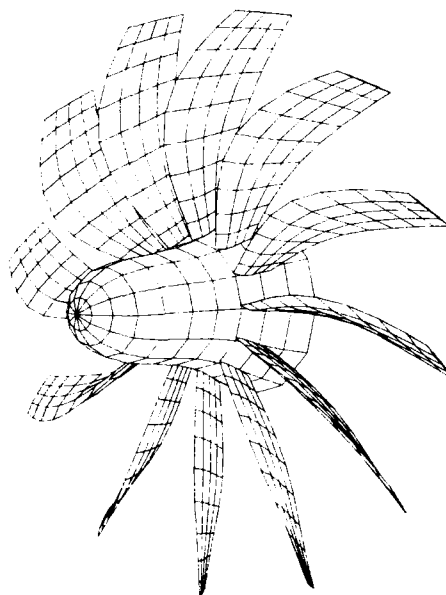


Fig 1 - Hélice HT3

Dans cet article, on présente uniquement la partie aérodynamique de la recherche. Les méthodes de calcul utilisées sont tout d'abord présentées, puis leur degré de validité est analysé à partir des comparaisons avec les résultats expérimentaux obtenus.

### 2. METHODES DE CALCUL

Dans le cadre de l'étude aérodynamique des hélices pour avion rapide (opération CHARME), de nombreuses méthodes ont été utilisées et évaluées. Une description détaillée de ces méthodes est fournie dans la référence [1]. On ne présentera ici que deux de ces méthodes : la méthode simple de Ligne Portante Courbe (programme LPC) et la méthode plus sophistiquée tridimensionnelle transsonique (programme Euler 3D).

### 2.1. Méthode de Ligne Portante Courbe (programme LPC)

Ce type de méthode, remarquable par sa simplicité, reste des plus employé pour la définition et le calcul de performances d'hélices classiques.

La méthode est basée sur le calcul du fonctionnement de chaque section de la pale, dans le champ de vitesse relative, superposition de la vitesse de l'écoulement  $\vec{V}_0$ , de la vitesse d'entraînement  $\vec{\Omega} \wedge \vec{r}$  et du champ de perturbation  $\vec{\delta V}$ .

Le champ de perturbation est calculé à l'aide d'une modélisation tourbillonnaire des pales et de leurs sillages, par application des formules de BIOT et SAVART qui, avec les notations de la figure 2, s'expriment :

$$\vec{\delta V} = -\frac{\delta \Gamma}{4\pi i} \int \frac{\vec{IM} \wedge d\vec{t}}{|\vec{IM}|^3}$$

Pour les hélices classiques (droites), l'induction se réduit à la contribution des tourbillons libres du sillage, de la forme

$$\textcircled{1} \quad \begin{cases} v = \delta v_x(\xi) = \int_{\xi_0}^1 \frac{d\Gamma}{d\xi_1} f(\xi, \xi_1, B, \lambda_0) d\xi_1 \\ u = \delta v_y(\xi) = \int_{\xi_0}^1 \frac{d\Gamma}{d\xi_1} g(\xi, \xi_1, B, \lambda_0) d\xi_1 \end{cases}$$

en posant

$$\xi = \frac{z}{R} \quad \text{et} \quad \xi_1 = \frac{z_1}{R}$$

$\lambda_0$  est le pas réduit de chacun des tourbillons hélicoidaux du sillage.

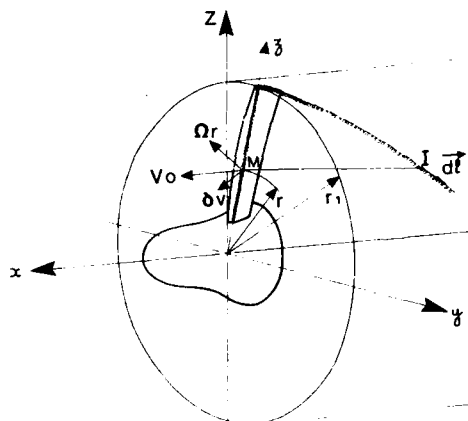


Fig. 2 - Induction d'une ligne portante droite.

La circulation  $\Gamma$  variable en envergure du tourbillon libre modélisant la pale est déterminée par application du théorème de Joukowski au niveau de chacun des profils.

$$\textcircled{2} \quad \begin{cases} \Gamma(\xi) = 1/2 \{ W C_z(\alpha, M_{rel}) \\ \alpha = \beta - \text{Arctg} \left( \frac{V_0 + v}{\Omega r - u} \right) \\ W = \sqrt{(V_0 + v)^2 + (\Omega r - u)^2} \\ M_{rel} = \frac{W}{C} \end{cases}$$

Les méthodes de Ligne Portante consistent à résoudre simultanément les équations  $\textcircled{1}$  et  $\textcircled{2}$ . Moyennant la détermination du  $C_z(\alpha, M_{rel})$  et du pas de sillage  $\lambda_0$ , on calcule par intégrations, les performances globales de l'hélice ; la traînée des différents profils est également prise en compte au niveau de ces intégrations.

Les fonctions  $f$  et  $g$  présentes dans  $\textcircled{1}$  sont calculées par intégration numérique des formules de BIOT et SAVART. Les intégrales du système  $\textcircled{1}$  sont traitées par une méthode analogue à celle de GLAUERT pour les ailes, en développant  $\Gamma$ ,  $f$  et  $g$  en séries trigonométriques. Le  $C_z$  et  $C_x$  des profils sont déterminés par interpolation dans un fichier de polaires expérimentales de profils.

L'originalité de la méthode réside dans le calcul exact du pas réduit  $\lambda_0(\xi)$  de chacun des tourbillons hélicoidaux du sillage à l'aide d'un processus itératif.

Pour traiter le cas de pales d'hélices comportant de la flèche, cette méthode a été modifiée d'une part en incorporant la théorie simplifiée de l'attaque oblique pour le fonctionnement des profils, et d'autre part en prenant en compte la géométrie d'une ligne portante courbe dans le calcul tourbillonnaire.

Ce dernier point est illustré par la figure 3, qui montre la nécessaire prise en compte de la distance axiale  $X_w$ , et du déphasage  $\psi$  entre les points J et M, pour le calcul du champ de perturbation.

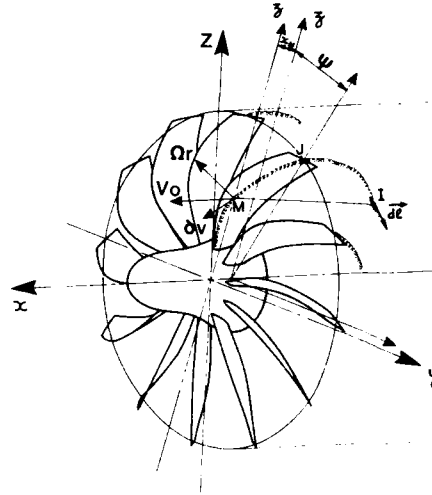


Fig. 3 - Induction d'une ligne portante courbe

Le système ① devient en conséquence :

$$\textcircled{1} \begin{cases} v = \delta v_x(\xi) = \int_{\xi_0}^1 \left[ \frac{d\Gamma}{d\xi_1} f_1(\xi, \xi_1, \lambda_0, \psi, \beta_n, B) + \Gamma h_x(\xi, \xi_1, \psi, \beta_n, B) \right] d\xi_1 \\ u = \delta v_\theta(\xi) = \int_{\xi_0}^1 \left[ \frac{d\Gamma}{d\xi_1} g_1(\xi, \xi_1, \lambda_0, \psi, \beta_n, B) + \Gamma h_\theta(\xi, \xi_1, \psi, \beta_n, B) \right] d\xi_1 \end{cases}$$

les fonctions  $f_1, g_1$  concernent le sillage ; les fonctions  $h_x$  et  $h_\theta$  concernent l'induction des lignes portantes courbes. Elles sont calculées par intégration numérique.

L'effet global de ces nouvelles fonctions est montré sur la figure 4, où sont comparées les répartitions de circulation pour une ligne portante droite et pour une ligne portante courbe typique, pour les mêmes répartitions de pas de sillage  $\lambda_0(\xi_1)$ . On remarque, que l'incurvation de la ligne portante se traduit par un décalage du maximum de circulation vers l'extrémité de la pale et par une inflexion dans les zones médianes.

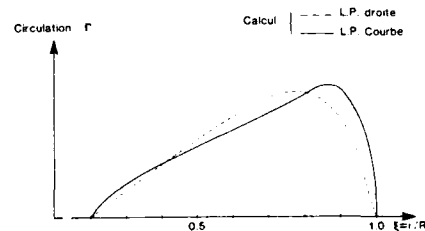


Fig. 4 - Influence d'une ligne portante courbe.

Ce résultat montre l'importance d'une modélisation correcte de la géométrie de pales comportant de la flèche, pour la prévision de la répartition de charge sur les pales de l'hélice.

La méthode de Ligne Portante Courbe (LPC) constitue l'outil de base pour la conception et le calcul des performances d'hélices pour avions rapides. Ses avantages principaux résident dans la souplesse d'emploi (simplicité des données géométriques relatives à l'hélice) et sa rapidité d'exécution (environ 10 secondes CPU sur CYBER 750). Son intérêt, comme on le montrera au paragraphe 4, concerne la prévision des performances globales (traction, puissance, rendement) de l'hélice, avec possibilité de prise en compte de l'interaction d'une nacelle moteur et possibilité de calcul de l'hélice en incidence.

Le programme LPC a également été étendu au calcul des doublets d'hélices coaxiales contra-rotatives (programme LPC2).

## 2.2. Méthode tridimensionnelle transsonique (programme Euler 3D)

Cette méthode a été initialement développée pour les turbomachines.

Dans l'hypothèse de fluide parfait, les équations d'Euler décrivant le comportement d'une particule le long d'une ligne de courant relative s'écrivent :

$$\textcircled{3} \quad \begin{cases} \text{(a)} & \text{div}(\rho \bar{W}) = 0 \\ \text{(b)} & \text{div}(\rho \bar{W} \otimes \bar{W} + p \bar{I}) + \rho \bar{F} = 0 \\ \text{(c)} & \text{div}(\rho I \bar{W}) = 0 \end{cases}$$

où  $I$  désigne la rothalpie :

$$I = h(p, \rho) + \frac{W^2}{2} - \frac{r^2 \Omega^2}{2}$$

et  $\bar{F}$  est la somme des accélérations d'entraînement et de Coriolis :  $\bar{F} = 2\Omega \bar{e}_z \wedge \bar{W} - r\Omega^2 \bar{e}_r$ ,

$\bar{e}_z$  et  $\bar{e}_r$  sont les vecteurs unitaires axial et radial du référentiel tournant.

Ce problème stationnaire est d'abord transformé en un problème pseudo-instacionnaire par introduction d'une variable "temps" fictive, qui permet de construire un procédé itératif convergent vers la solution stationnaire. Le système pseudo-instacionnaire est construit en remplaçant l'équation de l'énergie 3 (c) par la condition de rothalpie uniforme  $I = \text{Cte}$  et en traitant les formulations instacionnaires exactes des équations de continuité 3 (a) et de quantité de mouvement 3 (b).

$$\textcircled{4} \quad \begin{cases} \text{(a)} & \frac{\partial \rho}{\partial t} + \bar{\nabla} \cdot (\rho \bar{W}) = 0 \\ \text{(b)} & \frac{\partial \rho \bar{W}}{\partial t} + \bar{\nabla} \cdot (\rho \bar{W} \otimes \bar{W} + p \bar{I}) + \rho \bar{F} = 0 \end{cases}$$

Les quatre inconnues du problème sont la masse volumique  $\rho$  et les trois composantes de la quantité de mouvement relative  $\rho \bar{W}$ . La pression statique est déterminée par la condition de rothalpie uniforme  $I = \text{Cte}$  et par la relation thermodynamique :

$$p(\rho, \rho \bar{W}) = \frac{\gamma-1}{\gamma} \left( 1 + \frac{\Omega^2 r^2}{2} \right) \rho - \frac{\gamma-1}{2\gamma} \frac{(\rho \bar{W})^2}{\rho}$$

Le paramètre  $\gamma$  étant égal à  $\gamma = \frac{C_p}{C_v}$  et dans les applications usuelles  $\gamma = 1.4$ .

Le système  $\textcircled{4}$  est complété par un ensemble de conditions aux limites et de conditions initiales.

Des considérations de périodicité permettent de limiter le domaine de calcul à l'espace compris entre deux pales consécutives (figure 5).

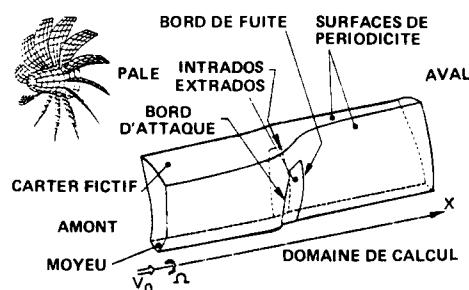


Fig. 5 - Domaine de calcul Euler 3D

Les conditions limites basées sur la résolution d'équations de compatibilité sont du type :

- périodicité sur les surfaces latérales, sauf sur les pales où une condition de glissement relatif est appliquée,
- glissement relatif sur le moyeu (casseroles et nacelles),
- direction de la vitesse imposée dans le plan amont,
- condition de pression (équilibre radial simplifié) ou condition de non-réflexion des ondes acoustiques dans le plan aval,
- glissement relatif, ou condition de pression, ou condition de non-réflexion des ondes acoustiques sur le carter fictif, selon le type de calcul (hélice en soufflerie ou atmosphère infinie).

Le maillage tridimensionnel est de type H, permettant une construction relativement simple. Un exemple de maillage est fourni sur la figure 6, où trois frontières du domaine de calcul ont été représentées.

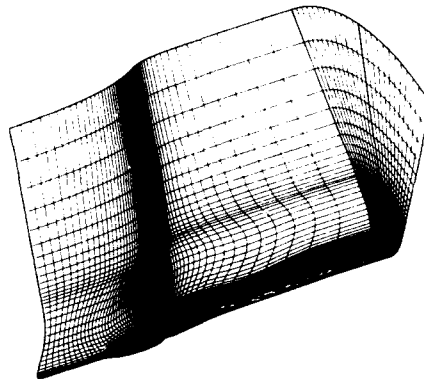


Fig. 6 - Surfaces frontières du maillage tridimensionnel Euler 3D

Les maillages usuels comportent approximativement 30 000 points, ce qui conduit à des temps de calcul d'environ 20 minutes CPU sur ordinateur CRAY 1S.

### 3. CONCEPTION DE L'HELICE HT3

La conception aérodynamique de l'hélice HT3 a été effectuée par l'ONERA, la conception structurale et la fabrication des pales par l'Aérospatiale et le moyeu et les modifications du banc d'essai par Ratier-Figeac.

Le point d'optimisation de l'hélice a été choisi par l'Aérospatiale division Avion : charge au disque  $C = 250 \text{ kW/m}^2$ , nombre de Mach de vol  $M = 0.75$  à  $Z = 10\,500 \text{ m}$  ( $Z = 35\,000 \text{ ft}$ ), vitesse de rotation périphérique  $\Omega R = 220 \text{ m/s}$  ; ceci correspond en notations adimensionnées à  $X = 1.82$  et  $\gamma = 3.12$ .

La méthodologie employée est présentée sur la figure 7. La conception articulée autour de la méthode Ligne Portante Courbe, compte tenu des lois de définition géométrique des pales et du moyeu ainsi que des caractéristiques aérodynamiques des profils bidimensionnels (profil isolé ou en grille, moyeu axisymétrique), permet de trouver la loi de vrillage la mieux adaptée pour optimiser le rendement de l'hélice au point de définition tout en gardant de bonnes performances aux autres points de vol caractéristiques de l'hélice.

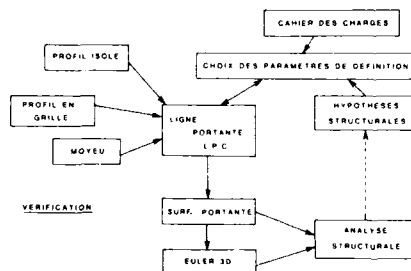


Fig. 7 - Définition d'une hélice pour avion rapide.

Les lois de flèche (empilement tridimensionnel des profils) et d'épaisseur relative de profils sont choisies en intégrant des contraintes d'ordre structural et aéroélastique.

La seconde phase de la conception aérodynamique concerne la vérification du bon fonctionnement aérodynamique de l'ensemble pales + moyeu, à l'aide de calculs tridimensionnels. A ce stade de la conception, on utilise essentiellement la méthode Euler 3D, qui permet notamment de vérifier l'absence de blocage de l'écoulement en embase de pales ; dans ces calculs, on peut prendre en compte itérativement l'effet des déformations de pales sous l'action des efforts centrifuges et aérodynamiques, calculées par exemple en utilisant un code éléments finis de structures en rotation.

Dans sa définition finale, l'hélice HT3 comporte 12 pales en flèche. Les profils sont modernes, spécialement adaptés au fonctionnement en régime transsonique. En particulier, la partie externe des pales est conçue autour du profil mince OR2204 ( $e/l = 0.035$ ) dont les caractéristiques à grand nombre de Mach sont très bonnes comme on peut le voir sur la figure 8 où ses performances sont comparées à celles du profil classique NACA 16304. Une vue de la forme en plan des pales, ainsi que l'empilage des profils de l'hélice HT3 sont fournis sur la figure 9.

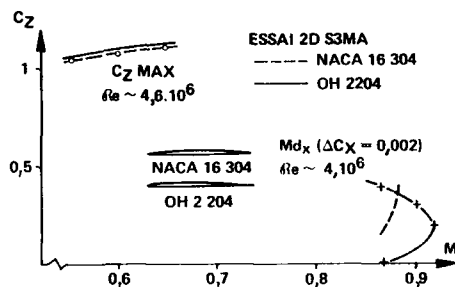


Fig. 8 - Performances du profil mince OH2204.

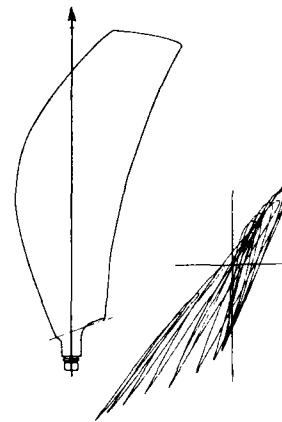


Fig. 9 - Pales de l'hélice HT3.

#### 4. COMPARAISON DES RESULTATS DE CALCUL AVEC L'EXPERIENCE

L'hélice HT3 a été essayée dans la grande soufflerie S1 Modane de l'ONERA. Une photographie de l'hélice de 1 mètre de diamètre dans la veine d'essai est présentée sur la figure 10. Le dispositif d'essai ainsi que les très nombreuses mesures effectuées sont schématiquement représentés sur la figure 11. On notera l'originalité de certaines des mesures, notamment des mesures de pression sur les pales, par l'intermédiaire de capteurs de pression miniatures implantés à l'intérieur des pales en matériau composite.

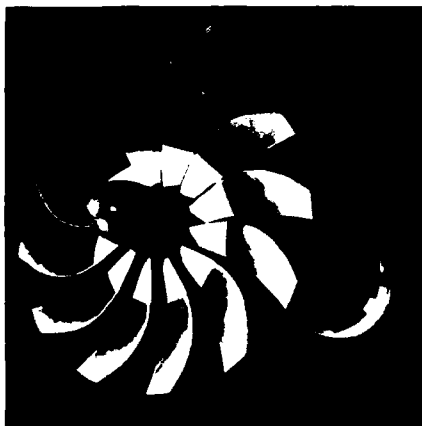


Fig. 10 - Essai de l'hélice HT3 dans la soufflerie S1 Modane de l'ONERA

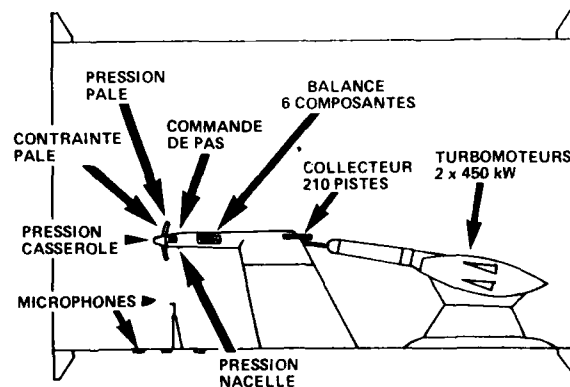


Fig. 11 - Mesures effectuées lors de l'essai de l'hélice HT3.

Des mesures de pression utilisant la même technique ont également été effectuées sur la casserole tournante [4].

Les performances mesurées au cours de cet essai sont bonnes comme le montre le tableau de la figure 12. En particulier on remarque que la bonne performance mesurée à grand nombre de Mach est très voisine de la prévision faite par la méthode LPC décrite au paragraphe 2 (le rendement net mesuré  $\eta = 0.79$  est très proche de la prévision  $\eta = 0.796$ ). A plus faible nombre de Mach, pour des points de vol correspondant au décollage et à la montée avion, la performance mesurée est supérieure à la prévision, laissant supposer que la prise en compte de la trainée de profil dans la méthode LPC, par l'intermédiaire de la trainée élémentaire de profils bidimensionnels, est probablement pessimiste pour ce type de pales de faible allongement et comportant de la flèche.

	ESSAI S1MA	CALCUL LPC
$M = 0,25$ $\gamma = 1,24 \quad x = 1,43$	0,633	0,583
$M = 0,5$ $\gamma = 2,3 \quad x = 1,4$	0,834	0,783
$M = 0,7$ $\gamma = 3,12 \quad x = 1,82$	0,810	0,807
$M = 0,75$ $\gamma = 3,12 \quad x = 1,82$	0,790	0,796

Fig 12 - Hélice HT3. Rendement net.

La validité de la méthode LPC n'est pas limitée à la prévision du niveau de rendement des hélices rapides. La figure 13 montre que l'évolution calculée du coefficient de puissance  $X$  avec le paramètre d'avancement  $\gamma$ , à calage de pale  $\beta$  fixé, est très voisine de l'évolution obtenue en essai, avec toutefois un léger écart d'environ  $2,5^\circ$  sur la valeur de l'angle de calage, qui peut être au moins partiellement attribué à la déformation des pales sous charge.

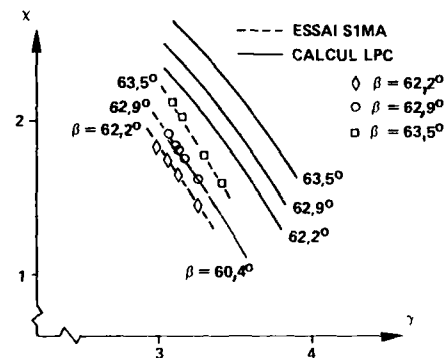


Fig 13 - Hélice HT3. Performances à  $M = 0,75$   
Comparaison calcul/expérience

La méthode Euler 3D a été utilisée au cours de la phase de conception pour s'assurer notamment de l'absence de blocage de l'écoulement dans le canal inter-pales près du moyeu. Un autre point important dans l'étude des résultats de calculs par la méthode Euler a été de vérifier que les nombres de Mach relatifs maximaux sur les profils n'étaient pas trop importants ( $Mr_{rel} \leq 1,4$  sur toute la pale pour  $M = 0,75$ ), afin d'éviter tout risque de décollement au pied du choc par interaction avec la couche limite.

La figure 14, montre un exemple de calcul sur l'hélice HT3, pendant la phase de conception de l'hélice.

La méthode Euler 3D a pu être évaluée à l'issue des essais en soufflerie de l'hélice HT3.

Sur la figure 15 les répartitions des pressions mesurées et calculées sont comparées sur un profil situé au rayon relatif  $\xi \approx 0,8$ , pour un essai à  $M = 0,7$ . On remarque que l'accord calcul/expérience est relativement bon.



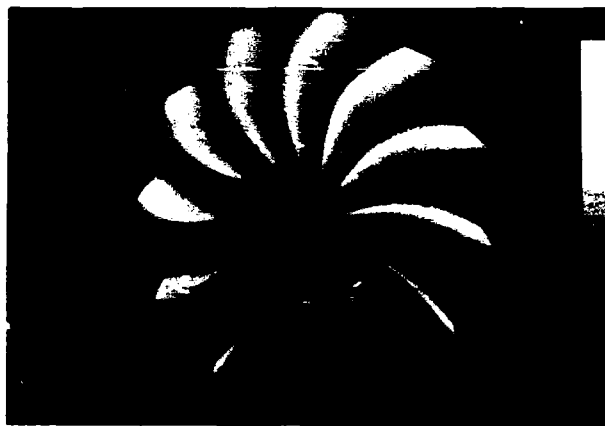
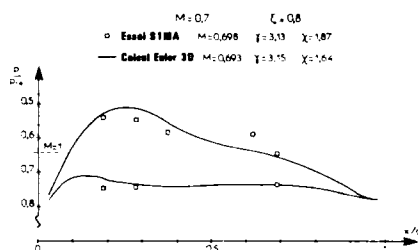
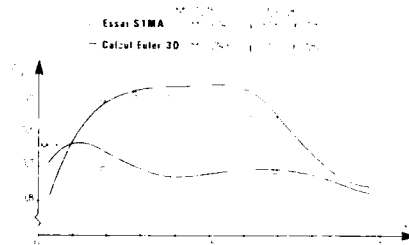


Fig. 14 - Hélice HT3. Calcul Euler 3D.

Fig. 15 - Hélice HT3 Pressions sur les pales.  $M = 0.7$ 

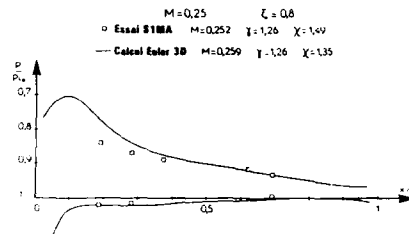
Le calcul sous-évalue toutefois légèrement les pressions maximales (et surévalue donc légèrement les nombres de Mach relatifs maximaux) tant à l'intrados qu'à l'extrados du profil ; la recompression mesurée de l'écoulement à l'extrados du profil apparaît également moins progressive que celle calculée.

Lorsque le nombre de Mach de l'écoulement est plus élevé ( $M = 0.75$  sur la figure 16) l'accord avec l'expérience reste acceptable, la même remarque concernant la surévaluation du nombre de Mach relatif maximal par le calcul peut être faite. On peut penser que les effets visqueux non pris en compte par la méthode Euler 3D pourraient expliquer au moins partiellement cet écart.

Fig. 16 - Hélice HT3. Pressions sur les pales.  $M = 0.75$ 

Le champ d'application traditionnel de la méthode Euler 3D concerne essentiellement les domaines transsoniques et supersoniques. Aux plus faibles nombres de Mach (domaines incompressible et subsonique compressible) la méthode n'est pas parfaitement adaptée. On remarque cependant sur la figure 17, que le fonctionnement du profil situé au rayon relatif  $\xi = 0.8$  est relativement bien prévu. C'est dans la partie de l'extrados proche du bord d'attaque que l'écart entre le calcul et l'expérience est le plus sensible ; bien que cette zone ne soit pas parfaitement décrite expérimentalement en raison du faible nombre de capteurs de pression dans cette région du bord d'attaque, il semble que la recompression sur l'extrados du profil soit assez mal prévue par ce calcul. Ceci pourrait être dû au type de maillage en  $H$  utilisé pour le calcul Euler 3D, qui n'est pas très bien adapté aux grands rayons de bord d'attaque des profils modernes utilisés sur l'hélice HT3 ; ce phénomène pourrait également être attribué à l'importance de la dissipation numérique nécessaire pour traiter ce cas difficile.

On peut souligner à cette occasion que des développements nouveaux sont en cours à l'ONERA afin d'améliorer la prise en compte des bords d'attaque des profils par une technique de sous-domaines dans le calcul Euler 3D.

Fig. 17 - Hélice HT3. Pressions sur les pales  $M = 0,25$ 

Dans l'état actuel les méthodes développées au cours de l'opération CHARME sont bien adaptées pour la prévision des performances et des caractéristiques de l'écoulement sur des hélices pour avion rapide simple-rotation.

##### 5. HÉLICES POUR AVIONS RAPIDES CONTRA-ROTATIVES

L'intérêt des hélices coaxiales contra-rotatives réside dans le fait que l'écoulement qui est dévié à la sortie de la première rangée de pales est redressé par la seconde rangée, minimisant ainsi la perte d'énergie cinétique due à la présence d'une composante de vitesse tangentielle dans le sillage d'une hélice simple-rotation ; cette solution est d'autant plus intéressante que la déviation à l'aval des hélices rapides simple-rotation est grande en raison de la très forte charge au disque ( $C > 250 \text{ kW/m}^2$ ) de ce type d'hélices.

Pour traiter le cas des hélices contra-rotatives des méthodes de calcul sont en cours de développement à l'ONERA. On ne présentera ici que des résultats de calculs obtenus avec la méthode LPC2, extension au cas des hélices contra-rotatives de la méthode LPC déjà décrite.

Comme pour les hélices simple-rotation, la méthode LPC2 calcule à partir d'une définition simple de la géométrie des pales (lois de définition), les performances de chacune des hélices fonctionnant dans le champ aérodynamique créé par l'autre.

La performance globale du doublet est obtenue par sommation des performances de chacune des hélices. Il faut signaler à ce sujet, que les calculs d'optimisation d'hélices contra-rotatives sont globalement plus coûteux que les hélices simple-rotation. En effet, le fonctionnement de chacune des rangées de pales dans le champ aérodynamique de l'autre nécessite un calcul itératif environ 5 fois plus long que le calcul d'une hélice simple-rotation ; de plus le choix des paramètres de fonctionnement de chacune des rangées de pales (répartition de la puissance, choix des régimes de rotation, des nombres de pales...) multiplie de façon importante les calculs nécessaires.

À titre de comparaison, nous avons étudié des hélices contra-rotatives basées sur la définition de l'hélice simple-rotation HT3. Une illustration du type d'hélice étudié est fournie sur la figure 18, dans une configuration hélice tractrice 6 + 6 pales.

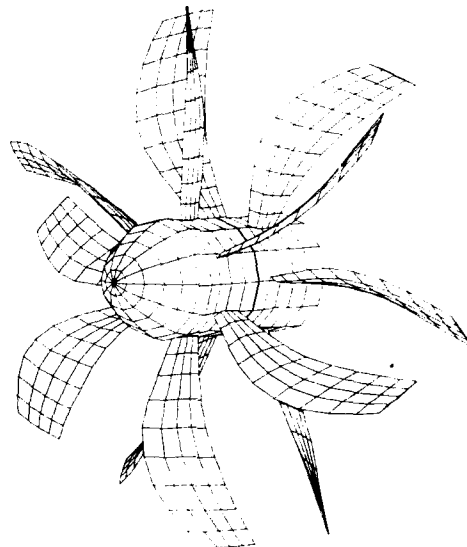


Fig. 18 - Exemple de doublet d'hélices contrarotatives 6 + 6 pales

Pour cette étude, la puissance appliquée sur chaque rangée de pales et la vitesse de rotation sont identiques, ce qui correspond souvent à une solution proche de l'optimum de performance. Les diamètres d'hélices et de moyeu sont identiques pour les deux rangées de pales.

Si l'on regarde le rendement induit de l'hélice qui ne prend en compte que les pertes induites dans le sillage de l'hélice (accélération de l'écoulement axial, déflexion tangentielle, non-uniformité de l'écoulement dues au nombre discret de pales) l'avantage intrinsèque des solutions contra-rotatives est pleinement démontré. Sur la figure 19, on remarque que l'augmentation du coefficient de puissance  $X$  (qui résulte uniquement de variations de la charge au disque  $C = P/D^2$  lorsque  $\gamma$  est fixé) fait beaucoup moins chuter le rendement induit des hélices contra-rotatives que celui des hélices simple-rotation par rapport à l'optimum que constitue le rendement de Froude. Les pertes de non-uniformité d'écoulement sont d'autant plus faibles que le nombre de pales est grand ; le rendement induit de la configuration 9 + 9 est d'environ 2 points supérieur à celui d'une configuration 6 + 6 pour  $X = 3$ . La répartition du nombre de pales entre la rangée amont et la rangée aval est assez indifférente en ce qui concerne le rendement induit ; en effet les solutions 6 + 9 et 9 + 6 sont sensiblement équivalentes, bien intercalées entre les solutions 6 + 6 et 9 + 9.

Ces conclusions partielles doivent être nuancées dès lors que l'on considère également les pertes par viscosité traduites dans la méthode LPC2 par la prise en compte de la traînée des profils comme il est fait sur la figure 20. Pour cette comparaison, les lois de définition et notamment la loi de largeur des cordes, sont conservées identiques pour toutes les hélices. On remarque que pour les grands coefficients de puissance l'avantage des solutions contra-rotatives à grand nombre de pales est toujours déterminant ; pour  $X = 2.5$ , la solution contra-rotative 9 + 9 a un rendement d'environ 12 points supérieur à l'hélice simple-rotation, et d'au moins 1 point supérieur à l'hélice contra-rotative 6 + 6. Aux faibles coefficients de puissance ( $X \leq 1$ ), la traînée des profils devient très importante pour toutes les configurations, la largeur des cordes employées dans cette étude devenant beaucoup trop importante ; la solution 6 + 6 est alors moins pénalisée que la solution 9 + 9, montrant qu'une optimisation sur des bases différentes de celles de cette étude serait nécessaire pour cerner au mieux les avantages respectifs de chacune des solutions.

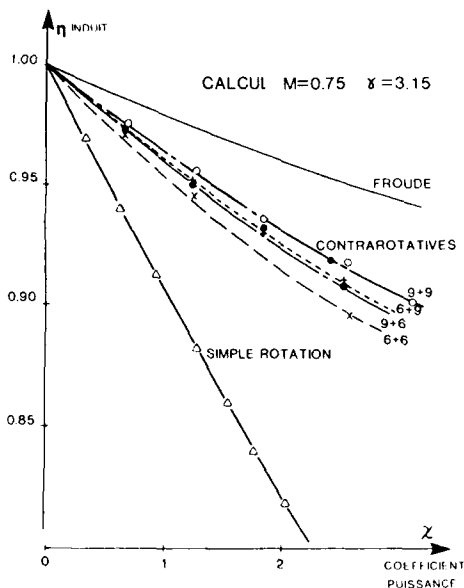


Fig 19 - Hélices contra-rotatives. Influence du coefficient de puissance sur le rendement induit.

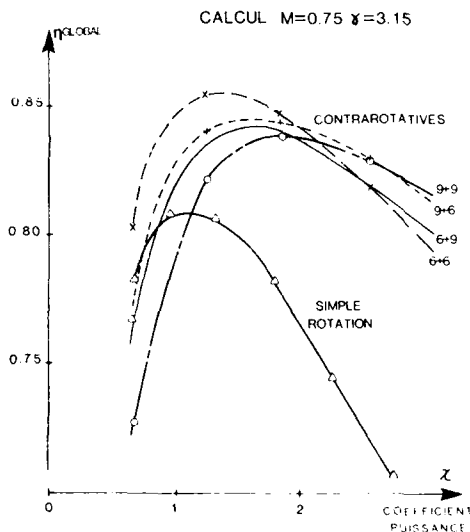


Fig 20 - Hélices contra-rotatives. Influence du coefficient de puissance sur le rendement global

Cette étude succincte montre à la fois l'intérêt de la solution hélice contra-rotative par rapport à la solution simple-rotation, et la difficulté de cerner au stade de l'avant-projet les paramètres d'optimisation de ces doublets. De telles études sont poursuivies activement à l'ONERA.

Il faut signaler que ces études sont menées au stade actuel de la recherche uniquement par calcul. Les bons résultats obtenus sur l'hélice simple-rotation HT3 laissent à penser que la démarche est correcte. Il serait toutefois nécessaire de valider les méthodes de calcul à l'aide d'un support expérimental qui pourrait être constitué au cours d'une opération CHARME2.

Par ailleurs, d'autres méthodes sont en cours de développement pour traiter ce type d'hélices contra-rotatives, notamment un code de résolution des équations d'Euler en tridimensionnel.

## 6. CONCLUSIONS

Les méthodes de calcul développées au cours de l'opération CHARME se sont avérées bien adaptées pour calculer le fonctionnement aérodynamique des hélices rapides simple-rotation.

Les performances de l'hélice HT3 essayée dans la soufflerie S1 Modane sont conformes aux prévisions faites à l'aide de la méthode globale de Ligne Portante Courbe. Le développement de l'écoulement transsonique sur les pales de cette hélice, est bien modélisé par le calcul Euler 3D, comme le montrent les comparaisons avec les mesures de pression faites en essai.

Les études s'orientent maintenant vers les doublets contra-rotatifs dont les potentialités ont été cernées à l'aide de calculs par une méthode globale (LPC2). Les développements futurs de ces études concerneront des méthodes plus sophistiquées, et une vérification expérimentale.

#### REFERENCES

- [1] - J.M. BOUSQUET  
"Methodes aérodynamiques utilisées en France pour l'étude des hélices pour avions rapides".  
AGARD CP 366, Toronto 1984. (English translation in La Recherche Aérospatiale N° 1985-1).
- [2] - J.M. BESSON, D. PETOT  
"Comportement dynamique d'un rotor de prop-fan".  
AGARD CP 366, Toronto 1984.
- [3] - H. GOUNET, S. LEWY  
"Prediction of single-rotation prop-fan noise by a frequency domain scheme".  
15th ICAS, London 1986 (ONERA TP 1986-100).
- [4] - J.M. BOUSQUET  
"Theoretical and experimental analysis of highspeed propeller aerodynamics".  
AIAA 86-1549 (ONERA TP 1986-64).

#### DISCUSSION

N. KROLL, Ge

- 1) How many grid points did you use in the Euler calculations ?
- 2) How was the non linear effects accounted for in your linear methods for the counter-rotating propellers ( $M = 0.76$ ) ?

Author's Reply

1) We used about 30000 points in an inter-blade calculation domain. Mesh is of "H" type.

2) In the curved lifting line method (LPC) non-linear effects are taken into account through lift and drag characteristics of 2D airfoils (experimental or calculated data).

T.J. SULLIVAN, US

In your paper, you show that the predicted global efficiency of the counter-rotating propellers is dependent upon the number of blades in each rotor. Can you comment on why the 9 + 6 combination is better than the 6 + 9 ?

Author's Reply

It must be pointed out that the parametric study presented on counter-rotating propellers has been done with keeping airfoils and chord width constant (the same as HT3 highspeed propeller). In this case the drag of a 9 bladed aft propeller is more important than the drag of a 9 bladed front propeller, which explains the slight superiority of the 9 + 6 combination over the 6 + 9. Other choices of airfoils and chord width may change this conclusion.

**ANALYSIS OF POSSIBLE TRANSMISSION  
ARRANGEMENTS APPLICABLE FOR DRIVING SINGLE  
OR TWIN COUNTERROTATING FANS ON PROPFAN ENGINES**

by

L. Battazzato and S. Turra  
Direzione Progettazione  
FIAT AVIAZIONE  
Corso Ferrucci 112 - 10100 TORINO  
Italy

**SUMMARY**

A number of different designs of propfan engines are now being defined by the main engine manufacturers in the world. Some of these designs require a reduction gearbox between the LP turbine and the propfan; the propfan itself is conceived as single stage, variable pitch blade or double counterrotating stage variable pitch solution.

In order to satisfy these requirements, the authors propose different mechanical arrangements of the reduction gearbox and, for given engine interfaces, compare their relative merits in order to eventually show the optimum solution.

The comparison is made on the basis of various aspects, namely: lightness, quietness, life, reliability, fail safety and maintainability. The analysis is carried out on the basis of the experience acquired by FIAT AVIAZIONE after thirty years of high level work on design, development and manufacturing of transmissions for aeronautical application.

**FOREWORD**

Starting from 1975 a lot of new studies have been conducted with the aim of defining new high efficiency aircraft engines: these are based on the use of the new technology high efficiency propellers that allowed to configure the new engines as an hybrid between the old turboprops and the modern turbofans with a very high bypass ratio.

With this aim in mind, a number of possible solutions have been conceived:

- the propeller is configured as single or double counter rotating blade row
- the propeller is rotating in the free air or is shrouded for containment and better noise abatement
- the propeller is on the front (tractor) or on the rear (pusher) of the engine
- the speeds of the propeller and of the drive turbine are independently optimized: consequently a geared transmission is needed in order to allow the single element to rotate at its own optimum speed
- as an alternative the two modules can be solidly mounted together and optimized as a single rotor
- the choice of the optimum solution can be heavily influenced by the type of installation on the aircraft (wing or tail mounting).

Finally the total panorama is complicated by the fact that today's technology is not ready for solving the totality of the problems. A lot of assumptions must be made based on future trends of present technology, on the use of new materials, on the adequacy of design solutions. These assumptions must be entered

into the equations of the problem in order to get the optimum solution: this is the reason why the studies made by different engine manufacturers in the world seem to conclude on different optimized configurations.

In this panorama, we in FIAT AVIAZIONE as expert on gearboxes, can offer our experience on the matter, by trying to show the best gearbox solution most suitable to propeller and turbine configurations, by putting in evidence the features or problems that need technology development because they are beyond the practice on past gearboxes for aircraft application.

In the past we had examples of turbofans with geared drive between turbine and fan: they had limited applications because of two main reasons:

- Turbofans in those days were not oriented to very high bypass ratios; the fan speed could be sufficiently high for a direct drive from the turbine without too important weight penalties on each single element.
- The gearbox technology was not ready yet for offering light, silent, reliable, durable, high power gearboxes whose behaviour would not deteriorate unacceptably the equivalent characteristics offered by the other modules of turbofan engines.

#### GEARBOX SOLUTIONS FOR DUAL OUTPUTS COUNTER ROTATING FANS

Among the various possible configurations of gearboxes capable of driving two counter rotating propellers, we evaluated some with offset and some with in line input and output shafts.

Generally the first ones ask for a higher number of bearings and gears, thus having a higher weight, higher overall dimensions and lower reliability. Also, eventually, the offset solutions give major problems in defining the air path within the fan and the other modules of the engine. Among the in line solutions, the Inline Differential Planetary (see fig.1) seems the most attractive because it has the lowest number of items and it has no meshing loads reacted on the structure. Consequently the gearbox generated vibration or noise transmitted to a/c structure and to ambient will be minimized.

This solution offers the possibility to assure a given RPM and torque distribution between the outputs to the fans, through the intervention of pitch control on each propeller. However we must underline that, should any failure arise causing the incapability of one fan to absorb the due torque, the other fan torque will change proportionally; in other words the failure of one fan cannot be covered by the other. Fig.2 proposes another Inline Differential Planetary with split path; in this case the extra added parts impact negatively on the weight and on the reliability of the system but allow to cover to a certain extent the single fan rupture because a constant input/output ratio is assured.

The same advantage would be offered by the Inline Multiple Stars of fig. 3; however gear meshing loads are in this case directly transferred to the structure with detrimental effects on weight, vibration and noise. It offers the possibility to reduce the outer dimensions of the gearbox and could then become attractive at high input/output gear ratios for which the previous solutions would require too large ring gears. We give in the following table the results of relative evaluations of the above three solutions.

	Inline Differential Planetary	Inline Differential Plan.with Split Path	Inline Multiple Stars
Design complexity:			
Number of gears	5 to 7	8 to 12	11 to 14
Number of bearings*	9 to 11	15 to 21	12 to 14
Outer diametral dimension	base	base	- 12% of base
Axial length	base	+ 10% of base	+ 30% of base
Vibration to structure	low	med.	high
Efficiency	99.2% possible	-.30%	-.40%
Reliability	base	failure probability: 70% higher than base	failure probability: 65% higher than base
Weight	base	+ 12% of base	+ 16% of base at 1:3 ratio - 4% of base at 1:7 ratio
* A different number of bearings could be required as a consequence of the integration of the gearbox in the engine.			

#### GEARBOX SOLUTIONS FOR SINGLE OUTPUT TO SINGLE ROW FAN

In this case too, a number of gearbox configurations has been studied and the relative merits evaluated. As said in the previous paragraph, the same difficulty for the engine overall configuration is created by gearboxes with offsets between input and output shafts.

Having then taken into consideration only the in line configurations, we propose three solutions:

- The Counterrotating Inline Star Gear System (fig.4) is the simplest arrangement, with sun and ring gears rotating in opposite directions and with star gears located on fixed structure. The number of elements is minimal.

The solution loses its feasibility for the high transmission ratios: in fact as the ratio increases the sun gear reduces its diameter and the number of stars that can be located in the available space diminishes. Consequently the ring gear, having concentrated loads in fewer points, must be stiffened thus causing its weight to increase over acceptable limits.

- These facts can be overcome with the solution shown in fig.5, Codirectional Inline Double Row Star Gear system. The multiple row star gears allows to mesh with the sun and the ring gears with smaller and more numerous stars.

- As an alternative, the Counterrotating Double Stage Inline Star Gear System shown in fig.6 allows to have a high total ratio thanks to the two step down gear meshings; in the second stage a very high contribution to the total ratio is achievable.

The loads transferred to the structure are in this case higher than in the previous cases: the noise and vibrations transferred to the support structure are expected higher and more difficult to be brought within acceptable limits.

In the following table the results of studies and the relative merits of the above three solutions are given.

	Counterrotating star gear system	Codirectional double row star gear system	Counterrotating double step star gear system
Design complexity :			
Number of gears	5 to 7	11 to 14	8 to 12
Number of bearings *	8 to 12	20 to 26	10 to 14
Outer diametral dimension	base	base	- 12% of base
Axial length	base	base	+ 30% of base
Vibration to structure	med.	med.	high
Efficiency	99.4% possible	- .4%	- .4%
Reliability	base	failure prob.: 110% higher than base	failure prob.: 40% higher than base
Weight	base	+10% of base at 1:3 ratio -8% of base at 1:7 ratio	+7% of base at 1:3 ratio -13% of " at 1:7 ratio
* A different number of bearings could be required as a consequence of the integration of the gearbox in the engine.			

#### REQUIREMENTS TO BE MET IN THE DESIGN OF THE GEARBOX

The design of the gearbox should be done trying to satisfy the characteristics normally required for a/c engines:

- lightness
- highest possible running temperature
- low noise and vibration generation
- long life
- reliability
- fail safety
- maintainability.

The designer knows that eventually the design will be a compromise among these requirements: the gearbox, for example, will be the lightest allowed by the life offered to the operator. Keeping this principle in mind, few remarks on each characteristic can be done.

#### Lightness and highest possible running temperature

All the parts in the gearbox must be sized carefully for a good result in this aspect.

The gears in particular concentrate the highest part of gearbox weight, so they must be considered with the maximum of care.

We in Fiat normally define the gears on the basis of bending stress and of flash temperature delta as per AGMA calculation method.

The optimization procedure we applied for each gear meshing of each proposed solution can be understood from the chart of fig.7 applicable to the sun/star gears meshing of the Counterrotating Star Gear System (fig.4), capable of the following characteristics:

- power 40.000 HP
- input speed 6.500 RPM
- ratio 1:5

Curve number 1 and 2 give the limit modulus/face width combinations for spur gear and helical gear respectively at the max assumed bending stress; curves 3a,b,c the limits at flash temperature deltas of 130, 90 and 70°F.

The first point we can deduce from the graph is the advantage obtainable with helical in comparison with spur gears: the face width can be reduced of some 10 to 15%. The choice of the best solution, highest permissible stress and flash temperature delta,



lies on point A, intersection of curves 2 and 3a.

In fact the chosen design point reduces the dimensions and then the weight, of the meshing gears to a minimum.

Indicatively, according to our experience, the temperatures we assume in the system are (in max take off hot day condition):

oil input to lube circuit	135°C
oil output to heat exchanger	160-165°C

The assumed flash delta temperature of 130°F can bring the local metal temperature even in the case of good lubrication and cooling up to 200-210°C.

The temperature level we suggest is tailored on the new gear materials now having increasing applications, namely:

- new carburizing steels capable of displacing the critical temperature from 170°C (as per the traditional carburizing steels such as SAE 9310) up to 300°C. Among these, we acquired good experience on Cartech 00053 and CBS 600.

- nitriding steel that could run at a temperature of 450°C without any structural damage.

The use of nitriding steels for large gears as in the present application must be checked carefully; in fact the high stress levels require evidently a perfect tooth geometry so that the teeth must be ground after heat treatment.

Now, considering that the max case thickness should be of the order of .4 mm, the deformations imposed on the gears during heat treatment must be such that the following grinding operation will not cause any local reduction of the case thickness under .3 mm in order not to cause underskin cracks when applying the meshing loads.

Consequently we can be quite sure that the larger gears required for this application shall be made of the carburizing steels mentioned above.

A small remark must still be done on running temperature: of course it is convenient to run at the max temperature allowed by materials for the required life; the oil heat exchanger would have the maximum temperature differential to the ambient air, so its dimensions and weight could be minimized.

At this point the evolution of gear material would allow an increase in temperature up to about 300°C: we must stay instead lower than 200-210°C as we said before because the present lubricants widely available for aeroengines and then preferred by operators have effectiveness, durability and stability problems at higher temperatures.

Anyway the capability of gears to operate safely at those temperatures offers them an optimum survivability characteristic in windmilling condition after leaking out the total quantity of oil in the case of possible failures in the oil system.

The same concepts underlined for gears shall be applied in designing the other parts of the transmission, such as shafts, splines, bearings.

Bearings in particular are the other very critical parts to be looked at carefully: materials like tungsten steel, CBS 600, M50, M50 NIL, offering structural stability up to 300°C are necessary; some of these steels are commonly used already, other ones have been developed and their technology is restricted in few companies or countries. In particular M50 NIL is very promising; bearing vendors using it claim they have been able to solve problems of premature failures and of inadequate damage tolerance experienced on other materials.

### Low noise and vibration generation

Modern jet engines have shown a great advantage over the geared turboprops because of their lower vibration and noise transmitted to the structure of the aircraft. The adoption of a high power speed decreaser gearbox will be accepted by operators only if the engine equipped with it will offer the same quietness as the present engines. Modern technology offers the way to minimize the variation of transmitted load in gear meshing, thus reducing the cause directly in its origin. The actions to be taken will consist mainly in the sense of reducing the variations in the actual transmission ratio of meshing gears or along the contact on the same pair of teeth or in the transition between subsequent pairs; in particular, the actions that we in Fiat showed useful in this aspect, are:

- increasing of the total contact ratio by:
  - . adopting higher addendums of spur gears (High Contact Ratio gears, having the profile contact ratio higher than 2, can be used, provided flash temperature limits are not exceeded)
  - . possibly adopting helical gears
  - . reducing the pressure angle
  - . increasing the number of teeth (by going to a finer pitch)
- improving the accuracy by:
  - . reducing the relative position error of tooth profiles
  - . reducing the position error of teeth relative to the gearshaft supports
- modifying the involute profile for avoiding that position errors and deformations of teeth under load cause sudden engagement of teeth when entering the contact, thus generating heavy shocks on the supports.

In fig. 8 we give an idea of the modification introduced on the epicyclic stage gear profile of a helicopter main gearbox previously defined with traditional gears; the contact ratio went up from 1,47 to 2,04 with a noise abatement in the relevant stage of 8 dB over the original 98 dB.

We underline the care we took in manufacturing these gears.

The position error of teeth has been reduced to the minimum obtainable with existing machine tools (0,002 mm tooth to tooth position error has been achieved. The profile correction has been studied carefully taking into account the deformation due to Hertzian stresses and to bending deflection of teeth and of their relevant supporting structure; the profile correction theoretically required has been manufactured with a precision of  $\pm 0,003$  mm.

### Long life and reliability

As we said before, the transmission should offer the assurance of satisfactory running for periods of time much longer than presently offered by turboprop main gearboxes; also it must be very light in order to assure competitiveness for the engine in comparison with the version with direct drive from turbine to fan.

In order to satisfy these requirements it is necessary to have in hands some technology development programs capable of giving the designer information on the points that are out of the common experience on the traditional designs (namely: new materials large bearings and gears, high temperatures, etc.).

For example an important problem to be solved is the one concerning the rotating seals in the gearbox; oil and air internal ambient must be sealed to its external where the main engine stream passes by. The dimensions of the gearbox require for the different designs and power levels some seals of the order of 600 to 1000 mm.

The most convenient design seems to rely on positive carbon seal, radial, segmented, oil cooled type, of which some samples are now being rig tested and developed in Fiat.

The characteristics demanded for these seals are of course the capability to perform the function of sealing the gearbox, and the capability to run in an optimized condition of oil cooling and lubrication such that the heat generated by friction would not cause oil coking and carbon deposition and eventually the unserviceability of the seals within the TBO.

More generally we can say that, in order to reach the very long required MTBR's (Mean Time Between Removals) it is necessary to have a reliable and sound design gearbox.

Under this aspect, according our past experience, a number of areas should be accurately checked when designing and when manufacturing the gearbox because anything forgotten there can cause unacceptable recurring problems and tedious interventions on fleet during service. A detailed analysis of the matter has been given on ref./1/.

#### Fail safety and safe life characteristic

The transmissions we propose are essentially fail safe at least to a certain extent of failure; in order to maximize this characteristic we suggest in the following table few features whose introduction should be considered in order to

- . increase the fail safety quality of the system
- . monitor incipient damages for allowing the intervention of the operator before they grow to their extreme level of unserviceability of the system

Features provided for giving fail safety characteristics to the gearbox design.	
Type of incipient failure	Possibility of survival/Detection method
1. Bearing rolling elements and rings; pitting and scuffing	The phenomenon progresses slowly/Chip detectors and vibration pick-ups
2. Gearing; pitting and scoring	The phenomenon progresses slowly/Chip detectors and vibration pick-ups
3. Gearing; partial or total loss of one or more teeth	Special shaping of the adjacent static parts in order to force chips out of meshing area is good design principle. The continuity of the drive is assured, when the missing tooth would be in contact, by the other gears offering unaffected contact/Chip detectors and vibration pick-ups.
4. Oil system; loss of lube function or loss of oil due to leakage	The transmission can run many minutes at reduced power after complete loss of oil thanks to the choice of adequate materials. Oil circuit pressure and temperature and vibration pick-ups.

Of course, the failure on structural parts leading to mismatch of gears cannot be suffered and would cause the immediate stop of the engine. These parts must be designed with a different approach, offering them a characteristic of safe life, characteristic to be demonstrated by calculation or by fatigue rig testing. Alternatively, a modern philosophy on the matter tends to design these structures with a damage tolerance characteristic: the damage tolerant parts should allow in any feature of theirs any damage to start and to grow within the operating time between two subsequent overhauls, without reaching the point where the system would be unserviceable. Many studies are in progress on the matter, but it is understandable that this characteristic is difficult to be shown both theoretically and practically; the maximum effort should be done anyway when designing the gearbox, for approaching the optimum condition as much as possible.

#### **Maintainability**

As usual for commercial engines, the design of the gearbox shall be conducted having in mind that the operator requires to ease the intervention on engines for maintenance purpose: the parts requiring the intervention should be

- easily accessible on aircraft
- quickly detachable from the engine as a separate module.  
This characteristic should apply both to the gearbox as a complete module and to any single accessory located on it such as the oil pump, the cooler etc.
- equipped with an accessible health monitoring system, capable of a simple and reliable indication to the operator

Clearly these principles shall be applied and the final design shall be optimized having in sight the designs of the total engine and of the installation on the aircraft: in other words, the optimized version should be the results of a strict collaboration among the designers of the gearbox, of the engine and of the a/c

#### **CONCLUSION**

The new large, efficient engines require that an important step forward should be done in the field of gearboxes. The challenge in future years for gearbox manufactures will be to show they are capable of producing light, efficient, reliable, quiet transmissions so that the engines will take advantage from them. Few difficult problems still require to be solved: modern technology already shows the ways of possible solution; these ways must be tried immediately in order to be ready for the contest.

#### **REFERENCE**

- (1) L. Battezzato, S. Turra - Possible technological answers to new design requirements for power transmission systems. Agard Conference Proceedings No. 369.

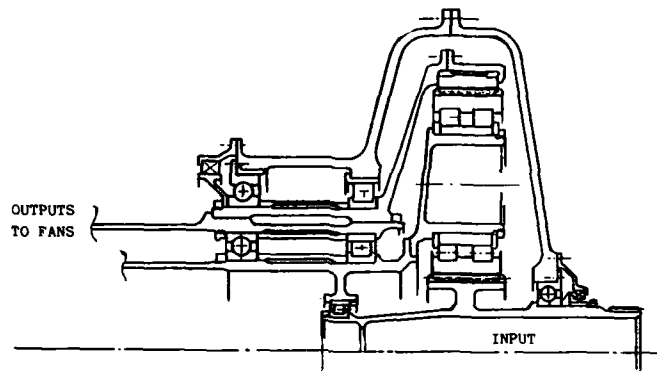


Fig. 1 - Inline Differential Planetary Solution - Schematic.

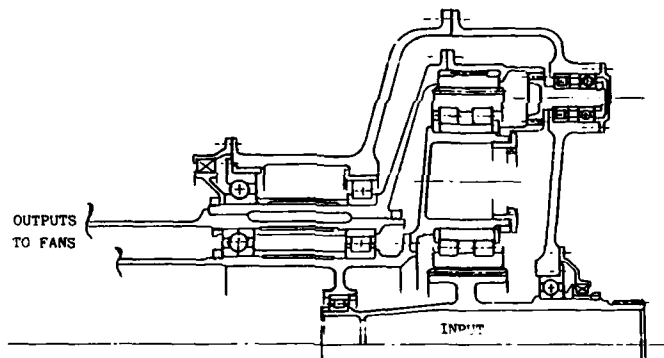


Fig. 2 - Inline Differential Planetary Solution with Split Path - Schematic.

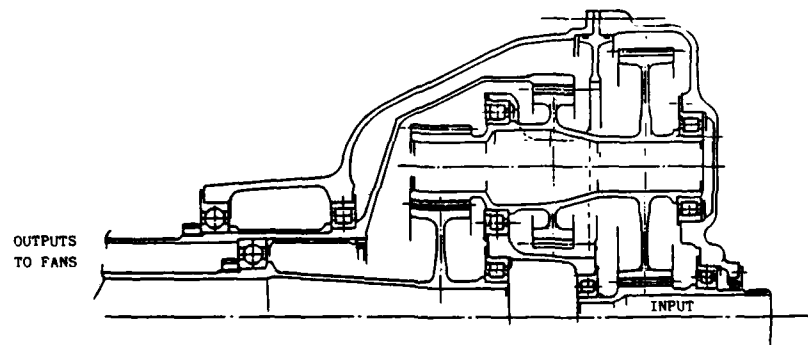
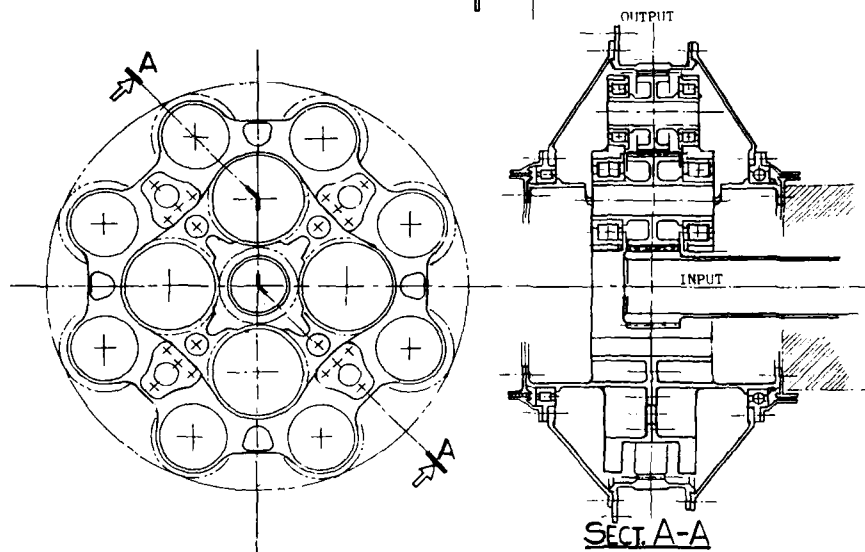
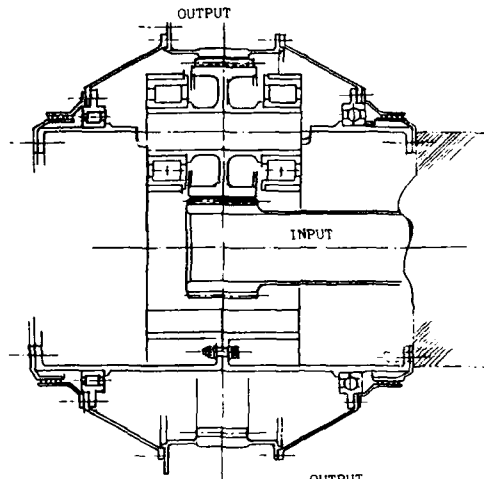


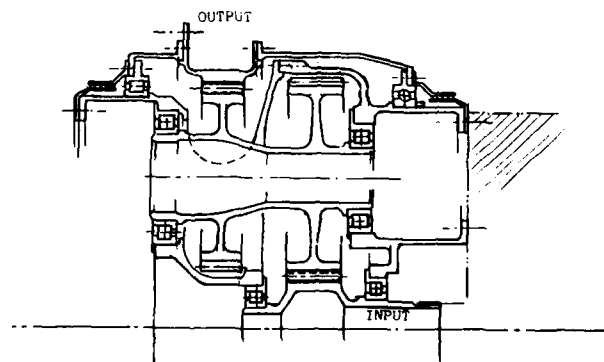
Fig. 3 - Inline Multiple Star Solution - Schematic.

Fig. 4 - Counterrotating  
Inline Star Gear System -  
Schematic.



Codirectional Inline Double Row Star Gear System - Schematic.

Fig. 6 - Counterrotating  
Double Stage Inline Star  
Gear System - Schematic.



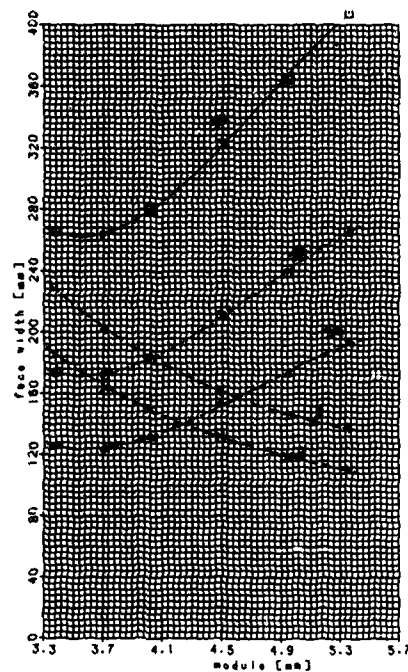


Fig. 7 - Optimization graph for the Sun - Star gear meshing of the Counter rotating Gear System (fig.4), based on the following assumptions:

transmitted power 40000 HP  
input speed 6500 RPM  
ratio 1:5  
ring gear pitch dia 38 ins

curve 1 : 55 KSI spur gear bending stress limit  
2 : 55 KSI helical gear bending stress limit  
3a: 130°F flash temp delta limit  
3b: 100°F flash temp delta limit  
3c: 70°F flash temp delta limit

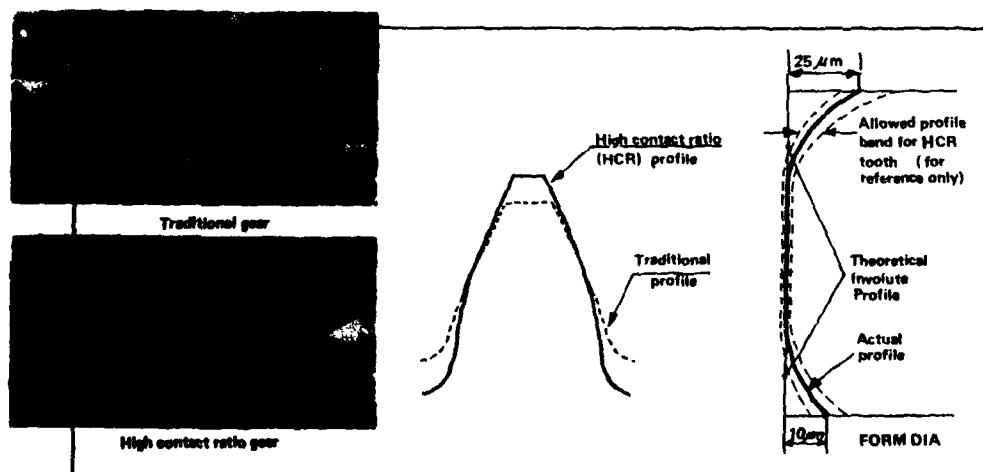


Fig. 8 - Application of HCR (high contact ratio) gears on the epicyclic stage of a helicopter gearbox designed and produced by Fiat.

# TRANSONIC BLADE DESIGN ON ROTATIONAL STREAM SURFACES

F. KLIMETZEK and E. SCHMIDT  
 Institut für Aero- und Gasdynamik, Universität Stuttgart  
 7000 Stuttgart-80, Germany

## ABSTRACT

A method enabling the computation of cascade profiles from prescribed velocity distributions in a relative system is presented. The optimisation of the velocity distribution to attain definite values in parameters such as turning angle, chord length or profile thickness is also included. Comparisons between the inverse design method with various analysis programs for cascades in both absolute and relative systems show good agreement.

## NOMENCLATURE

d	profile thickness	$T$	pitch
h	enthalpy	$\vec{w}, w$	velocity-vector, -magnitude
H	total enthalpy		
h	metric factor	$\beta_{u2}$	up-, downstream angle
l	chord length	$\beta$	stream angle
La	Laval number	$\lambda$	diverging angle of the stream-sheet
Ma	Mach number		( $\sin \lambda = \beta R / \partial m$ )
n	arc length on normal lines	$\rho$	density
R	radius	$\phi$	co-ordinate function
s	arc length on stream lines	$\psi$	stream function
t	stream-sheet thickness	$\omega$	angular velocity
		$\theta, m, z$	rotational co-ordinates

## INTRODUCTION

High pressure ratios and mass flow rates are prerequisites to increase power density in turbomachines. The resulting high velocities with steep gradients between suction and pressure sides of the blades lead to supercritical flows with local supersonic regions. To avoid losses due to boundary layer separation which frequently appears with shocks in the decelerated region, a careful blade profiling is of utmost importance.

In the sonic region, small changes of the profile contour lead to large changes in the velocity distribution thus making the well known analysis methods (e.g. /1,2,3/) laborious due to the many iterations.

It is more effective to prescribe velocity distributions, which can be optimised by boundary layer methods for low losses, and to use an inverse computation procedure that delivers the appropriate profile contour. Only a few methods /4,5,6/ exist for transonic flows.

The following method, based on Schmidt /7,8/, solves this inverse problem for supercritical cascades on rotational stream surfaces with variable sheet thickness in a relative system. This extension should lead to a more accurate prediction of fluid behaviour in highly loaded turbomachines.

## GOVERNING EQUATIONS

The inverse design makes it feasible to obtain low profile losses without strong shocks, so the following equations for stationary, isentropic flows are valid to cal-



$$\vec{w} \cdot \frac{\nabla \rho}{\rho} + \nabla \cdot \vec{w} = 0 \quad \text{continuity} \quad (1)$$

$$\nabla \left( h + \frac{W^2}{2} - \frac{\omega^2 R^2}{2} \right) = \vec{w} \times (\nabla \times \vec{w} + 2\vec{\omega}) \quad \text{motion} \quad (2)$$

$$\nabla H_R = \nabla \left( h + \frac{W^2}{2} - \frac{\omega^2 R^2}{2} \right) = 0 \quad \text{energy} \quad (3)$$

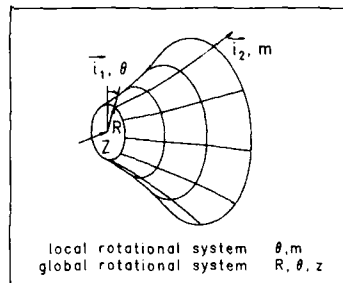


Figure 1: Co-ordinate systems in ISGAV-R

This paper considers flows in a mean  $S_1$ -plane /9/, i.e. we assume rotational  $S$  planes of variable sheet thickness. If one observes the equation of motion in a rotational co-ordinate system (Fig.1), it is obvious that flows on rotational stream surfaces exist only in flows that satisfy the simplified equation of motion  $(\nabla \times \vec{w}) + 2\vec{\omega} = 0$  /10/.

#### TRANSFORMATION INTO THE COMPUTATION PLANE

In the stationary case, streamlines  $s$  and their normals  $n$  can be used as co-ordinate lines. The stream function  $\psi$  is defined as a co-ordinate function on the normal lines, with

$$d\psi = \rho t (\vec{w} \times d\vec{n}) = \rho t W dn \quad (4)$$

and a function  $\phi$  on the streamlines

$$d\phi = h_1 ds \quad (5)$$

with  $h_1$  as a metric factor /11/. The transformation to this system on a rotational stream surface with  $w_m/W_u = \tan(\lambda)$  and  $\sin(\lambda) = \partial R / \partial m$  leads to the following set of equations:

$$\begin{aligned} \frac{h_1}{R \rho^2 t^2 W^2} \frac{\partial(R \rho t W)}{\partial \psi} + \frac{\partial \phi}{\partial \psi} &= 0 \\ \frac{\partial \phi}{\partial \psi} - \frac{\rho t}{R h_1} \frac{\partial(R W)}{\partial \psi} &= \frac{2\omega \sin(\lambda)}{W h_1} \end{aligned} \quad (6)$$

Flows in the absolute system allow a potential  $\phi$  with  $d\phi = W ds$  to be defined from the equation of motion with  $\omega = 0$ , i.e. in potential flows, the metric factor simplifies to  $h_1 = W$ .

#### DETERMINATION OF THE METRIC FACTOR

The orthogonality of the  $\phi, \psi$  co-ordinate system can be used to determine the metric factor  $h_1$ . The curl  $\vec{\omega} = \nabla \times \vec{w}$  in an orthogonal  $\phi, \psi$  system with  $\vec{w} = (W, 0)$  can be calculated using equations (4) and (5):

$$\nabla \times \vec{w} = -i_3 \frac{h_1}{\rho t W} \left( \frac{\partial W / h_1}{\partial \psi} \right) = i_3 \omega_{C3} \quad (7)$$

The equation of motion  $\nabla \times \vec{w} = -2\vec{\omega}$  leads to

$$\omega_{C3} = -2\omega_3 = 2\omega \sin(\lambda) \quad (8)$$

Integrating on normal lines  $\psi = \text{constant}$  results in

$$h_1(\psi) = h_{1u} \frac{W}{W_u} \exp \left( \int_{\psi_u}^{\psi} \frac{\omega \sin(\lambda)}{\rho t W^2} d\psi \right) \quad (9)$$

As  $h_1 = W$  is valid for the flows in an absolute system, it is used as the condition for the free integration constant  $h_{1u}$ , so that  $h_{1u}(\phi=0) = W_u$ .

## COMPUTATIONAL EQUATION

By eliminating the stream angle  $\delta$ , the system of equations (6) can be reduced to the final computational equation:

$$C_1 \frac{\partial^2 \ln(W)}{\partial \varphi^2} + C_2 \frac{\partial^2 \ln(W)}{\partial \psi^2} + C_3 \left( \frac{\partial \ln(W)}{\partial \varphi} \right)^2 + C_4 \left( \frac{\partial \ln(W)}{\partial \psi} \right)^2 + C_5 \frac{\partial \ln(W)}{\partial \varphi} + C_6 \frac{\partial \ln(W)}{\partial \psi} + C_7 = 0$$

$$C_i = f(W, R, t, h_i) \quad i=1..7 \quad (10)$$

For flows with constant stream sheet thickness and constant radius the introduction of the logarithm in the differentials reduces the terms  $C_5$  to  $C_7$  to zero.

The type of this quasilinear partial differential equation of second order changes according to the sign of  $C_1$ . It is elliptic for  $C_1$  positive ( $Ma < 1,0$ ), hyperbolic for  $C_1$  negative ( $Ma > 1,0$ ), and parabolic for  $C_1 = 0$  ( $Ma = 1,0$ ). For the numerical solution of this equation, finite differences are used. The adjustment to the different domains of dependence occurs by type-dependent switching between the respective difference stars /12/. The numerical treatment is given by the equation

$$C_1 r_{ij} + C_2 s_{ij} + C_3 t_{ij}^2 + C_4 u_{ij}^2 + C_5 t_{ij} + C_6 u_{ij} - \mu_{ij} (C_1 r_{ij} + C_3 t_{ij}^2 + C_5 t_{ij}) - \mu_{i-1,j} (C_1 r_{i-1,j} + C_3 t_{i-1,j}^2 + C_5 t_{i-1,j}) = C_7 \quad (11)$$

with  $r$  and  $t$  standing for the centered formulae of second- and first-order numerical differentiation in flow direction, and  $s$  and  $u$  for the same normal to flow direction. The switching factor is

$$\mu = 0 \text{ for subsonic flow}$$

$$\mu = 1 \text{ for supersonic flow}$$

The solution of the difference equation is performed by successive line overrelaxation (SLOR) /9/.

## TRANSFORMATION INTO THE PHYSICAL PLANE

From the computed velocity field, the flow angles can be calculated by integrating the continuity equation on normal lines and the equation of motion on streamlines.

$$\int_{b_1}^{b_2} db = \int_{\varphi_1}^{\varphi_2} \frac{-h_1}{\varphi t W} \frac{\partial \ln(\varphi R t W)}{\partial \varphi} d\varphi \quad (12)$$

$$\int_{b_1}^{b_2} db = \int_{\varphi_1}^{\varphi_2} \left( \frac{\varphi t W}{h_1} \frac{\partial \ln(R W)}{\partial \varphi} + \frac{2\omega \sin(\lambda)}{W h_1} \right) d\varphi \quad (13)$$

To avoid numerical inaccuracies in determining the derivatives on normal lines at the boundary, equation (13) is used only to compute the flow angle of the mean streamline. From the mean streamline to the boundary the flow angle can be calculated by using equation (12).

Analogously, using equations (4) and (5), the physical co-ordinates on streamlines can be calculated with:

$$\int_{\theta_1}^{\theta_2} R d\theta = \int_{\varphi_1}^{\varphi_2} \frac{\cos(\delta)}{h_1} d\varphi \quad \int_{m_1}^{m_2} dm = \int_{\varphi_1}^{\varphi_2} \frac{\sin(\delta)}{h_1} d\varphi$$

and on normal lines with:

$$\int_{\theta_1}^{\theta_2} R d\theta = \int_{\varphi_1}^{\varphi_2} \frac{-\sin(\delta)}{\varphi t W} d\varphi \quad \int_{m_1}^{m_2} dm = \int_{\varphi_1}^{\varphi_2} \frac{\cos(\delta)}{\varphi t W} d\varphi \quad (14)$$

### THE INVERSE DESIGN METHOD

The inverse design method for rotational stream sheets (ISGAV-R) consists of two modules.

- THE COMPUTATION MODULE  
It is used to compute the channel geometry along the boundary streamlines of the channel for a prescribed velocity distribution.
- THE OPTIMISATION MODULE  
A prescribed velocity distribution does not necessarily lead to a profile with desired parameters such as turning angle, pitch or profile thickness. The optimisation module interprets the result of the computation module and modifies the velocity distribution accordingly to achieve the desired parameter values by iteration.

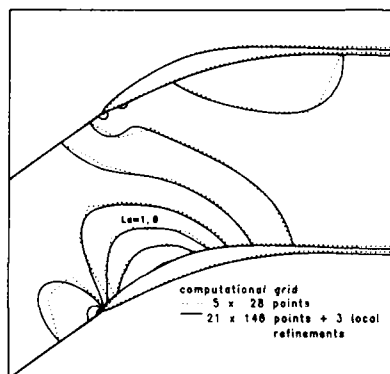


Figure 2: Comparison of the computed velocity fields and contours with a coarse grid (dotted) and a fine grid with local refinements at the stagnation point. (solid)

For the frequent recalls of the computation module in the optimisation stage, it is essential that the computation time be minimized. Reducing the number of mesh points is the simplest method. The necessary correction at the stagnation point is shown in reference /13/. As an example, Fig.2 depicts the computed isotachs (lines of constant velocity) for a plane supercritical cascade composed of a 21x140 main-grid with 3 additional grades of local refinements in the stagnation point region (solid lines) as compared to a solution of a computational grid comprising only 5x28 points (dotted).

Greater differences in the contours are observed only in the stagnation point region, the integral values such as turning angle or pitch differing by less than 1.5%. The ratio of the computation times is 54:1 at 8.8 CPU-seconds for the coarse grid solution with the CONVEX C1.

### THE COMPUTATION MODULE

Fig.3 represents the flow chart of the computation module. The simple basic-algorithm comprises of:

- Setting up of the computation grid in the  $\phi, \psi$  plane and of the boundary values from the prescribed velocity distribution.
- Computation of the velocity fields by the SLOR procedure.
- Computation of stream-angle fields and of local co-ordinates by integrating the velocity solution obtained above.

### BOUNDARY CONDITIONS

In supercritical flows, it is generally not possible to predict if a certain prescribed profile-velocity would lead to a convergent solution as it represents an "ill-posed problem" and thus a physical solution need not exist in this case. The non-elliptical type of differential equation in transonic and supersonic areas allows computation of the flow only in the domain of dependence. By completely prescribing the boundary values along the profile contour and by determining the sonic line during the course of the computation leads to the interaction between the elliptical subsonic differential equation and the parabolic type at the sonic line and the hyperbolic type in the supersonic field and thus to an overdetermination of the system of differential equations. By a "bad" prescription, the differential equation system cannot be solved, i.e. it leads to non-convergence of the numerical relaxation. A discontinuity in the velocity occurs within the computation field which can be concluded to be a shock.

If strong oscillating shocks appear in the field, the prescription of a weak shock on the boundary with consideration of the Rankine-Hugoniot relation is the only alternative. Otherwise, a total change of the velocity distribution with lower maximum velocity and different distribution of the circulation over the blade depth is needed.

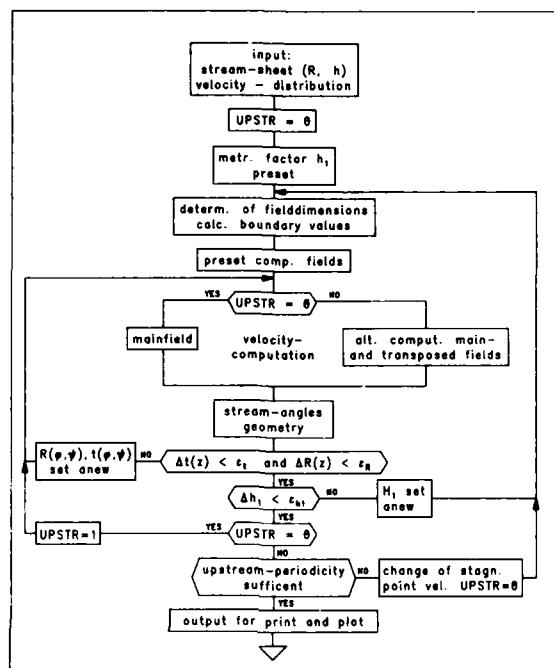


Figure 3: Flow-chart of the computation module.

Homogeneous flow is assumed at the channel grid entrance and exit so that the prescribed velocities could be set at the normals. The velocities must be periodic at the suction and pressure sides of the entrance and exit regions of the streamlines. Their distribution depends mainly on the profile nose form; in highly staggered cascades it is additionally influenced by the area of maximum velocity on the profile suction-side. In the program, the accurate velocity distribution on the stagnation streamline is computed iteratively by alternate computation between the main field and a transposed field comprising the stagnation line /13/. The trailing edge stagnation point being absent due to the wake and the velocity gradients being relatively weak, the distribution is less problematic downstream.

As the function of the axial co-ordinate  $z = f(\phi, \psi)$  is a result of the computation itself, the transformation of the prescribed radius and stream sheet thickness along the rotational axis  $z$  has to be performed iteratively. Starting from an empirical preset value, the geometry is determined, both fields then take on the new values of the axial co-ordinates and the velocity field is solved again. This procedure is repeated till the differences are within given limits of error.

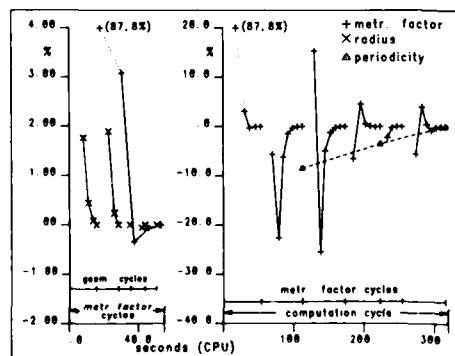


Figure 4: Convergence history of the maximum changes of the turning angle, radius, and metric factor for a rotor cascade within one computation cycle.

A further iteration occurs only when a rotor is computed in the relative system. The transformation of the prescribed velocity in the computation plane is carried out by integrating equation (5) to determine the normal function  $\phi$ . The suction side values can be integrated directly; the metric factor  $h_1$  of the pressure side streamline being unknown in the beginning of the computation. During the relaxation procedure the metric factor is determined anew iteratively according to equation (9). After fitting the radius and stream sheet thickness, the metric factors from the pressure side are used as new prescribed values and the  $\phi, \psi$ -computation grid is then determined anew. This iterative procedure is run till the maximum change in the metric factor is within a certain error limit.

Fig.4 shows the convergence history for a computation cycle (5x81 mesh points). The maximum change in the metric factor  $h_1$ , the upstream periodicity, as well as the radius for each solution of the velocity field

within a computation run for a rotor cascade for  $Ma_1 = 0.8$  is represented in this diagram. Depicted in the left figure is the convergence history of the metric factor as well as that of the radius within a cycle in adjusting the metric factor. If the computation grid dimension remains constant during one iteration of the metric factor, the radius and sheet thickness field values of the previous iteration are taken over as starting values, resulting in a reduction of the computation time between the geometric cycles. The convergence history of the metric factor as well as the upstream periodicity for a complete computation cycle is shown in the right section of Fig.4.

The distance between the periodically transposed boundary streamlines in the upstream region of the grid is defined as the upstream periodicity. In three periodicity-cycles, the maximum difference in the periodicity lies within the convergence limit of 0.5%. Due to the coarse computation grid used, a higher standard of accuracy is not meaningful here.

#### THE OPTIMISATION MODULE

To obtain a profile with minimum energy losses, the design of cascades starts with the development of the velocity prescription by a check on the state of the boundary layer. For a complete design of a compressor or a turbine and the dynamic loads expected from them, further properties such as turning, profile thickness, length or cascade numbers are stipulated. Therefore, it is generally necessary to modify the velocity prescription to satisfy all prerequisites.

Fig.5 depicts the optimisation module in a flow chart. Based on a velocity prescription, the necessary modifications due to the non-linearity of the computation equations are performed iteratively. The built-in modification functions are developed in such a way that the type of velocity distribution is maintained to a great extent, so as not to influence the boundary layer too greatly.

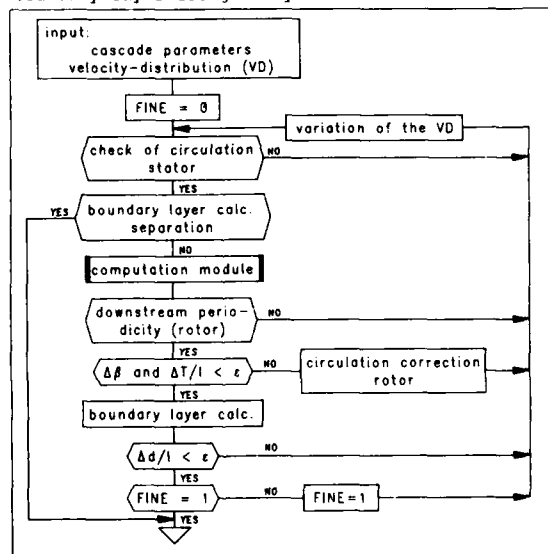


Figure 5: Flow-chart of the optimisation module.

To reduce the computation time, the first run for a coarse fitting with the desired parameter is carried out in a computation grid with only five mesh points perpendicular to the upstream (FINE=0).

The modification cycle starts with a control of the profile circulation and if necessary, with adapting the prescribed velocity distribution ( $\omega = 0$ ). After determining the geometry according to the computation module, the turning angle and the pitch cord ratio of the cascade is checked.

The profile circulation is obtained by evaluating the integrals:

$$\Gamma = - \oint \omega R \hat{i}_t ds - \int_D^E W_2 ds + \int_K^I W_1 ds \quad (15)$$

For stator flows with  $\omega = 0$ , the necessary circulation is only a function of the velocity and arc length, i.e. the velocity distribution can be checked for sufficient circulation right from the beginning; for rotor flows though, the geometry has to be known

to determine the first integral in equation (15). The adjustment between the turning angle and circulation has therefore to be carried out simultaneously. At first the profile arc length is varied to achieve the geometric periodicity of the wake. The actual circulation necessary for the turning angle is calculated using equation (15). The difference between the turning angles is a measure for the necessary modification in the profile circulation. An exact adaptation is still not possible, as the variation

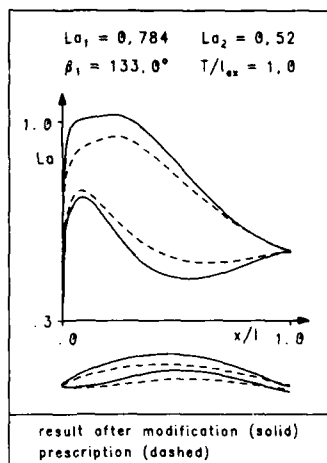


Figure 6: Comparison between prescription and the final result (velocity above; profile contour down) of the modification cycle.

of the velocity yields a new geometry so that the necessary circulation has to be determined iteratively. If the differences in the turning angles and the pitch lie within given tolerance limits, the boundary layer displacement thickness is then computed. The metal profile is determined by subtraction from the calculated potential profile contour and the camber-line and thickness distribution are then obtained. The minimum and maximum profile thickness is then tested for a given profile range.

When all prescribed parameters are fulfilled, the fine field computation is started (FINE=1), i.e. the adjusted velocity distribution is taken as the new prescribed velocity for a second run in the optimisation module, in which now all available local computation grid refinements are included.

A subsonic stator grid serves as an example for a modification iteration. Fig. 6 shows the velocity distributions as well as the metal profiles. Through the modification module, the prescribed velocity distribution is varied so that the turning angle of the new profile increases by  $10^\circ$ , the pitch cord ratio being constant and the maximum profile thickness limited to  $8.4\%$  ( $d/l$ ). In spite of large increments in the grid parameters, the plateau type velocity distribution is held constant (maximum velocity in the suction side at  $x/l = 25\%$ ) by the internal modification functions, so that boundary layer separation does not occur in spite of the higher maximum velocities.

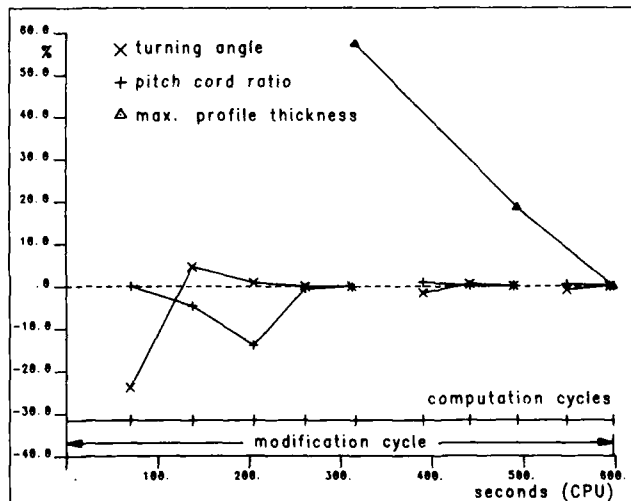


Figure 7: Convergence history of the changes in percentage of the turning angle, pitch cord ratio and maximum profile thickness for a stator cascade within a modification cycle.

the mean velocity level the desired profile thickness is attained in two iterations. The minimum influence on the turning angles and on the pitch by this modification can be clearly seen. A simple damping algorithm is implemented to prevent overswinging of the parameter during the modification cycle.

Fig. 7 presents the convergence history for the turning angles and profile thickness (11x142 mesh - points), the development within the computation cycles being not included. The large difference in the turning angle after the first computation cycle shows clearly that the wake is not periodic as the profile circulation of the predicted velocity distribution has already been adjusted. The desired turning angle is achieved in the successive iterations by contrarily varying the arc length of the prescribed velocity distribution on the pressure and suction sides; the circulation being held constant. This variation leads nevertheless through the consequent change of the stagger-angle to an increase in the axial blade length. The first computation of the profile thickness shows an increase of about 60% maximum thickness. By decreasing

## RESULTS

To verify the results of the inverse design method, comparative computations with analysis programs have been conducted.

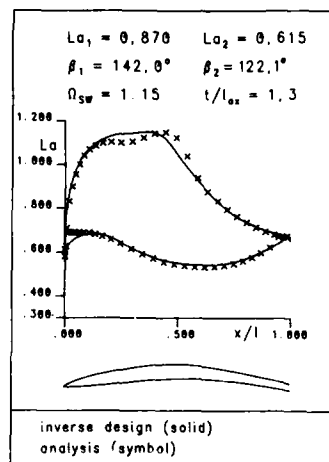


Figure 8: Comparison between the inverse design and analysis method for a plane supercritical cascade.

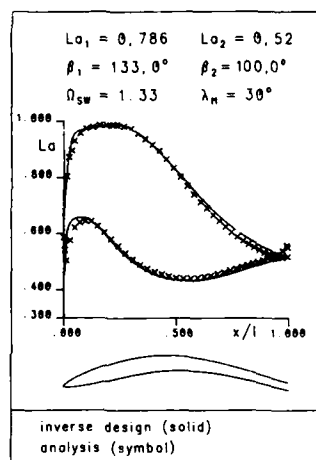


Figure 9: Comparison between the inverse design and analysis method for a stator cascade with variable radius.

Fig. 8 shows a plane supercritical cascade with  $La_1 = 0.87$  and a turning angle of  $20^\circ$ . To consider the increase of the side wall boundary layer, the sheet thickness between the leading and trailing edges is reduced by 15%. The profile contour shows the potential profile attained by the inverse procedure. In the comparative computation, a finite-flux element program (FFEM) [14] solving the compressible potential equation is utilized. Except for some differences in the leading edge area of the pressure side and in the local supersonic region there is very good agreement.

The profile contours shown in the subsequent figures have been produced by transforming the profile data on an equivalent cylindrical stream sheet.

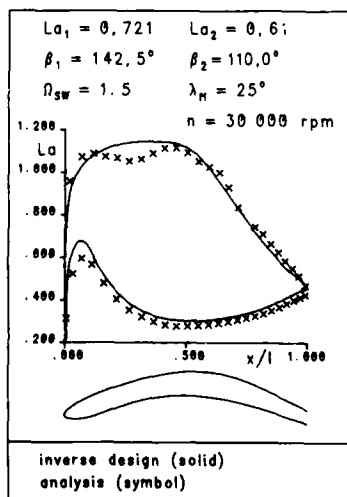


Figure 10: Comparison between the inverse design and analysis method for a rotor cascade with variable radius.

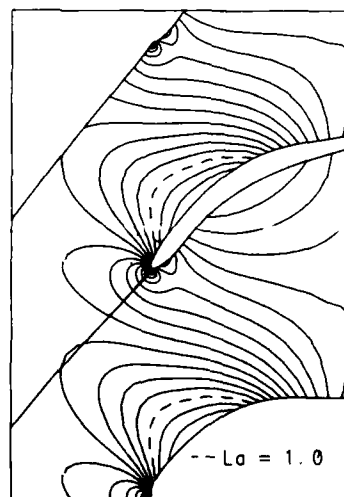


Figure 11: Stream surface of a rotor cascade in the meridian plane.

For flows on rotational stream surfaces, a time dependent finite volume computation method with a modified McDonald program /15/, has been used for comparison. Fig.9 shows the transformed profile contour of an inverse designed stator cascade. The cascade has been designed for high subsonic flow with  $La_1 = 0.786$  and a turning angle of  $33^\circ$ . The stream sheet has a mean divergence angle  $\lambda_m$  of  $30^\circ$ . Comparison between both methods shows excellent agreement.

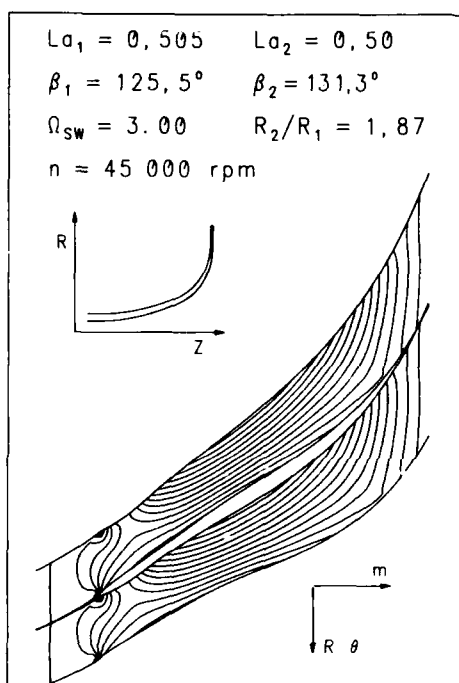


Figure 12: Stream surface of a radial rotor cascade in the meridian plane including the development of the stream surface.

As an example for design in the relative system, a rotor cascade with 30 000 rpm was chosen. Fig.10 shows the velocity distribution and the transformed profile contour. Being a preliminary test, the profile form has still not been optimised. The high loads lead to a strong supercritical velocity distribution. The stream surface represented in the meridian plane in Fig.11 shows the shockfree solution which can be identified distinctly by the smooth development of the sonic line as well as by the neighbouring lines of constant velocity. This comparison has likewise been computed with the modified McDonald program. The deviation in the supersonic region can be explained by the existence of a weak shock. The pressure side shows good agreement.

The efficiency of the inverse design method was tested on a radial compressor with 45 000 rpm. The upper left portion of Fig.12 shows the development of the stream surface. The divergence angle of the stream sheet at the trailing edge has been restricted to  $89.5^\circ$  due to non-uniqueness of the radius as a function of the axial co-ordinate.

The profile contour in the meridian plane with its respective lines of constant velocity is shown in the bottom part of Fig.12. The thickness in the front part of the profile shows that the velocity distribution needs to be optimised.

In our experience, the extended inverse design method is an effective procedure to design highly loaded axial compressor cascades on rotational stream surfaces and could also possibly be applied to radial compressors.

#### REFERENCES

- /1/ Denton, J.D. A Time Marching Method for Two- and Three-Dimensional Blade to Blade Flows; Aeronautical Research Council, R & M No.3775, London, Oct.1974.
- /2/ Ives, D.C. Second Order Accurate Calculation of Transonic Flow over Turbomachinery Cascades; AIAA-Journal, 17, 1979.
- /3/ Caspar, J.R. Calculation of Two-Dimensional Potential Cascade Flow using Finite Area Methods; AIAA-Journal, 18, 1980.
- /4/ Garabedian, P. A Systematic Method for Computer Design of Supercritical Airfoils in Cascade; Com. Pure Appl. Math., XXIX, 1976.
- /5/ Meauzè, G. An Inverse Time Marching Method for the Definition of Cascade Geometry; ASME 81-GT-167, 1981.



27-10

- /6/ Novak, R.A.      A Mixed-Flow Cascade Passage Design Procedure Based on a Power Series Expansion; Haymann-Haber, G. ASME 82-GT-121, 1982.
- /7/ Schmidt, E.      Numerische Berechnung und experimentelle Untersuchung des transsonischen Strömungsfeldes in stark umlenkenden Schaufelgittern; Dissertation, Institut für Aero- und Gasdynamik, Universität Stuttgart, 1976.
- /8/ Schmidt, E.      Computation of Supercritical Compressor and Turbine Cascades with a Design Method for Transonic Flows. ASME-Paper No.19-GT-30, 1979; Trans. ASME, J.Eng.Pow. Vol.102, Jan.1980, pp.68-74.
- /9/ Wu, C.            A General Theory of Three-Dimensional Flow in Subsonic and supersonic Turbomachines of Axial, Radial, and Mixed-Flow Types; ASME, 50-A-79, 1952.
- /10/ Vavra, M.H.      Aero-Thermodynamics and Flow in Turbomachines; Wiley, New York, 1960.
- /11/ Zanetti, L.      A Natural Formulation for the Solution of 2D or Axisymmetric Inverse Problems. International Conference on Inverse Design Concepts in Engineering Sciences ICIDES, 1984.
- /12/ Jameson, A.      Transonic Potential Flow Calculation Using Conservation Form; Proc. 2nd AIAA Conf. on Comp. Fluid Dynamics, Hartford, 1975.
- /13/ Schmidt, E.      Inverse Design of supercritical Nozzles and Cascades. Berger, P. Int. J. Num. Meth. Eng. Vol.22, No.2, Feb.86, pp.417-432
- /14/ Faden, M.        Verlustarme, superkritische Verdichtergitter. Weber, A. Teil II: Entwurf der Profildruckverteilung, Gitternachrechnung und experimentelle Überprüfung. Starcken, A. FVV-Abschlussbericht - FVV-Vorhaben Nr.325 Dezember 1986.
- /15/ Happel, H.W.    Anwendung neuer Entwurfskonzepte auf Profile für axiale Turbomaschinen. MTU Techn. Bericht 78/54A, München 1978.

## DISCUSSION

N. KROLL, Ge

1) You talked about local refinements. Do you use adaptative flow local refinements or do you prescribe regions in advance ?

2) The design problem is a non linear problem, and, I think, one problem of the method is to find a starting solution. Can you say something about the robustness of your code concerning starting solution and also concerning the pre-parameters in the design method ?

### Author's Reply

1) Since we prescribe the velocity distribution, the critical ranges within the computational grid are known in advance, so there is no need for an adaption of the grid refinements.

2) The starting solution of the velocity field calculation is always a linear interpolation between the prescribed boundary velocities. The only free-parameters of our SLOR method to solve the velocity field are the over-relaxation parameters. We have one subsonic and one supersonic parameter with linear slope in the sonic range.

For the starting velocity distribution within the optimisation cycle you can use any distribution you want. In the design of supercritical cascades the crucial point is the interaction between the calculated sonic line and the prescribed velocity distribution at the boundary. Therefore, if the prescription at the profile contour does not match, a shock appears within the flow field. But we have developed some methods to modify such velocity distribution.

R.G. THOMPSON, US

My question concerns supersonic flow. Do you see applicability for the method and the possibility to minimize the boundary layer blockage at the throat?

Author's Reply

The problem of supersonic flow upstream of the cascade lies in the correct prescription of the bow wave which has severe influence on the velocity distribution of the upstream stagnation streamlines of a flow channel. Therefore we calculated only flows with subsonic upstream velocities up to now.

With the prescription of an "optimized" velocity distribution we try to minimize the boundary layer thickness. Secondly we look for solutions which are shockless or at least which have only weak shocks. If this is not possible, we have to change the parameters of the cascade.

R.B. GINDER, UK

1) Which boundary layer calculation method do you use?

2) In choosing your velocity distribution, do you aim for any particular type of boundary layer behaviour, e.g. is the boundary layer well attached, or do you allow it to approach separation at some point on the surface. Do you aim for any particular distribution of the shape parameter,  $H$ ?

Author's Reply

1) The Rotta and the McNally codes are integrated in the method.

2) The only thing we look for is sufficient distance from separation. If we have separation within the modification of the velocity distribution, we just stop the calculation of the inverse design. We do not use inverse boundary layer methods.

# INVESTIGATION OF DIHEDRAL EFFECTS IN COMPRESSOR CASCADES

F.A.E. BREUGELMANS  
von Karman Institute for Fluid Dynamics  
B - 1640 Rhode Saint Genèse - Belgium

## ABSTRACT

An experimental investigation of the influence of blade dihedral on the secondary flow in a two dimensional NACA 65-series compressor cascade is performed. Different inlet boundary layer thicknesses are used on the endwalls.

Three different stacking lines have been chosen, namely a straight line inclined at 15°, 25° and 35°, a circular arc and an elliptic arc. The incidence range up to stall has been investigated and the local and overall losses are compared. The obtuse angle between the blade suction surface and the endwall has a beneficial effect on overall and secondary flow loss. Some limitations have to be accepted, depending on boundary layer thickness and incidence.

## NOMENCLATURE

AVR axial velocity ratio  
BL1 reference inlet boundary layer  
BL2 thickened inlet boundary layer  
DF diffusion factor  
P pressure  
q dynamic pressure  
Re Reynolds number  
V velocity  
i incidence angle  
 $\alpha$  angle of attack  
 $\beta$  flow angle =  $\text{ATAN}(V_\theta/V_x)$   
 $\gamma$  stagger angle in plane parallel to end wall  
 $\gamma$  exit yaw angle =  $\text{ATAN}(V_\theta/V_x)$   
 $\delta$  boundary layer thickness  
 $\delta^*$  boundary layer displacement thickness  
 $\Delta$  dihedral angle  
 $\epsilon$  sweep angle  
 $\theta$  boundary layer momentum thickness  
 $\theta^*$  exit bank angle =  $\text{ATAN}(V_\theta/V_\theta)$   
 $\sigma$  solidity  
 $\omega$  total pressure loss coefficient

## SUBSCRIPTS

0 stagnation conditions  
1 inlet  
2 outlet  
BL boundary layer  
cl based on chord and inlet velocity  
MS midspan  
PROF profile  
s spanwise with  $\Delta=0^\circ$  as reference direction  
sec secondary flow related  
T overall  
x axial component  
 $\theta$  pitchwise direction

## SUPERSCRIPTS

— pitchwise integrated  
— pitch- and spanwise integrated  
' tangent to camberline

## INTRODUCTION

The annulus wall boundary layer build up from the blade end clearance effects, the boundary layer centrifugation, skewing and the blade-to-blade pressure gradient producing a cross flow, yield the secondary flow field. The accurate prediction of the detailed flow distribution is closely related to the secondary problem. The type of vortex law chosen for a given meridional flow path produces the radial equilibrium and the positioning in space of the blade elements generates additional radial force components. The freedom in choosing the stacking line, within the mechanical constraints, can introduce sweep and dihedral which will exert a control on the secondary flow evolution.

The dihedral or lean angle effect on the radial equilibrium are discussed by Vavra [1] and Smith [2, 3] who showed that the effect on the radial pressure gradient is proportional to the tangent of the dihedral angle. Smith discusses in detail the dihedral and sweep effects and advises on incidence angle and solidity to be considered for the cascade. Novak [4] discusses the lean angle effect on a turbine nozzle configuration in which a reversal of the spanwise distribution of the mean static pressure in the blade is predicted with and without 10° lean angle. At the trailing edge plane, only a slight difference between the two cases is observed since there the transverse pressure gradient becomes zero. The effect of fillet geometry, studied by Debruge [5] included also the considerations of dihedral in the prediction of the boundary layer development in the corner.

Numerous experimental investigations of secondary flow development have been performed. Salvage [6] derived his conclusions on longitudinal and crosswise boundary layer development and on secondary flow magnitude and distribution based on 43 different compressor cascade experiments. Dejc & Trojanowski [7] describe experiments in annular turbine nozzle cascade where positive and negative dihedral angles ( $\Delta$ ) of +13° and -14° produce large variation of the loss in the hub region. Other experiments with  $\Delta=20^\circ$  to -20° show a symmetric influence on tip and hub with an increase of the mid span loss. In this case, the model has a small aspect ratio. It is mentioned that the meridional contouring has to be combined with leaning the blades and this geometrical freedom provides a larger control on the degree of reaction. It is suggested to use a curved blade in order to obtain a beneficial effect at the root and tip radius. The experiments are carried out on a curved blade with 0° dihedral at the tip. An improvement is observed over the lower 2/3 of the span when compared to the radial blades. The aspect ratio and hub-tip ratio seem to be a factor in the loss distribution, since they determine the relative importance of the secondary flow with respect to main flow, as defined by the radial pressure gradient.

Breugelmans et al. [8] showed the important influence of the dihedral angle upon the cascade performance at nominal incidence. Different inlet boundary layer thicknesses were investigated. The conclusion was that a moderate dihedral of 15°, forming an obtuse angle between blade suction and wall, yields an important gain. This beneficial effect can be obtained on both blade extremities when a curved stacking line is used. A circular arc one and an elliptic arc one are investigated from the point of view of

overall and local losses but also the blade pressure distribution and blade midspan boundary layer evolution.

#### EXPERIMENTAL FACILITY AND INSTRUMENTATION

##### THE FACILITY

The experimental rig is the low speed cascade tunnel C-1 of the von Karman Institute. It is a continuous flow facility with a rectangular cross section of 127x500 mm (Fig. 1). A large centrifugal blower pumps air into the settling chamber, equipped with screens. A large contraction guides the flow into the rectangular duct towards the rectilinear cascade model.

The inlet duct is equipped with slots in the endwalls and with porous and deformable walls at the top and bottom in order to remove the boundary layer build-up in and control the axial velocity ratio across the cascade. However, suction through the slots is not applied and solid endwalls are used in order to avoid any recirculation through porous walls for these tests.

The inlet velocity can be controlled by the continuous speed adjustment of the 18 KW DC blower. The amount of suction, when applicable, can be controlled independently by valves in the piping to the 45 KW DC suction blower. The inlet flow survey plane is fixed at 120 mm in front of the blade mid chord position, the downstream surveys can be performed in the span- and pitchwise directions in planes parallel to the blade trailing edges. The maximum air speed is 40 m/s and the tunnel of the non return type, discharging into the atmosphere. Compressor and turbine cascades can be accommodated.

##### THE INSTRUMENTATION

The upstream flow field is measured with a directional probe of the NACA short prism type [9]. The downstream surveys are performed with a multihead probe in which the total pressure sensing port is separated from the directional ports by 20 mm. The probe is described in [8] and shown in Fig. 2.

The calibration curves are determined using the techniques of [9, 10] in which yaw, pitch, static and dynamic coefficients are determined for yaw and pitch angle variation of  $\pm 30^\circ$ . This calibration confirmed the insensitivity to angular variations of the total pressure reading. The pressure tapings are connected to strain gage pressure transducers, whose signal is amplified and stored on a magnetic tape using a micro-processor controlled 8 channel data logger.

The blade surface boundary layer profiles are measured with a classical single hot wire mounted on a 0.1 mm step-by-step displacement carriage.

##### THE CASCADE MODEL

The blades are NACA 65-12A<sub>1</sub>-10 airfoils as described in [12] with a chord of 127 mm, solidity and aspect ratio of unity, a stagger angle of  $28.9^\circ$  and a nominal air inlet angle of  $45^\circ$  corresponding to an incidence angle of  $-1.1^\circ$  when dihedral is zero. The straight blade cascade, the inclined and curved blade model are shown in Fig. 3. The effect of dihedral is investigated for dihedral angles from  $0^\circ$  (reference) to  $35^\circ$  [8]. Dihedral, or the blade not normal to the endwall, is introduced by rotation of the two dimensional blade around the chordwise direction. This operation introduces a change of the incidence angle, adds a slight sweep angle to the cascade model and modifies slightly the aspect ratio and solidity. The incidence angle is corrected by a modification of the stagger angle according to :

$$\Delta\gamma = \left( \beta_1' - \gamma \right)_{\Delta=0} - \text{ARCTG} \frac{\text{tg}(\beta_1' - \gamma)_{\Delta=0}}{\cos \Delta} \quad \text{or} \quad \begin{array}{cc|cc} \Delta & & \Delta\gamma & \\ \hline 0^\circ & \text{Reference} & 25^\circ & -1.5^\circ \\ 15^\circ & & 35^\circ & -3.1^\circ \end{array}$$

TABLE 1

The sweep angle, formed by the projection of the leading edge on an axial plane and the normal to the endwall is eliminated by a rotation around an axis normal to the plane formed by leading edge and chord. The  $35^\circ$  dihedral model and the sweep angle compensation are illustrated in Fig. 4. These rotation angles are  $9.2^\circ$ ,  $14.9^\circ$  and  $12.8^\circ$  for the three values of the dihedral. The solidity increases from 1.0 (reference) to 1.01, 1.03 and 1.06 with an aspect variation from 1.0 (reference) to 1.02, 1.06 and 1.14 for the increasing dihedral angle. The effective blade maximum thickness changes from 10%, 11.0% and 12.2% as well as the effective camber angle. These effects are not corrected for in the blade construction since two dimensional blades are cast and the ends cut to fulfil the no-sweep requirement with a zero clearance fit at the endwalls, 127 mm apart.

The circular arc stacking lines formed an angle of  $+15^\circ$ ,  $+25^\circ$ ,  $+35^\circ$  and  $-15^\circ$  with the endwall, where  $+15^\circ$  means an obtuse angle between blade suction surface and the wall. The elliptic arc stacking is chosen to have a span of 127 mm and an angle of  $+25^\circ$  with the wall. This circular stacking introduces a small amount of sweep  $9.2^\circ$  of the leading edge of the blades and the sweep angle decreases from the wall towards the mid-span position. The following definitions are used :

- \*  $15^\circ\text{S}$  : stacking along a straight line,
- \*  $15^\circ\text{CO}$  : stacking along a circular arc with the obtuse angle on the suction surface,
- \*  $15^\circ\text{CA}$  : stacking along a circular arc with the acute angle on the suction surface.
- \*  $15^\circ\text{EL}$  : stacking along an elliptic arc.

##### MEASUREMENTS AND DATA REDUCTION

The measurements are performed in planes parallel to the cascade leading and trailing edge plane. The inlet flow survey is performed at a plane 56 mm axially in front of the leading edges; the inlet boundary layer on both endwalls is measured with a boundary layer probe, which is exchanged for a NACA prism type

measured at 21 equally spaced traversing planes 10 mm axially downstream of the trailing edge. This distance is kept constant for all spanwise measurements. Two inlet boundary layers are used : the naturally developed one and an artificially thickened one using triangular vortex generators fixed on the endwalls, 1 m upstream of the central blade. The boundary layer parameters on the endwall are given in table 1.

	BL1	BL2	BL1'	BL2'
	Reference Straight Blades	7 mm Edge Vortex Generators	Reference Curved Blades	9 mm Edge Vortex Generators
$\delta$	18 mm	32 mm	27 mm	50 mm
$\delta^*$	2.3	3.5	4.4	8.0
$\theta$	1.7	2.1	2.9	5.7

TABLE 1

Turbulence levels in the inlet plane at the midspan position of  $Tu=0.8\%$  and  $1.25\%$  are measured for the two inlet boundary layer thicknesses.

The local total pressure loss coefficient and the downstream flow vector are obtained through the calibration curves of the multiple head probe. Mass and area averaged quantities are calculated for each pitchwise survey. The following procedure is used in defining these values : the average value,  $\bar{X}$ , of the parameter  $X(s,\theta)$ , a function of two variables, is given by

$$\bar{X} = \frac{\int_{\theta_1}^{\theta_2} \int_{s_1}^{s_2} X(s,\theta) W(s,\theta) ds d\theta}{\int_{\theta_1}^{\theta_2} \int_{s_1}^{s_2} W(s,\theta) ds d\theta}$$

where  $W(s,\theta)$  is a weighting function dependent, in general, upon the two spatial variables. A double bar ( ) over a flow property indicates the results of averaging over the entire half plane of measurement. For  $s$  equal to a constant, the equation degenerates into the form

$$\bar{X}(s) = \frac{\int_{\theta_1}^{\theta_2} X(s,\theta) W(s,\theta) d\theta}{\int_{\theta_1}^{\theta_2} W(s,\theta) d\theta}$$

Thus, a single bar (—) over a flow property indicates that the quantity results from pitchwise averaging. The spanwise position at which this average was made is indicated by either the subscript MS if the midspan is implied or by (s) if the spanwise position is arbitrary. For area averaging, the weighting function,  $W$ , is given by :  $W = 1$ ; everywhere.

For mass flow averaging in incompressible flows :  $W(s,\theta) = \rho V(s,\theta) \cos\theta(s,\theta)$ , since density is constant and where  $V \cos\theta$  is the axial component of the velocity vector at  $(s,\theta)$ . This procedure can now be applied to the total pressure and flow angle by substitution of  $X$  through  $P_{02}$  and  $\theta_2$ .

#### TOTAL PRESSURE LOSS COEFFICIENTS

The overall (or global) total pressure loss coefficient

$$\omega_T = \frac{(\bar{P}_{01})_{MS} - \bar{P}_{02}}{(\bar{q})_{MS}} \quad \text{where } (\bar{q}_1)_{MS} \text{ is the dynamic head at midspan read on the upstream probe}$$

$$\text{A local loss coefficient, } \omega(s,\theta) \text{ may be defined as : } \omega(s,\theta) = \frac{(\bar{P}_{01})_{MS} - P_{02}}{(\bar{q}_1)_{MS}}$$

Average results for  $\bar{\omega}(s)$  :

$$\bar{\omega}(s) = \frac{(\bar{P}_{01})_{MS} - \bar{P}_{02}(s)}{(\bar{q}_1)_{MS}} \quad \text{pitchwise integrated loss coefficient}$$

Loss in total pressure attributed to secondary flow is here defined as follows :  $\bar{\omega}_{sec} = \bar{\omega}_T(s) - \bar{\omega}_{BL}(s)$ , where  $BL(s)$  is the loss measured at the same plane due to the boundary layer

In the same way :  $\bar{\omega}_{sec} = \bar{\omega}_T - \bar{\omega}_{BL}$ .

#### OUTLET FLOW ANGLE AVERAGING

Two types of outlet flow angle are encountered :

$\theta_2$  : local

$\bar{\theta}_2$  : pitchwise mass average, obtained with the above described method.

### EXPERIMENTAL RESULTS

All experiments are performed at an inlet Reynolds number of  $Re=2.1 \times 10^5$ . The inlet flow uniformity is checked for three passages in the center of the cascade. Adjustments can be made only by the upper and lower walls since no suction is applied in this investigation. The downstream traverses explore the central passage while allowing for a suitable overlap due to the physical separation of the probe total pressure point from the others.

The influence of two different inlet boundary layers, BL1 and BL2, on the cascade performance is investigated from nominal to stall incidence angle. Four different stacking lines are considered, i.e., the reference zero dihedral, the 15° dihedral with straight stacking line (15°S), the circular arc stacking line (15°CO) and the elliptic arc stacking line. A limited number of experiments are performed with 15°CA and 25°CO stacking lines. The discussion will be limited to the total pressure losses in these different configurations.

The inlet total pressure loss due to the boundary layers BL1 and BL2 is presented in figure 5.

#### TOTAL PRESSURE LOSSES FOR STRAIGHT AND INCLINED BLADES

The total pressure loss coefficient ( $\omega$ ) contours for the 0° and 15° dihedral with the reference and artificially thickened inlet boundary layer are shown in figure 6. The aspect ratio is exaggerated in the plottings due to the different scale factors for the span- and pitchwise directions. The accumulation of losses in the suction surface endwall corners are shown, and slight difference are caused by the non identical inlet boundary layer on the left and right hand side (0° dihedral). A small amount of dihedral (15°) produces a sufficient spanwise pressure gradient to suppress almost completely the development of a large loss zone in the larger corner. The losses along the endwall, between two successive blades, equal the inlet boundary layer loss on the right hand endwall when excluding the blade wakes. On the opposite wall, a large secondary flow loss zone develops, spreading out to midspan and covering 100% of the pitch at the endwall for 35° dihedral case as reported in the references.

The pitchwise integrated loss values are compared in figure 7 on which the inlet boundary layer loss profile is also shown. The difference is caused by the secondary flow development through the blading. The application of dihedral changes this spanwise distribution in an important manner. Very quickly, a doubling of losses occurs on the acute angle side while one approaches the inlet loss distribution on the right hand side for 15° to 35° dihedral. The losses at 25° dihedral reached a level where the inlet boundary layer effect does not modify the distribution and the high losses region occupies 25% of the area.

The overall loss is compared in figure 8 to the 0° dihedral configuration, using the left and right hand side of the blade span. The overall losses are rapidly reduced on the half span with the obtuse corner and this at moderate dihedral angles for both inlet boundary layer thicknesses. The blade half span with the acute corner demonstrates a sharp increase in loss with respect to the reference case as shown and the beneficial effect cannot compensate the detrimental evolution on the opposite endwall.

The diffusion factor, DF, is calculated at the spanwise minimum loss position using the expression

$$DF = 1 - \frac{\bar{V}_2}{\bar{V}_1} + \frac{\bar{V}_{\theta 1} - \bar{V}_{\theta 2}}{2 \bar{V}_1}$$

where the inlet midspan velocity and the pitchwise averaged outlet velocity components are used. The axial velocity ratio is calculated using the pitchwise averaged velocity component  $\bar{V}_{x2}$ . The DF increases from 0.29 ( $\Delta=0^\circ$ ) to 0.33 ( $\Delta=35^\circ$ ) and AVR from 1.15 to 1.19 for the reference inlet boundary layer case. A lower DF of 0.24 and higher AVR 1.21 is observed for the artificially thickened inlet boundary layer.

The secondary loss is that part of the total loss which is not present in the inlet wall boundary layer and in the midspan blade wake, under the assumption that the sidewall flows have not merged over the blade suction surface. The inlet boundary layer profiles are shown in figure 5, together with the pitchwise averaged total pressure losses. The secondary loss (Fig. 7) is reduced already by almost 50% for a moderate dihedral of 15° and little or no benefit is obtained on the obtuse angle side of the cascade model for a further increase in dihedral. The large increase in secondary loss on the opposite side is strongly dependent on inlet boundary layer thickness and dihedral as shown. The evolution towards a limit loss level, as for the total loss, seems to occur.

#### TOTAL PRESSURE LOSS CONTOURS FOR THE CURVED BLADES

The results of the experiments on an inclined blade demonstrated the improvement of the flow conditions in the obtuse corner. A beneficial effect on both endwalls can be obtained by applying a curved stacking line of 30° camber. In a preliminary series of tests a C-7 blade of 45° camber was used. The total pressure distribution is shown in figure 9 and the most striking feature is the wake thickening at the midspan position. The streamtube divergence, due to dihedral, causes an additional diffusion in this high turning cascade and any beneficial effects in the endwall region may be cancelled by the increased midspan losses. A systematic investigation is started with different curved stacking lines and the influence of incidence angle is included.

A selection is made for the presentation of the losses in the exit plane. The thick inlet boundary layer case with the reference, 15° dihedral straight and 15° dihedral curved stacking cascade model has been chosen for the inlet flow angles of 45°, 50° and 55°. The cascade aspect ratio of unity is modified in the plottings due to the different scale factors in the span- and pitchwise directions. The location of two blade wakes can easily be observed as well as the 15° inclination or curvature of the trailing edge, with the suction surface pointing downwards. The accumulation of the losses in the suction surface endwall corners are shown and the differences between left and right hand side, for the symmetrical models, are caused by the presence of inlet instrumentation ports.

A small amount of dihedral (15°) prevents the thick inlet boundary layer to grow into a large secondary flow loss zone on the obtuse corner, while on the acute corner or left side an important spanwise extension of

the losses is observed. A very thick wake over the entire span occurs at  $\alpha_i = 55^\circ$ . The observations of [8] are confirmed for the minimum loss incidence.

The curved stacking (15°CO) model shows higher losses and thicker wakes at the midspan location due to the local streamtube divergence through the cascade under the influence of the transverse component of the blade forces. The flow separation over the entire span at  $\alpha_i = 55^\circ$  is delayed as can be observed in figure 10, but a local separation around the midspan is measured. Further comparisons, using local and averaged data, are made in the following paragraphs.

#### MIDSPAN LOSSES

The midspan losses are presented in function of the inlet flow angle  $\alpha_i$  to the different cascade models, the different inlet boundary layers BL1 and BL2 being the parameters (Fig. 11).

The NACA two dimensional minimum loss value is confirmed for the reference boundary layer, while a three times higher minimum loss occurs for BL2. The operating range, defined by twice the minimum loss, is limited to  $\alpha_i = 52^\circ$  and  $54^\circ$  for BL1 and BL2 respectively. The axial velocity ratio AVR is 1.0 (BL1) and 1.04 (BL2) at the midspan minimum loss point, with an increase to 1.13 (BL1) and 1.08 (BL2) at stall conditions.

The effect of dihedral in the case of a straight stacking (15°S) is observed at the midspan location. The beneficial effect of the obtuse corner shows up in the lower losses but stall occurs in a more abrupt way and the losses at midspan are higher than for the reference cascade in the case BL1.

The midspan loss for the curved stacking case 15°CO has a different evolution for BL1 and BL2. The losses are the same as the reference cascade for BL1, but an important improvement is observed at the positive incidence angles when a thick inlet boundary layer, BL2, is present. The incidence range is seriously reduced for the negative incidence angles.

The midspan losses for the 25°EL model are lower than for 15°CO at moderate incidence angles. The rate of change is much larger when approaching the stall conditions.

A comparison of the reference model with the 15°CO model shows that the AVR is lower and the diffusion factor higher for the midspan section of the curved stacking. The discrepancy is largest for the case BL1 and occurs in the positive incidence range. This indicates a streamtube divergence due to the spanwise component of the blade force (Fig. 12).

#### EFFECT OF INCIDENCE ON ENDWALL LOSSES

The beneficial effect of an obtuse angle, obtained by the dihedral, between blade suction surface and endwall has been demonstrated. A comparison can be made of the local pitchwise averaged total pressure loss distribution for the reference, 15°S and 15°CO model with the two different inlet boundary layers, BL1 and BL2. The figures illustrate the artificially thickened boundary layer case in the different cascade models.

The incidence effect on the endwall losses in combination with 15° dihedral is shown in figures 13a-b. The comparison of the reference and 15°S model shows that over the last 25% of the blade span, losses increase rapidly and are incidence angle dependent. The positive effect of 15° dihedral in the obtuse corner is observed for the reference and artificially thickened boundary layer of the minimum loss and moderate positive incidence angles ( $\alpha_i = 50^\circ$ ). The beneficial action of dihedral is lost at high incidence angle ( $\alpha_i = 55^\circ$ ) for the case of BL1. Only in the case of the thicker inlet boundary layer, a positive result may be expected (Fig. 13a).

A similar comparison is shown for the 15° curved stacking model (15°CO). The influence on the endwall loss distribution is marginal or negative at  $\alpha_i = 45^\circ$ . A positive trend can be detected between  $\alpha_i = 50^\circ$  to  $52^\circ$  for the thick inlet boundary layer, the stall at high incidence angles ( $\alpha_i = 55^\circ \dots 57^\circ$ ) is worse than in the reference cascade model. The additional diffusion of the midspan streamtube is now (model 15°CO) dominating the entire separated flow (Fig. 13b).

#### SPANWISE AVERAGED LOSSES (Fig. 14a-b)

The different models are compared on the basis of the spanwise averaged losses over 50% of the span and considering only the obtuse angle side. The increase in the secondary loss,  $w_{SEC} = w_{BL} - w_{BL1}$ , is observed for higher inlet flow angles in the case of the reference cascade model. The evolution is the same for the two inlet boundary layers, BL1 and BL2.

The 15°S cascade model demonstrates a decrease of the secondary flow losses, the endwall flow is strongly influenced in the obtuse corner and the losses are smaller than the ones in the inlet plane to the cascade in the case of BL2. An abrupt increase is observed at an inlet flow angle of  $51^\circ$ . The improvement mentioned in [8] is confirmed and, when compared to the reference cascade, extends over a limited incidence range ( $+7^\circ$ ) for BL1 and over the total range up to stall for the BL2 inlet boundary layer.

The curved stacking model, 15°CO, does not provide an improvement for the reference inlet boundary layer BL1. A remarkable reduction of the losses is obtained in the range from  $+6^\circ$  incidence angle towards stalls: zero and negative incidences should be avoided due to the large losses in case of a thick inlet boundary layer BL2.

A comparative test has been performed with a 15°CA cascade model and the averaged spanwise losses for the case BL1 are given in table 2. This demonstrated clearly the positive and negative dihedral effect and no further investigations have been made with this cascade model, forming an acute angle between suction surface and endwall.

$\beta_1$ [°]	15°CO	15°CA
45	10.5%	14.5%
50	12 %	21.5%
55	15%	26 %

TABLE 2

The elliptic stacking line demonstrated identical overall losses as the circular one (Fig. 14a). A substantial improvement can be observed at moderate incidence angles. The stall occurs at 9° incidence angle (Fig. 14b).

#### BLADE PRESSURE DISTRIBUTION - BOUNDARY LAYER EVOLUTION

The blade pressure distribution has been measured at 4%, 12.5%, 30% and 50% of the span. A comparison will be made between the reference blade ( $\Delta=0^\circ$ ) and the elliptic stacking line model for the reference and artificially thickened inlet boundary layer in Figs. 15a, b.

The increased loading at 50% chord, and midspan is observed as well as the unloading near the endwalls for the 25°EL cascade (Figs. 15a) at 45° inlet flow angle.

At the higher inlet flow angle of 50° and the artificially thickened inlet boundary layer, one can observe a plateau pressure over the whole span for  $\Delta=0^\circ$ . This is a local separation and does not exist for the 25°EL model (Fig. 15b) as was shown by oil flow visualization.

The evolution of the boundary layer thickness for the reference blade  $\Delta=0^\circ$  and the elliptic stacking  $\Delta=25^\circ$ EL is shown in Fig. 16, from the 50% to 90% chord position. Different inlet flow angles have been used for these midspan surveys. The appearance of a separation bubble is observed as well as its upstream motion for increasing inlet angles ( $\Delta=0^\circ$ ). The large increase of the midspan boundary layer thickness in the case  $\Delta=25^\circ$ EL is demonstrated.

#### CONCLUSION

Four different stacking of a NACA-65 series blade section are investigated in a cascade arrangement with two different inlet boundary layers. The inlet flow angle range covered is  $\beta_1=40^\circ$  to  $57.5^\circ$ .

The 15° dihedral stacking along a straight line shows an improvement in the total pressure losses for the two inlet boundary layer thicknesses. An abrupt increase of the loss occurs near the stalling inlet angle where a decrease of the loss is only observed for the thick inlet boundary layer.

The effect of a 15° dihedral stacking along an arc of a circle fades out towards the midspan position where an increased diffusion is observed due to the streamtube divergence. No difference is observed with the reference cascade model in the case of the reference inlet boundary layer. A remarkable improvement of the spanwise averaged losses is obtained for medium to stalling incidence angles when a thick inlet boundary layer is present.

A moderate amount of dihedral (15°) correctly applied can improve the flow in the endwall region in conditions such as occurring in multistage compressors.

#### REFERENCES

- VAVRA, M.H.: Aero-thermodynamics and flow in turbomachines. Wiley & Sons, 1960.
- SMITH, L.H. & YEH, H.: Sweep and dihedral effects in axial flow turbomachinery. ASME Tr., Series D: J. Basic Engrg, Vol. 85, No 2, Sept 1963, pp 401-416.
- SMITH, L.H.: The radial equilibrium equation of turbomachinery. ASME Tr., Series A: J. Engrg for Power, Vol. 88, No 1, Jan 1966, pp 1-12.
- NOVAK, R.A. & HEARSEY, R.M.: A nearly three dimensional intra blade computing system for turbomachinery. ASME Tr., Series I: J. Fluids Engrg, Vol. 99, No 1, March 1977, pp 154-166.
- DEBRUGE, L.L.: The aerodynamic significance of fillet geometry in turbocompressor blade rows. ASME Tr., Series A: J. Engrg for Power, Vol. 102, No 4, Oct 1980, pp 984-993.
- SALVAGE, J.W.: Investigation of secondary flow behaviour and endwall boundary layer development through compressor cascades. VKI TN 107, June 1974.
- DEJC, M.E. & TROJANOWSKY, B.M.: Untersuchung und Berechnung axialer Turbinenstufen. Berlin, VEB Verlag Technik, 1977, pp 405-413.
- BREUGELMANS, F.A.E.; CARELS, Y.; DEMUTH, M.: Influence of dihedral on the secondary flow in a 2D compressor cascade. ASME Tr., Series A: J. Engrg for Gas Turbines and Power, Vol 106, NO 3, July 1984, pp 578-584; also VKI Preprint 1983-08.
- ERWIN, J.R.: Experimental techniques. in "Aerodynamics of Turbines and compressors", Vol. X of High Speed Aerodynamics and Jet Propulsion. Princeton U. Press, 1964, pp 167-269.
- SHEPHERD, I.C.: A four hole pressure probe for fluid measurement in three dimensions. ASME Tr., Series I: J. Fluids Engrg, Vol. 103, No 4, Oct 1981, pp 590-594.



11. TREASTER, A.L. & YOCUM, A.M.: *The calibration and application of five hole probes.*  
Pennsylvania State U., TM 78-10, 1978.
12. FELIX, A.R. & EMERY, J.C.: *A comparison of typical NGTE and NACA axial flow compressor blade sections in cascade at low speed.*  
NACA TN 3937, 1957, p. 25.

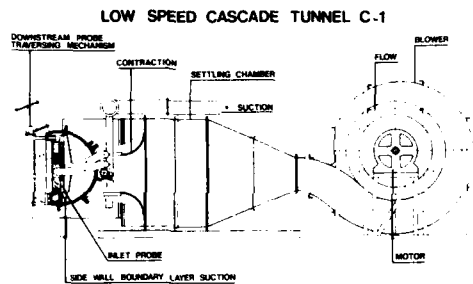


FIG. 1 - THE C-1 LOW SPEED CASCADE FACILITY.

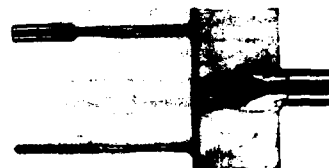


FIG. 2 - THE MULTHEAD PRESSURE PROBE



FIG. 3 - THE REFERENCE, INCLINED AND CURVED BLADE MODELS

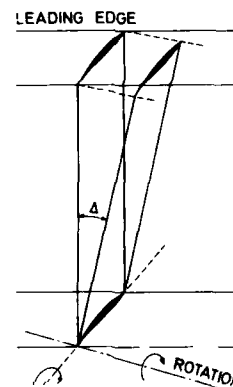


FIG. 4 - SWEEP ANGLE COMPENSATION

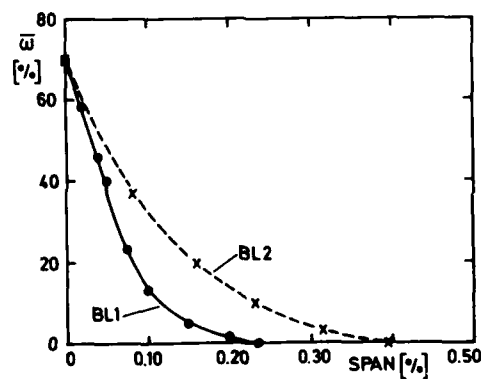


FIG. 5 - INLET BOUNDARY LAYER PROFILES

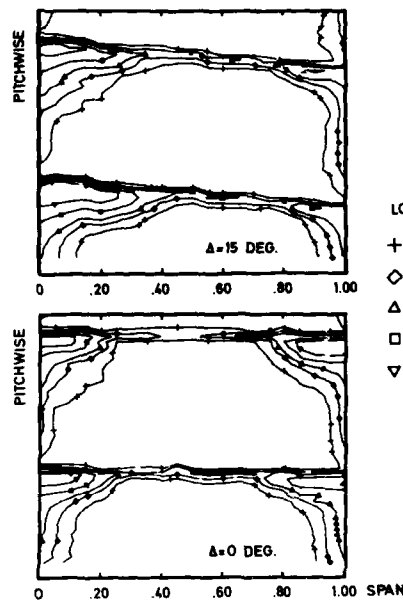


FIG 6a - REFERENCE INLET BOUNDARY LAYER  
ISOLOSS CONTOURS.  
 $\Delta = 0^\circ$  AND  $15^\circ$ .

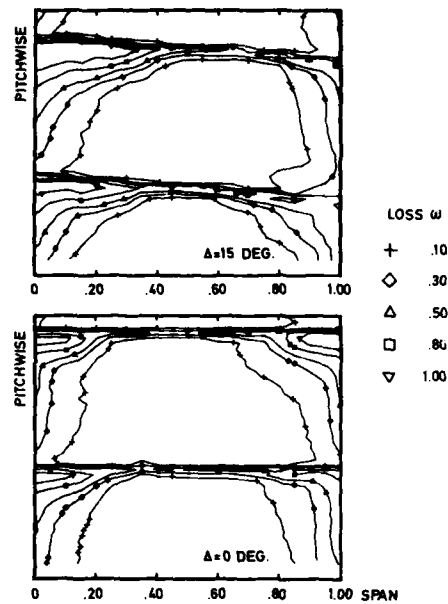


FIG 6b - THICK INLET BOUNDARY LAYER  
ISOLOSS CONTOURS  
 $\Delta = 0^\circ$  AND  $15^\circ$ .

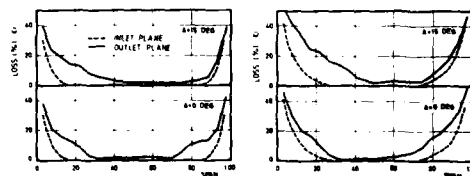


FIG 7 - REFERENCE AND THICK INLET BOUNDARY  
LAYER SPANWISE LOSS DISTRIBUTION.

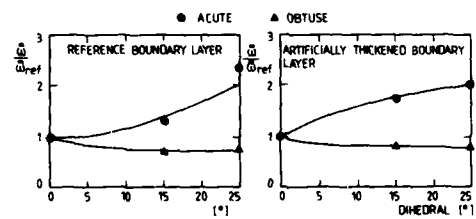


FIG 8 - OVERALL LOSS

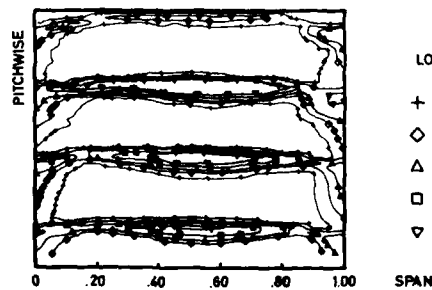


FIG 9 - CURVED C-7 BLADE - ISOLOSS CONTOURS

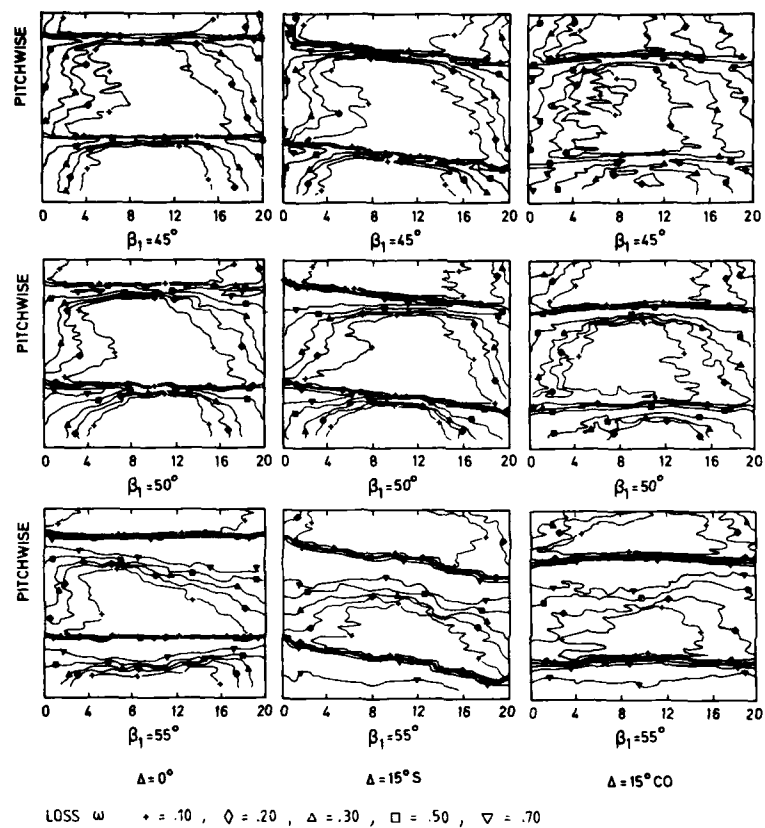
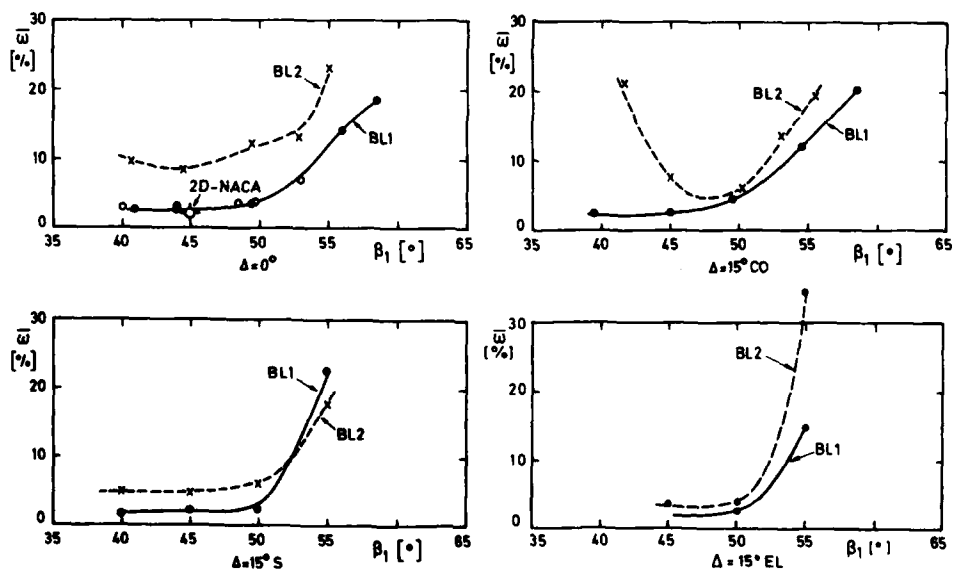


FIG 10 - INFLUENCE OF INLET FLOW ANGLE-ISO  
LOSS CONTOURS  $\Delta = 0^\circ, 15^\circ S, 15^\circ CO$



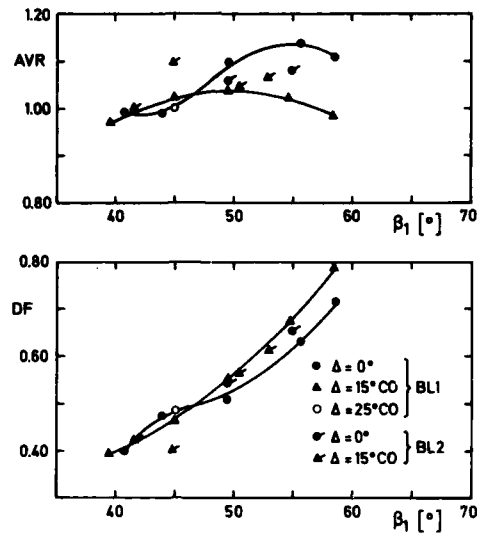
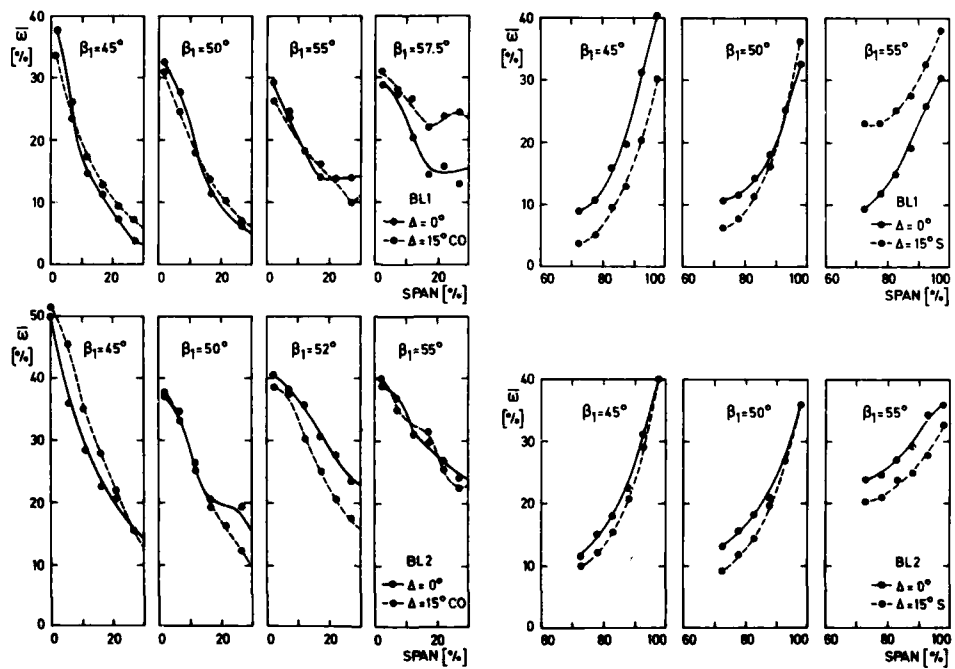


FIG 12 - AXIAL VELOCITY RATIO AND DIFFUSION FACTOR

FIG 13a - LOSSES IN THE ENDWALL REGION  
 $\Delta = 0^\circ$  AND  $15^\circ \text{S}$ FIG 13b - LOSSES IN THE ENDWALL REGION  
 $\Delta = 0^\circ$  AND  $15^\circ \text{CO}$

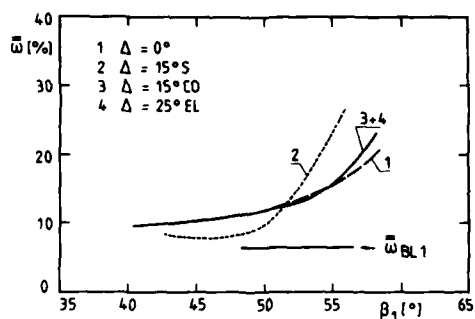


FIG. 14a - INTEGRATED LOSSES FOR THE  
REFERENCE INLET BOUNDARY LAYER.  
 $\Delta = 0^\circ, 15^\circ S, 15^\circ CO, 25^\circ EL$

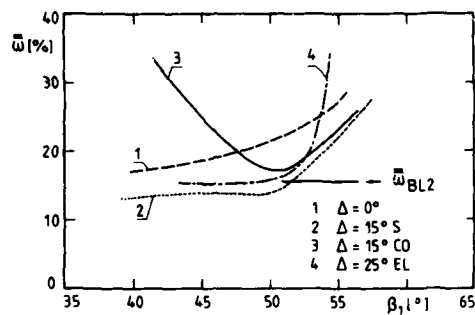


FIG. 14b - INTEGRATED LOSSES FOR THE THICK  
INLET BOUNDARY LAYER  
 $\Delta = 0^\circ, 15^\circ S, 15^\circ CO, 25^\circ EL$

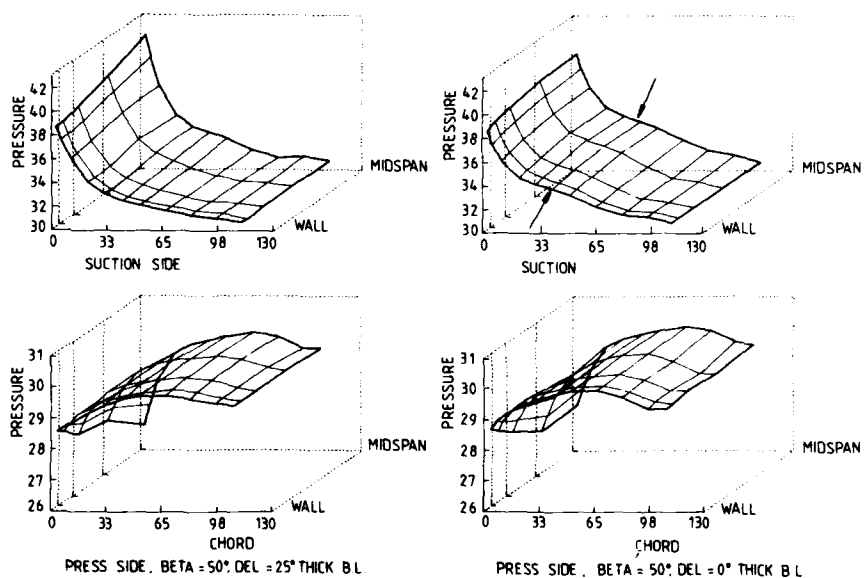
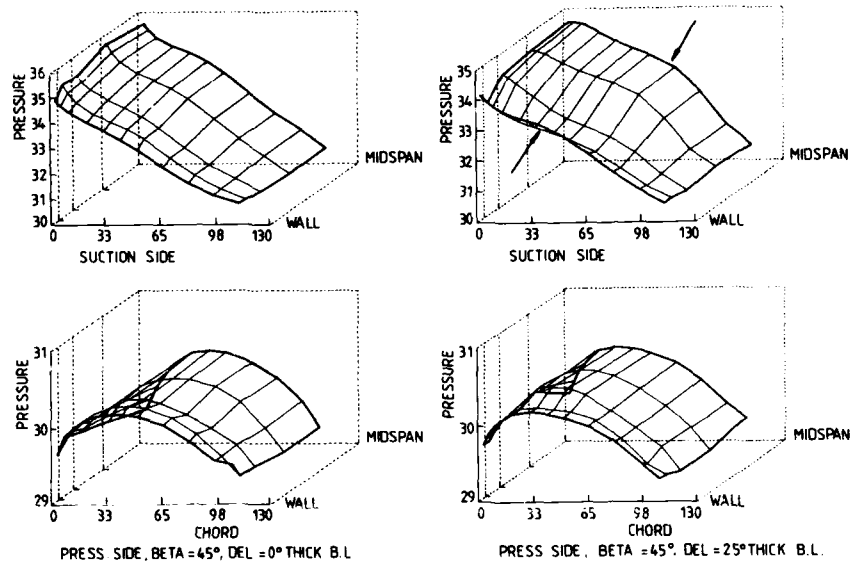
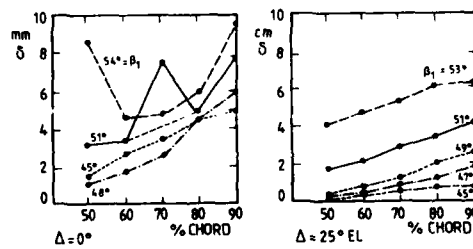


FIG. 15a - BLADE PRESSURE DISTRIBUTION REFERENCE BLADE,  $25^\circ$  ELIPT  $\beta_1 = 45^\circ$

FIG 15b - BLADE PRESSURE DISTRIBUTION. REFERENCE BLADE, 25° ELIPT.  $\beta_1 = 56^\circ$ FIG. 16 - BLADE SUCTION SURFACE  
BOUNDARY LAYER EVOLUTION

### DISCUSSION

J. HOURMOUZIADIS, Ge

Thank you very much for such a magnitude of useful information, Professor Breugelmans. I would like to comment firstly ; your experience agrees perfectly well with our experience on low pressure turbines.

You showed that loss increases at mid-span with the thicker boundary layer for the curved blade, at negative incidence which indicates that you must have some kind of a laminar separation. Do you have an explanation why this happens with thicker boundary layer only ?

Author's Reply

Usually, if you incorporate beneficial effect, you will see the positive result much easier if you have very dirty flow coming in, namely in our case a very thick boundary layer. And that there is why we are doing a lot of effort to get very thick wall boundary layer and a lot of secondary flow.

Now, if you see on the vectors at mid-stream for the curved blades, they may seem to diverge and that of course puts additional diffusion on it. Now, do not forget the Reynolds number of the test we run is low speed and it is 200 000, so certainly air profiles sit there where transition is moving back and forth. That's probably the reason why we have, at 50-51 degrees for the reference blade, a circulating bubble very good visible with flow visualisation on the surface, as it moves up. This disappears if you put in the beginning, due to side blade force, an additional diffusion.

J. HOURMOUZIADIS, Ge

My second question is on the effect of leaned and curved blades. We have been doing that now for several years in our production turbines and our impression is that the primary effect on long blades is the rearrangement of the two-dimensional loading of the profile. In fact, we have not been able to identify any significant effect on secondary losses. Have you been able to separate two-dimensional losses from secondary losses ?

Author's Reply

Not entirely. You could do this by looking at the mid-span loss. The mid-span losses are not 2D losses because they are much too high. We have aspect ratio of 1 with 30 % boundary layer coming in, on both sides. This is completely different situation than in a turbine with a much long aspect ratio. Secondly, this is a compressor cascade, so pressure gradient and so on, are opposite to what we have in turbine. That is probably the reason why it is harder to see it in turbine, where you expand the flow sufficiently and where it is very hard to measure any boundary layer at the outlet.

K.D. PAPAILLIOU, Gr

I would name two possible sources for improvement or disprovement of secondary losses in the measurements that you have presented. One is the mechanism that creates the rolling up of the vortex, so acting directly on the secondary loss. The other would be the transport of material that has been lost somewhere and goes elsewhere discharging locally the blade and, not entirely in fact, but indirectly improving locally the performance of the blade.

However, this lost material is going elsewhere and it is the total effect which we have to look at.

Could you comment on this two mechanism in order to explain what is your feeling about the improvement of designing, in this direction ?

**Author's Reply**

Comment is : we have to wait a few more years. That is exactly the test under way now, using rotating hot wires to get the fluctuating components and hoping to find the vortex in the corner and how it moves. May be we have the answer in two years.

H. WEYER, N1

Please, comment on the effects of spanwise contraction (AVDR) on losses, in particular what is the reason of increased loss of the plane cascade with thickened boundary layer ?

**Author's Reply**

The axial velocity density variation is 8 or 10 %, I believe. The increased loss is due to the aspect ratio of 1 and to the 30 % boundary layer, on both sides.

L. FOTTNER, Ge

Should one take into account the incidence according to the boundary layers by making the camber different near the wall ?

**Author's Reply**

That is something you certainly should do in a machine because the local high entropy at the ends. For a high speed machine, when you have a very narrow incidence range, you must adapt the leading edge to the local flow and that is the all story of the end-bend and the 3D design. That is just following the flow and not hoping the flow will follow the blades.



# ETUDE PHENOMENOLOGIQUE DU FLOTTEMENT DE BLOCAGE SUR LA BASE DES RESULTATS D'UNE THEORIE LINEAISEE

par Pascal FERRAND  
Laboratoire de Mécanique des Fluides - ECOLE CENTRALE DE LYON (E.C.L.)  
B.P. 163 - 69131 ECULLY CEDEX - FRANCE

## RESUME

Le flottement de blocage se produit sur des redresseurs fonctionnant en incidence négative avec un col sonique proche de l'entrée du canal interaube suivi d'un choc droit. Une modélisation monodimensionnelle dans les canaux interaubes et bidimensionnelle hors grille a été développée de telle sorte qu'il soit aisé de mener une étude variationnelle des différents paramètres. Les résultats sont basés sur l'expérience de TANIDA et SAITO. Une étude phénoménologique est ainsi présentée, centrée sur la mise en évidence des dépendances du gradient de vitesse longitudinal stationnaire et du mouvement du choc. Les résultats obtenus ne sont pas contradictoires avec d'autres résultats publiés mais remettent en cause les interprétations qui y sont associées. Il apparaît, par exemple, que le mouvement du choc est tributaire des fluctuations qui se développent dans la zone amont au choc alors que la contribution du domaine aval reste modérée. Ces résultats montrent pour la première fois comment agir aérodynamiquement pour limiter les risques de flottement.

## PARAMETRIC STUDY OF CHOKE FLUTTER WITH A LINEAR THEORY

## ABSTRACT

The choke flutter problem arises in the stator, the incidence is slightly negative and the inlet Mach number is subsonic. A one-dimensional unsteady approach is used in blade channel and out of the cascade, the equations describe the unsteady two dimensional periodical flow field. The results are compared to experimental data from TANIDA et SAITO tests. A parametric study has been developed to understand the influence of stationary velocity gradient and shock wave movement. The results obtained don't contradict with each other but give different explanation. For example, it means that the shock wave movement depends highly of upstream perturbations but weakly of downstream flow. For the first time, these results point out the possibilities to limit the choke flutter domain.

## 1. INTRODUCTION

Le flottement de blocage apparaît à régime partiel et à fort débit (figure A), principalement sur des redresseurs d'étages intermédiaires de compresseurs. Un flottement en configuration bloquée peut aussi se produire sur turbine, mais la structure de l'écoulement diffère de celle décrite.

Flottement supersonique désamorçé

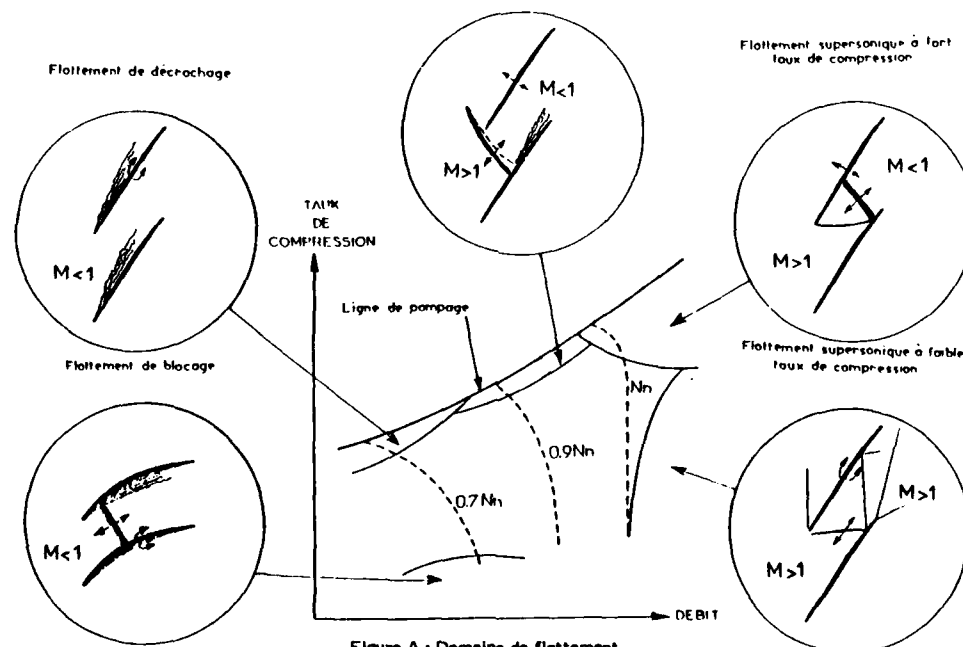


Figure A : Domaine de flottement

Les incidences sont faibles ou même négatives. Les nombres de Mach amont et aval sont subsoniques. Le canal est traversé par un col puis par un choc droit situé, généralement, entre le quart et la mi-corde. Il existe un couplage interaube, les aubes vibrant en flexion ou en torsion. On attribue généralement ce flottement au mouvement du choc ; l'influence des effets visqueux n'est pas déterminée. Les mécanismes d'apparition de ce type de flottement sont méconnus, très peu de recherches ayant été effectuées sur ce problème.

Notre objectif est d'utiliser une théorie représentative du flottement de blocage [1] pour analyser les causes d'apparition de ce phénomène dans une configuration aussi simple que possible. La méthode ayant été validée [2] à partir de l'expérience de TANIDA et SAITO [3], c'est sur cette configuration que nous développerons notre étude.

## 2. RAPPEL DES HYPOTHESES DE LA METHODE

L'amplitude des mouvements vibratoires des aubes à l'approche du flottement est suffisamment faible pour qu'une théorie linéarisée puisse être appliquée. L'écoulement est séparé en huit zones (notées de A à H) comme défini figure B.

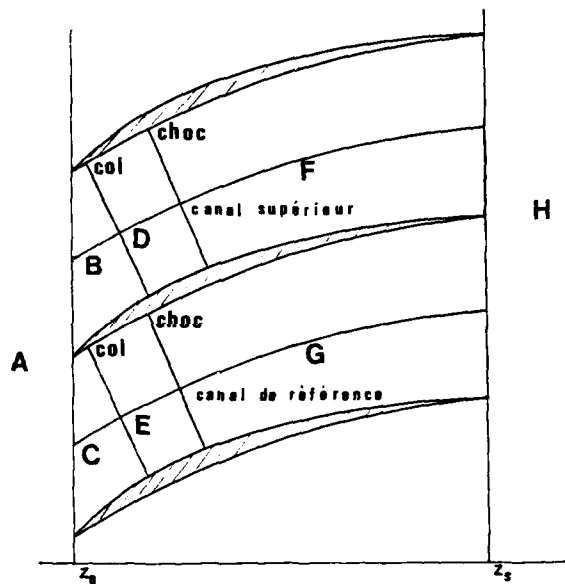


Figure B : Domaine de calcul

Dans les zones A et H (hors grille), l'écoulement est supposé bidimensionnel compressible subsonique. Si l'écoulement moyen peut être considéré constant, des solutions analytiques peuvent être obtenues [4]. Les périodicités spatiales (suivant la circonférence) et temporelles sont séparées en appliquant une décomposition en série trigonométrique pour la première direction ( $\theta$ ) et une décomposition en série complexe pour la seconde ( $t$ ).

Les zones internes aux canaux interaube sont séparées par le col et le choc. Dans toutes ces zones (de B à G), l'écoulement est supposé monodimensionnel compressible. Les effets visqueux sont pris en compte par un calcul couplé écoulement sain - couche limite instationnaire, l'effet de cette dernière étant introduit par un apport de débit. Les mouvements vibratoires des aubes provoquent des évolutions de sections instationnaires qui sont introduites comme des termes sources.

Les conditions d'écoulements bidimensionnels hors grille et le déphasage entre chaque aube imposent un calcul sur deux canaux adjacents qui encadrent une aube de référence. C'est sur celle-ci que seront déterminées les répartitions de pression intrados-extrados après avoir imposé une condition sur l'angle instationnaire de sortie pour résoudre le système.

La structure de la méthode (sous forme de matrices de transfert) est telle qu'il est possible d'analyser l'influence d'un paramètre indépendamment des autres. C'est cette particularité qui est utilisée dans la présente étude pour essayer d'analyser les causes d'apparition du flottement de blocage.

## 3. CONFIGURATION ANALYSEE

TANIDA et SAITO [3] ont essayé de simuler le flottement de blocage rencontré en turbomachine en plaçant une seule aube au milieu d'un canal à parois parallèles (figure C).

L'aube est un profil symétrique à double arc de cercle. La corde est de 50 mm et l'épaisseur relative de 0,1. Les parois ne sont pas profilées, ce qui constitue deux canaux limités par deux parois (le profil et la paroi extérieure) non symétriques. Le pas relatif peut varier de 1,5 à 0,25 ; néanmoins, les principales expériences ont été effectuées pour le plus petit pas relatif.

Le profil peut osciller en rotation autour de la mi-corde pour une fréquence de 60 Hz ou de 100 Hz, ce qui donne des fréquences réduites faibles (inférieures à 0.10). L'amplitude de l'oscillation  $\delta\alpha$  est de plus ou moins 0.5°.

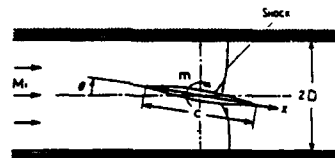


Figure C: Expérience TANIDA et SAITO

On admet que l'oscillation de ce profil isolé entre deux parois fixes schématise un flottement présentant un déphasage interaube de 180 degrés. En effet, pour une position instantanée du profil, en un point d'un canal, la section du canal sera minimale alors que le point homologue de l'autre canal présentera une section maximale. Donc, d'un point de vue évolution des sections, cette expérience reproduit bien la structure d'un flottement en opposition de phase. Par contre, cette opposition de phase qui se retrouve sur grille réelle entre deux positions instantanées de deux aubes limitrophes, n'existe pas dans cette expérience du fait de l'immobilité des parois. Cette différence se traduit nécessairement par une structure de l'écoulement instationnaire hors grille différente.

Les configurations analysées se réfèrent à des conditions expérimentales repérées par le rapport de pression statique de sortie à pression totale d'entrée (PS/PT) pour un pas relatif de 0,25 et une fréquence de 100 Hz.

La figure 1 montre l'évolution comparée théorie - expérience de la partie imaginaire du coefficient de moment normalisée par le produit de la pression dynamique et de l'angle de torsion  $\delta\alpha$ . L'écoulement est subsonique pour un rapport de pression supérieur à 0,74 et transsonique en deçà, la plus faible valeur correspondant à une onde de choc proche du bord de fuite.

Les données stationnaires utilisées sont celles relevées expérimentalement. L'accord est bon, compte tenu de la dispersion des résultats expérimentaux, sauf dans la zone subsonique où, pour toutes les configurations étudiées, la valeur théorique était trop négative.

Le flottement apparaît lorsque la partie imaginaire du coefficient de moment ( $\text{Im}(C_m)$ ) est positive. On constate que la prédiction du passage stable - instable est correcte.

#### 4. ETUDE PHENOMENOLOGIQUE

Nous allons essayer de comprendre ce qui conditionne le changement de signe de  $\text{Im}(C_m)$  en étudiant l'évolution de la partie imaginaire du coefficient de pression statique ( $\text{Im}(PS)$ ) le long de la corde et ce pour différents points de fonctionnement.

Compte-tenu du mouvement de torsion autour de la mi-corde, la partie imaginaire ( $\text{Im}(PS)$ ) est stabilisante lorsqu'elle est négative le long de la première demi-corde et positive le long de la seconde moitié.

L'étude suivante a été menée pour deux pas relatifs (0,25 et 0,50), un mouvement vibratoire et deux fréquences (60 Hz et 100 Hz). L'écart de fréquence n'ayant pas fait apparaître de différences significatives, seuls les résultats obtenus pour la fréquence la plus élevée sont présentés. Il est à noter, néanmoins, que pour cette fréquence, pratiquement seuls les effets visqueux stationnaires influencent le flottement alors que pour des fréquences de l'ordre de 1 000 Hz (fréquence réduite de l'ordre de l'unité), la contribution des couches limites instationnaires devient importante [5].

##### 4.1. Rôle des gradients longitudinaux de vitesse stationnaire le long du profil

Il est intéressant de comparer les évolutions le long de la corde de la dérivée logarithmique de la vitesse stationnaire (notée  $DU/U$ ) (figures 2,4,6) et de  $\text{Im}(PS)$  (figures 3,5,7). Ces dernières figures décrivent l'évolution de  $\text{Im}(PS)$  le long de la corde sur l'extrados et l'intrados, ce qui correspond en fait à la ligne moyenne du canal supérieur et inférieur de l'aube de référence. Dans les cas étudiés, correspondant à l'expérience, les mouvements étant en opposition de phase, les valeurs de  $\text{Im}(PS)$  sont égales en module mais de signe opposé. Le calcul du coefficient de moment s'effectuant à partir de la différence extrados moins intrados, c'est cette dernière courbe (en trait continu) que nous analysons dans la suite de cet article.

Pour le premier point transsonique (rapport 0,710), quelques oscillations apparaissent sur le gradient  $U$  - vitesse (figure 2), sans doute provoquées par l'imprécision des données. Le gradient présente un minimum au col (situé en 0,45) suivi d'une augmentation de l'accélération dans la partie supersonique. L'évolution correspondante de  $\text{Im}(PS)$  (figure 3) est constante dans la première partie (avec une très légère bosse au quart de la corde), puis croît (en valeur négative) jusqu'au col avant de décroître jusqu'au choc, ce qui donne alors une évolution inversée par rapport au gradient de vitesse. On peut remarquer à l'aval du choc une décélération élevée qui se traduit par un fort amortissement de la pression instationnaire.

Pour un rapport de pression de 0.642 (choc plus reculé), les évolutions de  $DU/U$  (figure 4) et de  $\text{Im}(PS)$  (figure 5) sont légèrement différentes du point précédent à l'aval du col. Après le col, on observe une augmentation plus brutale de l'accélération suivie d'une légère diminution puis d'une décélération juste à l'amont du choc. A l'aval de celui-ci, la décélération est faible et se stabilise autour d'une valeur de  $DU/U$  de 0.36. La partie imaginaire  $\text{Im}(PS)$  est identique au point précédent jusqu'au col. Par contre, elle diffère dans la zone supersonique. Après le col, le module décroît plus rapidement (ce qui correspond à l'accroissement plus rapide de l'accélération) puis continue de décroître mais plus modérément jusqu'à recroître légèrement au point précédent le choc et qui subit, lui, une décélération. Après le choc, le module reste pratiquement constant. Qualitativement, on observe donc bien un lien entre l'évolution de la partie imaginaire du coefficient de pression et le logarithme du gradient de vitesse longitudinal, exclusion faite de la traversée du choc (celle-ci sera étudiée plus loin).

L'analyse du point de fonctionnement présentant un rapport de pression statique à totale de 0.594 confirme les mêmes tendances. Une forte augmentation de l'accélération (figure 6) dans la partie supersonique suivie d'une très légère décélération à l'amont du choc engendre une diminution continue, mais pas brutale, du module de  $Im(Ps)$  (figure 7) jusqu'au choc. A l'aval de celui-ci, l'écoulement accélère avec un maximum entre le choc et le bord de fuite, ce qui se traduit par une augmentation continue du module de  $Im(PS)$ .

Les dérivées de l'écoulement stationnaire sont calculées dans chaque zone (figure B) en considérant chaque limite de zone comme une frontière, donc en décentrant, en amont ou en aval, les points limitrophes. Pour un point courant, les dérivées sont calculées au quatrième ordre :

$$\frac{\partial f}{\partial x} = \frac{1}{12 \Delta x} [f(x-2\Delta x) - 8f(x-\Delta x) + 8f(x+\Delta x) - f(x+2\Delta x)]$$

Pour le point précédent, la frontière (aval dans ce cas), la formule suivante est appliquée :

$$\frac{\partial f}{\partial x} = \frac{1}{6 \Delta x} [f(x-2\Delta x) - 6f(x-\Delta x) + 3f(x) + 2f(x+\Delta x)]$$

Et à la frontière :

$$\frac{\partial f}{\partial x} = \frac{1}{2 \Delta x} [f(x-2\Delta x) + 3f(x) - 4f(x-\Delta x)]$$

Une imprécision apparaît au niveau du col puisque celui-ci n'est qu'une frontière fictive. L'erreur introduite est bien sur d'autant plus importante que le nombre de points de discrétisation est faible.

En calculant des dérivées centrées à travers le col, on obtient pour le point 0.642, la courbe en pointillé présentée figure 4. Compte tenu du faible nombre de points (21 sur la corde), un écart important apparaît puisque le point précédant le col présente une pointe d'accélération et non un creux. Les résultats de la partie imaginaire de la pression sont illustrés figure 8. Cette modification se traduit sur  $Im(PS)$  par une valeur plus faible du module au bord d'attaque (de l'ordre de 20 %) et surtout par une forte diminution locale au point présentant la plus forte accélération (près du col). Dans la zone supersonique, l'accélération diminue continûment, ce qui se traduit par un léger accroissement du module de  $Im(PS)$ . La sensibilité de la partie imaginaire du coefficient de pression au gradient de vitesse près du col est donc évidente.

La figure 9 permet de mieux se rendre compte de la correspondance entre  $DU/U$  et  $Im(PS)$ . Cette analyse ayant été effectuée indépendamment de la discontinuité à travers le choc, les courbes ont été tracées en prenant comme origine les valeurs des variables à l'amont et à l'aval du choc (la discontinuité à travers celui-ci n'apparaît donc pas). Le gradient  $DU/U$  a été, dans ces conditions, superposé au terme  $Im(PS)$  ; on constate, qu'aux oscillations près, les pentes des courbes évoluent dans le même sens sauf dans le dernier quart de corde où on observe une inversion des pentes.

Il ressort de cette analyse qu'une forte accélération provoque une importante régression du module de la partie imaginaire du coefficient de pression et inversement pour une faible accélération ; par ailleurs une diminution de la décélération provoque plutôt une diminution du module de  $Im(PS)$  mais cette dépendance est moins nette (et peut même s'inverser). Il semblerait que pour cette zone décélétratrice (généralement aval au choc), l'évolution de  $Im(PS)$  dépende aussi des valeurs de cette variable au niveau du choc. On remarque une sensibilité très grande au gradient  $DU/U$  près du col puisqu'il semble avoir une influence locale mais aussi sur le niveau des fluctuations à l'entrée du canal. Enfin, les évolutions de  $Im(PS)$  dans la zone supersonique semblent dépendre à un moindre niveau (qu'à l'amont du col) des valeurs locales de  $DU/U$ .

Dans l'étude qui nous intéresse, l'axe de torsion étant situé à la mi-corde, les valeurs négatives de  $Im(PS)$  sur la première demi-corde sont stabilisantes alors qu'elles sont déstabilisantes sur la seconde moitié. C'est donc en fonction du rapport de ces deux évolutions que le système sera stable (valeur négative de la partie imaginaire du coefficient de moment) ou au contraire instable (valeur positive de  $Im(Cm)$ ).

Pour cette étude (à ce niveau il semble délicat de généraliser), une forte accélération près du col est donc déstabilisante dans la mesure où elle diminue le niveau du module de  $Im(PS)$  à l'entrée du canal (et donc sur toute la première demi-corde) alors que l'effet à l'aval du col, surtout local, n'engendre pas de diminution importante du couple déstabilisant (distance trop faible de l'axe de torsion).

La dépendance entre le gradient longitudinal de vitesse et la stabilité est trop fonction du mouvement vibratoire (flexion, torsion, position de l'axe de torsion) et des positions, par rapport à l'axe éventuel de torsion, du col et du choc pour qu'il soit possible de trouver une relation générale directe. Par ailleurs, le choc crée une discontinuité du module de  $Im(PS)$  qu'il est nécessaire d'analyser pour étudier la stabilité.

#### 4.2. Influence du choc

Les différentes courbes présentées au paragraphe précédent montrent clairement que le niveau de  $Im(PS)$  à l'aval du choc est fortement tributaire de la discontinuité à travers celui-ci. En tout premier lieu, il est intéressant d'analyser l'effet associé à l'intensité du choc. La figure 10 présente en pourcentage la variation du module de  $Im(PS)$  à travers le choc normalisée par la valeur amont au choc en fonction de la variation du nombre de Mach normalisée aussi par la valeur amont pour différents points de fonctionnement obtenus pour les pas relatifs de 0.25 et 0.5. Il apparaît nettement que pour les chocs faibles (valeurs de  $\Delta M/M$  inférieures à 35 % ( $M_1 = 1.2$ ), les variations de  $Im(PS)$  sont systématiquement faibles (inférieures à 15 %). Ainal, lorsque le choc est faible, même si les conditions d'écoulement sont défavorables (voir paragraphe suivant), l'influence de celui-ci sur  $Im(PS)$  restera modérée. Par contre, pour des chocs plus intenses, l'amplitude de la variation de  $Im(PS)$  n'est pas directement liée à l'intensité du choc bien que celle-ci y contribue. Il semble donc qu'une intensité supérieure à 35 % ( $M_1 > 1.20$ ) soit une condition nécessaire mais non suffisante pour créer un accroissement remarquable du module de  $Im(PS)$  à travers le choc. Pour la plupart des cas étudiés, l'influence du choc est déstabilisante, il est donc important d'étudier les paramètres qui conditionnent la variation de  $Im(PS)$  à travers celui-ci.

D'un point de vue stabilité, le fait que ce soit les chocs forts qui soient déstabilisants pondère le résultat précédent. En effet, ce qui importe au niveau stabilité, c'est la valeur de la partie imaginaire du coefficient de moment or celle-ci est obtenue par intégration le long du profil, par le produit de la force associée à  $\text{Im}(\text{PS})$  et de la distance au centre de torsion. Donc si le choc est faible, celui-ci est proche du col et donc de l'axe de torsion ; ainsi le domaine instable (aval au choc) est important. Inversement, pour un choc intense (donc proche du bord de fuite), le domaine instable est beaucoup plus réduit. Bien que dans les cas analysés, cet effet compensateur n'était pas suffisant pour inverser l'influence due à l'intensité du choc, il est possible qu'il n'en soit pas de même pour d'autres géométries.

#### 4.2.1. Influence du gradient de vitesse au niveau du choc

##### Gradient amont au choc

Le paragraphe 4.1. a montré le rôle du gradient de vitesse longitudinal stationnaire sur  $\text{Im}(\text{PS})$ . Ce gradient conditionne aussi l'amplitude de ce terme à travers le choc. Ainsi nous avons étudié l'influence de la valeur de ce gradient juste à l'amont du choc. Le point ayant un rapport de pression de 0.659 présente une faible valeur de  $\text{DU}/\text{U}_1$  (0.062) à l'amont du choc. Il a donc été possible de pratiquement annuler ce gradient ( $\text{DU}/\text{U}_1 = 0,003$ ) en ne modifiant que légèrement la valeur de la vitesse, 10 % de la corde en amont du choc. La répartition le long de la corde de  $\text{Im}(\text{PS})$  pour le point ainsi obtenue (figure 12) est à comparer à la répartition initiale (figure 11). La variation relative  $\Delta \text{Im}(\text{PS})/\text{Im}(\text{PS}_1)$  passe ainsi de 0.85 à 2.73.

Ainsi, la déstabilisation est considérable lorsque la valeur du gradient de vitesse à l'amont du choc tend vers zéro. On notera de plus que l'amplitude de la variation de  $\text{Im}(\text{PS})$  pour le point de référence était déjà très importante et vraisemblablement liée à la faible valeur de  $\text{DU}/\text{U}_1$  (0.062).

Le tableau ci-dessous donne les valeurs des parties imaginaires et réelles des nombres de Mach amont  $\text{M}_{1c}$  et aval  $\text{M}_{2c}$  au choc ainsi que les parties imaginaires et réelles du mouvement du choc  $X_c$  (normalisé par la corde) pour le point de référence et le point à faible gradient  $\text{DU}/\text{U}_1$ .

	$\text{Im}(\text{M}_{1c})$	$\text{Im}(\text{M}_{2c})$	$\text{Im}(X_c)$	$\text{Re}(\text{M}_{1c})$	$\text{Re}(\text{M}_{2c})$	$\text{Re}(X_c)$
PS/PT = 0.659 DU/U = 0.062	0.0078	0,0093	0.0146	-0.0464	-0.037	-0.070
PS/PT = 0.659 DU/U = 0.003	0.0077	0.0083	0.0777	-0.0462	-0.041	0.0066

Les valeurs sensiblement égales de  $\text{Im}(\text{M}_{1c})$  et de  $\text{Re}(\text{M}_{1c})$  montrent que la modification de la vitesse stationnaire 10 % avant le choc n'a pas de conséquence sur l'écoulement instationnaire amont au choc. Par contre, on remarque un écart de près de 20 % sur  $\text{Im}(\text{M}_{2c})$  mais les valeurs restent faibles. La variation instationnaire de l'intensité du choc reste modérée et diminue même pour la plus faible valeur de  $\text{DU}/\text{U}$ . Par contre, l'amplitude du mouvement croît légèrement en module (passant de 7,1 % à 7,8 %) mais surtout il s'établit un transfert de phase tel que le mouvement du choc est en opposition de phase avec le mouvement vibratoire (partie imaginaire de  $X_c$  prépondérante) pour la plus faible valeur de  $\text{DU}/\text{U}$ . Ainsi, les variations de  $\text{Im}(\text{PS})$  semblent plus sensibles au mouvement instationnaire du choc qu'à sa variation d'intensité.

Nous avons essayé de confirmer ce résultat par une étude pour un autre rapport de pression (0.642). Pour ce cas, nous avons effectué un balayage en modifiant uniquement la valeur de  $\text{DU}/\text{U}$  à l'amont du choc de -0.85 (valeur de référence) à + 0.80. La figure 13 illustre les résultats obtenus sur la partie imaginaire du coefficient de moment ainsi que sur les parties réelles et imaginaires du déplacement instationnaire du choc. On peut remarquer que la partie imaginaire du déplacement du choc présente un maximum pour une valeur nulle de  $\text{DU}/\text{U}$ . Une valeur négative de ce gradient est plus pénalisante qu'une valeur positive. Enfin, lorsque l'amplitude de ce gradient est importante, l'influence est alors limitée.

Ces résultats vont dans le sens d'une intuition : le choc a du mal à se stabiliser sur une position précise lorsque l'accélération est faible (faible divergent). Néanmoins, le fait que le mouvement du choc soit déphasé (cause essentielle de l'instabilité) ne trouve pas d'explication évidente. On remarque, toujours sur la figure 13, que la partie imaginaire du coefficient de moment est directement proportionnelle à la partie imaginaire du déplacement du choc. Il existe donc une relation directe entre la stabilité et le gradient de vitesse amont au choc.

L'étude de la formulation de la loi de transfert du choc montre que le terme  $\text{DU}/\text{U}$  apparaît dans la matrice CX associée au mouvement du choc et dans les termes de la matrice CX dépendant des fluctuations d'entropie  $\delta y_3$  et de masse volumique  $\delta y_1$  :

$$\begin{bmatrix} \delta y_1 \\ \delta y_2 \\ \delta y_3 \end{bmatrix}_{\text{Aval}} = [CY] \cdot \begin{bmatrix} \delta y_1 \\ \delta y_2 \\ \delta y_3 \end{bmatrix}_{\text{Amont}} + [CX] \cdot \delta X_{\text{choc}} + [CA] \cdot \delta A$$

La détermination de l'écoulement instationnaire à l'aval du choc requiert la connaissance du mouvement du choc. Celui-ci est obtenu notamment en exprimant  $\delta X_c$  en fonction des variables  $\delta y$  de part et d'autre du choc donc en inversant la matrice CX. Si la partie réelle du coefficient lié  $\delta y_3$  de la matrice CX est petite, alors la résolution tendra à déterminer une forte valeur du déplacement  $\delta X_c$ , toutes choses égales par ailleurs. Lorsque les perturbations à l'aval du choc seront recalculées, la partie réelle du coefficient lié  $\delta y_3$  de la matrice CX étant importante (fonction du rapport des masses volumiques d'où l'influence de l'intensité du choc), la fluctuation d'entropie sera très grande. Cette importante fluctuation d'entropie crée une forte augmentation de la fluctuation de pression (fonction de  $\delta y_1 + \delta y_3$ ). Ainsi par exemple, pour le rapport de pression de 0.642, la fréquence de 100 Hz et la valeur nulle de DU/U à l'amont du choc, la fluctuation d'entropie passe d'une valeur de  $9.10^{-4}$  à une valeur de  $8.10^{-3}$  - i.2,5.10<sup>-3</sup>. Si de plus la valeur des perturbations amont au choc avait été nulle, la fluctuation d'entropie aurait été de  $4,5.10^{-3}$  - i.3,5.10<sup>-3</sup> ce qui aurait accru la valeur de la partie imaginaire.

#### Gradient aval au choc

Pour le pas relatif de 0.50, les perturbations sont fortement amorties à l'aval du choc tout comme pour les rapports de pression 0.710 et 0.676 du pas relatif de 0.25. Pour ces configurations, le gradient DU/U est négatif et élevé en module (sauf pour 0.676 où c'est le point suivant qui présente une valeur élevée).

Nous avons testé l'influence de ce gradient en imposant une valeur nulle juste à l'aval du choc pour le rapport de pression de 0.710. La répartition de pression instationnaire (figure 14, à comparer à la figure 3) montre clairement un amortissement plus faible sur les deux points après le choc, le niveau restant plus négatif (jusqu'au bord de fuite) que dans la configuration standard. Le mouvement est ainsi moins bien amorti, la valeur de la partie imaginaire du coefficient de moment étant de -0.056 contre -0.148. Néanmoins, l'amortissement aval subsiste et le gradient DU/U n'est donc pas le seul responsable de cet amortissement. En fait, la contribution de ce point est identique à celles des autres points contrairement au gradient amont au choc.

Un résultat, sous-jacent à l'ensemble de ceux présentés, apparaît : la contribution de l'aval sur le mouvement du choc semble secondaire. En effet, ce sont principalement les termes (stationnaires et instationnaires) situés à l'amont qui contribuent à modifier de façon significative la discontinuité de Im(PS) à travers le choc. Ainsi, contrairement à ce que l'on pourrait supposer (par extrapolation du fonctionnement stationnaire où la position du choc dépend de la pression aval), le déplacement du choc est peu sensible aux conditions de sortie.

Il serait alors possible de penser que les théories [6] qui utilisent une hypothèse d'homotropie à travers le choc (ce qui leur permet de déterminer le mouvement du choc indépendamment de l'aval) sont bien adaptées au problème posé. En réalité, les résultats obtenus montrent au contraire que le mouvement du choc engendre un accroissement très important de la fluctuation d'entropie.

Par ailleurs, ces résultats montrant la faible dépendance de l'aval contredisent l'interprétation de SHIRATORI et TANIDA [7]. En effet, ceux-ci, en observant que le déphasage du mouvement du choc semble proportionnel à la fréquence réduite, supposent que ce déphasage est lié au temps de remontée d'une perturbation du bord de fuite au choc.

#### 5. CONCLUSION

L'exploitation d'une modélisation du flottement de blocage à l'aide d'une théorie linéarisée a permis de développer une étude sur l'influence du gradient de vitesse longitudinal stationnaire. Cette étude révèle une correspondance directe entre l'évolution, le long de la corde, de ce gradient de vitesse et de la partie imaginaire du coefficient de pression instationnaire.

Il apparaît par ailleurs, que ce même gradient de vitesse juste à l'amont du choc conditionne le mouvement (et surtout son déphasage) du choc instationnaire qui lui-même détermine le niveau de la partie imaginaire du coefficient de pression jusqu'au bord de fuite. Ainsi, les faibles valeurs du gradient de vitesse au niveau du choc nuisent à la stabilité. Consécutivement à ces résultats, on peut remarquer une forte dépendance du mouvement du choc vis à vis de l'amont et inversement une faible influence de l'aval.

#### REFERENCES

1. FERRAND P.  
Linearized theory of the choked flow in an annular oscillating cascade.  
Symposium "Unsteady aerodynamics of turbomachines and Propellers". Cambridge. Sept. 1984.
2. FERRAND P.  
Etude théorique des écoulements instationnaires en turbomachine axiale. Application au flottement de blocage.  
Thèse de Doctorat d'Etat. Université LYON I. Mars 1986.
3. TANIDA Y. et SAITO Y.  
A study on choking flutter.  
Symposium IUTAM sur l'Aérodélasticité dans les turbomachines. Revue Française de Mécanique.  
Octobre 1976.
4. FERRAND P.  
Modélisation d'écoulements présentant deux périodicités : étude des interactions distorsion circonférentielle - pompage et décrochage tournant - pompage dans les compresseurs.  
Journal de Mécanique Théorique et Appliquée. Vol. 5, n° 2, p. 259-275, 1986.
5. COUSTEIX J., DESOPPER A., HOUEVILLE R.  
Recherches sur les couches limites turbulentes instationnaires.  
A.A.A.F. 13ème Colloque d'Aérodynamique Appliquée, Lyon, Nov. 1976.
6. MICKLOW J. and JEFFERS J.  
Semi-actuator disk theory for compressor choke flutter.  
NASA CR 3426, Juin 1986.
7. SHIRATORI et TANIDA Y.  
Aerodynamic characteristics of an airfoil oscillating in transonic flow between parallel walls.  
International Gas Turbine Congress, Tokyo, GTSJ, 1983.

#### REMERCIEMENTS

Nous remercions la S.N.E.C.M.A. pour le soutien financier qu'elle a apporté à cette recherche.

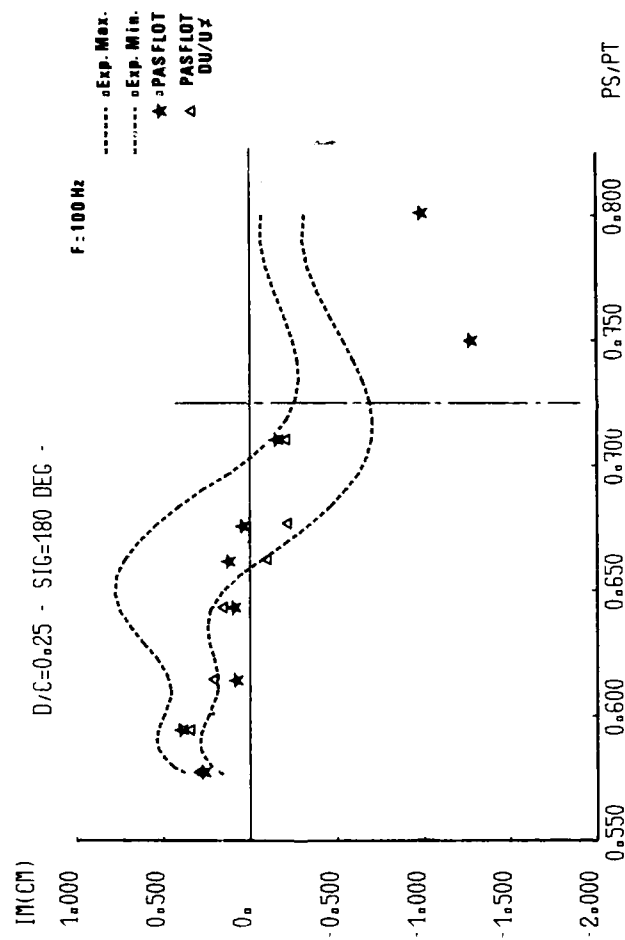


Fig 1

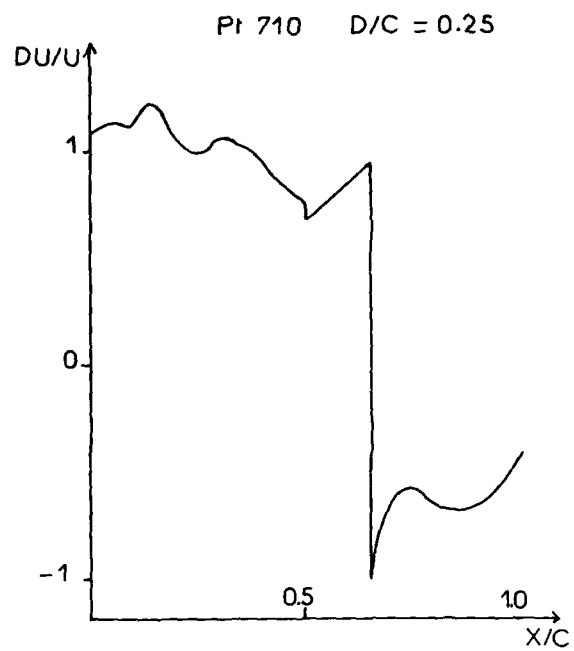


Fig 2

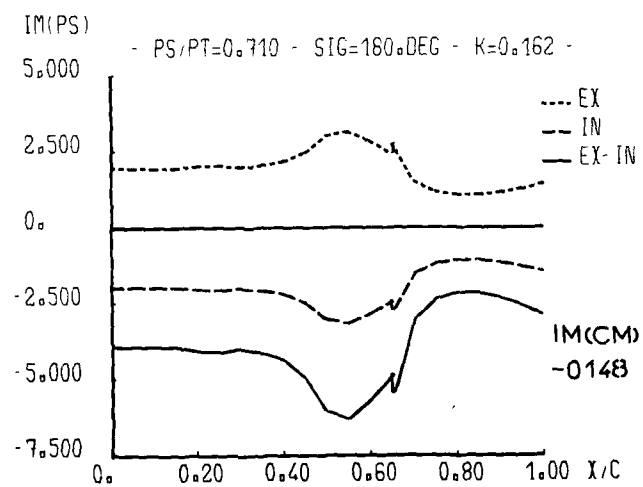


Fig 3



Pt 642

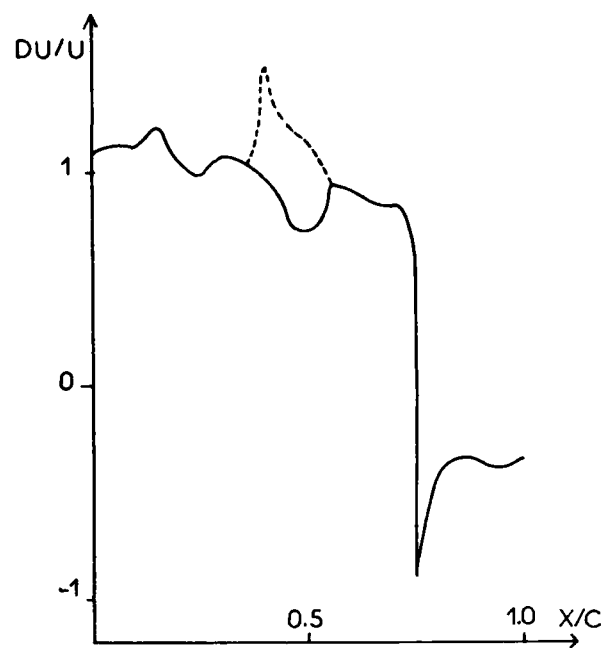


Fig 4

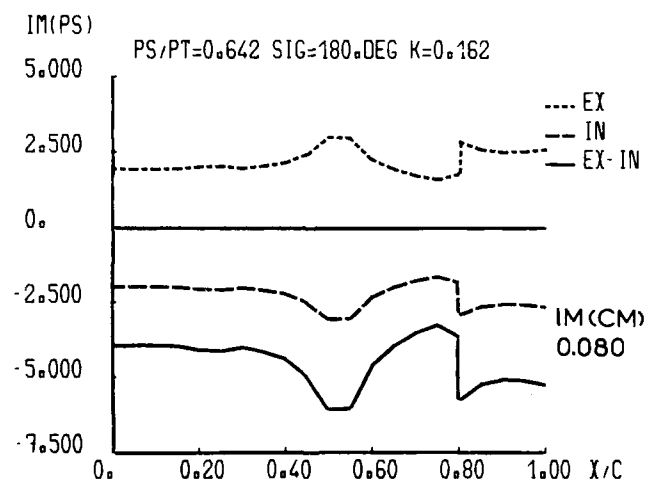


Fig 5

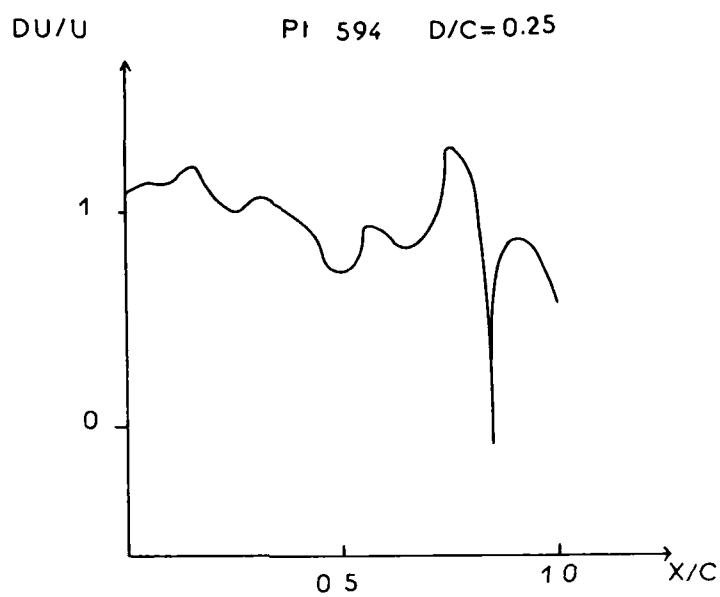


Fig 6

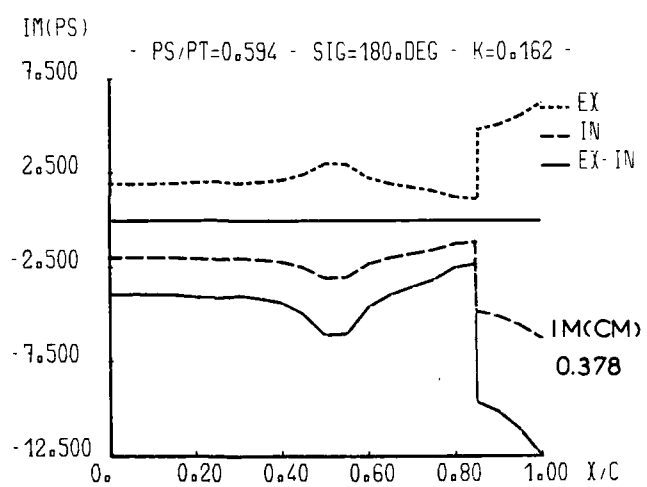


Fig 7

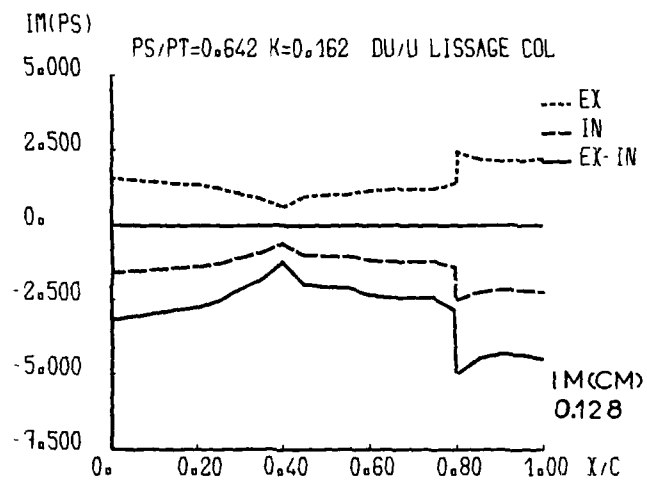


Fig 8

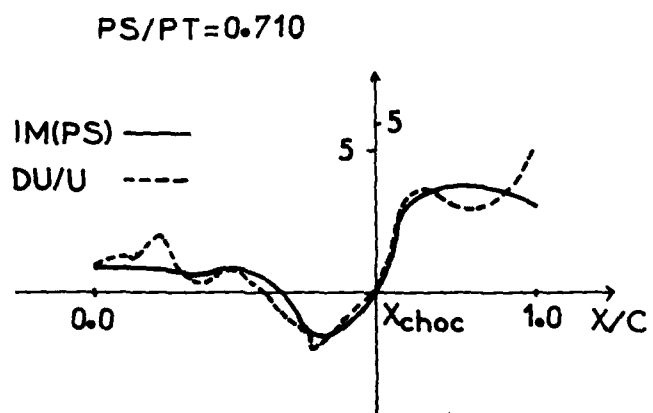


Fig 9

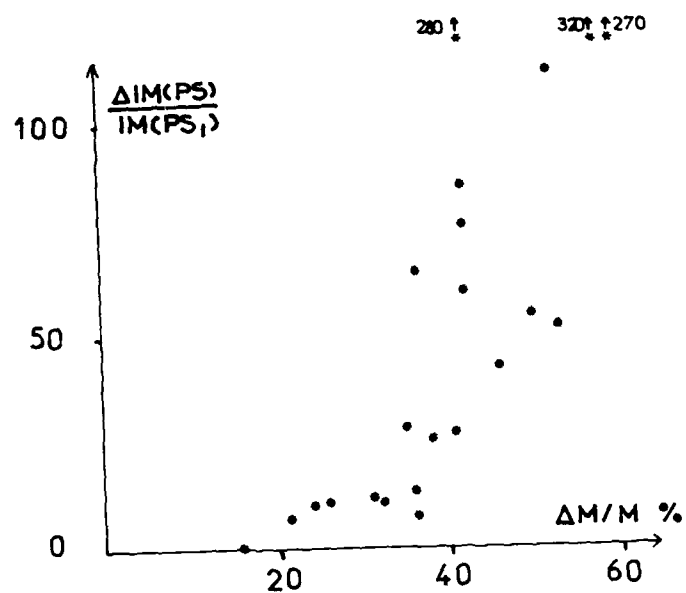


Fig 10

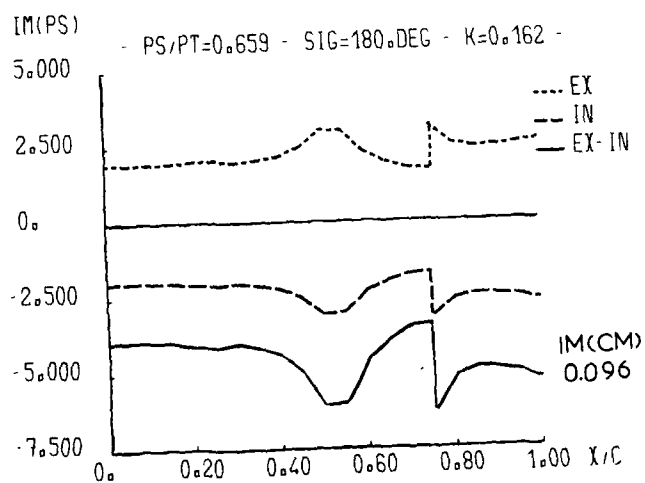


Fig 11

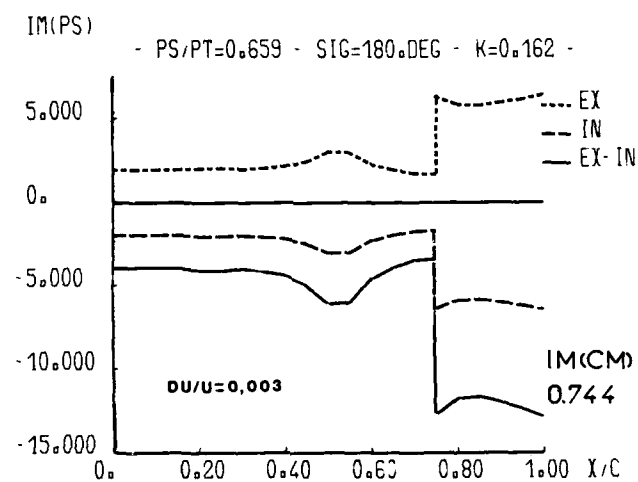


Fig 12

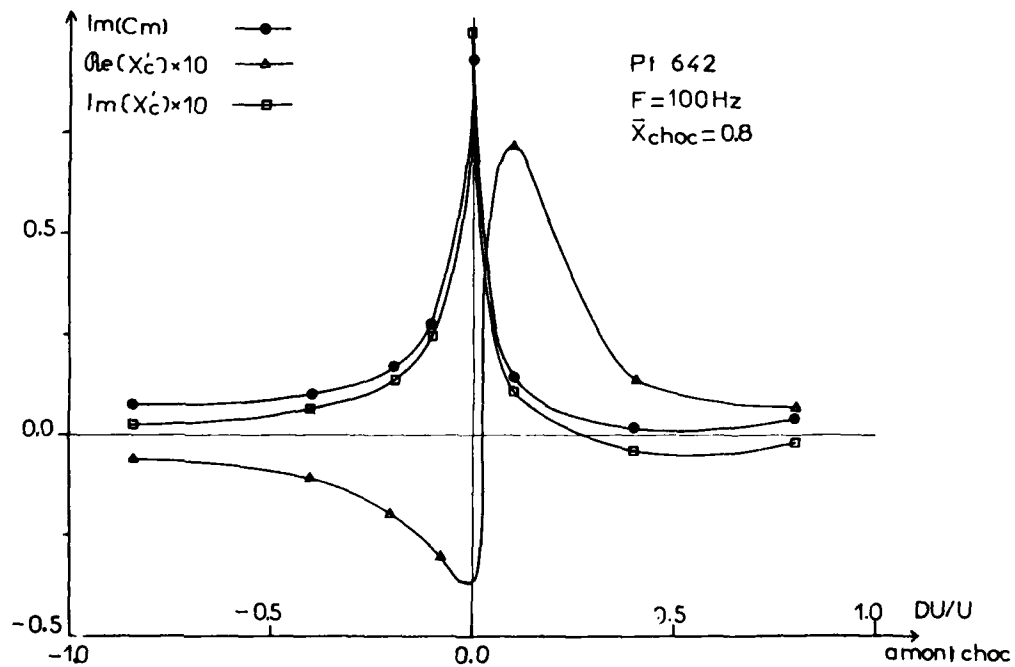


Fig 13

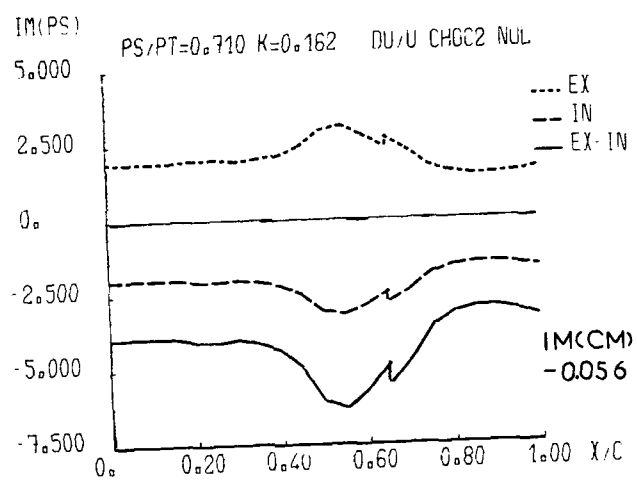


Fig 14

## POSSIBILITIES FOR ON-LINE SURGE SUPPRESSION BY FAST GUIDE VANE ADJUSTMENT IN AXIAL COMPRESSORS

by  
W. Rieß  
U. Blöcker  
Institut für Strömungsmaschinen  
Universität Hannover

Appelstr. 9  
D-3000 Hannover  
Germany

### SUMMARY

The usual surge suppression regulation is realized by integration of a fixed limit-line into the regulation system at a safe distance to the stability limit of the compressor. Since additional reserves for deterioration or fouling have to be included, an interesting part of the characteristic field with high efficiency is excluded so from practical use.

With appropriate means for detection of the onset of stall and surge and by fast response of the guide vane adjustment an adaptive system for surge suppression could be realized, which takes into account the actual state of the compressor.

Experimental results for stall detection and for different modes of guide vane adjustment are presented. A six-stage axial compressor is equipped with fast acting guide vane adjustment in all stages. First experimental results are presented.

### 1. INTRODUCTION

For control of mass flow rate and pressure ratio of a multistage axial compressor different control modes are applied, dependent on the characteristics of the system and of the compressor drive. Usually the variable speed control is very efficient, if a compressor drive with a low-loss possibility for speed regulation, e.g. a steam turbine, a gas turbine or an electric motor with suitable equipment, is available. For a fixed speed drive (usually a 3-phase electric motor) other modes of compressor regulation, as throttling or blow-off are widely used. More recently the application of variable guide vanes for about half of all stages of a compressor as a highly efficient and versatile means of regulation finds increasing interest.

For axial compressors in two-shaft gas turbines or gas generators in jet engines, marine and stationary applications, where mass flow rate and pressure ratio control is effected largely by speed variation, variable guide vanes are applied as additional control means for high pressure ratio machines with narrow characteristic fields and for further optimisation of the stage flow conditions in part load conditions. Usually an additional blow-off device is used for surge control /1/.

In modern turbojet engines the characteristic field of the highly loaded compressors is quite narrow and usually the stationary operating line is situated in the high efficiency region near the surge limit. During transient conditions as acceleration, afterburner ignition etc., the dynamic shift of the operating line to the left can result in surge or, at least, rotating stall. Therefore a sufficient margin for operating conditions like these has to be incorporated in the regulating system. Furthermore engine deterioration by fouling, blade erosion, blade clearance increase by wear or mechanical damage will invariably lead to a shift of the surge limit towards higher mass flow rates and further decrease of the surge margin, which has to be taken care of in the positioning of the operating line. In total, the conventional concept of surge control by introduction of a sufficient fixed margin for all eventualities into the regulation system renders a considerable part of the - anyway rather limited - characteristic field of the compressor non-available for normal stationary operation at high efficiency. The basic shortcoming of this solution are the lack of actual information on the real position of the surge limit and - in addition - the time-lag occurring in the regulation via fuel flow rate.

A quick-acting, condition-oriented, on-line surge suppression system could be realized with a real-time surge-onset detection and a quick-acting, individual guide vane control system, which would first change guide vane positions towards a configuration with higher stability and, probably, lower efficiency and then, in cooperation with the compressor regulating system, approach a new stable and efficient operating point.

Considerable experience with the detection and measurement of flow instabilities in axial compressors /2/ and with the influence of guide vane control on the characteristic field /3/ are the basis for the concept, which is presented here.

### 2. AXIAL-FLOW COMPRESSOR TEST FACILITY

Our experimental research activities concerning multistage axial compressors are rea-

lized in a test facility comprising two different compressors, a three-stage type and a six-stage type with variable guide vanes in all stages. Figures 1 and 2 show the cross-sections and in table 1 the main design data are listed.

The aerodynamic design parameters of both experimental compressors render a performance similar to real machines encountered in practice e.g. in power-plant gas turbines, chemical industry and in turbojet-engines. The similarity of design and performance refers to equal inlet hub ratios, inlet relative Mach numbers and in particular stage pressure ratios.

Both compressors are equipped with a diffuser throttling device in order to avoid classical surge cycles during the experiments at the surge limit to reduce the operating risk to a minimum. The plenum on the pressure side of the test rig between outlet and throttling valve with a volume of about  $6 \text{ m}^3$  is reduced thus to a volume  $0,03 \text{ m}^3$  (3-stage) resp.  $0,024 \text{ m}^3$  (6-stage). This facility renders possible all experimental investigations near and beyond the surge limit without excessive loading. Previous experiments confirmed, that for highly loaded multistage compressors the position of the stability limit is not influenced by this modification.

The diffuser throttling device consists of a movable throttling ring (fig. 1 and 2, pos. f) which is positioned by a stepping motor (pos. g). For experimental investigations carried out directly at the stability limit the high accuracy and reproducibility of the positioning system is of considerable advantage.

The two compressors exhibit a similar pattern of flow instabilities, explained in detail in chapter 4. The experiments comprising a fast acting guide vane control are limited to the six-stage compressor with its variable geometry.

The detection of instationary flow conditions is realized by semiconductor pressure transducers. Their geometrical arrangement for three different cases is shown in fig. 3. In configuration I thirteen transducers are distributed flush mounted to the casing wall in the axial gaps between rotor and stator. This arrangement permits the detection of incipient unsteady flow conditions in all stages. For the analysis of the dynamic phenomena in circumferential direction five transducers have been distributed peripherally in the axial gap before the second rotor as shown in configuration II. The development and extension of unsteady flow conditions in radial direction was measured by means of configuration III. Four pressure probes, designed for this purpose and furnished with suitable transducers, have been installed on different radii according to fig. 3.

The six-stage compressor is additionally equipped with a three-channel-FM/FM-telemetry (fig. 2, pos. c) for monitoring the cyclic stress of the blading resulting from this extreme operation. Furthermore, indications for instationary flow conditions from an independent source are made available thus. The vibrations of one blade in each of any three different rotors, measured with strain gauges, are transmitted simultaneously. The three-stage compressor, is equipped with a single-channel-FM/FM-telemetry system (fig. 1, pos. b), serving the same purposes. The signal patterns have been recorded by a multi-channel analog magnetic tape, then digitized and processed in a digital computer.

### 3. GUIDE VANE SETTING AND COMPRESSOR PERFORMANCE

Each of the guide vane rows of the six-stage compressor can be set individually and independently from all others. This results theoretically in an infinite number of possible combinations of guide vane positions within a wide range of stagger angle. Purely random combinations are mostly ineffective or detrimental, systematic combinations seem to have more practical value. Therefore several "guide vane setting laws" were defined and the resulting compressor performance was investigated in a comprehensive experimental program /3/. Fig. 4 shows the compressor characteristic field for variable speed with constant nominal stagger angles for all guide vane rows, while three different compressor maps for variable guide vanes for three different modes of setting angle variation are shown in fig. 5, 6 and 7. The different values of the parameter K characterize the amount of guide vane angle variation according to the different modes.  $K = 0$  indicates the design configuration. Obviously the three different setting modes exemplify the three basic possibilities of decreasing (I LE), identical (II LE) and increasing (III LE) angle variation along the compressor. The linear distribution is the most simple way of realisation only, non-linear distributions are equally possible and might be even better.

In many modern turbojet-engines variable guide vanes in several compressor stages are adopted in addition to the usual variable speed control /4, 5/. Generally the guide vane adjustment is performed rather slowly compared with the fuel regulation and realizes a better adaption of the characteristic field to the operating conditions, as rotational

	Dim.	Three-Stage Compressor	Six-Stage Compressor
No. of Stages	-	3	6
Degree of Reaction	-	0.5	0.84
Tip Diameter of Blading	mm	540	540
Rotational Speed	rpm	17000	14575
Blade Tip Speed	m/s	302	259
Relative Inlet Mach Number	-	0.75	0.84
Stage Pressure Ratio	-	1.26	1.12
Overall Pressure Ratio	-	2.0	2.0
Hub/Tip Ratio	-	0.405	0.44
Mass Flow Rate	kg/s	11	10.2
Power Input	kW	900	850
Blade Profile Type	-	NACA 65	NACA 65 (modified)
Vortex Flow Pattern	-	Radial Body (modified)	Free Vortex
No. of Blades	-	16V./26 Ro./21 St./26 Ro./25 St./26 Ro./29 St./28	16V./21 Ro./17 St./42

Table 1: Design Data of Experimental Compressors



speed and inlet temperature. A decrease of speed will cause some opening of the front guide vanes and some closing of the rear ones. So the stability of flow can be enhanced.

In the six-stage compressor (fig. 2) the design position of all guide vanes is because of mechanical reason also the fully-open position, only closing is possible, i.e. only negative adjustment angles  $\Delta\alpha_s$  in fig. 5, 6 and 7 can be realized.

The compressor maps in figures 5, 6 and 7 show systematic differences concerning the form of the operating field, the position of the surge limit and the pattern of the efficiency-curves. The relative positions of the stability limits are additionally plotted in fig. 7. Obviously the patterns of the stability limits and consequently the shift of the operating field are considerably dependent on the selected adjustment mode.

These results of /3/ indicate, that each specific part-load working line of the compressor can also be realized with an optimum adjustment mode, which assures best efficiencies in all stages.

Normally a high-efficiency flow condition in a stage assures stable flow conditions, too. However, the optimum efficiency will often be situated close to the stability limit, so that an appropriate stability margin is not realized. If incipient instability can be detected, the guide vane positions can be adapted in consequence.

#### 4. FLOW INSTABILITIES IN COMPRESSORS - "ROTATING STALL" AND "SURGE"

Research concerning flow instabilities in compressor traditionally was centered on the physical appearance of these phenomena and on the formulation of governing parameters and definition of limit values for stability, important for compressor design and operation. Obviously the experimental research preferred fully development instabilities for its investigation.

For the development of an on-line surge suppression by fast guide vane adjustment and the implementation of an appropriate control system the timely detection of the onset of instabilities is of utmost importance.

A practical possibility is offered by signals transmitted from semiconductor pressure transducers, as mentioned above, which are installed in the casing according to configuration I in fig. 3.

In /6/ G.R. LUDWIG reported that pressure transducers are useful sensors for detecting incipient rotating stall. With an improved version of a rotating stall control system, which was acting with variable inlet guide vanes and bleed doors, he was able to suppress rotating stall, but only after it had occurred for a short time (about 90 milliseconds). Before its disappearance a stall cell had already rotated up to seven times. The few stall cycles had no noticeable effect on the tested compressor (J-85). However, with a larger plenum on the pressure side as e.g. in industrial installations, surge would have occurred immediately according to our experimental experience. In addition the successful tests carried out by G.R. LUDWIG were restricted to rotational speeds of about 75 % of rated value.

The basic disadvantages of this type of stall suppression are the triggering of surge, if the system stability is not sufficient, and the additional stressing of the blading. They could be avoided, if development of rotating stall was suppressed completely by early detection and quick corrective action. No limitations to part-speed would be necessary then.

Comprehensive experimental investigations on unsteady flow phenomena at the Institute of Turbomachines in two rather different compressors (fig. 1, fig. 2) revealed quite similar behavior /2/. The strong influence of the form of the compressor characteristic in combination with the pressure side plenum could be proven again in accordance with E.M. GREITZER /7/. The two test compressors proved to exhibit static instability, consequently the stability limit was not influenced by the system configuration, as could be shown experimentally.

Based on this statement most of our experiments on compressor instability were conducted utilizing the diffuser throttling ring, the very small plenum volume precluded any surge oscillations, so that complete characteristic fields including the region left of the stability limit could be measured, e.g. fig. 8 for the experimental compressors. Mass flow rate and pressure ratio are time averaged values resulting from the stationary equipment.

A detailed evaluation including the results of the instationary pressure measurements reported below revealed a specific pattern of a characteristic line with respect to the different types of flow instability. According to the schematic presentation in fig. 9 the characteristic beginning at the choking line describes the stable operation of the compressor with increasing pressure ratio corresponding to increased throttling. A short distance before the stability limit increasing, non-periodic pressure fluctuations indicate instability region 1, which is probably due to stochastic flow separation at blade tip.

Upon reaching the stability limit the operating point moves very rapidly through the instability region 2 (transient) and comes to rest on a macroscopically stable characteristic,

which describes the instability region 3 with a stable full span stall. Further throttling moves the operation point on this line to the left with increasing extension of the stall cell, but quasi-stationary operation can be realized (with a very small pressure-side plenum!) down to very low net mass flow rates, where complete flow separation, instability region 4, begins.

Fig. 10 shows the corresponding development of instationary pressure signals from transducers in two different positions. Short sections of the time-dependent pressure signals measured during a slow throttling manœuvre characterize the different instability regions.

Of specific interest is the considerable increase of the fluctuation level in the instability region 1, which could be utilized for detection of incipient instability. Frequency analysis of these signals revealed a negligible periodicity, so that an interpretation as stochastic separation seems more appropriate than a part span rotating stall.

Upon reaching the stability limit the pressure signals change rapidly and within three to five revolutions a single-cell full-span rotating stall in all stages develops, which remains stable in the small plenum configuration.

Tests with a large plenum volume revealed the same development of a full-span stall. The corresponding drop in pressure ratio through the "transient" portion of the characteristic serves then as a trigger for the considerably slower surge cycle (fig. 11). Each new surge cycle is initiated by a new rotating-stall period.

Fig. 12 and 13 resp. show simultaneously the signals of pressure transducers in different positions during the transient from instability region 1 to region 2 with full-span stall on the real time scale for the 3-stage and the 6-stage compressor. Apart from the very rapid passage through the transient part of the characteristic, it is obvious that only some of the transducers show considerably increased fluctuation level just before reaching the stability limit.

For a reliable on-line detection of incipient flow instability it will be necessary to investigate the most effective positions for instationary pressure transducers for the different modes of stall. In addition a suitable signal processing, e.g. the evaluation of the a.c.-part of the pressure signal within a specific frequency range, and the definition of limit values for the fluctuation intensity from the experimental results.

Since the stability limit for multi-stage axial compressors with sufficient aerodynamic loading is identical for large and small plenum volumes, all experimental investigations concerning the flow stability can be conducted at low risk for the integrity of the blading by use of the diffuser throttling ring.

In total the following facts resulting from the analysis of the experimental data can be utilized for the intended regulating system:

- The stability limit of a multistage compressor is preceded by a region of irregular pressure fluctuations
- These fluctuations can be detected by suitably placed pressure transducers of adequate sensitivity
- The position of the stability limit and the preceding pressure fluctuations are independent of the volume of the pressure-side plenum.

##### 5. DESIGN OF THE FAST ACTING GUIDE VANE ADJUSTMENT

The design of the guide vane adjustment equipment was based on a number of fundamental considerations /8/

- a) Each guide vane row can be adjusted independently to assure great experimental flexibility
- b) The adjustment mode can be chosen individually for each stage in order to be able to realize many different "adjustment laws" for the complete compressor
- c) The adjustment speed is variable between very high values - about 90° stagger angle variation per second - for quick-acting suppression of imminent flow instabilities and quasi-stationary movement for subsequent adaption of the blade angles to optimum position for a new operating point.

In order to fulfill these criteria, the guide vane adjustment system is realized as a electro-hydraulic regulating system.

For a future industrial application the layout can be based on the results of our intended investigations and might result thus in a more or less simpler configuration with sufficient capabilities.

The main parts of our experimental adjustment system shown in fig. 14 are the control unit (pos. A) for regulating oil supply and the distributor block (pos. B), which feeds the six adjustment units, consisting each of a four-way servo-valve (pos. C), a hydraulic power cylinder (pos. D) and the electronic control system (pos. E), which are shown only for one adjusting ring. The momentary position of the hydraulic actuator, which corresponds to the stagger angle of the pertinent guide vane row, is measured by a linear potentiometer (pos. I). The control system comprises adjustable limits in both directions of the movement and an adjustable speed from 90° per second to slow motion. It will be operated

in the final configuration by an on-line control computer.

Fig. 15 demonstrates the compact design of the adjustment system for one stage. Servo-valve (pos. a), hydraulic actuator (pos. c) and linear potentiometer (pos. d) are arranged on a support block (pos. b), which contains the connecting bare holes for the hydraulic oil. Length of connections and oil volume were reduced thus to a minimum, assuring a very quick response of the hydraulic system. The motion of the actuator is transmitted via the connecting rod (pos. e), the adjustment ring (pos. f) and the levers to the guide vanes.

#### 6. OPERATION OF THE FAST ACTING GUIDE VANE ADJUSTMENT

The action of the Fast Guide Vane Adjustment System has to be integrated in the control system of an axial compressor in a suitable way.

The realization of an efficient control method necessitates complete information regarding the operational characteristics of the compressor: Experimentally determined stage characteristics in combination with a through-flow calculating code /3, 5/ can be used for the determination of the compressor characteristic.

A considerable number of stage characteristics for different guide vane setting modes have been measured for the six-stage test compressor with adjustable guide vanes /9/. A computer program for the calculation of the compressor characteristic field from stage characteristics has been established: Combined with data on the system supplied by the compressor and the intended control function this program can realize a surge suppression regulation utilizing an on-line computer. In an industrial application a specialized micro-processor will probably be sufficient, as soon as sufficient knowledge on structure, operation and capability of such a system will be acquired.

The regulating process with a fast guide vane adjustment can be exemplified in fig. 16 for a control mode with constant pressure ratio  $\pi$ . Starting point is OP1, where the compressor is operating on characteristic a) (defining a certain combination of guide vane positions in the different stages) at optimum efficiency: If the mass flow, due to a disturbance in the system supplied, is suddenly reduced, the operating point of the compressor moves on characteristic a) into instability region I. The resulting increased pressure fluctuation is detected by pressure transducers, a regulating signal is deduced and the fast-acting system moves the guide vanes accordingly, so that the stability limit will not be reached. The operating point is transferred to characteristic b), which has been calculated by the on-line computer and results from the modified position of the guide vanes. When the dynamic phenomena have ceased, the compressor operates in point OP2. It is important, that characteristic b) is chosen so, that this point has sufficient distance from instability region I and - consequently - from the stability limit: Efficiency is of minor importance in OP2.

During the fast movement of the guide vanes from characteristic a) to b) the stability limit (indicated by lines with small circles) may also be subjected to a dynamic modification. The exact nature of the dynamic regulating process in the characteristic field is being investigated experimentally at the moment. Three possible curves are shown in fig. 16. Curve I would be an ideal result, since the pressure ratio  $\pi$  remains constant. Curve II has to be avoided, since it crosses the stability limit and this results in a multistage compressor with high aero-dynamic loading instantly in a transient development of full span stall or surge. The drawback of curve III is, that the pressure ratio  $\pi$  drops off shortly, but in a dynamic regulating process this is probably admissible.

If the new steady state of the system supplied is characterized by point OP3, the guide vane adjustment is moved slowly so that via curve IV a new characteristic with optimum efficiency and safe distance to stability limit is reached.

Fig. 16 shows a schematic example only. From the great many of possible solutions the real behavior of compressors under dynamic guide vane regulation conditions will be determined experimentally. With these information an optimum regulating strategy, the suitable positioning of the instability detectors and the necessary configuration of the guide vane adjustment system can be defined.

#### 7. EXPERIMENTAL RESULTS

Measurements during a typical regulating process with the fast acting guide vane adjustment system are shown in fig. 17. The guide vane position is changed from characteristic III LE(k) (fig. 7) to I LE(k) (fig. 5) with a corresponding shift of the stability limit to considerably smaller mass flow rates, as fig. 7 shows. In the test the starting point is situated on characteristic III LE(1), the end point on characteristic I LE(1,5). The compressor speed was 11.120 rpm, a value below nominal speed, the guide vane adjustment time was 110 msec.

The left part of fig. 17 shows the pressure fluctuations at the starting point conditions before the guide vane adjustment. Transducers 3 and 5 in stages 1 and 2 indicate an operation in the I. instability zone with increased pressure fluctuations. Similarly the strain gauge signals from a rotor blade in the 1. stage express increased instability. The signals of transducers 7, 9, 11 and 13 in stages 3, 4, 5 and 6 show normal behavior without instability, likewise the strain gauge signals of rotors 2 and 5, not shown in fig. 17, are not increased.

During this test the crossing at the stability limit was not intended, but the operating point of the compressor was to be moved from the 1. instability zone by operation of the rapid guide vane adjustment to a characteristic with sufficient distance from the stability limit.

The regulating process is shown in the middle part of fig. 17 for a total of 270 msec, the guide vane adjustment itself takes 110 msec. During the rapid guide vane movement, already, a considerable reduction of the pressure amplitudes in stages 1 and 2 to 66 % and 76 % resp. of the initial values is effected. Similarly the rotor blade vibration diminishes to 69 %.

The right part of fig. 17 shows the new stabilized operating point: the pressure ratio has been kept constant at 1.567, the mass flow is reduced slightly for 2.9 % to 5.156 kg/sec, a very small speed increase of 0.9 % can be noted. Similar tests at nominal speed resulted in speed increases of 2.5 to 3 %. In total the test proved that a rapid stabilisation of the compressor at constant pressure ratio can be realized, a quite practicable result for real compressor operation. The data of the pressure transducers are given in a relative scale intentionally, because the interest during the first experiments was concentrated mainly on the qualitative behavior of the system.

Fig. 18 shows the results of a different test with a rather identical starting point on characteristic III LE(1) with a pressure ratio of 1.615, mass flow of 5.468 kg/sec at 11 377 rpm. The pressure signals of stage 1 and 2 indicate the 1. instability zone. The guide vane position was changed to that of characteristic I LE(3), i.e. the guide vanes are closed considerably more than in fig. 17.

The now stable operating point shows a pressure ratio of 1.495 and 5.084 kg/sec mass flow at 11 117 rpm.

Right after the beginning of the regulating process the pressure reduction in stages 2 to 6 starts and takes about 800 msec, while the guide vane movement is completed after 188 msec. The decrease of speed is caused by a simultaneous action of the speed regulating system.

The amplitudes of the pressure fluctuations in stage 1 and 2 diminish to 53 % and 88 % resp. of the initial value and prove the increased distance of the new operating point from the stability limit.

These two examples of initial tests show, that by a rapid guide vane adjustment the operating point of the compressor can be moved quickly into a part of the characteristic field with higher stability. During the regulating process the compressor remained stable without onset of rotating stall. Somewhat disadvantageous is the speed increase coupled with the guide vane adjustment. In a computerized control system, however, an appropriate action of the speed regulation could be anticipated and initiated.

Actually conducted tests at nominal speed rendered qualitatively similar results, so that the principles of operation can be generalized.

In the tests up to now the diffuser throttle ring was utilized exclusively for realizing the operating point of the compressor, i.e. the pressure-side volume of the system was very small. Since our former investigations had proved that the stability limit is not dependent on this pressure-side volume, the experimental results should be valid. Test with a high pressure-side volume will be conducted later.

## 8. Conclusion

The concept of an on-line anti-surge regulating system is based on the detection of incipient instability by pressure fluctuations and the rapid shifting of the compressor operating point by a quick acting guide vane adjustment system.

The system has been developed, built and tested on an experimental compressor. The results are consistent with the basic ideas. Further extensive experimental work will be centered first on dynamic operation, i.e. movement of the operating point towards the stability limit before the regulating process, and then closing of the control loop, i.e. automatic initiation of the regulation process by pressure fluctuation sensors and microprocessor calculation of the new stable operating point will be aimed at.

## 9. References

- /1/ Traupel, W.; Thermische Turbomaschinen - Band II, 3. Auflage, Springer-Verlag, 1982, pp. 98-121.
- /2/ Schlamann, U., Teipel, I., Rieß, W.; Experimentelle Untersuchung der Strömungsphänomene des Rotating Stall und des Pumpens bei mehrstufigen, hochbelasteten Axialverdichtern. VDI-Fortschritt-Berichte, Reihe 7, Nr. 91, Düsseldorf, 1985.
- /3/ Rieß, W., Kiesow, H.-J.; Experimentelle Untersuchung des Einflusses von Leitschaufelverstellgesetzen auf das Betriebsverhalten von Stufen und Stufengruppen eines Axialverdichters, VDI-Berichte 572.1, VDI-Verlag, Düsseldorf, 1985, pp. 421-436.
- /4/ Hagen, H.; Fluggasturbinen und ihre Leistungen, Wissenschaft + Technik-Verlag, Karlsruhe, 1982, pp. 25-42, pp. 297-306.

- /5/ Dettmering, W., Bitterlich, W., Grahl, K.; Theoretische Untersuchung über die Verbesserung des Flugverhaltens von Strahltriebwerken bei variablen Flugaanforderungen durch kombinierte Leitschaufel- und Schubdüsenanpassung, Forschungsberichte des Landes Nordrhein-Westfalen Nr. 2416, Westdeutscher Verlag 1974.
- /6/ Ludwig, G.R.; Tests of an improved Rotating Stall Control System on a J-86 Turbo-jet-Engine, Aerodynamic Research Department, 1979, AFAPL-TR-79-2080, New York 14225.
- /7/ Greitzer, E.M.; Flow Instabilities in Axial Fans and Compressors Including Surge Prediction, International Seminar Advanced Turbomachinery Performance, Munich, 1985.
- /8/ Rieß, W., Blöcker, U.; Auslegung und Konstruktion einer schnellen Leitschaufelverstellung für einen sechsstufigen Axialverdichter, Sonderforschungsbereich 211, Universität Hannover, Seminarbericht 1984, pp. 75-96.
- /9/ Kiesow, H.-J.; Leitschaufelverstellung bei mehrstufigen Axialverdichtern, Dissertation, Universität Hannover, 1984.

# 10. FIGURES

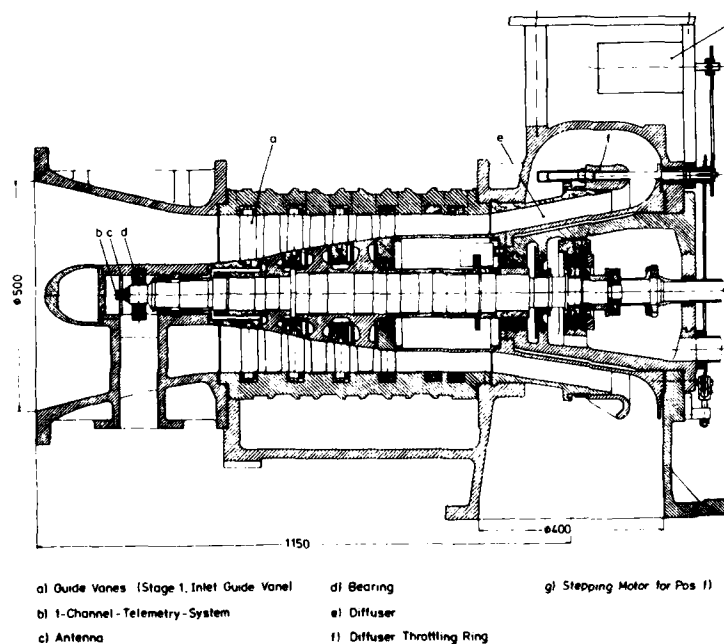


Fig. 1 Three-Stage Experimental Axial-Flow Compressor

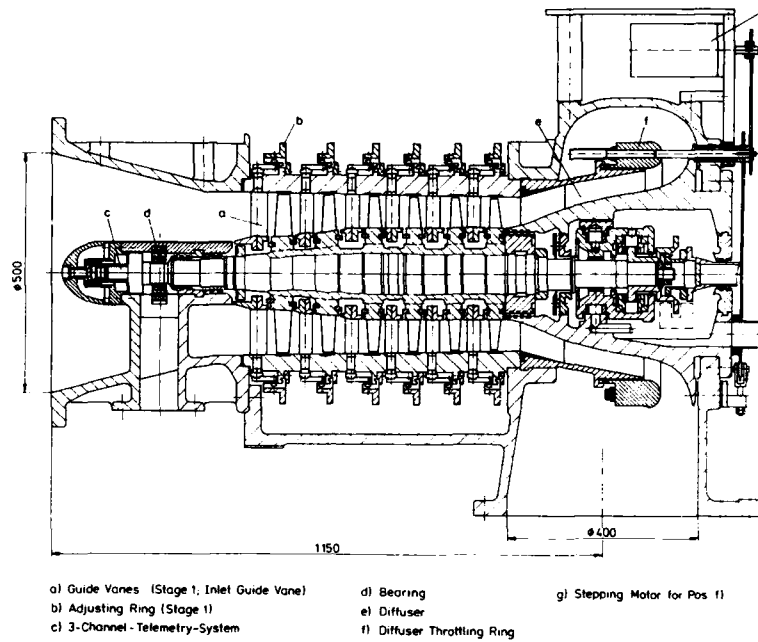


Fig. 2 Six-Stage Experimental Axial-Flow Compressor

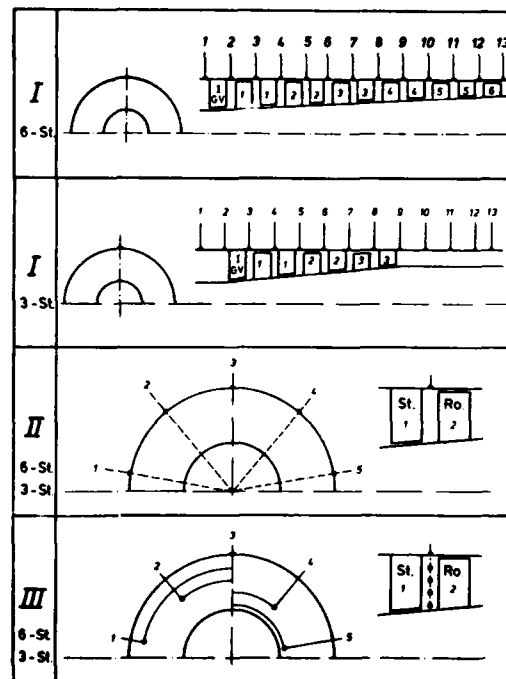
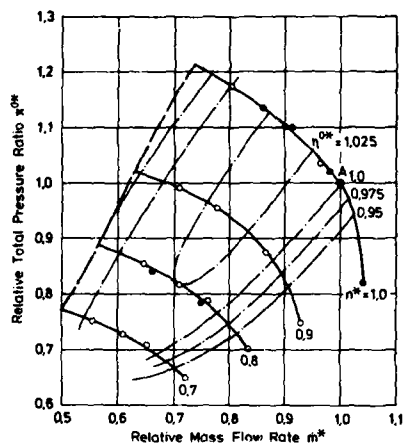
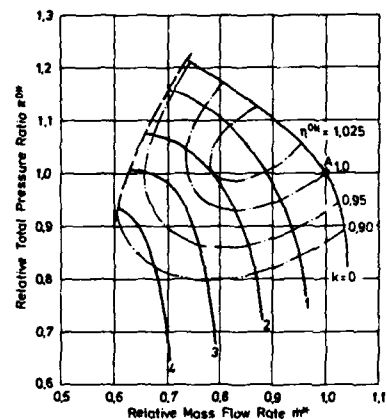


Fig. 3 Configuration of Pressure Transducers Distribution



A : Design Point  
 $n^*$  : Rotational Speed Ratio  
 $\pi^*$  : Relative Total Efficiency  
 ○ : Measured Points

Fig. 4 Compressor Map for Variable Speed (DLE(0)N); Guide Vane Setting at Design Values



Adjustment Rule: I LE(k)  
 A : Design Point  
 k : Number of Adjustment Characteristic  
 $\pi^*$  : Relative Total Efficiency

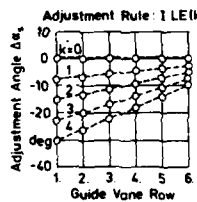
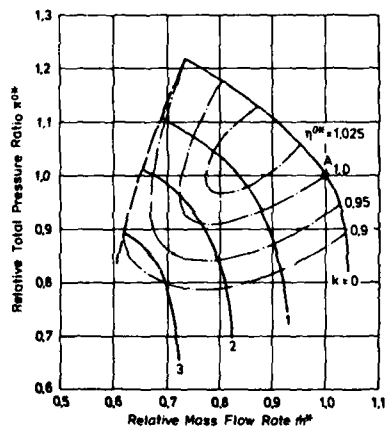


Fig. 5 Compressor Map for Variable Guide Vane Setting (I LE(k)) at Design Speed



Adjustment Rule: II LE(k)  
 A : Design Point  
 k : Number of Adjustment Characteristic  
 $\pi^*$  : Relative Total Efficiency

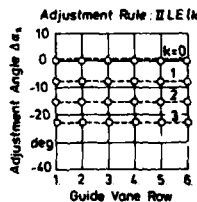
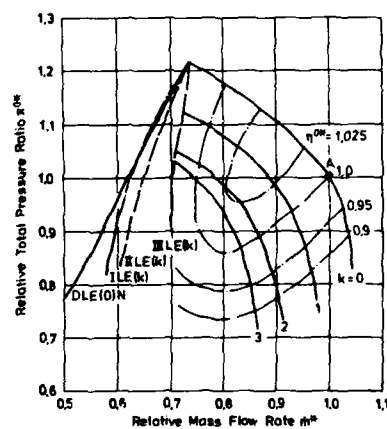


Fig. 6 Compressor Map for Variable Guide Vane Setting (II LE(k)) at Design Speed



Adjustment Rule: III LE(k)  
 A : Design Point  
 k : Number of Adjustment Characteristic  
 $\pi^*$  : Relative Total Efficiency

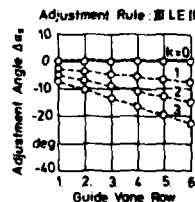


Fig. 7 Compressor Map for Variable Guide Vane Setting (III LE(k)) at Design Speed

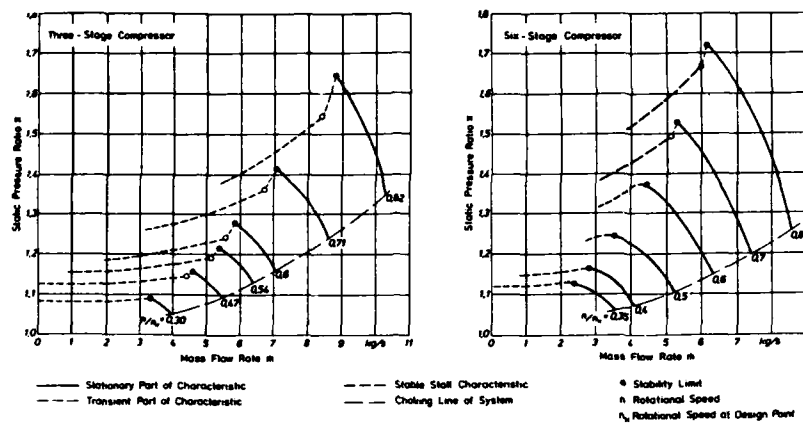


Fig. 8 Measured Compressor Maps for Variable Speed Ratios

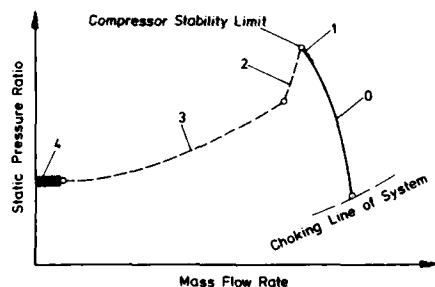


Fig. 9 Complete Schematic Compressor Characteristic for Highly-Loaded Multi-Stage Axial-Flow Compressors without System Instability

Explanation of Numbers used in Fig. 9, Fig. 10, Fig. 12 and Fig. 13:

- 0: Stationary Part of Characteristic  
 1: Instability Region 1  
 - Flow Separation at Rotor Blade Tip  
 2: Instability Region 2  
 - Transient Regime  
 3: Instability Region 3  
 - Stable Full Span Stall (one Cell)  
 4: Instability Region 4  
 - Complete Flow Separation

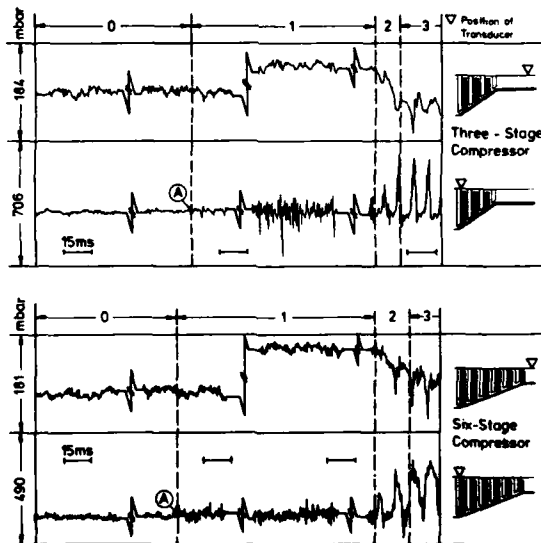


Fig. 10 Patterns of Unsteady Pressure Fluctuations in different Instability Regions for both Experimental Compressors



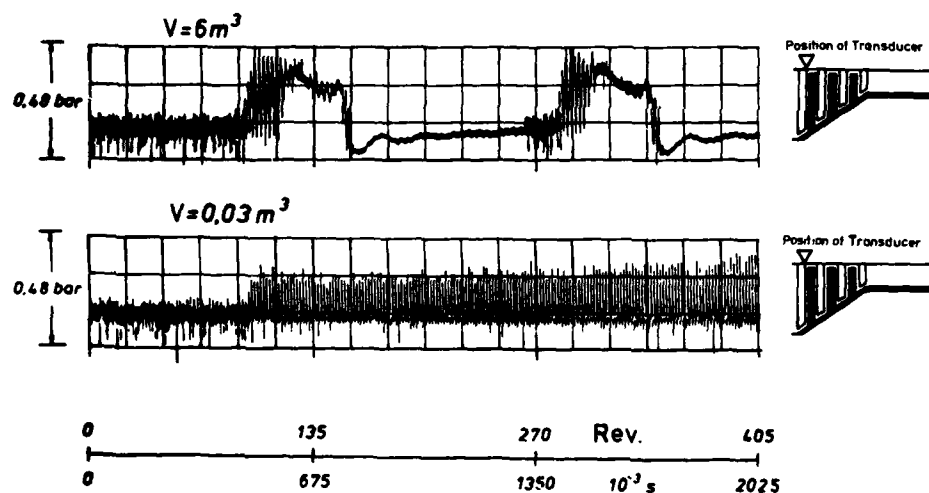


Fig. 11 Pattern of Unsteady Pressure Fluctuations for Surge (Large Pressure Side Volume) and Full Span Stall (Small Pressure Side Volume)

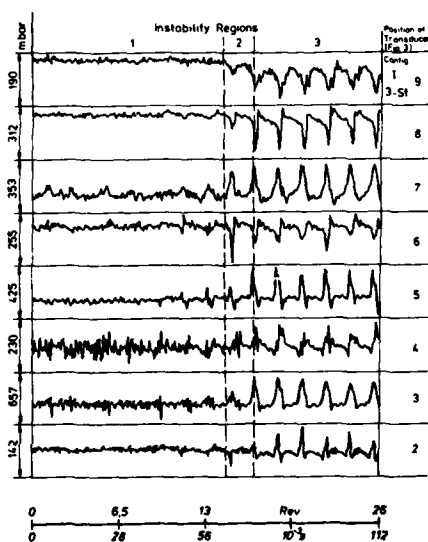


Fig. 12 Patterns of Instability Development in the Blading of the Three-Stage Compressor

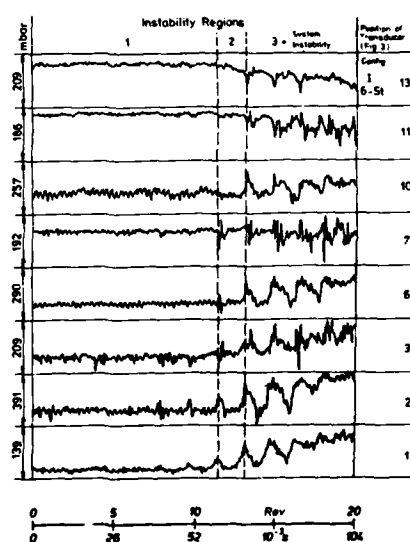


Fig. 13 Patterns of Instability Development in the Blading of the Six-Stage Compressor

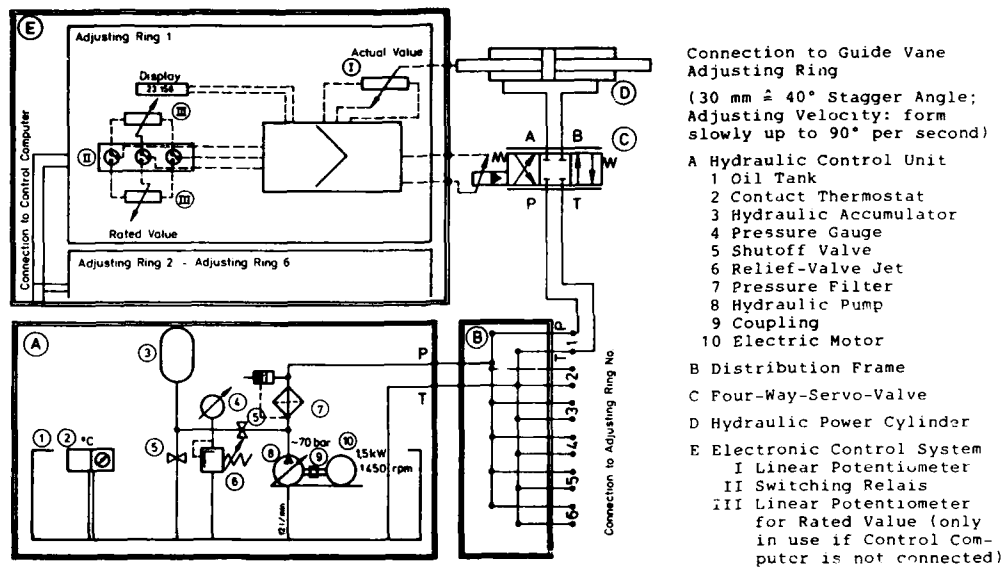


Fig. 14 Electrohydraulic Control System for Fast Acting Guide Vane Adjustment

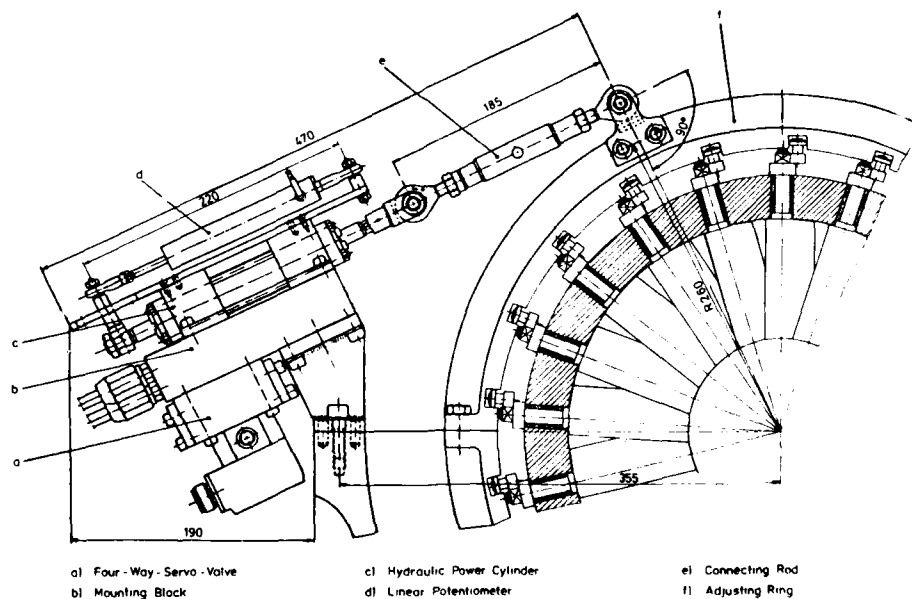


Fig. 15 Fast Acting Guide Vane Adjustment Device (for one Stage)

Fig. 16 Regulating Process with Fast Guide Vane Adjustment System ( $\pi = \text{const.}$ )

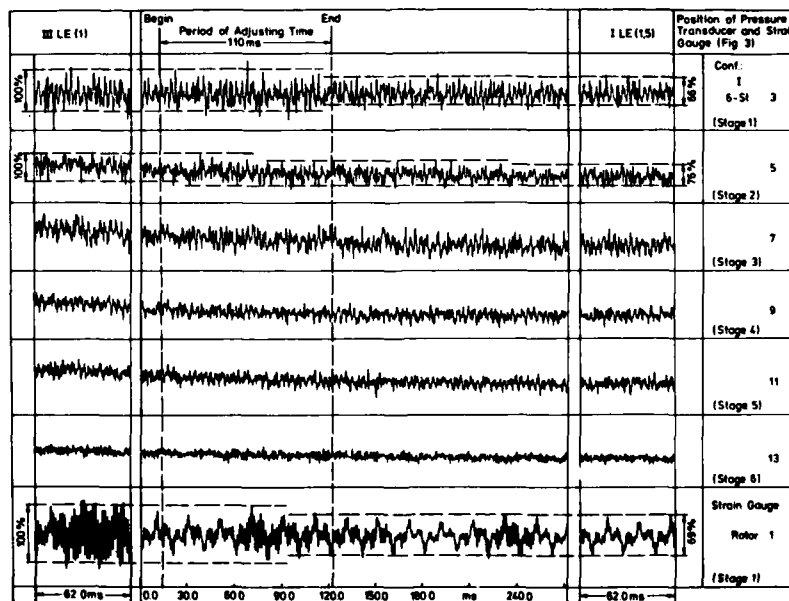
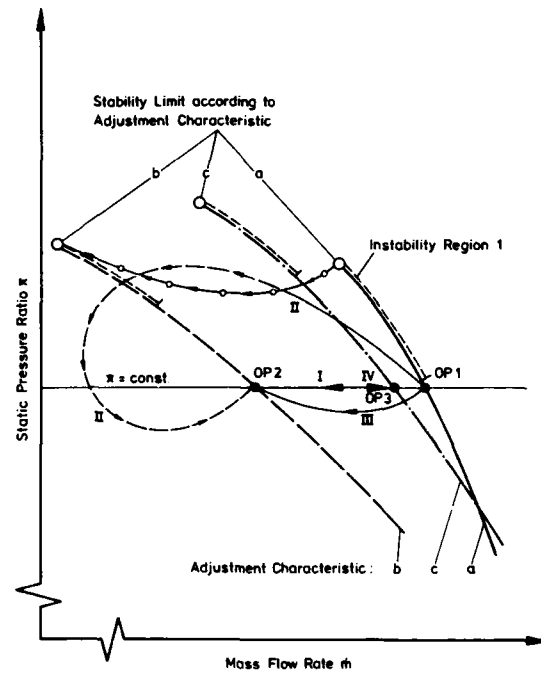


Fig. 17 Regulating Process with Fast Acting Vane Adjustment System:  
 - Starting Point: III LE(1);  $\dot{m} = 5,309 \text{ kgs}^{-1}$ ;  $\pi = 1,567$ ;  $n = 11,123 \text{ rpm}$   
 - End Point : I LE(1,5);  $\dot{m} = 5,156 \text{ kgs}^{-1}$ ;  $\pi = 1,567$ ;  $n = 11,222 \text{ rpm}$

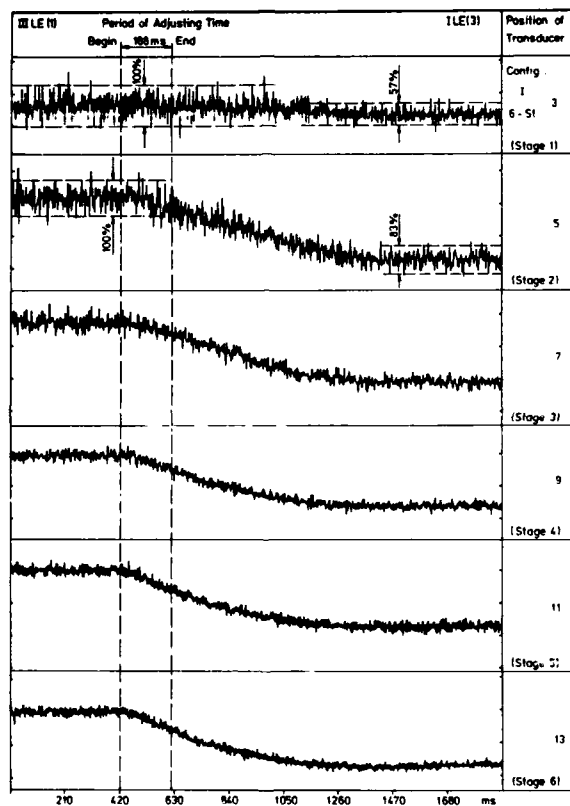


Fig. 18 Adjusting Process with Fast Acting Guide Vape Adjustment System  
 - Starting Point: III LE(1);  $\dot{m} = 5,468 \text{ kgs}^{-1}$ ;  $\pi = 1,6151$ ;  $n = 11,377 \text{ rpm}$   
 - End Point : I LE(3);  $\dot{m} = 5,084 \text{ kgs}^{-1}$ ;  $\pi = 1,495$ ;  $n = 11,117 \text{ rpm}$

### DISCUSSION

**J.F. CHEVALIER, Fr**

Vous avez montré des essais avec un compresseur dont les volumes amont et aval sont très petits. Votre système de contrôle peut-il fonctionner avec des volumes amont et aval beaucoup plus grands ?

**Author's Reply**

The upstream volume of the system is quite large (700 mm Ø pipe, 6 m long plus filter chamber). The downstream volume can be chosen large (6 m<sup>3</sup>) or small (0.003 m<sup>3</sup>) with two different throttles. The situation of the stability limit and the pressure fluctuation behaviour has been proven experimentally not to be influenced by the downstream volume. Therefore many of the experiments are conducted with small volume to avoid surge and endangering the compressor.

A closed-loop control system has not been used up to now, it will be tried later in the project with large and small volume.

**N.A. CUMPSTY, UK**

Could you give more information on guide vanes, how fast, how large is the angle of adjustment and how large is the error of setting ?

**Author's Reply**

The maximum adjustment speed of the guide vanes is actually 90°/sec, the hydraulic system is capable of more. The real adjusting range is + 0°/-30° because of mechanical reasons. The setting error of individual vanes is less than 0.5°. The positioning accuracy of the hydraulic system is very high. The inaccuracies of positioning from elastic deformations are small because of its rugged design.

**K.R. GARWOOD, UK**

During the experiments have any measurements of the torque or stresses generated in the variable geometry system been made, during the transient high rate of stagger changes ?

**Author's Reply**

We have not measured this torque reaction. The first results that I have presented here are carried out by the maximum variation speed. The adjustment mechanism is, as you have seen, very rugged. It can tolerate all the dynamic forces and, in fact, up to now we didn't care for dimensioning. Practical use would necessarily cause detail dimensioning of the mechanism.

# RADIAL COMPRESSOR DESIGN USING AN EULER SOLVER

M.Sc. Jan Tore Billdal  
Division of Hydro- and Gas Dynamics  
Norwegian Institute of Technology, Norway  
and  
M.Sc. Andrew Wilson  
RTR, A/S Kongsberg Våpenfabrikk, Norway

## Summary

The steady inviscid flow through a radial compressor is computed by solving the 3-D Euler equations on both a H-type and O-type grid. The centered finite volume method with an explicit integration scheme is used to solve the equations. The numerical programmes were developed as a tool in the design process of new, high pressure radial compressors, with complex geometries and splitterblades.

Special emphasis is placed on transonic compressors, and the capability of predicting complex three-dimensional flows is demonstrated. Preliminary experience using Euler solver in design work is described with the future developments expected on this subject.

## Introduction

It is common to show results from a 3-dimensional program which agree well with well documented and abundant test data. In the normal design environment, that data is not normally so forthcoming, and the designer is usually limited to such measurements as upstream and downstream pressures and temperatures, mass flow and the shroud static pressures. These must in some way be assessed in terms of design criteria such as blockage, loss distribution and slip factor. In turn these criteria are fed back into the design process.

The Euler solver cannot implicitly cater for the correct viscous effects in the compressor and the solution obtained will be without regard to the criteria our experience tells us is correct. (The flow in the exducer section of a centrifugal compressor is dominated by 3-dimensional viscous flows). In the absence of anything better the Euler solver can be used to give a more accurate picture of the flow in the inducer section up to the splitter blade leading edge, and to give some basic understanding of the secondary flows in the exducer.

Little is normally presented about the problem in running a 3-dimensional program when things can often go wrong. The test cases presented here represent a high pressure ratio, supersonic inlet compressor, and a low pressure ratio compressor, both with splitter blades and their own problems. Two different types of boundary conditions are discussed and two different grids are compared.

First the numerical method used to solve the time-dependent Euler equations is described. This is an explicit time-marching finite-volume procedure.

## Algorithm description

### Governing equations

The equations which are solved are the time dependent Euler equations in a Cartesian reference frame rotating with a uniform angular velocity  $\Omega$  around the x-axis. Expressed in integral form one gets:

$$\frac{\partial}{\partial t} \int_V \bar{q} \, dV + \int_S \bar{H} \cdot \bar{n} \, dS = \int_V \bar{k} \, dV \quad (i)$$

where in 3-D space:

$$\bar{q} = \begin{bmatrix} \rho \\ \rho u \\ \rho v \\ \rho w \\ E \end{bmatrix}; \quad \bar{H} = \begin{bmatrix} \rho \bar{v} \\ \rho u \bar{v} + p \bar{e}_x \\ \rho v \bar{v} + p \bar{e}_y \\ \rho w \bar{v} + p \bar{e}_z \\ (E+p) \bar{v} \end{bmatrix}; \quad \bar{k} = \begin{bmatrix} 0 \\ 0 \\ 2\Omega \rho \omega + \Omega^2 \rho y \\ -2\Omega \rho v + \Omega^2 \rho z \\ \rho \Omega^2 (y v + z w) \end{bmatrix} \quad (2)$$

Here  $\bar{q}$  are the conservative variables and  $\bar{H}$  the flux tensor,  $S$  the closed surface that bounds the volume  $V$  with unit vector  $\bar{n}$ , positive pointing outwards. The primitive variables  $\rho, u, v, w$  and  $p$  are, respectively, density, velocity components in  $x$ -,  $y$ - and  $z$ -directions and pressure. Total energy per unit volume is expressed as

$$E = \frac{p}{\gamma-1} + \frac{1}{2} \rho \bar{v}^2; \quad \bar{v} = u \bar{e}_x + v \bar{e}_y + w \bar{e}_z \quad (3)$$

where  $\bar{v}$  is the relative fluid velocity, and  $\gamma$  is the ratio of specific heats. The right hand side of eq. (1) are the lower order terms due to Coriolis and centrifugal accelerations.

#### Spatial discretization

The numerical method used here to integrate the Euler equations in space is a centered finite volume method. The advantage of this method is that the governing equations are solved in a Cartesian coordinate system, and one only needs to know the volume and surface normal directions of the cells. The curvature of the mesh is not considered in computing surface normals, since only projections of fluxes and forces in the  $x$ -,  $y$ - and  $z$ -directions are used. The integral-conservative form of eq. (1) has no space derivative and therefore no special treatment of the flow discontinuities is needed, i.e. shocks and slip surfaces.

The computational domain is divided into hexahedral cells denoted by subscripts  $i, j, k$ . When the conservative variables  $\bar{q}$  are defined at the cell centers, a system of ordinary differential equations is obtained by applying eq. (1) separately to the interior cells. This gives the semi-discrete scheme:

$$V_{i,j,k} \frac{d}{dt} \bar{q}_{i,j,k} + N(\bar{q}_{i,j,k}) = \bar{k} \quad (4)$$

where

$$N(\bar{q}_{i,j,k}) = \bar{H}_{i+1/2,j,k} + \bar{H}_{i-1/2,j,k} + \bar{H}_{i,j+1/2,k} + \bar{H}_{i,j-1/2,k} + \bar{H}_{i,j,k+1/2} + \bar{H}_{i,j,k-1/2} \quad (5)$$

$$\begin{aligned} \bar{H}_{i+1/2,j,k} &= [\bar{F} dA_x + \bar{G} dA_y + \bar{H} dA_z]_{i+1/2,j,k} \\ &\dots\dots\dots \\ \bar{H}_{i,j,k-1/2} &= [\bar{F} dA_x + \bar{G} dA_y + \bar{H} dA_z]_{i,j,k-1/2} \end{aligned}$$

$\bar{H} \cdot \bar{n} = [\bar{F} n_x + \bar{G} n_y + \bar{H} n_z]$  is the flux components in respectively the  $x$ -,  $y$ - and  $z$ -directions evaluated at the six surfaces of the cell, and  $d\bar{A} = [dA_x, dA_y, dA_z]$  is the vector element of the cell surface, positive pointing outwards. The flux vectors are calculated by interpolating flow variables, with equal weight, from the two cells that share the face. This averaging is done without accounting for the difference in volumes of neighboring cells. The scheme is second order accurate if the grid is sufficiently smooth.

The discrete scheme, eq. (4), is not dissipative, allowing nonphysical shocks (expansion shocks) and also nonlinear instabilities (oscillations with alternate sign at odd even mesh points) being possible. This instability can be explained as follows, ref. 3. In real flow energy is transferred from large eddies to small eddies. This energy at small eddies is dissipated into internal energy through friction. If our scheme is non-dissipative, energy which is transferred from the longer to the shorter wavelengths will accumulate at the shortest wavelengths possible on the mesh. This accumulated energy is then transformed back to the longer wavelengths, which represent a nonphysical phenomena. To avoid this a constant fourth order dissipative term is added to the discrete scheme throughout the domain. In order to capture shocks a variable second order term is added locally by a pressure sensor designed to detect these discontinuities.

The artificial viscosity terms are added to the semi-discrete scheme and we get:

$$V(d/dt) \bar{q} = N(\bar{q}) + e_2 \bar{D}_2(\bar{q}) + e_4 \bar{D}_4(\bar{q}) \quad (6)$$

$\bar{D}_2$  is a variable-coefficient second-order difference operator while  $\bar{D}_4$  is a constant-coefficient fourth-order difference operator. The parameters  $e_2$  and  $e_4$  are user defined constants. Details can be found in ref. 1.

### Boundary conditions

One of the most important aspects of internal flow lies in the formulation and implementation of appropriate boundary conditions. Stability and convergence of the numerical scheme is sensitive to the conditions imposed. Here, the two distinct types involved in internal flow will shortly be described with special attention to the inflow/outflow conditions.

#### Inflow/outflow boundaries:

In order to reduce the domain of computation, artificial boundaries are often introduced up- and/or down-stream of the blade leading and trailing edges respectively. For the unsteady Euler equations, which are of hyperbolic type, the correct conditions to specify at these planes are determined using the theory of characteristics. In the subsonic case four conditions at inflow and one at outflow must be specified, while for supersonic flow five conditions at inlet and none at outlet are specified. The classical choice in turbomachinery flow calculations, assuming a subsonic axial velocity, is to specify total pressure, total temperature, meridional- and blade-to-blade flow angles. If the flow is transonic at inlet, i.e. the axial velocity is subsonic while the relative velocity is supersonic, there exists a relationship between Machnumber and flow angle, the unique incidence condition. Then the swirl velocity is specified instead of the blade-to-blade angle. Additional purely numerical boundary conditions are added by extrapolation from the interior domain.

The initial condition can be considered as a perturbation of the sought steady solution and, as a result, waves will start propagating in the entire computational domain. The steady solution is found after the elimination of these waves, which is caused by the following two processes; internal damping in the interior domain or elimination or damping during their interaction with the boundaries. Internal damping due to artificial viscosity introduced through the numerical scheme leads to damping of the waves, but this viscosity should be as small as possible since it introduces an error in the steady solution. Waves striking solid walls are reflected without being either amplified or damped. If the inlet/outlet boundary is suitably modelled a perfectly absorbing condition can be constructed for all waves striking these planes. Engquist and Majda (ref. 2) presented a mathematical theory of local absorbing boundary conditions at artificial boundaries. Here the first approximation of their hierarchical theory is applied. This is done by transforming the original coordinate system  $(x, y, z)$  to a local system  $(\tilde{x}, \tilde{y}, \tilde{z})$  located on the boundary, with the  $\tilde{x}$ -coordinate normal to the surface and positive into the computational domain while the other two are tangent to the surface. By transforming eq. (4) to this local coordinate system while neglecting pitchwise and spanwise derivatives and introducing characteristic variables, a decoupled set of five scalar equations can be found. The number of conditions to be imposed equals the number of characteristic directions which enter the domain, and is given by:  $d\tilde{x}/dt = \lambda_i$ ,  $i=1, \dots, 5$ . According to the sign of the corresponding eigenvalue a new vector is constructed by either specifying or extrapolating the characteristic variables. At inlet the new  $w$ -vector is constructed according to:

$$\begin{aligned} \lambda_1 > 0, \quad w^{(i)} &= w_{\text{spec}}^{(i)} \\ \lambda_i > 0, \quad w^{(i)} &= w_{\text{extr}}^{(i)} \end{aligned} \quad (7)$$

It is then transformed back to conservative variables, and the flux through the inlet boundary cell-surface is calculated. It can be shown that this technique gives stable boundary conditions and absorbs waves very efficiently.

#### Solid- and periodic boundaries:

The mesh is constructed such that cell surfaces lie on the solid- and periodic boundaries. Since the conservative variables are defined at the centre of the cells, all convective fluxes are zero at solid walls. The only contribution to the flux comes from the wall pressure which is extrapolated from the interior domain. The periodicity condition imposed along periodic boundaries is such that these cells are updated just as interior cells.

### Time discretization

With the boundary conditions and the artificial viscosity included, our complete space difference operator becomes:

$$\frac{d\tilde{q}}{dt} = F(\tilde{q}) \quad (8)$$

The time is discretized according to:

$$\begin{aligned} \tilde{q}_{n+1}^* &= \tilde{q}_n + \Delta t F(\tilde{q}_n) \\ \tilde{q}_{n+1}^{**} &= \tilde{q}_n + \frac{1}{2} \Delta t F(\tilde{q}_n) + \frac{1}{2} \Delta t F(\tilde{q}_{n+1}^*) \\ \tilde{q}_{n+1} &= \tilde{q}_n + \frac{1}{2} \Delta t F(\tilde{q}_n) + \frac{1}{2} \Delta t F(\tilde{q}_{n+1}^{**}) \end{aligned} \quad (9)$$



where

$$\bar{q}_n = \bar{q}(n\Delta t)$$

This is an explicit three-stage, second order accurate scheme well suited for obtaining a steady solution. It is stable with a CFL condition of 2. Since the time-dependence of the solution is of no concern here local time-stepping is applied in order to accelerate the convergence to a steady-state solution.

## Results

### General note on splitter blades

Inclusion of splitter blades in the solution of aerodynamic flows in centrifugal compressors presents an extremely difficult problem to the program. The presence of a sharp leading edge in a flow with a high diffusion rate, such as at the shroud, adds a high instability factor to the process of finding a solution. Great care must also be taken with the geometry around the leading edge of the splitter blade in order to allow it to tolerate the likely incidence range even in the early stages of convergence.

It is normally required to find a solution with the shock in the inducer section. If during the early stages of convergence the shock forms in the exducer passage, then it must be forced forward into the inducer. This is complicated by the splitter blade leading edge with its own unique incidence condition and shock system. Back pressure and second order viscosity must be controlled very carefully by this process.

### Low pressure ratio compressor

The first case is one of 2.2:1 in overall stage pressure ratio and a design inlet mach number of 0.8 at shroud. The geometry is first run with a relatively short downstream region and with classical boundary conditions (fig. 1). At the hub, the loading on the splitter blade is considerably less than on main blade (as judged by the difference between the suction and the pressure surface mach numbers). On the shroud, there is a "collapse" of loading on the suction surface of main blade, caused by a break-down in the solution at the leading edge from which it never recovers. This is brought about by a high incidence on the blade during the early stages of the solution which introduces an unreasonably high loss in total pressure (fig. 2).

The second has the same geometry as that of the first but the exit boundary conditions are changed to absorbing. These have the ability of regulating the distribution of mass flow more naturally at the exit boundary, and therefore the difference in flow between main - splitter blade and splitter - main blade. The distribution of loading between the blades is now more even at the hub. The "collapse" of loading on the shroud is still present but not so severe (fig. 2).

Downstream calculating region is now extended and the program is run with classical exit boundary conditions (fig. 1). The loading distribution at hub is not as good as that from the second run, but a full solution at the shroud has been obtained, with a fair agreement between main and splitter blades (fig. 3).

The final run is with absorbing boundary conditions on the extended downstream grid, the best solution is seen both for hub and shroud.

### High pressure ratio compressor

The second test case is one of 8.5:1 in stage pressure ratio and it has a design inlet mach number of 1.36 at shroud. This type of compressor geometry presents the severest problems in running of 3-dimensional Euler solver for three main reasons. The use of absorbing conditions have proved to be unstable and a switch to the classical boundary conditions is necessary to allow the positioning of the inducer shock in the final stages of the calculation.

The second problem is that due to the absence of boundary layer blockage, a lower total pressure loss, and the wrong blade exit angle, the implied pressure ratio is much higher than desired and can often lead to a break-down in the solution caused by overloading in the exducer section. This problem is overcome to a large extent by steadily increasing the back pressure during the solution, and forcing the shock towards the front. The effective mass flow behind the shock reduces as the back pressure is increased and the shock gets weaker. The results shown are of this compressor run with splitter blades and an H-grid (fig. 10,11,12).

The geometry has also been run with an O-grid but without splitter blades (fig. 7,8,9). This is compared with an H-grid without splitter blades and a comparison is made of the solution around the leading edge (fig. 4,5,6).

### Future work

It is intended to develop the grid further to include a C-grid and even a combined C-H grid. These would provide the advantages of the O-grid at the leading edge and the advantages of the H-grid in the passages between the blades and in the downstream region. Of course the final step in the development of the program is the solution of the full Navier-Stokes equations. It is believed to be more sensible to develop this than to develop the Euler method to overcome all the problems encountered in the running of centrifugal compressors.

### Conclusion

The use of an Euler-solver has demonstrated in the design of centrifugal compressors. As it stands it cannot be completely relied upon and the use of traditional methods with their empirical rules must continue for a long time into the future. There is no doubt however that it can contribute to our basic understanding of complex three-dimensional flow.

### References

1. Rizzi, A., Eriksson, L.E. "Computation of flow around wings based on the Euler equations", J. Fluid Mech. (1984), vol. 148, pp. 45-71.
2. Engquist, B., Majda, A. "Absorbing boundary conditions for the numerical simulation of waves", Math. Comp., vol. 31, pp. 629-651.
3. Sod, G.A. "Numerical methods in fluid dynamics", Cambridge University Press 1985.

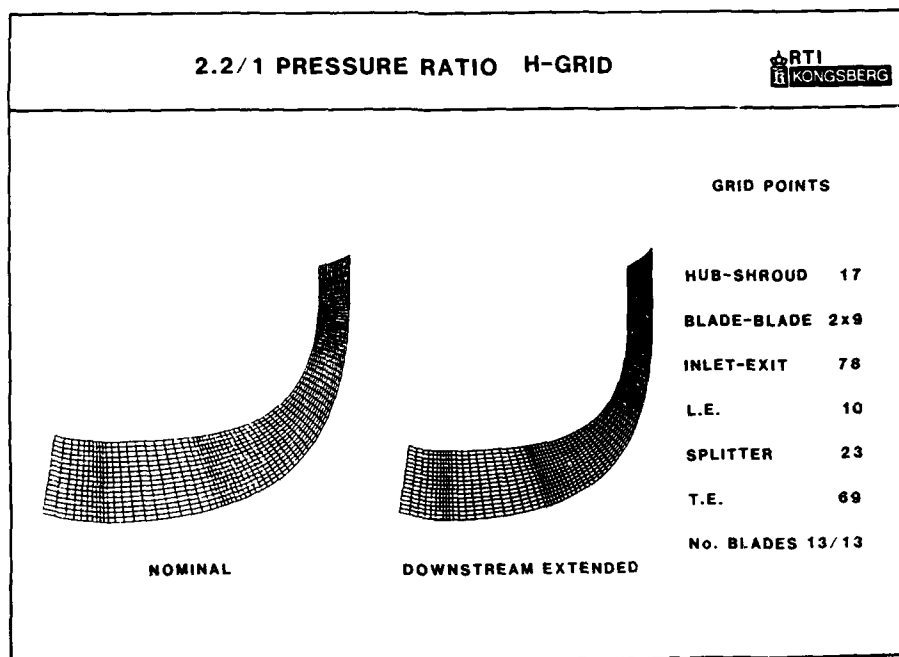


FIGURE 1

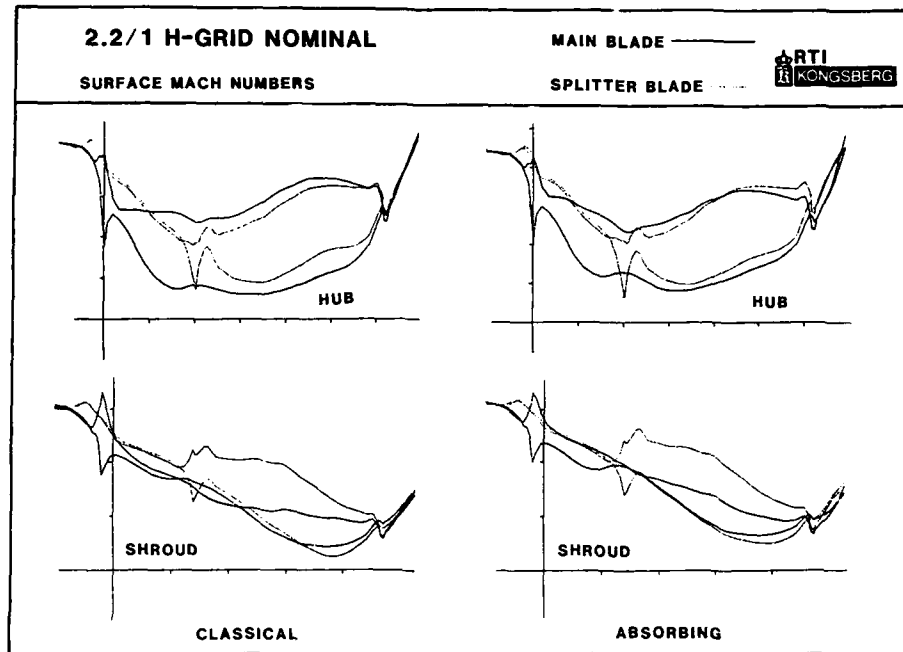


FIGURE 2

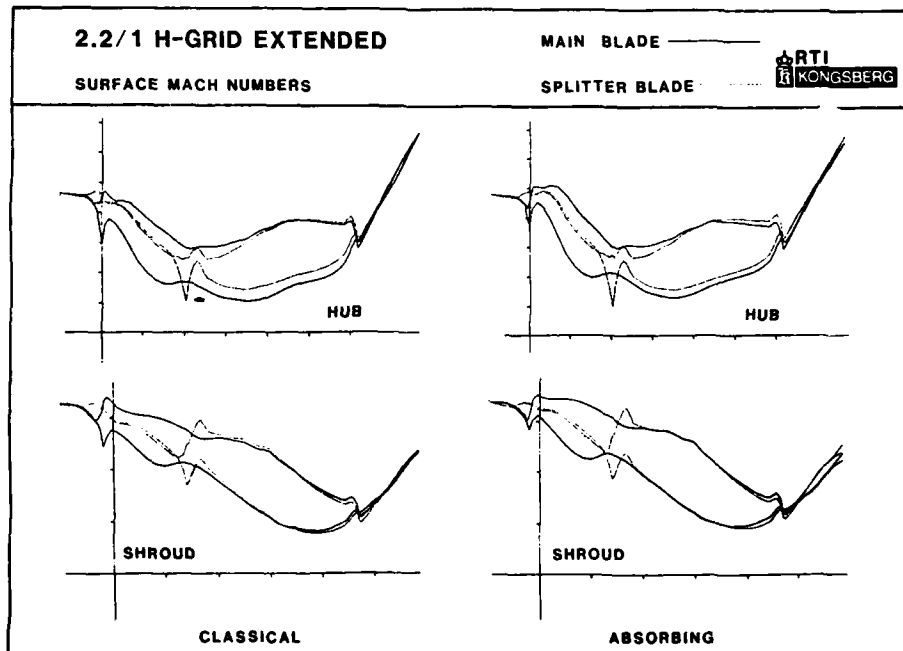


FIGURE 3

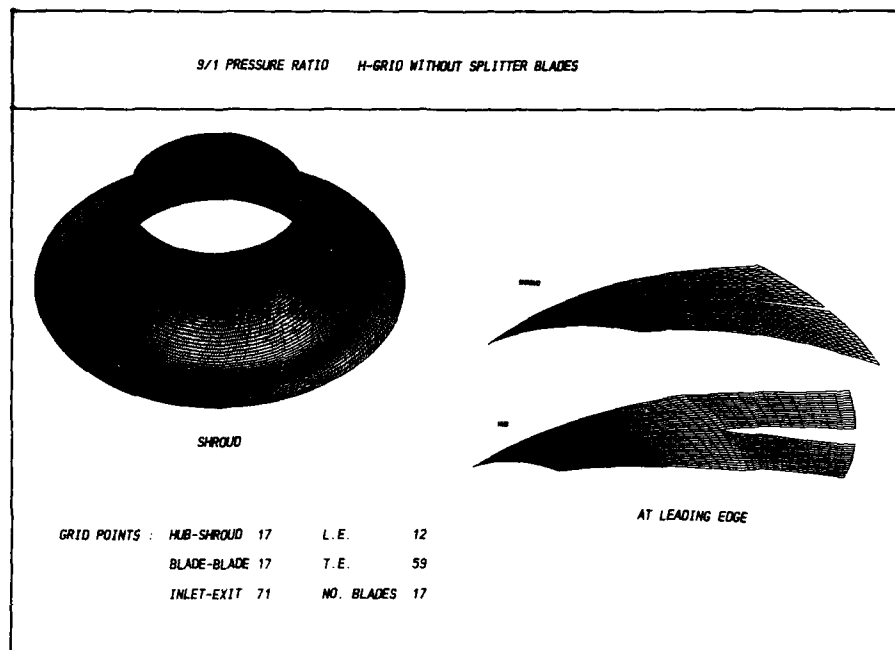


FIGURE 4

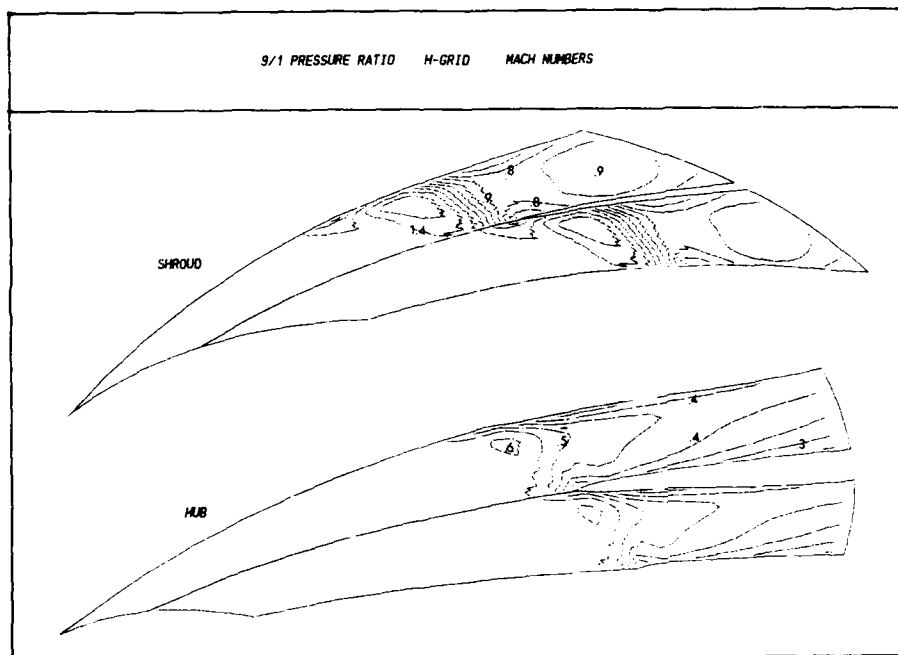
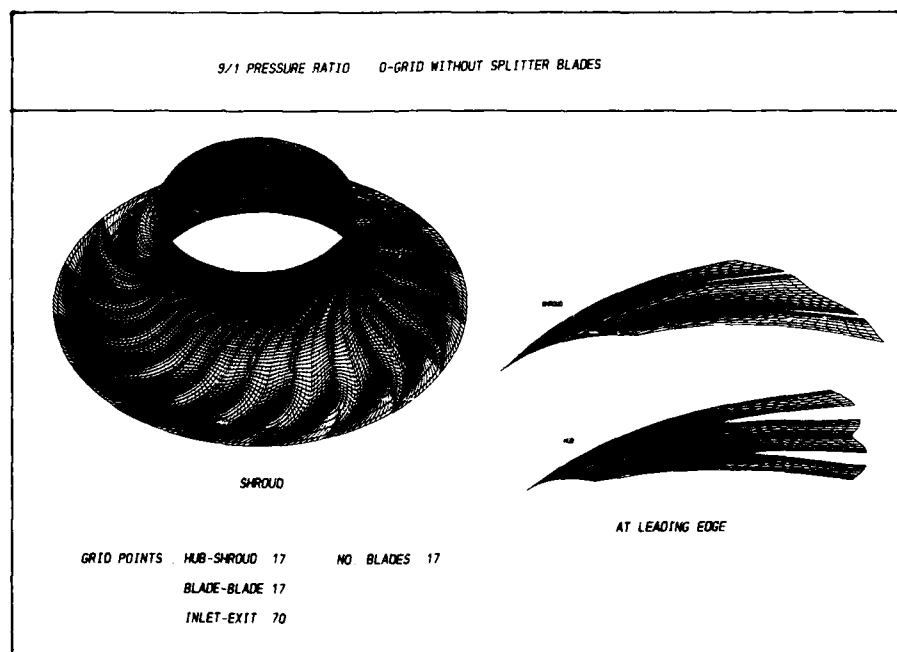
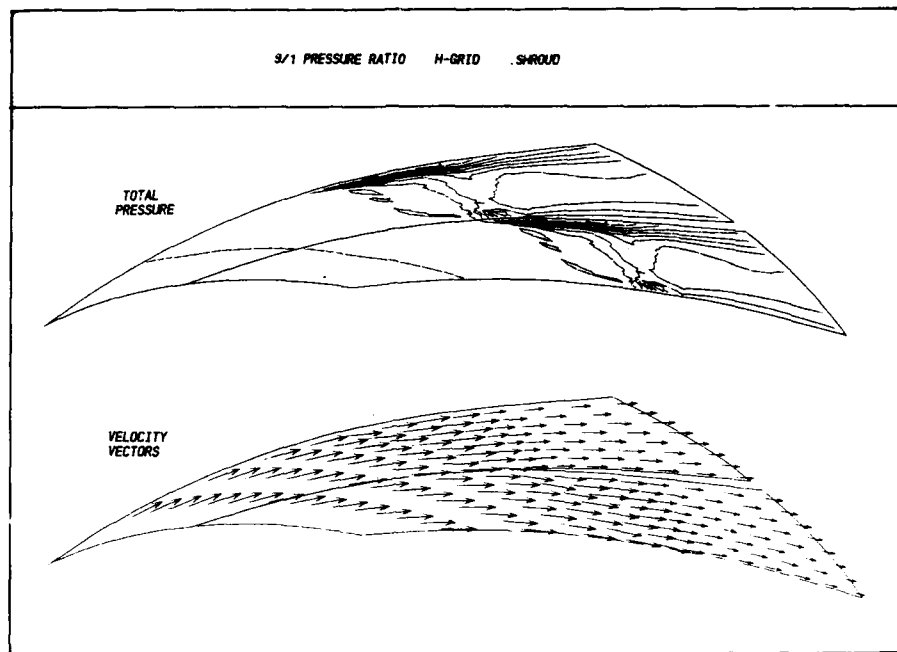


FIGURE 5



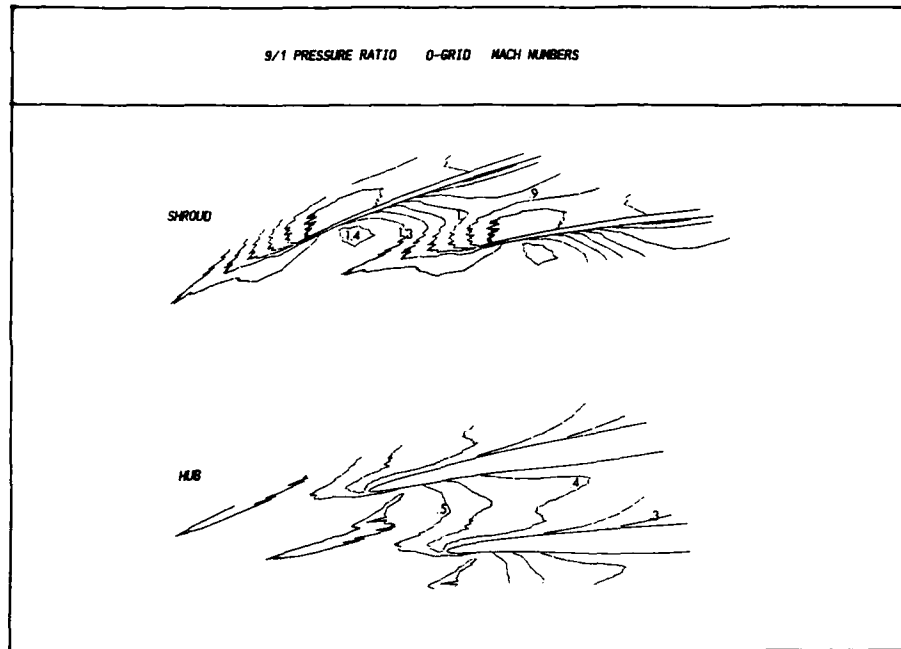


FIGURE 8

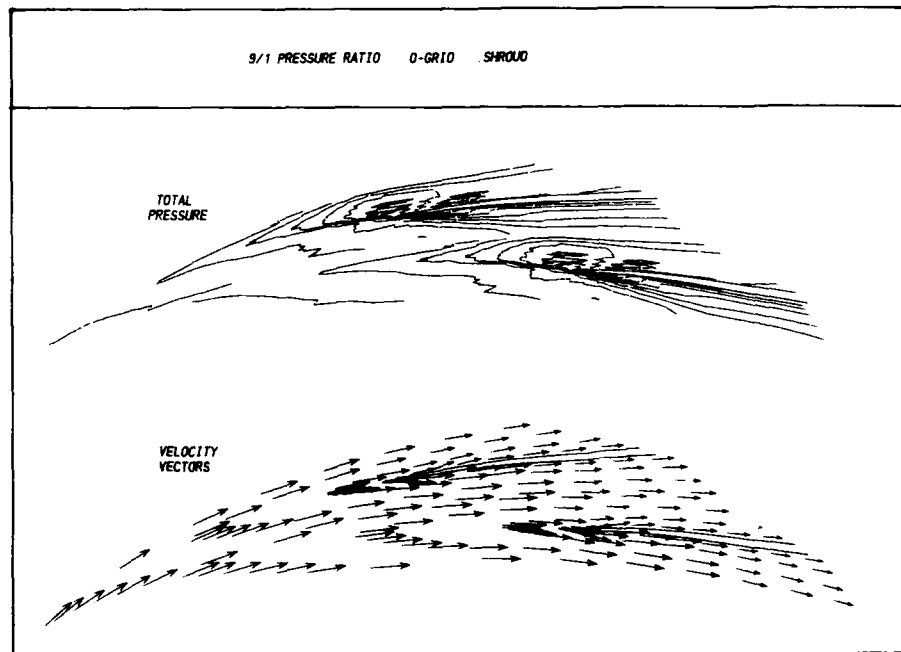


FIGURE 9

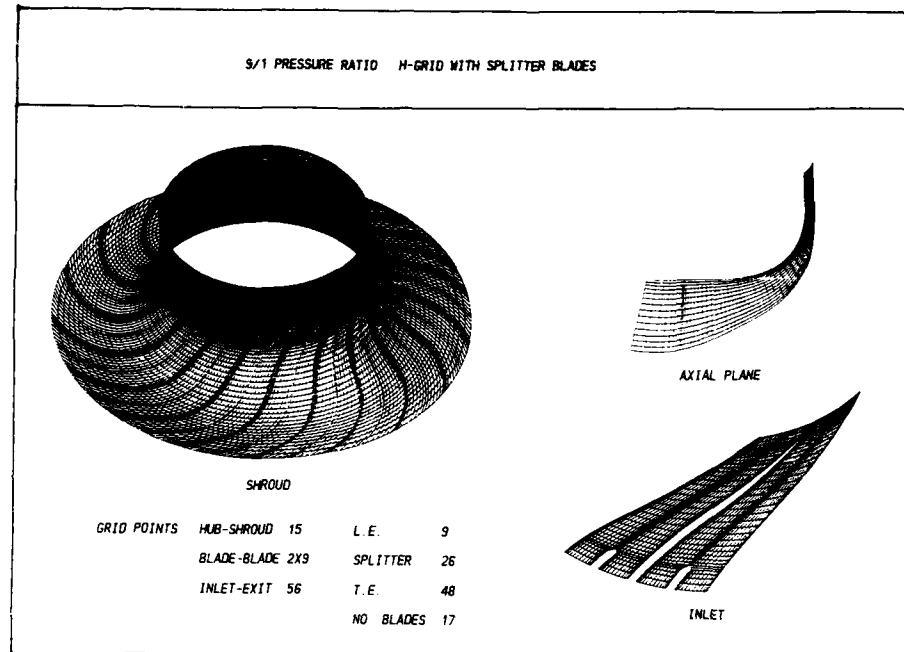


FIGURE 10

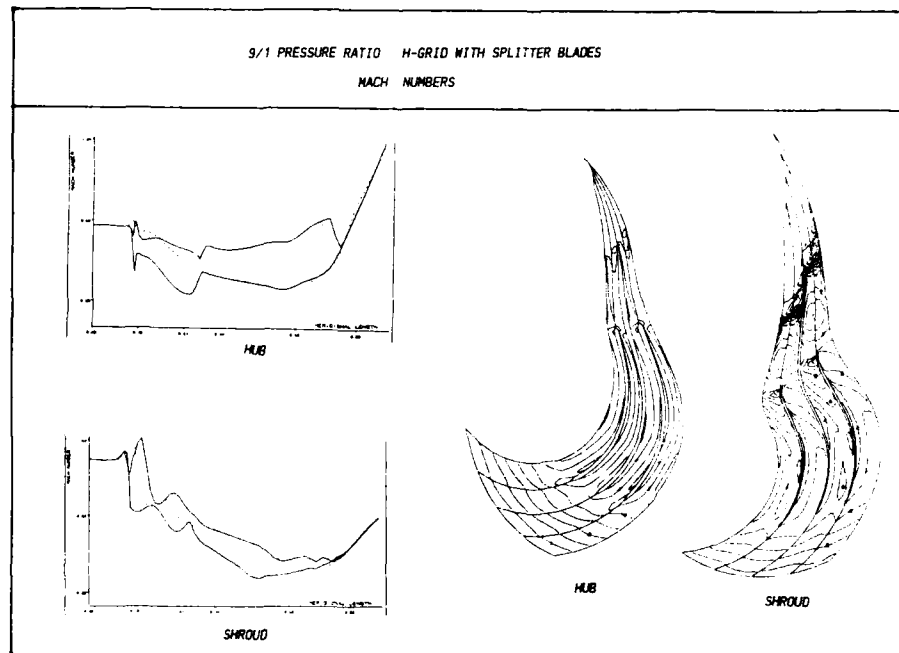


FIGURE 11

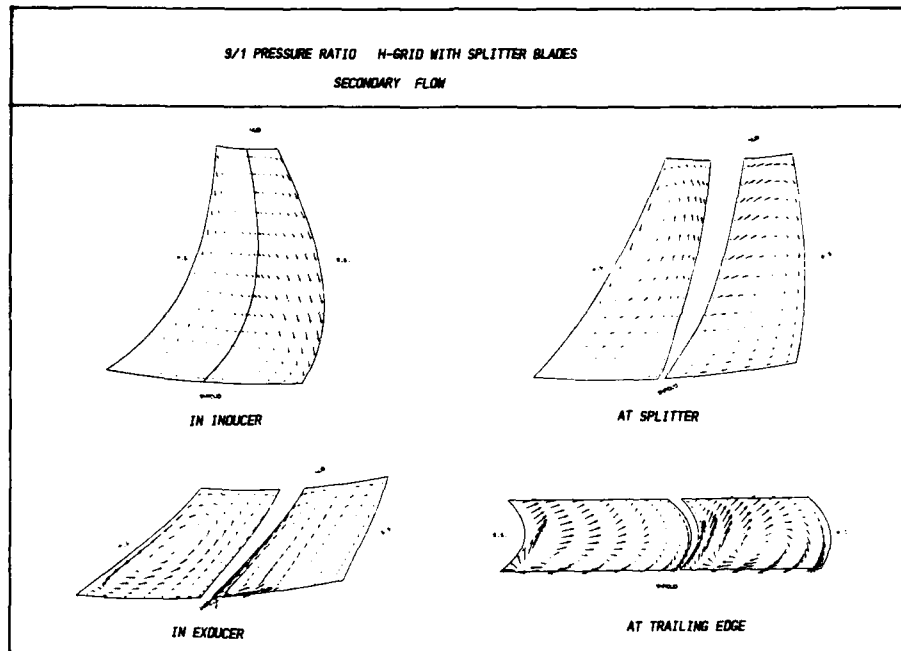


FIGURE 12



## DISCUSSION

Y. RIBAUD, Fr

Avez-vous appliqué des critères de cohérence pour vos calculs d'écoulement ? Si oui êtes-vous satisfait des résultats ?

### Author's Reply

In the checking of the solution, we do an integration of the mass flow up the channel, from the inlet station to the exit station. We are very happy with the solution.

In the development of the program, rothalpy has been checked through the compressor but not entropy.

N. KROLL, Ge

1) How does the picture of secondary flow change if you refine the grid, that is, how does the secondary flow calculated with the Euler solver depend on discretization error ?

2) Do you notice differences in the smoothness of contour plots using classical and absorbing boundaries conditions ?

### Author's Reply

1) This compressor has only been run with the grid we have presented.

2) The contour profiles would come out different. The absorbing boundary conditions have the ability of continuing the local solution at the exit boundary.

J.D. DENTON, UK

It is a significant achievement to obtain an Euler solution at such a high pressure ratio (9 : 1). I and others have tried without much success because of the very strong transients which occur on starting the calculation and which never settle down.

What is the development which makes your Euler solver work better than others in this application ?

### Author's Reply

The calculation of this compressor has not been easy and has taken many months of work. The convergence and quality of the solution must be controlled carefully during the run. The exit static pressure is gradually increased and the second order viscosity gradually reduced. Additionally, absorbing boundary conditions are used in the early stages, changing to classical boundary conditions at exit for the final convergence. This is currently a manual process.

## Secondary Flow Measurements with L2F-Technique in Centrifugal Compressors

by

H. Krain

DFVLR-Institut für Antriebstechnik  
Linder Höhe  
5000 Köln 90, W.-Germany

## ABSTRACT

The flow character of a 30 deg. backswept impeller is analyzed by means of the L2F-measurement technique available at DFVLR. Significant cross flows, noticeable distortions of the through flow patterns and considerable velocity fluctuations are found inside the blade passages of the impeller. The distortions of the velocity patterns are smoothing towards the impeller exit. A detailed analysis of the measured data reveals the existence of two counterrotating channel vortices that are significantly influencing the overall flow character.

## NOMENCLATURE

$c$	= absolute velocity	$x$	} = cylindrical coordinates
$c_m$	= meridional velocity	$r$	
$c_p$	= square of the velocity fluctuations	$z$	
$c_\phi$	= circumferential vortex velocity	$x/s$	= dimensionless shroud length
$c_{\phi L}$	= component of vortex velocity measured by laser velocimetry	$y/t$	= dimensionless blade pitch
$c'_n$	= fluctuating velocity parallel to mean absolute velocity	$z/b$	= dimensionless channel depth
L2F	= Laser-Two-Focus	$\beta_b$	= blade angle
$\dot{m}$	= mass flow rate	$\beta_L$	= flow angle measured by L2F-technique
$n/n_0$	= dimensionless shaft speed	$\Delta\beta$	= difference angle between blade angle and flow angle
PS	= pressure side	$\eta_{Stt}$	= total/total isentropic efficiency
$p$	= static pressure	$\nu$	= kinematic viscosity
$r_{max}$	= maximum radius of potential vortex part	$\pi_t$	= total pressure ratio
$r_0$	= radius of solid-body vortex	$\rho$	= density
SS	= suction side	$\omega$	= angular velocity
$Tu$	= turbulence intensity $Tu = \sqrt{c_p}/c$	SUBSCRIPTS	
$u$	= circumferential velocity		
$w_b$	= relative velocity parallel to the blade surface		
$w_L$	= relative velocity derived from L2F-measurements		
		0	= ambient condition
		1	= rotor inlet
		2	= rotor exit
		3	= diffuser inlet
		4	= diffuser exit

## INTRODUCTION

The research activities on centrifugal compressors are focused on increasing the performance and economy as well as on improving the design techniques for these machines. Extensive experimental studies are required to accomplish today's knowledge about the real flow character in centrifugal compressors as e.g. about unsteady flows, boundary-layers, secondary flows etc.. This is the most promising approach for establishing realistic flow models that subsequently can be used for a further improvement in performance and economy of centrifugal compressors [1,2,3,4,5]. Great progress has been achieved in the experimental field by the development of the non-intrusive optical velocimeters which enable the users to analyze the internal flow fields of turbomachines. Even the flow character inside the rotating blade channels can be analyzed by these measurement techniques [6,7,8,9]. Generally, the absolute flow vectors and flow fluctuations can be measured inside the machine at any point accessible by the laser light from outside. For the results to be presented the "Laser-2-Focus" velocimeter (L2F) available at DFVLR has been applied for detailed flow studies. This paper deals primarily with the secondary flows and the corresponding flow fluctuations analyzed with the L2F-technique in a 30 deg. backswept rotor. Today, two widely differing definitions of turbomachinery secondary flows are in use. The academic definition of secondary flows is associated with the development of stream-wise vorticity [10,11] whereas the technical definition associates secondary flows with all cross flows that are not following the blades [12,13]. The technical definition of secondary flows will be the basis of this paper.

## TEST COMPRESSOR AND INSTRUMENTATION

The test compressor is a single stage centrifugal compressor designed for a total stage pressure ratio of 4.0:1 and a mass flow rate of 4.0 kg/s running at a rotor tip speed of  $u_t = 470$  m/s. The compressor stage is composed of a 30 deg. backswept impeller coupled with a vaneless constant area diffuser. Fig. 1 shows the performance characteristic of this centrifugal compressor stage. Maximum achieved total/total isentropic stage efficiency is 84%, maximum pressure ratio - for 105% design shaft speed - is 4.5:1. The rotor was designed with a CAD-method de-

veloped at DFVLR [3,14]. It has 24 blades and its tip diameter is 400 mm.

The compressor flow characteristics were analyzed by using conventional as well as optical measurement techniques. Total pressures and total temperatures were measured at the compressor inlet and exit to determine the performance characteristic (Fig.1). Additionally, the static pressure development was measured from rotor inlet to the diffuser exit. 24 tapings distributed over the circumference were used at the rotor discharge to determine the mean static pressure at the rotor exit that has been used to derive the rotor efficiency. The equations of continuity and energy were applied and a zero blockage was assumed for this derivation. Maximum achieved total/total isentropic impeller efficiency was 94%.

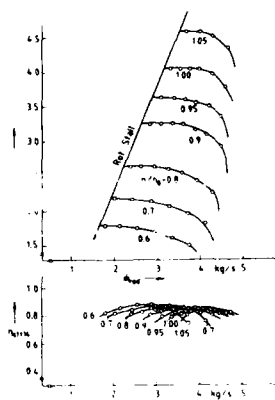


Fig.1 Performance map of the centrifugal compressor stage

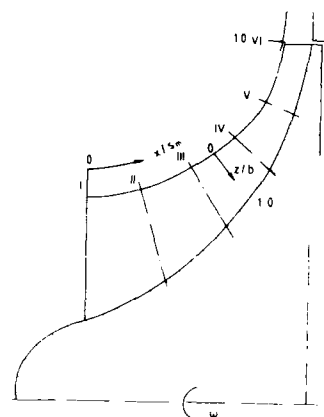


Fig.2 Arrangement of the optical measurement planes

The arrangement of the measurement planes in the rotor area used for the optical measurements inside the moving rotor blade channels is shown in Fig. 2. Detailed laser measurements were carried out at 6 measurement planes orientated perpendicular to the shroud contour. Up to 16 measurement points are automatically measured by the L2F-technique across one blade pitch [15]. At each plane measurements were carried out at 5  $z/b$ -positions ( $z/b=0.1, 0.3, 0.5, 0.7, 0.9$ ) permitting the reconstruction of a 3-D impeller flow pattern.

The measurement accuracy is satisfactory. Generally the error of mean velocity measurements is less than  $\pm 1\%$  and the uncertainty of flow angle measurements is less than  $\pm 1$  deg.. In regions of separated flow, however, the error to be expected may rise to  $\pm 3\%$  or  $\pm 3$  deg..

#### THROUGH FLOW AND SECONDARY FLOW

Figs. 3-8 are representing the through flow character of the 30 deg. backswept impeller. Lines of constant dimensionless meridional velocity  $c_m/u$ , are plotted in these figures for the six measurement planes shown in Fig. 2. The plotted results were obtained for the design point ( $\dot{m}=4.0$  kg/s,  $n/n_0=1$ ).

Only small variations in the meridional velocity profile are present at measurement plane I (Fig. 3,  $x/s=0$ ). As expected, the meridional velocity profile is increasing slightly from the pressure to the suction side and is almost constant from hub to shroud which agrees with the design approach i.e., during the design procedure of this impeller a constant meridional velocity profile has been assumed from hub to shroud.

Fig. 4 shows the meridional velocity pattern obtained at measurement plane II ( $x/s=0.2$ ). A comparison with plane I reveals that the meridional velocity is slightly accelerated from plane I to plane II, which, of course, is not true for the mean relative velocity that is continuously decelerated from rotor inlet to rotor exit. Maximum meridional velocities are present in the middle of the flow channel. A positive velocity gradient is observed from hub to shroud. In the pitchwise direction the velocities are decreasing towards the blade surfaces. A discrete boundary layer profile, however, is not analyzed by these measurements which is due to the measurement position not permitting measurements very close to the blade surfaces.

Fig. 5 shows the meridional velocity pattern measured at plane III ( $x/s=0.4$ ). Altogether, the velocity profile analyzed at this measurement plane is very similar to that found at plane II (Fig. 4). A significant difference is only seen in the shroud/pressure side area. Here, a considerable gradient and a strong reduction are indicated for the through flow velocity component. In comparison to the overall flow channel the area covered by the low velocity fluid is rather small.

From plane III to plane IV (Fig. 6,  $x/s=0.6$ ) the low velocity fluid area is increasing covering now a greater portion of the pitchwise extension. The points of minimum velocities are again located close to the shroud but compared to plane III they have now shifted from the pressure side towards the mid-pitch position. Close to the shroud ( $z/b=0-0.4$ ) maximum meridional velocities are present in the vicinity of the blade surfaces and the area of low velocity fluid is embedded in high velocity fluid areas.

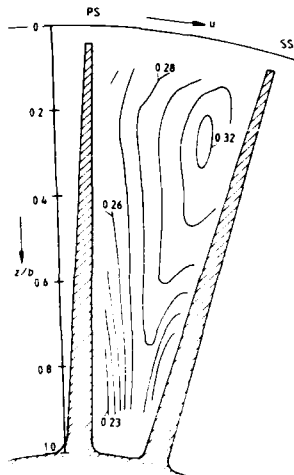


Fig. 3 Lines of const. meridional velocity  $c_m/u_2$  at plane I ( $\dot{m}=4.0$  kg/s,  $n/n_0=1$ )

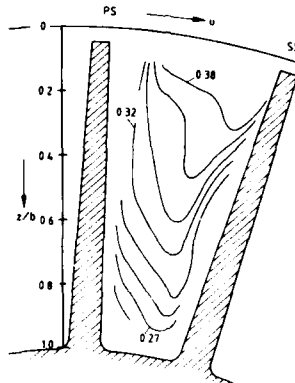


Fig. 4 Lines of const. meridional velocity  $c_m/u_2$  at plane II ( $\dot{m}=4.0$  kg/s,  $n/n_0=1$ )

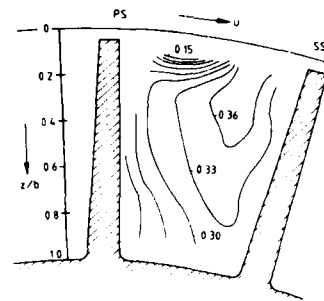


Fig. 5 Lines of const. meridional velocity  $c_m/u_2$  at plane III ( $\dot{m}=4.0$  kg/s,  $n/n_0=1$ )

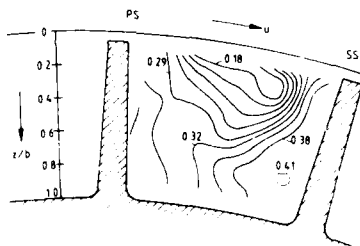


Fig. 6 Lines of const. meridional velocity  $c_m/u_2$  at plane IV ( $\dot{m}=4.0$  kg/s,  $n/n_0=1$ )

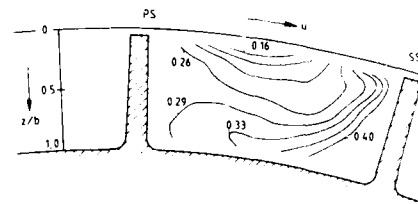


Fig. 7 Lines of const. meridional velocity  $c_m/u_2$  at plane V ( $\dot{m}=4.0$  kg/s,  $n/n_0=1$ )

A similar flow character is present at plane V (Fig. 7,  $x/s=0.8$ ). But here, blade loading has already significantly decreased in the middle of the flow channel ( $z/b=0.5$ ) which can be deduced from the lines of constant meridional velocity that are now almost extending from the pressure to the suction side of the blade.

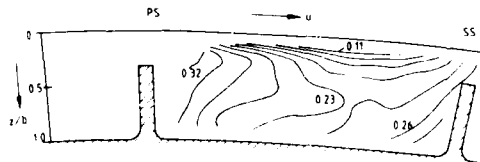


Fig. 8 Lines of const. meridional velocity  $c_m/u_2$  at plane VI ( $\dot{m}=4.0$  kg/s,  $n/n_0=1$ )

Fig. 8 illustrates the through flow character at plane VI ( $x/s=1.004$ ) that is located at the impeller exit. Due to the laser beam orientation, measurements at  $z/b=0.1$  and  $z/b=0.3$  had to be taken outside of the rotor which is also the reason for the large tip gap plotted in Fig. 8. The low velocity fluid is now concentrated in the vicinity of the shroud. Only small velocity gradients are present in the flow channel area ( $z/b=0.3-1.0$ ) indicating a very regular meridional velocity distribution at this measurement position. The reduction in the through flow velocity component, primarily observed in the shroud areas of measurement planes III to VI, is associated with significant cross flows. These effects are pointed out in Figs. 9-14. In these figures the difference angle  $\Delta\beta$  between the blade and flow angle is plotted versus measurement area. Fig. 9 illustrates the flow angle distribution at plane I (Fig. 2). An almost blade-congruent flow is present at this measurement position. Noticeable differences between the flow and blade angle are only seen in the hub/pressure side area which is due to the displacement effects of the thick blades. A throughout blade congruent flow is observed in planes II and III (Figs. 10, 11). Here the flow properly follows the blades. The differences between the flow angle and blade angle found in the hub/pressure side area of plane I have now faded out, negligible  $\Delta\beta$ 's are present in planes II and III.

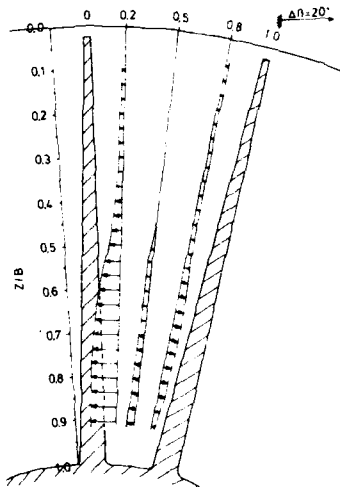


Fig. 9  $\Delta\beta$ -distribution at plane I  
( $\dot{m}=4.0$  kg/s,  $n/n_0=1$ )

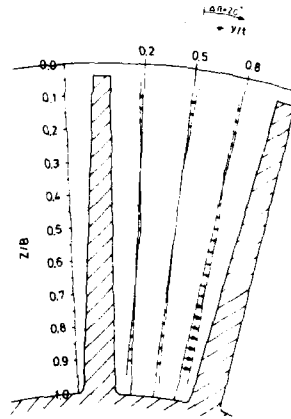


Fig. 10  $\Delta\beta$ -distribution at plane II  
( $\dot{m}=4.0$  kg/s,  $n/n_0=1$ )

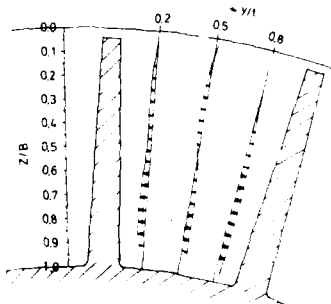


Fig. 11  $\Delta\beta$ -distribution at plane III  
( $\dot{m}=4.0$  kg/s,  $n/n_0=1$ )

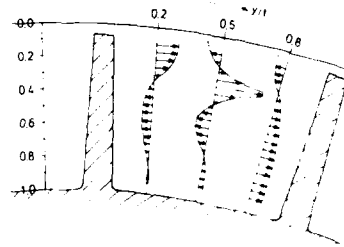


Fig. 12  $\Delta\beta$ -distribution at plane IV  
( $\dot{m}=4.0$  kg/s,  $n/n_0=1$ )

Fig. 12 shows the  $\Delta\beta$ -distribution for plane IV. The secondary flow pattern analyzed at this measurement position looks very irregular. In the hub/pressure side area ( $y/t=0.2$ ,  $z/b>0.4$ ) the flow has a component towards the pressure side, whereas, close to the suction side ( $y/t=0.8$ ), the flow vectors are primarily pointing in the circumferential direction. A very strange looking secondary flow pattern is present at the middle of the flow channel ( $y/t=0.5$ ). At this measurement position, the flow directions are changing repeatedly from shroud to hub. Looking at the entire flow channel, a distinct secondary flow direction cannot be derived from these measurements. On the contrary, the secondary flow seems to go in any direction. A similar secondary flow character is present at measurement plane V (Fig. 13). Again a distinct cross flow direction is not seen at this measurement position.

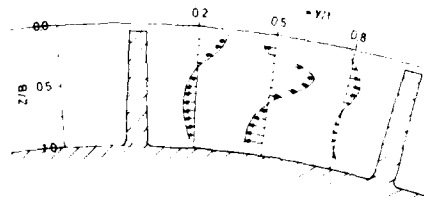


Fig. 13  $\Delta\beta$ -distribution at plane V  
( $\dot{m}=4.0$  kg/s,  $n/n_0=1$ )

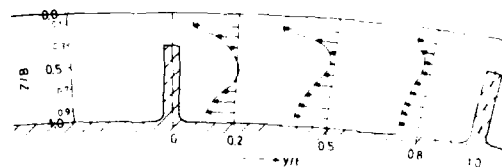


Fig. 14  $\Delta\beta$ -distribution at plane VI  
( $\dot{m}=4.0$  kg/s,  $n/n_0=1$ )

In contrast to measurement planes IV and V the cross flows are clearly directed towards the pressure side of the blade at measurement plane VI which is located at the rotor exit (Figs. 2, 14). This effect is well known in centrifugal compressor aerodynamics. Generally it is called the slip effect of centrifugal compressor impellers.

## INSTANTANEOUS RESULTS

The unsteady flow effects throughout the rotor were also analyzed with the L2F-technique. As expected, maximum flow fluctuations were present in the areas of great velocity gradients. This is pointed out in Figs. 15-20.

RV 61, PLANE I  
 $\dot{m}=4\text{ kg/s}$   
 $n/n_0=1$

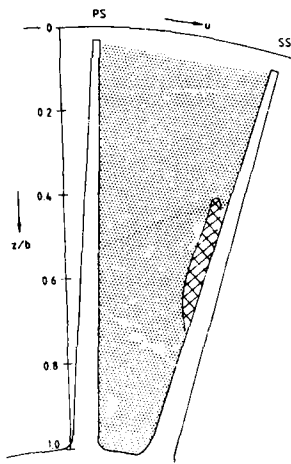


Fig.15 Velocity fluctuations  $c_p$  at plane I ( $\dot{m}=4.0\text{ kg/s}$ ,  $n/n_0=1$ )

RV 61, PLANE II  
 $\dot{m}=4\text{ kg/s}$   
 $n/n_0=1$

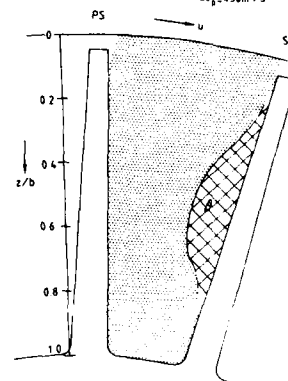


Fig.16 Velocity fluctuations  $c_p$  at plane II ( $\dot{m}=4.0\text{ kg/s}$ ,  $n/n_0=1$ )

In these figures the kinetic energy ( $c = c_u^2$ ) of the velocity fluctuations parallel to the mean absolute velocity vector is plotted versus the flow area. Only low flow fluctuations are present at measurement planes I and II (Figs. 15,16). Here the fluctuation intensities are varying between  $150\text{ m}^2/\text{s}^2$  and  $300\text{ m}^2/\text{s}^2$ . The corresponding turbulence intensities ( $Tu$ ) are varying between 3 and 8%.

RV 61, PLANE III  
 $\dot{m}=4\text{ kg/s}$   
 $n/n_0=1$

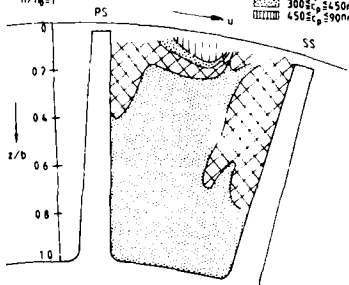


Fig.17 Velocity fluctuations  $c_p$  at plane III ( $\dot{m}=4.0\text{ kg/s}$ ,  $n/n_0=1$ )

RV 61, PLANE IV  
 $\dot{m}=4\text{ kg/s}$   
 $n/n_0=1$

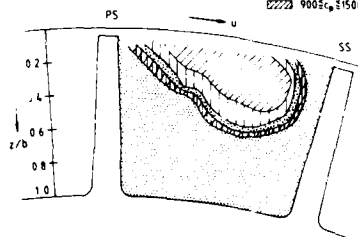


Fig.18 Velocity fluctuations  $c_p$  at plane IV ( $\dot{m}=4.0\text{ kg/s}$ ,  $n/n_0=1$ )

RV 61, PLANE V  
 $\dot{m}=4\text{ kg/s}$   
 $n/n_0=1$

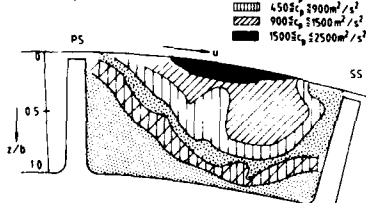


Fig.19 Velocity fluctuations  $c_p$  at plane V ( $\dot{m}=4.0\text{ kg/s}$ ,  $n/n_0=1$ )

RV 61, PLANE VI  
 $\dot{m}=4\text{ kg/s}$   
 $n/n_0=1$

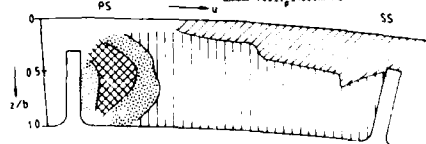


Fig. 20 Velocity fluctuations  $c_p$  at plane VI ( $\dot{m}=4.0\text{ kg/s}$ ,  $n/n_0=1$ )

The flow fluctuations are continuously increasing towards the impeller exit (Figs. 17-20), which is primarily true for the shroud area, whereas only low fluctuations ( $c_p \approx 150 \text{ m}^2/\text{s}^2$ ) are present in the hub area. In the hub areas of planes I to II the fluctuation intensity  $c_p$  does not exceed  $150 \text{ m}^2/\text{s}^2$ . However, the flow area portion with low fluctuation intensities is continuously decreasing from rotor inlet to rotor exit. At measurement plane VI (Fig. 20) the low fluctuation intensities have almost vanished. A small area with low fluctuation intensities is only present close to the pressure side. On the other hand, the high fluctuation intensity areas are increasing continuously from rotor inlet to rotor exit. Maximum fluctuation intensities of  $2.500 \text{ m}^2/\text{s}^2$  have been measured in the shroud area of plane V (Fig. 19). However, the area covered by these very high fluctuations is rather small. Towards the impeller exit the fluctuation intensities in the shroud area are again decreasing. Maximum fluctuation intensities at the impeller exit are  $1.500 \text{ m}^2/\text{s}^2$  (Fig. 20). At this measurement plane the turbulence intensity varies from 4 to 10% which seems to be an appropriate turbulence level for a diffuser inlet flow [16].

#### VORTEX ANALYSIS

The results presented indicate significant cross flows and flow fluctuations in the areas of reduced meridional velocities. Reduced meridional velocities and strong gradients in the meridional velocity profiles are primarily present close to the shroud. The interrelationship of these phenomena can be best explained by a study of the vortex flow inside of the impeller channel passages. Information about the vortex flow of a centrifugal compressor rotor is obtained from the lines of constant relative flow angles (isoclines). The existence of a real vortex can be deduced from the shape of the isocline pattern. The basic relations for the isoclines of a real vortex analyzed by means of the LZF-velocimetry were originally derived by A. Binder [17,18].

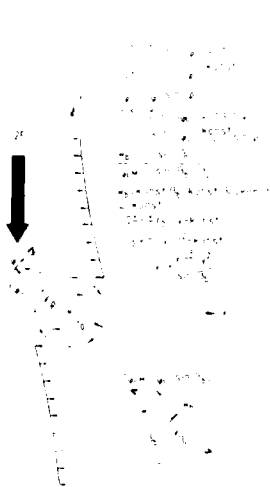


Fig. 11 Measurement of vortex flow with LZF-measurement technique

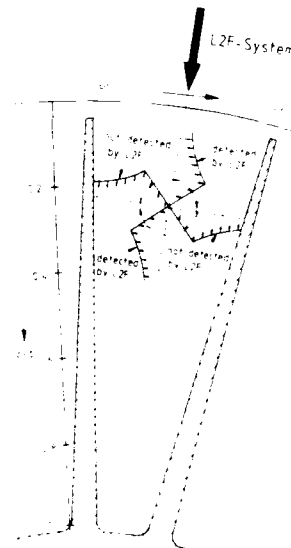


Fig. 12 Components of vortex flow detected by LZF-technique

These equations are submitted in Fig. 13. They are valid for a vortex composed of a solid-body vortex part ( $\Omega \cdot r$ ) and of a potential vortex part ( $\Gamma/r$ ). Any real vortex will have a similar shape. The velocity distribution of such a vortex is shown in Fig. 14. Principally the LZF-velocimeter can only measure the velocity component perpendicular to the laser beam axis whereas the component parallel to the laser beam axis is not measured. Inside of the flow channel the blade tangential relative velocity  $w_t$  is superimposed on the vortex velocity  $c$ . As a result the LZF-velocimeter will measure the relative flow angle  $\gamma$ , indicated in Fig. 15. From the velocity triangle it can easily be derived that the isoclines of a real vortex are described by the following simple equations:

$$\gamma = \text{konst.} \quad \rightarrow \quad c \cdot r = r_0 \quad (1)$$

$$\left. \begin{aligned} \gamma/r^2 &= \text{konst.} \\ x &= \frac{\sqrt{r^2 - y^2}}{\sin \alpha_0} \end{aligned} \right\} \quad r_0 < r \quad (2)$$

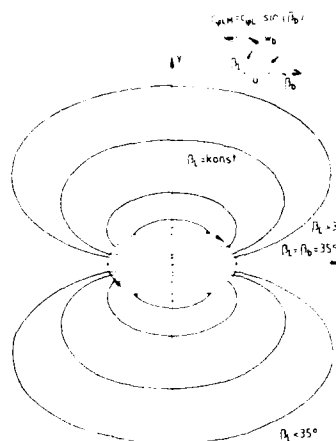


Fig. 23 Isocline structure for a real vortex, composed of a solid-body and a potential vortex part

The corresponding isoclines are shown in Fig. 23 indicating that the isoclines are parallel in the solid-body vortex area whereas the isoclines are elliptical in the potential-vortex area. The vortex center is located in the middle of the parallel isoclines. The idea described was used to look for vortices in the impeller flow. Isoclines were plotted from the L2F-measurement results and a real vortex was assumed to be present when an isocline pattern similar to that shown in Fig. 23 was analyzed.

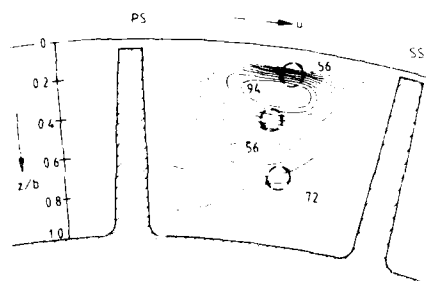


Fig. 24 Isocline pattern ( $\beta_r = \text{konst.}$ ) measured at plane IV ( $\dot{m} = 4.0 \text{ kg/s}$ ,  $n/n_0 = 1$ )

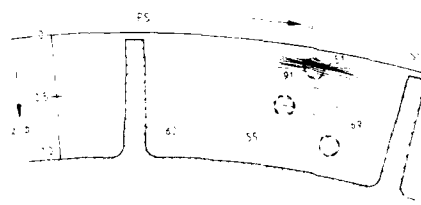


Fig. 25 Isocline pattern ( $\beta_r = \text{konst.}$ ) measured at plane V ( $\dot{m} = 4.0 \text{ kg/s}$ ,  $n/n_0 = 1$ )

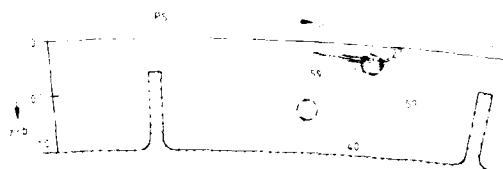


Fig. 26 Isocline pattern ( $\beta_r = \text{konst.}$ ) measured at plane VI ( $\dot{m} = 4.0 \text{ kg/s}$ ,  $n/n_0 = 1$ )

Figs. 24, 25 and 26 are showing the isocline patterns for measurement planes IV, V and VI. The isocline patterns are showing a distinct vortex development at these measurement planes. Two counterrotating channel vortices were found at planes IV and V. Only one channel vortex was analyzed at plane VI. Close to the shroud considerable flow angle differences and parallel isoclines were analyzed at planes IV to VI. The isocline pattern indicates a solid-body vortex part in this area which seems to be initiated by the relative motion between the rotor blades and the casing.

A comparison with Figs. 3-20 clearly shows that high reductions of the through flow velocity component, strong flow angle differences and fluctuations are primarily present in the areas of increased vortex development. The vortices are generating secondary flows in the pitchwise as well as in the hub-to-shroud direction. Since the L2F-velocimeter is capable of measuring the velocity components in the pitchwise direction (Fig. 22), the cross flow in this direction caused by the vortex development can be derived from the L2F-measurements. These results are shown in Figs. 9-14. Obviously, the strange looking cross flow patterns at measurement planes IV and V (Figs. 12 and 13) are easily explained with the vortex model. A comparison between Figs. 14 and 26 - which are showing the results obtained at the impeller exit - is suggesting that the slip effects of the 30 deg. backswept impeller can also be attributed to the vortex development. Obviously, the vortices analyzed at the impeller discharge are predominantly sweeping the flow in the negative circumferential direction. These effects are clearly marked in



the hub and shroud area whereas the cross flow towards the pressure side of the blade is suppressed in the middle of the flow channel which seems to be due to the counter-rotating vortices (Fig. 26).

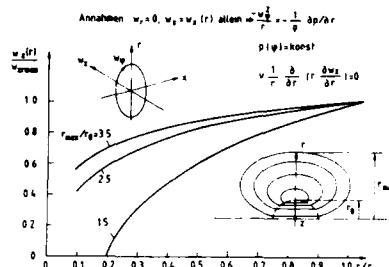


Fig. 27 Through flow velocity distribution in a vortex

The low through flow velocities in the shroud areas of measurement planes IV, V and VI (Figs. 6, 7 and 8) are also supposed to be due to the vortex development. It is well known that the through flow velocity component of a swirling flow is decreasing from the vortex edge towards the vortex center [19, 20, 21]. Fig. 27 illustrates this effect for three vortices. A vortex with an axial velocity component varying only in the radial direction is assumed ( $w_r = w_r(r)$ ). The radial velocity component is assumed to be zero ( $w_r = 0$ ). For these assumptions the following relations can be derived from the Navier-Stokes equations:

$$w_\theta^2/r = \frac{1}{r} \frac{\partial p}{\partial r} \quad (3)$$

$$p(r) = \text{konst.} \quad (4)$$

$$v \frac{1}{r} \frac{\partial}{\partial r} \left( r \frac{\partial w_\theta}{\partial r} \right) = 0 \quad (5)$$

Equation (5) can easily be integrated and the result of the integration is shown in Fig. 27.

The through flow velocity has a maximum at the vortex edge ( $r/r_{\max} = 1$ ) and is decreasing towards the vortex center. The descent towards the center strongly depends on the radius ratio  $r_{\max}/r_0$  that relates the potential vortex part to the solid-body vortex part of the overflow vortex. Qualitatively the results obtained are in good agreement with the measurement results found for the impeller flow. In the impeller the through flow velocity is also decreasing in those areas where the vortices are present. The distorted actual through flow patterns are also supposed to be due to the vortex development inside of the flow passages.

#### REFERENCES

- [1] Japikse, D.; Osborne, C.: "Optimization of Industrial Centrifugal Compressors". ASME-Paper 86-GT-221 part 6A, p.14.
- [2] Japikse, D.; Osborne, C.: "Optimization of Industrial Centrifugal Compressors". ASME-Paper 86-GT-222 part 6B, p.16.
- [3] Krain, H.: "A CAD Method for Centrifugal Compressor Impellers". ASME Journal of Engineering for Gas Turbines and Power, Vol.106, April 1984, pp.482-488.
- [4] Casey, M.V.: "The Aerodynamic Development of High-Performance Radial Compressor Stages for Industrial Turbocompressors". VDI Bericht 572.1, pp.167-181.
- [5] Krain, H.; Rogge, H.: "Design and Manufacturing of High Pressure Ratio Centrifugal Compressor Impellers". VDI Bericht 572.1, pp.437-460 (in German).
- [6] Weyer, H.B.; Dunker, R.: "Dual Beam Laser Anemometry Study of the Flow Field in a Transonic Compressor". AGARD-CP-214, March 1977, pp.8.1-8.11.
- [7] Wisler, D.C.; Mossey, P.W.: "Gas Velocity Measurements within a Compressor Rotor Passage Using the Laser Doppler Velocimeter". Journal of Engineering for Power, TRANS.ASME, Series A, Vol.95, April 1973, p.91.
- [8] Eckardt, D.: "Detailed Flow Investigations within a High-Speed Centrifugal Compressor Impeller". TRANS.ASME, September 1976, pp.390-402.
- [9] Krain, H.: "A Study on Centrifugal Impeller and Diffuser Flow". ASME Journal of Engineering for Power, Vol.103, No.4, October 1981, pp.688-697.
- [10] Hawthorne, W.R.: "Secondary Circulation in Fluid Flow". Proc. Roy. Soc. A. Vol.206, 1951, pp.374-387.

- [11] Horlock, J.H.: "Recent Developments in Secondary Flow".  
AGARD-CP-214, 1977, pp.1.1-1.18.
- [12] Gallus, H.; Kümmel, W.: "Secondary Flows and Annulus Wall Boundary Layers in Axial-Flow Compressor and Turbine Stages".  
AGARD-CP-214, 1977, pp.4.1-4.15.
- [13] Eckardt, D.; Krain, H.: "Secondary Flow Studies in High-Speed Centrifugal Compressor Impellers".  
AGARD-CP-214, pp.18.1-18.13.
- [14] Krain, H.: "Interdependence of Centrifugal Compressor Blade Geometry and Relative Flow Field".  
ASME-Paper 85-GT-85.
- [15] Schodl, R.: "Optical Techniques for Turbomachinery Flow Analysis".  
Nato Institute, Izmir 1984.
- [16] Rundstadler, P.W., Jr.; Dolan, F.X.; Dean, R.C., Jr.: "Diffuser Data Book".  
Creare, TN-186, 1975, p.88.
- [17] Binder, A.: "Instationary Flow Effects in the Rotor of a Turbine".  
Thesis, University of Aachen, DFVLR-FB 85-66. p.157 (in German).
- [18] Binder, A.; Förster, W.; Mach, K.; Rogge, H.: "Unsteady Flow Interaction Caused by Stator Secondary Vortices in a Turbine Rotor".  
ASME-Paper 86-GT-302, p.8.
- [19] Meldau, E.: "Drallströmung im Drehhohlraum".  
Thesis University of Hannover, 1935 (in German).
- [20] Acrivlellis, M.: "Untersuchungen an turbulenten Drallströmungen hinter einem radialen Leitapparat".  
Thesis, University of Karlsruhe, 1974 (in German).
- [21] Neuburger, W.: "Calculation of Compressible Swirling Flows in Pipes, Annuli and on Rotating Cylinders".  
DFVLR-FB 80-21, p.107 (in German).

### DISCUSSION

J. MOORE, US

Can you tell us what the tip clearance was in this impeller and what is its distribution through the impeller ?

Author's Reply

When the impeller was operating at the design point, the tip clearance at the impeller inlet was 0.5 mm, and 0.2 mm at the impeller exit.

J. HOURMOUZIADIS, Ge

You observed secondary flow pattern primary in the rear half of the impeller, and you said it's because the relative motion of the impeller casing. There is also relative motion in the front part of the impeller. Do you have an explanation why it was predominant in the rear part ?

Author's Reply

There are significant differences in velocities through the impeller. In the rear part they are greater than in the impeller inlet and I think that is the reason for this phenomena.

34-10

H. VIGNAU, Fr

A quelle distance minimale des parois avez-vous effectué des mesures ?

Author's Reply

The measurements results shown during this presentation have been taken at 1.6 mm from the wall, at the impeller exit. We also carried out measurements very close to the wall, at 0.5 mm from it. These results have not been presented here.

## METHODE DE PREVISION DES LIMITES DE FONCTIONNEMENT EN DEBIT DES COMPRESSEURS CENTRIFUGES

H. MITON, C.N.R.S.-I.M.F.M., 1, rue Honnorat, 13003 Marseille (France)

G. SENATORE, I.M.F.M., 1, rue Honnorat, 13003 Marseille (France)

J. CHAUVIN, L.E.M.F.I., Bât. 502, Campus Universitaire, 91405 Orsay Cedex (France)

Les phénomènes qui imposent le débit minimum de fonctionnement d'un compresseur centrifuge ne sont pas toujours clairement identifiés. Si le pompage et le décrochage tournant sont souvent observés à débit partiel, il n'est pas certain que ce soient seulement ces phénomènes purement stationnaires qui imposent la "ligne de pompage". L'approche qui a été retenue ici consiste à déterminer cette ligne en appliquant uniquement des critères de charge dans la région axiale de la roue mobile et la partie semi-aubée du diffuseur. La limite de fonctionnement est supposée atteinte lorsque roue et diffuseur sont simultanément décrochés. Les résultats d'une méthode d'analyse simple appliquée à deux compresseurs de caractéristiques géométriques très différentes montrent un assez bon accord entre la limite de fonctionnement définie par ce critère et la ligne de pompage expérimentale.

## Liste des symboles

V	: Vitesse absolue
Va	: Vitesse débitante
Vu	: Vitesse tangentielle
W	: Vitesse relative
M	: Nombre de Mach absolu
Mw	: Nombre de Mach relatif
U	: Vitesse d'entraînement
N	: $U_2 / \sqrt{T_{01}}$
X	: Rapport des vitesses débitantes sortie/entrée roue
$\phi$	: Coefficient de débit : $Va_1/U_2$
DPmax	: Coefficient de charge limite
$\Phi_1$	: Potentiel des vitesses
B	: Angle entre la vitesse relative et la vitesse débitante
T	: Température
$\rho$	: Densité
To	: Température totale
q	: Rapport des chaleurs spécifiques
Cp	: Chaleur spécifique à pression constante
nr	: Rendement de la roue mobile
$\pi$	: Rapport de pression totale
L	: Facteur de forme de Truckenbrodt (potentiel de déformation)
R	: Rayon
Rm	: Rayon moyen
Rp	: Rayon de pied
Rt	: Rayon de tête
S	: Section de passage
Zr	: Nombre de pales de la roue
B*	: Angle formé par les pales avec la direction radiale à la sortie de la roue
n	: Direction du maillage
s	: Direction du maillage
$\lambda$	: Coefficient de glissement

## Indices

1	: Entrée de la roue mobile
tr	: Col de la roue mobile
2	: Sortie de la roue mobile
3	: Entrée du diffuseur
*	: Col du diffuseur
4	: Sortie compresseur

## I. INTRODUCTION

Si le débit maximum d'un compresseur centrifuge peut être déterminé sans ambiguïté, dans la mesure où l'on sait prévoir la saturation de ces différents composants, les phénomènes qui imposent son débit minimum ne sont pas toujours clairement identifiés.

Il convient d'abord de préciser les phénomènes généralement mis en cause :

- le pompage vrai
- le décrochage tournant

et d'effectuer une remarque concernant l'usage de ces termes.

Le pompage "vrai" intéresse l'ensemble du compresseur et son circuit. Son amplitude peut être importante (fluctuations de la vitesse atteignant 100 % du niveau moyen). Sa fréquence est généralement faible. Il peut se produire dès que la pente de la courbe caractéristique débit-pression globale du compresseur présente une certaine valeur positive. Son apparition et son amplitude sont fortement influencées par le circuit récepteur. Il n'est pas nécessairement provoqué par le décrochage tournant.

Le terme de "décrochage tournant" désigne en réalité plusieurs phénomènes de nature complètement différente du précédent. Il s'agit d'instabilités de même type que celles observées dans les compresseurs axiaux, présentant certaines caractéristiques propres aux compresseurs centrifuges. En particulier, on peut déceler un décrochage tournant dans une seule partie du compresseur non ressenti dans d'autres parties de la machine, même voisines.

Les informations dont on dispose de ce point de vue sont souvent ambiguës. Il est en effet d'usage de désigner la limite de fonctionnement d'un compresseur par le terme de "ligne de pompage", sans que l'on puisse toujours identifier expérimentalement le phénomène réellement en cause. Il est dans ces conditions difficile d'établir une méthode de prévision si l'on ne connaît pas sur quelles bases cette ligne a été réellement déterminée, bases qui dans certains cas peuvent être même quelque peu subjectives. Le pompage et plus fréquemment le décrochage tournant sont souvent observés à débit partiel ; il n'est cependant pas certain que dans tous les cas, ces phénomènes purement instationnaires imposent la ligne de pompage. Des décollements de la couche limite dans certaines régions du compresseur, même stationnaires dans un repère fixe ou mobile, mais toujours à l'origine de phénomènes instationnaires intenses à travers le mouvement relatif, peuvent parfaitement perturber le fonctionnement à faible débit. Par ailleurs, en raison de leur influence sur le profil des courbes caractéristiques des différents éléments de la machine, ces décollements peuvent contrôler par ce biais l'apparition des phénomènes instationnaires décrits ci-dessous. Enfin, au-delà de l'aspect phénoménologique du problème, si l'on s'en tient au point de vue de la prévision, il est évident que, décrochage stationnaire relatif à un composant, décrochage tournant ou pompage ont une cause commune et ne sont que les différentes conséquences d'une charge excessive imposée à l'écoulement dans certaines parties de la machine. Deux approches ont été envisagées pour traiter ce problème dont la nature n'est donc pas toujours clairement définie, même lors des essais :

- Analyse détaillée de la stabilité de l'écoulement. Cette approche largement utilisée dans les compresseurs axiaux revient à identifier le pompage avec une instabilité de l'écoulement suivant le temps. Elle paraît avoir été surtout mise en oeuvre pour traiter le cas des diffuseurs lisses (Réf. 1 à 4). Entrent également dans cette catégorie les travaux basés sur l'étude de la pente des courbes caractéristiques débit-pression. Appliquées à l'ensemble du circuit, ces méthodes permettent de prévoir le pompage "vrai".

Toutefois, la stabilité de chaque composant (roue, diffuseur, volute) peut être étudiée séparément, approche "localisée" qui paraît mieux adaptée à la prévision du décrochage tournant (voir par exemple les Réf. 11 et 12 pour le cas des diffuseurs aubés). Il est cependant permis de s'interroger sur la validité des approches linéaires dans les compresseurs centrifuges en raison de l'amplitude des phénomènes instationnaires, même au point de fonctionnement nominal.

- Application de critères de charge (souvent très empiriques) dans certaines parties de la machine faisant intervenir des caractéristiques géométriques (nombre d'aubes, rapports de rayons) et certaines performances locales ou globales. Cette approche, finalement voisine de celle adoptée dans ce travail, tend à identifier l'entrée en "pompage" à l'apparition de certains phénomènes stationnaires. S'appliquant de façon "localisée" aux différents éléments de la roue et du diffuseur, elle paraît également intéresser particulièrement les machines plus fortement concernées par le décrochage tournant que le pompage "vrai".

## II. RAPPEL DE CERTAINES OBSERVATIONS EFFECTUEES AU VOISINAGE DE LA LIGNE DE POMPAGE.

Pour proposer un modèle, il apparaît nécessaire de tenter d'éclaircir dans quel ordre les différents phénomènes susceptibles d'imposer la ligne de "pompage" sont généralement observés. Le décrochage tournant a été moins étudié que pour les compresseurs axiaux. Il a bien été observé expérimentalement sur des roues et des diffuseurs de compresseurs centrifuges. FRIGNE et VAN DEN BRAEMBUSSCHE (Réf. 5) ont étudié un compresseur équipé d'un diffuseur lisse, et mis en évidence que plusieurs régimes de décrochage tournant précèdent généralement l'entrée en pompage "vrai". Dans la roue mobile, trois types de décrochages tournant se distinguant par leur amplitude et leur fréquence peuvent être obtenus.

- décrochage "faible"
- décrochage progressif, d'amplitude continuellement variable lorsque le point de fonctionnement se déplace sur la courbe caractéristique (peut n'apparaître qu'à certaines vitesses de rotation)
- décrochage "brutal", c'est-à-dire apparaissant brusquement à l'amplitude maximum à partir d'un certain débit.

Le décrochage tournant de type "progressif" montre une amplitude maximum à un débit intermédiaire entre le débit donnant le rapport de pression maximum et le débit correspondant à l'apparition du décrochage brutal. C'est souvent à ce débit intermédiaire qu'apparaît le pompage "vrai" (défini en tant qu'instabilité du débit d'amplitude importante) qui peut également être déclenché par le décrochage "brutal".

Dans les diffuseurs, deux types de décrochage tournant ont été mis en évidence par les mêmes auteurs :

- décrochage à haute fréquence pour les plus grands débits ;
- décrochage à basse fréquence pour les débits plus faibles (précédant une entrée éventuelle en pompage "vrai").

Ces auteurs ont observé, par ailleurs, que si l'entrée en décrochage de la roue mobile est réalisée, il peut empêcher l'apparition du décrochage tournant dans le diffuseur pour des débits plus faibles.

Si ce problème paraît avoir été étudié de façon très détaillée pour les diffuseurs lisses (Réf. 5 et 6), type de machine qui présente moins d'intérêt actuellement, il paraît difficile d'avoir des informations aussi précises concernant les diffuseurs aubés.

Dans ce domaine, des travaux concernant la stabilité des différentes parties du diffuseur ont cependant été effectués. Par exemple, BAGHADI (Réf. 7) a pu mettre en évidence une influence stabilisatrice de la partie lisse et semi-aubée (pente de la courbe caractéristique toujours négative). Le régime de fonctionnement, stable ou instable, du diffuseur se voit ainsi imposé par la partie aubée.

On ne dispose cependant pas d'informations précises permettant de savoir si à une telle instabilité est associé un décrochage tournant ou un pompage "vrai".

Il ressort de cette première analyse sommaire, que dans les compresseurs centrifuges, le pompage "vrai" est généralement précédé par un régime de décrochage tournant intéressant au moins la roue mobile. D'autre part, un compresseur peut parfaitement être le siège d'un phénomène décrochage tournant de type "progressif", avant d'atteindre sa ligne de pompage.

En ce qui concerne le décrochage tournant dans les diffuseurs aubés, son occurrence paraît avoir été moins

bien mise en évidence.

Il convient enfin de rappeler, d'un point de vue pratique, que si le décrochage tournant est un phénomène très critique dans les compresseurs axiaux, les compresseurs centrifuges, de par leur structure plus compacte, sont généralement à l'abri des risques de rupture par contrainte d'origine aérodynamique (sauf si les pressions de fonctionnement sont élevées).

### III. L'APPROCHE RETENUE

En conséquence il apparaît que l'un des points essentiels est d'identifier correctement les composants de la machine dont le comportement est à l'origine des événements se produisant à la limite acceptable de fonctionnement.

De ce point de vue, le travail de YOSHINAKA (Réf. 8) est particulièrement significatif. Cet auteur associe l'entrée en "pompage" au décollement simultané de la région d'entrée de la roue (bord d'attaque-col) et du diffuseur (région semi-aubée) (Fig. 1).

Celle des deux régions entrant en décrochage pour le débit le plus faible entraîne alors le pompage au moment de son décollement.

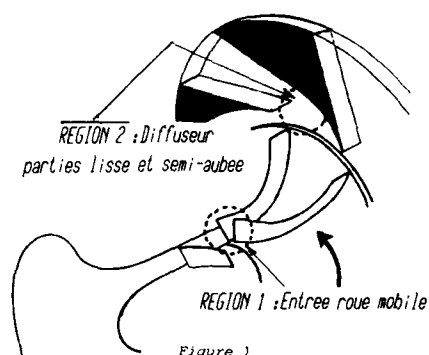


Figure 1

Cette approche donne un sens nouveau aux méthodes basées sur les critères de charge en ce sens que l'apparition du phénomène n'est plus la conséquence du comportement d'un seul élément du compresseur, mais de plusieurs. Cette hypothèse est confrontée par l'auteur à des résultats expérimentaux globaux pour une série de compresseurs à rapports de pression élevé (11:1). Les roues et diffuseurs sont identiques, et les compresseurs se différencient uniquement par le taux de prérotation en amont de la roue. Un accord satisfaisant est obtenu, sauf en régime de rotation intermédiaire avec prérotation nulle où la prévision est optimiste. Cette différence peut être due à une interaction forte diffuseur-roue mobile, en raison d'un décrochage tournant "brutal" dans cette dernière.

Au vu de ces résultats, il nous a paru intéressant de vérifier ce concept du critère de double décollement sur des géométries différentes, ainsi que la formulation et les valeurs numériques des formules de charge limite, puis la sensibilité des résultats obtenus aux paramètres mis en jeu.

Dans un premier temps, un programme de calcul de performances du type "ligne moyenne" a été établi. Il s'agit, pour la roue, d'une méthode de "niveau II" suivant la classification de JAPISKE (Réf. 9). Moyennant, à ce stade, un certain nombre de recalages expérimentaux, elle a permis d'évaluer les charges, puis les conditions de décrochage, dans les avant-roues et les régions semi-aubées de deux compresseurs "tests" de géométrie très différente.

Avec des temps de calcul extrêmement réduits, il paraît ainsi possible de prévoir la "ligne de pompage" avec une erreur généralement inférieure à 10 % sur le débit et d'identifier généralement sans ambiguïté le composant responsable.

Ces premiers résultats ont conduit à entreprendre une deuxième étape, dans laquelle les charges limites sont calculées pour chaque compresseur à chaque vitesse de rotation. Ces calculs font intervenir une méthode de type "trois zones" (écoulement sain et couches limites) appliquées localement dans les deux régions critiques. Si cette étude est toujours en cours, les résultats partiels qui sont présentés paraissent confirmer les conclusions proposées à l'issue de la première étape.

#### 4. LES DEUX PRINCIPALES COMPOSANTES DE LA METHODE DE PREVISION

##### 4.1. Calcul à la ligne moyenne

Il s'agit d'une méthode directe dans laquelle la géométrie, le nombre de tours et le débit sont donnés. Les objectifs sont de calculer rapidement, avec une précision suffisante, les grandeurs caractéristiques (angles, vitesses, pressions) de l'écoulement :

- de l'entrée au col dans la partie axiale de la roue mobile ;
- de la sortie de la roue au col du diffuseur.

En conséquence, cette méthode présente les caractéristiques suivantes :

- a) Calcul sur une ligne de courant représentative unique (rapidité d'exécution) ;
- b) Bonne précision à la traversée de la roue pour donner les conditions correctes à l'entrée du diffuseur ;
- c) Evaluation assez grossière des performances de la partie aubée du diffuseur et de la région de refoulement dont l'importance n'est pas essentielle dans le cadre de ce travail.

Pour satisfaire le point b, on utilise certains résultats d'origine expérimentale notamment le rendement de la roue. Le glissement est calculé suivant la formule de ECK, adaptée au cas du compresseur étudié (voir tableau + 2 An. 1). Le niveau de correction est faible et dans la précision des méthodes de type II d'après JAPISKE (Réf. 9). Cette référence justifie également le fait que cette correction puisse être effectuée une seule fois dans tout le champ : la déviation standard de correction d'angle pour reproduire les performances expérimentales est de l'ordre du degré sur l'ensemble de celui-ci.

Les blocages au niveau du col du diffuseur sont évalués, soit (dans la première étape : § 5), suivant les formules d'origine expérimentale proposées par KENNY (Réf. 13), soit (dans la deuxième étape : § 6) par calcul du développement de la couche limite.

Compte tenu des informations d'origine expérimentale utilisées, ce calcul n'a donc pas la prétention d'être une méthode générale de prévision du champ caractéristique complet d'une machine quelconque.

Une description complète en est donnée dans la référence 20, et un résumé en Annexe 1.

## 4.2. Pr vision du d crochage des composants

On utilise des coefficients de charge limite caract risant l'accroissement de pression statique   la travers e de la r gion consid r e.

-   l'entr e de la roue mobile :

$$DP_{\max 1-th} = P_{th} - P_1/P_{01} - P_1$$

entre le bord d'attaque et le col, divis  par la diff rence entre la pression d'arr t et la pression statique.

-   l'entr e du diffuseur :

$$DP_{\max 3-4} = P_4 - P_3/P_{03} - P_3$$

Deux sources sont utilis es pour la d termination de la valeur limite :

- formules empiriques de type KENNY (R f. 13) (Fig. 6) relev es pour des diffuseurs   canaux et ailet s de compresseurs PRATT et WHITNEY, donnant un rapport de pression de 6:1, sensiblement plus  lev  que celui des deux machines consid r es ici. Suivant ces formules, la charge limite est fonction seulement du nombre de Mach au bord d'attaque des aubages.

- calcul local suivant un mod le   trois zones ( coulement sain, plus couches limites), non coupl es pour la roue, coupl e pour le diffuseur. Les r sultats de ces calculs permettent d' tablir des courbes de type KENNY pour chaque type de machine et chaque r gion consid r e.

## 4.3. Les compresseurs  tudi s

La m thode de pr vision bri vement pr sent e dans le paragraphe pr c dent a  t  mise en oeuvre pour deux compresseurs sensiblement diff rents pour lesquels on dispose au moins d'un certain nombre de r sultats d'essais :

- compresseur DFVLR (R f. 10)
- compresseur TURBOMECA (R f. 14)

Les principales caract ristiques de ces machines sont repr sent es dans le tableau 1 ci-dessous :

Tableau 1	Roue				Diffuseur			
	* Rp/R2	* Rt/R2	* type pales	* nbr. pales	* R3/R2	* nbr. pales	*	*
DFVLR	* 0.2	* 0.7	* radiales	* 14	* 1.1	* 27	*	*
TURBOMECA	* 0.35	* 0.603	* couch�es	* 16	* 1.024	* 15	*	*

## 4.4. Validation du calcul   la ligne moyenne

Les performances de ces deux compresseurs ont  t  d termin es par mise en oeuvre de la m thode de calcul   la ligne moyenne. Les rendements de la roue mobile ont  t  estim s d'apr s les maximum mesur s le long de chaque isovitesse (voir A1.5). Les courbes repr sent es sur les figures 2 et 3 correspondant aux deux compresseurs, donnant une seule valeur par d bit, ont  t  ainsi obtenues.

Par ailleurs, le facteur de glissement a  t  fix    une valeur unique adapt    partir de la formule de ECK.

Les r sultats ainsi obtenus sont pr sent s sur les figures 4 et 5.

Compte tenu de la m thode utilis e pour  valuer le rendement des roues mobiles, les rapports de pression calcul s co ncident r ellement avec les valeurs mesur es seulement pr s de la ligne de pompage, c'est- -dire, lorsque la valeur du rendement utilis e dans le calcul est voisine du rendement r el. Les probl mes qui nous int ressent prenant place pr cis ment dans cette r gion du champ, ces r sultats peuvent  tre consid r s comme satisfaisants.

Figure 2

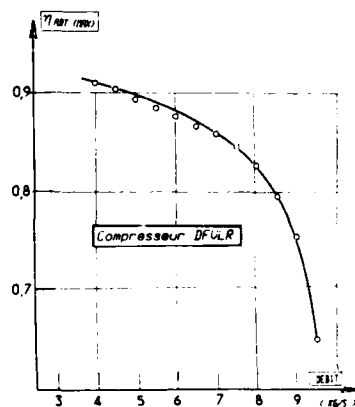
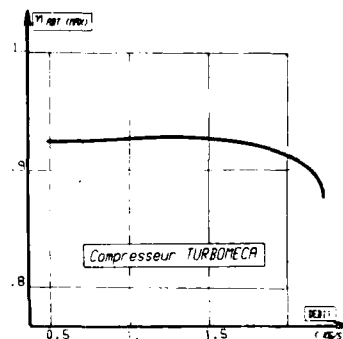


Figure 3



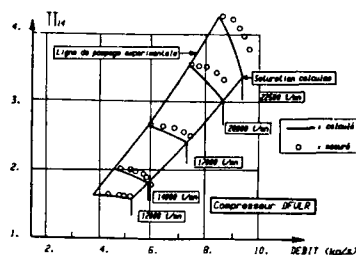


Figure 4

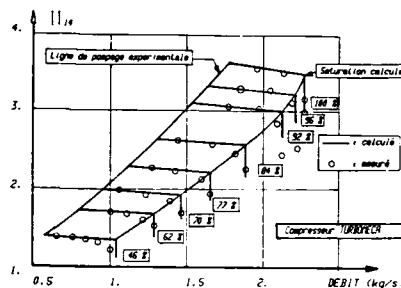


Figure 5

##### 5. MISE EN OEUVRE DE LA METHODE DE PREVISION AVEC CRITERES DE CHARGE EXPERIMENTAUX (Première étape)

###### 5.1. Critères de charge limite pour la partie semi-aubée du diffuseur

On dispose, pour évaluer la charge limite de la partie semi-aubée du diffuseur, des courbes d'origine expérimentales établies par KENNY (Fig. 6 et Réf. 13) pour les diffuseurs à canaux. Dans le domaine subsonique ou transsonique qui nous intéresse ici, le coefficient de charge limite varie de 0.35 pour les faibles valeurs du nombre de Mach, à 0.4 pour  $Mw_3 = 1$ . Il croît ensuite rapidement jusqu'à 0.5, maximum obtenu pour  $Mw_3 = 1.15$ , représentant un nombre de Mach critique au delà duquel le décollement de la couche limite par choc limite l'accroissement de pression dans la partie semi-aubée du diffuseur.

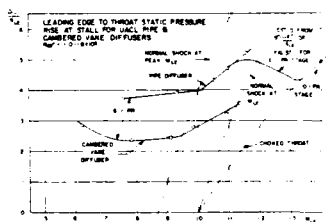


Figure 6

Il est intéressant de remarquer que YOSHINAKA (Réf. 8), dont les résultats ont été rapportés plus haut, utilise dans son modèle théorique un coefficient uniformément égal à 0.4, indépendant du nombre de Mach. Ce critère constitue en quelque sorte une simplification de celui proposé par KENNY. Des formulations différentes font intervenir d'autres paramètres que le nombre de Mach. On peut citer HERBERT et CAME (Réf. 11), pour qui le paramètre dominant est le rapport des surfaces  $A_w/A_g$  où  $A_w$  représente la surface mouillée de l'espace semi-aubée,  $A_g$  la surface géométrique du col. Ces auteurs notent également une certaine influence sur la charge limite du nombre d'aubes du diffuseur, ainsi que des performances du collecteur monté en aval. Cependant, les résultats qu'ils présentent ne permettent pas de comprendre de façon très claire l'influence de ces paramètres ou composants du compresseur. HELDER et GILL (Réf. 12) ont étudié l'influence du nombre d'aubes de la roue mobile sur la charge limite. Cette tentative est intéressante dans la mesure où elle permet de prendre indirectement en compte l'influence des phénomènes instationnaires sur le fonctionnement de la partie semi-aubée du diffuseur. Cependant, leurs résultats présentent une dispersion importante et leur nature purement expérimentale ne permet pratiquement pas d'introduire cette influence dans un modèle théorique. Dans ces conditions, les critères de KENNY ont été appliqués directement aux deux diffuseurs étudiés.

###### 5.2. Critères de charge limite pour la région d'entrée de la roue mobile.

Il n'existe à notre connaissance pas de relations semblables à celles de KENNY pour la partie du rotor située entre l'entrée et le col des canaux (les relations basées sur le facteur de diffusion du type Lieblein étant difficilement applicables aux aubages d'une roue centrifuge). Ainsi, on a été contraint, dans une première étape, d'appliquer au rotor les critères du même type que pour le diffuseur, c'est-à-dire supposer qu'il existe un coefficient de charge limite uniquement fonction du nombre de Mach relatif à l'entrée  $Mw_1$ .

###### 5.3. Application de relations de charge limite type KENNY aux compresseurs DFVLR et TURBOMECA.

Le calcul à la ligne moyenne fournit les caractéristiques de l'écoulement ( $w$ ,  $p$ ,  $T$ ) dans les deux régions critiques :

- avant-roue : de l'entrée au col formé par la pales (les valeurs sont alors pondérées par le débit) ;
  - région semi-aubée du diffuseur : du bord d'attaque des aubages à l'entrée des canaux inter-aubes.
- Pour chaque point de fonctionnement, le coefficient de charge entre la sortie et l'entrée de ces deux régions est alors calculé et comparé au coefficient de charge critique déterminé d'après les valeurs du nombre de Mach relatif en amont de la roue et du diffuseur, données par le calcul monodimensionnel. Ces charges limites sont représentées sur la figure 7 pour le compresseur DFVLR et la figure 8 pour le compresseur



TURBOMECA, dans le domaine limité par la vitesse de rotation la plus faible et la plus élevée.

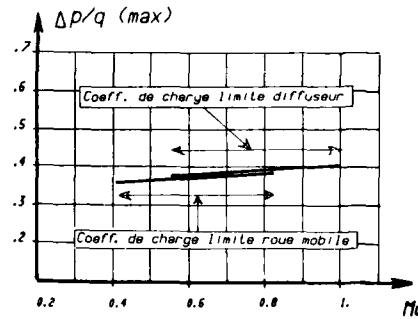


Figure 7

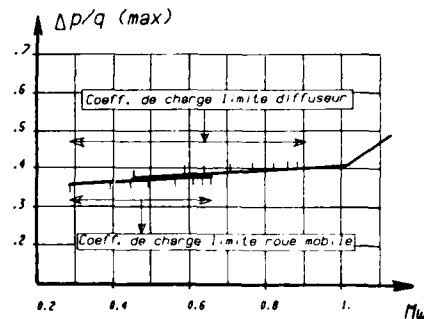


Figure 8

Sur chaque isovitesse, on obtient ainsi deux points de fonctionnement particuliers, correspondant, l'un à l'entrée du décrochage du diffuseur, l'autre à l'entrée en décrochage de l'avant-roue. En joignant les différents points correspondants aux différentes isovitesse représentées dans le champ, celui-ci se trouve ainsi séparé en 4 régions :

- Zone 1 : Diffuseur décroché et roue non décrochée.
- Zone 2 : Diffuseur et roue décrochés.
- Zone 3 : Diffuseur non décroché et roue décrochée.
- Zone 4 : Diffuseur et roue décrochés.

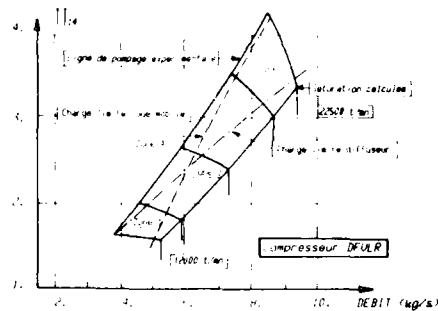


Figure 9

contre, à l'autre extrémité du champ, c'est le diffuseur qui paraît le plus résistant. Les résultats concernant le compresseur TURBOMECA sont représentés sur la figure 10.

On constate que dans ce cas, la zone 1 disparaît pratiquement, ce qui rend la roue responsable de l'entrée en pompage dans tout le domaine de fonctionnement du compresseur. La courbe de charge limite correspondant au décrochage de la roue coïncide sensiblement avec la ligne de pompage (à moins de 5 %) pour les isovitesse les plus basses (46 %) et les plus élevées (de 84 % à 100 %). Par contre, pour les vitesses de rotation intermédiaires, l'écart est plus important, encore de l'ordre de 10 % pour un débit de 1 kg/s. Ces résultats, si ils sont encore insuffisants pour valider la présente méthode de prévision de la ligne de pompage, sont cependant encourageants dans la mesure où ils permettent d'obtenir une approximation souvent acceptable du débit minimum de fonctionnement et aussi d'identifier généralement sans ambiguïté si la roue ou le diffuseur sont responsables du pompage en mettant en oeuvre des moyens de calcul très simples.

Suivant le type de prédiction proposée par YOSHINAKA, dont le principe est suivi ici, la zone correspondant au double décrochage de la roue et du diffuseur coïncide avec la région de "pompage" ou de décrochage tournant.

Dans le cas du compresseur DEULR (Fig. 9), les 4 zones se situent de façon à peu près symétrique par rapport au centre du domaine de fonctionnement. On constate sur la figure que la frontière de la zone 4 coïncide avec la ligne de pompage à moins de 4 % du débit pour les 2 isovitesse les plus basses (12000 à 17000 t/mn) et les plus élevées (20000 et 22500 t/mn), l'écart entre le débit d'intersection des deux courbes limites et le débit de pompage expérimentale est de l'ordre de 10 % le long de l'isovitesse moyenne (17000 t/mn), ce qui paraît excessif dans le cadre d'une méthode de prévision satisfaisante.

Le composant responsable de l'entrée en régime de pompage est cependant assez bien identifié par le calcul. Le long des isovitesse les plus basses, c'est l'entrée de la roue mobile qui décroche pour les débits les plus faibles ; par

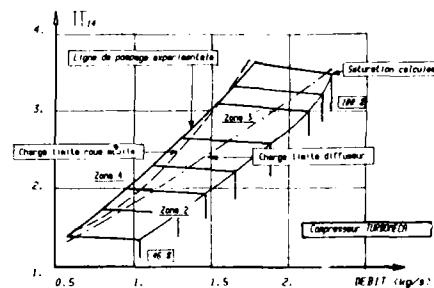


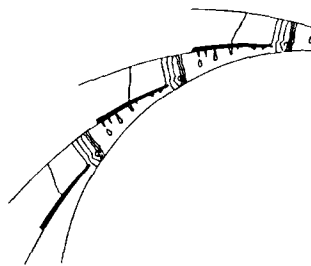
Figure 10

## 6. MISE EN OEUVRE DE LA METHODE DE PREVISION AVEC CRITERES DE CHARGE CALCULES (deuxième étape).

### 6.1. Résultats des calculs de charge limite pour les diffuseurs DFVLR et TURBOMECA.

L'écoulement est calculé par la méthode décrite dans la Réf. 20 et dans l'annexe A2 en partant de l'entrée du diffuseur jusqu'à une certaine distance en aval du col (représentant 5 à 6 fois la distance entre les flasques) pour des conditions à la sortie de la roue fournies par le calcul monodimensionnel.

Figure 11



La figure 11 montre un exemple de résultat de calcul concernant l'écoulement potentiel (courbes isomach dans la partie semi-aubée du compresseur TURBOMECA pour un nombre de Mach à la sortie de la roue égal à 0.91). On remarque que le calcul prévoit un choc de faible intensité à l'entrée du canal inter-aube. Suivant le nombre de Mach et la direction d'écoulement à la sortie de la roue (ou débit), le calcul de couche limite couplé à celui de l'écoulement potentiel (voir annexe A2) indique un décollement soit en aval du col, soit en amont. La figure 12 montre ainsi deux types d'évolution du potentiel de déformation  $L$  à travers les parties lisses et semi-aubée. Le décollement est obtenu pour  $L = 0$ . Faisant varier systématiquement le débit à l'entrée sur une isovitesse ( $M$  étant sensiblement constant), il est possible de reconstituer le cheminement du décollement dans cette région, puis de déterminer par interpolation son débit critique provoquant un décollement juste dans le col. Les pressions correspondantes obtenues par le calcul de l'écoulement potentiel permettent alors d'obtenir pour chaque nombre de Mach un coefficient de charge limite pour les parties lisses et semi-aubée du diffuseur.

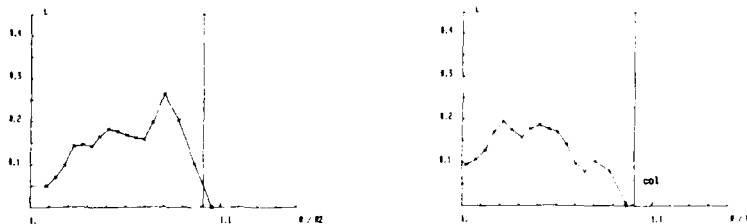


Figure 12

Les coefficients de charge limite calculés sur cette base sont représentés sur la figure 13 pour le compresseur DFVLR et la figure 14 pour le compresseur TURBOMECA. La comparaison des figures 7 et 13 met en évidence, pour le compresseur DFVLR, que le niveau du coefficient de charge critique est sensiblement plus élevé que celui prévu d'après KENNY. Pour les trois premières isovitesses (nombre de Mach  $< 0.9$ ), le niveau moyen atteint 0.6 contre 0.4 dans le cas précédent. Les deux courbes présentent cependant une allure semblable, le changement de pente de la courbe de KENNY, correspondant à l'apparition d'un choc au bord d'attaque pour  $Mw = 1$ , étant également observé mais à un nombre de Mach plus faible (0.8). Le calcul de la charge limite n'ayant pu, à l'heure actuelle, être effectué pour la roue, on a conservé sur la figure 13 l'évolution utilisée dans la première étape. Des conclusions analogues peuvent être tirées concernant le compresseur TURBOMECA. Le niveau de charge limite obtenu reste voisin de 0.5. L'influence du choc au bord d'attaque semble moins ressentie avec ce type de diffuseur. Cependant, le nombre de Mach au bord d'attaque est lui limité à 0.9 pour la vitesse de rotation la plus élevée. Concernant la roue mobile, la remarque effectuée concernant le premier compresseur s'applique également ici.

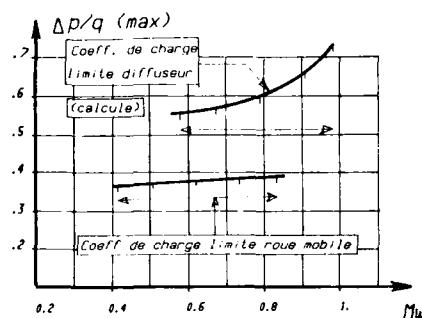


Figure 13

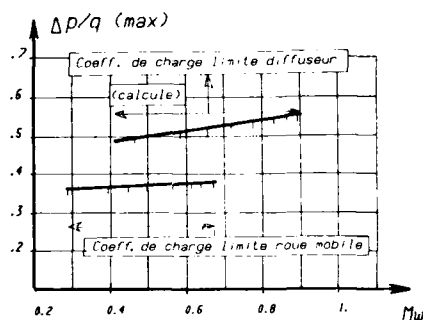


Figure 14

#### 6.2. Conséquences de ce calcul pour la prévision de la ligne de pompage.

Il est intéressant de replacer dans le plan débit-pression la courbe de décrochage du diffuseur, obtenue à l'issue de ce calcul, pour examiner notamment la sensibilité du débit de décrochage vis-à-vis de la charge limite.

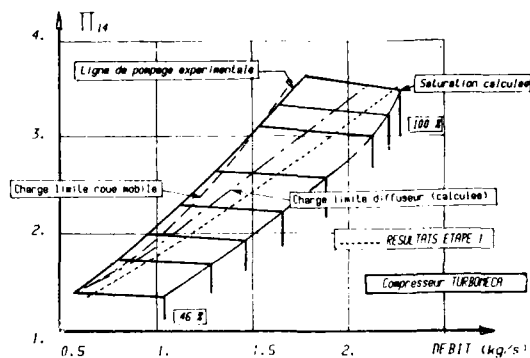


Figure 15

Dans le cas du compresseur TURBOMECA (Fig. 15, l'accroissement de la charge limite du diffuseur obtenu par rapport à la première étape (voir Fig. 8 et 14) se traduit naturellement par un déplacement de la courbe de décrochage vers la gauche de la figure. Si, en terme de débit absolu, il paraît plus important pour les vitesses de rotation élevées, en débit relatif, ce déplacement est à peu près constant de la vitesse de rotation la plus basse à la plus élevée ( $\sim 5\%$  à  $\sim 6\%$  environ). Compte tenu de la différence importante entre les coefficients de charge limite utilisés, ce déplacement de la courbe de décrochage paraît donc relativement modéré. Il n'est, en tous cas, pas suffisant pour modifier l'identité du composant responsable. Sauf peut-être pour la vitesse de rotation la plus faible, c'est encore la roue, et elle seule, qui paraît imposer la limite de fonctionnement.

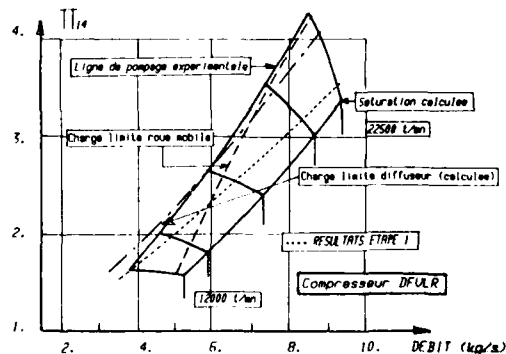


Figure 16

Le cas du compresseur DEVLK (Fig. 16) est un peu plus complexe à analyser. Aux vitesses de rotation élevées, le déplacement vers la gauche de la courbe de décrochage est du même ordre de grandeur que dans le cas du compresseur précédent (c'est-à-dire voisin de 5 %). Pour les isovitesse les plus basses, le déplacement est, par contre, plus important (- 10 %, au moins), notamment à 12000 t/mn. Le composant qui impose un débit minimum de fonctionnement reste inchangé (diffuseur pour les faibles vitesses de rotation, roue pour les vitesses élevées).

Cependant, à 12000 t/mn (vitesse de rotation la plus faible), la courbe de décrochage du diffuseur passe derrière la ligne de pompage expérimentale, ce qui paraît contredire localement la définition de cette ligne adoptée dans le présent travail.

Différentes explications peuvent être cependant avancées, expliquant de telles positions respectives de la courbe de décrochage du diffuseur et de la ligne de pompage.

D'abord l'imprécision de la méthode de calcul doit nécessairement être prise en compte (choix de la ligne moyenne, en particulier) pouvant donner une erreur de quelques % sur le débit. Ce type d'incertitude sera certainement réduit par une meilleure expérience de la méthode. Par ailleurs, il peut être imaginé la préexistence d'un décollement tournant dans la roue, provoquant un second décollement prématuré dans le diffuseur. Ce type de phénomène ne peut être pris en compte par la méthode, où chaque composant est supposé alimenté par un écoulement moyen stationnaire (Cf. plus loin). De ce point de vue, il faut remarquer que le décrochage de l'avant-roue à 12000 t/mn se produit pour un débit relativement éloigné du débit de la ligne de pompage. Il est donc probable que les conditions d'alimentation du diffuseur ne sont pas très satisfaisantes, lorsqu'on s'approche de celle-ci. De ce point de vue, il est permis de soulever le problème, qui semble avoir été envisagé par JAPISKE (Réf. 9) de la définition elle-même d'un écoulement moyen en présence de phénomènes instationnaires intenses.

Jusqu'à quelle mesure est-il permis de calculer et d'utiliser des conditions stationnaires à l'entrée d'un diffuseur situé en aval d'une roue mobile dont la partie radiale est le siège de décollements importants et inévitables ("jet-sillage"), alimentée de façon médiocre par l'avant-roue ?

Il s'agit, bien entendu, d'un problème qui dépasse le cadre de ce compte-rendu, mais qui peut-être, sera à prendre en compte dans le futur, même de façon grossière, pour calculer les conditions à l'entrée du diffuseur à partir de l'écoulement supposé obtenu à la sortie de la roue.

## 7. CONCLUSION

Une méthode de prévision de la ligne de pompage pour les compresseurs centrifuges est proposée. Basée sur des observations effectuées par YOSHIMAKA (Réf. 8), son principe peut être résumé dans le fait qu'un compresseur centrifuge ne peut entrer en régime de pompage (plus vraisemblablement en régime de décrochage tournant notable), que si des décollements dans la partie axiale de la roue et la partie semi-axiale du diffuseur existent simultanément.

Cette approche du problème, qui masque, sans aucun doute, un certain nombre d'éléments de la physique des phénomènes, ne semble cependant pas contredite par l'expérience. Elle présente, par ailleurs, l'avantage de distinguer dans une machine une région responsable de l'entrée dans la zone de pompage. Bien qu'il soit encore largement prématuré de tirer des conclusions définitives et de donner une allure de généralité aux observations effectuées, on peut cependant rappeler les principales étapes et résultats de ce travail. Une comparaison expérience-calcul effectuée sur cette base et des résultats d'essais a été réalisée, concernant deux compresseurs ne présentant aucune caractéristique commune. La prévision de la situation (décollée ou non l'écoulée) des deux principaux composants a été effectuée de deux façons. Dans un premier temps, en appliquant aux deux éléments supposés les plus sensibles (roue et diffuseur) des formules de charge limite établies expérimentalement sur certains types de compresseurs. Les résultats obtenus lors de cette étape sont cohérents, sans pour autant que l'on puisse être assuré de leur validité en raison du manque d'informations sur les phénomènes se produisant réellement dans les machines à faible débit. Une coïncidence souvent satisfaisante est observée entre les lignes de pompage, relevée expérimentalement et définie suivant la notion proposée plus haut.

Dans un deuxième temps, les charges limites ont été déterminées pour le diffuseur, en tenant compte de l'évolution de la couche limite. Les résultats obtenus sont assez différents sur ce plan (on observe un accroissement des charges calculées par rapport aux valeurs utilisées dans la première partie, mesurées sur des compresseurs particuliers KENNY). Cependant, une évolution relativement modérée des débits de décrochage du diffuseur a été observée. Par ailleurs, les composants identifiés, en un premier temps, comme responsables de l'entrée dans la zone de pompage ne sont pas inversés. Si certains points demandent à être éclaircis, ces résultats ne sont donc pas négatifs. On peut penser, en particulier, qu'un calcul des charges limites guidé par l'évolution des couches limites pour la roue mobile, en cours actuellement, ne devrait pas modifier de façon très sensible les présentes conclusions.

Sur un plan pratique, ces observations ont également un intérêt, puisqu'elles tendent à prouver qu'il suffit de disposer d'une bonne approximation de la charge limite pour pouvoir déterminer de façon satisfaisante les débits minimum de fonctionnement du compresseur.

## REFERENCES

1. JENSEN W. : Rotating stall in radial vaneless diffusers. ASME Trans. J. of Basic Eng., Vol. 86, N° 4, pp. 756-758, Dec. 1964
2. SHENO Y., KINOSHITA Y., ISHIDA M. : Asymmetric flow in vaneless diffusers of centrifugal blowers. ASME Trans. J. of Fluids Eng., Vol. 99, N° 1, pp. 104-114, March 1977
3. ABDELHAMID A. : Analysis of rotating stall in vaneless diffusers of centrifugal compressors. ASME paper 80 GT 184
4. SHENO Y., NISHI M. : Prediction of flow separation in a diffuser by a boundary layer calculation. ASME Trans. J. of Fluids Eng., Vol. 99, N° 2, pp. 379-389, June 1977
5. FRIGNE P., VAN DEN BRAEMBUSSCHE R. : Distinction between different types of impeller and diffuser rotating stall in a centrifugal compressor with vaneless diffuser. ASME Trans. J. Eng. for Gas Turbines and Power, Vol. 106, N° 2, pp. 468-474, April 1984
6. VAN DEN BRAEMBUSSCHE R. : Surge and stall in centrifugal compressors. VKI Lecture Series 1984 on Flow in Centrifugal Compressors, May 29-30 1984
7. BACHARDI S. : The effect of rotor blades wakes on centrifugal compressor diffuser performance. A comparative experiment. ASME Trans. J. Basic Eng., Vol. 99, N° 1, pp. 45-52, March 1977

8. YOSHINAKA T. : Surge responsibility and range characteristics of centrifugal compressors. Proceed. of the Tokyo Joint Gas Turbine Congress, pp. 381-390, 1977
9. JAPISKE D. : A critical evaluation of three centrifugal compressor with pedigree data sets. Part 5. Studies in component performances. ASME Trans. J. of Turbomachinery, Vol. 109, pp. 1-9, January 1987
10. KRAIN H. : A study on centrifugal impeller and diffuser flow. ASME Trans. J. Engrg. for Power, Vol. 103, N° 4, pp. 688-697, Oct. 1981
11. CAME P.M., HERBERT M.V. : Design and experimental performance of some high pressure ratio centrifugal compressors. AGARD CP 283, Nov. 15, 1980
12. ELDER R.L., GILL M.E. : A discussion of the factors affecting surge in centrifugal compressor. ASME Paper 84 GT 194, June 1984
13. KENNY D. : Supersonic radial diffusers. "Advanced compressors". AGARD LS 39, May 1970
14. Rapport interne TURBOMECA, Juillet 1985
15. LE FOLL J. : A theory of representation of the properties of the boundary layer on a plane. Proc. Seminar on Advanced Problems in Turbomachinery VKI, 1965
16. PAPAILIOU K.D. : Optimisation des dispositifs décélérateurs à forte charge fondée sur une théorie intégrale de la couche limite. Thèse d'Etat, Université Claude Bernard de Lyon, 1974
17. HUO S. : Optimisation based on boundary layer concept for compressible flow. ASME Paper 74 GT 63, April 1974
18. PANARAS A.G. : Calculation of a boundary layer interacting with a normal shock by a discontinuity analysis. VKI TN 121, Oct. 1976
19. VERDONCK G. : Vaned diffuser inlet flow conditions for a high pressure centrifugal compressor. ASME Paper 78 GT 50
20. SENATORE C. : Etude théorique de l'écoulement dans les compresseurs centrifuges. Thèse de Doctorat. Université d'Aix-Marseille II, May 1987

## REMERCIEMENTS

Les auteurs remercient la D.R.E.T. d'avoir autorisé la publication de ce travail.

## ANNEXE 1 : METHODE DE CALCUL A LA LIGNE MOYENNE

Il s'agit d'une méthode de calcul directe qui s'applique sur une ligne moyenne supposée représentative. Les caractéristiques géométriques de l'étage (y compris le pré-distributeur si il existe) sont réputées connues, y compris les sections géométriques de l'avant-roue et du diffuseur aubé. Le débit et le nombre de tours sont donnés.

## A1.1. Calcul de l'écoulement à l'entrée de la roue mobile

Une localisation exacte du col demande une connaissance tridimensionnelle de l'écoulement que l'on ne possède pas. Aussi, celui-ci est-il défini approximativement à un rayon donné par la distance mesurée suivant la perpendiculaire à l'extrados d'une pale, passant par le bord d'attaque de l'aube suivante. Cette appréciation s'est avérée correcte pour les compresseurs qui ont servi de cas test à la présente méthode (Cf. calcul du débit de saturation).

Entre l'amont et le col, l'écoulement relatif subit une déflexion d'autant plus importante que l'angle d'entrée  $B_1$  est élevé.

Ce phénomène se produit aussi pour des vitesses supersoniques en amont, la compression s'effectuant alors partiellement à travers une onde de choc dont le pied est situé sur l'extrados. La présence de cette onde, qui peut être située à une distance assez en amont de l'avant-roue, modifie le col aérodynamique par l'intermédiaire du blocage. La position réelle de l'onde, ainsi que le blocage créé, ne sont pas pris en compte dans la modélisation. Par application de l'équation de continuité à chaque rayon, on détermine des conditions correspondantes au niveau du col. Le facteur de charge DP (Cf. § 4.2) peut alors être obtenu au rayon moyen  $r_{1m}$  défini par :

$$(a1) \quad \rho_1 \cdot V_{a1} \cdot \pi \cdot R_{m1}^2 = \pi \int_{R_{p1}}^{R_{t1}} \rho_1 \cdot W_{a1} \cdot r \cdot dr$$

Cette valeur du facteur de charge est alors comparée à une valeur maximum donnée expérimentalement (§ 5) ou calculée (§ 6).

## A1.2. Calcul de l'écoulement à la sortie de la roue mobile.

$B_{2*}$  désignant l'angle formé par les pales à la sortie de la roue avec la direction radiale, la vitesse tangentielle à la sortie de la roue s'écrit :

$$(a2) \quad V_{u2} = \lambda \cdot (U_2 - V_{a2} \cdot \tan B_{2*})$$

On en déduit le rapport des températures totales absolues entrée-sortie par application de l'équation de Euler :

$$(a3) \quad T_{02}/T_{01} = 1 + (1 - RR_{12} \cdot \tan \alpha_{1m} \cdot \phi - \lambda \cdot R_{12} \cdot \tan B_{2*} \cdot X \cdot \phi) \cdot N^2 / C_p$$

où :

$$RR_{12} = R_{m1}/R_2$$

L'équation de continuité écrite à la traversée de la roue mobile donne le rapport  $X$  des vitesses axiales et radiales entre l'entrée et la sortie de la roue, que l'on peut écrire en fonction du rapport des températures totales et du rendement polytropique totale à totale  $\eta_x$  de la roue :

$$(a4) \quad X = (T_1/T_2)^{1/(g-1)} \cdot (T_{02}/T_{01})^{g(1-\eta_x)/(g-1)} \cdot S_1/S_2$$

Le rapport des températures s'exprimant en fonction de celui des températures totales et des vitesses et

des angles, les équations (a3) et (a4) forment un système donnant le rapport des vitesses débitantes à la traversée de la roue et ainsi, l'ensemble des éléments de l'écoulement à sa sortie, à partir, outre ses caractéristiques définies plus haut :

- du rendement de la roue  $\eta_r$  (voir § A.5)
- du coefficient de glissement  $\lambda$  (voir § A.6)

#### A1.3 Calcul de l'écoulement à la traversée de la partie semi-aubée et dans le col du diffuseur.

Un calcul analogue au précédent, mais simplifié (la température d'arrêt étant ici supposée constante) donne la vitesse débitante et l'inclinaison de la vitesse par rapport à la direction radiale à l'entrée de la région semi-aubée. On obtient alors facilement le coefficient de charge associé au diffuseur.

#### A1.4 Calcul du rapport de pression global du diffuseur.

Ce rapport de pression est calculé en supposant un rendement constant pour la partie aubée du diffuseur et le système de refoulement situé en aval.

#### A1.5 Détermination du rendement de la roue mobile

Les rendements de roue sont des données du schéma de calcul choisi dans cette phase de validation de la méthode. On a choisi d'utiliser les rendements expérimentaux fournis par les constructeurs des roues étudiées. Ces rendements dépendent essentiellement de deux paramètres : débit et vitesse de rotation. En réalité, si on examine les diagrammes correspondants, on constate que les différentes courbes correspondant à chaque vitesse de rotation présentent une enveloppe qui n'est fonction que du débit, tout en donnant une bonne approximation du rendement pour les débits voisins du régime de pompage qui nous intéressent ici. Les valeurs du rendement utilisées sont donc celles données par l'enveloppe. Ceci s'est avéré suffisant, du moins dans le cadre des objectifs actuels.

#### A1.6 Calcul du facteur de glissement

Le facteur de glissement est calculé au départ suivant la formule de ECK (Réf. 5) :

$$(a6) \quad \lambda = (1 + \pi \cdot \cos(B^*)) \cdot (2 \cdot Z_r \cdot (1 - R_{m1}/R_2))^{-1}$$

puis recalé à une valeur unique dans tout le champ pour respecter au mieux l'ensemble des niveaux de pression.

Le tableau 2 ci-dessous donne les valeurs ainsi calculées et celles effectivement utilisées.

Tableau 2

	* Valeur standard (a6) *	* Valeur utilisée *
DFVLR	. 83	. 88
TURBOMECA	. 86	. 86

### ANNEXE 2 : METHODE DE CALCUL DE LA CHARGE LIMITE (Diffuseur)

On réalise un couplage entre une méthode de relaxation isentropique exacte pour le calcul de l'écoulement sain et d'un calcul de couche limite sur les flasques. Le calcul de l'écoulement potentiel et celui de la couche limite sont liés suivant un procédé itératif. Un maillage sur lequel sont évaluées les différentes grandeurs relatives à l'écoulement est préalablement déterminé. L'ensemble du calcul est mis en oeuvre sur un domaine limité à un canal.

#### A2.1 Calcul de l'écoulement aube à aube

Le fluide est supposé parfait et non visqueux, l'écoulement stationnaire et isentropique. Le maillage choisi est curviligne et orthogonal (Fig. A).

La méthode de calcul est du type quasi 3D, basée sur la résolution exacte de l'équation du potentiel. Une application de cette méthode aux diffuseurs de compresseurs centrifuges (aubes épaisses) a déjà été effectuée par VERDONCK (Réf. 19).

Pour prendre en compte le caractère elliptique ou hyperbolique des équations suivant le nombre de Mach local, deux schémas numériques ont été adoptés :

- centré (cas subsonique)
- décentré aval (cas supersonique)

Il en résulte la forme suivante de l'équation discrétisée du potentiel :

$$\Phi(s, n) = F(\Phi(s+1, n), \Phi(s-1, n), \Phi(s, n+1), \Phi(s, n-1), \Phi(s-1, n+1), \Phi(s-1, n-1), \Phi(s+1, n-1), \Phi(s+1, n+1))$$

$$\Phi(s, n) = F(\Phi(s-3, n), \Phi(s-2, n), \Phi(s-1, n), \Phi(s, n+1), \Phi(s, n-1), \Phi(s-2, n+1), \Phi(s-2, n-1), \Phi(s-1, n+1))$$

Une relaxation du potentiel des vitesses est effectuée à chaque itération suivant :

$$\Phi_{K(s, n)} = r \cdot \Phi_{K(s, n)} + (1-r) \cdot \Phi_{K-1(s, n)}$$

où K représente le numéro de l'itération et r le facteur de relaxation variant de 0.1 à 0.5. Cette méthode qui ne prend pas en compte les relations de Rankin Hugoniot ne peut donc prendre en compte les ondes de choc de forte intensité.

## A2.2 Calcul de la couche limite

Les caractéristiques des couches limites situées sur les flasques du diffuseur, assimilées à des parois planes, sont estimées par la méthode de LE FOLL-PAPALIOU-HUO (Réf. 15 à 17) qui résout les équations dites de la couche limite sous une forme intégrale.

Le saut des grandeurs intégrales de cette couche limite à la traversée des ondes de choc (détectées à ce niveau par une méthode de capture) est calculé par la méthode proposée par PANARAS (Réf. 18).

## A2.3 Couplage Calcul potentiel - Calcul couche limite

Les vitesses potentielles sont dans un premier temps déterminées dans le plan aube à aube. Après un certain nombre d'itérations, la couche limite sur les flasques est déterminée en prenant comme écoulement extérieur celui qui existe sur la ligne centrale du maillage, supposée représentative de l'écoulement moyen. Les blocages méridiens de la veine sont alors réinjectés dans le calcul potentiel. Cette technique est répétée jusqu'à convergence.

Généralement, le calcul de la couche limite n'est effectué que toutes les 20 itérations du calcul potentiel. On laisse ainsi à l'écoulement un temps d'adaptation, ce qui donne un gain de temps.

## A2.4 Calcul des charges limites

Cette méthode de calcul donne l'état de la couche limite dans le col formé par les pales de la roue mobile ou à la sortie de la région semi-aubée (col du diffuseur). On considère que l'état critique est atteint lorsqu'un décollement de la couche limite est observé dans ce col. Il est alors aisé de calculer le coefficient de charge en fonction du nombre de Mach à l'entrée. Des exemples sont donnés dans le texte.

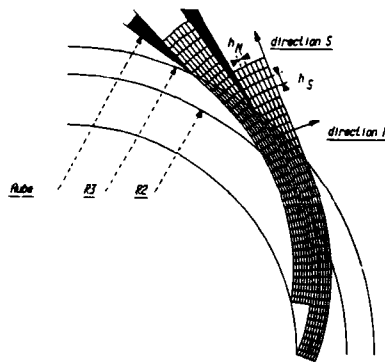


Figure A

# Design and Development of an Advanced F100 Compressor

Charles M. Love  
Senior Project Engineer  
Pratt & Whitney  
Engineering Division  
P. O. Box 109600  
West Palm Beach, FL 33410-9600

## ABSTRACT

The aerodynamic and mechanical design features of an advanced F100 compressor are described. The design objectives were to increase the efficiency and stability, along with simplifying the mechanical configuration in order to reduce the number of parts. Test results from a compressor rig and core engine are shown. Comparisons of the performance to the current F100 compressor are made. Results of testing with inlet pressure distortion are shown. Configuration features to improve reliability, durability, maintainability, and producibility are described.

## PROGRAM OVERVIEW

In the late 1970's Pratt & Whitney realized that military power plants would soon need increased performance, and a compressor with significantly improved efficiency was required. In 1980, configuration studies began to define an F100 replacement compressor. Compatibility with existing F100 engine models was an important consideration. The overall length and interfaces of the new compressor with the intermediate and diffuser cases had to remain the same, as did rotor speed, flow rate and pressure ratio.

Ultimately, a nine stage compressor with a larger annulus area and increased diameter flowpath was selected. This compressor was eventually tested in two compressor rigs and two core engine configurations under combined funding provided first by P&W independent research and development program and subsequently by the U.S. Air Force.

In late 1984, the U.S. Air Force defined new engine requirements for an F100 Improved Performance Engine (IPE). These requirements led to the choice of a 10 stage compressor with higher airflow and pressure ratio than the nine stage compressor that had been under development. This new 10 stage compressor incorporates the same aerodynamic design philosophy as the 9 stage and in fact uses the identical rear 5 stages. This 10 stage compressor is approximately 3 inches longer than the production and 9 stage compressors. However, by shortening the diffuser and combustor, the total length of the engine remained unchanged.

At the time of this writing, the 10 stage design has been completed but only limited testing has been done. Therefore, the aerodynamic performance results reported will be from the 9 stage configuration. The mechanical design description will be for the 10 stage configuration.

## AERODYNAMIC DESIGN

The 9 stage F100 replacement compressor was designed with constraints that would make it essentially a "plug-in" for the production model. The overall length and interfacing dimensions remained unchanged as did rotor speed, flow rate and pressure ratio. The aerodynamic design goals included:

Pressure Ratio	8.2
Adiabatic Efficiency	86%
Stall Margin	24%

Achievement of these goals would provide an approximate 4 point efficiency improvement and stall margin equal to the production compressor. In addition, a reduced stall line sensitivity to inlet pressure distortion was desired.

The compressor configuration that was selected evolved from "meanline design" studies of many different designs. These studies were done with the P&W analytical model that has been developed to accurately predict efficiencies and stall margins for multistage axial compressors and fans. This model allows for rapid analysis and performance prediction of the potential efficiency and stall margin levels of a compressor without having completed a detailed design. The model was used to select number of stages, flowpath shape, aspect ratio, solidity, reaction, and stage work distribution.



Within the constraints of the configuration studies, 8, 9, or 10 stages could have been selected. The predicted efficiency potential was highest with 8 stages, and the 10 stage design would have the greatest stall margin, but any of the three could meet the 24% objective. The 9 stage was selected because of its better efficiency potential over the 10 stage and its better stability potential over the 8 stage.

The selected configuration is shown in comparison to the production compressor in Figure 1. The concept for the improved efficiency is based on higher work per stage

- o MAINTAIN F100 INTERCHANGEABILITY
- o INCREASED WHEEL SPEED THROUGH INCREASED AVERAGE DIAMETER
- o LOWER ASPECT RATIO AIRFOILS

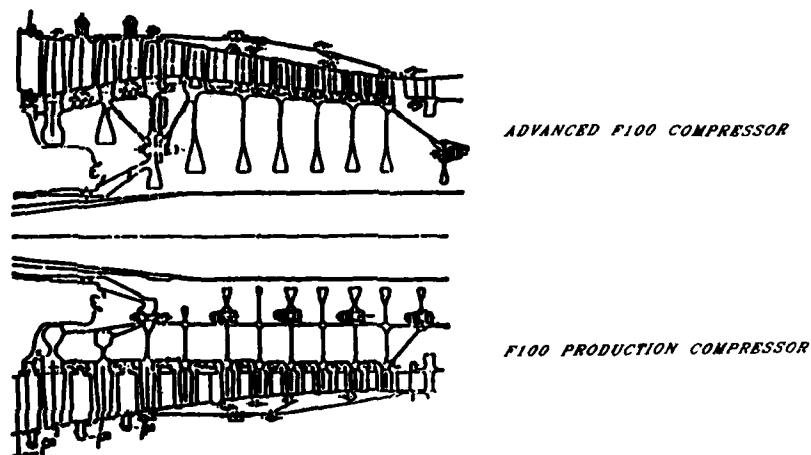


FIGURE 1. BACKGROUND/CONCEPT OF ADVANCED F100 COMPRESSOR

and increased annulus area. This is accomplished with a higher average wheel speed which results from increasing the diameter of the middle stages. In addition there is a benefit due to lower aspect ratio airfoils. The increased stage loading required for 9 stages instead of 10 results in a need for slightly higher solidity stages. A balance between rotor and stator loading levels was achieved by selection of the stage reactions.

Following the configuration selection, a detailed design was initiated. This design was performed using an axisymmetric streamline design model. Radial distributions of loss and work input were selected to completely define the velocity triangles. Airfoil shapes were selected using P&W cascade data in all rows except the first rotor where higher Mach numbers dictated a design composed of multiple circular arcs.

For adequate starting and off-design operation a start bleed and 3 rows of variable geometry were selected. The start bleed was located aft of the 4th compressor stage.

For the initial aerodynamic evaluations of the compressor, a rig with its own separate drive source was used. This testing was done in P&W's X-27 test stand in East Hartford, Connecticut. This test facility provides standard sea-level atmospheric inlet conditions.

The compressor rig configuration consisted of a flight-type rotor, "boiler plate" split cases, and adjustable stator rows with synchronizing rings in all stages. Instrumentation consisted of a full complement of inlet and exit rakes for pressure and temperature measurements and up to 5 radial location pressure and temperature sensors on the vane leading edges of each stage to acquire stage data for aerodynamic analysis and development. Flow rate was determined by a calibrated orifice.

# PERFORMANCE RESULTS

The first rig test of the advanced F100 compressor was conducted in mid-1982. Overall performance results showed good efficiencies, but stall margins below goals. Analysis of the interstage data revealed premature stalling was occurring because of insufficient work input and inadequate leading edge camber in the airfoils. Adjustments were made to the airfoil designs based on the data analysis. New rotor airfoils were procured while stator modifications were made by a reforming process. The second rig test of the modified design was conducted in the same test facility in mid-1983.

The performance of the second test configuration is shown in Figure 2. The results

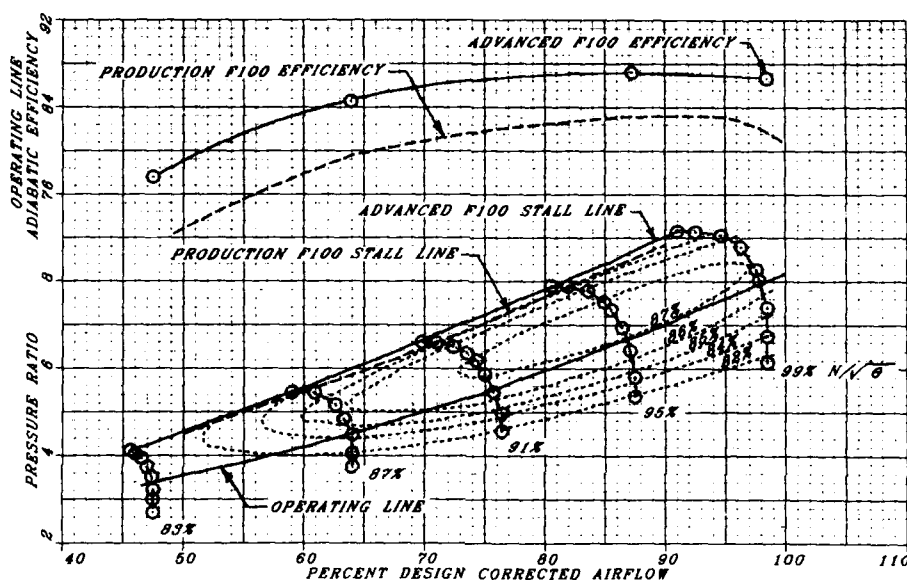


FIGURE 2. ADVANCED F100 COMPRESSOR - SECOND RIG TEST

were considered to be excellent. Efficiency and stall margins met or exceeded goals over the entire operating range. Shown for reference are the stall line and operating line efficiencies of the production F100 compressor. Efficiency improvement of over 4 points was demonstrated. In addition, this configuration showed very little loss of efficiency from the peak value on the speedline to the operating line. Also, there was a broad range of high efficiency as speed and flow were varied. This broad range of good efficiency covered the entire flight regime from subsonic to high supersonic flight conditions.

Analysis of the interstage data showed that the stages were well matched and were achieving the desired work and range levels.

A comparison of the goals and achieved performance levels are shown in Table I.

Table I

Aerodynamic Performance		
	Goal	Achievement
Efficiency	86.0	86.5
Stall Margin	24	30

Following the successful completion of the second rig test it was decided that additional evaluation of this configuration in a core engine was desirable. The core engine test facility had capabilities for increased inlet pressure and temperature which would allow a more severe structural evaluation of the design and would also allow evaluations of the interactions of the compressor, burner, and turbine during starting and stall recovery. For this testing a full complement of airfoil strain gages was installed. This would also allow for testing with inlet pressure distortions and flutter evaluations without excessive risk of blade failures.

The core engine tests were conducted in late 1983 and early 1984 at P&W's C-21 facility in West Palm Beach, Florida. The performance data confirmed the results from the rig. In addition, the measurements of turbine discharge conditions and fuel flows confirmed that the compressor efficiency was higher than the production compressor by the amount indicated by the compressor efficiency measurements.

A distortion screen covering half of the compressor face was fabricated for testing and comparison of results to the production compressor. The stall lines of the compressors are compared in Figure 3. Limitations on engine turbine inlet temperature prevented

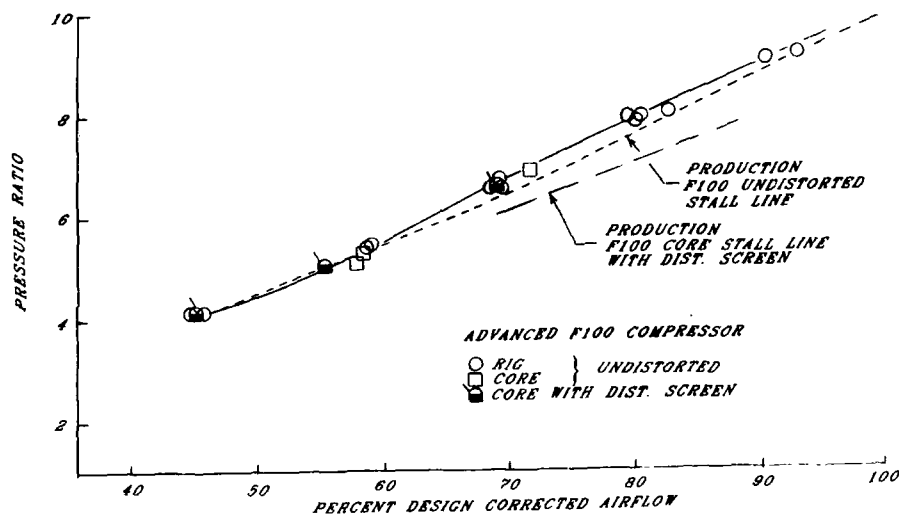


FIGURE 3. ADVANCED F100 COMPRESSOR SHOWS EXCELLENT DISTORTION TOLERANCE

determining the stall line for the advanced compressor above approximately 90% speed. It can be seen that there was very little loss of stall line due to the presence of the distortion screen, whereas the production compressor did show a loss. It can also be seen that the advanced compressor stall line with the distortion screen is higher than the undistorted production compressor stall line.

Starting evaluations were conducted by varying fuel flow rates between the minimum self-sustaining value and the value to cause compressor stall. Transient data were recorded to determine pressure ratio and flow rate. A comparison of these results is shown in Figure 4. The advanced compressor shows a slightly lower stall line than the

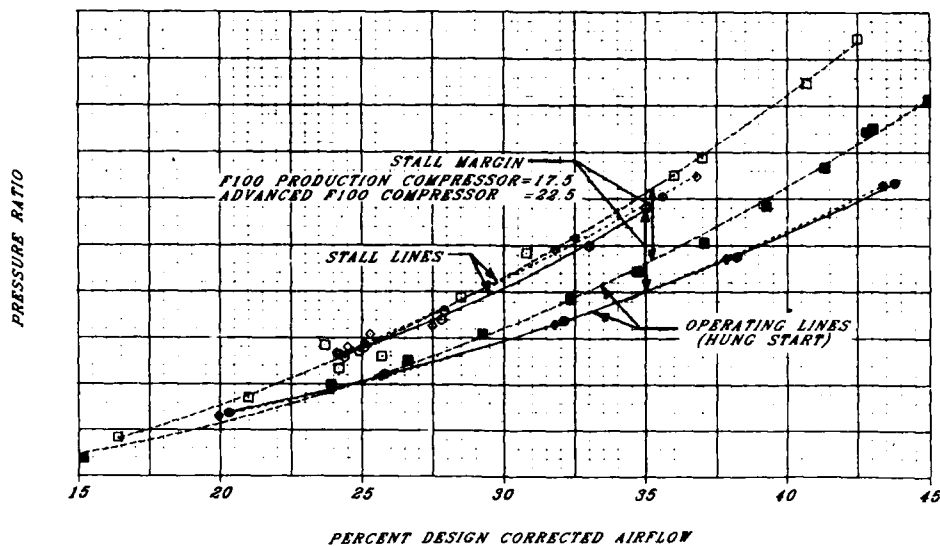


FIGURE 4. ADVANCED F100 COMPRESSOR - START REGION PERFORMANCE

production compressor. But because of its higher efficiency, the operating line is also lower, resulting in a higher stall margin for the advanced compressor.

Tests were conducted to determine the recoverability characteristics after a stall for both the advanced and production compressors. Intentional stalls were induced over a range of speeds and variable vane geometry settings. The speed boundary at which compressor rotating stall occurs was determined. These boundaries are shown in Figure 5. It is desirable to have the recovery boundary as low as possible in flow and

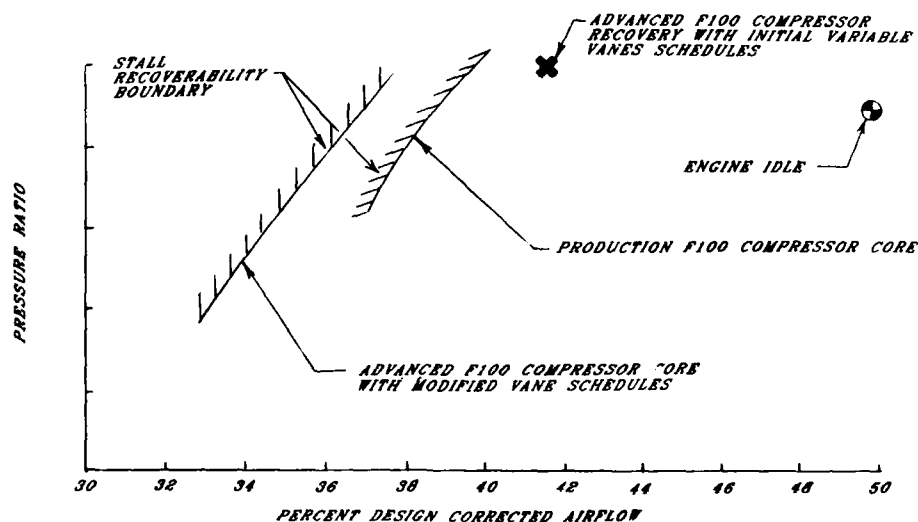


FIGURE 5. VARIABLE VANES OPTIMIZED ON ADVANCED COMPRESSOR CORE FOR RECOVERABILITY

pressure ratio to preclude a stalled compressor from decelerating into the non-recoverable (rotating stall) condition. Although the boundary for the advanced compressor with the initial variable geometry settings was higher in pressure ratio and flow than the production compressor, it was well below the engine idle speed. Modifications to the variable vane settings proved to be effective in moving the boundary to lower flows. The best recovery boundary achieved is shown to be below the production compressor boundary, however, the starting characteristics and efficiency were not as desirable as with the initial vane settings.

#### MECHANICAL DESIGN

The advanced F100 compressor, through the use of design innovations, manufacturing processing improvements and material advancements, is designed to achieve an 8000 total accumulated cycles (TAC) low cycle fatigue (LCF) life with a 4000 TAC service inspection interval.

The advanced F100 compressor configuration uses a drum rotor, shrouded stator configuration with four rows of variable stator vanes. The rotor system features an inertia-welded, damage tolerant process (DTP) titanium 1st/2nd stage drum, an independent 3rd stage disk/hub assembly and an inertia-welded DTP IN100 4th through 10th stage drum. The rear drum rotor is inertia-welded to an IN100 compressor drive shaft. This system forms a rigid rotating member with improved durability and performance retention. Each disk has integral knife-edge seals coated with aluminum oxide for wear protection. Rotor blade material for stages 1 through 4 is titanium, while nickel-based alloys are utilized for the remaining stages. The case structure consists of an axially split, titanium front and rear case for ease of maintainability. The stator vanes are all nickel-based alloy, the 1st, 2nd and 3rd stages being individual vanes and the 4th through 10th being fixed cast rings. Rapid solidification rate (KCR) nickel (alloy Y) material is used as a blade tip abradable rubstrip coating while all inner seals utilize small-cell honeycomb rubstrips. The compressor cross-sections in Figures 6 and 7 illustrate the significant design features of the advanced F100 compressor.

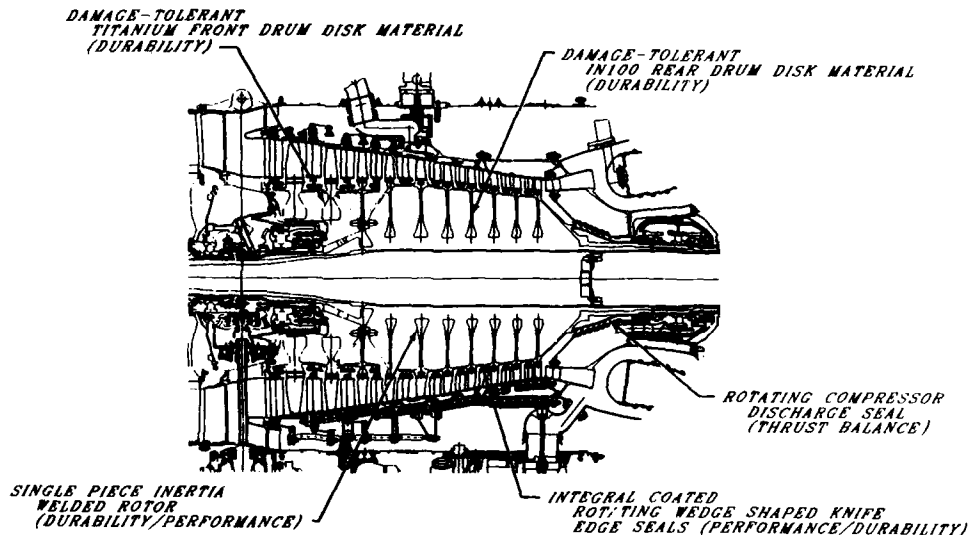


FIGURE 6. ADVANCED F100 DESIGN FEATURES - ROTATING STRUCTURES

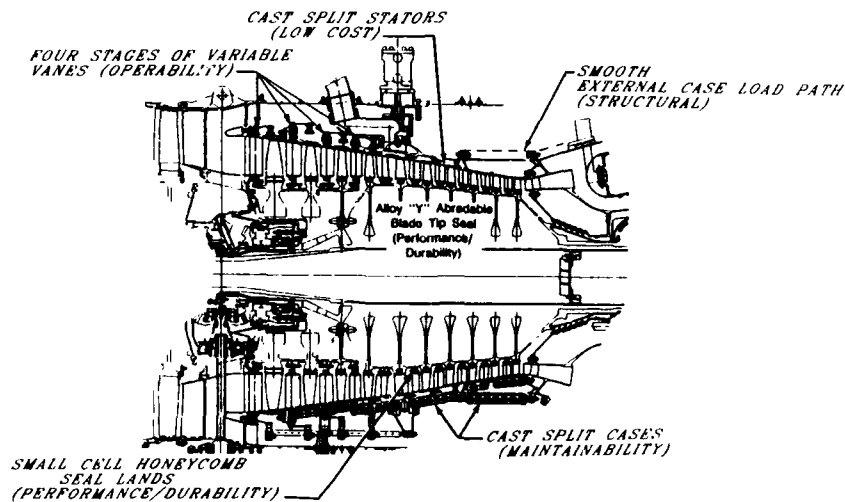


FIGURE 7. ADVANCED F100 DESIGN FEATURES - STATIC STRUCTURES

The rotor consists of only three major components: (1) an inertia-welded two-stage front drum rotor assembly, (2) an independent mid-rotor disk/hub assembly, and (3) a 7-stage inertia-welded rear drum rotor assembly that includes a compressor rear drive shaft. The three components are attached by body-bound studs located at the third disk. The current production F100 compressor rotor is made up of individual disks and spacers that are bolted together. Figure 8 shows a comparison of the two rotors. The advanced F100 compressor rotor will have a substantial reduction in number of parts and mechanical joints, thus providing a stiffer, more reliable component.

With the exception of the fan/compressor intermediate case and IGV outer support case, the advanced F100 compressor design incorporates a split case concept for drum rotor compatibility and ease of maintainability. The split cases are bolted together at the horizontal centerline. Figure 9 illustrates the case configuration. Two major case structures encompass the rotor system. A forward case, which extends from the 1st- to the 7th-stator vane, incorporates variable stator vanes, abradable blade tip liner segments and start bleed provisions. The rear case, which extends from the 7th-stator vane to the diffuser case outer front flange is designed to isolate the hotter compressor case temperatures from those of the cooler fan air for improved blade tip clearance control. All cases are designed for an 8000 TAC life.

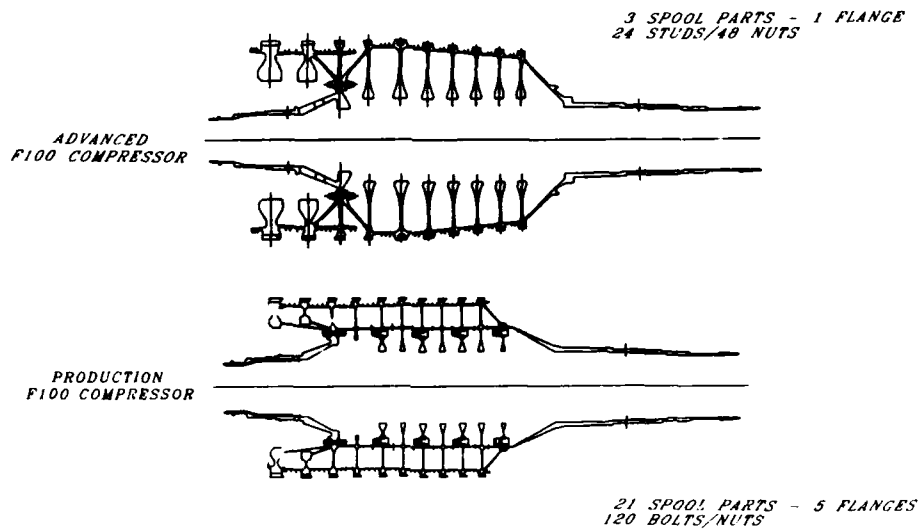


FIGURE 8. ADVANCED F100 COMPRESSOR - FEWER PARTS

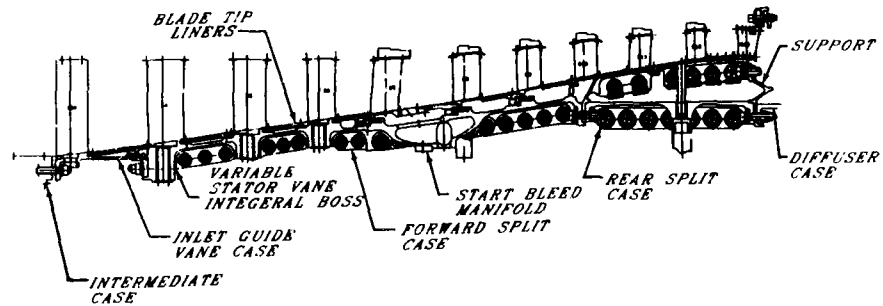


FIGURE 9. ADVANCED F100 COMPRESSOR CASES - DESIGN FEATURES

## SPECIAL MANUFACTURING TECHNIQUES

## Inertia-Weld Rotor Attachment Process

Advanced manufacturing processes are an integral part of the program development phase and have contributed greatly to achieving production of highly reliable, durable engine parts. Inertia welding, a unique form of friction welding, comes under this category. The process is used extensively in the manufacture of the high compressor drum rotor. A total of 11 inertia weld joints are used to attach the various details of the rotor assembly. The weld locations are shown in Figure 10. This process provides a consistent, high quality weld necessary for today's advanced technology rotor systems.

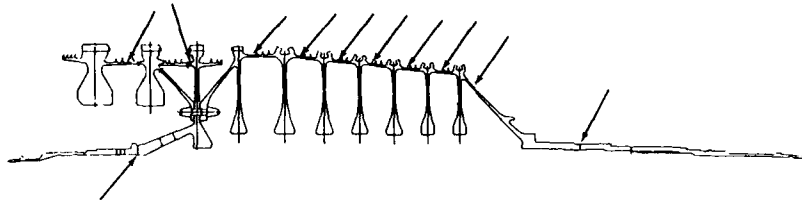


FIGURE 10. ADVANCED F100 COMPRESSOR ROTOR SYSTEM INERTIA - WELD LOCATIONS

Inertia welding utilizes kinetic energy stored in a flywheel system for all of the heating and much of the forging required. The basic process is shown in Figure 11.

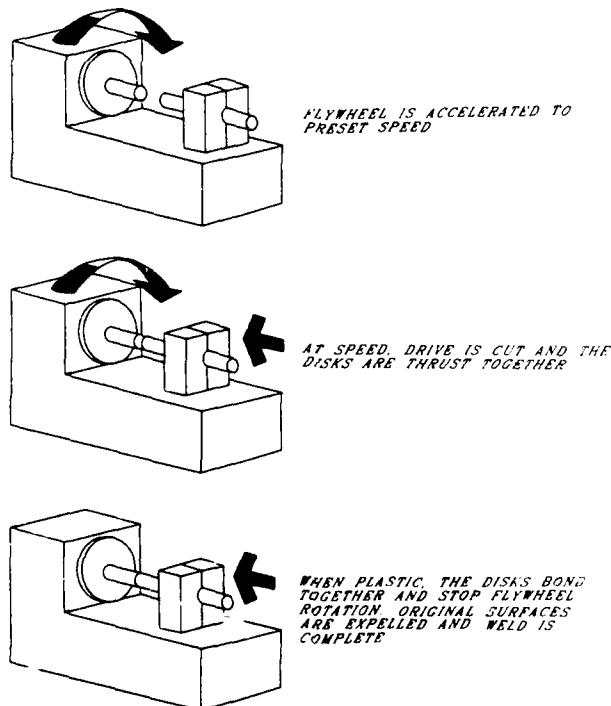


FIGURE 11. INERTIA WELD PROCESS



One disk detail is fixed in a stationary holding device. The adjacent disk, clamped in a spindle chuck with an attached flywheel, is accelerated rapidly. At a predetermined speed driving power is cut and two disks are thrust together. Friction between the disks decelerates the flywheel converting stored energy to frictional heat. This heat is enough to soften, but not melt, the two parts. The energy level is established to be sufficient to achieve forging temperatures. The rate of energy consumption is determined by the weld itself. When fully consumed the weld is completed and the flywheel rotation stops. Solid-state bonding, rather than welding may be a more appropriate term for the process. Advantages of this process include:

1. Preweld surface cleanliness insignificance because rubbing tends to disrupt and expel films and flaws.
2. Minimization of the heat-affected zone.
3. Localized heating and the absence of melting make welding better suited for joining dissimilar metal combinations.
4. Weld joints having forged properties can be as strong as base material.
5. Easily achievable process automation.

#### SUMMARY

1. A 9-stage advanced F100 compressor has been aerodynamically developed to achieve a 4 point efficiency improvement and a 6 point stall margin increase relative to the current F100 production compressor.
2. This compressor has shown reduced sensitivity to inlet pressure distortion.
3. Rotating stall boundaries have been shown to be well below engine idle speed.
4. Start region testing has shown improved stall margin due to higher efficiency and a lower operating line.
5. A 10 stage higher airflow and pressure ratio compressor has been designed using the proven aerodynamic concepts, including identical rear five stages, demonstrated by the 9-stage compressor.
6. Through innovative design concepts, manufacturing processing improvements, and material advancements this configuration provides improved reliability, durability, maintainability, and producibility.

#### DEFINITIONS

Work Coefficient	$\frac{\text{Enthalpy Rise}}{\text{Number Stages (Average Wheel Speed)}^2}$
Aspect Ratio	Blade Height/Chord
Solidity	Chord/Tangential Gap
Reaction	$\frac{\text{Rotor Static Pressure Rise}}{\text{Stage Static Pressure Rise}}$
Stall Margin %	$\left[ \frac{\text{Stall Pressure Ratio}}{\text{Operating Line Pressure Ratio}} - 1 \right] \times 100$ Constant Flow
Adiabatic Efficiency	$\left[ \frac{\text{Ideal Enthalpy Rise}}{\text{Actual Enthalpy Rise}} \right] \times 100$

# DISCUSSION

H.J. LICHTFUSS

- 1) Can you mention the radial tip clearance ?
- 2) The shown absolute efficiency levels are they Reynolds corrected ?
- 3) Can you please comment on the influence of low aspect ratio blades on efficiency ?

Author's Reply

- 1) The average tip clearance for the data shown was .009 inches.
- 2) Yes. The tests were conducted at a Reynolds Index of approximately .76. The efficiencies have been adjusted by Pratt & Whitney standard empirically based adjustment technique to the Reynolds Index equivalent to operation at sea level static conditions downstream of the 3-stage fan.
- 3) The choice of aspect ratio for best efficiency depends upon the aerodynamic loading. The more highly loaded the compressor the lower the required aspect ratio for best efficiency.

L. BATTEZATO, It

Can you please give informations about the dimensions of the parts (discs and distance pieces) being friction welded in the compressor drum. Also I would be interested in knowing the force and the speed imposed on the parts being welded.

Author's Reply

The joins which are welded together are on the order of 200/1000 of an inch thick.

R.G. THOMPSON, US

What is the commitment of the F-100 advanced compressor to full scale engineering development ?

Author's Reply

The full scale development program is currently in progress with production scheduled for 1990.

J. ALBRECHT, Ge

What operating blade tip clearances do you attempt in this engine with bled casing ?

**Author's Reply**

It is 15/1000 of an inch, averaged value.

**J.F. CHEVALIER, Fr**

- 1) For what reason is the advanced 9-stage compressor surge line insensitive to distortion ?
- 2) With the very low damping of the integral drum rotor, how do you avoid vibration ?

**Author's Reply**

- 1) The advanced 9-stage compressor is probably less sensitive to distortion because of its lower flow coefficient.
- 2) All I can say is that our experience to date with these rotors has shown no vibration problems.

## CONCEPTION ET ESSAIS D'UN ETAGE DE TETE

### D'UN COMPRESSEUR HP AVANCE

par

Marius GOUTINES

Société Nationale d'Etude et de Construction de  
Moteurs d'Aviation (S.N.E.C.M.A.)  
77550 MOISSY-CRAMAYEL (FRANCE)

et

Henri NAVIERE

Ecole Centrale de Lyon

36, Avenue Guy de Collongue, 69130 ECULLY (FRANCE)

### RESUME

Les études d'un compresseur haute pression avancé montrent que le rotor d'un étage de tête est supersonique sur toute l'envergure de ses aubes.

La SNECMA a dessiné et construit un compresseur monoétage qui est représentatif pour évaluer les performances et notamment les écoulements secondaires. Les essais sont réalisés par l'Ecole Centrale de Lyon qui a construit un banc d'essais de deux mégawatts pour accueillir ce compresseur.

Nous décrivons d'abord le projet du compresseur, la géométrie de la veine et les triangles des vitesses choisis au point de fonctionnement nominal. Les profils supersoniques sont optimisés par des calculs directs résolvant les équations d'Euler tridimensionnelles. Les profils subsoniques sont optimisés par une méthode directe potentielle couplée à un calcul de couche limite. Les performances globales ont été relevées. Les champs aérodynamiques mesurés et moyennés azimuthalement sont comparés à des prévisions théoriques dans la zone des écoulements secondaires pariétaux.

### 1 - INTRODUCTION

Dans un projet moderne de turboréacteur on cherche à abaisser le poids, la complexité et le coût en réduisant le nombre d'étages du compresseur haute pression. L'élévation du rapport de pression élémentaire qui en résulte conduit en général à des coefficients de charge aérodynamique ( $\Delta H/U^2$ ) plus élevés mais aussi à des vitesses de rotation plus élevées. Les études préliminaires au dessin des compresseurs montrent alors, que le premier étage a un rotor supersonique sur toute la hauteur de pale. Il importe donc de savoir prédire avec suffisamment de précision les performances d'un tel étage (rendement isentropique et marge au pompage) pour juger de son intérêt. Un des points les plus méconnus est le développement des écoulements et des pertes secondaires au moyen d'un rotor supersonique.

C'est pourquoi la SNECMA a décidé de dessiner et de fabriquer un compresseur monoétage, avec roue directrice d'entrée, dont les nombres de Mach relatifs du rotor, soient représentatifs de ceux d'un étage de tête d'un compresseur haute pression avancé. Les essais et une grande partie de l'analyse des résultats expérimentaux sont réalisés par la Société METRAFLU et l'Ecole Centrale de Lyon qui ont construit un banc d'essais de 2 mégawatts pour accueillir ce compresseur appelé "EC13". Les principaux buts de cette étude sont les suivants :

- valider les méthodes de dessin de compresseurs dont l'écoulement relatif à l'amont du rotor est entièrement supersonique.
- Analyser finement les écoulements secondaires en présence de chocs pour asseoir les méthodes de prévisions correspondantes.

### 2 - CONCEPTION AERODYNAMIQUE DU COMPRESSEUR

#### 2.1. - Caractéristiques générales

Au point de dessin, et dans des conditions d'alimentation standard ( $P_{to} = 1$  atmosphère,  $T_{to} = 15^\circ\text{C}$ ), les principales caractéristiques du compresseur sont les suivantes :

. Nombre de Mach relatif, amont rotor	$Mw1 = 1.1 \text{ à } 1.3$
. Rapport de moyeu, amont rotor	$\pi E = 0.75$
. Débit spécifique	$D/S_E = 180 \text{ kg/s/m}^2$
. Rapport de pression d'arrêt	$\pi = 1.84$
. Nombre de Mach axial moyen en sortie	$M_{X_5} = 0.48$
. Le compresseur est équipé d'une roue directrice d'entrée (RDE)	

La vitesse d'entraînement périphérique est limitée supérieurement pour des raisons aérodynamiques (limitation du nombre de Mach relatif incident en tête et surtout en pied de la roue mobile) et des raisons mécaniques (limitations des efforts centrifuges). Elle est fixée à 455 m/s.

Le rapport de moyeu choisi à l'entrée du rotor est un compromis permettant de limiter le nombre de Mach relatif incident au pied de la roue mobile à une valeur voisine de 1.1, tout en ayant une vitesse d'entraînement suffisante pour assurer le rapport de pression.

Le nombre de Mach axial à la sortie du compresseur résulte de l'étude d'optimisation de futurs compresseurs multi-étages.

## 2.2. Dessin de la veine et triangles de vitesse

La figure 1 présente la coupe méridienne de la veine. La convergence s'effectue à la fois par le profil de paroi interne et par le profil de paroi externe afin de mieux optimiser la répartition radiale des paramètres aérodynamiques. Les écartements choisis entre deux grilles adjacentes permettent l'introduction de sondes de pression et de température ainsi que des visées "LASER" dans de bonnes conditions.

Les principales caractéristiques structurales adoptées pour les aubages tiennent compte à la fois des exigences aérodynamiques et mécaniques.

Les allongements sont de l'ordre de 2 pour la roue directrice d'entrée, 1.2 pour la roue mobile et 1.5 pour le redresseur.

Le rapport de pression de la roue mobile, hors pertes secondaires, est de 1.892 et ne présente pas de variation radiale. Les pertes totales de la roue directrice d'entrée sont de 0.5%. Les pertes de profil de la roue mobile sont modélisées comme suit :

- Les pertes dues aux couches limites (sillages) sont établies à l'aide de corrélations qui sont dérivées des travaux de Lieblein [1]

- Les pertes par choc sont données par une méthode simplifiée mise au point à la SNECMA. Cette méthode tient compte des écarts entre le point de fonctionnement réel des profils et le point de désamorçage de ceux-ci [2]

Les pertes secondaires sont, pour l'instant, calculées par une méthode intégrale simplifiée qui fournit les épaisseurs caractéristiques des zones visqueuses pariétales en amont et en aval de chaque rangée d'aubages ainsi que les bilans d'enthalpie et d'entropie [3], [4]. La figure 2 donne l'évolution du coefficient d'obstruction ( $K_d$ ) et des épaisseurs de déplacement ( $\delta^+$ ,  $\delta^e$ ) des zones visqueuses de moyeu et de carter.

L'optimisation aérodynamique nous a conduit à adopter une roue directrice d'entrée quicrée une prérotation de  $5^\circ$  au pied et de  $19^\circ$  en tête. La giration résiduelle en aval du redresseur est de  $11^\circ$  au pied et de  $15^\circ$  en tête. La figure 3 fournit les nombres de Mach amont ( $M_{w1}$ ), aval ( $M_{w2}$ ) et la déviation de l'écoulement vus par la roue mobile. On remarque que l'aube mobile est entièrement supersonique à l'amont et que le profil de pied doit réaliser une déviation de  $18^\circ$  à un nombre de Mach d'attaque de 1.1. Les ralentissements et les facteurs de diffusion de Lieblein du rotor sont fournis par la figure 4 qui montre qu'il s'agit d'un compresseur chargé. Le nombre de Mach absolu maximum en amont du redresseur est de 0.76. Les ralentissements et les déviations de l'écoulement vus par le redresseur sont représentés sur la figure 5.

## 2.3. Dessin des aubages

Nous ne présenterons pas le dessin des profils de la roue directrice d'entrée qui présente peu de difficulté aérodynamique.

### 2.3.1. Dessin de l'aubage du rotor

Les profils supersoniques de la roue mobile sont créés par une méthode mixte (géométrique et aérodynamique) créée à la SNECMA. Cette méthode intègre les notions classiques d'incidence unique en écoulement amorcé, de marge au blocage, de position relative du col aérodynamique par rapport au système de chocs obliques et de chocs droits et d'écart flux-profil. Une première critique des profils est réalisée à l'aide d'un calcul résolvant les équations d'Euler bidimensionnelles sur une nappe de courant de révolution (calcul dit 2.5D) [5].

Au vu des résultats de ce calcul, les profils sont modifiés pour atténuer l'intensité des chocs et les décélérations trop importantes qui pourraient provoquer de forts décollements des couches limites des profils. Le processus est répété plusieurs fois pour dégrossir le dessin des profils. Les calculs résolvant les équations d'Euler réellement tridimensionnelles [6], [7] sont engagés très tôt dans la procédure d'optimisation des profils ; ils conduisent à apporter des modifications au dessin initial jusqu'à l'obtention d'une roue mobile aérodynamiquement satisfaisante.

Les figures 6 et 7 fournissent les résultats des calculs tridimensionnels au point de dessin.

les pics de survitesses juste en amont des chocs droits sont des imperfections numériques (schéma aux différences finies de Mac-Cormack) et n'ont pas de signification physique.

Ce travail d'optimisation a conduit à définir une roue mobile comportant 44 aubes dont les pas relatifs et les épaisseurs relatives maximales sont compatibles avec les exigences de résistance statique et dynamique.

Les marges au blocage sont de l'ordre de 5%. La forme des profils est ajustée jusqu'à obtenir, par le calcul effectué en fluide parfait, une surdéviation de l'ordre de 2° pour prendre en compte les phénomènes visqueux.

### 2.3.2. Dessin de l'aubage du redresseur

les profils du redresseur sont créés par une méthode inverse [8] permettant le dessin de profils plans. L'aube est ensuite engendrée par enroulement conforme de ces profils sur les nappes de courant issues du calcul méridien. Les calculs aérodynamiques 2.5D sont exécutés sur les profils gauches à l'aide d'une méthode résolvant l'équation complète du potentiel [9]. Ce calcul est couplé à un calcul de couche limite [10,11] qui utilise une méthode intégrale et qui prend en compte les courbures de paroi, la convergence transversale et les décollements faibles. Au vu des résultats obtenus, notamment ceux concernant l'état de la couche limite, les profils sont modifiés par la méthode inverse et le procédé est réitéré jusqu'à l'obtention d'un aubage satisfaisant.

On cherche en particulier à obtenir une marge en incidence satisfaisante et de faibles pertes de pression totale dans les conditions nominales. La figure 8 fournit, en deux points de fonctionnement, les répartitions de nombre de Mach et le facteur de forme des couches limites relatives au profil de pied du redresseur.

## 3 - BANC D'ESSAIS ET MESURES

Le banc d'essais de 2000 Kw installé au laboratoire de l'Ecole Centrale de Lyon a été conçu pour recevoir des compresseurs axiaux ou centrifuges. Il est équipé pour la surveillance mécanique des maquettes, les mesures de leurs caractéristiques aérodynamiques stationnaires, globales ou locales. Des mesures instationnaires peuvent également être implantées dans le banc d'essai.

### 3.1. - Description du local banc

Le local banc comprend d'une part la chaîne motrice, d'autre part la chaîne aéraulique et leurs annexes.

3.1.1. La chaîne motrice est constituée d'un moteur électrique synchrone auto-piloté fournissant la puissance nominale de 2MW à 3000 tr/mn. La variation de vitesse est obtenue par un ensemble onduleur-hacheur à thyristor dont la fréquence nominale est de 100 Hz et un courant nominal de 1300A. Le moteur entraîne un multiplicateur de vitesse à un train d'engrenages permettant d'atteindre la vitesse de 17000 tr/mn au niveau de l'accouplement de la maquette d'essai.

Cet accouplement est constitué d'un empilage de lames de type "flector". L'ensemble est monté rigidement sur un châssis qui permet également la fixation de la maquette et est scellé sur un massif béton, posé sur plots élastiques, dissocié des bâtiments. La fréquence propre de l'assemblage obtenu est alors très largement inférieure aux vitesses en utilisation normale du banc.

3.1.2. La chaîne aéraulique est en boucle ouverte (fig.9). A l'amont du compresseur elle comporte :

- a) Une cheminée d'aspiration garnie de panneaux filtrants et une batterie de silencieux acoustiques. Elle débouche, sur le local banc, dans une chambre de tranquillisation.
- b) Une manche d'entrée, propre au compresseur, placée symétriquement dans le plan vertical de la chambre de tranquillisation.

A l'aval du compresseur le circuit de refoulement comprend : a) une manche de sortie fixe, b) une conduite de raccordement munie d'une manchette élastique qui amortit les vibrations et absorbe les dilatations, c) une conduite de sortie qui comporte une vanne d'urgence et un registre de réglage du débit, d) un conduit collecteur qui débouche dans une cheminée d'évacuation avec un joint gonflable pour assurer l'étanchéité. En effet, la conduite de sortie est mobile pour permettre son adaptation en fonction de la position relative de la volute de la maquette par rapport à une conduite munie d'un venturi interchangeable en fonction des gammes de débit à mesurer et d'un silencieux d'évacuation.

Des éléments annexes permettant de recueillir les mesures électriques de température et de pression sont implantés sur le site.

### 3.2. - Moyens de mesures

Ces moyens sont regroupés dans le local de mesure. Celui-ci est protégé mécaniquement et acoustiquement. Il est isolé des vibrations à l'aide d'une dalle sur plots élastiques et l'alimentation électrique des appareils passe par un transformateur d'isolement.

Les mesures de surveillance mécanique, vibrations, contraintes et températures sont sous contrôle manuel constant de l'opérateur de banc. Les mesures aérodynamiques sont effectuées à l'aide d'un calculateur associé à des périphériques.

3.2.1. Mesures stationnaires : ce sont d'une part les mesures permettant la caractérisation globale de la maquette, d'autre part celles obtenues par des sondes introduites dans différents plans de mesure prédéterminés. Les sondes utilisées pour le compresseur "ECL 3" sont de deux types : sonde de type "cylindrique" et sonde de type "cobra" (fig.10). La première permet d'obtenir une bonne qualité des mesures près de la paroi carter car le diamètre de sonde est identique au diamètre de l'orifice de passage. La distance de l'extrémité de sonde au plan de mesure des pressions ne permet pas de mesurer au moyeu. Inversement, la sonde "cobra" permet cette approche mais reste imprécise au carter. Ces sondes sont donc utilisées complémentaires, ce qui permet en outre un recoupement des résultats dans les zones éloignées des parois. Les valeurs obtenues sont l'angle absolu de l'écoulement grâce aux pressions directionnelles gauche et droite, la pression d'arrêt, la température d'arrêt et la pression statique. Cette dernière est lue directement pour la sonde "cobra" ou déduite de l'étalonnage des pressions directionnelles pour la sonde "cylindrique". Les sondes sont télécommandées depuis le local de mesures par l'intermédiaire de chariots porte-sonde assurant la rotation et le déplacement radial, eux-mêmes pouvant être mis en place sur des chariots de déplacement azimutal.

3.2.2. Mesures instationnaires : Elles permettent, soit des mesures de pressions statiques pariétales, soit du champ de vitesse dans la machine. Les mesures effectuées par anémométrie laser ne perturbent pas l'écoulement, donc sont aptes aux explorations près des parois et dans des veines de dimensions réduites, d'autre part elles autorisent des mesures dans les éléments mobiles, en particulier dans les passages inter-aubes. On obtient alors le champ de vitesse par la méthode dite "à temps de vol" à l'aide d'un anémomètre à 2 points (fig.11) étudié et réalisé à l'Ecole Centrale de Lyon (système optique et électronique). 6 hublots de verre ont été implantés dans le carter externe du compresseur afin de mettre en oeuvre l'anémométrie laser suivant 9 axes de visée différents (fig.12).

Le compresseur ECL3 compte aujourd'hui environ 200 h de rotation à l'Ecole Centrale de Lyon et un certain nombre de résultats expérimentaux ont été acquis.

#### 4 - RESULTATS DES PREMIERS ESSAIS

##### 4.1. - Performances globales

Les essais ont été réalisés avec un calage fixe de la roue directrice d'entrée. Le champ de caractéristiques débit standard - rapport de pression est représenté en variables réduites sur la figure 15. Ce champ a été obtenu avec un jeu très faible en sommet de l'aube mobile (de l'ordre de 0.2 mm). On remarque que, sur la ligne de fonctionnement et à la vitesse de rotation nominale le débit projet est obtenu à 1% près. La marge par rapport au pompage est de 15%. On observe, sur l'isovitesse de rotation nominale, un rendement maximal de 0.86.

L'analyse détaillée de l'écoulement montre qu'un certain nombre de modifications permettrait d'accroître cette valeur (vrillage des aubes de la roue directrice d'entrée, adaptation plus fine du redresseur aux écoulements secondaires délivrés par le rotor.

##### 4.2. - Etude de l'écoulement

L'écoulement en un point de fonctionnement situé sur l'isovitesse nominale a été caractérisé par des mesures de pression totale, de température totale et de direction du vecteur vitesse dans les plans 1, 2 et 3 (cf. fig.1). Afin de valider notre méthode de calcul d'écoulements secondaires visqueux [12], on a réalisé un couplage du calcul de l'écoulement méridien avec ladite méthode de calcul d'écoulements secondaires. Bien entendu, seules les données expérimentales de la zone "saine", non perturbée par les écoulements secondaires visqueux, sont introduites dans le calcul méridien. La comparaison théorie-expérience se fait dans les zones pariétales de moyeu et de carter (fig. 14 à 17). On remarque que le recoupement calcul-mesures est satisfaisant sauf dans la zone de carter à l'aval de la roue mobile où la prédiction théorique donne des phénomènes secondaires trop accentués ; en particulier, les accroissements de température calculés sont un peu trop forts. Ces mesures seront donc utilisées pour améliorer la schématisation des écoulements secondaires, notamment dans les rotors supersoniques.

#### 5 - CONCLUSIONS

la SNECMA, en collaboration avec l'Ecole Centrale de Lyon, s'est dotée de moyens expérimentaux pour étudier l'aérodynamique des étages de tête de compresseurs haute pression avancés qui ont des nombres de Mach relatifs élevés à l'amont du rotor :

- Un étage réalisant un rapport de pression de 1.84 et ayant des nombres de Mach relatifs à l'amont du rotor compris entre 1.1 et 1.3, a été réalisé et essayé sur un banc construit à cet effet par l'Ecole Centrale de Lyon. Les objectifs en marge au pompage et en débit ont été atteints. Le rendement maximal est satisfaisant (0.86) mais il peut être amélioré en adaptant plus précisément le redresseur aux écoulements secondaires délivrés par le rotor.

- Les caractérisations précises de l'écoulement par des sondages de pression et température sont en cours. Des essais de vélocimétrie LASER suivront. Ces données expérimentales permettront de mettre au point les codes de calcul des écoulements secondaires dans les compresseurs supersoniques. Les premières tentatives présentées laissent bien augurer des capacités du code de calcul.

REMERCIEMENTS

Nous remercions MM. J.BROCHET, J.R.L.BARTON et les techniciens, notamment P.MOREAU, qui ont participé à la conception et à l'analyse des résultats d'essais du compresseur ECL 3.

Les travaux décrits dans cet article ont été réalisés grâce au soutien de la Direction des Recherches, Etudes et Techniques du Ministère de la Défense.

REFERENCES

- [1] NASA "Aerodynamic Design of Axial - Flow Compressors (Revised)" NASA-SP-36 1965
- [2] J.NAVILLE - Prédiction de performances d'aubages des compresseurs à divers régimes de fonctionnement au moyen de corrélations" - Thèse C.N.A.M. - 1983
- [3] G.MELLOR, G.WOOD, "An Axial End-wall Boundary Layer Theory" ASME. Journal of Basic Engineering vol.93, 1971, pp 200-216
- [4] F.LEBOEUF, A.COMTE, K.D.PAPAILIOU "Calculation Concerning the Secondary flows in a Compressor Bladings" - AGARD CP-214, La Haye, 1977, paper 2
- [5] H.VIVIAND, J.P.VEUILLLOT. "Méthodes pseudo-instationnaires pour le calcul d'écoulements transsoniques" - ONERA - Publication 1978-4
- [6] J.BROCHET. "Calcul numérique d'écoulements internes tridimensionnels transsoniques" La recherche aérospatiale, vol.5, sept. 1980, pp 301-315
- [7] T.DERRIEN. "Calcul tridimensionnel dans les aubages de compresseurs munis de nageoires" AGARD. 68th (B) Symposium of the propulsion and energetics panel, 1986 CPP 400/401, Conférence n°14
- [8] G.KARADIMAS. "Calcul analytique des grilles d'aubes" - 7ème colloque d'Aérodynamique Appliquée de l'AFITAE - Lyon 4/6 Nov.1970
- [9] T.S.LUU, G.MONFORT. "Blade-to-Blade transsonic flow calculation in axial turbomachines" Sixth International Symposium on Air Breathing Engines (ISABE)
- [10] K.D.PAPAILIOU. "Optimisation des dispositifs décélérateurs à forte charge fondée sur une théorie intégrale de la couche limite" - Thèse de Doctorat ès Sciences, Université de Lyon I, 1974
- [11] G.M.ASSASSA. "Calcul par des méthodes intégrales de couches limites laminares ou turbulentes incompressibles ou compressibles incluant des zones faiblement décollées" Thèse de doctorat ès Sciences, Université de Lyon I, 6 Mai 1976.
- [12] F.FALCHETTI, J.BROCHET. "Calcul des Ecoulements secondaires dans un compresseur multi-étages" AGARD - 69 th Symposium of the propulsion and energetics panel PARIS, 4,8 mai 1987, Conférence n°40



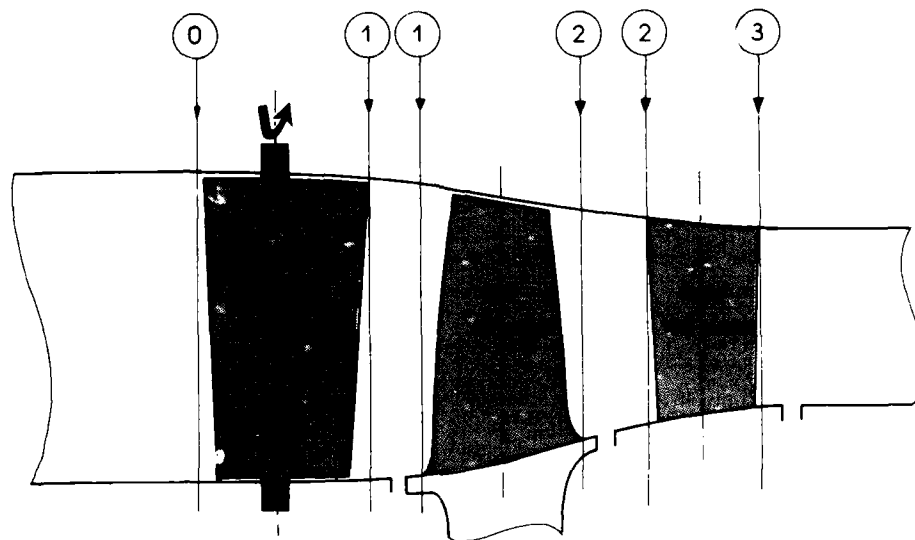


FIG.1 COUPE MERIDIENNE DU COMPRESSEUR "E.C.L.3"

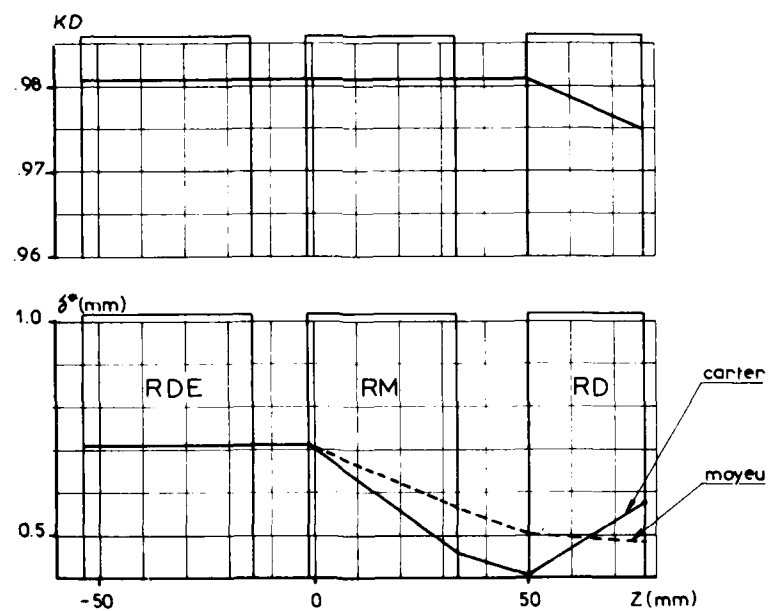


FIG.2 EVOLUTION DU COEFFICIENT D'OBSTRUCTION (KD)  
ET DES EPAISSEURS DE DEPLACEMENT ( $\delta^*$ )  
DES ZONES VISQUEUSES DE MOYEU ET DE CARTER

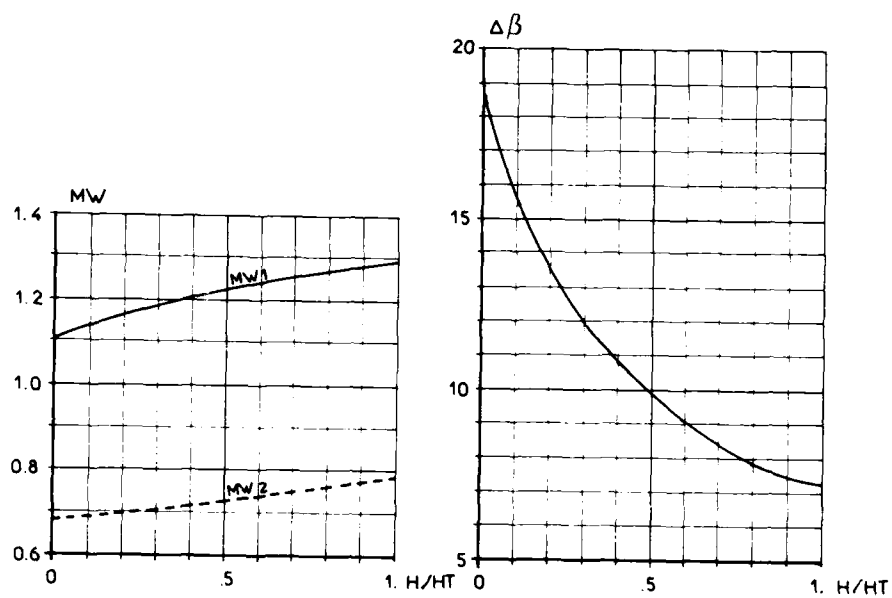


FIG. 3 NOMBRES DE MACH RELATIFS ET DEVIATIONS DANS LA ROUE MOBILE

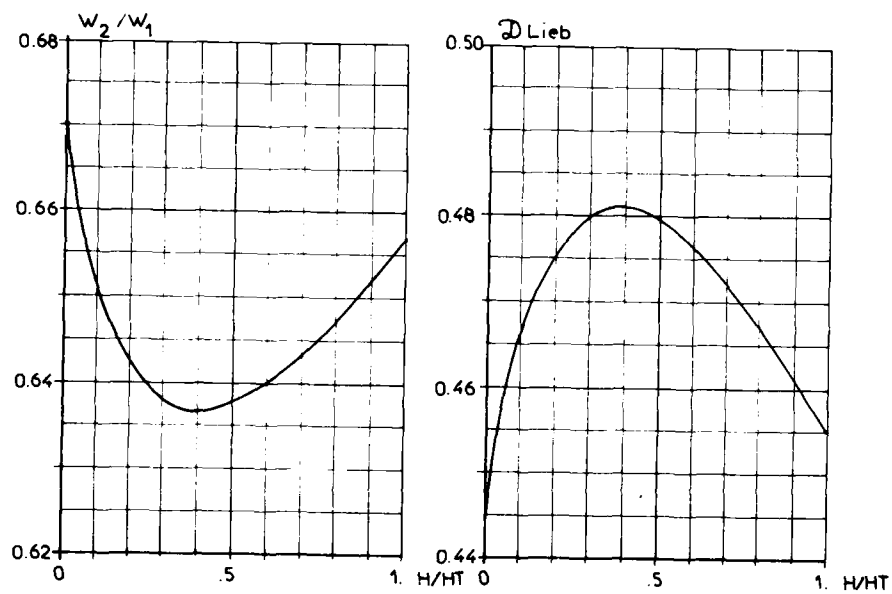


FIG. 4 RALENTISSEMENTS ET FACTEURS DE DIFFUSION DE LIEBLEIN DE LA ROUE MOBILE

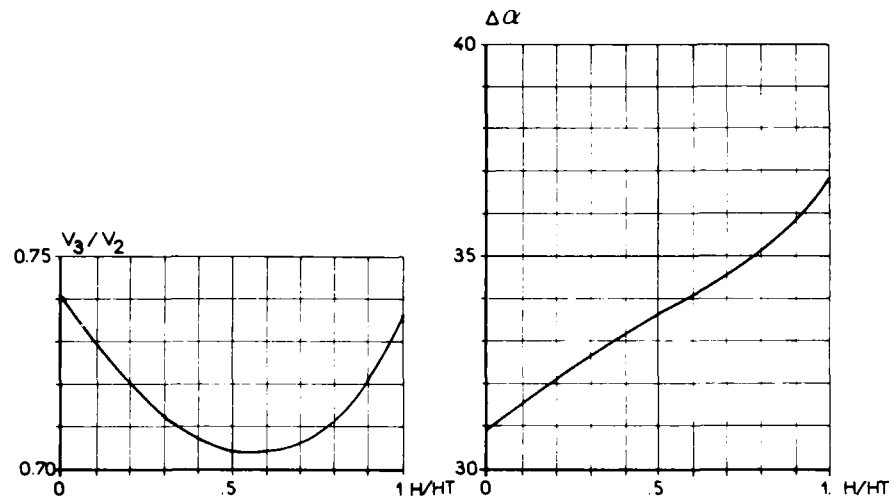


FIG. 5 RALENTISSEMENTS ET DEVIATIONS DE L'ÉCOULEMENT  
VU PAR LE REDRESSEUR

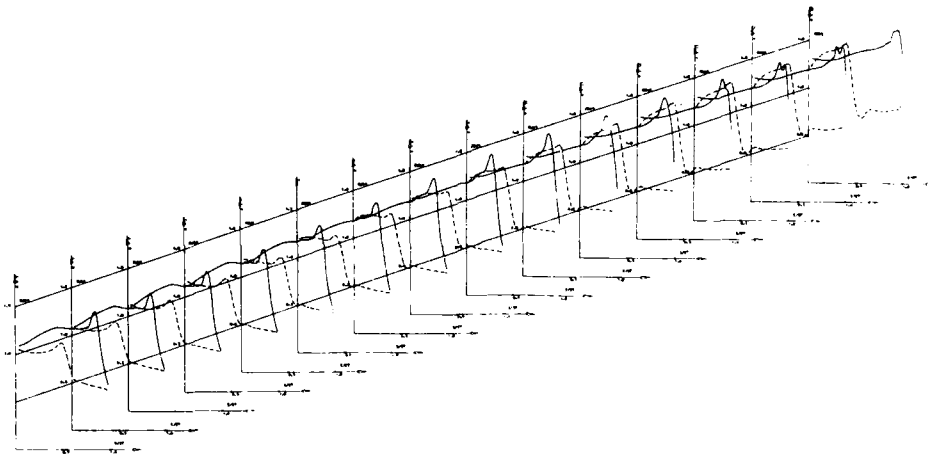


FIG. 6 CALCUL 3D SUR LA ROUE MOBILE  
REPARTITIONS DU NOMBRE DE MACH SUR L'EXTRADOS  
ET L'INTRADOS

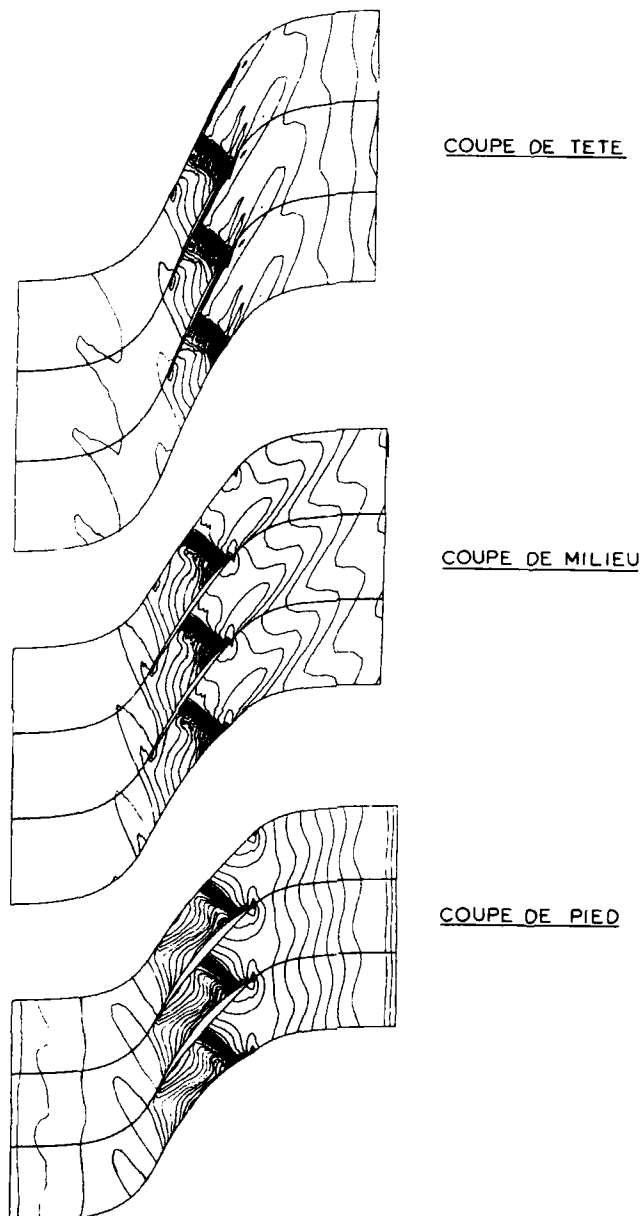


FIG. 7g      CALCUL 3D SUR LA ROUE MOBILE  
VISUALISATION DES LIGNES ISO-NOMBRE DE MACH

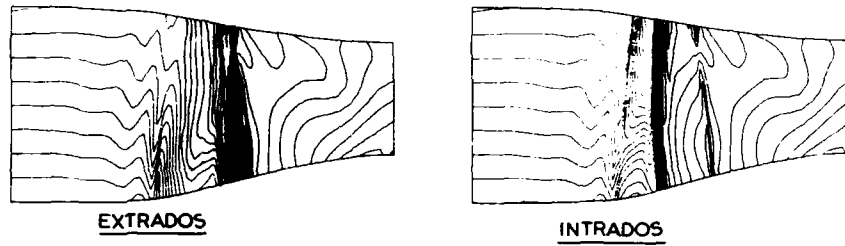


FIG. 7b CALCUL 3D SUR LA ROUE MOBILE  
VISUALISATION DES LIGNES ISO-NOMBRE DE MACH

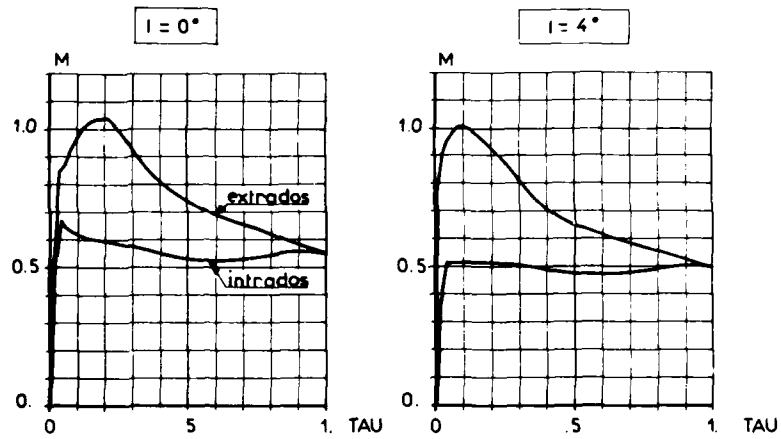


FIG. 8a PROFIL DE PIED DU REDRESSEUR  
REPARTITION EXTRADOS ET INTRADOS DU NOMBRE DE MACH

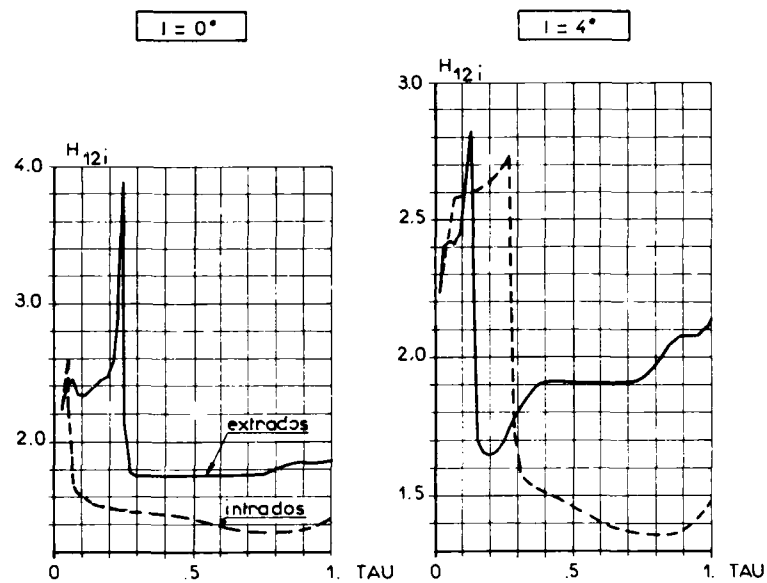


FIG. 8b PROFIL DE PIED DU REDRESSEUR  
FACTEUR DE FORME DES COUCHES LIMITES DU PROFIL

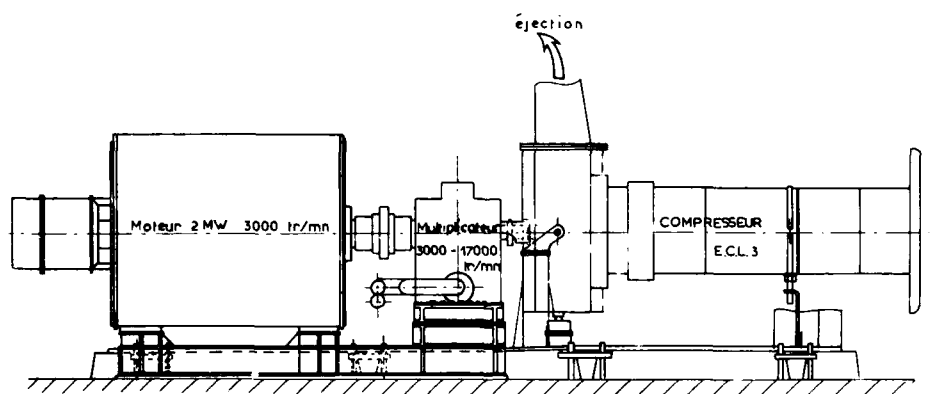


FIG. 9 SCHEMA DU BANC D'ESSAIS DU COMPRESSEUR E.C.L. 3

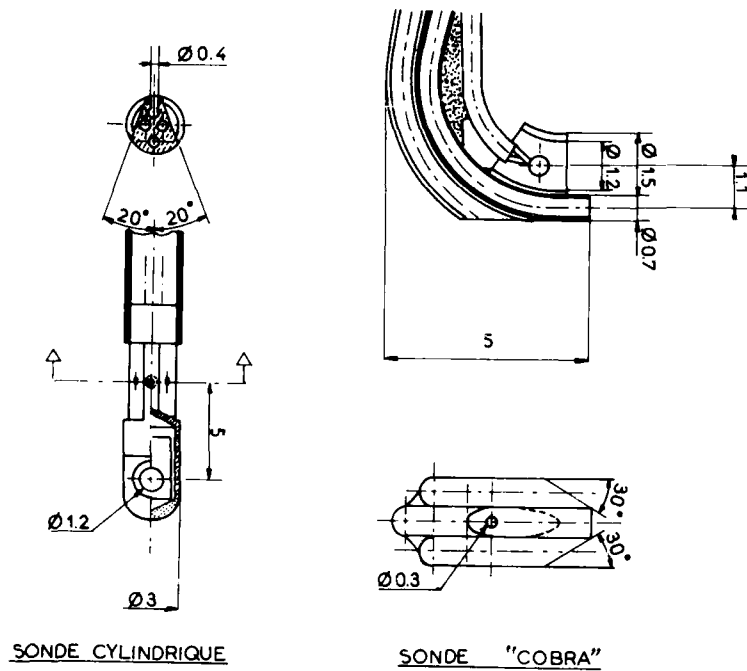


FIG: 10

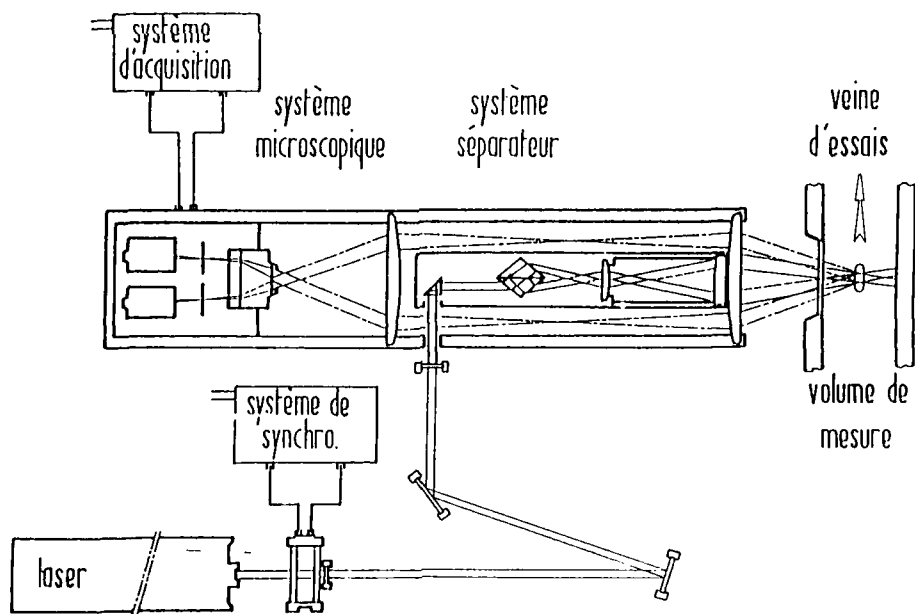


FIG. 11 SCHEMA DE LA NOUVELLE CHAÎNE OPTIQUE DE L'ANEMOMETRE LASER

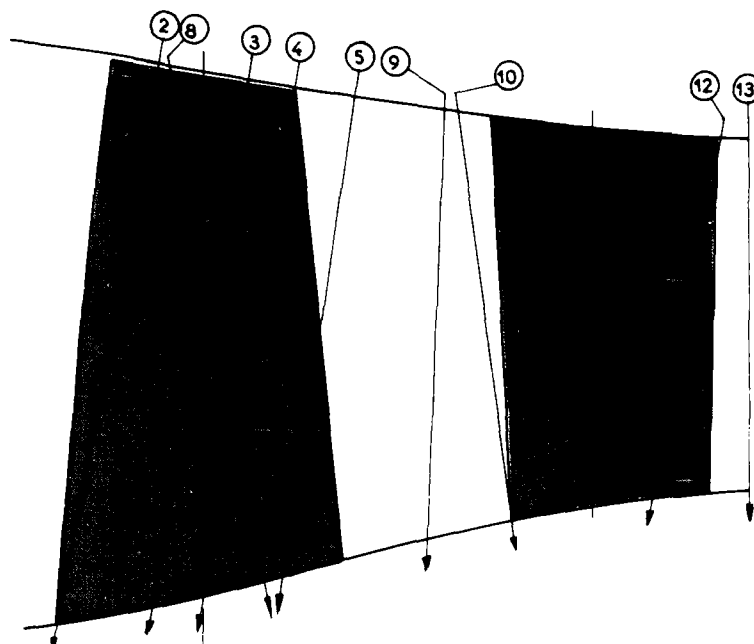


FIG: 12 AXES DE VISEE DES HUBLOTS DE VELOCIMETRIE LASER

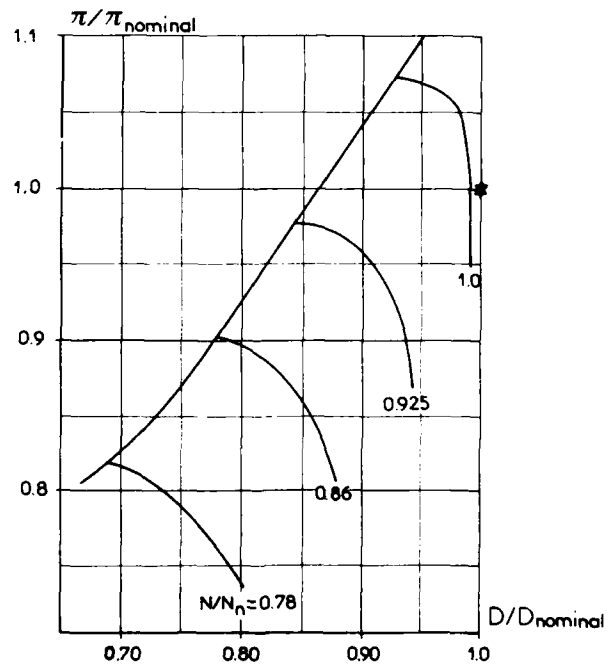
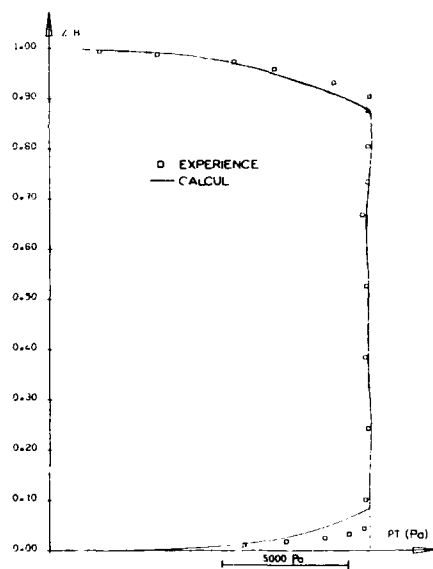
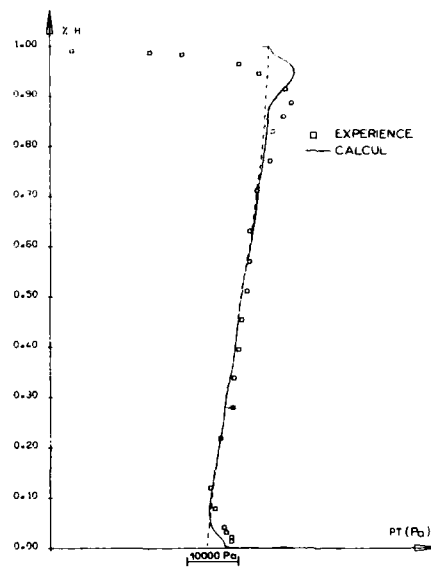


FIG: 13 CHAMP DE CARACTERISTIQUES EXPERIMENTAL  
DEBIT - RAPPORT DE PRESSION



## DISTRIBUTIONS RADIALES

$$N/N_h = 1. \quad \pi = 1.904$$

FIG. 14 PRESSION D'ARRET ABSOLUE  
AVAL RDEFIG. 15 PRESSION D'ARRET ABSOLUE  
AVAL RM

## DISTRIBUTIONS RADIALES

$$N/N_h = 1. \quad \pi = 1.904$$

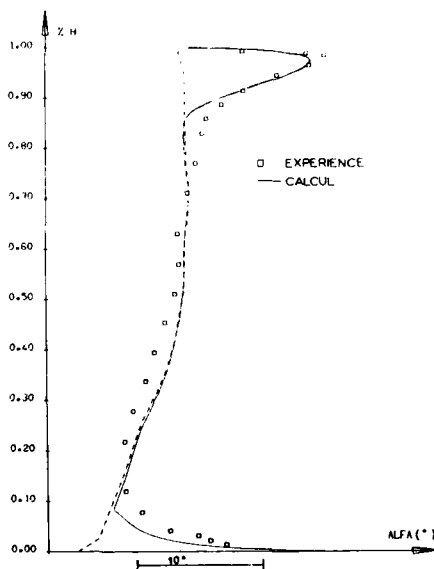
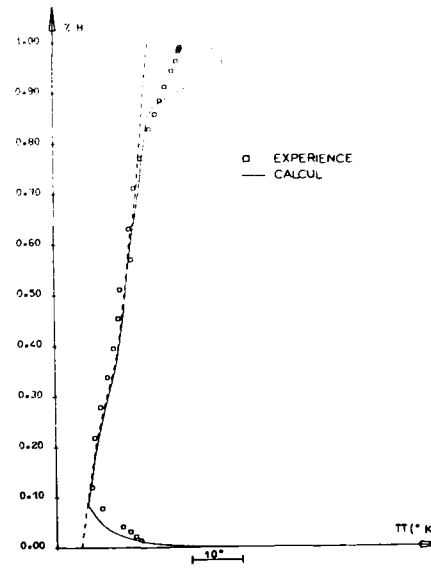


FIG. 16 ANGLE ABSOLU AVAL RM

FIG. 17 TEMPERATURE D'ARRET ABSOLUE  
AVAL RM

## DISCUSSION

R.G. THOMPSON, US

What was the motivation to design a high hub ratio compressor ?  
Normally one would employ lower hub ratio to lower the relative Mach numbers, into the rotor.

### Author's Reply

In the design of core engine with multi-stage high pressure compressor, there are some technological and structural limitations in increasing rotational speed and lowering hub radius on the front stages. Moreover, if one wants to obtain high pressure ratio per stage, particularly on the hub region, it is necessary to have sufficient hub speed and so that hub-to-tip ratio cannot be significantly lowered.

We also point out that this work is mainly devoted to the design process for supersonic rotors and to the analysis of secondary flows. It is not a complete study of a multi-stage HP compressor.

F. BREUGELMANS, Be

- 1) A des nombres de Mach compris entre 1.1 et 1.2, l'onde de choc dans le rotor est détachée et est relativement normale à l'extrados de l'aube. Elle se propage donc loin en amont et peut interférer avec le bord de fuite du pré-distributeur. Est-ce qu'il y a eu des considérations de ce genre pour déterminer la distance axiale entre le pré-distributeur et le rotor ?
- 2) S'attend-on à des problèmes de fonctionnement du rotor supersonique quand on fera varier le calage de la pale du pré-distributeur ?

### Réponse de l'Auteur

1) La distance axiale entre la roue directrice d'entrée et le rotor a été choisie pour pouvoir effectuer correctement des sondages et de la vélocimétrie LASER. Aucune considération relative à la propagation des ondes de choc issues du rotor n'est intervenue.

2) Le calage des aubes de la roue directrice d'entrée peut être modifié en fonction de la vitesse de rotation étudiée. Il n'est pas prévu de fixer la vitesse de rotation et de "piloter" le compresseur en agissant sur le calage des aubes de la roue directrice d'entrée.

Les aubes ont été optimisées à la vitesse de rotation maximale. Aux faibles vitesses de rotation, l'écoulement est subsonique relativement au rotor, et on ne s'attend donc pas à des problèmes de fonctionnement. Le problème se posera peut-être aux régimes intermédiaires (90 %). A l'heure actuelle, nous n'avons pas fait d'essais à différents calages de la roue directrice d'entrée.

## EXPERIMENTAL INVESTIGATION OF A SUPERCRITICAL COMPRESSOR ROTOR BLADE SECTION

by  
 R. Fuchs, R. Kaymaz, H. Starken, W. Steinert  
 Institut für Antriebstechnik  
 DFVLR  
 Linder Höhe  
 D 5000 Köln 90  
 W.-Germany

## SUMMARY

A controlled diffusion rotor blade section was designed for a supercritical inlet Mach number of  $M_1=0.85$  and a flow turning of  $20^\circ$ . The blade section has been tested in a cascade wind tunnel under various inlet flow conditions and axial velocity density ratios. Detailed investigation about transition and separation points were carried out at the design and at two off design inlet flow conditions. The results are presented and discussed.

## NOMENCLATURE

$c$ = chord	$\delta_1$ = boundary layer displacement thickness
$H_{12}$ = shape factor $\delta_1/\delta_2$	$\delta_2$ = boundary layer momentum thickness
$M_{12}$ = Mach number	$\omega$ = total pressure loss coefficient = $(p_{t1}-p_{t2})/(p_{t1}-p_1)$
$p$ = static pressure	$\Omega$ = axial velocity density ratio (AVDR)
$p_t$ = total pressure	
$t/c$ = pitch to chord ratio	
$x$ = coordinate in chordwise direction	
$\eta$ = coordinate in circumferential direction	
$\beta$ = flow angle with reference to circumferential direction	
$\beta_s$ = stagger angle with reference to circumferential direction	

## SUBSCRIPTS

1 = inlet plane  
 2 = outlet plane

## 1. INTRODUCTION

In recent years considerable improvement has been achieved in the design of axial flow turbomachines by making use of numerical blade design methods [1,2,3,4]. Different names have been used like "custom tailoring", "controlled diffusion" or "prescribed velocity distribution" to characterize these designs. A similar concept has been developed in the "Institut für Antriebstechnik of the DFVLR" in Cologne in cooperation with the "Institut für Aerodynamik und Gasdynamik" of the University of Stuttgart. In Cologne the compressor blade surface Mach number distribution has been optimized by application of boundary layer calculations and cascade tests [5,6,7], whereas in Stuttgart the required inverse design code has been established [8,9].

This method has been applied in the past mainly for stator blade sections [10,11]. But there is also a big interest in the improvement of rotor blade sections, especially at supercritical operating conditions. Therefore a research program was initiated by the German gas turbine industry and carried out in Stuttgart and Cologne in order to develop a supercritical blade section with low losses and large operating range with respect to the inlet flow angle.

This paper describes the experimental cascade test results of the blade section

- SKG-FVV 3.3 developed within this program. The aim of the experiments was
- to check the design code and the direct code, used to develop the blade section, by measuring surface Mach numbers, losses and turnings. This is published in [12,13].
  - to check the boundary layer calculation by measuring transition and separation points.
  - to identify the reason for the loss rise at high inlet Mach numbers.
  - to identify the reason for the loss rise at high and low inlet flow angles.

## 2. EXPERIMENTAL SET UP

## 2.1 CASCADE WIND TUNNEL

The DFVLR transonic cascade wind tunnel is a continuously running facility operating in a closed cycle driven by two radial flow compressors with a flow capacity of  $10\text{ m}^3/\text{s}$  each. One of these compressors is connected to the suction system which is used to reduce the upstream side wall boundary layer through protruding slots and to vary the axial velocity density ratio via slotted side walls. The pressure ratio of four renders possible a Mach number range from 0 to 1.4 and a variation of the axial velocity density ratio even at supersonic inlet velocities.

The cascade span is 168mm and the cascade height can be varied between 150mm and 450mm. Fig. 1 shows a cross section of the tunnel.

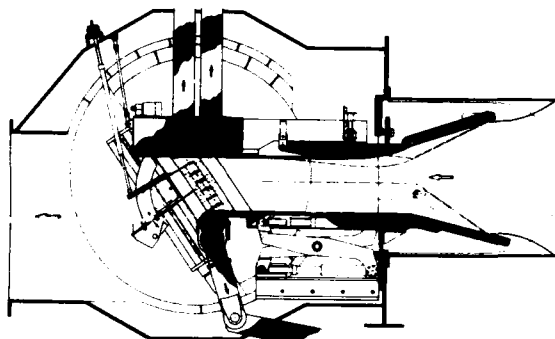


Fig. 1 Cross sectional view of the transonic cascade wind tunnel of the DFVLR-Institut für Antriebstechnik

The blades are mounted between plexiglass windows in the rotatable side walls of 2m diameter. By turning the side walls the inlet flow angle  $\beta_1$  is adjusted before running the wind tunnel. The upper floor is fixed and carries the variable half nozzle. The bottom floor can be moved horizontally and vertically to adjust the geometry of the bottom by-pass passage.

Inlet total pressure and temperature were measured in the settling chamber. In a plane half a gap axially upstream of the leading edges the inlet static pressure was measured ahead of the center blades at one side wall (Fig. 2). In the same plane (measuring plane I) the periodicity of inlet velocity and inlet flow angle was checked by three flow angle probes.

In a plane half a gap axially downstream of the trailing edges the total pressure, static pressure and flow angle distribution were measured by moving a combined probe stepwise over slightly more than one blade pitch at cascade midspan. The traversing system provides rotation around the upstream probe head for angle measurements.

The effect of variation of the axial velocity density ratio in the cascade midspan by suction through slotted side walls is shown in Fig. 3.

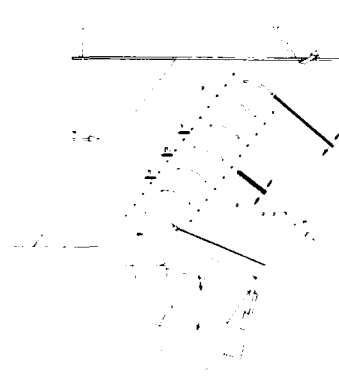


Fig. 2 Test section arrangement with measurement positions

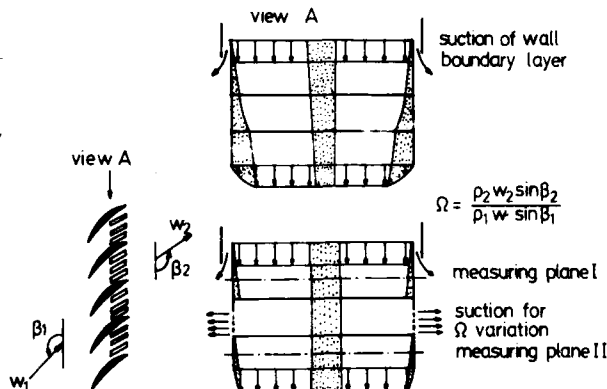


Fig. 3 Test section cross view without (top) and with (bottom) boundary layer suction on the side walls

The design geometry and flow data of the cascade SKG-FVV 3.3 are:

inlet Mach number	$M_1=0.85$	
inlet flow angle	$\beta_1=142.0^\circ$	with reference to circumferential direction
outlet flow angle	$\beta_2=122.0^\circ$	"
stagger angle	$\beta_2=129.8^\circ$	"
pitch-chord ratio	$t/c=1.0$	
AVDR	$\Omega=1.15$	

Six blades of 70mm chord length have been installed in the wind tunnel. The third blade was equipped with 16 pressure taps on the suction side and the fourth blade with 14 pressure taps on the pressure side in such a way that the flow in one blade passage could be recorded.

## 2.2 TEST PROGRAM

The inlet flow angle  $\beta_1$  was varied from  $138^\circ$  to  $145^\circ$  and the AVDR from 1.0 to 1.2. The Mach number was varied from 0.60 to 0.88 at the design inlet angle  $142^\circ$  only. The other inlet angles were tested at the design Mach number 0.85 only.

It has to be remarked that instead of the design Mach number 0.85 in the experiments a reduced Mach number of 0.84 was adjusted. The reason for that is the flow acceleration between the measuring plane I (Fig. 2), where  $M_1$  was determined, and the cascade inlet plane due to growing side wall boundary layers.

## 2.3 VISUALIZATION OF BOUNDARY LAYER BEHAVIOUR ON PROFILE SURFACES

Three methods have been used for boundary layer visualization on the profile surfaces: the azobenzene sublimation method, the ink tracing method and the surface oil flow technique. The pictures produced by these methods give information of:

- the laminar separation bubble
- the secondary flow pattern
- the backflow in separated areas
- wedges of turbulent flow by isolated excrescences

The great advantage of these methods is in giving information not only point by point but also over the whole profile surface area, especially in case of the azobenzene- and the oil surface technique. This is of importance for the knowledge of the transition line position, which is influenced a great deal by local disturbances causing turbulent wedges.

In the ink tracing method coloured ink is introduced into the profile surface boundary layer through one or more profile pressure taps. By this method boundary layer separation can be detected. But it is difficult to analyse turbulent reattachment after laminar separation in the front part of the blade. In this case a second test run may be performed by introducing ink into a pressure tap further downstream. Alternatively ink of different colour may be released out of several pressure taps.

The second technique is a method of sublimation [14]. The model is sprayed by a mixture of azobenzene and gasoline. Spray distance should be large enough to enable evaporation of gasoline before coating the profile and bonding of the small parts of azobenzene on the profile surface. By that surface roughness is low enough to avoid natural transition. Visualization of the transition line works by quicker sublimation of azobenzene in the turbulent boundary layer region because mixing is more intensive.

The third method used is the surface oil flow technique [15]. The coating material is a mixture of oil, titanium dioxide ( $\text{TiO}_2$ ) and oleic acid. The proportions of the mixture depend on flow Mach number and total pressure level. The proportions for the tests presented are: oil (g) :  $\text{TiO}_2$  (g) : oleic acid (drops) = 1 : 1 : 1. Oil in use was Shell Carnea 460.

## 3. EXPERIMENTAL RESULTS

### 3.1 TOTAL PRESSURE LOSSES VERSUS INLET MACH NUMBERS

The variations of the total pressure loss coefficient for various inlet Mach numbers and three different inlet flow angles are presented in Fig. 4.

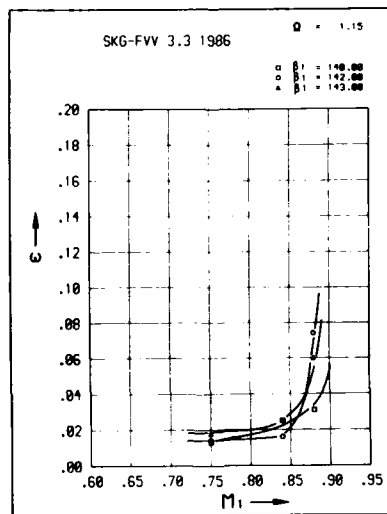


Fig. 4 Loss coefficient versus inlet Mach number at three different inlet flow angles

Looking first at the design inlet flow angle  $\beta_1 = 142^\circ$ , very low values of loss coefficient  $\omega$  not much more than 1% up to the experimental design Mach number  $M_1 = 0.84$  can be seen. If the Mach number exceeds 0.85 the losses increase rapidly. The same increasing tendency is shown in Fig. 4 for the lower and higher inlet flow angles.

An explanation for this characteristic increase can be given by Fig. 5. This figure presents the surface profile Mach number distribution for the three Mach numbers of Fig. 4  $M_1 = 0.75$  (top left), 0.84 (top right), 0.88 (bottom) and  $\beta_1 = 142^\circ$ . Under each Mach number curve the loss coefficient distribution is shown, which was measured close behind the cascade exit plane (measuring plane II Fig. 2). In case of the low Mach number  $M_1 = 0.75$  as well as at the design Mach number  $M_1 = 0.84$  a very small and narrow wake is to be seen. That means no boundary layer separation occurred and the losses are therefore extremely low.

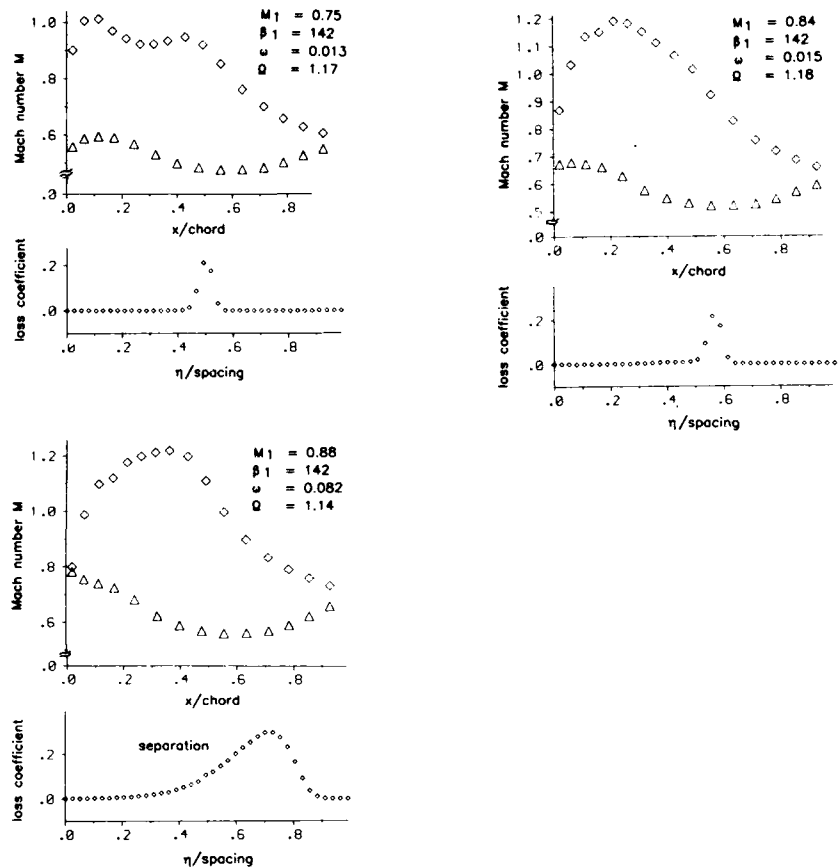


Fig. 5 Profile Mach number and loss distribution in the cascade outlet plane at three different inlet Mach numbers

In contrast to this the bottom part of Fig. 5 shows a large wake mainly widened towards the suction side. In this case the higher Mach number  $M_1 = 0.88$  leads to an increasing maximum Mach number on the suction surface, followed by an increasing deceleration which is realized by a compression shock. The shock strength obviously leads to shock induced separation and therefore to high total pressure losses.

On the other hand, the measured suction surface Mach number distribution downstream of the shock position at 50% of the profile length shows no region of constant Mach number due to separation rather than a continuous deceleration.

### 3.2 LOSSES VERSUS INLET FLOW ANGLE

In Fig. 6 the loss characteristics are shown for inlet flow angle variations at design Mach number and two different axial velocity density ratios (AVDR). Loss minimum can be found at design condition  $\beta_1 = 142^\circ$  and at slightly negative incidence angles. The low loss incidence range is quite small and the losses increase steeply at lower and higher inlet flow angles.

Two loss curves are presented for AVDRs  $\Omega=1.15$  and  $1.05$ . Both curves are of similar increasing character in the positive as well as in the negative range. The loss curve is shifted to higher inlet flow angles with increasing AVDR. At positive incidences this phenomenon is caused by a decreased suction surface diffusion and at negative incidences by an increased supersonic diffusion.

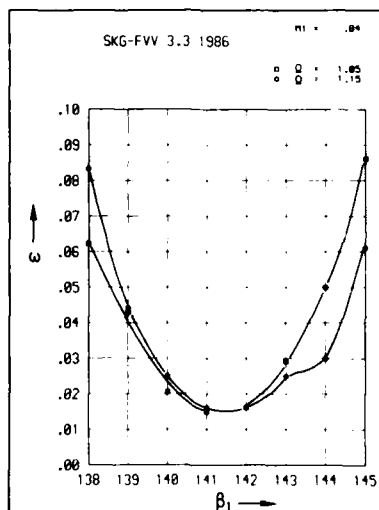


Fig. 6 Cascade losses versus inlet flow angle at design inlet Mach number and two different AVDRs

### 3.3 BOUNDARY LAYER BEHAVIOUR

The intent of the boundary layer investigation was to find out the reason for the loss increase at high and low inlet flow angles, respectively high positive and negative incidences. Therefore, three different flow cases have been selected and the methods described in chapter 2.3 have been applied. The flow cases are the design point condition at  $\beta_1=142^\circ$  and the off-design conditions at  $\beta_1=138^\circ$  and  $\beta_1=145^\circ$ , the latter of which are the minimum and maximum measured inlet flow angle.

#### 3.3.1 THEORETICAL PREDICTIONS

With the inviscid-viscous interaction method, described in [12,13] (flux finite element method coupled with McNally integral boundary layer method) the boundary layer has been calculated. In table 1 the predicted positions of the transition and separation points are presented for both blade surfaces. As free stream turbulence level the measured value of 2.3% has been used.

At  $\beta_1=138^\circ$  laminar turbulent transition is calculated at 52% of chord followed by a shock induced turbulent separation at 63% on the suction surface. At the design incidence, transition is predicted at 29% with no separation and at  $\beta_1=145^\circ$  the transition moved further upstream to 17% followed by a shock induced separation at 27% of chord. On the pressure surface the transition point moves downstream from 10% to 28% of chord with increasing incidence and no separation was calculated in this incidence range.

inlet flow angle $\beta_1$	surface	transition x/c	separation x/c
138°	suction	0.52	0.63
	pressure	0.10	--
142°	suction	0.29	--
	pressure	0.21	--
145°	suction	0.17	0.27
	pressure	0.28	--

Table 1 Calculated transition and separation point positions (method described in [12,13])

### 3.3.2 MEASUREMENTS AT DESIGN INLET FLOW ANGLE ( $\beta_1=142^\circ$ )

The results of the azobenzene test are shown on the top of Fig. 7. The left picture shows the suction surface with the laminar-turbulent transition visible at 42% of chord which is different from the theoretical prediction at 29%. However, the ink test showed a laminar separation starting at 30% of chord along one half of the blade span.

This asymmetric picture is confirmed by the corresponding oil flow pattern shown in Fig. 7 (bottom), with the additional information of a laminar separation bubble ending around 42% of chord.

An explanation for this phenomenon is, that the boundary layer is just at the border of laminar separation and small differences either in inlet flow angle or turbulence level cause this effect. The transition point location, theoretically predicted near the point of laminar separation, seems to substantiate this assumption, although small differences between calculated and measured surface velocities may also be responsible for this.

On the pressure surface the azobenzene test and especially the oil flow pattern do not show a distinct transition point rather than a certain transition region between 22 to 34% of chord. This is in reasonable agreement with the theoretical prediction of 21%. From the ink test it can be concluded that no laminar separation bubble does exist on the pressure surface and that the turbulent boundary layer is not separated on both surfaces. The latter is confirmed by the low loss level of 1.5% measured at the design point.

### 3.3.3 MEASUREMENTS AT MINIMUM INLET FLOW ANGLE ( $\beta_1=138^\circ$ )

At this high loss level condition in Fig. 8 both the ink test as well as the oil flow pattern show a severe laminar flow separation at 45% of chord over the whole span of the suction surface. The theory predicts transition at 52% and a shock wave at 63% of chord followed by turbulent separation. The differences between theory and experiment are due to the fact that the prediction does not yet include the upstream influence of the shock boundary layer interaction leading to a lambda shock system. However, the surface Mach number distribution again does reveal the separation just as little as the shock wave. The shock wave pressure rise is smeared out and the separated flow exhibits a considerable pressure increase. A possible existence of flow reattachment was excluded by an additional test introducing ink out of a rear pressure tap into the separated region (Fig. 8, middle).

By releasing ink out of the first and the fourth pressure tap and applying the surface oil flow technique it was found that on the pressure side a very short laminar separation bubble existed just near the leading edge. After turbulent reattachment the boundary layer remained unseparated.

The theory did not reveal the measured suction peak, which is probably terminated by a shock wave, and predicted the transition point therefore at 10% of chord.

### 3.3.4 MEASUREMENTS AT MAXIMUM INLET FLOW ANGLE ( $\beta_1=145^\circ$ )

The theory predicted at this inlet flow angle transition at 17% and shock induced turbulent separation at 27% of chord on the suction surface. From the oil flow pattern in Fig. 9 (bottom) transition was observed between about 17 and 22%. It looks like a laminar separation bubble, but the ink test (Fig. 9, top) did not confirm this. It showed only a turbulent separation occurring at around 60% of chord. Due to instationary and secondary flow effects, especially at high incidences, the visualization results are not as distinct as in the other flow cases and spanwise variations are difficult to avoid. Nevertheless there is a clear difference between the measured and calculated separation point probably due to the separation criteria ( $H_{12}=2.5$ ) used within the shock interaction model.

Again from the blade Mach number distribution alone the turbulent boundary layer separation cannot be detected at all.

On the pressure surface, ink and oil flow pattern (Fig. 9) showed a transition region between 28 and 35% and no boundary layer separation. The transition prediction is in good agreement with the beginning of the transition region similarly as it was the case at design inlet flow angle.

## 4. CONCLUSION

The loss behaviour of a supercritical compressor rotor cascade has been investigated experimentally. The reason for the loss rise at high inlet Mach numbers and at high positive and negative incidences could be identified by analysing oil flow patterns, ink traces, and wake measurements.

In all cases early boundary layer separation, caused or influenced strongly by shock-boundary layer interactions, was observed on the blade suction side.

In spite of this, the surface pressure distributions showed a considerable pressure rise downstream of the separation point. Therefore, it is not possible in this Mach number range to detect a boundary layer separation using only the blade surface pressure distribution. The measured positions of transition and separation points are valuable information for the improvement of viscous codes. Comparisons with a viscous-inviscid interaction method are encouraging.



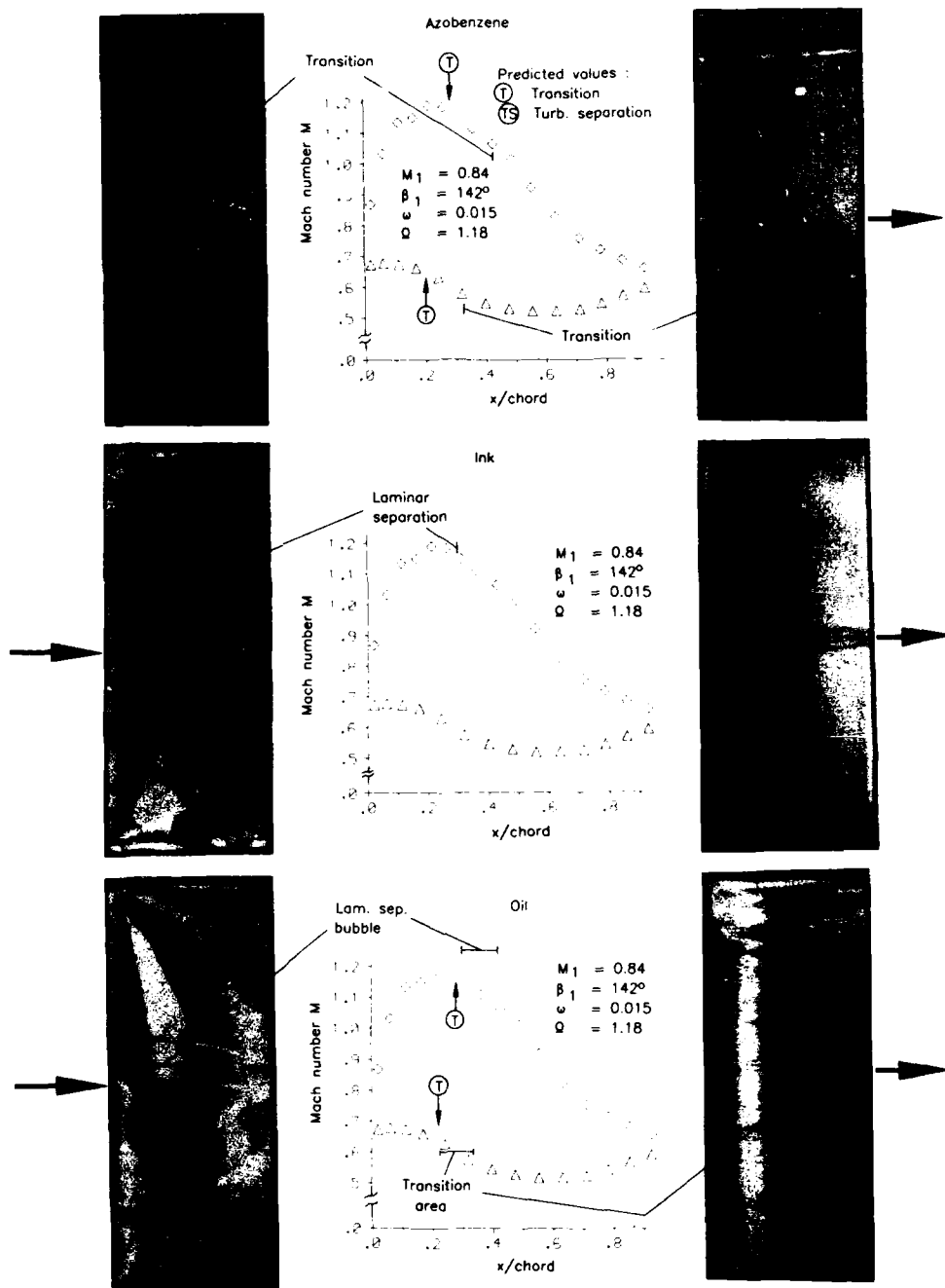


Fig. 7 Patterns of azobenzene (top), ink (middle) and oil (bottom) of suction side (left) and pressure side (right) together with profile Mach number distribution at  $\beta_1=142^\circ$

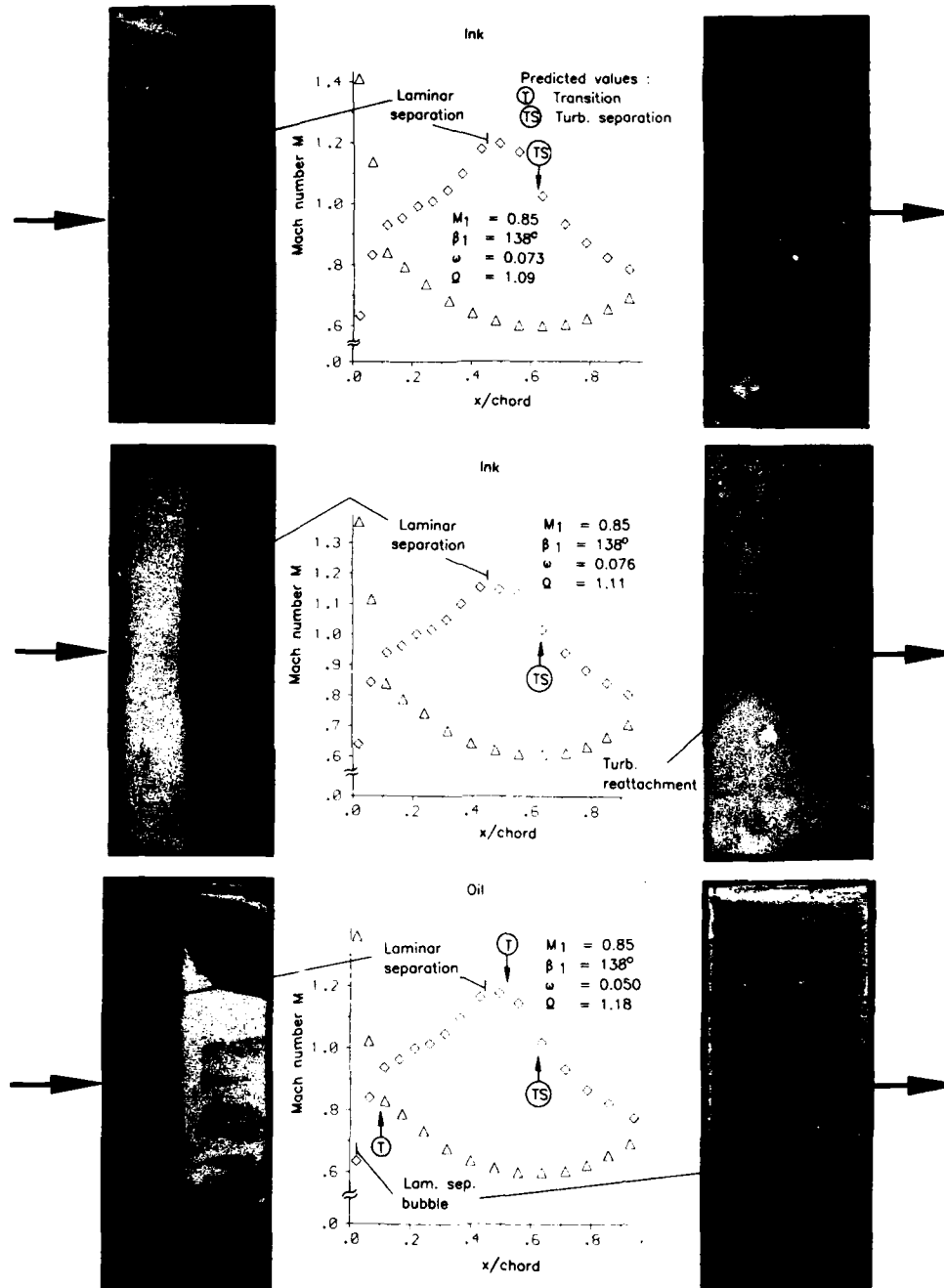


Fig. 8 Patterns of ink with front injection (top), rear injection (middle) and oil (bottom) of suction side (left) and pressure side (right) together with profile Mach number distribution at  $\beta_1 = 138^\circ$

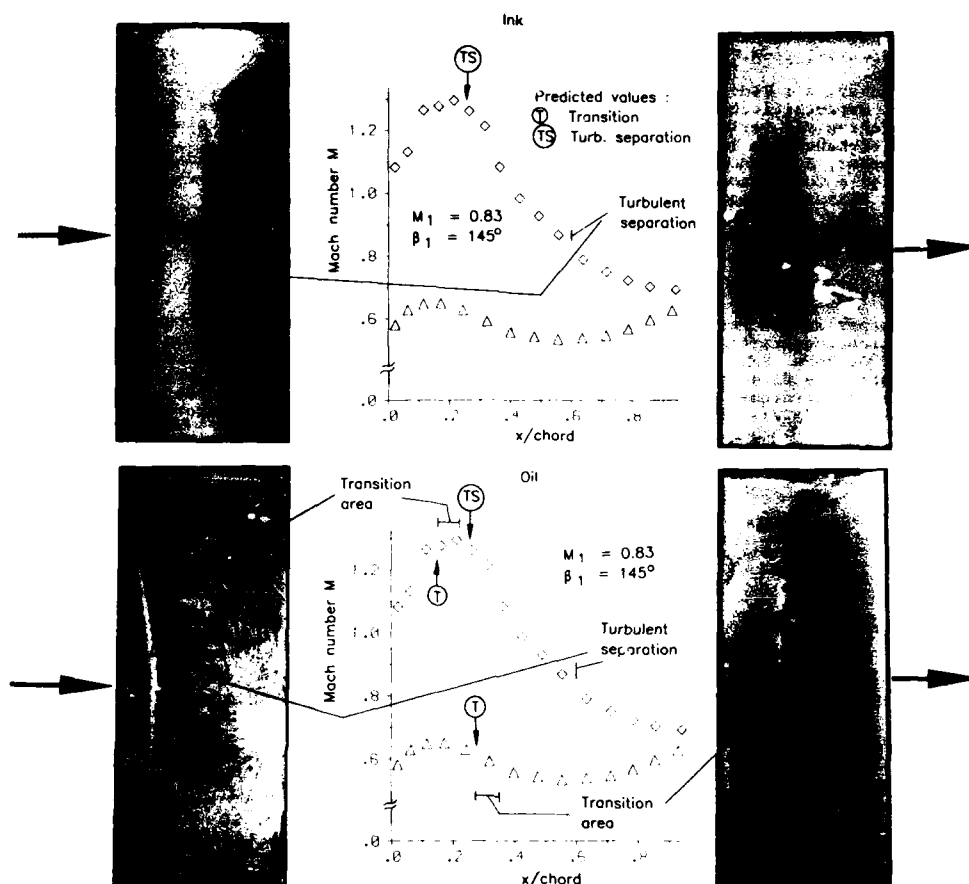


Fig. 9 Pattern of ink (top) and oil (bottom) of suction side (left) and pressure side (right) together with Mach number distribution at  $\beta_1=145^\circ$

#### 5. REFERENCES

- [1] Stephens, H.E.: "Application of Supercritical Airfoil Technology to Compressor Cascades: Comparison of Theoretical and Experimental Results", AIAA-Paper 78-1138 AIAA 11th Fluid and Plasma Dynamics Conference, Seattle, July 1978.
- [2] Hobbs, D.E.; Weingold, H.D.: "Development of Controlled Diffusion Airfoils For Multistage Compressor Application", ASME-Paper 83-GT-211.
- [3] Wisler, D.C.: "Loss Reduction in Axial-Flow Compressors Through Low-Speed Model Testing", ASME-Paper 84-GT-184.
- [4] Behlke, R.F.: "The Development of a Second-Generation of Controlled Diffusion Airfoils for Multistage Compressors", ASME-Paper 85-IGT-9.
- [5] Rechter, H.; Schimming, P.; Starken, H.: "Design and Testing of Two Supercritical Compressor Cascades", ASME-Paper 79-GT-11, San Diego, March 1979.
- [6] Weber, A.; Rechter, H.; Starken, H.: "Verlustarme, superkritische Verdichterprofile", Teil II: Nachrechnung; Experiment, FVV-Abschlußbericht, FVV-Vorhaben Nr. 266, Heft 344-2, 1984.
- [7] Fuchs, R.; Kaymaz, R.; Steinert, W.: "Experimentelle Untersuchung des superkritischen Verdichtergitters, SKG-FVV 3.3", DFVLR IB-325-14-1986.
- [8] Schmidt, E.: "Computation of Supercritical Compressor and Turbine Cascades with a Design Method for Transonic Flows", Journal of Engineering for Gas Turbines and Power, Vol.102, January 1980.
- [9] Schmidt, E.; Klimetzek, F.: "Verlustarme, superkritische Verdichterprofile", Teil I: Inverses Profilauslegungsverfahren ISGAV, FVV-Abschlußbericht, FVV-Vorhaben Nr. 266, Heft 344-1, 1984.
- [10] Dunker, R.; Rechter, H.; Starken, H.; Weyer, H.: "Redesign and Performance Analysis of a Transonic Axial Compressor Stator and Equivalent Plane Cascades With Subsonic Controlled Diffusion Blades", Journal of Engineering for Gas Turbines and Power, Vol.106, April 1984.

- [11] Rechter, H.; Steinert, W.; Lehmann, K.: "Comparison of Controlled Diffusion Airfoils With Conventional NACA 65 Airfoils Developed for Stator Blade Application in a Multistage Axial Compressor", Journal of Engineering for Gas Turbines and Power, Vol.107, April 1985.
- [12] Weber, A.; Faden, M.; Fuchs, R.; Starken, H.; Jawtusch, V.; Kaymaz, R.: "Verlustarme, superkritische Schaufelgitter", Erweiterung des Anwendungsbereichs der Berechnungsverfahren für verlustarme, superkritische Schaufelgitter; FVV-Abschlußbericht Teil II, Vorhaben Nr. 325, Heft 392-2. 1987.
- [13] Weber, A.; Faden, M.; Starken, H.; Jawtusch, V.: "Theoretical and Experimental Analysis of a Compressor Cascade at Supercritical Flow Condition", ASME-Paper to be published at Anaheim, June 1987.
- [14] Pankhurst, R.C., Holder, D.W.: "Wind-Tunnel Techniques", Pitman, London, 1952.
- [15] Maltby, R.L. (Ed.): "Flow Visualization in Wind Tunnels Using Indicators", AGARDograph 70, April 1962.

#### ACKNOWLEDGEMENTS

This paper is the result of a research program initiated by the "Forschungsvereinigung Verbrennungskraftmaschinen e.V." (FVV), accompanied by a working group directed by Dr.-Ing. D. Bohn, KWU, Mülheim and performed in the "Institut für Antriebstechnik", DFVLR, under the director Prof. Dr.-Ing. G. Winterfeld. The program has been sponsored by the German government through the "Arbeitsgemeinschaft Industrieller Forschungsvereinigungen e.V." (AIF), Köln, (AIF Nr. 5946 and 6761). All the support is greatly acknowledged.

#### DISCUSSION

N.A. CUMPTSY, UK

Can you give any more information about this rise in loss at  $M_1 = 0.88$  ? Why does the separation not appear in the pressure distribution ?

Author's Reply

The loss rise at  $M_1 = 0.88$  is due to the fact, that the higher inlet Mach number with respect to the design flow case leads to an increasing maximum Mach number on the suction surface followed by an increasing deceleration which is realized by a compression shock. The shock strength leads to shock induced separation and therefore to high total pressure losses.

The deceleration downstream of the separation point may be caused by the channel type flow region ducted by the opposite pressure side. J. Hourmouziadis (MTU) notified similar results in turbine cascades, where a dependency on the boundary layer thickness at the separation point was observed.

J. MOORE, US

Can you please answer a few questions about your interesting experimental and computational studies ? What were the blade Reynolds numbers and what was inlet free stream turbulence intensity ? What were the endwall boundary layer parameters at the cascade inlet ? Also, in the calculations, how were the AVDR's distributed axially through the cascade ?

Author's Reply

The blade Reynolds numbers varied between  $1.1$  and  $1.2 \cdot 10^6$  and the free stream turbulence level was  $2.5\%$ . Measurements were taken only in cascade midspan and no endwall boundary layer parameters are therefore available.

In the calculations the AVDR's were distributed linearly between leading and trailing edge plane equivalent to the design procedure.

R.G. WILLIAMSON, Ca

The pitchwise loss distribution at  $M = 0.88$  of Figure 5 shows not only a deeper and broader wake, but also an appreciable pitchwise shift of the wake towards the pressure side of the blade. Could you explain this ?

Author's Reply

The pitchwise shift of the wake in Figure 5 has no physical meaning. The pitchwise position of the wake depends on the starting position of the traversing probe which was arbitrarily chosen somewhere between two adjacent profile trailing edges.

N.J. SEYB, UK

I had five questions but three have already been asked. My remaining questions are :

- 1) Were the boundary layer predictions based on a measured or predicted pressure distribution ?
- 2) If the boundary layer predictions were based on predicted pressure distributions, could you please comment on the agreement with the measured pressure distribution ?

Author's Reply

The boundary layer predictions were based on predicted pressure distributions. The comparison predictions - experiments of the pressure distributions will be presented by Weber et al. at the ASME Gas Turbine Conference in Anaheim (ASME Paper n° 87-GT-256).

# CALCUL DES ÉCOULEMENTS SECONDAIRES DANS UN COMPRESSEUR AXIAL MULTISTAGE

F. FALCHETTI - J. BROCHET  
SNECMA, Centre de Villaroche  
77550 MOISSY CRAMAYEL - FRANCE

## Résumé

La SNECMA a industrialisé et étendu le domaine d'application d'une méthode de calcul des écoulements secondaires au cas des compresseurs multistages. Cette méthode prend en compte les phénomènes secondaires au moyen d'une correction visqueuse apportée à un écoulement méridien classique. Cette correction est calculée en moyenne azimutale dans tout le plan méridien, y compris à l'intérieur des aubages, en résolvant un système d'équations déduites des équations de Navier-Stokes 3D, parabolisées. Le couplage entre le calcul des écoulements secondaires et le calcul méridien est assuré de façon classique par des injections de débit.

Après un rappel des principes de la méthode, nous présentons dans cet article une application à un compresseur multistages, et montrons l'intérêt de cette méthode pour le dessin des aubages à extrémités vrillées.

## Abstract

SNECMA has developed and extended the use of a secondary flow computation method for multistage axial flow compressors. This method takes into account the secondary phenomena through a viscous correction applied to a through flow calculation. This correction is calculated in the complete meridian plane, including the bladerows. A set of equations is solved, which are deduced from 3D parabolized and pitchwise averaged Navier-Stokes equations. A classical coupling process between the secondary flow and the through-flow computations is insured through mass flow injection.

After reviewing the main features of the method, this paper presents an application to a multistage compressor, and shows the interest of this method when designing end-bend blades.

## Nomenclature

$B$	= coefficient de blocage
$h$	= hauteur de veine
$h_m, h_b$	= métriques
$k_i, j$	= courbure ( $= \frac{1}{h_i h_j} \frac{\partial h_i}{\partial u_j}$ )
$(m, b, \theta)$	= système de coordonnées curvilignes axisymétriques
$p$	= pression statique
$P$	= pression totale
$(s, b, n)$	= système de coordonnées intrinsèques, orthogonal
$u_m, u_b$	= coordonnées selon les directions $m$ et $b$
$T$	= température totale
$\vec{v}$	= vitesse absolue
$\vec{w}$	= vitesse relative
$(z, r, \theta)$	= système de coordonnées cylindriques
$\alpha$	= angle absolu de l'écoulement ( $= \tan^{-1}(v_g/v_m)$ )
$\beta$	= angle relatif de l'écoulement ( $= \tan^{-1}(w_g/w_m)$ )
$\beta'$	= angle du profil
$\delta$	= épaisseur de la couche limite
$\delta_m^*$	= épaisseur de déplacement méridienne ( $= \pi \int_0^{\delta} r (\tilde{u}_m - \tilde{u}_m) db$ )
$\delta_n^*$	= épaisseur de déplacement transversale ( $= \int_0^{\delta} r \tilde{u}_m db$ )
$\delta q$	= déficit de débit ( $= 2\pi B (r \tilde{u}_m - \tilde{u}_m) \delta_m^*$ )
$\Delta Q_m, \Delta Q_b$	= composantes du déficit de force d'aubage
$\Delta Q_{sm}$	= déficit de pression statique
$\phi$	= angle entre les directions $z$ et $m$
$\vec{\omega}$	= vitesse angulaire de rotation
$\tilde{\omega}$	= vorticité relative ( $= \nabla \wedge \vec{w}$ )
$\rho$	= masse volumique
$\nu_t$	= viscosité cinématique turbulente
$\bar{\sigma}$	= tenseur des tensions visqueuses

indices inférieurs :

$\circ$	= valeur à la paroi
$m, b, \theta$	= composantes d'un vecteur dans le système de coordonnées axisymétriques
$s, b, n$	= composantes d'un vecteur dans le système de coordonnées intrinsèques
$\delta$	= valeur à la limite extérieure de la couche visqueuse

indice supérieur :

$\wedge$	= relatif à l'écoulement sain non visqueux
----------	--

### Introduction

La demande de consommation spécifique et de coût d'exploitation direct toujours moins élevés a conduit à la recherche de compresseurs de plus en plus chargés aérodynamiquement et avec de meilleurs rendements. La réalisation de cet objectif passe par une meilleure analyse et un contrôle plus efficace des différentes sources de pertes. Les écoulements secondaires constituent une importante source d'irréversibilités, surtout dans les étages arrière des compresseurs HP, où les rapports de moyeu sont élevés et où les allongements sont faibles. Les écoulements secondaires sont liés au développement des couches limites sur les parois du moyeu et du carter. Leur présence peut modifier notablement l'écoulement, de sorte que leurs effets doivent être modélisés de façon précise et pris en compte de façon complète dans le dessin des aubages pour atteindre de bonnes performances.

La SNECMA a développé depuis une douzaine d'années une méthode originale de conception de soufflantes et de compresseurs axiaux qui met en oeuvre un ensemble complet de méthodes numériques. Le calcul des écoulements secondaires intervient dès le début de cette méthode de conception, au niveau du calcul méridien, avec lequel sont optimisées les valeurs des principaux paramètres aérodynamiques (forme de la veine, emplacement des roues, triangles des vitesses). A ce stade de la conception, les méthodes de calcul des écoulements secondaires comme celle de Mellor et Wood [1] sont très pratiques car elles peuvent facilement être couplées au calcul méridien et elles sont capables de traiter un compresseur complet en quelques secondes, ce qui permet des études paramétriques. La SNECMA utilise une version améliorée de ce code écrite par Papailiou [2] et elle possède aujourd'hui une dizaine d'années d'expérience avec ce programme. Cependant cette méthode calcule uniquement le blocage et l'effet global des écoulements secondaires sur les performances de chaque roue. Elle ne donne pas l'évolution radiale des effets secondaires, qui est une information indispensable pour le dessin des profils d'aubes près des parois. Dans ce contexte il est apparu utile de disposer d'une méthode numérique, qui, comme celle de Mellor, appréhende les phénomènes secondaires par une correction visqueuse apportée à un calcul méridien, mais qui fournit des informations moins globales que la méthode de Mellor. Certains ont répondu à ce besoin en introduisant, entre autres éléments, des familles de profils de vitesse dans la méthode de Mellor (par exemple [3], [4]). Cette approche est intéressante mais elle a l'inconvénient de faire appel à beaucoup de lois empiriques. D'autres chercheurs à l'Ecole Centrale de Lyon (FRANCE) et à l'Université d'Athènes (GRECE) ont préféré repartir des équations de base (équations de Navier Stokes 3D) et construire une nouvelle méthode numérique, mieux adaptée au besoin exprimé ci-dessus (de [5] à [7]). Cette méthode est conçue pour calculer la valeur locale, moyennée en azimut des effets secondaires dans un compresseur complet, y compris dans les roues aubées. Les écoulements secondaires sont traités comme deux couches limites 3D couplées à un calcul méridien, qui représente l'écoulement sain, non visqueux. Sur le plan numérique, cette méthode entre à la fois dans la catégorie des méthodes de couche limite de paroi et celle des méthodes d'écoulement secondaire [8]. La vitesse longitudinale est calculée en résolvant un système d'équations intégrales et en utilisant un profil de la famille de Kühn et Nielsen [9]. La vitesse transversale est obtenue à partir de l'équation différentielle de transport de la vorticité longitudinale.

La SNECMA a industrialisé la méthode que le Docteur F. LEBOEUF a mise au point sur des compresseurs et des turbines monoétages [10]. Elle a plus récemment étendu son domaine d'application au cas des compresseurs multiétages. Cet article a pour but de présenter les développements de cette méthode numérique, qui ont permis son application aux compresseurs multiétages et de montrer comment elle peut utilement servir à la conception des aubages. Auparavant, les caractéristiques fondamentales de cette méthode seront exposées.

## 1. Méthode de calcul

### 1.1. Une approche de type couche limite

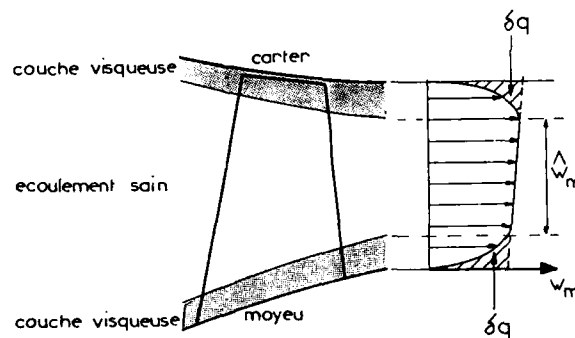


Fig. 1 - Modélisation de l'écoulement méridien

De façon classique pour une approche de type couche-limite, l'écoulement est représenté dans cette méthode de calcul par un modèle à trois zones : deux zones dites "visqueuses" au voisinage des parois du moyeu et du carter de la machine, séparées par une zone dite saine, non visqueuse. Les caractéristiques de l'écoulement en zone saine sont supposées être correctement représentées par les résultats d'un calcul méridien "non visqueux". Les écoulements secondaires sont alors appréhendés par une correction visqueuse apportée à l'écoulement sain, due à la présence de couches limites sur le moyeu et le carter. Nous noterons que le calcul méridien n'est pas entièrement de nature non visqueuse. En effet les couches limites de profils  $\gamma$  sont prises en compte sous la forme de pertes et d'écart flux-profil. Les écoulements secondaires sont calculés avec un niveau d'approximation comparable avec celui du calcul méridien. La méthode calcule la valeur moyennée en azimut des effets secondaires dans tout le plan méridien, y compris à l'intérieur des aubages. Les couches visqueuses sur le moyeu et le carter sont traitées séparément, avec comme écoulement extérieur de référence la valeur à la paroi de l'écoulement sain. L'écoulement complet est reconstitué en fin de calcul. Un couplage classique méridien-couche visqueuse est réalisé par des injections de débit  $\delta q$  au niveau des parois moyeu et carter, qui représentent le déficit de débit des couches visqueuses (Fig.2)

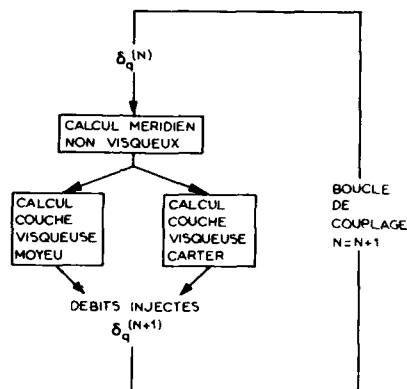


Fig.2 : Couplage calcul méridien - Ecoulement secondaire

### 1.2. Equations fondamentales

La correction visqueuse relative à chaque paroi est obtenue en résolvant un système d'équations dérivées des équations de Navier-Stokes, stationnaires et parabolisées dans la direction de l'écoulement. Les équations de base sont trois équations intégrales, écrites dans le système de coordonnées  $(m, b, \theta)$  (Fig.5)

La première est l'équation intégrale de continuité moyennée en azimut. Elle est intégrée depuis la paroi ( $b = 0$ ) jusqu'à la frontière extérieure de la couche limite ( $b = \delta$ )

$$\frac{\partial}{\partial m} \int_0^\delta B r \rho w_m db = (B r \rho w_m)_\delta \left( \frac{\partial \delta}{\partial m} - h_m \frac{w_\theta}{w_m} \right)_\delta \quad (1)$$

Le second membre de cette équation, qui représente l'augmentation de débit dans la couche limite, est calculé avec le modèle empirique de la loi d'entraînement de Head [11].

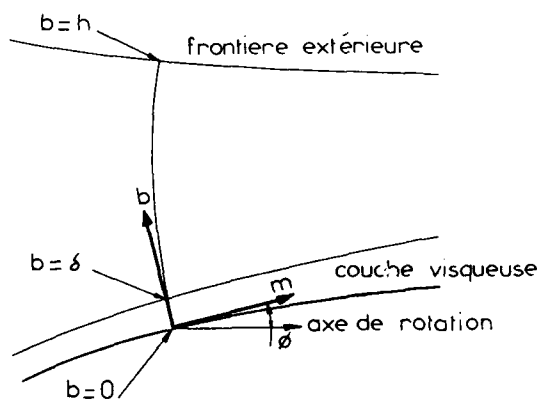


Fig. 3 - Intégration des équations suivant l'envergure



Les deux autres équations fondamentales sont les composantes selon  $m$  et  $\theta$  de l'équation intégrale de quantité de mouvement, moyennée en azimut. Celles-ci sont écrites sous forme déficitaire par rapport à l'écoulement sain, et intégrées depuis la paroi ( $b = 0$ ) jusqu'à la limite extérieure du domaine fluide ( $b = h$ ) (cf Fig. 4)

$$\frac{1}{\partial u_m} \int_0^h Br(\hat{v}_m^2 - v_m^2) db - [Brh_m(\hat{v}_m \hat{\omega}_m + \tau_{bm})]_{b=0} - \int_0^h Brh_m \sin \theta (\hat{v}_\theta^2 - v_\theta^2 + \tau_{\theta\theta}) db = \Delta D_{1m} + \Delta D_{3m} \quad (2)$$

$$\begin{aligned} \frac{1}{\partial u_m} \int_0^h Br(\hat{v}_\theta \hat{\omega}_m - v_\theta \omega_m) db - [Brh_m(\hat{v}_\theta \hat{\omega}_b + \tau_{b\theta})]_{b=0} + \int_0^h Brh_m \cos \theta (\hat{v}_\theta \hat{\omega}_b - v_\theta \omega_b + \tau_{\theta b}) db \\ + \int_0^h Brh_m \sin \theta (\hat{v}_\theta \hat{\omega}_m - v_\theta \omega_m + \tau_{\theta m}) db = \Delta D_{1\theta} \end{aligned} \quad (3)$$

Dans les équations (2) et (3), les quantités  $\Delta D_{1m}$  et  $\Delta D_{1\theta}$  sont les composantes du vecteur  $\overrightarrow{\Delta D_1}$ , lequel représente l'effet visqueux sur la force d'aubage. Au second membre  $\Delta D_{3m}$  est un terme de correction visqueuse sur la pression statique moyenne. Dans les expressions précédentes, les termes liés aux fluctuations azimutales ont été supprimés, car leurs effets sont négligeables dans les compresseurs. L'expression complète de ces équations est donnée en référence [6].

Le traitement de ces deux équations est différent selon que le calcul est fait dans les aubages ou à l'extérieur : en zone libre d'aubage, les termes de force d'aubage  $\Delta D_1$  sont nuls, et les équations (2) et (3) sont résolues. En zone aubée au contraire, les termes  $\Delta D_{1m}$  et  $\Delta D_{1\theta}$ , non nuls, sont éliminés entre les deux équations par la relation empirique (4).

$$\Delta D_{1m} + (1 - \epsilon) \tan \beta^* \Delta D_{1\theta} = 0 \quad (4)$$

Une seule équation reste alors à résoudre. Dans la relation empirique (4), l'introduction du paramètre  $\epsilon$  déjà utilisé par Mellor et Wood [1], est nécessaire pour les applications à des compresseurs multi-étages. En effet, l'hypothèse d'un déficit de force perpendiculaire à l'aubage ( $\epsilon = 0$ ) conduit avec cette méthode numérique à une croissance indéfinie de l'épaisseur de déplacement  $\delta_m^*$  à la traversée d'un compresseur multi-étage, ce qui est contraire à la réalité (Fig. 12). Nous obtenons des valeurs correctes de blocage dans les compresseurs basse pression avec des valeurs de  $\epsilon$  voisines de 0,7.

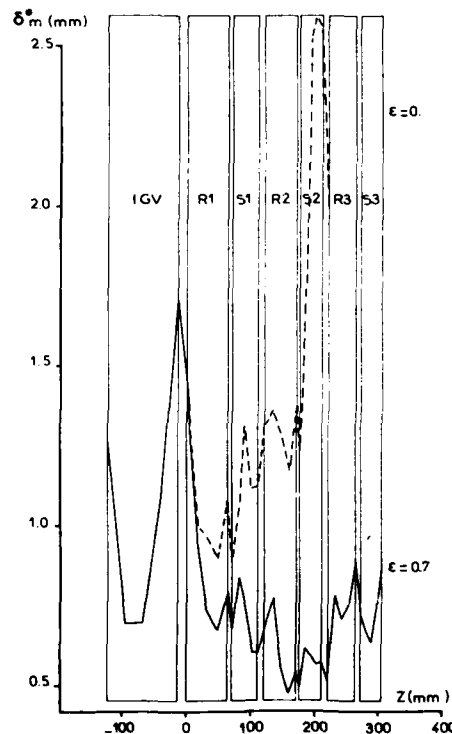


Fig. 4 : Influence du coefficient  $\epsilon$  sur l'épaisseur de déplacement au moyeu d'un compresseur à 3 étages

### 1.3. Modèle pour le calcul des champs de vitesse secondaire

La résolution des équations fondamentales (1), (2) et (3) dépend de la détermination des trois composantes de la valeur moyennée en azimut du vecteur vitesse.

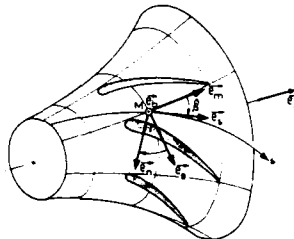


Fig. 5 : Système orthogonal de coordonnées intrinsèques

Certaines expériences montrent qu'il est possible de décrire la composante de vitesse dans la direction principale  $s$  (celle de l'écoulement sain) par certaines familles de profils analytiques. En revanche de telles descriptions semblent difficiles pour les deux autres composantes de vitesse  $w_n$  et  $w_b$ , en particulier à l'intérieur des roues aubées. En pratique, la composante longitudinale  $s$  est décrite par un profil de Kühn et Nielsen [9].

La composante transversale  $w_n$  est obtenue par une méthode différentielle dérivée des théories classiques de calcul d'écoulements secondaires : résolution d'une équation de transport pour obtenir la vorticité secondaire, longitudinale :

$$\frac{1}{Br \Gamma h_m} \frac{\partial}{\partial u_m} (Br h_b \Gamma w_m \Omega_s) - (\Omega_s + 2 \Omega_b) \left[ \frac{\cos \beta}{Br \Gamma h_m} \frac{\partial Br \Gamma w_s}{\partial u_m} + k_{sn} w_n - \frac{w_n}{Br \Gamma h_m} \sin \beta \frac{\partial Br \Gamma}{\partial u_m} \right] + (\Omega_b + 2 \Omega_b) \left( w_b k_{sb} - \frac{1}{Br h_b} \frac{\partial Br w_s}{\partial u_b} \right) + (\Omega_n + 2 \Omega_n) \left( w_n k_{nn} + \frac{\sin \beta}{Br h_m} \frac{\partial Br w_s}{\partial u_m} \right) = \frac{v_l}{\theta} \frac{\partial^2 \Omega_s}{\partial u^2} \quad (5)$$

puis, résolution d'une équation de Laplace dans le plan transversal :

$$\Delta \psi = -\Omega_s \quad (6)$$

faisant intervenir une fonction de courant vérifiant :

$$w_n = -\frac{\partial \psi}{\partial b} \quad (7)$$

Dans l'équation (5), les termes d'origine visqueuse sont très simplifiés, seul subsiste le second membre, où la viscosité turbulente est issue d'un modèle de turbulence de Cebeci-Smith, de type longueur de mélange.

La troisième composante de vitesse est quant à elle obtenue en résolvant une forme appropriée de l'équation de continuité (Eq.8)

$$Br \Gamma w_b(b) - Br \Gamma w_b(0) = \frac{\partial}{\partial m} \int_0^b Br \Gamma w_m db \quad (8)$$

Le calcul de la vitesse est complété par ceux de la pression statique et de la température totale. L'écart de pression statique avec l'écoulement sain est calculé en résolvant la composante selon  $b$  de l'équation de quantité de mouvement. La température totale  $T$ , qui intervient dans le calcul de la masse volumique  $\rho$ , est obtenue en résolvant la forme non visqueuse de l'équation de l'énergie : conservation de la rothalpie le long des lignes de courant.

### 1.4. Architecture générale de la méthode

Nous nous intéressons ici à l'architecture d'ensemble de la méthode. Nous considérons le traitement d'une paroi (le moyeu par exemple) à une certaine itération de couplage avec le calcul méridien. Les données initiales du calcul sont d'une part les valeurs de l'écoulement sain à la paroi, d'autre part les caractéristiques de la couche visqueuse dans le plan amont du calcul. L'écoulement sain à la paroi est issu d'un calcul méridien prenant en compte des injections de débit  $\delta q_i$  calculées à l'itération de couplage précédente. Les écoulements secondaires pour la paroi considérée, sont calculés en résolvant les équations du paragraphe précédent, plan par plan, depuis l'amont jusqu'à l'aval (processus parabolique). L'écoulement étant supposé stationnaire par rapport à chaque aubage, le domaine de calcul est divisé en autant de sous-domaines que de roues, et un changement de repère est effectué à chaque passage d'un sous domaine à l'autre (Fig.6 et 11)

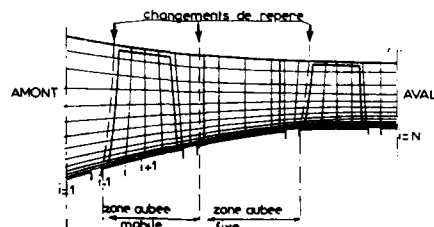


Fig. 6 : Domaine de calcul - Maillage au moyeu

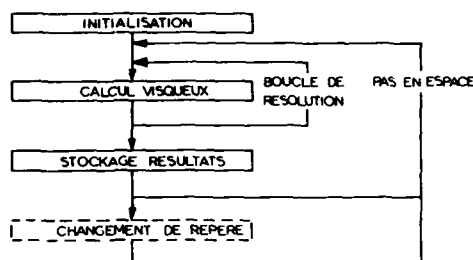


Fig. 7 : Calcul des écoulements secondaires sur une paroi

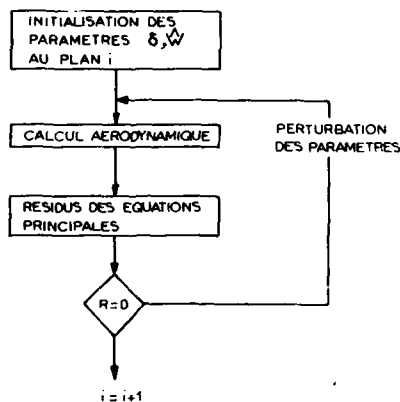
La parabolisation des équations conduit à des temps de calcul raisonnables, mais peut entraîner des problèmes de stabilité à cause des effets elliptiques qui ont été négligés. Ces effets sont surtout liés au champ de pression statique qui, à une faible correction visqueuse près, coïncide avec celui de l'écoulement sain. Dans notre modèle, ces effets sont restitués de façon approchée, en résolvant une équation supplémentaire relative à l'écoulement sain, en même temps que les équations pour l'écoulement visqueux. En pratique cette équation se présente comme une équation en  $\hat{w}_m$  et calcule les effets de blocage et de courbure à la paroi sur l'écoulement sain, induits par les variations du déficit de débit de la couche visqueuse entre deux itérations de couplage. Après discrétisation, cette équation s'écrit sous la forme vectorielle (Eq. 9)

$$\begin{bmatrix} \hat{w}_m \end{bmatrix} = A \begin{bmatrix} \delta q_i \end{bmatrix} + B \quad (9)$$

où  $A$  est une matrice carrée d'ordre  $N$ . Une fois connu  $\hat{w}_m$ , les autres grandeurs de l'écoulement sain, dont la pression statique, sont mis à jour en conservant  $\hat{p}$  et  $\hat{T}$ , entre deux itérations de couplage. La correction ainsi apportée à l'écoulement sain assure une bonne stabilité numérique et permet une convergence rapide du processus de couplage calcul visqueux - calcul méridien (Fig. 12).

Il nous reste à préciser de quelle façon les équations sont résolues dans un plan de calcul d'indice  $i$  donné.

Les résidus des équations principales (1) et (2) sont considérés comme des fonctions implicites de paramètres convenablement choisis (en pratique, la vitesse  $\hat{w}$  de l'écoulement sain à la paroi et l'épaisseur  $\delta$  de la couche limite). Un processus de minimisation classique (Gauss-Newton) optimise les valeurs de ces paramètres (Fig. 8)

Fig. 8 : Résolution des équations principales au plan  $i$

Pour chaque valeur testée des paramètres principaux ( $\dot{Q}, \delta$ ), le champ aérodynamique est calculé en suivant l'organigramme simplifié de la figure 9.

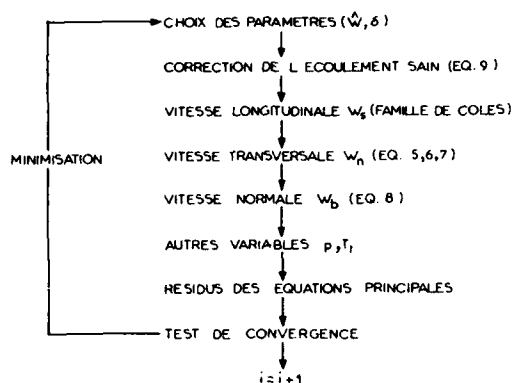


Fig. 9 : Calcul aérodynamique dans le plan  $i$

## 2. Application à un compresseur multiétagé

Nous présentons une application sur un compresseur basse pression de trois étages avec une roue directrice d'entrée (Fig.10), et pour lequel nous disposons de mesures suffisamment proches des parois. Les deux premières roues mobiles ont une nageoire respectivement à 60 % et 55 % de hauteur. Le point de fonctionnement étudié correspond à un taux de compression de 3,48. Compte tenu des valeurs assez faibles du rapport de moyeu (0,3 à l'entrée, 0,725 à la sortie), les couches limites de parois occupent une fraction assez faible de la veine (Fig.11). La détermination de l'écoulement sain de référence ne pose donc pas d'ambiguïté. Celui-ci est modélisé par un calcul méridien dans lequel sont imposées les distributions radiales de pression et température totale à l'aval des roues mobiles, de pression totale et d'angle absolu à l'aval des redresseurs. Ces distributions correspondent aux valeurs mesurées, sauf près des parois où les forts gradients sont éliminés (Fig.11).

Les résultats de la méthode de calcul des écoulements secondaires sont présentés pour les plans de sortie du second redresseur et de la troisième roue mobile (stations 6 et 7, Fig. 10). Nous constatons un excellent recoupement des valeurs expérimentales au moyeu comme au carter en ce qui concerne la pression totale (Fig. 11-A-B), l'angle absolu (Fig. 11C-D) et l'angle relatif (Fig. 12-A). Seule, la température totale calculée diffère largement de celle mesurée près des parois (Fig. 12 B). Ceci est probablement lié à la non-prise en compte de la forme visqueuse de l'équation de l'énergie dans la méthode actuelle, et également à la non-prise en compte des phénomènes de mélange. ([15] à [17])

Nous notons enfin le bon accord entre les valeurs calculées de la pression statique et les mesures effectuées aux parois (Fig. 12 C et D), preuve que le blocage induit par les couches limites de paroi est correctement calculé.

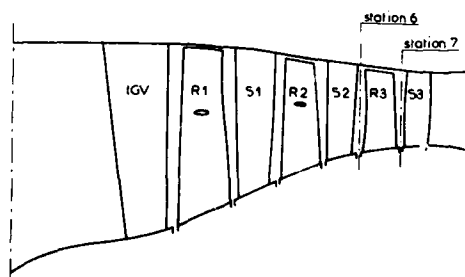


Fig. 10 - Compresseur BP à trois étages  
Vue méridienne de la veine

### 3. Application au dessin d'aubages

La méthode de calcul qui vient d'être présentée constitue un outil pratique pour dessiner les aubages. Elle a l'avantage de calculer les phénomènes secondaires dans tout le plan méridien, et son niveau d'approximation est comparable à celui du calcul méridien avec lequel sont choisis les principaux paramètres aérodynamiques. La SNECMA l'utilise en particulier pour dessiner les redresseurs avec extrémités vrillées, dont la géométrie permet une augmentation du rendement et de la marge au pompage d'un compresseur multi-étage. Dans l'exemple représenté en Fig. 13A, ces redresseurs se distinguent des aubages classiques par une forte augmentation de l'angle de calage des profils près des parois. Cette transformation géométrique répond à deux objectifs : Vers le bord d'attaque, l'augmentation de l'angle des profils permet de mieux adapter l'aubage à l'écoulement incident (Fig. 13B) ; vers le bord de fuite, l'augmentation de l'angle des profils permet de réduire la charge aérodynamique près des parois, et donc de limiter le développement des phénomènes secondaires. Ceci permet également d'atténuer les variations sur la hauteur de l'angle absolu à la sortie du redresseur (Fig. 13C et 13D). Par composition des vitesses, l'angle d'incidence sur la roue mobile suivante s'en trouve légèrement réduit (Fig. 13E).

La méthode de calcul des écoulements secondaires, couplée au calcul méridien, fournit les informations nécessaires au réglage de l'angle des profils près des parois en calculant les angles à l'entrée et à la sortie des redresseurs et roues mobiles. Enfin, de façon plus générale, cette méthode permet de mesurer l'effet de ces modifications géométriques sur le développement des phénomènes secondaires.

### Conclusion

La SNECMA a industrialisé et étendu au cas des compresseurs axiaux multi-étages une méthode de calcul mise au point par le Docteur F. Leboeuf sur des compresseurs et turbines mono-étages [6]. Cette méthode repose sur la modélisation de l'écoulement méridien par un écoulement sain séparant deux couches visqueuses de paroi. Elle a l'avantage de pouvoir calculer la valeur moyenne en azimut des phénomènes secondaires dans tout le plan méridien, y compris à l'intérieur des aubages.

La comparaison calcul - expérience sur un compresseur basse pression de trois étages montre un excellent accord en ce qui concerne le blocage, la pression totale et les angles. Seule la température totale calculée présente des écarts notables avec l'expérience. Ceux-ci sont attribués en partie à l'absence de résolution de l'équation complète de l'énergie.

Cette méthode de calcul est d'un grand intérêt pour la conception des aubages, en particulier des redresseurs à extrémités vrillées.

### Remerciements

Cette étude est financée par la DRET (Direction des Recherches, Etudes et Techniques) et la SNECMA (Société Nationale d'Etude et de Construction de Moteurs d'Aviation). Les auteurs tiennent à remercier le Professeur K.D. Papailiou, de l'Université d'Athènes, et le Docteur F. Leboeuf, pour leurs encouragements et suggestions précieuses au cours de cette étude.

### Références

- [1] Mellor G., Wood G., "An axial End-wall Boundary Layer Theory", - ASME Journal of Basic Engineering Vol. 93, 1971, pp 200-216
- [2] Leboeuf F., Comte A., Papailiou K.D., "Calculation Concerning The Secondary Flows in a Compressor Bladings" AGARD-CP-214, La Haye, 1977, Paper 2.
- [3] De Ruyck J., Hirsch C., "Investigation of an Axial Compressor End-Wall Boundary Layer Prediction Method", ASME Journal of Engineering for Power, Vol. 103, 1981, pp. 20-32.
- [4] Simon Ch., Grahel K.G., "Comparison of Endwall Boundary Layer Calculation Methods for Axial-Flow Compressor Stage", ISABE 85-7071.
- [5] Comte A., Ohayon G., Papailiou K.D., "A Method for the calculation of the wall layers inside the passage of a compressor cascade with and without tip clearance effect", ASME Journal of Engineering for Power, vol. 105, 1983
- [6] Leboeuf F., "Annulus End-Wall Boundary Layer Theory", VKI Lecture Series, 1984-05
- [7] Papailiou K.D., "A Contribution to the Calculation of Secondary Flows in an Axial-Flow Compressor" 6-Th ISABE, Paris, June 1983, pp. 439 446.
- [8] Sitaram N., Lakshminarayana B., "End-Wall Flow Characteristics and Overall Performance of an Axial flow Compressor Stage", NASA CR 3671, February 1983.
- [9] Kuhn G.D., Nielsen J.N., "Prediction of Turbulent Separated Boundary Layers", AIAA, 6 th Fluid and Plasma Dynamic Conference, July 1973.
- [10] Leboeuf F., Brochet J., "The Use of Secondary Flows Computation in the Compressor Design Process", Fluid Engineering Division, Vol. 32 "Three Dimensional Flow Phenomena in Fluid Machinery", pp 63.72, ASME Winter Annual Meeting, Miami, November 1985.

- [11] Head M.R., "Entrainment Approach", V.K.I. Short Course on "Turbulent Boundary Layers", March 1968.
- [12] Hawthorne W.R. "Some Formulae for the Calculation of Secondary Flows", GICC Rp. 298, 1955.
- [13] Bradshaw P., Cebeci I., Whitelaw J.H., "Engineering Calculation Methods for Turbulent Flows" Academic Press, 1981.
- [14] Ohayon G., "Contribution à l'étude des écoulements secondaires dans les compresseurs axiaux, avec effet de jeu radial", Engineer - Dr.Thesis, Lyon I (France), 1979
- [15] Adkins G.G., Smith L.H., "Spanwise Mixing in Axial Flow Turbomachines", ASME Journal of Engineering for Power, n°1, Vol.104, pp.97-110.
- [16] Gallimore S.J., Cumpsty N.A., "Spanwise Mixing in Multistage Axial flow Compressors : Part I - Experimental Investigation". ASME Journal of Turbomachinery Vol 108, July 1986, pp. 2-9.
- [17] Gallimore S.J., "Spanwise Mixing in Multistage Axial flow Compressors : Part II - Through-flow Calculations Including Mixing", ASME Journal of Turbomachinery, Vol.108, July 1986, pp 10-16.

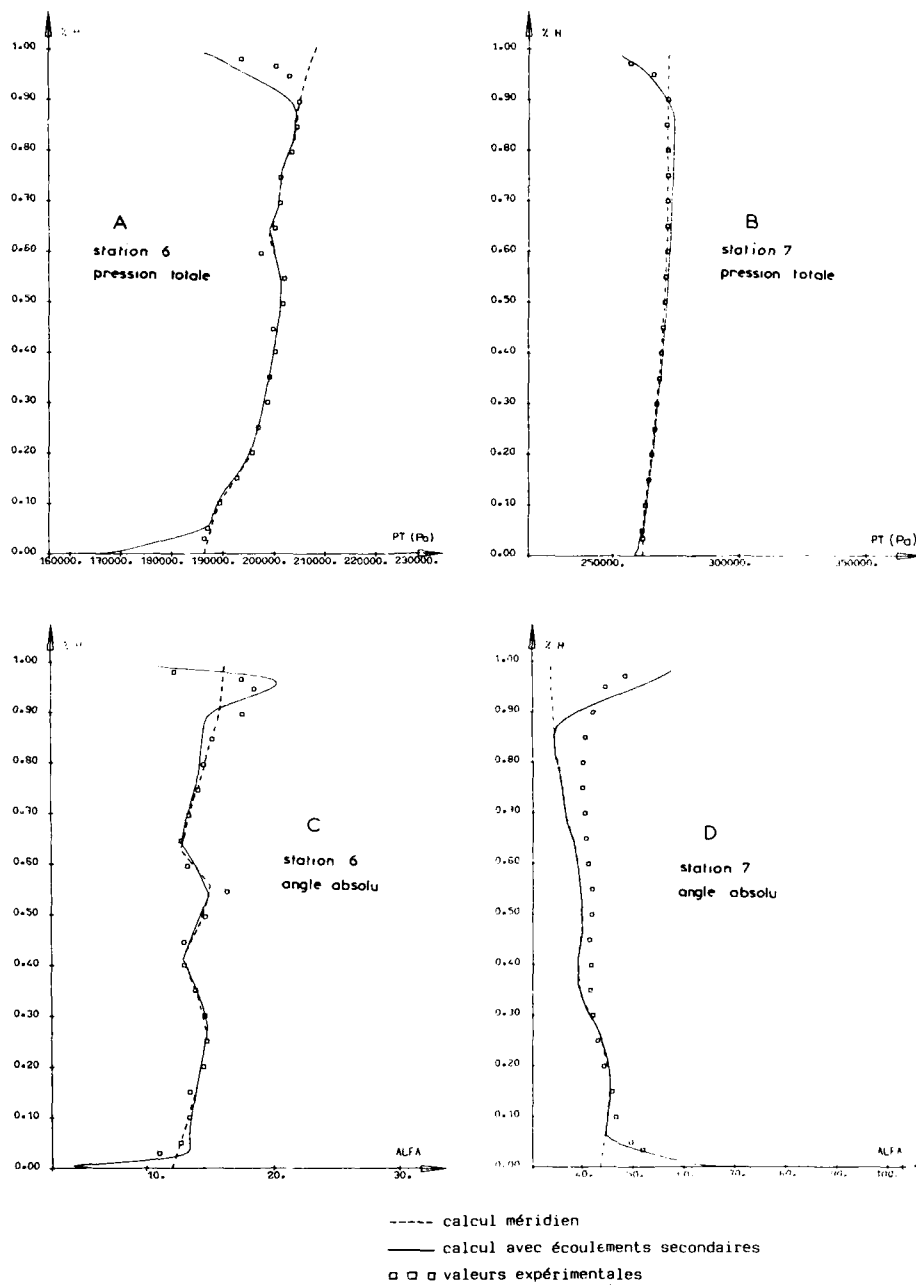
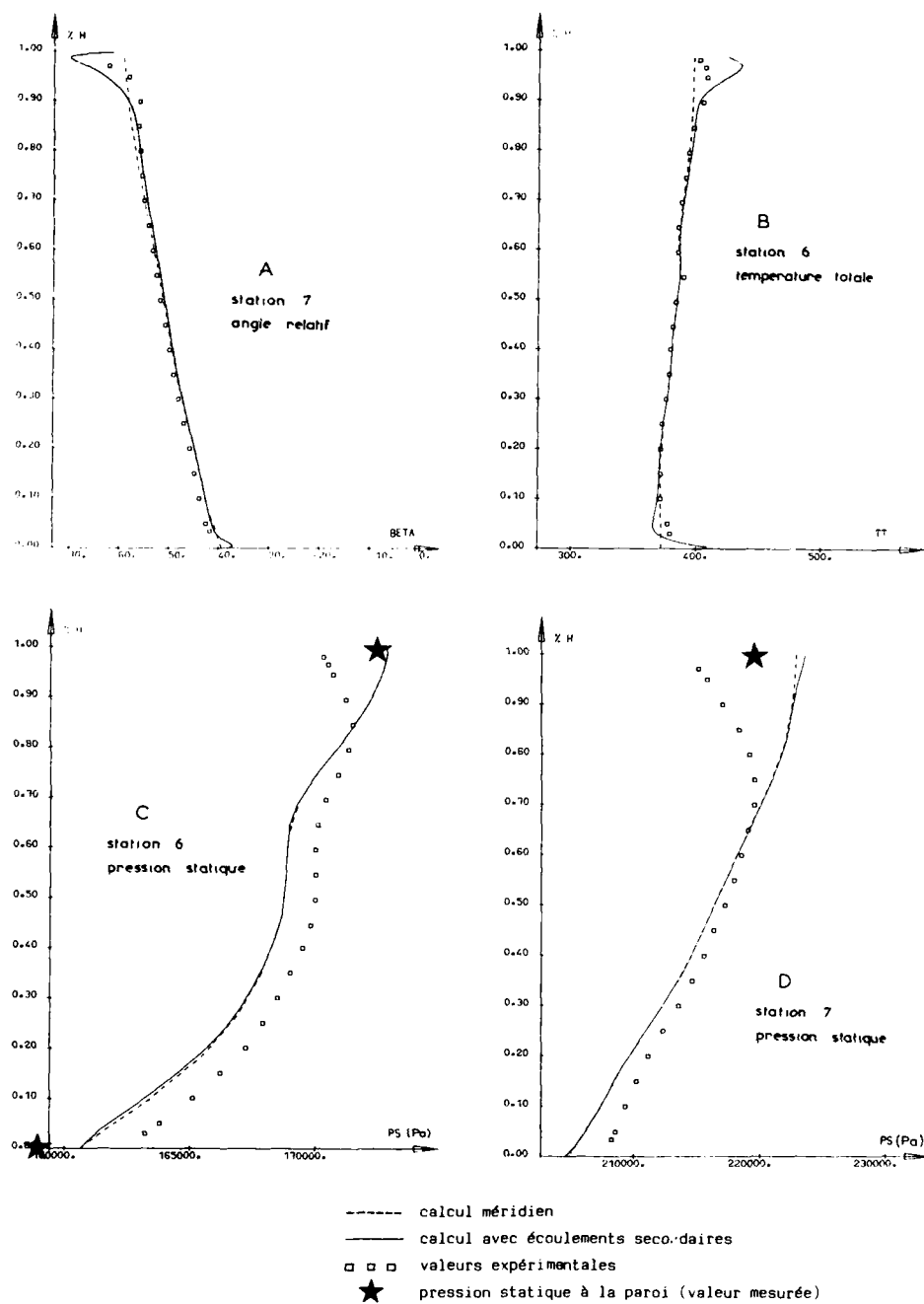
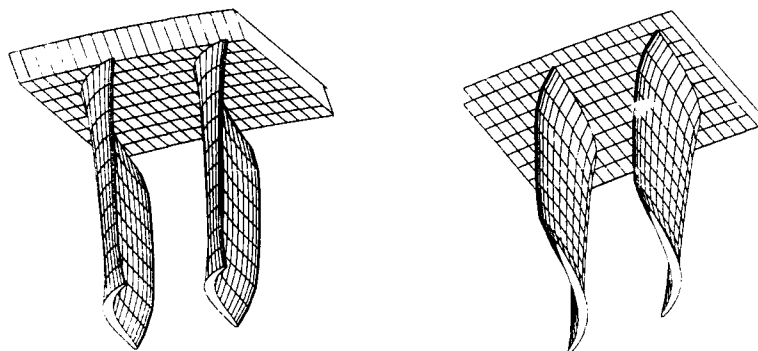


Fig. 11 - COMPRESSEUR BP à 3 ETAGES  
COMPARAISON CALCUL - EXPERIENCE

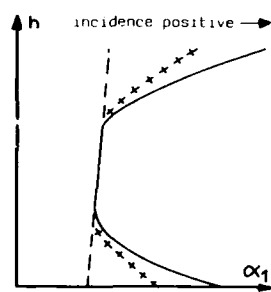


**Fig. 12 COMPRESSEUR BP A TROIS ETAGES**  
**COMPARAISON CALCUL - EXPERIENCE**



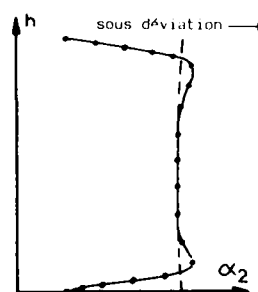


A - Stator SNECMA avec "end-bend"

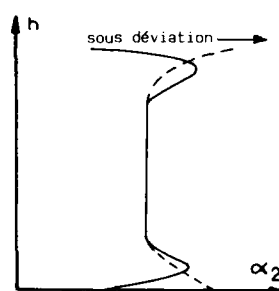


+++++: angle du profil au bord d'attaque

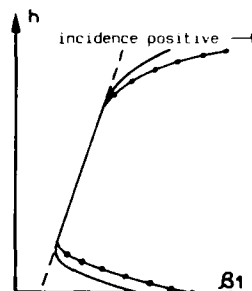
B - Angle d'entrée du stator



C - Angle de sortie d'un stator conventionnel



D - Angle de sortie d'un stator avec "end-bend"



E - Angle d'entrée de la roue mobile suivante

----- calcul méridien  
 ••••• calcul avec écoulements secondaires (stator conventionnel)  
 ——— " " " " (stator avec end-bend)

Fig. 13 CONCEPTION D'AUBAGES AVEC "END-BEND" A LA SNECMA

### DISCUSSION

N. KROLL, Ge

How are the elliptic effects accounted for in the solution process ?

Author's Reply

The elliptic effects neglected in the parabolic process are related to the static pressure gradients in the marching direction. These are taken into account by solving an approximate inviscid flow equation simultaneously with the wall layer equations. This equation is expressed in the form of a correction of the external flow according to the blockage induced by the wall shear layers.

This strong coupling ensures a good numerical stability. For more details on this point, you may refer to F. Leboeuf, "Annulus End-Wall Boundary Layer Theory", VKI Lecture Series 84-05.

K.R. GARWOOD, UK

Having presented data on how you propose to design the stators, how would you propose to design the rotor blades, particularly the casing sections ?

Author's Reply

This is a difficult problem and investigations are currently under way.

REPORT DOCUMENTATION PAGE			
1. Recipient's Reference	2. Originator's Reference	3. Further Reference	4. Security Classification of Document
	AGARD-CP-421	ISBN 92-835-0433-X	UNCLASSIFIED
5. Originator	Advisory Group for Aerospace Research and Development North Atlantic Treaty Organization 7 rue Ancelle, 92200 Neuilly sur Seine, France		
6. Title	ADVANCED TECHNOLOGY FOR AERO GAS TURBINE COMPONENTS		
7. Presented at	the Propulsion and Energetics Panel 69th Symposium held in Paris, France 4-8 May 1987.		
8. Author(s)/Editor(s)	Various		9. Date September 1987
10. Author's/Editor's Address	Various		11. Pages 456
12. Distribution Statement	This document is distributed in accordance with AGARD policies and regulations, which are outlined on the Outside Back Covers of all AGARD publications.		
13. Keywords/Descriptors	<div style="display: flex; justify-content: space-between;"> <div> Compressors Turbines Combustors Afterburners </div> <div> Cooling effects Propellers Drive systems </div> </div>		
14. Abstract	<p>The Conference Proceedings contains 34 papers presented at the Propulsion and Energetics Panel 69th Symposium on Advanced Technology for Aero Gas Turbine Components, which was held 4-8 May 1987 in Paris, France</p> <p>The Symposium was arranged in the following sessions: Requirements and Design Considerations (7), Turbines (8), Combustion (3), High Speed Propellers (5), and Compressors (11). Questions and answers follow each paper.</p> <p>The Symposium was aimed at highlighting the development of advanced components for new aero gas turbine propulsion systems, and it provided engineers and scientists with a forum to discuss recent progress in these technologies and to identify requirements for future research.</p>		

<p>AGARD Conference Proceedings No.421 Advisory Group for Aerospace Research and Development, NATO ADVANCED TECHNOLOGY FOR AERO GAS TURBINE COMPONENTS Published September 1987 456 pages</p> <p>The Conference Proceedings contains 34 papers presented at the Propulsion and Energetics Panel 69th Symposium on Advanced Technology for Aero Gas Turbine Components, which was held 4-8 May 1987 in Paris, France.</p> <p>The Symposium was arranged in the following sessions: Requirements and Design Considerations (7), Turbines (8), P.T.O.</p>	<p>AGARD-CP-421</p> <p>Compressors Turbines Combustors Afterburners Cooling effects Propellers Drive systems</p>	<p>AGARD Conference Proceedings No.421 Advisory Group for Aerospace Research and Development, NATO ADVANCED TECHNOLOGY FOR AERO GAS TURBINE COMPONENTS Published September 1987 456 pages</p> <p>The Conference Proceedings contains 34 papers presented at the Propulsion and Energetics Panel 69th Symposium on Advanced Technology for Aero Gas Turbine Components, which was held 4-8 May 1987 in Paris, France.</p> <p>The Symposium was arranged in the following sessions: Requirements and Design Considerations (7), Turbines (8), P.T.O.</p>	<p>AGARD-CP-421</p> <p>Compressors Turbines Combustors Afterburners Cooling effects Propellers Drive systems</p>
<p>AGARD Conference Proceedings No.421 Advisory Group for Aerospace Research and Development, NATO ADVANCED TECHNOLOGY FOR AERO GAS TURBINE COMPONENTS Published September 1987 456 pages</p> <p>The Conference Proceedings contains 34 papers presented at the Propulsion and Energetics Panel 69th Symposium on Advanced Technology for Aero Gas Turbine Components, which was held 4-8 May 1987 in Paris, France.</p> <p>The Symposium was arranged in the following sessions: Requirements and Design Considerations (7), Turbines (8), P.T.O.</p>	<p>AGARD-CP-421</p> <p>Compressors Turbines Combustors Afterburners Cooling effects Propellers Drive systems</p>	<p>AGARD Conference Proceedings No.421 Advisory Group for Aerospace Research and Development, NATO ADVANCED TECHNOLOGY FOR AERO GAS TURBINE COMPONENTS Published September 1987 456 pages</p> <p>The Conference Proceedings contains 34 papers presented at the Propulsion and Energetics Panel 69th Symposium on Advanced Technology for Aero Gas Turbine Components, which was held 4-8 May 1987 in Paris, France.</p> <p>The Symposium was arranged in the following sessions: Requirements and Design Considerations (7), Turbines (8), P.T.O.</p>	<p>AGARD-CP-421</p> <p>Compressors Turbines Combustors Afterburners Cooling effects Propellers Drive systems</p>

<p>Combustion (3), High Speed Propellers (5), and Compressors (11). Questions and answers follow each paper.</p> <p>The Symposium was aimed at highlighting the development of advanced components for new aero gas turbine propulsion systems, and it provided engineers and scientists with a forum to discuss recent progress in these technologies and to identify requirements for future research.</p> <p>ISBN 92-835-0433-X</p>	<p>Combustion (3), High Speed Propellers (5), and Compressors (11). Questions and answers follow each paper.</p> <p>The Symposium was aimed at highlighting the development of advanced components for new aero gas turbine propulsion systems, and it provided engineers and scientists with a forum to discuss recent progress in these technologies and to identify requirements for future research.</p> <p>ISBN 92-835-0433-X</p>
<p>Combustion (3), High Speed Propellers (5), and Compressors (11). Questions and answers follow each paper.</p> <p>The Symposium was aimed at highlighting the development of advanced components for new aero gas turbine propulsion systems, and it provided engineers and scientists with a forum to discuss recent progress in these technologies and to identify requirements for future research.</p> <p>ISBN 92-835-0433-X</p>	<p>Combustion (3), High Speed Propellers (5), and Compressors (11). Questions and answers follow each paper.</p> <p>The Symposium was aimed at highlighting the development of advanced components for new aero gas turbine propulsion systems, and it provided engineers and scientists with a forum to discuss recent progress in these technologies and to identify requirements for future research.</p> <p>ISBN 92-835-0433-X</p>

END

DATE  
FILMED

10 - 88